DETERMINATION OF MAGMA FERTILITY INDICATORS FOR PORPHYRY SYSTEMS IN WESTERN ANATOLIA AND CENTRAL TAURIDES

A THESIS SUBMITTED TO
THE GRADUATE SCHOOL OF NATURAL AND APPLIED SCIENCES
OF
MIDDLE EAST TECHNICAL UNIVERSITY

BY

AKIN ÇİL

IN PARTIAL FULFILLMENT OF THE REQUIREMENTS
FOR
THE DEGREE OF DOCTOR OF PHILOSOPHY
IN
GEOLOGICAL ENGINEERING

AUGUST 2025

Approval of the thesis:

DETERMINATION OF MAGMA FERTILITY INDICATORS FOR PORPHYRY SYSTEMS IN WESTERN ANATOLIA AND CENTRAL TAURIDES

submitted by **AKIN ÇİL** in partial fulfillment of the requirements for the degree of **Doctor of Philosophy** i**n Geological Engineering, Middle East Technical University** by,

Prof. Dr. Naci Emre Altun
Dean, **Graduate School of Natural and Applied Sciences** _____

Prof. Dr. Erdin Bozkurt
Head of the Department, **Geological Engineering** _____

Assist. Prof. Dr. Ali İmer
Supervisor, **Geological Engineering, METU** _____

Examining Committee Members:

Prof. Dr. Kaan Sayıt
Geological Engineering, METU _____

Assist. Prof. Dr. Ali İmer
Geological Engineering, METU _____

Prof. Dr. Tolga Oyman
Geological Engineering, Dokuz Eylül University _____

Assoc. Prof. Dr. Hüseyin Evren Çubukçu
Geological Engineering, Hacettepe University. _____

Assist. Prof. Dr. Erkan Yılmazer
Geological Engineering, Aksaray University _____

Date: 25.08.2025

I hereby declare that all information in this document has been obtained and presented in accordance with academic rules and ethical conduct. I also declare that, as required by these rules and conduct, I have fully cited and referenced all material and results that are not original to this work.

Name Last name : Akın Çil

Signature :

ABSTRACT

DETERMINATION OF MAGMA FERTILITY INDICATORS FOR PORPHYRY SYSTEMS IN WESTERN ANATOLIA AND CENTRAL TAURIDES

Çil, Akın
Doctor of Philosophy, Geological Engineering
Supervisor: Assist. Prof. Dr. Ali İmer

August 2025, 340 pages

Porphyry systems are closely associated with magmatism in arc, back-arc, and post-collisional settings. Arc-related porphyries are typically Cu-rich, whereas back-arc and post-collisional settings more commonly host Au-rich porphyry deposits. Magma oxidation state, water content, and volatile budget are key parameters that enhance the fertility of arc or post-collisional magmas in terms of porphyry formation since fertile magmas are generally oxidized, hydrous, and enriched in volatiles such as S, Cl, and F. Although whole-rock geochemistry has been widely applied in fertility assessment, the use of precise mineral geochemistry has gained popularity for understanding magmatic controls on porphyry deposit formation. This study investigates Late Cenozoic back-arc and post-collisional magmatism in Western Anatolia and the Central Taurides, segments of the Neotethyan orogenic belt that experienced prolonged Oligo–Miocene to Quaternary magmatism with a progressive southward-younging trend. The region hosts significant porphyry systems within intermediate to felsic intrusions of high-K calc-alkaline to mildly

alkaline affinity. A multi-proxy approach, combining zircon U–Pb dating with zircon and apatite trace element analyses, demonstrates that fertile magmas are characterized by elevated Eu/Eu*, Yb_n/Dy_n, and ΔFMQ in zircon, and positive Eu/Eu* and Cl contents in apatite. By contrast, whole-rock fertility proxies such as Sr/Y and La/Yb fail to distinguish fertile from barren systems, emphasizing the robustness of mineral-scale indicators. Overall, this study establishes zircon and apatite geochemistry as reliable tools to evaluate magma fertility in Anatolia and provides insights applicable to other post-collisional segments of the Tethyan metallogenic belt.

Keywords: Porphyry Systems, Magma Fertility, Zircon and Apatite Geochemistry, Late Cenozoic Magmatism, Western Anatolia and Central Taurides

ÖZ

BATI ANADOLU VE ORTA TOROSLAR PORFİRİ SİSTEMLERİYLE İLİŞKİLİ MAGMA ÜRETKENLİK GÖSTERGELERİNİN BELİRLENMESİ

Çil, Akın
Doktora, Jeoloji Mühendisliği
Tez Yöneticisi: Dr. Öğr. Üyesi Ali İmer

Ağustos 2025, 340 sayfa

Porfiri sistemleri, yay, yay-arkası ve çarpışma sonrası ortamlarda gelişen magmatizma ile yakından ilişkilidir. Yay ile ilişkili porfiriler genellikle Cu bakımından zenginken, yay-arkası ve çarpışma sonrası ortamlarda daha çok Au bakımından zengin porfiri yatakları gelişmektedir. Üretken magmalar genellikle oksidize, sulu ve S, Cl, F gibi uçucular bakımından zengin olduklarından, magma oksidasyon seviyesi, su içeriği ve uçucu bütçesi, porfiri oluşumu açısından yay veya çarpışma sonrası magmaların üretkenliğini artıran temel parametreler olarak görülmektedir. Her ne kadar tüm kayaç jeokimyası uzun süredir üretkenlik değerlendirmelerinde kullanılsa da, son yıllarda porfiri yataklarının oluşumunu kontrol eden magmatik süreçleri anlamada mineral ölçeğinde jeokimyanın kullanımı giderek önem kazanmıştır. Bu çalışma, Oligo–Miyosen'den Kuvaterner'e kadar uzanan ve güneye doğru gençleşme eğilimi gösteren uzun süreli magmatizmanın gözlendiği Neotetis orojenik kuşağının Batı Anadolu ve Orta Toroslar segmentlerindeki Geç Senozoyik yay-arkası ve çarpışma sonrası magmatizmasını

incelemektedir. Bölgesel ölçekte önemli porfiri sistemleri genellikle yüksek-K'lu kalk-alkalen ile hafif alkalen karakterli ortaç–asidik kayaçlarla ilişkilidir. Zirkon U–Pb tarihlendirmeleri ile zirkon ve apatit iz element analizlerini birleştiren çoklu parametreli yaklaşım, üretken magmaların zirkonda yüksek Eu/Eu*, Yb_n/Dy_n ve ΔFMQ değerleriyle; apatitte ise pozitif Eu/Eu* ve yüksek Cl içerikleriyle ayırt edilebildiğini ortaya koymaktadır. Buna karşılık, Sr/Y ve La/Yb gibi tüm-kayaç üretkenlik göstergeleri verimli ve verimsiz sistemleri ayırt etmede yetersiz kalmakta, mineral ölçeğindeki göstergelerin güvenilirliğini vurgulamaktadır. Sonuç olarak, bu çalışma zirkon ve apatit jeokimyasını Anadolu'daki magma üretkenliğinin değerlendirilmesinde güvenilir araçlar olarak ortaya koymakta ve Tetis metalojenik kuşağının diğer çarpışma sonrası segmentlerine de uygulanabilir yeni yaklaşımlar sunmaktadır.

Anahtar Kelimeler: Porfiri Sistemler, Magma Üretkenliği, Zirkon ve Apatit Jeokimyası, Geç Senozoyik Magmatizma, Batı Anadolu ve Orta Toroslar



To my father

Nurettin Çil

ACKNOWLEDGMENTS

I would like to express my deepest gratitude to my supervisor, Assist. Prof. Dr. Ali İmer, for his invaluable guidance, everlasting patience, and encouragement throughout the course of this study. It would be impossible without his never-ending support starting from the beginning until the very end.

Also, I am grateful to the examining committee because of their constructive criticism and valuable suggestions to improve the quality of this work.

I wish to thank Prof. Dr. Ersin Koralay for his efforts during the sample preparation. Special thanks to Dr. Massimo Chiaradia and Prof. Dr. Robert Moritz for their invaluable scientific contributions to this study.

I am deeply grateful to my friends Atilla, Burak, Orkun, Devin, Gamze, Görkem, Hakan, Meryem, and Taner for their advices and encouragements during the thesis writing process.

This thesis could not have been written without the 1001-The Scientific and Technological Research Projects Funding (Project no: 122Y016) and 2214A-International Research Fellowship Programme for PhD Students funding programs granted by TÜBİTAK.

Special thanks to Ariana Resources, Tüprag/Eldorado, TÜMAD, and ESAN companies for their permission and support, as well as their exploration and mining teams who aided sample collection and guidance.

I would like to express my very special thanks to my family for their trust, patience, guidance and financial support throughout my entire life. I would not be able to succeed without their inspiration.

TABLE OF CONTENTS

ABSTRACT v

ÖZ …..... vii

ACKNOWLEDGMENTS x

TABLE OF CONTENTS xi

LIST OF TABLES xv

LIST OF FIGURES xvi

LIST OF ABBREVIATIONS xxxviii

CHAPTERS

1 INTRODUCTION 1

1.1 Review of Subduction and Post-subduction Magmatism 5

1.2 Porphyry Deposits 9

1.2.1 Effects of Magma Oxidation Level, Water Content and Sulfide Saturation on Mineral Chemistry 16

1.3 Magmatism and Metallogeny of the Western Anatolia and Central Taurides 21

1.4 Thesis Research Question/Statement of Problem/Motivation 30

1.5 Methodology 34

1.5.1 Field Studies 34

1.5.2 Laboratory Work 39

2 MAGMATISM AND METALLOGENY IN CENTRAL TAURIDES 49

2.1 Regional Sampling Studies 50
2.1.1 Konya Volcanic Complex (16–8 Ma) 50
2.1.2 Karacadağ-Melendiz Volcanics (7–1 Ma) 58
2.1.3 Develidağ Volcanic Complex (6–5 Ma) 63
2.2 Mineralogy and Petrography 65
2.2.1 Konya Volcanic Complex (16–8 Ma) 65
2.2.2 Karacadağ-Melendiz Volcanics (7–1 Ma) 69
2.2.3 Develidağ Volcanic Complex (6–5 Ma) 71
3 MAGMATISM AND METALLOGENY IN WESTERN ANATOLIA 73
3.1 Regional Geology and Field Observations 73
3.1.1 Balıkesir District (25 Ma) 73
3.1.2 Kütahya-Simav District (22-17 Ma) 76
3.1.3 İzmir-Afyon-Uşak District (15–9 Ma) 83
3.1.4 Bodrum Peninsula (11–9 Ma) 91
3.2 Mineralogy and Petrography 93
3.2.1 Balıkesir District (25 Ma) 93
3.2.2 Kütahya-Simav District (22–17 Ma) 96
3.2.3 Uşak District (16–14 Ma) 99
3.2.4 Salihli Pluton (15 Ma) 102
3.2.5 Kırka-Afyon-Isparta (21-4 Ma) 102
3.2.6 Bodrum Peninsula (11–9 Ma) 104

4 LITHOGEOCHEMISTRY 107
4.1 Central Taurides 115
4.1.1 Konya Volcanic Complex 115
4.1.2 Karacadağ-Melendiz and Develidağ Volcanic Complexes 120
4.2 Western Anatolia 124
4.2.1 Biga Peninsula 124
4.2.2 Kütahya-Simav District 128
4.2.3 Kırka-Afyon-Isparta District 132
4.2.4 Uşak District 137
4.2.5 Manisa District 141
4.2.6 Bodrum Volcanic Complex 145
5 INDICATOR MINERAL ANALYSES RESULTS 149
5.1 Mineral Geochemistry and Isotopic Analyses 149
5.1.1 Zircon Analyses 149
5.1.2 Apatite Chemistry 213
5.1.3 Amphibole Geochemistry 226
5.1.4 Biotite Geochemistry 231
5.1.5 Magnetite-Ilmenite Geochemistry 236
6 DISCUSSION 241
6.1 Temporal and Spatial Evolution of the Late Cenozoic Magmatism 242
6.2 Tectonomagmatic Evolution of the Central Taurides and the Western Anatolia 247

6.3 Assessment of the Porphyry Ore Forming Potential of the Late Cenozoic Magmatism using Whole-rock, Zircon, and Apatite Fertility Indicators 263
6.3.1 Central Taurides 268
6.3.2 Western Anatolia 274
7 CONCLUSIONS 291
REFERENCES 295
APPENDICES 325
CURRICULUM VITAE 339

LIST OF TABLES

TABLES

Table 1.1. Details of samples collected from the Central Taurides after fieldwork. 36
Table 1.2. Details of samples collected from the Western Anatolia after fieldwork and selected for petrographic analysis. 37
Table 4.1. Whole-rock lithogeochemistry data for the Late Cenozoic units across the Western Anatolia and the Central Taurides 109
Table 5.1. Summary table of U-Pb zircon ages of Central Tauride samples..... 154
Table 5.2. Summary table of U-Pb zircon ages obtained from samples collected from the Western Anatolia sector. 159
Table 5.3. Summary table of zircon trace element abundances and other key parameters. 173
Table 5.4. Isotopic ratios obtained from zircon Hf isotope analyses. 211
Table 5.5. Representative EPMA and LA-ICP-MS results for the apatite. 215
Table 5.6. Representative EPMA analytical results of amphiboles from the studied localities. 230
Table 5.7. Representative EPMA analytical results of biotites from the studied localities. 233
Table 5.8. Representative EPMA analytical results of magnetite/ilmenite from the studied localities..... 238

LIST OF FIGURES

FIGURES

Figure 1.1. Porphyry deposits/occurrences in Türkiye and their relation with the metallogenic belt in western Tethyan-Eurasian metallogenic belt (Kuşcu et al., 2019). 3
Figure 1.2. A) Structure and processes beneath an oceanic island arc where primary hydrous basaltic arc magmas are derived from partial melting of the metasomatized asthenospheric mantle wedge (Richards, 2011). B) Representation of a MASH zone development at the base of the crust where basaltic arc magmas pool at their level of neutral buoyancy, differentiate, and interact with crustal rocks and melts. Evolved, less dense, andesitic magmas rise into the mid-to-upper crust where they pool at their new level of neutral buoyancy to form batholithic complexes. Along with volcanic structures, porphyry and epithermal deposits may form at shallower levels above these batholithic complexes where exsolved magmatic fluids ascend, cool, and interact with near-surface upper crustal rocks (Richards, 2011). 6
Figure 1.3. Schematic cross section of common subduction-related tectonic settings that can potentially host porphyry or other magmatic-hydrothermal systems (Richards, 2011). A) Generation of porphyry Cu±Mo as a product of typical arc magmatism. B) Crustal thickening and subsequent partial melting of SCLM due to post-collisional thermal rebound and formation of porphyry Cu±Mo±Au mineralization. C) Delamination of SCLM and partial melting of lower crust due to the upwelling of hot asthenospheric mantle and formation of post-collisional porphyry Cu±Mo±Au. D) Formation of post-collisional alkalic epithermal Au mineralization in post-collisional extensional settings. The extension causes the thinning of the continental crust and partial melting under the influence of heat added

to the SCLM and continental crust, and the formation of vein-type deposits localized along the normal faults..... 7
Figure 1.4. Schematic cross-section of batholih-cupola volcanic system with associated porphyry Cu±Au and linked high sulfidation Cu-Au epithermal deposits (Richards, 2011)..... 12
Figure 1.5. Schematic model illustrating the contrasting magmatic and hydrothermal evolution of porphyry Cu systems in thick vs. thin crust. Thick crust settings promote early sulfide saturation, Fe depletion, and prolonged hydrothermal activity, resulting in large, Au-poor deposits. In contrast, thin crust systems delay sulfide saturation, enhancing Cu–Au fertility but form smaller, Au-rich deposits due to shorter-lived magmatic-hydrothermal systems and shallow vapor–sulfide melt interaction. (Park et al., 2021). 14
Figure 1.6. Simplified map of Central Taurides and Western Anatolia showing the distribution of significant magmatic domains..... 22
Figure 1.7. Distribution of Late Cenozoic magmatic districts and related mineral occurrences/deposits in A) Western Anatolia, B) Kırka-Afyon-Isparta region and Konya Volcanic Complex, C) Central Taurides, and D) Bodrum Peninsula. Sample locations are also included. Distribution of magmatic units and structural features are from MTA (2002). 25
Figure 2.1. Simplified geological map of the west of Konya (Gündüz et al., 2025). Published K/Ar (Besang et al., 1977; Platzman et al.,1998), and U-Pb zircon ages (Rabayrol et al., 2019a) are also shown. Lithologies are from MTA (2002)..... 51
Figure 2.2. Field photographs of volcanic units from the Sulutaş Volcanic Suite within the Konya Volcanic Complex. (A) ~1 m-thick lamprophyre sill intruding Paleozoic metamorphic basement units, located approximately 3 km north of Tatköy. (B) Andesite porphyry outcrops situated just south of Tatköy. 52

Figure 2.3. Field and drill core photographs from the İnlice area within the KVC. (A) View of the İnlice open pit showing zones of intense silicification and advanced argillic alteration hosting high-sulfidation epithermal Au mineralization. (B) Andesitic dike cutting through altered and mineralized andesite porphyry on the SE wall of the open pit. (C) Weakly-propylitized andesite porphyry from drill hole INES-201, located north of the pit. (D) Andesite porphyry showing weak potassic alteration and associated M- and B-type veinlets. Propylitic alteration occurs as an overprint. (E) Residual vuggy silica and alunite cross-cutting potassic-altered andesite porphyry. (F) Quartz-sericite/clay-pyrite alteration and quartz-pyrite stockworking in porphyrytic andesite(?) from deeper levels of drill hole INES-201. 54
Figure 2.4. Field and core photographs from the Doğanbey, Çukurağıl, and Damlapınar prospects within the KVC. (A) Erosion-resistant units displaying silicification and advanced argillic alteration at the Doğanbey epithermal–porphyry prospect. (B) Porphyritic volcanic unit with quartz–alunite alteration exposed at the DGBD-01 drill collar site at Doğanbey. (C) Quartz–kaolinite-altered porphyritic volcanic rock observed in drill hole DGBD-02 at Doğanbey. (D) Silica caps at the Çukurağıl epithermal prospect. (E) Hand specimen of weakly–altered andesite porphyry exposed at the Damlapınar prospect. 55
Figure 2.5. Field and outcrop photographs from the Karacaören and Ketenli prospects within the KVC. (A) Altered andesite porphyries overlain by Pliocene lavas within the Karacaören license area; inset shows representative outcrop of quartz veins hosted in the alteration zone. (B) Andesite porphyry outcrop exposed near Saraycık Village within the Karacaören license. (C) Tuffs overlain by weathered lavas near Ketenli Village. (D) Moderately weathered andesitic agglomerates containing fresh andesite clasts, southern part of the Ketenli license. (E) Outcrop of silicified breccia with fine-grained disseminated pyrite in the matrix, southern

Ketenli sector. (F) Silica ridges with approximate NNE orientation in southern Ketenli; fresh andesitic lavas and agglomerates are visible in the background hills. 57
Figure 2.6. Field views and core photographs from sampling locations in Melendiz area. (A) Hydrothermally-altered units within the Melendiz Dağ volcanic complex, located east of Niğde (view looking west). (B) Agglomerate displaying quartz–illite–chlorite(?) alteration in drill core from the Çömlekçi prospect. (C) Erosion-resistant altered lava flows at the Karanlıkdere locality. (D) Altered (chlorite–illite?) massive basaltic andesite/andesite sample from Karanlıkdere. 59
Figure 2.7. Field photographs of the Karacadağ caldera. (A) Layered lava flows and volcaniclastic deposits (block faulted to the left of image) rimming the caldera (view toward the west with town of Yeşilyurt in the background). (B) An andesitic(?) dome developed in the eastern part of the caldera center. (C, D) Strongly clay-silica-altered, Fe-(hydr)oxide-stained andesite porphyry. Red arrow in (D) show fault striations (E) Brecciated andesite porphyry with dark gray silica matrix..... 60
Figure 2.8. Field and drill core photographs from the DVC and the associated Öksüt HS epithermal Au-Cu deposit. (A) Andesitic dome occupying in the northern part of the DVC, which is also the host to Öksüt gold mineralization (view to the north from the Öksüt village). (B) View of the Güneytepe open pit, looking east. The upper part of the pit exposes Early Pliocene basalt to basaltic andesite lava flows overlying altered and mineralized andesite porphyry. (C) Drill core of potassically-altered (biotite-K-feldspar-magnetite) andesite porphyry from the deeper part of the Keltepe pit. Green color is due to late propylitic alteration (D) Deformed magnetite vein with K-feldspar halos in potassically-altered andesite porphyry. 64
Figure 2.9. Transmitted light microphotographs of igneous rock samples from İnlice and Damlapınar areas in KVC. (A) Strongly altered andesite dyke within the İnlice open pit. Hornblende is completely replaced, whereas plagioclase in both

groundmass and phenocrysts is partially kaolinized; biotite shows partial opacitization and clay alteration (PPL). (B) Weakly-altered andesite porphyry from drill hole INES-201 with relatively well-preserved plagioclase and biotite phenocrysts (XPL) (C) Strongly kaolinized andesite porphyry host to the İnlice HS epithermal Au mineralization (PPL). (D) Weakly-altered pyroxene-bearing andesite porphyry from the Damlapınar prospect (XPL). 66
Figure 2.10. Transmitted-light microphotographs of igneous rocks from the Karacaören and Ketenli sectors of the KVC. (A) Andesite porphyry from Karacaören showing weak carbonate–chlorite–illite alteration. Plagioclase and hornblende phenocrysts have been partially replaced by carbonate, and hornblende has been partially opacitized (XPL). (B) Dacitic agglomerate from Ketenli with embayed quartz and zoned plagioclase phenocrysts set in a fine-grained matrix (XPL). 68
Figure 2.11. Transmitted-light microphotographs of Late Miocene–Pliocene igneous rock samples from the Niğde–Kayseri region. (A) Andesite porphyry from the Çömlekçi (Melendiz) prospect, showing low-temperature alteration; plagioclase phenocrysts are largely fresh, whereas a large hornblende crystal has been replaced by clay minerals (XPL). (B) Least-altered andesite poprhyry from Çömlekçi displaying quartz–plagioclase–biotite as the main phenocrysts (XPL). (C) Dacitic lava flow from Süleymanpınarı containing quartz, plagioclase, and biotite phenocrysts set in partially devitrified glassy matrix (XPL). (D) Completely carbonatized hornblende phenocryst in altered andesitic lava from Karanlıkdere area (XPL)Weakly-altered dacite porphyry from Süleymanpınarı with large, medium-grained plagioclase and biotite crystals; opaque inclusions within biotite are magnetite (XPL). (E) Plagioclase-phyric andesite porphyry containing hornblende and magnetite phenocrysts from the Karacadağ caldera (XPL). (F) Clinopyroxene-bearing andesite porphyry host rock of the Öksüt HS epithermal Au-Cu deposit in the DVC (XPL)..... 70

Figure 3.1. Simplified geologic map of the Biga Peninsula and the Kütahya–Simav area highlighting principal magmatic centers (Miocene–Pliocene) and the spatial distribution of porphyry and epithermal deposits/occurrences (MTA, 2002; Yılmaz et al., 2013; Bickford et al., 2016; Baker et al., 2016; Delibaş et al., 2017; Kuşcu et al., 2019; Özel, 2024). 75
Figure 3.2. Drill core photographs from hole BKS-317, which intersects porphyry-style mineralization within the northern sector of the Balya skarn system. (A) Clay-altered agglomerate from the volcanic–volcaniclastic sequence overlying the porphyry system. Clasts include andesitic and basaltic lithologies. (B) Weakly-altered granodiorite porphyry cross-cut by a D-type quartz–pyrite vein, surrounded by a narrow sericitic halo. (C) Granodiorite porphyry exhibiting potassic alteration, cut by A- and B-type quartz–sulfide veins. Pinkish potassium feldspar halos are prominent around the veins. (D) B-type quartz–pyrite–molybdenite vein crosscutting potassically-altered granodiorite porphyry. 76
Figure 3.3. Simplified geologic map of the Kütahya–Simav region, showing major magmatic centers and the distribution of porphyry and epithermal mineralizations (MTA, 2002). 78
Figure 3.4. Field photographs from the Sındırgı and Eğrigöz areas in the Kütahya region. (A) Open pit at the Kızıltepe low-sulfidation epithermal Au–Ag deposit, located north of Sındırgı. Clay-altered microgranite/microgranodiorite units are exposed to the south of the pit (looking towards northeast). (B, C) Partially clay-altered and propylitized volcaniclastic units exposed ~2.5 km east of the Kızıltepe Au–Ag deposit. (D) Outcropping granite and crosscutting aplitic dike near Gökçeler village, west of Simav, situated at the southern margin of the Eğrigöz Pluton. (E) Weakly-altered granitic rocks with mafic enclaves at the northern edge of the Eğrigöz Pluton, spatially associated with skarn-type mineralization. 79

Figure 3.5. Field photographs from the Salihli Granite. (A) General view of the southern margin of the granitic intrusion juxtaposed against the Bayındır Nappe. This contact forms part of the E–W-trending Alaşehir Detachment. (B, C) Partially mylonitized granite at detachment contact containing flattened mafic enclaves. ...80
Figure 3.6. Field photographs of altered magmatic units from the Pınarbaşı Cu-Mo prospect, located approximately 1 km north of Pınarbaşı Village (NW of Gediz). (A) Surface exposure of quartz–sericite-altered microgranite, representing the main mineralized host unit. (B) Well-exposed altered microgranite along a stream bed. (C) NW-trending andesite porphyry dyke crosscutting the microgranite. (D) A transported block of andesitic porphyry containing mafic enclaves. 81
Figure 3.7. Surface and drill core photographs from the Çatalçam Au-Ag-Pb-Zn-Mo prospect. (A) Quartz–clay–carbonate–altered andesite porphyry hosting the main ore zone, exposed east of Duğla Village, crosscut by oxidized stockwork quartz–pyrite veins. (B) Andesite porphyry exhibiting quartz–illite–carbonate alteration, intruded by a propylitized basaltic andesite dyke. (C) Phreatomagmatic breccias developed within the andesite porphyry; some breccia clasts display porphyry-style alteration and include B-type porphyry veins. (D) Quartz–illite–carbonate–altered andesite porphyry showing intense quartz–pyrite stockworking veinlets, cross-cut by basaltic andesite dyke. 82
Figure 3.8. Geologic map of the Uşak-Güre basin, showing the location of the Elmadağ, Itecektepe, and Beydağı volcanic centers (modified after Karaoğlu et al., 2010). The inset map illustrates the distribution of magmatic belts across Anatolia. 84
Figure 3.9. Drill core photographs representing different intrusive phases of the Kışladağ porphyry Au deposit. (A) Early-stage monzonite porphyry (INT1) exhibiting intense potassic alteration. (B–E) Various monzonite porphyry and latite phases belonging to the syn-mineralization INT2 stage, crosscutting INT1 within the

open pit. (F) Porphyritic latite dyke (INT3) with partial alteration, intruding both INT1 and INT2 phases in the open pit. 85
Figure 3.10. Drill core photographs from the Sayacık porphyry Au prospect. (A) Monzonite displaying intense quartz–white mica–tourmaline–pyrite alteration. The dark-colored veinlet crosscutting the sample is filled with tourmaline. (B) Altered monzonite crosscut by an altered latite porphyry intrusion. 86
Figure 3.11. Map showing distribution of alkaline igneous rocks of Kırka-Afyon-Isparta with related fault systems, and radiometric age data determined on the volcanic rocks (Savaşcın and Oyman, 1998, modified after Savaşçın et al., 1994). Radiometric data from Sunder (1982), Besang et al. (1977), Lefevre et al. (1983), and Rabayrol et al. (2019b). 88
Figure 3.12. Field photographs of igneous exposures within the AVC to the north and east of Sandıklı. (A) Latitic lava flows exposed north of Sandıklı. (B) General view of the central zone of the A-S porphyry prospect, characterized by hydrothermally altered and mineralized rocks, where drilling activities have also been conducted. (C) Trachyte dykes crosscutting altered volcanic units in the central zone of the A-S porphyry prospect. (D) Altered syenite porphyry from the central zone of the A-S porphyry prospect. (E) Moderatelyaltered latite from the central zone of the A-S porphyry prospect. (F) Weakly-altered latite porphyry from the southern sector of the A-S porphyry prospect. 89
Figure 3.13. Field photographs of volcanic and volcaniclastic units from the southern Sandıklı and southern Balçıkhisar areas within the AVC. (A) Latite dyke cross-cutting a syenite porphyry unit located ~1 km east of Bektaş Village, south of Sandıklı. Close-up view of the (B) syenite porphyry and (C) latite at the same location. (D) Roadcut exposure of a volcaniclastic succession overlain by terrestrial clastic sediments ~3 km south of Balçıkhisar Village. (E–F) Syenite and lamproite clasts observed within the volcaniclastic succession south of Balçıkhisar. 90

Figure 3.14. Simplified geological map of Bodrum Peninsula showing the distribution of lithological units (MTA, 2002; Çubukçu et al., 2021; modified from Ulusoy et al., 2004). 91
Figure 3.15. Field and hand specimen photographs of igneous rocks from the Bodrum Peninsula. (A) Pyroclastic succession exposed south of Türkbükü and hand specimen of trachyandesite clasts within this unit. (B) Resistant ridges composed of trachyandesite with pervasive quartz–alunite alteration in the Dağbelen area (view towards southwest). (C) Massive, fresh to weakly-altered trachyandesite outcrop at the same location in B. (D) Quarry near Turgutreis exposing a shallow monzonitic intrusion. (E) Weakly-altered basaltic trachyandesite outcrop near Gümüşlük. 93
Figure 3.16. Transmitted-light microphotographs of igneous rock samples associated with porphyry-style mineralization from Balya. (A–B) Diorite porphyry affected by potassic alteration (biotite–K-feldspar); biotite phenocrysts have been partially replaced by chlorite (PPL and XPL, respectively). (C) Granodiorite porphyry overprinted by potassic alteration (XPL). (D) Hornblende phenocryst in granodiorite porphyry replaced by secondary biotite and magnetite (opaque; XPL). 94
Figure 3.17. Transmitted-light microphotographs of igneous rock samples from the Çatalçam porphyry–epithermal prospect. (A) Andesite porphyry from deeper levels of the epithermal system with chloritized hornblende and illite-altered groundmass. Fine-grained opaque phases are pyrite intergrown with chlorite (PPL). (B) Altered basaltic andesite dyke with partially chloritized hornblende and better-preserved biotite. Groundmass exhibits pervasive illite alteration, and the opaque phases are disseminated pyrite grains (PPL)..... 95
Figure 3.18. Transmitted-light microphotographs of igneous rock samples from the Sındırgı and Eğrigöz areas. (A) Weakly-altered microgranodiorite exposed north of Sındırgı, near Kızıltepe Au deposit (PPL). (B) Agglomerate from east of Kızıltepe. Hornblende and biotite are partially opacitized, whereas plagioclase-rich fine-

grained groundmass shows partial alteration into clays (PPL). (C) Dacitic tuff from the same locality as (B), where hornblende crystals are completely opacitized, whereas biotite is well preserved. Quartz typically occurs as angular crystal fragments (PPL). (D) Fresh granite from the southern margin of the Eğrigöz Pluton near Gökçeler Village. (E) Granite from the northern part of the Eğrigöz Pluton, immediately north of Söğüt Village. Sample contains a higher proportion of hornblende compared to granite sample in (D) (PPL). (F) Weakly-altered granite from the northern margin of the Eğrigöz Pluton (XPL). 98
Figure 3.19. Transmitted-light microphotographs of igneous rock samples from the Pınarbaşı porphyry Cu–Mo prospect. (A) Altered dacite porphyry dyke crosscutting the monzonite. Quartz and K-feldspar are accompanied by biotite that has been variably replaced by sericite. Secondary calcite occurs as fracture-fill (XPL). (B) Altered monzonite porphyry host to the porphyry mineralization. Biotite is secondary in origin and plagioclase crystals have been partially replaced by sericite (XPL). 99
Figure 3.20. Transmitted-light microphotographs of core samples from igneous units in the Kışladağ and Sayacık porphyry Au systems. (A) Early monzonite porphyry from Kışladağ (INT1), showing abundant fine-grained biotite aggregates formed during potassic alteration. Fine-grained groundmass consists predominantly of secondary K-feldspar intergrown with quartz (PPL). (B–D) Various monzonite porphyry phases from Kışladağ (INT2) intruding early-phase monzonite porphyries. These display moderate to high intensity quartz–white mica–tourmaline alteration. Sample KSLD-06 in (C) shows lower intensity alteration, whereby ferromagnesian phases have been partially preserved (PPL and XPL). (E–F) Altered late-stage latite porphyry dyke from Kışladağ (INT3; XPL). (G–H) Monzonitic–latite porphyries from Sayacık, exhibiting intense quartz–white mica–tourmaline alteration (PPL and XPL). 101

Figure 3.21. Transmitted-light microphotographs of igneous rock samples from the Salihli Granitoid. (A) Medium-grained, equigranular granite showing no evidence of deformation (XPL). (B) Foliated granite from the southern contact zone of the granitoid, which has been subjected to tectonic stress and partial mylonitization. Biotite crystals display a pronounced preferred orientation (XPL).....102
Figure 3.22. Transmitted-light microphotographs of igneous rock samples from the AVC. (A) Porphyritic lamproite from south of Balçıkhisar, containing phenocrysts of leucite, pyroxene, and phlogopite in a K-feldspar–rich groundmass (PPL). (B) Leucitite from south of Balçıkhisar, characterized by abundant leucite enclosed in a dark groundmass rich in K-feldspar and carbonate (PPL). (C) Fresh micromonzonite from the A–S porphyry prospect, showing porphyritic texture with euhedral K-feldspar and biotite phenocrysts in a quartzofeldspathic groundmass (XPL). (D) Trachytic dyke from the A–S porphyry prospect, composed mainly of slender prismatic biotite and tabular K-feldspar phenocrysts in a fine-grained K-feldspar–rich groundmass with minor quartz; greenish minerals are tourmaline (PPL). (E) Syenite porphyry host unit of the A–S porphyry mineralization, characterized by K-feldspar, biotite, and quartz with minor chlorite (PPL). (F) Porphyritic latite from the A–S porphyry prospect, with phenocrysts of hornblende, biotite, K-feldspar, and plagioclase (XPL).....103
Figure 3.23. Transmitted-light microphotographs of igneous rock samples from the Bodrum Peninsula. (A) Trachyandesite containing well-preserved biotite, plagioclase, hornblende, and pyroxene (XPL). (B) Basaltic trachyandesite with trachytic texture, dominated by clinopyroxene and plagioclase with subordinate biotite (XPL). (C) Trachyandesite composed of pyroxene and plagioclase with lesser large orthoclase crystals (XPL). (D) Medium-grained monzonite showing carbonate–clay alteration (XPL).....105

Figure 4.1. Classification diagram for mineralized samples in the Central Taurides and the Western Anatolia based on immobile trace elements (after Winchester and Floyd, 1977). 108
Figure 4.2. Classification diagrams based on whole-rock geochemical data for KVC. (A) TAS diagram (Le Maitre et al., 1989), with the alkaline/subalkaline division after Irvine and Baragar (1971). (B) K_2O vs. SiO_2 diagram (Peccerillo and Taylor, 1976). (C) Alumina Saturation Index (Shand, 1927). Data from Çelik, 1999, Kurt et al., 2003, Asan and Ertürk, 2013, Asan et al., 2021; Rabayrol and Hart, 2021. 116
Figure 4.3. A) Primitive mantle-normalized trace element and B) chondrite-normalized REE diagrams for igneous rocks from the KVC. Normalization values are from Sun and McDonough (1989). 117
Figure 4.4. Selected trace element discrimination diagrams for igneous lithologies from the KVC and SVS: (A) $(La/Sm)_N$ vs. $(Dy/Yb)_N$, (B) Eu/Eu* vs. SiO_2, (C) Sr/Y vs. SiO_2, (D) La/Yb vs. SiO_2, (E) Sr/Y vs. Y, and (F) La/Yb vs. Yb. Normalization values are from Sun and McDonough (1989). 119
Figure 4.5. Classification diagrams based on whole-rock geochemical data for Central Taurides. (A) TAS diagram (Le Maitre et al., 1989), with the alkaline/subalkaline division after Irvine and Baragar (1971). (B) K_2O vs. SiO_2 diagram (Peccerillo and Taylor, 1976). (C) Alumina Saturation Index (Shand, 1927). Data from Innocenti et al. (1975); Temel et al. (1988); Aydın (2008); Güçtekin and Köprübaşı (2009); Gençalioğlu-Kuşcu and Geneli (2010); Koralay (2010); Kürkçüoğlu (2010); Koralay et al. (2011); Reid et. al. (2017); Di Giuseppe (2018); Aluç et al. (2020); Rabayrol and Hart (2021); Aydın et al. (2022). 121
Figure 4.6. A and C) Primitive mantle-normalized trace element and B and D) chondrite-normalized REE diagrams of volcanic rocks from Central Taurides. Normalization values are from Sun and McDonough (1989). 122

Figure 4.7. Selected trace element discrimination diagrams for igneous lithologies from the Central taurides: (A) $(La/Sm)_N$ vs. $(Dy/Yb)_N$, (B) Eu/Eu* vs. SiO_2, (C) Sr/Y vs. SiO_2, (D) La/Yb vs. SiO_2, (E) Sr/Y vs. Y, and (F) La/Yb vs. Yb. Normalization values are from Sun and McDonough (1989). 123
Figure 4.8. Classification diagrams based on whole-rock geochemical data for Biga Peninsula. (A) TAS diagram (Le Maitre et al., 1989), with the alkaline/subalkaline division after Irvine and Baragar (1971). (B) K_2O vs. SiO_2 diagram (Peccerillo and Taylor, 1976). (C) Alumina Saturation Index (Shand, 1927). Data from Delaloye and Bingöl (2000); Ece and Schroeder (2007); Ece and Wampler (2008); Özışık (2009); Altunkaynak et al. (2012); Aydar (2018); Özel (2024). 125
Figure 4.9. A) Primitive mantle-normalized trace element and B) chondrite-normalized REE diagrams for igneous rocks from the Biga Peninsula. Normalization values are from Sun and McDonough (1989). 126
Figure 4.10. Selected trace element discrimination diagrams for igneous lithologies from the Biga Peninsula: (A) $(La/Sm)_N$ vs. $(Dy/Yb)_N$, (B) Eu/Eu* vs. SiO_2, (C) Sr/Y vs. SiO_2, (D) La/Yb vs. SiO_2, (E) Sr/Y vs. Y, and (F) La/Yb vs. Yb. Normalization values are from Sun and McDonough (1989). 127
Figure 4.11. Classification diagrams based on whole-rock geochemical data for Kütahya-Simav district. (A) TAS diagram (Le Maitre et al., 1989), with the alkaline/subalkaline division after Irvine and Baragar (1971). (B) K_2O vs. SiO_2 diagram (Peccerillo and Taylor, 1976). (C) Alumina Saturation Index (Shand, 1927). Data from Tufan (2005); Aydoğan et al. (2008); Özgenç and İlbeyli (2008); Akay (2009); Hasözbek et al. (2011); Jacob (2011); Altunkaynak et al. (2012); Oyman et al. (2013); Semiz et al. (2015); Delibaş et al (2017); Özen and Arık, 2019; Rabayrol and Hart (2021).....129

Figure 4.12. A) Primitive mantle-normalized trace element and B) chondrite-normalized REE diagrams of Late Cenozoic igneous rocks from the Kütahya-Simav region. Normalization values are from Sun and McDonough (1989). 130
Figure 4.13. Selected trace element discrimination diagrams for igneous lithologies from the Kütahya-Simav district: (A) $(La/Sm)_N$ vs. $(Dy/Yb)_N$, (B) Eu/Eu* vs. SiO_2, (C) Sr/Y vs. SiO_2, (D) La/Yb vs. SiO_2, (E) Sr/Y vs. Y, and (F) La/Yb vs. Yb. Normalization values are from Sun and McDonough (1989)..... 131
Figure 4.14. Classification diagrams based on whole-rock geochemical data for Kırka-Afyon-Isparta volcanics. (A) TAS diagram (Le Maitre et al., 1989), with the alkaline/subalkaline division after Irvine and Baragar (1971). (B) K_2O vs. SiO_2 diagram (Peccerillo and Taylor, 1976). (C) Alumina Saturation Index (Shand, 1927). Data from Francalanci et al. (2000); Akal (2003); Çoban and Flower (2006); Akal (2008); Dilek and Altunkaynak (2010); Prelevic et al. (2012); Akal et al. (2013); Prelevic et al. (2015); Kuşcu et al. (2019); Sönmez and Kuşcu (2020); Rabayrol and Hart (2021)..... 133
Figure 4.15. A) Primitive mantle-normalized trace element and B) chondrite-normalized REE diagrams for igneous rocks from Kırka-Afyon-Isparta region. Normalization values are from Sun and McDonough (1989)..... 134
Figure 4.16. Selected trace element discrimination diagrams for igneous lithologies from the Kırka-Afyon-Isparta region: (A) $(La/Sm)_N$ vs. $(Dy/Yb)_N$, (B) Eu/Eu* vs. SiO_2, (C) Sr/Y vs. SiO_2, (D) La/Yb vs. SiO2, (E) Sr/Y vs. Y, and (F) La/Yb vs. Yb. Normalization values are from Sun and McDonough (1989)..... 136
Figure 4.17. Classification diagrams based on whole-rock geochemical data for Uşak. (A) TAS diagram (Le Maitre et al., 1989), with the alkaline/subalkaline division after Irvine and Baragar (1971). (B) K_2O vs. SiO_2 diagram (Peccerillo and Taylor, 1976). (C) Alumina Saturation Index (Shand, 1927). Data from Innocenti et

al. (2005); Ersoy et al. (2010); Karaoğlu et al. (2010); Prelevic et al. (2012); Baker et al. (2016); Kuşcu et al. (2019); Rabayrol and Hart (2021).....138
Figure 4.18. A) Primitive mantle-normalized trace element and B) chondrite-normalized REE diagrams for igneous rocks for Kışladağ and Sayacık porphyry systems and the surrounding volcanic rocks in Uşak. Normalization values are from Sun and McDonough (1989). 139
Figure 4.19. Selected trace element discrimination diagrams for igneous lithologies from the Uşak district: (A) $(La/Sm)_N$ vs. $(Dy/Yb)_N$, (B) Eu/Eu* vs. SiO_2, (C) Sr/Y vs. SiO_2, (D) La/Yb vs. SiO_2, (E) Sr/Y vs. Y, and (F) La/Yb vs. Yb. Normalization values are from Sun and McDonough (1989). 140
Figure 4.20. Classification diagrams based on whole-rock geochemical data for Salihli granitoid. (A) Total Alkali–SiO_2 (TAS) diagram (Le Maitre et al., 1989), with the alkaline/subalkaline division after Irvine and Baragar (1971). (B) K_2O vs. SiO_2 diagram (Peccerillo and Taylor, 1976). (C) Alumina Saturation Index (Shand, 1927). 142
Figure 4.21. A) Primitive mantle- and B) chondrite-normalized multi-element diagrams for Salihli Pluton. Normalization values are from Sun and McDonough (1989). 143
Figure 4.22. Trace element discrimination diagrams for the Salihli and Turgutlu plutons showing parameters relevant to porphyry fertility assessment: (A) $(La/Sm)_N$ vs. $(Dy/Yb)_N$, (B) Eu/Eu* vs. SiO_2, (C) Sr/Y vs. SiO_2, (D) La/Yb vs. SiO_2, (E) Sr/Y vs. Y, and (F) La/Yb vs. Yb. Subscript *N* indicates chondrite normalization (Sun and McDonough, 1989).....144
Figure 4.23. Classification diagrams based on whole-rock geochemical data for Bodrum Peninsula. (A) TAS diagram (Le Maitre et al., 1989), with the alkaline/subalkaline division after Irvine and Baragar (1971). (B) K_2O vs. SiO_2

diagram (Peccerillo and Taylor, 1976). (C) Alumina Saturation Index (Shand, 1927). Data from Çubukçu et al. (2021); Rabayrol and Hart (2021). 145
Figure 4.24. A) Primitive mantle- and B) chondrite-normalized multi-element diagrams for Bodrum Volcanic Complex. Normalization values are from Sun and McDonough (1989). 146
Figure 4.25. Selected trace element discrimination diagrams for igneous lithologies from the BVC: (A) $(La/Sm)_N$ vs. $(Dy/Yb)_N$, (B) Eu/Eu* vs. SiO_2, (C) Sr/Y vs. SiO_2 , (D) La/Yb vs. SiO_2, (E) Sr/Y vs. Y, and (F) La/Yb vs. Yb. Normalization values are from Sun and McDonough (1989). 147
Figure 5.1. Concordia and weighted mean age diagrams of U-Pb dated zircons from KVC. 156
Figure 5.2. Concordia and weighted mean age diagrams of U-Pb dated zircons from prospects near Melendiz Stratovolcano and from Karacadağ caldera from the Karapınar Volcanic Vent. 158
Figure 5.3. Concordia and weighted mean age diagrams of U-Pb dated zircons from Kırka-Afyon-Isparta district. 161
Figure 5.4. Concordia and weighted mean age diagrams of U-Pb dated zircons from the Biga Peninsula. 164
Figure 5.5. Concordia and weighted mean age diagrams of U-Pb dated zircons from the Bodrum Peninsula. 166
Figure 5.6. Concordia and weighted mean age diagrams of U-Pb dated zircons from the Salihli Pluton. 167
Figure 5.7. Concordia and weighted mean age diagrams of U-Pb dated zircons from the Kütahya-Simav district. 168
Figure 5.8. Concordia and weighted mean age diagrams of U-Pb dated zircons from the Uşak district. 170

Figure 5.9. Diagrams illustrating the geochemical relationships of zircons analyzed from the Konya region of Central Anatolia. A) Eu/Eu* vs. Dy/Yb, B) Hf/Y vs. Th/U, C) Th/U vs. Yb_N/Gd_N, D) Eu/Eu* vs. Th/U, E) Eu/Eu* vs. $1000\times(Ce/Nd)_n/Yb$, and F) Magma fO_2 (ΔFMQ) vs. Ti-in-zircon temperature (°C). 181
Figure 5.10. Zircon multi-element variation diagrams of the Konya district. 182
Figure 5.11. Diagrams illustrating the geochemical relationships of zircons analyzed from the Karacadağ-Melendiz-Develidağ area. A) Eu/Eu* vs. Dy/Yb, B) Hf/Y vs. Th/U, C) Th/U vs. Yb_N/Gd_N, D) Eu/Eu* vs. Th/U, E) Eu/Eu* vs. $1000\times(Ce/Nd)_n/Yb$, and F) Magma fO_2 (ΔFMQ) vs. Ti-in-zircon temperature (°C). 185
Figure 5.12. Zircon multi-element variation diagrams of volcanic and sub-volcanic rocks from the Karacadağ-Melendiz-Develidağ region. 186
Figure 5.13. Diagrams illustrating the geochemical relationships of zircons analyzed from the Biga Peninsula. A) Eu/Eu* vs. Dy/Yb, B) Hf/Y vs. Th/U, C) Th/U vs. Yb_N/Gd_N, D) Eu/Eu* vs. Th/U, E) Eu/Eu* vs. $1000\times(Ce/Nd)_n/Yb$, and F) Magma fO_2 (ΔFMQ) vs. Ti-in-zircon temperature (°C). 188
Figure 5.14. Zircon multi-element variation diagrams of the Oligo-Miocene igneous rocks from the Biga Peninsula. 190
Figure 5.15. Diagrams illustrating the geochemical relationships of zircons analyzed from the Kütahya-Simav district. A) Eu/Eu* vs. Dy/Yb, B) Hf/Y vs. Th/U, C) Th/U vs. Yb_N/Gd_N, D) Eu/Eu* vs. Th/U, E) Eu/Eu* vs. $1000\times(Ce/Nd)_n/Yb$, and F) Magma fO_2 (ΔFMQ) vs. Ti-in-zircon temperature (°C). 194
Figure 5.16. Zircon multi-element variation diagrams of Middle Miocene igneous rocks from the Kütahya-Simav region. 195
Figure 5.17. Diagrams illustrating the geochemical relationships of zircons analyzed from the Kışladağ and Sayacık porphyry Au systems in Uşak district. A) Eu/Eu* vs. Dy/Yb, B) Hf/Y vs. Th/U, C) Th/U vs. Yb_N/Gd_N, D) Eu/Eu* vs. Th/U, E) Eu/Eu*

vs. 1000×$(Ce/Nd)_n$/Yb, and F) Magma fO_2 (ΔFMQ) vs. Ti-in-zircon temperature (°C). 197
Figure 5.18. Zircon multi-element variation diagrams of igneous rock samples from the Uşak district. 198
Figure 5.19. Diagrams illustrating the geochemical relationships of zircons analyzed from the Salihli Pluton. A) Eu/Eu* vs. Dy/Yb, B) Hf/Y vs. Th/U, C) Th/U vs. Yb_N/Gd_N, D) Eu/Eu* vs. Th/U, E) Eu/Eu* vs. 1000×$(Ce/Nd)_n$/Yb, and F) Magma fO_2 (ΔFMQ) vs. Ti-in-zircon temperature (°C). 199
Figure 5.20. Zircon multi-element variation diagrams of granitic rocks of the Salihli Granitoid. 200
Figure 5.21. Diagrams illustrating the geochemical relationships of zircons analyzed from the Kırka-Afyon-Isparta region. A) Eu/Eu* vs. Dy/Yb, B) Hf/Y vs. Th/U, C) Th/U vs. Yb_N/Gd_N, D) Eu/Eu* vs. Th/U, E) Eu/Eu* vs. 1000×$(Ce/Nd)_n$/Yb, and F) Magma fO_2 (ΔFMQ) vs. Ti-in-zircon temperature (°C). 202
Figure 5.22. Zircon multi-element variation diagrams of the volcanic and sub-volcanic rocks from the Kırka-Afyon-Isparta region. 204
Figure 5.23. Diagrams illustrating the geochemical relationships of zircons analyzed from the Bodrum district. A) Eu/Eu* vs. Dy/Yb, B) Hf/Y vs. Th/U, C) Th/U vs. Yb_N/Gd_N, D) Eu/Eu* vs. Th/U, E) Eu/Eu* vs. 1000×$(Ce/Nd)_n$/Yb, and F) Magma fO_2 (ΔFMQ) vs. Ti-in-zircon temperature (°C). 207
Figure 5.24. Zircon multi-element variation diagrams of volcanic, volcaniclastic, and sub-volcanic rocks of the BVC. 209
Figure 5.25. Temporal variation in εHf_{zircon} values of selected igneous systems in Western Anatolia. 212
Figure 5.26. Box and whisker plots of the halogen contents of apatites from the Western Anatolia and the Central Taurides. 214

Figure 5.27. Box and whisker plots of the trace element compositions for the apatites from the Western Anatolia and the Central Taurides. 224
Figure 5.28. Back-scattered electron (BSE) images of amphibole, biotite, and magnetite/ilmenite grains selected for EPMA under the scanning electron microscope. 227
Figure 5.29. Classification diagram of amphiboles from Late Cenozoic magmatic systems (after Leake et al., 1997). 228
Figure 5.30. Classification diagram of biotites from Late Cenozoic magmatic systems. A) 10*TiO_2-(FeO+MnO)-MgO ternary plot to discriminate primary and secondary biotites (after Nachit et al., 2005). B) Biotite compositional plots on binary classification diagram (after Rieder et al., 1998). C) Biotite discrimination diagram (after Abdel-Rahman, 1994). 235
Figure 5.31. Classification of magnetite and ilmenite based on A) TiO_2-FeO-Fe_2O_3 system (after Sassi et al., 2004), and B) Ti^{+4}-Fe^{3+}+Mg+Mn-Fe^{3+}+Cr+V+Al system. 240
Figure 6.1. Temporal and spatial distribution of the Late Cenozoic magmatism in the Central Taurides and the Western Anatolia. The sample locations and the obtained U-Pb ages are included in the map. 244
Figure 6.2. Diagrams showing temporal variations of key zircon-derived porphyry fertility parameters for Late Cenozoic magmatism in the Central Taurides. 250
Figure 6.3. Diagrams showing temporal variations of key zircon-derived porphyry fertility parameters for Late Cenozoic magmatism in the Western Anatolia. 257
Figure 6.4. Apatite fertility diagrams (A to C) and chondrite normalized rare earth multi-element diagrams (D) for the Western Anatolian and Central Taurides samples. 267
Figure 6.5. Zircon fertility parameters for the Erenlerdağ-Alacadağ Volcanics and Sulutaş Volcanic Suite. A) Zircon (Eu/Eu*)/$Yb_N \times 10^4$ plotted against Ce/√(UxTi) in

zircon. Shaded fields are after Loucks et al. (2024) and represent ranges for zircons from porphyry Cu ore-forming intrusions and from infertile arc igneous suites. B) $Dy_{(n)}$ vs. $Yb_{(n)}/Gd_{(n)}$. C) Eu/Eu* vs. P (ppm). D) Ce/Nd vs. Dy/Yb diagram. E) Eu/Eu* vs Sr (ppm). F) ΔFMQ vs. $(Eu/Eu^*)/(Dy_N/Yb_N)$ as suggested by Tapia et al. (2025). Subscript *N* indicates chondrite-normalized values. Fertility parameters used in C, D, and E are suggested by Carrasco-Godoy et al. (2024). 270
Figure 6.6. Zircon fertility parameters for the Niğde-Kayseri sector. A) Zircon $(Eu/Eu^*)/Yb_N \times 10^4$ plotted against Ce/√(UxTi) in zircon. Shaded fields are after Loucks et al. (2024) and represent ranges for zircons from porphyry Cu ore-forming intrusions and from infertile arc igneous suites. B) $Dy_{(n)}$ vs. $Yb_{(n)}/Gd_{(n)}$. C) Eu/Eu* vs. P (ppm). D) Ce/Nd vs. Dy/Yb diagram. E) Eu/Eu* vs Sr (ppm). F) ΔFMQ vs. $(Eu/Eu^*)/(Dy_N/Yb_N)$ as suggested by Tapia et al. (2025). Subscript *N* indicates chondrite-normalized values. Fertility parameters used in C, D, and E are suggested by Carrasco-Godoy et al. (2024). 271
Figure 6.7. Zircon fertility parameters for the Biga. A) Zircon $(Eu/Eu^*)/Yb_N \times 10^4$ plotted against Ce/√(UxTi) in zircon. Shaded fields are after Loucks et al. (2024) and represent ranges for zircons from porphyry Cu ore-forming intrusions and from infertile arc igneous suites. B) $Dy_{(n)}$ vs. $Yb_{(n)}/Gd_{(n)}$. C) Eu/Eu* vs. P (ppm). D) Ce/Nd vs. Dy/Yb diagram. E) Eu/Eu* vs Sr (ppm). F) ΔFMQ vs. $(Eu/Eu^*)/(Dy_N/Yb_N)$ as suggested by Tapia et al. (2025). Subscript *N* indicates chondrite-normalized values. Fertility parameters used in C, D, and E are suggested by Carrasco-Godoy et al. (2024). 275
Figure 6.8. Zircon fertility parameters for the Kütahya-Simav region. A) Zircon $(Eu/Eu^*)/Yb_N \times 10^4$ plotted against Ce/√(UxTi) in zircon. Shaded fields are after Loucks et al. (2024) and represent ranges for zircons from porphyry Cu ore-forming intrusions and from infertile arc igneous suites. B) $Dy_{(n)}$ vs. $Yb_{(n)}/Gd_{(n)}$. C) Eu/Eu* vs. P (ppm). D) Ce/Nd vs. Dy/Yb diagram. E) Eu/Eu* vs Sr (ppm). F) ΔFMQ vs.

(Eu/Eu*)/(Dy_N/Yb_N) as suggested by Tapia et al. (2025). Subscript *N* indicates chondrite-normalized values. Fertility parameters used in C, D, and E are suggested by Carrasco-Godoy et al. (2024). 276
Figure 6.9. Zircon fertility parameters for the Kırka-Afyon-Isparta district. A) Zircon (Eu/Eu*)/$Yb_N \times 10^4$ plotted against Ce/√(UxTi) in zircon. Shaded fields are after Loucks et al. (2024) and represent ranges for zircons from porphyry Cu ore-forming intrusions and from infertile arc igneous suites. B) $Dy_{(n)}$ vs. $Yb_{(n)}/Gd_{(n)}$. C) Eu/Eu* vs. P (ppm). D) Ce/Nd vs. Dy/Yb diagram. E) Eu/Eu* vs Sr (ppm). F) ΔFMQ vs. (Eu/Eu*)/(Dy_N/Yb_N) as suggested by Tapia et al. (2025). Subscript *N* indicates chondrite-normalized values. Fertility parameters used in C, D, and E are suggested by Carrasco-Godoy et al. (2024). 278
Figure 6.10. Zircon fertility parameters for the Kışladağ and Sayacık porphyry systems in Uşak. A) Zircon (Eu/Eu*)/$Yb_N \times 10^4$ plotted against Ce/√(UxTi) in zircon. Shaded fields are after Loucks et al. (2024) and represent ranges for zircons from porphyry Cu ore-forming intrusions and from infertile arc igneous suites. B) $Dy_{(n)}$ vs. $Yb_{(n)}/Gd_{(n)}$. C) Eu/Eu* vs. P (ppm). D) Ce/Nd vs. Dy/Yb diagram. E) Eu/Eu* vs Sr (ppm). F) ΔFMQ vs. (Eu/Eu*)/(Dy_N/Yb_N) as suggested by Tapia et al. (2025). Subscript *N* indicates chondrite-normalized values. Fertility parameters used in C, D, and E are suggested by Carrasco-Godoy et al. (2024). 280
Figure 6.11. Zircon fertility parameters for the Salihli Pluton. A) Zircon (Eu/Eu*)/$Yb_N \times 10^4$ plotted against Ce/√(UxTi) in zircon. Shaded fields are after Loucks et al. (2024) and represent ranges for zircons from porphyry Cu ore-forming intrusions and from infertile arc igneous suites. B) $Dy_{(n)}$ vs. $Yb_{(n)}/Gd_{(n)}$. C) Eu/Eu* vs. P (ppm). D) Ce/Nd vs. Dy/Yb diagram. E) Eu/Eu* vs Sr (ppm). F) ΔFMQ vs. (Eu/Eu*)/(Dy_N/Yb_N) as suggested by Tapia et al. (2025). Subscript *N* indicates chondrite-normalized values. Fertility parameters used in C, D, and E are suggested by Carrasco-Godoy et al. (2024). 283

Figure 6.12. Zircon fertility parameters for the Bodrum Peninsula. A) Zircon (Eu/Eu*)/$Yb_N \times 10^4$ plotted against Ce/√(UxTi) in zircon. Shaded fields are after Loucks et al. (2024) and represent ranges for zircons from porphyry Cu ore-forming intrusions and from infertile arc igneous suites. B) $Dy_{(n)}$ vs. $Yb_{(n)}/Gd_{(n)}$. C) Eu/Eu* vs. P (ppm). D) Ce/Nd vs. Dy/Yb diagram. E) Eu/Eu* vs Sr (ppm). F) ΔFMQ vs. (Eu/Eu*)/(Dy_N/Yb_N) as suggested by Tapia et al. (2025). Subscript *N* indicates chondrite-normalized values. Fertility parameters used in C, D, and E are suggested by Carrasco-Godoy et al. (2024). 285
Figure 6.13. Various fertility parameters used to identify porphyry mineralization. A) Zircon Eu/Eu* (>0.4). B) Zircon 1000x(Eu/Eu*)/Yb. (>2). C) Zircon ΔFMQ (>1). D) Apatite Eu/Eu* (>0.5). E) Whole-rock Sr/Y (>40). F) Whole-rock La/Yb (>20). The gray fields for the whole rock lithogeochemistry data indicates the adakite-like field (Defant and Drummond, 1990; Richards, 2011). 289

LIST OF ABBREVIATIONS

ABBREVIATIONS

AVC – Afyon Volcanic Complex

BVC – Bodrum Volcanic Complex

ICP‐MS – Inductively Coupled Plasma Mass Spectrometry

ICP-OES – Inductively Coupled Plasma Optical Emission Spectrometry

INAA – Instrumental Neutron Activation Analysis

KVC – Konya Volcanic Complex

LOI – Loss on Ignition

MASH – Melting Assimilation Storage Homogenization

PGE – Platinum Group Elements

SCLM – Subcontinental Lithospheric Mantle

SML – Subduction Modified Lithosphere

SVS – Sulutaş Volcanic Suite

TEMB – Tethyan-Eurasian Metallogenic Belt

WAVP – Western Anatolian Volcanic Province

CHAPTER 1

INTRODUCTION

Porphyry deposits significantly contribute to the production of various base and precious metals, mainly including Cu, Au, and Mo (Sinclair, 2007; Sillitoe, 2010) as well as many other important base and precious metals. Porphyry-type deposits are typically associated with intrusive bodies that are situated at shallow depths (an average of 2–5 km) within volcanic-plutonic complexes. These deposits can also be related to high/intermediate sulfidation epithermal and skarn/carbonate vein-type mineralizations in different sections of the same formation environment (Sillitoe, 2010). One of the most important factors for the development of these magmatic-hydrothermal deposits (especially porphyry-type ore deposits) is the physico-chemical properties of their source magmas. This is because the metals precipitated in porphyry and associated magmatic-hydrothermal systems are largely provided by the magma itself (Richards, 2011), and these mantle-derived magmas must be capable of transporting metals to the upper crustal depths. Mantle-derived magmas are typically enriched in siderophile and chalcophile metals compared to the crustal magmas, regardless of their tectonic setting. However, for metal transport from the mantle to the upper crust, magmas are required to have high water and volatile contents and they also should be oxidized (Ballard et al., 2002; Cooke et al., 2005; Sillitoe, 2010; Dilles et al., 2015; Lu et al., 2016; Loader et al., 2017). Such oxidized and volatile-rich magmas primarily develop in subduction zones where continental arcs are formed, or in collisional to post-collisional settings formed after major periods of subduction (Richards, 2009).

The geology of Anatolia has been significantly affected by the formation of the Tethys Ocean basins and the tectonic processes that caused their subsequent disappearance during the Alpine Orogeny. As a natural result of ocean opening and closure, the region has seen the development of arcs, back-arc-related to collisional/post-collisional magmatic products. These products are observed in regions such as the Eastern Pontides, Eastern and Central Taurides, Biga Peninsula, and Western Anatolia, which are also among the most important metallogenic regions in Türkiye. Therefore, Türkiye forms one of the most important and high-potential segments of the Tethyan-Eurasian Metallogenic Belt (TEMB; Jankovic, 1997) in terms of base and precious metal mineralizations. However, when examining these metallogenic regions, it is apparent that economic porphyries in Türkiye are noticably less common than epithermal and skarn/carbonate vein-type deposits. In addition, Türkiye also has fewer economic porphyry deposits compared to neighboring sectors of the TEMB such as Iran and Bulgaria. Among the economic porphyry mineralizations, the Kışladağ porphyry Au (Uşak), Cevizlidere porphyry Cu-Mo-Au (Tunceli), and Halilağa porphyry Cu-Au (Çanakkale) systems are the most prominent examples. Recent mine-site drilling activities have revealed the economic potential of the Çöpler intermediate-sulfidation epithermal system overlying a marginally economic porphyry Cu-Au system. Other notable porphyry deposits/prospects in Türkiye include the Tepeoba porphyry Mo (Balıkesir), Karakartal/Mavidere porphyry Cu-Au (Erzincan), and Ardala porphyry Cu-Mo-Au (Artvin) mineralizations.

In Anatolia, a widespread volcanism and plutonism developed during the Late Cenozoic period (Figure 1.1) due to back-arc opening and continent-continent collision processes, extending from the Central Taurides (the Kayseri-Konya transect) to the Aegean coast in Western Anatolia. Although the magmatic belt extending between these two regions appears to be continous along the E–W axis, the Late Cenozoic magmatism in Central Taurides and Western Anatolia has been

influenced by different tectonomagmatic processes. Consequently, the temporal-spatial evolution and character of magmatism in the two regions show some differences. Middle Miocene and younger magmatic activity in the Central Taurides sector mainly developed due to continent-continent collision and delamination, whereas in Western Anatolia, contemporaneous magmatism is related to back-arc opening and the gradual southward progression of the north-dipping Neotethys oceanic lithosphere throughout the Cenozoic (Keskin, 2003; Biryol et al., 2011; Cosentino et al., 2012; Schildgen et al., 2012; Jolivet et al., 2013; Delph et al., 2017; Uzel et al., 2020).

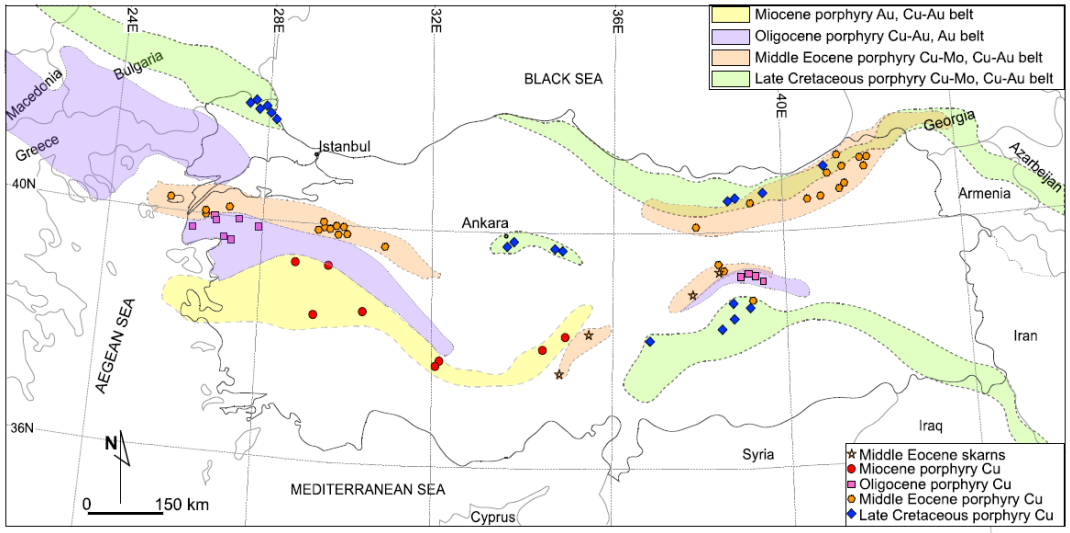


Figure 1.1. Porphyry deposits/occurrences in Türkiye and their relation with the metallogenic belt in western Tethyan-Eurasian metallogenic belt (Kuşcu et al., 2019).

Despite these fundamental tectonic differences, it is observed that suitable magmatic conditions for porphyry and associated epithermal-skarn/carbonate-vein type mineralization developed in both sectors of the magmatic belt, particularly during the Miocene (Kuşçu et al., 2019; Rabayrol et al., 2019a, 2019b; Rabayrol and Hart, 2021). However, it is also noted that not all magmatic phases with suitable magma chemistry resulted in fertile magmas (and thus economic mineralization).

Additionally, differences in the economic metal content are found between magmatic centers with similar chemistry.

In a small number of regional metallogenic studies conducted up until today (e.g., Kuşcu et al., 2019; Rabayrol et al., 2019a, 2019b; Rabayrol and Hart, 2021), the tectonomagmatic processes directly affecting porphyry-type mineralization in the Late Cenozoic belt of the Central Taurides–Western Anatolia have been outlined in broad terms. However, in these studies, where the magmatic evolution of the region is primarily examined in the light of geochronological and whole-rock geochemical data, it has not been possible to accurately or sufficiently resolve the productive magmas from other magmas based on specific whole-rock geochemical parameters (such as Sr/Y, La/Yb, Eu/Eu*, and Fe^{3+}/Fe^{2+} ratios) in terms of mineralization. These parameters are widely used to monitor whether mantle-derived magmas have reached the appropriate chemistry to develop porphyry-type mineralization, as they rise and undergo increased crustal interaction. In such cases where conventional whole-rock productivity parameters from the literature have proven to be ineffective in establishing the relationship between porphyry mineralization and magma chemistry, an important alternative is the use of geochemical/isotopic compositions of indicator minerals such as zircon, apatite, magnetite, and amphibole. This is because source magma characteristics such as volatile content and oxidation state cannot be accurately determined through lithogeochemical means once magmas are crystallized. On the other hand, indicator mineral chemistry combined by high-resolution geochronology are proven to be more powerful tools to understand these parameters that are crucial in terms of mineralization potential in magmatic-hydrothermal systems.

1.1 Review of Subduction and Post-subduction Magmatism

Andean- or Cordilleran-type arc magmatism develops where oceanic lithosphere subducts beneath the continental and/or accreted transitional lithosphere. Subduction magmatism involves dehydration of subducting oceanic lithosphere and subsequent metasomatism and partial melting of the asthenospheric mantle wedge. Following the Melting, Assimilation, Storage, Homogenization (MASH; Hildreth and Moorbath, 1988) processes, intermediate composition magmas may generate porphyry and epithermal deposits if conditions are satisfied. In complex arc settings, it is often challenging to attribute any given pluton and any associated mineral deposit to a particular subduction or collision event since the magmatism commonly continues following the collision, with a shift in the magmatic locus (Richards, 2011). In continent-continent zones or termination of subduction, on the other hand, timing of cessation of subduction magmatism can be identified with more certainty (Richards, 2011). Therefore, collisional orogens including parts of the Neo-Tethyan belt between SE Europe hosts some of the clearest examples of post-subduction-related magmatic-hyrdothermal deposits (Richards, 2011). Cessation of subduction prevents the addition of fresh supply of fluids, volatiles, and other slab-derived materials to the mantle wedge. Typical arc and post-subduction magmas display broadly similar geochemical signatures – that is that they are hydrous and generally oxidized, due to similar metasomatized source of subduction-related magmatism.

Typical I-type, calc-alkaline (mostly medium-K) arc magmas that were produced through MASH processes (Figure 1.2) in the lower crust commonly display relatively high Sr/Y and La/Yb ratios due to the suppression of early plagioclase crystallization and the preferential partitioning of Y and middle and heavy rare earth elements into amphibole and garnet (Green and Pearson, 1985; Richards, 2009, 2012). In collisional settings, arc contraction may lead to crustal thickening and delamination of the sub-continental lithospheric mantle (SCLM). Partial melting

occurs in the depressed lower crustal rocks as isotherms rebound or hot asthenospheric melts invade, which in turn results in generation of more felsic magmas with commonly calc-alkaline to mildly alkaline character carrying crustal radiogenic isotopic signatures (Richards, 2009). Amphibole and/or garnet that are present in the previously-metasomatized lower crustal source rocks may cause the high Sr/Y and La/Yb signatures of these magmas (Richards, 2009). This similarity may lead to misidentification of these rocks as adakites in some cases.

In post-subduction environments where earlier arc undergoes extension, upwelling of subduction-metasomatized asthenosphere and/or lithosphere may cause decompression melting to the generate mafic alkaline (shoshonitic or hawaiitic) magmas (Richards, 2009, 2011; Figure 1.3).

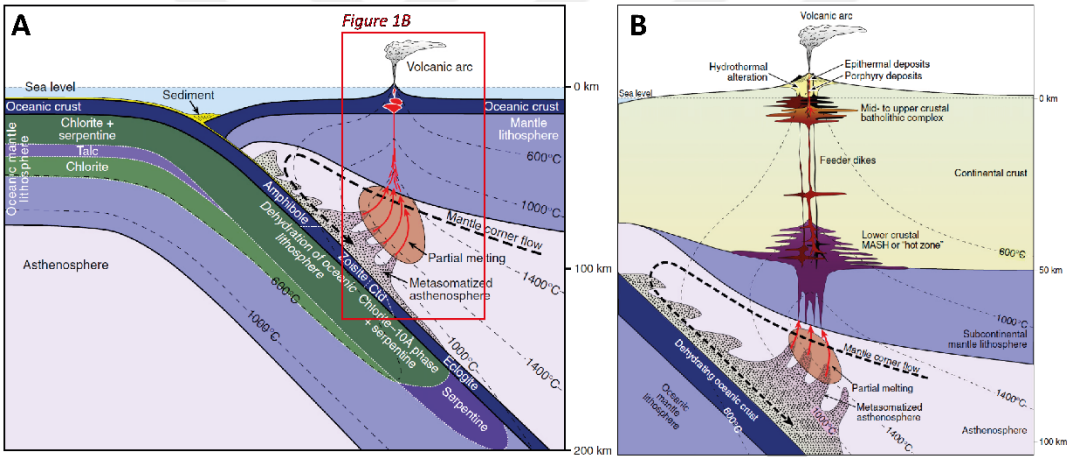


Figure 1.2. A) Structure and processes beneath an oceanic island arc where primary hydrous basaltic arc magmas are derived from partial melting of the metasomatized asthenospheric mantle wedge (Richards, 2011). B) Representation of a MASH zone development at the base of the crust where basaltic arc magmas pool at their level of neutral buoyancy, differentiate, and interact with crustal rocks and melts. Evolved, less dense, andesitic magmas rise into the mid-to-upper crust where they pool at their new level of neutral buoyancy to form batholithic complexes. Along with volcanic structures, porphyry and epithermal deposits may form at shallower levels above these batholithic complexes where exsolved magmatic fluids ascend, cool, and interact with near-surface upper crustal rocks (Richards, 2011).

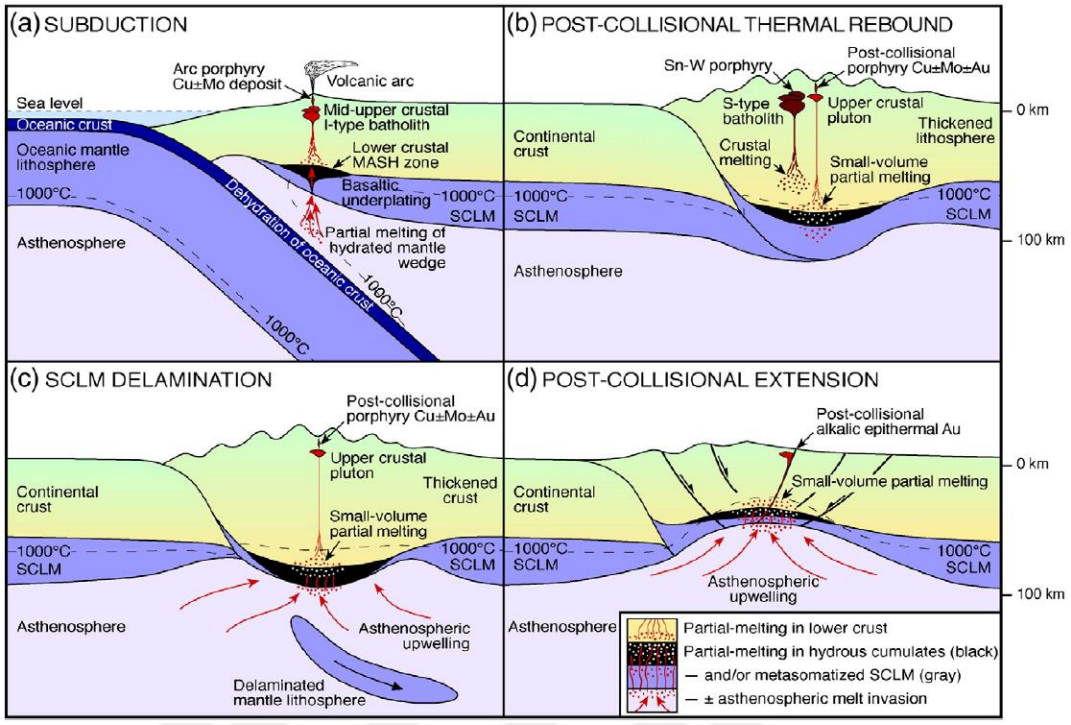


Figure 1.3. Schematic cross section of common subduction-related tectonic settings that can potentially host porphyry or other magmatic-hydrothermal systems (Richards, 2011). A) Generation of porphyry Cu±Mo as a product of typical arc magmatism. B) Crustal thickening and subsequent partial melting of SCLM due to post-collisional thermal rebound and formation of porphyry Cu±Mo±Au mineralization. C) Delamination of SCLM and partial melting of lower crust due to the upwelling of hot asthenospheric mantle and formation of post-collisional porphyry Cu±Mo±Au. D) Formation of post-collisional alkalic epithermal Au mineralization in post-collisional extensional settings. The extension causes the thinning of the continental crust and partial melting under the influence of heat added to the SCLM and continental crust, and the formation of vein-type deposits localized along the normal faults.

Post-subduction-related magmas in both collisional or extensional arcs segments are heavily sourced from subduction-modified (i.e., metasomatized) lithosphere and/or asthenosphere. Therefore, post-subduction magmas display many geochemical and isotopic similarities with the preceding arc magmatism. However, post-subduction processes are considered to be transient when compared to the steady-state subduction due to lower degrees of partial melting and lower magma volumes, thus,

magmas produced in this way will tend to be spatially isolated, and mildly alkaline in character (Hawkesworth et al., 1993; Pearce and Stern, 2006; Richards, 2011; Holwell et al., 2019).

Post-subduction-related magmas in both collisional or extensional arcs segments are heavily sourced from subduction-modified (i.e., metasomatized) lithosphere and/or asthenosphere. Therefore, post-subduction magmas display many geochemical and isotopic similarities with the preceding arc magmatism. However, post-subduction processes are considered to be transient when compared to the steady-state subduction due to lower degrees of partial melting and lower magma volumes, thus, magmas produced in this way will tend to be spatially isolated, and mildly alkaline in character (Hawkesworth et al., 1993; Pearce and Stern, 2006; Richards, 2011; Holwell et al., 2019).

Porphyry Cu ± Mo ± Au deposits in subduction-related arc settings are fundamentally linked to the generation and evolution of oxidized, hydrous magmas in supra-subduction zones. These magmas typically originate from partial melting of a subduction-metasomatized mantle wedge, producing basaltic melts that ascend and interact with the overlying crust (Sillitoe and Hedenquist, 2003; Richards, 2009). During ascent, extensive magma–crust interaction, coupled with fractional crystallization, yields intermediate to felsic calc-alkaline compositions characterized by elevated oxidation states—commonly ~2 log units above the fayalite–magnetite–quartz buffer (ΔFMQ)—and high water contents (≥4 wt.% H_2O) (Richards, 2011). These conditions are critical for ore formation since the high oxidation state suppresses early sulfide saturation, preventing premature sequestration of chalcophile and siderophile metals (e.g., Cu, Au, Mo) into cumulate phases, while the high water content promotes fluid saturation in the upper crust, enabling efficient partitioning of metals into exsolved magmatic–hydrothermal fluids (Candela and Holland, 1984; Hamlyn et al., 1985). As a result, first-stage arc magmatism

efficiently generates Cu-rich, relatively Au-poor porphyry systems, leaving behind a hydrous cumulate and lithospheric mantle residue enriched in residual sulfides.

These deep cumulate and lithospheric mantle zones act as long-term metal reservoirs. Over time, tectonic changes such as subduction termination, lithospheric thickening, slab break-off, mantle lithosphere delamination, or post-collisional extension can trigger renewed melting of these subduction-modified lithospheric sources (Richards, 2009; Park et al., 2021). When such fertile, hydrous residues are re-melted, the residual sulfide phases (commonly enriched in Au and platinum-group elements) can be dissolved back into the silicate melt, generating magmas with elevated Au/Cu ratios (Solomon, 1990; Richards, 2005). These post-subduction melts often display mildly alkaline affinities, are less sulfur-rich than arc-derived counterparts, and tend to form Au-rich porphyry Cu–Au and low-sulfidation epithermal Au deposits.

The transition from first-stage arc magmatism to second-stage post-subduction magmatism therefore represents a critical shift in metallogenic potential. While arc magmatism primarily contributes large-scale Cu endowment through direct metal flux from mantle-derived melts, post-subduction remelting mobilizes metals from pre-enriched lithospheric sources, resulting in distinctive Au-rich signatures. Understanding this dual-stage metal transfer process is essential for accurately evaluating mineral prospectivity in regions with complex arc and post-arc tectonomagmatic histories.

1.2 Porphyry Deposits

Porphyry deposits are considered as one of the most significant sources for base and precious metals, especially of Cu, Mo, and Au. Such deposits are genetically linked

to magmatism generated in convergent tectonic settings, more specifically, arc, back-arc, and post-subduction environments (Richards, 2003, 2014; Sillitoe, 2010).

Porphyry deposits have very complex formation processes that start with magma production in the mantle, followed by magma ascent and differentiation within the crust, ultimately leading to fluid exsolution and ore formation in shallow crustal depths (Richards, 2003, 2005, and 2011; Wilkinson, 2013; Park et al., 2021). These successive processes have to be formed one after the other, and in the event of any failure in link in this chain, porphyry mineralization either does not occur at all or the ores will be subeconomic.

The formation of porphyry-type deposits, which is directly related to subduction tectonomagmatism, begins with partial melting of the subducting oceanic lithosphere and metasomatism of the peridotite-rich mantle wedge through addition of volatiles and fluid-mobile elements (i.e., large ion lithophile elements; LILE), forming primary arc basalts (Tatsumi et al., 1986; Arculus, 1994). Basaltic magmas rise in the mantle wedge due to density difference and initially accumulate in the MASH zone at the base of the crust (Hildreth and Moorbath, 1988) then migrate into lower and middle crustal levels and eventually make their way into shallow crustal depths (Richards, 2005). Afterwards, depending on the magma chamber processes, mineralization occurs when volatiles and metals separate from the melt and precipitate through fluid phases (Figure 1.4).

The first stage of all these processes – namely, magma production in a subduction environment – is controlled by tectonic processes such as the stress conditions prevailing in the subduction environment, the duration of the subduction and the subduction angle of the subducting plate (Tosdal and Richards, 2001; Sillitoe, 2010; Loucks, 2021). However, when we look at the orogenic belts in the world, it is noteworthy that a very small amount of porphyry mineralization is observed compared to the high volume of arc magmas produced in environments where all

these variables develop appropriately. It is claimed that this scarcity in porphyry formation is due to the conditions that develop during the differentiation of magmas with suitable chemistry produced in the mantle during the crustal transition (Chiaradia et al., 2012; Wilkinson, 2013; Loucks, 2014 and 2021; Chiaradia and Caricchi, 2017; Lee and Tang, 2019).

Two of the most important characteristics of arc magmas that make them potentially productive for porphyry mineralization are their oxidized and hydrous nature as well as their high volatile budgets (Lee and Tang, 2019; Meng et al., 2021; Richards, 2021; Grondahl and Zajacz, 2022). While the oxidation levels of mid-ocean ridge basalts are in the range of $-1<\Delta FMQ\ buffer<+1$, oxygen fugacity of arc magmas are two log units above ΔFMQ buffer (Ballhaus, 1993; Brandon and Draper, 1996; Kelley and Cottrell, 2009; Cottrell and Kelley, 2011). The high oxidation level of arc magmas ensures that sulfur remains in oxidizing form up to the upper crust levels and thus, sulfur and especially chalcophile-siderophile metals (such as Fe, Cu, Au, platinum group elements) can be transported together in arc magmas without being lost to sulfide species (Richards, 2009 and 2011; Wilkinson, 2013). Since porphyry systems are characterized by circulation of large volumes of hydrothermal fluids, the high H_2O contents for their parental arc magmas is a must (Cline and Bodnar, 1991; Richards, 2005 and 2011).

Early petrogenetic models argue that the high fO_2 and H_2O levels observed in arc magmas are the result of mantle metasomatism caused by volatiles released from the subducting oceanic lithosphere (Davidson, 1996; Noll et al., 1996; de Hoog et al., 2001). However, since similar fO_2 values are observed in the primary arc and oceanic ridge basalts, it is claimed that arc magmas acquired their critical properties for porphyry mineralization through magmatic differentiation during their passage through the lower-middle crust (Lee et al., 2005; Chiaradia and Caricchi, 2017). Similarly, recent studies have suggested that the thickness of the crust, through which

magmas rise to the continental arc environment, directly controls the porphyry potential of arc magmas (Chiaradia et al., 2012; Lee and Tang, 2020; Tang et al., 2020).

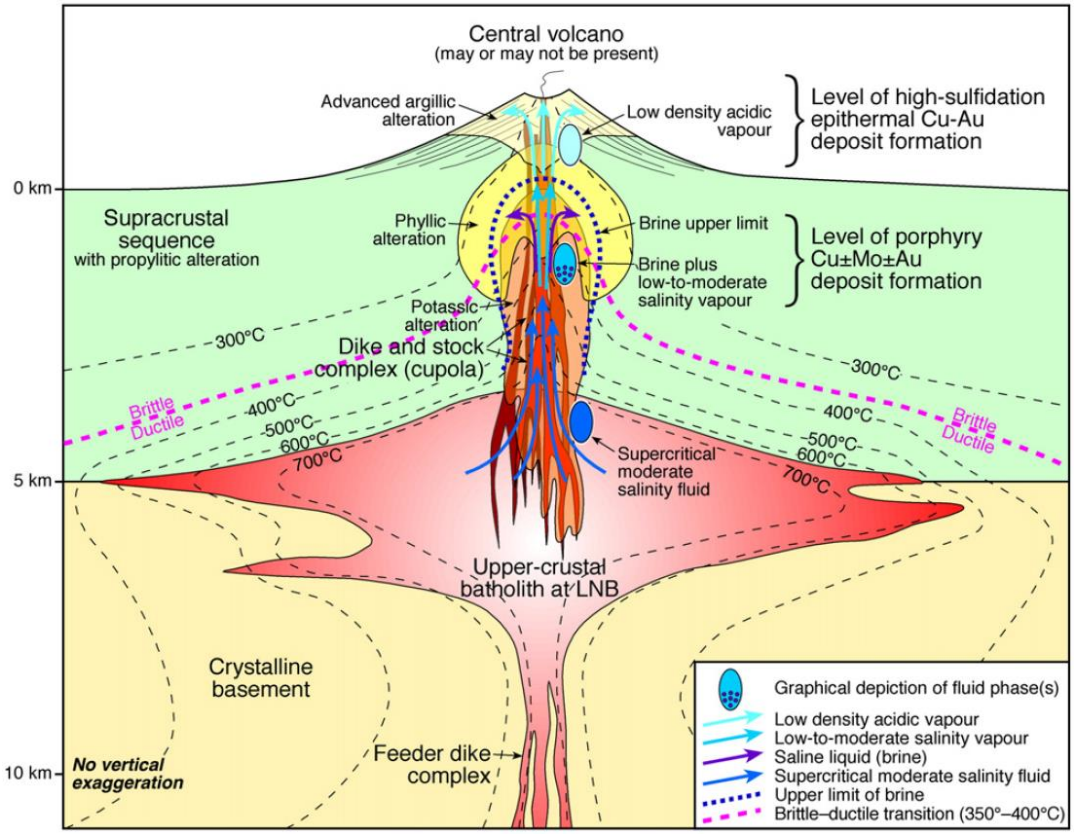


Figure 1.4. Schematic cross-section of batholih-cupola volcanic system with associated porphyry Cu±Au and linked high sulfidation Cu-Au epithermal deposits (Richards, 2011).

In arc environments where the continental crust is thick (>40 km), magmas differentiate to higher oxidation levels due to long-term (>2 m.y.; Annen et al., 2006, Chiaradia and Caricchi, 2017) and intense fractional crystallization at lower-mid crustal levels (Chiaradia, 2014; Lee et al., 2014; Chin et al., 2018). Higher degrees of fractional crystallization of arc magmas through interaction with thick continental crust help them attain optimal features (i.e. high fO_2 and H_2O content) especially for

Cu-Mo-rich porphyry mineralization (Figure 1.5). During the differentiation of typical calc-alkaline, I-type magmas, which are thought to be associated with porphyry Cu systems, early amphibole and Fe-oxide or garnet fractionation occur in the lower crustal levels, while plagioclase crystallization is suppressed (Zimmer et al., 2010; Richards, 2011b; Loucks, 2014). In addition, garnet fractionation in the lower crust in particular is thought to result in depletion of ferric iron in the magma, thereby leading to the typical calc-alkaline fractionation trends observed in arc magmas (Tang et al., 2018 and 2019; Lee and Tang, 2020). The remaining iron in the magma oxidizes gradually, while dissolved sulfide oxidizes into sulfate. Consequently, porphyry fertile igneous suites generally display high Sr/Y and La/Yb and Fe^{3+}/Fe^{2+} ratios (Kay and Mpodozis, 2001; Richards and Kerrich, 2007; Chiaradia et al., 2012; Richards, 2011b; Richards et al., 2012; Lee and Tang, 2020). The close association between high Sr/Y and La/Yb igneous rocks with porphyry systems has been attributed by some researchers to a genetic link between adakites and porphry mineralization (Thieblemont et al., 1997; Sajona and Maury, 1998; Oyarzun et al., 2001).

In addition to high oxidation levels and water contents of arc magmas, another factor that is thought to play an active role in the formation of porphyry systems is the degree of sulfide saturation of magmas (Wilkinson, 2013). Some researchers have suggested that silicate magmas attained sulfide saturation at some point during their evolution, based on the magmatic sulfide phase inclusions observed in the phenocrystal phases of lower crustal cumulates and arc volcanics (Hattori, 1997; Halter et al., 2002; Stavast et al., 2006; Wilkinson, 2013). As magmas begin to differentiate deeper in regions with thick continental crust, they reach sulfide saturation early (i.e., before reaching upper crustal levels; Park et al., 2021). Chalcophile and siderophile metals in magma tend to enter the magmatic sulfide phase that separates from the silicate magma. Therefore, it has been suggested that early and deep sulfide saturation of arc magmas will cause loss of primarily Au and

platinum group elements (PGE), and to a lesser extent copper, to deep crystallized magmas, thus preventing these metals from reaching the upper crust level (Figure 1.5; Park et al., 2019; Bai et al., 2020). However, some researchers suggest that even if arc magmas, which differentiate within the thick continental crust, reach sulfide saturation, at least some of the copper and molybdenum will remain in the silicate magma, and thus the early sulfide saturation has limited effect on the formation of porphyry Cu-Mo-Au and associated high-sulfidation Au-Cu mineralizations (Audetat and Pettke, 2006; Simon et al., 2008).

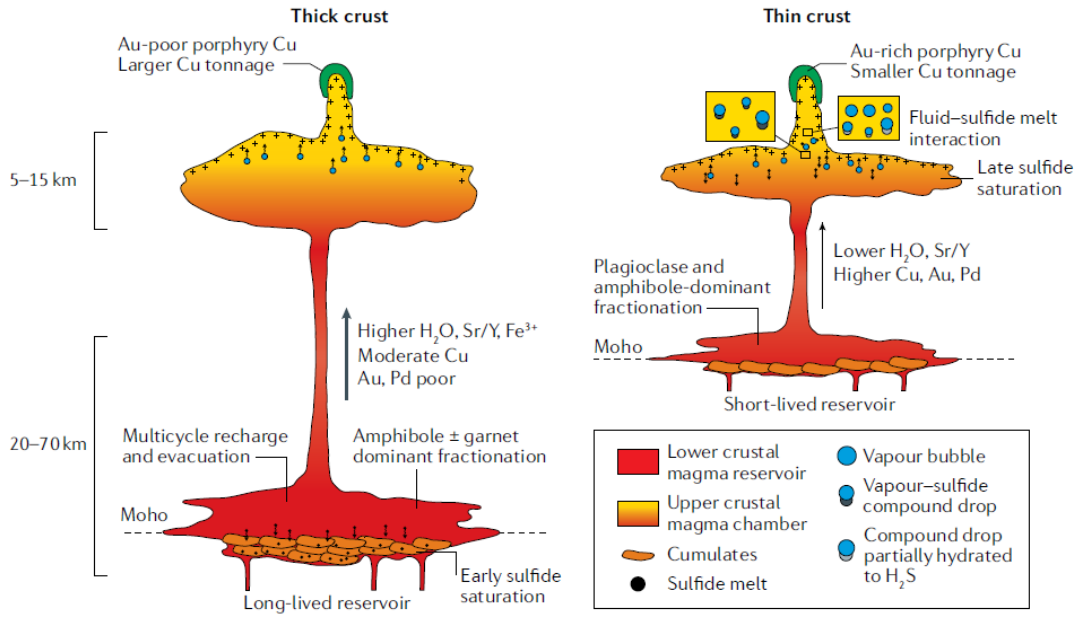


Figure 1.5. Schematic model illustrating the contrasting magmatic and hydrothermal evolution of porphyry Cu systems in thick vs. thin crust. Thick crust settings promote early sulfide saturation, Fe depletion, and prolonged hydrothermal activity, resulting in large, Au-poor deposits. In contrast, thin crust systems delay sulfide saturation, enhancing Cu–Au fertility but form smaller, Au-rich deposits due to shorter-lived magmatic-hydrothermal systems and shallow vapor–sulfide melt interaction. (Park et al., 2021).

In contrary to the above, porphyry mineralization may also develop in post-collisional environments that commonly develop during widespread extension

following Andean-type arc magmatism, usually due to delamination or steepening/break-of the subducting lithosphere. Although crustal thicknesses are limited in such orogenic belts (<40 km, generally <25 km), the nature of magmatism and associated mineralization may follow a different course compared to typical continental arc environments (Richards, 2009 and 2011a). Compared to typical Andean-type arc environments where the fluids cause the melting, melting is observed due to the rise of the hot asthenosphere in back-arc, collisional and post-collision environments (Davies and von Blanckenburg, 1995). Metasomatised early arc magmatism in the lower crustal region are exposed to remelting thus, magmas produces in this process display typical arc characteristic in terms of mineralogy and geochemistry (Harris et al., 1986). However, the degree of partial melting is less and magmas are generally of high K calc-alkaline or alkaline composition (Harris et al., 1986; Davies and von Blanckenburg, 1995; Jiang et al., 2006). During the remelting of the lower crust, magmatic sulfide phases that reached saturation and precipitated in this region due to previous arc magmatism may also melt and be transported to magma chambers at shallow levels. Porphyry Au ± Cu ± PGE systems are predominantly derived from such magmas, since these phases are particularly rich in gold (and in copper to an extent) and sulfide saturation is achieved relatively later (i.e., at upper crustal levels) in the thin continental crust after the collision (Richards, 2009 and 2011a; Park et al., 2019). In addition, since the magma composition is relatively alkaline and the Au solubility is higher in alkaline (especially potassic and ultrapotassic) magmas (Rock and Groves, 1988; Richards, 2009; Zajacz et al., 2010), porphyry type deposits with high gold content are generally found after this collision and they are associated with back-arc tectonic environments.

Magmatic differentiation is limited in post-collisional or back-arc settings observed along tensional or extentional deep fault zones since the crustal thickness is thinner. Therefore, unlike typical porphyry Cu systems developed in arc environments, source intrusion rocks present lower Sr/Y and La/Yb ratios (Chiaradia, 2014;

Richards, 2015; Figure 1.5). However, since the origin of the source magmas is early stage arc magmatism, their oxidation levels and water contents are high just like arc magmas (Richards, 2011b).

1.2.1 Effects of Magma Oxidation Level, Water Content and Sulfide Saturation on Mineral Chemistry

Oxidation levels and water and volatile (S, Cl, Fl) contents of magmas can be monitored by various mineralogical and geochemical parameters. Among the parameters based on major-trace element and REE compositions of magmatic systems, the ratios of whole-rock Sr/Y, La/Yb, V/Sc, Eu_N/Eu_N* and Fe^{3+}/Fe^{2+} are useful to obtain a general idea to understand the oxidation level and water content at the first stage (Richards, 2011b; Richards et al., 2012; Loucks, 2014). However, whole-rock compositions are prone to be affected by secondary processes such as alteration or metamorphism. Detailed mineral chemistry analyses and, if possible, accompanying dating studies are required to precisely determine these parameters and their changes in a multi-phase magmatic system. The mineral phases that are sensitive to magma redox conditions and water/volatile contents and frequently found in average intermediate-felsic rocks are zircon, apatite, amphibole and Fe-Ti oxides (magnetite-ilmenite).

Zircon: Zircon, which is a common accessory phase in moderate-acidic igneous rocks, is a magma fO_2 sensitive mineral (Burnham and Berry, 2012). Although REEs are usually +2 or +3 valence in magma, in cases where the oxidation level is high, especially Ce and Eu switch to +4 valence (Ballard et al., 2002; Hoskin and Schaltegger, 2003) and can relocate Zr, which is also +4 valence, in zircon. High Ce^{4+}/Ce^{3+} and Eu_N/Eu_N* ratios are observed in oxidized magmas due to Ce^{4+} and Eu^{4+} differentiation into zircon (Ballard et al., 2002; Dilles et al., 2015). Negative Eu anomaly disappears with increasing oxidation level (Hoskin and Schaltegger, 2003).

In addition, when the trace element composition of zircon, which can be precisely dated by in-situ methods, is evaluated together with the zircon Hf isotope composition ($^{176}Hf/^{177}Hf$), especially in regional metallogenic studies, detailed information on the origin of the magmatic system that source the mineralization, the history of crustal differentiation and mineralization potential can be obtained. Because magmas produced in subduction zones may be contributed by varying amounts from many different sources such as 1) the subducting oceanic lithosphere, 2) the ocean floor sediments added to the mantle from the arc trench, 3) the mantle wedge, and 4) the continental/oceanic crust in the upper plate (Ringwood, 1977; Gill, 1981; Davidson, 1996). In addition, metasomatized lower crustal melting or insertions from asthenospheric sources may occur during post-collisional magmatism. While Hf, which is in the high field strength element group such as Zr, behaves incompatible with phases such as garnet and spinel during mantle melting (Hawkesworth and Kemp, 2006), Lu, a REE, shows higher compatibility with the mantle than Hf during mantle melting. Therefore, the continental crust has relatively low Lu and higher Hf content (Patchett et al., 1984; Kinny and Maas, 2003; Hawkesworth and Kemp, 2006). Thus, the continental crust contribution has non-radiogenic ratios of $^{176}Hf/^{177}Hf$, while the depleted mantle is characterized by a radiogenic ratio of $^{176}Hf/^{177}Hf$ (Patchett et al., 1984). Since the upper mantle is more depleted in terms of Hf content than Lu, mantle-derived magmas have a higher Lu/Hf ratio than CHUR and therefore radiogenic (positive εHf) values. On the contrary, magmas derived from continental crust with high Hf content and low Lu/Hf ratio show less radiogenic (negative εHf) values (Kinny and Maas, 2003). Thus, by using zircon Hf isotope compositions, mantle, crust or mixed mantle-crust contributions in the formation of granitoid rocks can be determined.

Apatite: Apatite, another common accessory mineral of igneous rocks with intermediate-acidic composition, is sensitive to magma oxidation level (Belousova et al., 2002; Pan and Fleet, 2002) and can accurately record the volatile (especially

Cl, F and S) amounts carried by apatite magmas. (Piccoli and Candela, 1994; Streck and Dilles, 1998; Parat et al., 2002). While negative Eu and Ce anomalies are observed in reducing magmas, the negative anomaly disappears as the oxidation level increases (Belousova et al., 2002; Pan et al., 2016; Bromiley et al., 2021).

In studies examining the formation conditions of porphyry deposits, apatite is widely used to monitor the S and halogen (Cl, F) budgets of magmatism. Among these, S is one of the building blocks of porphyry systems since almost all ore minerals in the porphyry Cu-Mo-Au deposits are sulfide minerals. In addition, sulfate phases such as anhydrite and alunite are abundant in different porphyry alteration zones (Seedorff et al., 2005; Sillitoe, 2010). The behavior of sulfur, which is one of the rare elements that can be found in many different valences (from reducing S^{2-} to oxidizing S^{+6}) in nature, depends on oxidation level (Jugo et al., 2010). The amount of sulfur (as SO_3) in apatite, which is in the form of S^{+6}, increases with the oxidation level and the amount of sulfur present in the environment (Peng et al., 1997; Parat and Holtz, 2005; Boyce et al., 2010; Parat et al., 2011; Webster and Piccoli, 2015; Zhu et al., 2018).

During the formation of porphyry mineralization in the upper crustal levels, magmatic boiling occurs after magmas reach volatile saturation. Meanwhile, metals such as Cu and Fe combine with Cl and form chloride complexes, which are evacuated from magma by fluids with high salinity and transported to mineralization zones. Therefore, high magmatic Cl content is critical for Cu transition from magma to hydrothermal fluid, with efficient decomposition of water-rich magmas at lower-mid crustal levels (Tattich et al., 2021). The Cl and F amounts of magmas and the origins of these halogens can be determined by apatite analysis (Piccoli and Candela, 1994). Sources of mineralization from different intrusion phases found in most of the largest porphyry systems in the world appear to have relatively high S and Cl contents. In many economic porphyry deposits, apatites in the ore bearing source

intrusions have higher S and Cl contents than barren intrusions (i.e. Chelle-Michou and Chiaradia, 2017; Zhu et al., 2018; Xing et al., 2021).

In the Gangdese Batholith (Tibet), which hosts many large and medium-sized porphyry systems, it has been revealed that the highest $S_{apatite}$ compositions are associated with intrusions that host porphyry mineralization, the source magmas reach high oxidation levels by passing through the thick continental crust, and because of that a significant amount of sulfur is transported into the upper crust as sulfate that is dissolved in the magma (Tang et al., 2020). In addition, the observation of S and Cl zoning along the lines from the center to the periphery on single apatite crystals indicates the increasing $SO_{2(g)}$ gas output (degassing) in the volcano-plutonic environment (Dilles et al., 2015; Richards et al., 2017; Tattich et al., 2021). The rapid separation of SO_2 from magma to volcanic levels is one of the most important mechanisms in the formation of high-sulfidation epithermal Au-Cu deposits associated with porphyry intrusions.

Amphibole: The high-water level (approximately 2–6% by mass) of primary basalts in oxidized arc magmas is ideal for porphyry mineralization (Cline and Bodnar, 1991; Chelle-Michou et al., 2017; Chiaradia and Caricchi, 2017; Du and Audetat, 2020; Lee and Tang, 2020). The presence of amphibole phenocrysts in intermediate-felsic magmatic systems indicates that the magmatic water content is at least 4% by mass (Burnham, 1979; Rutherford and Devine, 1988; Ridolfi et al., 2010). Petrological models suggested that the optimum magma water content should be >6% by mass for porphyry mineralization (Chiaradia, 2020). The stability of amphibole in magma is controlled by water content and magma oxidation level (Sisson and Grove, 1993). Therefore, amphibole compositions are widely used in petrogenetic studies to determine magma oxidation level, temperature and pressure conditions at which crystallization occurs, and magma water content (Ridolfi et al., 2010; Zhang et al., 2012; Mutch et al., 2016).

In studies on the chemistry of amphiboles in porphyry systems, Wang et al. (2014) revealed that, following the Paleocene-Eocene magmatism, which represents the last phase of subduction along the Gangdese Belt, the magmatism that took place in the post-collisional phase in Miocene was relatively water rich and oxidized. It has also been suggested that amphibole phenocrysts formed from source magmas in classical porphyry regions located along the Andes Belt in South America and the Rocky Mountains in North America have relatively high water and Cl amounts (Chambefort et al., 2013; Chelle-Michou and Chiaradia, 2017; Zhu et al., 2018).

Magnetite-Ilmenite: In rocks derived from oxidized arc and post-collisional magmas, magnetite is observed as microphenocrysts. The main oxide phase, which has a more reducing chemistry and crystallizes from relatively "dry" magmas, is generally ilmenite and magnetite is not observed in this type of rocks. In plutonic and sub-volcanic units prone to porphyry mineralization, ilmenite is often found (but in relatively small amounts) as a separate phase or separated by exsolution during cooling. If magnetite and ilmenite microphenocrysts are found in the same rock as different crystals (that is, they do not show intergrowth or exsolution), the magma oxidation level can be expressed according to the fayalite-magnetite-quartz buffer over their main element oxide compositions (Buddington and Lindsley, 1964; Ghiorso and Sack, 1991; Ghiorso and Evans, 2008).

Sulfide Saturation: In order to determine whether sulfide saturation, which is one of the important factors affecting the porphyry mineralization potential, occurs in a magmatic system, petrographic examination and subsequent geochemical analyzes can be applied. Petrographic studies are carried out to detect magmatic sulfide phases in fresh or slightly altered igneous rock samples. However, since magmatic sulfide phases are found as very fine-grained (<50 micron) inclusions in silicate or oxide minerals, especially in rocks with intermediate-felsic composition, electron microscopy or electron microprobe investigations can be applied to detect them. On

the other hand, whole-rock platinum group element (PGE; Pt, Pd, Rh, Ir, Re and Os) compositions are used to monitor the chalcophile and siderophile element productivity and sulfide saturation levels of magmas. The main reasons for this are that PGEs have a much higher dissociation coefficient to immiscible sulfide phases than other chalcophile and siderophile metals (Mungall and Brenan, 2014) and that immobile PGEs are less affected by hydrothermal alteration and deformation than other chalcophile and siderophile metals. (Crocket, 2000). The ratios of PGEs, especially Pd and Pt to each other and to MgO, vary according to the degree of sulfide saturation (Cocker et al., 2016; Park et al., 2019). It is because Pd behaves incompatible whereas Pt behaves compatible before the magma reaches sulfide saturation and the Pd/Pt ratio starts to decrease since Pd is more chalcophile than Pt (Park et al., 2016; Hao et al., 2017). Park et al. (2018) were able to separate barren magmas from porphyry Cu and porphyry Au-Cu systems depending on the degree of sulfide saturation with the help of these parameters.

1.3 Magmatism and Metallogeny of the Western Anatolia and Central Taurides

Since Anatolia is part of the Alpine-Himalayan Orogenic Belt, the Mediterranean belt contains important examples of post-collisional and post-arc magmatism (i.e. Lustrino and Wilson, 2007). The temporal and spatial distribution of the aforementioned magmatic activities is mainly related to the geodynamic factors related to the gradual subduction of branches belonging to the Tethys Ocean in the African-Eurasian convergence zone during the Late Mesozoic-Cenozoic periods (Şengör and Yılmaz, 1981; Lustrino and Wilson, 2007).

Although the Late Cenozoic magmatism in Western Anatolia and Central Taurides, which is the focus of this study (Figure 1.6), shows some similarities in terms of temporal and magmatic products, it basically emerged as a result of different

geodynamic processes during the closure of the Southern Neotethys. The westward escape of the Anatolian Plate during the Arabian Peninsula–Eurasian convergence in Eastern Anatolia, the separation of the Southern Neotethys lithosphere (subducting Aegean/Hellenic, Cyprus, and Arabian plates) and their different movements play the main role in this (i.e. Facenna et al., 2006; Le Pichon and Kremeer, 2010; van Hinsbergen et al., 2010; Biryol et al., 2011).

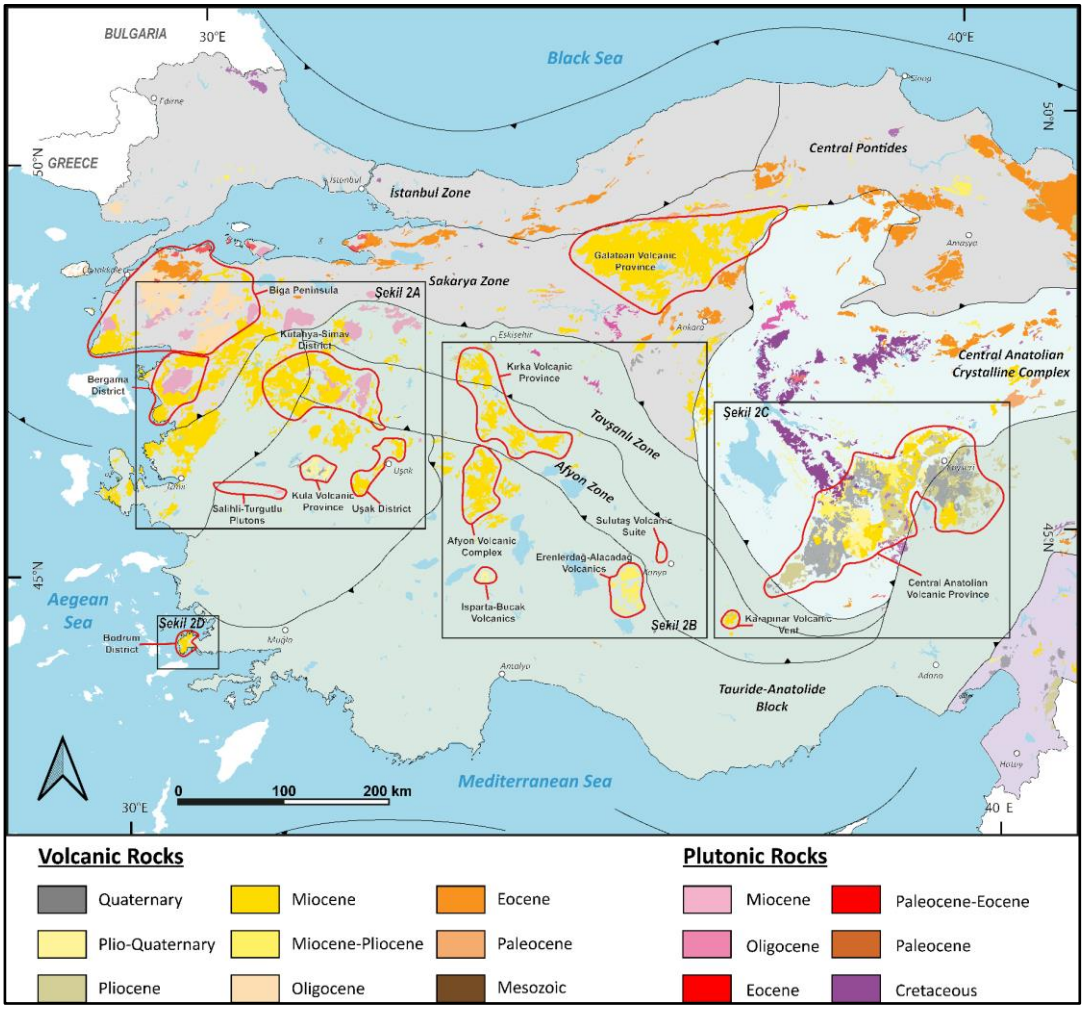


Figure 1.6. Simplified map of Central Taurides and Western Anatolia showing the distribution of significant magmatic domains.

One of the most widely distributed areas of Late Cenozoic post-collisional volcanism in Anatolia is the Western Anatolian Volcanic Province (WAVP). The geological-geodynamic evolution of the WAVP is mainly controlled by the post-collisional extensional tectonic dynamics that have affected Western Anatolia since the Late Paleocene, following the collision of the Pontide-Anatolide/Tauride continental blocks (Dilek and Altunkaynak, 2010).

Discussions on the mechanisms of stress dynamics triggering the formation of WAVP are still up-to-date and the main hypotheses regarding these mechanisms are as follows; (i) the westward escape of the Anatolian Plate (McKenzie, 1978) following the collision of the Arabian-Eurasian microcontinents along the Bitlis-Zagros subduction zone in eastern Anatolia; (ii) gravitational collapse of thickened crust (Dewey, 1988; Hetzel et al., 1995; Ersoy et al., 2010); (iii) back-arc extension due to the regression of the northward-plunging African oceanic lithosphere (Jackson and McKenzie, 1988; Kreemer et al., 2003) and (iv) the melting due to the uplift of the hot asthenosphere as a result of the slab break-off of the oceanic lithosphere subducting under the Western Anatolia (Agostini et al., 2007; Dilek and Altunkaynak, 2009; Prelevic et al., 2010).

Among these, models which have been more accepted in recent years include progressive migration of Late Cenozoic magmatism from north to south progressively due to combined effects of back-arc extension due to retreat of subducting lithosphere towards south and slab tear at the edge of subducting lithosphere (van Hinsbergen et al., 2010; Prelevic et al., 2012; Palmer et al., 2019). Depending on these mechanisms, in the Oligo-Miocene period, in the south of the İzmir-Ankara-Erzincan Subduction Zone (and the Biga Peninsula), graben development, core complex outcropping and magmatism were observed with normal faulting in the Menderes Massif. There are two different views on the extensional tectonism prevailing in the region. The first opinion is that tectonism is continuous

and uninterrupted since Oligo-Miocene (Jolivet et al., 2013), and the latter is that the region has experienced two different phases (Bozkurt, 2003; Gessner et al., 2013; Uzel et al., 2015). However, the main point that is common between these two views and has metallogenic importance is that regional magmatism and associated Au-Cu mineralizations generally occur along graben-horst structures developed by tension (Kuşcu et al., 2019; Rabayrol and Hart, 2021).

In summary, in many studies carried out in WAVP, the tectonomagmatic evolution of the region and especially the temporal variation of magmatism along the structural lines due to tensional tectonism have been revealed by whole-rock geochemistry, mineral chemistry and accompanying isotope geochemistry (Sr-Nd-Pb) data. Accordingly, while the Early-Middle Miocene high-K calc-alkaline magmatism display typical arc/back-arc chemistry produced in the subduction environment, it is observed that asthenospheric contribution gradually increased whereas the effect of lithospheric contribution and subduction-related magmatism is decreased since the Late Miocene.

The Central Taurides Late Cenozoic magmatism is widely observed along the line extending between Konya-Aksaray-Niğde-Nevşehir-Kayseri and in the region including the Cappadocia Volcanic Provence just to the north. Unlike WAVP, it is developed due to collision and post-collision processes, rather than back-arc extension. One of the main reasons for the difference is the delamination of the lower crust below the Cyprus lithosphere and Central Anatolia into the mantle, which is thought to have occurred in the east of slab-tear below the area between the Kırka-Afyon-Isparta and Konya due to different rates in the Tauride-Anatolide–Pontide convergence (Göğüş et al., 2017; Reid et al., 2017).

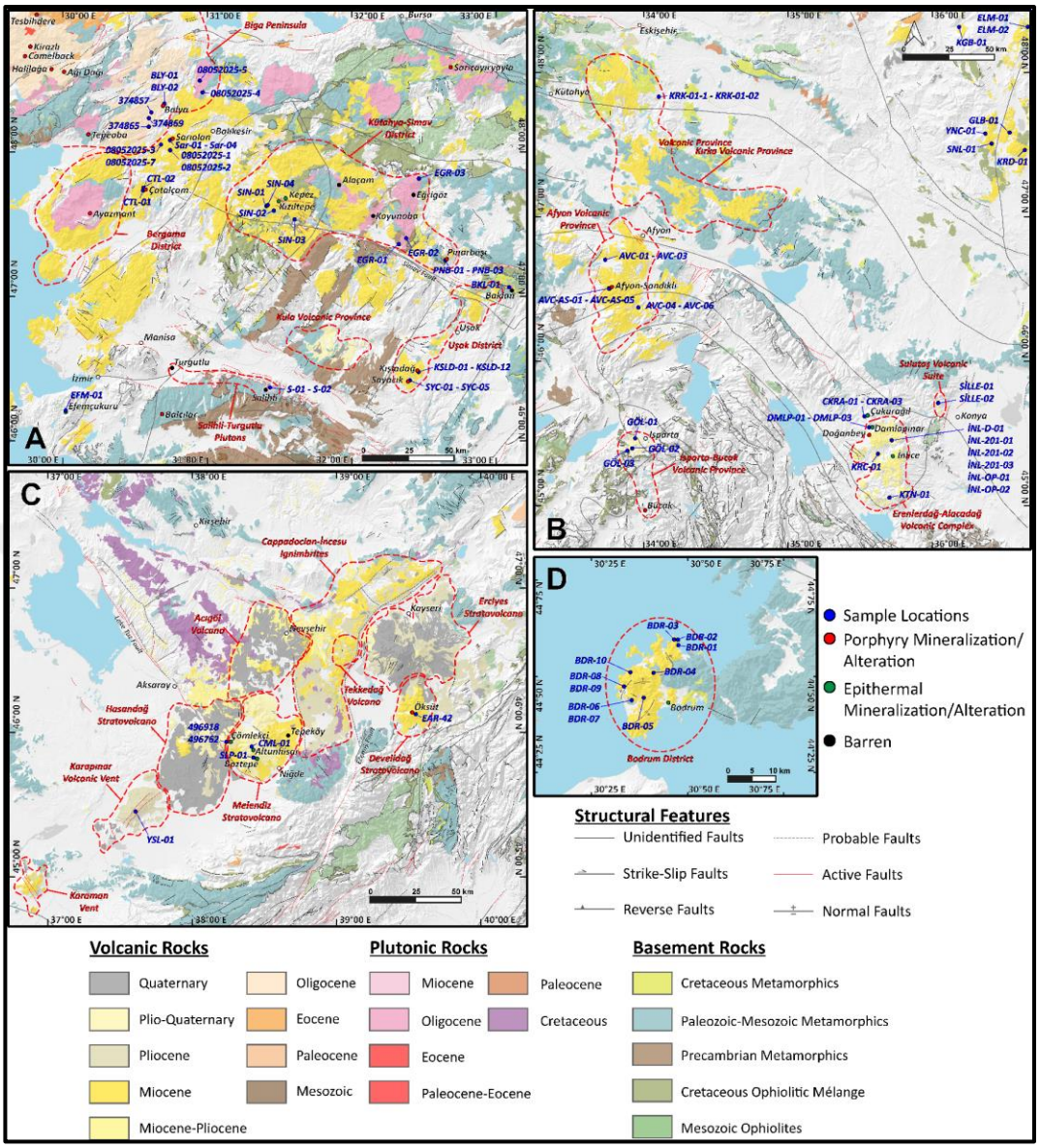


Figure 1.7. Distribution of Late Cenozoic magmatic districts and related mineral occurrences/deposits in A) Western Anatolia, B) Kırka-Afyon-Isparta region and Konya Volcanic Complex, C) Central Taurides, and D) Bodrum Peninsula. Sample locations are also included. Distribution of magmatic units and structural features are from MTA (2002).

Late Cenozoic magmatism in the Central Taurides began in the Early–Middle Miocene (20–12 Ma) following the closure of the Southern Neotethys and the

collision of the Tauride-Anatolide Block and the Arabian Peninsula (Robertson et al., 2007; Okay et al., 2010). Subsequent volcanic activity started in the Late Miocene (~11 Ma), right after the decrease in the rate of African-Eurasian convergence, with the transition from compressional to extensional tectonism in the region (Delph et al., 2017). This magmatic phase has continued until today, except for very short periods of quiescence. However, periods of increased magmatic productivity are generally restricted to 9–8 Ma and 7–5 Ma (Aydar et al., 2012). Starting from about 8 Ma, the Central Taurides experienced a major uplift of ≥2 km, with the effect of the lithospheric delamination and mantle upwelling (Cosentino et al., 2012, Schildgen et al., 2012).

The magmatism in the region from the Late Miocene to the present has been associated with the subduction of the lithospheric mantle under Central Anatolia (Bartol and Govers, 2014; Delph et al., 2017; Göğüş et al., 2017). As a result, widespread ignimbrite development and stratovolcano (Hasandağ, Erciyes, Melendiz, Develidağ, Tekkedağ) and dome formation, monogenetic lava flow and volcanic cone formation were observed (Innocenti et al., 1975; Pasquare et al., 1988; Toprak and Göncüoğlu, 1993; Aydar et al., 1995). Unlike in Western Anatolia, magmatism has developed along fault zones that have dominant strike-slip component but display short periods of tension-related deformation rather than horst-graben and detachment faults. These still active structural lines are the Ecemiş Fault Zone (Koçyiğit and Beyhan, 1998; Jaffey et al., 2001), Tuz Gölü Fault Zone (Koçyiğit, 2003; Derman et al., 2003; Özsayın et al., 2013) and the Akşehir Fault Zone (Koçyiğit et al., 2000; Özsayın and Dirik, 2011) from east to west, respectively.

While the volcanic units present different compositions ranging from basalt to andesite-dacite and rhyolite, they show arc character with predominantly high-K calc-alkaline or weakly alkaline chemistry (i.e., Gencalioğlu-Kuşcu and Geneli, 2010; Kürkcüoğlu, 2010; Reid et al., 2017). This indicates significant contribution

from the metasomatized mantle lithosphere in the post-collisional environment. However, in the Pliocene-Quaternary period, calc-alkaline magmatism was occasionally accompanied by alkali basalts with within-plate geochemical characteristics (Aydın, 2008; Güçtekin and Köprübaşı, 2009; Doğan-Külahçı et al., 2018). This situation has been interpreted as the young volcanism being of quite heterogeneous chemistry and derived from different origins (lithospheric and asthenospheric) (i.e., Gencalioğlu-Kuşcu and Geneli, 2010; Reid et al., 2017; Doğan-Külahçı et al., 2018).

While Late Cenozoic magmatism in Western Anatolia and Central Taurides produced porphyry and epithermal systems rich in gold, the region is largely devoid of other hydrothermal base and precious metal mineralization types including skarn and volcanic-hosted massive sulfide deposits. In western Anatolia, the only known porphyry mineralization related to Early Miocene magmatism is hosted in Pınarbaşı monzonite at the edge of the Menderes Massif. The age of porphyry Mo-Cu mineralization along the stockwork quartz veins was determined as ~18 Ma by Re-Os molybdenite dating (Delibaş et al., 2017). The Kızıltepe low-sulfidation Au-Ag deposit, which is the most important gold mineralization of this magmatic phase, developed simultaneously with the Pınarbaşı Cu-Mo system within the dacitic-rhyolitic volcanics in the same vicinity (Yılmaz et al., 2013). On the other hand, Fe-skarn zones with little economic significance were identified around the ~21 Ma aged (Ring and Collins, 2005) Eğrigöz Pluton (Oyman et al., 2013; Uğurcan and Oyman, 2016), although Eğrigöz and some other Middle Miocene intrusions may be responsible from formation of replacement-type Au-Sb ores such as in Tavşan (Oğuz, 2024) and Gördes (Günay, 2020).

The Middle Miocene (16–14 Ma) is the most productive period in terms of Au mineralization in the WAVP. The Kışladağ porphyry Au deposit, which is one of the largest gold systems in the entire Tethyan Belt, formed in relation to a multi-phase

monzonite porphyry stocks that was emplaced at 15.8–14.9 Ma (Baker et al., 2016; Paolillo et al., 2021). Similarly, the rhyolitic dikes that were involved in formation of the large Efemçukuru intermediate-sulfidation epithermal Au-Ag deposit are dated at around 13.3 Ma (Oyman et al., 2003; Boucher, 2016). Similar to Kışladağ, The Sayacık porphyry system, which hosts Kışladağ-like porphyry Au mineralization, was discovered in deep drillholes located approximately 6 km southwest of Kışladağ. The mineralization and its host latitic intrusion were dated using Re–Os molybdenite and U–Pb zircon techniques, yielding ages of 14.50 Ma and 14.51 Ma, respectively (Bickford et al., 2016).

In the Middle–Late Miocene, the AS porphyry Cu-Au prospect, in the furher south, was formed associated with 12.5-10.5 Ma aged, porphyritic textured monzonite, latite and trachyte which belong to the second phase magmatic units of the Afyon Volcanic Complex (Rabayrol, 2019; Sönmez and Kuşcu, 2020). Skarn and high-sulfidation epithermal Au formations associated with 9 Ma aged monzonite and trachy-andesites were observed in different parts of the similar aged volcano-plutonic system in the Bodrum Peninsula (Rabayrol and Hart, 2021). However, the economy of the aforementioned epithermal system has not been proven until now. Although ultrapotassic products and especially widespread lamproite formations of Late Miocene-Quaternary magmatism have high potential to be the source of porphyry-epithermal type mineralizations in terms of their composition (Müller and Groves, 1993; Jensen and Barton, 2000), no mineralization related to these rocks has been identified so far.

In the Late Cenozoic magmatic belt of the Central Taurides, no economic porphyry system has been recognized to date. On the other hand, barren or weakly-mineralized zones of porphyry-style alteration have been observed in sub-volcanic rocks located in deeper parts of some of the high-sulfidation epithermal Au systems.

The Develidağ Volcanic Complex, located approximately 45 km south of Kayseri, contains the Öksüt high-sulfidation epithermal Au-Cu deposit, the most important gold mineralization known in Central Anatolia. Most of the epithermal Au-Cu mineralization is observed in a diatreme breccia complex (Aluç et al., 2020; Yurdakul et al., 2021) nested within a dome structure comprising calc-alkaline andesite-dacite porphyries that were emplaced in the Late Miocene (6–5.3 Ma; Jaffey and Robertson, 2004; Rabayrol et al., 2019; Aluç et al., 2020). Alteration and mineralization in the diatreme breccia and the surrounding andesitic porphyry unit were dated at between 5.7 and 5.5 Ma (Yurdakul et al., 2021). $^{40}Ar/^{39}Ar$ age data obtained from secondary biotite from the potassic alteration intersected beneath epithermal mineralization (Yurdakul et al., 2021) as well as U-Pb garnet ages (Ali İmer, unpublished data) obtained from peripheral skarn zones indicate that epithermal-porphyry-skarn alteration occurred contemporaneously with Late Miocene magmatic activity.

Further west of the belt, the widespread volcanics to the west and south of Konya (Konya Volcanics) currently appear to be the most fertile igneous products in the Central Taurides sector as they contain several important gold-mineralized systems. The İnlice high-sulfidation epithermal Au deposit found here was formed in ~9 Ma aged calc-alkaline andesites (Hall et al., 2007; Terzi, 2020; Kuşcu et al., 2019; Rabayrol et al., 2019a). While there are similar formations such as Çukurağıl, Oğlakçı and Karacaören in different parts of the belt, the Doğanbey Cu-Mo-Au prospect is the only known porphyry system in the region. In the prospect located at the center of an eroded volcanic outlet, the mineralization is within calc-alkaline andesite-dacite porphyries (Keller et al., 1977; Temel et al., 1998; Kuşcu et al., 2019; Rabayrol et al., 2019a).

In the area between the Konya and Kayseri sectors, where epithermal-porphyry mineralization is observed, the younger (5–3 Ma; Türkecan et al., 2003; Kuşcu et al.,

2019; Rabayrol et al., 2019a) andesitic-dacitic units contain local epithermal alteration and weak mineralization (Altunhisar, Melendiz, Tepeköy), yet no porphyry system has been identified so far in this region.

1.4 Thesis Research Question/Statement of Problem/Motivation

The genetic relationship between subduction-related, calc-alkaline arc magmas and the porphyry Cu formation has been well documented through numerous studies since the 1999s (Richards, 2003; Seedorff et al., 2005; Sillitoe, 2010). Recent studies, on the other hand, revealed that high-K calc-alkaline or alkaline magmas formed at final stages of subduction or collisional/post-collisional tectonic environments are largely responsible from formation of Au-rich porphyry deposits, and Cu-rich systems with low to no gold are much rare in such tectonic settings (Heinrich and Neubauer, 2002; Richards et al., 2006, 2012; Richards, 2015; Heinrich, 2024).

Considering the general metallogenic structure in Anatolia situated at the western part of Tethyan-Eurasian Metallogenic Belt (TEMB), it is indicated that most of the important porphyry and associated epithermal mineralizations in the region are associated with back-arc or post-collisional magmatism instead of subduction magmatism (Kuşcu et al., 2010, 2013 and 2019; İmer et al., 2013 and 2015; Richards, 2015; Rabayrol, 2019a, b; Rabayrol and Hart, 2021). In addition, Anatolia hosts a large number of economic epithermal deposits, while it appears to lack Cu-rich porphyry mineralization (Yiğit, 2009; Oyman, 2019). This is in striking contrast with the neighboring regions along TEMB such as Iran, Greece, Bulgaria, Georgia, and Armenia that have numerous significant porphyry deposits (Moritz et al., 2016; Richards and Sholeh, 2016; Zürcher et al., 2016; Baker, 2019). There are two prominent porphyry systems in Anatolia in terms of their copper contents, the Cevizlidere (Tunceli) porphyry Cu-Mo-Au prospect and the Halilağa (Çanakkale) porphyry Cu-Au deposit. Among these, the first is developed at during the late

Oligocene during the collision between Arabia and Eurasia (İmer et al., 2015), whereas the latter is formed in a post-collisional environment in the middle Eocene (Brunetti, 2016). In the Eastern Pontides, on the other hand, the economic potential for subduction-related porphyry Cu-Mo mineralization is limited (Delibaş et al., 2016, 2019). Apart from these, other significant or potential porphyry systems in Anatolia are Kışladağ, AS porphyry, Doğanbey, Karakartal/Mavidere, and Ardala, which are relatively enriched in gold.

This study includes porphyry systems with variable metal enrichments that are related to Late Cenozoic magmatism in the Western Anatolia and Central Taurides. Different metal endowments are shown by these deposits/prospects since some are classified as gold-only porphyries (Kışladağ and Sayacık; Baker et al, 2016; Bickford et al., 2016), some as porphyry Cu-Mo (Pınarbaşı, Doğanbey; Hall et al., 2007; Delibaş et al., 2017), and porphyry Cu-Au (Afyon-Sandıklı; Sönmez and Kuşcu, 2020; Rabayrol and Hart, 2021), and epithermal Au deposit with deeper roots of high grade (>1% by mass) copper mineralization and porphyry-style alteration (Öksüt; Yurdakul et al., 2021). Although many of these systems have been studied previously, these studies are mostly at the deposit scale and mainly focus on the nature and tectonism of magmatic activity, style of mineralization and alteration, geochronology and geochemistry of magmatism/mineralization/alteration, and physico-chemical characteristics of hydrothermal fluids (Oyman et al., 2003; Baker et al., 2016; Delibaş et al., 2017; Aluç et al., 2020; Hanilçi et al., 2020; Sönmez and Kuşcu, 2020; Yurdakul et al., 2021; Terzi et al., 2024). However, the effects of spatial and temporal changes due to regional magmatism on the differences in metal contents in these deposits are either unknown or studies are too local to be interpret regionally. Additionally, there are alkaline ultrapotassic lamproitic occurences in Western Anatolia since 8 Ma due to changes in the magma origin. In the regions where there is back-arc extension, there are several examples of such rocks with a potential to host high grade gold mineralization (Müller and Groves, 1993 and 2002),

yet there is no discovery related to these rocks in Western Anatolia, and the reason(s) for the absence of such discoveries are not completely understood.

In recent studies focusing on regional metallogenic evolution, general comments were made based on magmatism/alteration age data, major, trace and rare earth element (REE) compositions of magmatic units, and whole-rock Sr-Nd-Pb isotope geochemical data (Kuşcu et al., 2019; Rabayrol, 2019a, b; Rabayrol and Hart, 2021). In all these studies, it has been determined that Late Cenozoic porphyry and associated epithermal mineralizations in Western Anatolia and Central Taurides are derived from high-K calc-alkaline or weakly alkaline magmas with arc chemistry, fertile magmas receive significant contributions from lithospheric sources and mineralizations are compressed at certain time intervals. (16–8 Ma in Western Anatolia, 14–9 Ma in Central Taurides) has been suggested. Kuşcu et al. (2019) stated that magmatism is represented by gradually increasing Sr/Y and La/Yb ratios during the transition from weak mineralization to productive periods. However, Rabayrol and Hart (2021) claimed that the productivity of magmatic systems in Western Anatolia and Central Taurides cannot be understood and barren and fertile magmas cannot be differentiated by the whole-rock geochemical parameteres (high Sr/Y, La/Yb and Fe^{3+}/Fe^{2+} ratios) which represents the alkalinity as well as oxidation states of magmas.

On the other hand, in recent years, geochemical studies on magmatic oxidation levels, which are the most important factors in the formation of this type of mineralization, and on minerals sensitive to water and volatile content, have accelerated in order to better understand the magmatic controls on porphyry-type mineralizations (e.g. Ballard et al., 2002; Wang et al., 2014; Lu et al., 2016; Chelle-Michou and Chiaradia, 2017; Lee et al., 2017 and 2020; Zhu et al., 2018; Nathwani et al., 2021). When these studies on zircon, apatite and amphiboles that are sensitive to these parameters are used together with U-Pb zircon dating, the temporal and

spatial development of ore-forming magmas can be determined with high resolution, thus the impact of magmatism on mineralization in prospect/deposit, district and metallogenic region scale can be resolved. On the other hand, magma oxidation level and sulfur content are parameters that are difficult to determine by analysis of crystallized igneous rocks.

In the first of two recent studies using methods for detailed mineral chemistry, Georgatou et al. (2021) investigated the Miocene aged felsic volcanics from the Beydağı Volcanics around Kışladağ and the vicinity of Doğanbey (Konya) and enclaves found in young alkaline basalts in Kula, and stated the presence of early sulfide saturation at the lower crust, and determined the temperature and pressure conditions. In another study, Paolillo et al. (2021), using an approach similar to the one proposed here, determined magma productivity between different intrusion units in the Kışladağ porphyry Au deposit by zircon petrochronology. With high resolution U-Pb dating, trace element and Hf isotope analyzes performed on zircons, it is determined that the early phase intrusions in Kışladağ were more productive in terms of porphyry mineralization, then the productivity decreased with the mixing of undifferentiated, mafic magmas developing in the lower crust, and this may be due to the extentional tectonism that started in the vicinity.

There is no other study in the magmatic belt stretching along the Western Anatolia and Central Taurides that uses “fertility indicator” minerals such as zircon and apatite which are resistant to alteration and surface weathering, and in this proposed study, this approach will be applied to the aforementioned mineralized belt. In this study, detailed geochemical and geochronological analyses of zircon, apatite, amphibole, and magnetite-ilmenite phases in samples collected from Late Cenozoic porphyry mineralizations (Kışladağ, Sayacık, Doğanbey, AS porphyry, Pınarbaşı, and Öksüt) and barren magmatic systems in Western Anatolia and Central Taurides will be carried out. Thus, the oxidation levels, water-volatile contents and sulfide saturation

levels of the source magmas will be determined. The analyzes to be made are evaluated together with the geochemical/geochronological data in the literature to obtain answers to the following question;

i. Whether there are differences between oxidation levels, water-volatile contents, sulfide saturation levels and magma source of fertile and barren intrusion systems in terms of mineralization,

ii. Which magmatic factors control the different metal contents of the porphyry formations in the region,

iii. What similarities and/or differences exist between the contributions of Late Cenozoic magmatism in the Western Anatolia–Central Taurides to the metallogeny of the region.

1.5 Methodology

This thesis will focus on determination of porphyry fertility indicators through detailed petrography and mineral/whole-rock geochemistry in order to understand the relationship between mineralized hydrothermal systems and barren plutonic and sub-volcanic rocks and Late Cenozoic magmatism in Western Anatolia and Central Taurides. This study will require several steps of both field and intensive laboratory studies which will begin with the collection of the igneous rock samples from drillholes/outcrops.

Methods in the study can roughly be divided into two categories.

1.5.1 Field Studies

The Late Cenozoic magmatic belt stretching between the Central Taurides and Western Anatolia hosts numerous intrusive centers, some of which are already recognized for their association with porphyry–epithermal–skarn mineralization.

Using a combination of regional geological maps and previously published datasets, a number of localities were identified within the belt for the purpose of regional sampling. Several of these localities are known to contain either well-developed ore deposits, potential prospects, or weakly mineralized systems of minor economic interest. As the thesis progressed, a number of newly reported porphyry systems from ongoing exploration programs were also added to the study through direct collaboration with mining companies, which allowed access to fresh drill core and surface exposures.

When planning the sampling campaign, it is aimed to represent the magmatic evolution of both the Central Taurides (Table 1.1) and Western Anatolian (Table 1.2) segments. Particular care was taken to include rock suites spanning a broad temporal range, from Late Oligocene–Early Miocene intrusions to younger pulses, many of which are Pliocene in age. This strategy was intended to reflect the full range of magmatic episodes potentially linked to ore formation in the region. Fieldwork was carried out between May 2022 and July 2024, with the majority of samples collected during the main field campaign in April 2023, when field access and exposure conditions were optimal.

At each locality, attempts were made to sample all distinct lithological units as identified either in the outcrop or in drill core. For outcrop samples, at least 2–3 kg of least-altered rock was collected per sample to preserve primary magmatic geochemical signatures and minimize the influence of weathering. Since porphyry and epithermal mineralizing systems typically derive from intermediate to felsic intrusions, most of the collected material reflects these compositions. However, the more mafic phases and lamprophyre dikes were deliberately included, by collecting larger bulk samples (7–8 kg) from these units to ensure sufficient material for comprehensive mineralogical and geochemical work. In active exploration sites, sampling was performed on drill cores in consultation with the operating companies,

and witness samples were archived on site in accordance with standard industry procedures. Where drill holes intersected short-interval drill cores intersected magmatic units, it is tried to collect as much representative material as possible to capture any variation in composition and texture.

Table 1.1. Details of samples collected from the Central Taurides after fieldwork.

Sample ID	Region	Field	Easting	Northing	Rock Type
INL-D-01	Konya	İnlice	419453.1	4179450.9	Andesite dyke
INL-OP-01	Konya	İnlice	419453.1	4179450.9	Andesite porphyry
INL-OP-02	Konya	İnlice	419453.1	4179450.9	Andesite porphyry
INL-201-01	Konya	İnlice	419453.1	4179450.9	Andesite porphyry
INL-201-02	Konya	İnlice	419453.1	4179450.9	Andesite porphyry
INL-201-03	Konya	İnlice	419453.1	4179450.9	Andesite porphyry
SİLLE-02	Konya	SVS	443341.0	4200427.0	Andesite porphyry
DMLP-01	Konya	Damlapınar	407104.5	4186658.1	Basaltic andesite
DMLP-02	Konya	Damlapınar	407104.5	4186658.1	Basaltic andesite
KRC-01	Konya	Karacaören	411868.0	4171972.0	Andesite porphyry
KTN-01	Konya	Ketenli	417931.0	4147964.0	Dacitic agglomerate
CKRA-01	Konya	Çukurağıl	404694.8	4192713.3	Andesite porphyry?
CKRA-02	Konya	Çukurağıl	404694.8	4192713.3	Andesite porphyry?
CKRA-03	Konya	Çukurağıl	404694.8	4192713.3	Andesite porphyry?
EAR-42	Develidağ	Öksüt	715725.0	4236105.0	Andesite porphyry
YLS-01	Karapınar	Yeşilyurt	568980.0	4179201.0	Andesite porphyry
SLP-01	Melendiz	Süleymanpınarı	633131.0	4209350.0	Andesitic agglomerate
SLP-02	Melendiz	Süleymanpınarı	633131.0	4209350.0	Andesitic agglomerate
SLP-03	Melendiz	Süleymanpınarı	633131.0	4209350.0	Andesite porphyry
496762	Melendiz	Çömlekçi	618290.0	4217347.0	Andesite porphyry
496918	Melendiz	Çömlekçi	618290.0	4217347.0	Andesite porphyry
CML-01	Melendiz	Çömlekçi	632047.0	4215318.0	Andesite porphyry
CML-07	Melendiz	Çömlekçi	632047.0	4215318.0	Andesite porphyry

? indicates the uncertainty of the rock type due to the loss of primary minerals and textures during intense hydrothermal alteration

Every sample collected in the field was described macroscopically on site, labeled with precise geographic coordinates, and, where applicable, drill‑hole metadata were recorded. Photographs were taken before removal to document context, and the material was sealed in heavy plastic or canvas sample bags to preserve integrity

during transport and storage. This systematic yet field‐responsive approach ensured that the resulting dataset captures not only the chemical variability of the magmatic centers but also the geological context necessary for interpreting their potential link to porphyry‐style mineralization.

Table 1.2. Details of samples collected from the Western Anatolia after fieldwork and selected for petrographic analysis.

Sample ID	Region	Field	Easting	Northing	Rock Type
CTL-01	Biga	Çatalçam	538677.2	4357055.0	Andesite porphyry
CTL-02	Biga	Çatalçam	538812.7	4358468.0	Andesite porphyry
TRD-17	Biga	Turplu	560687.0	4397778.0	Dacite porphyry
SAR-01	Biga	Sarıalan	552594.0	4384847.0	Andesite porphyry
SAR-02	Biga	Sarıalan	552594.0	4384847.0	Basaltic andesite
SAR-03	Biga	Sarıalan	552594.0	4384847.0	Basaltic andesite
SAR-04	Biga	Sarıalan	552594.0	4384847.0	Andesite
374857	Biga	Hallaçlar	545056.0	4400597.0	Dacite
374865	Biga	Hallaçlar	544542.0	4394902.0	Dacite
374869	Biga	Hallaçlar	544174.0	4398313.0	Dacite
BLY-01	Biga	Balya	549790.5	4403331.2	Andesite porphyry
BLY-02	Biga	Balya	549790.5	4403331.2	Andesite
EFM-01	İzmir	Efemçukuru	498176.7	4237934.2	Rhyolite dyke
KRK-01-2	Kırka	Kırka	296598.0	4367121.0	Basaltic trachyandesite
AVC-01	Afyon	Afyon V. Complex	265329.0	4280447.0	Latite
AVC-02	Afyon	Afyon V. Complex	265333.0	4280455.0	Latite
AVC-03	Afyon	Afyon V. Complex	265333.0	4280455.0	Lamproite
AVC-04-1	Afyon	Afyon V. Complex	282540.0	4254157.0	Leucitite
AVC-04-2	Afyon	Afyon V. Complex	282540.0	4254157.0	Leucitite
AVC-05	Afyon	Afyon V. Complex	282540.0	4254157.0	Lamproite
AVC-06	Afyon	Afyon V. Complex	282540.0	4254157.0	Leucitite
AVC-AS-01	Afyon	A-S Porphyry	267059.0	4265038.0	Micromonzonite
AVC-AS-02	Afyon	A-S Porphyry	267046.0	4265065.0	Diabase dyke
AVC-AS-03	Afyon	A-S Porphyry	267046.0	4265065.0	Trachyte porphyry
AVC-AS-04	Afyon	A-S Porphyry	267113.0	4264728.0	Syenite porphyry
AVC-AS-05	Afyon	A-S Porphyry	267036.0	4264740.0	Latite porphyry
GÖL-01	Isparta	Isparta	282899.0	4184178.0	Basaltic trachyandesite
GÖL-02	Isparta	Isparta	281806.0	4180344.0	Andesite
GÖL-03	Isparta	Isparta	278472.0	4178909.0	Tephriphonolite

Table 1.2. continued

Sample ID	Region	Field	Easting	Northing	Rock Type
KSLD-01 to 12	Uşak	Kışladağ	688753.8	4261649.7	Monzonite porphyry
SYC-01	Uşak	Sayacık	684048.2	4257023.0	Monzonite porphyry
SYC-02	Uşak	Sayacık	684048.2	4257023.0	Monzonite porphyry
SYC-03	Uşak	Sayacık	684048.2	4257023.0	Monzonite porphyry
SYC-04	Uşak	Sayacık	684048.2	4257023.0	Monzonite porphyry
SYC-05	Uşak	Sayacık	684048.2	4257023.0	Monzonite porphyry
S-01	Manisa	Salihli	608175.0	4251761.0	Granite
S-02	Manisa	Salihli	608158.0	4251768.0	Granite
SIN-01	Simav	Sındırgı	604896.0	4349336.0	Dacite porphyry
SIN-02	Simav	Sındırgı	608927.0	4346929.0	Dacite/Andesite
SIN-03	Simav	Sındırgı	620177.0	4342416.0	Dacite/Andesite
SIN-04	Simav	Sındırgı	605607.0	4349856.0	Dacite/Andesite
EGR-01-1	Simav	Eğrigöz	676392.0	4330175.0	Granite
EGR-01-2	Simav	Eğrigöz	676392.0	4330175.0	Granite
EGR-02	Simav	Eğrigöz	680323.0	4333495.0	Granite
EGR-03	Simav	Eğrigöz	686390.0	4365530.0	Granite
PNB-01	Simav	Pınarbaşı	701785.0	4322255.0	Dacite porphyry
PNB-02	Simav	Pınarbaşı	701730.0	4322278.0	Monzonite
PNB-03	Simav	Pınarbaşı	701791.0	4322049.0	Monzonite
BDR-01	Bodrum	Bodrum	533504.0	4110244.0	Trachyandesite
BDR-02-1	Bodrum	Bodrum	533401.0	4111385.0	Trachyandesite
BDR-02-2	Bodrum	Bodrum	533401.0	4111385.0	Trachyandesite
BDR-02-3	Bodrum	Bodrum	533401.0	4111385.0	Trachyandesite
BDR-03	Bodrum	Bodrum	532633.0	4111433.0	Trachyandesite
BDR-04-01-1	Bodrum	Bodrum	528367.0	4104527.0	Basaltic trachyandesite
BDR-04-01-2	Bodrum	Bodrum	528367.0	4104527.0	Basaltic trachyandesite
BDR-04-2	Bodrum	Bodrum	528367.0	4104527.0	Basaltic trachyandesite
BDR-05	Bodrum	Bodrum	526361.0	4099376.0	Trachyandesite
BDR-06	Bodrum	Bodrum	523865.0	4098846.0	Micromonzonite
BDR-07	Bodrum	Bodrum	523865.0	4098846.0	Monzonite
BDR-08	Bodrum	Bodrum	522258.0	4101692.0	Trachyandesite
BDR-09	Bodrum	Bodrum	522258.0	4101692.0	Trachyandesite
BDR-10-1	Bodrum	Bodrum	523562.0	4104622.0	Trachyandesite
BDR-10-2	Bodrum	Bodrum	523562.0	4104622.0	Basaltic trachyandesite

1.5.2 Laboratory Work

1.5.2.1 Sample Preparation

Following the field campaigns, all samples collected from the selected sites underwent a series of preparation and mineral separation procedures at the sample processing and heavy mineral laboratories of Middle East Technical University, Dokuz Eylül University, and the University of Geneva. The workflow was specifically designed to extract zircon and apatite grains suitable for geochemical and isotopic analysis.

The initial stage involved primary breaking of the rocks. Samples were first fed through a jaw crusher and reduced to coarse gravel‐sized fragments to liberate mineral grains without excessive breakage. The crushed material was subsequently milled using a disc pulverizer until a fine, homogeneous powder was obtained, maximizing grain liberation while minimizing the formation of ultra‐fine slurries that could complicate later separations. Following pulverization, each sample was sieved through a two‐stage system, first at 500 μm and then at 64 μm. The fraction between these two size thresholds (i.e., < 500 μm but > 64 μm) was retained for heavy mineral concentration, as this interval typically yields the highest recovery of accessory zircons and apatites with minimal inclusions.

The selected size fraction was processed on a Wilfley shaking table to concentrate the dense mineral fraction. The resulting heavy separates were then subjected to magnetic separation to remove strongly and moderately magnetic phases such as magnetite, ilmenite, and some mafic silicates. The non‐magnetic fraction was further refined using high‐density liquids, primarily diiodomethane and bromoform, to isolate the accessory mineral concentrate enriched in zircon and apatite. The final heavy mineral separates were meticulously handpicked under a

stereomicroscope. During this step, particular attention was given to selecting well‑formed, inclusion‑poor zircon grains of sufficient size, as well as apatites with minimal alteration and clear internal zoning where present.

The selected accessory minerals were mounted using two different preparation protocols depending on the analytical requirements and hosting facility. At Dokuz Eylül University, zircons and apatites were embedded in epoxy resin mounts, while at the University of Geneva they were placed on glass discs to facilitate subsequent in‑situ analytical techniques. All mounts were progressively polished using fine diamond abrasives until the internal surfaces of the crystals were fully exposed, ensuring a flat and contamination‑free analytical surface suitable for high‑precision microanalytical work.

1.5.2.2 Petrographic Analyses

A total of sixty‑three thin sections were prepared from the representative samples collected in the targeted sites across the Central Taurides and Western Anatolia (Table 3.1). Thin‑section preparation was carried out at the Mineral Analysis and Technology Department of the General Directorate of Mineral Research and Exploration (MTA). The sections were examined petrographically to determine rock types, primary mineral assemblages, textural characteristics, and the extent and nature of hydrothermal alteration. Particular attention was given to the identification of alteration minerals and the classification of alteration facies to establish the paragenetic sequence of each sample.

The petrographic results were essential for screening the most suitable specimens for subsequent geochemical and mineral separation work. Samples preserving accessory indicator minerals such as zircon, apatite, hornblende, biotite, and magnetite–ilmenite with minimal overprint from hydrothermal alteration, metamorphism, or

weathering were prioritized. This selection ensured that the subsequent trace‐element and isotopic analyses would reflect primary magmatic signatures rather than secondary processes.

All petrographic analyses were conducted using a Nikon CiPOL polarizing microscope equipped with both transmitted and reflected light systems in the Department of Geological Engineering at Middle East Technical University. During the thin‐section study, representative photomicrographs were taken from each sample to document mineralogical and textural features in detail and to complement the descriptive petrographic dataset. This combined approach of systematic petrography and photographic documentation provided a robust foundation for integrating field observations with mineralogical and geochemical interpretations in the later stages of the study.

1.5.2.3 Lithogeochemistry

A comprehensive lithogeochemical dataset comprising major, trace, and rare earth element (REE) compositions of rocks from the target locations as well as from other regional igneous exposures in the Western Anatolia and in the Central Taurides was compiled from numerous studies that were already available in the literature. Therefore, lithogeochemical analyses were not considered as an integral for the majority of the sampled magmatic systems. However, several sites included newly identified or previously unstudied porphyry systems, which necessitated the generation of new geochemical data. A total of eleven whole‐rock analyses were conducted on fresh samples from these locations, including four samples from the Sarıalan mineralization, two from the Çatalçam porphyry field, two from the Sayacık intrusion, a single dyke sample collected from within the İnlice open pit, and two additional specimens from the Damlapınar project area. Upon compilation, this data was evaluated to filter out potential effects of hydrothermal alteration.

In addition to these, major‐oxide, some trace‐element, and platinum group element (PGE) analyses were performed on fifteen additional samples representing a range of magmatic domains. These included recently discovered Balya mineralization, volcanic units from the Afyon Volcanic Complex and Afyon–Sandıklı prospect, granitoid bodies such as Eğrigöz and Salihli, as well as surface exposures from Kırka, Bodrum, Konya, and Isparta, together with further samples from the Damlapınar project area. This broader suite was designed to capture both volcanic and plutonic end‐members relevant to the Late Cenozoic magmatic belt. However, as the analytical results for these samples yielded concentrations below the respective detection limits, the dataset was not useful to have meaningful interpretation and therefore has not been incorporated into the scope of this thesis. However, their major oxide contents are included in the lithogeochemical interpretations.

All geochemical analyses were carried out at ALS Laboratories. Major and trace element concentrations were measured using a combination of inductively coupled plasma optical emission spectrometry (ICP‐OES) and inductively coupled plasma mass spectrometry (ICP‐MS), while platinum group elements were determined via instrumental neutron activation analysis (INAA). Analytical precision was continuously monitored through replicate measurements of certified reference materials; based on these checks, relative uncertainties were estimated at approximately ±5% for major oxides and ±10% for trace elements.

For integration with the compiled literature dataset, all new whole‐rock analyses were corrected for volatile loss-on-ignition (LOI) and recalculated to 100% volatile-free basis prior to plotting and interpretation. This normalization step ensured consistency between datasets and allowed robust comparison of magmatic trends and potential fertility indicators across the full range of studied systems.

1.5.2.4 U-Pb Zircon Geochronology

Following sample preparation, the epoxy mounts were subjected to cathodoluminescence (CL) imaging at the Scanning Electron Microscopy Laboratory of the University of Lausanne. These CL images were used to characterize internal zoning, crystal morphology, and potential alteration domains, enabling the selection of the most suitable zircon grains for in-situ U–Pb geochronological analyses. In total, 1,308 analytical spots were measured, which were used to obtain U-Pb zircon ages of 61 samples in total. The positioning of the analysis points was guided by several criteria, including zircon internal structures, grain size, and the presence or absence of inclusions that could compromise isotopic integrity. Parallel to the U–Pb age determinations, trace element and rare earth element (REE) analyses were performed along adjacent transects to the dated domains, ensuring direct geochemical context for the crystallization ages.

Geochronological analyses were carried out at the Institute of Earth Sciences, University of Lausanne (Switzerland), using a LA‐ICP‐MS system. Zircon crystallization ages were obtained with an ASI RESOlution 193 nm ArF excimer laser system coupled to a Thermo Fisher Scientific Element XR sector‐field ICP‐MS, equipped with a S155 dual‐volume ablation cell. Laser settings included a pre‐ablation of 3 pulses at 38 µm followed by a main ablation spot diameter of 30 µm, operated at a 5 Hz repetition rate with an energy density of 2.8 J/cm² on the sample surface. Helium was used as the carrier gas at 0.5 L/min, with a minor addition of nitrogen (1 mL/min) to enhance sensitivity. The selection of isotopes and acquisition parameters followed protocols broadly comparable to those described by Ulianov et al. (2012).

Instrumental mass bias and accuracy were monitored using well‐characterized reference zircons GJ‐1 (Jackson et al., 2004) and Plešovice (Sláma et al., 2008).

Raw time‐resolved count rate spectra were reduced and processed offline using the LAMTRACE software package (Jackson, 2008), ensuring consistent background subtraction and signal integration for all analytical sessions.

1.5.2.5 Mineral Geochemistry

1.5.2.5.1 Zircon Trace Element Analyses

Zircon trace element analyses were performed using the same analytical setup (LA‐ICP‐MS) system at the Institute of Earth Sciences, University of Lausanne, as employed for the U–Pb geochronological analyses. Instrumental optimization and analytical protocols followed the procedures outlined by Ulianov et al. (2012). The laser ablation system was operated with an energy density of approximately 3.2 J/cm² on the sample surface, a repetition rate of 10 Hz, and a standard spot diameter of 25 µm. In cases where zircon crystals provided sufficiently broad growth zones, the spot size was increased to 35 µm to enhance signal intensity and improve counting statistics.

To ensure direct geochemical context for the dated domains, laser spots for trace element analysis were placed as close as possible to the U–Pb analytical sites or, where spatial constraints prevented this, within the same growth zone identified in the CL images. Each analysis consisted of a 70–80 second background acquisition followed by approximately 40 seconds of ablation and data collection. NIST‐SRM‐612 silicate glass was employed as the external calibration standard, while BCR-2G served as the internal standard to correct for ablation yield and instrumental drift.

Due to the high zirconium concentrations inherent to zircon, detector saturation occasionally resulted in undetectable niobium signals. Similarly, analyses of grains

with elevated Al (> 15 ppm), Ba (> 0.05 ppm), or Ca (> 100 ppm) were generally excluded, as such compositions often indicated the presence of inclusions or alteration features. Raw data were reduced offline using the LAMTRACE software package (Jackson, 2008), which allowed careful inspection of time‐resolved count rate (cps) spectra. This step was critical for identifying analytical artifacts, including inadvertent sampling of mineral inclusions or subtle heterogeneities within the zircon domains that were not apparent under optical microscopy.

1.5.2.5.2 In-situ Zircon Hf Isotope Analyses

Following U–Pb geochronology and trace/REE analyses, hafnium isotope measurements were carried out on the same zircon grains to provide complementary constraints on magma source characteristics and crust–mantle interactions. Hf isotope analyses were performed at the Department of Earth Sciences, University of Geneva (Switzerland), using a Thermo Scientific Neptune Plus multi‐collector ICP‐MS (MC‐ICP‐MS) coupled to a Teledyne–Photon Machines Analyte G2 ArF excimer laser system.

Laser ablation was conducted with an energy density of approximately 4 J/cm², a repetition rate of 5 Hz, and a spot diameter of 40 µm; in a limited number of cases where sufficient zircon surface area was available, the spot size was increased to 50 µm to enhance signal intensity. Helium was used as the carrier gas, with a minor admixture of nitrogen added prior to entry into the Ar plasma to improve sensitivity. Analyses were conducted at low mass resolution over 120 cycles for standards (~1 second integration per cycle) and between 80 and 120 cycles for unknowns, depending on zircon thickness.

Throughout each analytical session, reference zircons Plešovice (Sláma et al., 2008), Mud Tank (Black and Gulson, 1978), Munich Zircon (MUN; Fisher et al., 2011) and

GJ‐1 (Jackson et al., 2004) were measured at the beginning, end, and approximately every fifteenth sample to monitor accuracy and correct for instrumental mass bias. Blank positions were inserted at the same frequency as standards but left unablated, serving as a background correction for downstream data reduction.

Raw datasets were processed offline using custom Excel templates. Blank‐subtracted signals were corrected for isobaric interference from ^{176}Lu and ^{176}Yb on mass 176 following the procedure of Fisher et al. (2011). Mass bias corrections for ^{176}Hf/^{177}Hf ratios were calculated using the exponential law and the βHf and βYb factors derived from measured ^{179}Hf/^{177}Hf and ^{173}Yb/^{171}Yb ratios, using the reference values of Patchett and Tatsumoto (1981; ^{179}Hf/^{177}Hf = 0.7325) and Thirlwall and Anczkiewicz (2004; ^{173}Yb/^{171}Yb = 1.1234). The contributions of ^{176}Yb and ^{176}Lu were corrected using ^{176}Yb/^{173}Yb = 0.786954 and ^{176}Lu/^{175}Lu = 0.02645, respectively (Thirlwall and Anczkiewicz, 2004).

To identify potential heterogeneities such as mineral inclusions or inherited zircon cores with distinct ^{176}Hf/^{177}Hf ratios, time‐resolved signal profiles were inspected for each analysis. Any spectra showing anomalous shifts or mixing trends were excluded from the final dataset. Initial ^{176}Hf/^{177}Hf ratios and corresponding $\varepsilon Hf_{(t)}$ values were calculated using the measured ^{206}Pb/^{238}U ages of the dated domains in combination with the CHUR parameters of Bouvier et al. (2008; ^{176}Hf/^{177}Hf = 0.282785; ^{176}Lu/^{177}Hf = 0.0336) and the ^{176}Lu decay constant of $\lambda = 1.87 \times 10^{-11}$ yr^{-1} (Söderlund et al., 2004).

Uncertainties in age‐corrected εHf values were estimated as 2σ based on the long‐term in‐house reproducibility of Temora zircon εHf(t) values. Although the Temora standard was not included in the analytical run, its long‐term laboratory reproducibility was used because the measured ^{173}Yb/^{177}Hf ratios of the analyzed zircons more closely matched those of Temora than those of the other standards.

1.5.2.5.3 Electron Microprobe Analyses

Following detailed petrographic characterization, a subset of polished thin sections deemed suitable for mineral chemistry was selected for in‐situ quantitative analysis. Prior to measurement, all mounts were coated with a thin layer of carbon to ensure optimal conductivity. Electron microprobe analyses (EMPA) were conducted over the course of five analytical sessions—one at the University of Lausanne and four at the University of Geneva. The use of two laboratories was dictated by instrument availability.

Measurements at Lausanne were performed using a JEOL JXA‐8350F HyperProbe, while those at Geneva employed a JEOL JXA‐iHP200F HyperProbe. In both laboratories, the analytical protocol was standardized to ensure consistency between datasets. Operating conditions included an accelerating voltage of 15 kV, a beam current of 20 nA, and a focused beam diameter of 1 μm. Individual point analyses were acquired with a counting time of 120 seconds to achieve high analytical precision, particularly for trace components in accessory minerals.

Analyses targeted apatite alongside rock‐forming mafic silicates and oxides, specifically amphibole, biotite, and magnetite/ilmenite. Calibration was performed using a suite of well‐characterized mineral and oxide standards: albitic plagioclase for Na, wollastonite for Ca and Si, Al_2O_3 for Al, MgO for Mg, hematite for Fe, rhodonite for Mn, metallic Ni for Ni, orthoclase for K, TiO_2 for Ti, Cr_2O_3 for Cr, $SrTiO_3$ for Sr, and barite for Ba. This combination provided matrix‐matched standards for all analyzed elements, minimizing inter‐element correction factors and ensuring data quality across both laboratories.

CHAPTER 2

MAGMATISM AND METALLOGENY IN CENTRAL TAURIDES

In the Central Taurides, Late Cenozoic magmatic activity is interpreted to have initiated around ~20 Ma and continued into the Quaternary. Late Cenozoic volcanic and sub-volcanic rocks form widespread exposures across the Konya–Aksaray–Niğde–Nevşehir–Kayseri region. Due to the thick cover of volcanic and volcaniclastic lithologies as well as limited erosion, coeval, deep plutonic rocks are not exposed and such lithologies were not encountered at depth in localities where drill core data is available. The onset of this magmatism during the Miocene is widely attributed to the convergence of the Tauride–Anatolide–Pontide domains, coupled with the subduction of the Cyprus lithosphere and a process interpreted as "delamination of the lower crust into the mantle" beneath Central Anatolia (Delph et al., 2017; Göğüş et al., 2017; Reid et al., 2017).

For the purposes of this study, the sampled areas within the Central Taurides were subdivided into distinct sectors based on their geographic distribution and the relative ages of their magmatic units (Figure 1.7). Within the Central Taurides, which occupy the portion of the Tauride orogenic belt between the Ecemiş and Kırkkavak fault zones, two principal sectors of well‐developed Late Cenozoic magmatism were identified. The first of these lies in the eastern part of the belt, encompassing the Aksaray–Niğde–Kayseri corridor, where volcanic centers such as Melendiz, Karacadağ, and Develidağ define a suite of eruptive products with ages ranging from 6 to 1 Ma. This sector is particularly notable for pervasive hydrothermal alteration within parts of the volcanic sequence.

The second sector is located to the west, extending from the vicinity of Konya city center in the north to Seydişehir in the south. Here, extensive volcanic exposures define what is collectively referred to in this study as the Konya Volcanic Complex. Together, these sectors provide a representative framework for investigating the temporal and geochemical evolution of Late Cenozoic magmatism across the Central Tauride belt.

2.1 Regional Sampling Studies

2.1.1 Konya Volcanic Complex (16–8 Ma)

The Konya Volcanic Complex (KVC) is widely exposed approximately 30 km west of city of Konya and extending farther south towards Seydişehir (Figure 2.1). It comprises a thick sequences of volcanic and volcaniclastic rocks with local sub-volcanic intrusions. Magmatic activity in KVC is dated to the Late Miocene–Pliocene (Keller et al., 1977; Temel et al., 1998). The northern part of this vast volcanic system is commonly referred to as the Sulutaş Volcanic Suite (SVS) or the Sille Volcanics (Asan et al., 2021), whereas the southern exposures are collectively termed as the Erenlerdağ–Alacadağ Volcanic Complex (Keller et al., 1977; Tatar et al., 2002). Based on stratigraphic correlations and geochronological studies, magmatic activity appears to have initiated in the north as the SVS developed and migrated progressively southward through time (Asan et al., 2019, 2024).

The earliest magmatic products within the SVS (Figure 2.1) are bimodal alkaline basalt–dacite suites dated to ca. 16 Ma, followed by the emplacement of lamprophyric sills and dykes (13.5–12.5 Ma), and succeeded by high‐K basalt–andesite–dacite volcanic units dated between 13 and 11 Ma (Asan et al., 2019). For this study, samples were collected from previously investigated localities, including meter‐thick lamprophyric sills intruding the Paleozoic basement north of Tatköy

(Figure 2.2A) and younger calc‑alkaline andesitic porphyries south of Tatköy (Figure 2.2B), both originally documented by Asan et al. (2019).

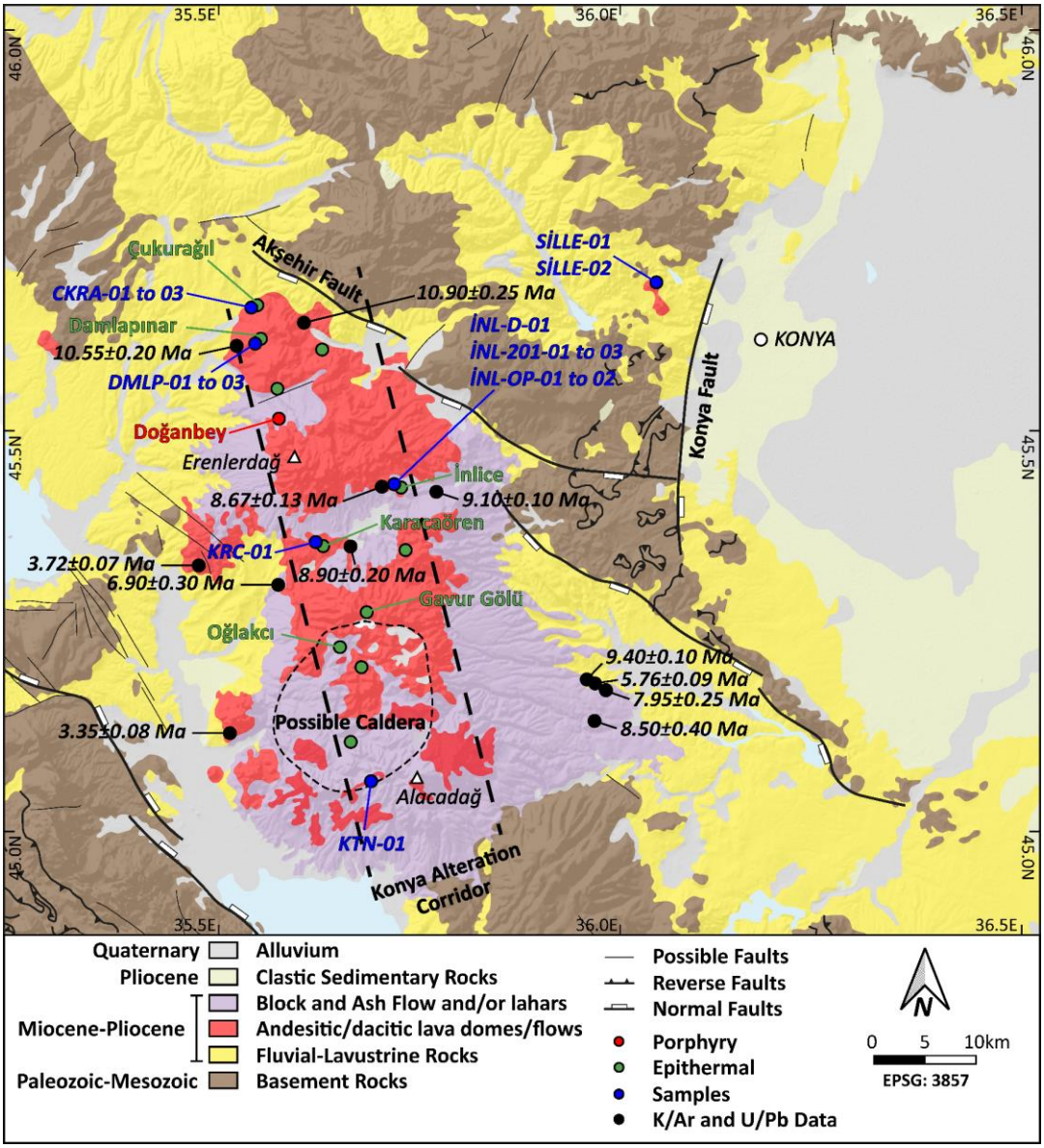


Figure 2.1. Simplified geological map of the west of Konya (Gündüz et al., 2025). Published K/Ar (Besang et al., 1977; Platzman et al.,1998), and U-Pb zircon ages (Rabayrol et al., 2019a) are also shown. Lithologies are from MTA (2002).

South of the SVS, the Erenlerdağ–Alacadağ Volcanic Complex forms a broad belt intruding ophiolitic and carbonate basement units on both sides of the Konya–Seydişehir corridor (Figure 2.1). This sector is dominated by andesitic lava flows and andesitic–dacitic domes overlain by extensive pyroclastic deposits and nuée ardente sequences (Temel et al., 1998; Terzi et al., 2023). Sampling in this area focused on volcanic and shallow intrusive units exhibiting hydrothermal alteration and, in some cases, Au ± Cu ± Mo mineralization. Fieldwork was carried out in collaboration with ESAN Eczacıbaşı, with samples collected from surface exposures and drill cores from the İnlice high-sulfidation epithermal Au deposit, as well as from outcrops within other prospects including the Çukurağıl, Damlapınar, Karacaören, and Ketenli licences (Figure 2.3–2.4).

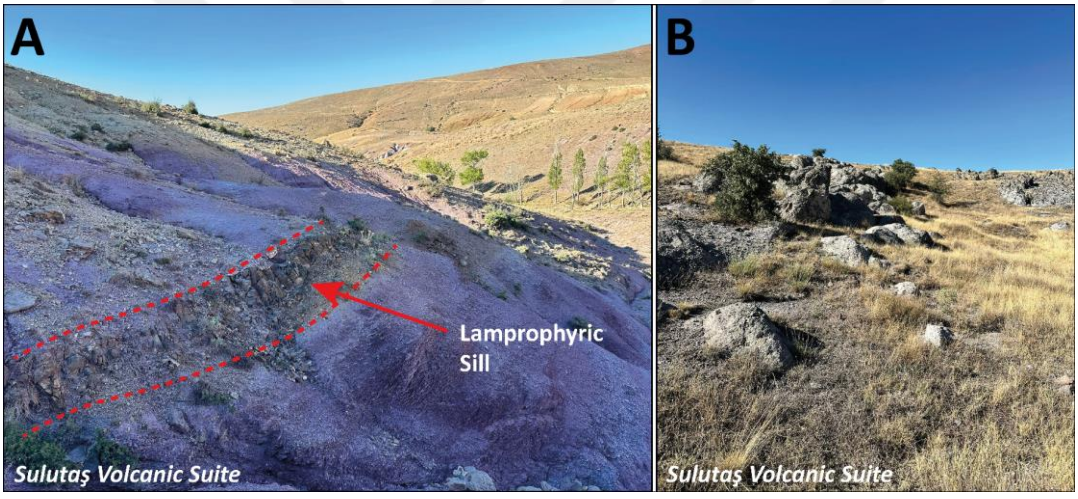


Figure 2.2. Field photographs of volcanic units from the Sulutaş Volcanic Suite within the Konya Volcanic Complex. (A) ~1 m-thick lamprophyre sill intruding Paleozoic metamorphic basement units, located approximately 3 km north of Tatköy. (B) Andesite porphyry outcrops situated just south of Tatköy.

At İnlice (Figure 2.1), investigations were conducted within the active open pit area exposing the high‐sulfidation (HS) epithermal Au mineralization (Figure 2.3A–B) and also on core samples from drill hole INES‐201 located immediately to the north of the open-pit area (Figure 2.3C–F). The andesitic porphyries hosting the gold

mineralization display intense hydrothermal alteration with a well‐developed zonation pattern typical of HS epithermal Au systems (Terzi et al., 2023). A central zone of silicification hosts bulk of the mineralized breccias and vein networks, and is itself surrounded first by quartz–alunite and then by quartz–kaolinite alteration domains (Figure 2.3A). Due to the pervasive alteration along the pit walls, fresh andesitic porphyry was not available for sampling within the main ore zone. Thus, a moderately propylitized andesitic dyke cross-cutting quartz-alunite-clay altered units was sampled from the southeastern pit wall (Figure 2.3B).

Drill hole INES‐201 (~1000 m total depth) was aimed to test the deeper levels of the epithermal system and its potential connection to a porphyry center. Two distinct magmatic phases and associated alteration assemblages were documented along this drill hole. The upper 70 m of INES-201 comprises an andese porphyry that shows weak potassic alteration overprinted by moderate-intensity propylitic (chlorite–epidote–sericite–carbonate–pyrite) alteration (Figure 2.3C–D). Within the potassic alteration zones, magnetite‐rich M‐type veins and cross‐cutting 1–2 cm‐thick B‐type veinlets containing granular quartz alongside minor chalcopyrite and pyrite, and rare molybdenite and bornite were observed. These also have symmetrically-developed magnetite bands along vein margins. From ~70 m and continuing down to ~900 m, INES-201 intersected a thick zone of vuggy residiual quartz and quartz–alunite–kaolinite alteration likely representing the northwestern extension of the İnlice HS system (Figure 2.3E). This alteration assemblage transitions downward into zones of quartz–white mica alteration with abundant quartz–pyrite and gypsum–anhydrite stockworks overprinting recognizable andesitic porphyry textures (Figure 2.3F).

At Doğanbey, located ~20 km northeast of İnlice (Figure 2.1), historical work by Stratex plc. identified significant Mo and Au anomalies during surface sampling, suggesting the presence of a porphyry system. Field mapping and drill core

inspection confirmed intense acidic alteration (silica–alunite–clay) similar to that at İnlice (Figure 2.4A–B). Surface exposures are dominated by erosion‐resistant silicified zones with no fresh magmatic rocks preserved, while drill core intersections display the same quartz–alunite assemblages underlain by porphyritic units retaining magmatic textures but affected by moderate intensity quartz–clay alteration (Figure 2.4C).

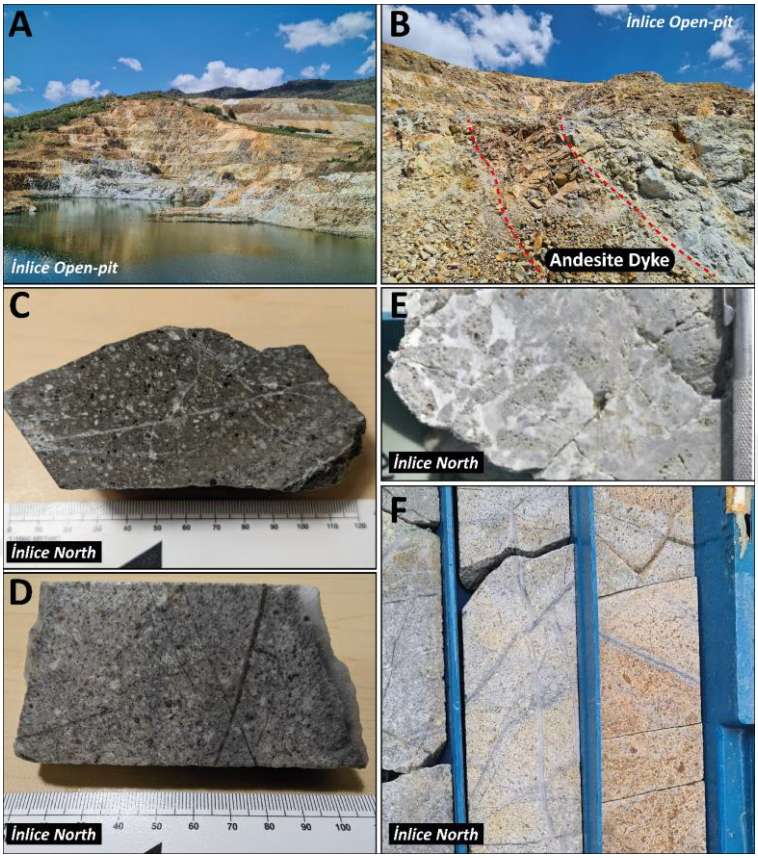


Figure 2.3. Field and drill core photographs from the İnlice area within the KVC. (A) View of the İnlice open pit showing zones of intense silicification and advanced argillic alteration hosting high-sulfidation epithermal Au mineralization. (B) Andesitic dike cutting through altered and mineralized andesite porphyry on the SE wall of the open pit. (C) Weakly-propylitized andesite porphyry from drill hole INES-201, located north of the pit. (D) Andesite porphyry showing weak potassic alteration and associated M- and B-type veinlets. Propylitic alteration occurs as an overprint. (E) Residual vuggy silica and alunite cross-cutting potassic-altered

andesite porphyry. (F) Quartz-sericite/clay-pyrite alteration and quartz-pyrite stockworking in porphyrytic andesite(?) from deeper levels of drill hole INES-201.

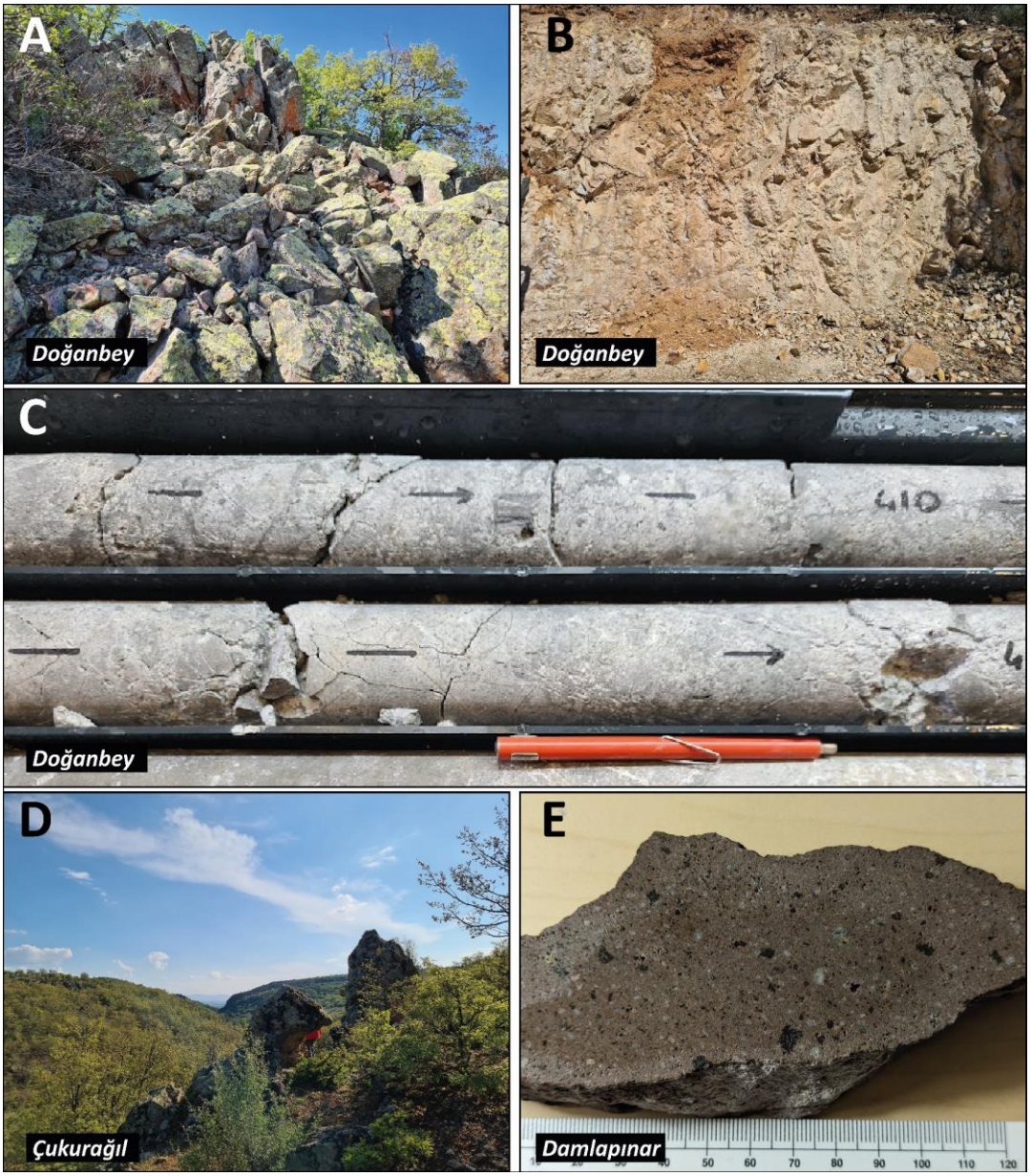


Figure 2.4. Field and core photographs from the Doğanbey, Çukurağıl, and Damlapınar prospects within the KVC. (A) Erosion-resistant units displaying silicification and advanced argillic alteration at the Doğanbey epithermal–porphyry prospect. (B) Porphyritic volcanic unit with quartz–alunite alteration exposed at the DGBD-01 drill collar site at Doğanbey. (C) Quartz–kaolinite-altered porphyritic

volcanic rock observed in drill hole DGBD-02 at Doğanbey. (D) Silica caps at the Çukurağıl epithermal prospect. (E) Hand specimen of weakly–altered andesite porphyry exposed at the Damlapınar prospect.

At Çukurağıl and Damlapınar, located 4–6 km north of Doğanbey, surface exposures are characterized by silica caps (Figure 2.4D) enveloped by quartz–clay altered andesitic lavas. Weakly-propylitized andesitic units still retain porphyritic textures in the outcrop with relatively well‐preserved ferromagnesian minerals (biotite, and hornblende) and plagioclase phenocrysts (Figure 2.4E).

Karacaören, located ~11 km southwest of İnlice near Saraycık village, exposes altered Miocene volcanic and volcaniclastic units overlain by fresh Pliocene lavas. Initial exploration by Stratex reported weak Au anomalies in the altered Miocene sequence and local intervals of Au mineralization during limited drill testing. ESAN Eczacıbaşı subsequently acquired the license to evaluate a potential analogue to the İnlice HS epithermal Au system. Silica–clay alteration zones are structurally controlled along a NW-trending stream south of the Saraycık village (Figure 2.5A–B), where andesitic to dacitic lavas and tuffs have largely lost their primary mineralogy. On the flanking ridges, relatively fresh porphyritic andesites crop out, with relatively well-preserved biotite and hornblende (both weakly altered into chlorite) and plagioclase phenocrsyts. The altered Miocene units are unconformably overlain by dark‐colored Pliocene lava flows.

The Ketenli license, located ~25 km south of İnlice, extends ~7 km from Ketenli village southward toward Seydişehir. As in İnlice and Karacaören, alteration is hosted within Miocene andesitic lavas and dacitic–rhyolitic tuff–agglomerate successions (Figure 2.5C–F). In the northern sector, domes form prominent topography surrounded by thick crystal‐lithic tuff sequences containing plagioclase ± K‐feldspar ± quartz with subordinate hornblende and biotite. Andesitic lava flows display similar mineralogy with lower quartz content. These units show silica flooding with chlorite–clay (illite–smectite?)–hematite–pyrite

alteration, while the surrounding tuffs exhibit intense kaolinization associated with opaline silica–smectite (halloysite?)–pyrite assemblages (Figure 2.5C).

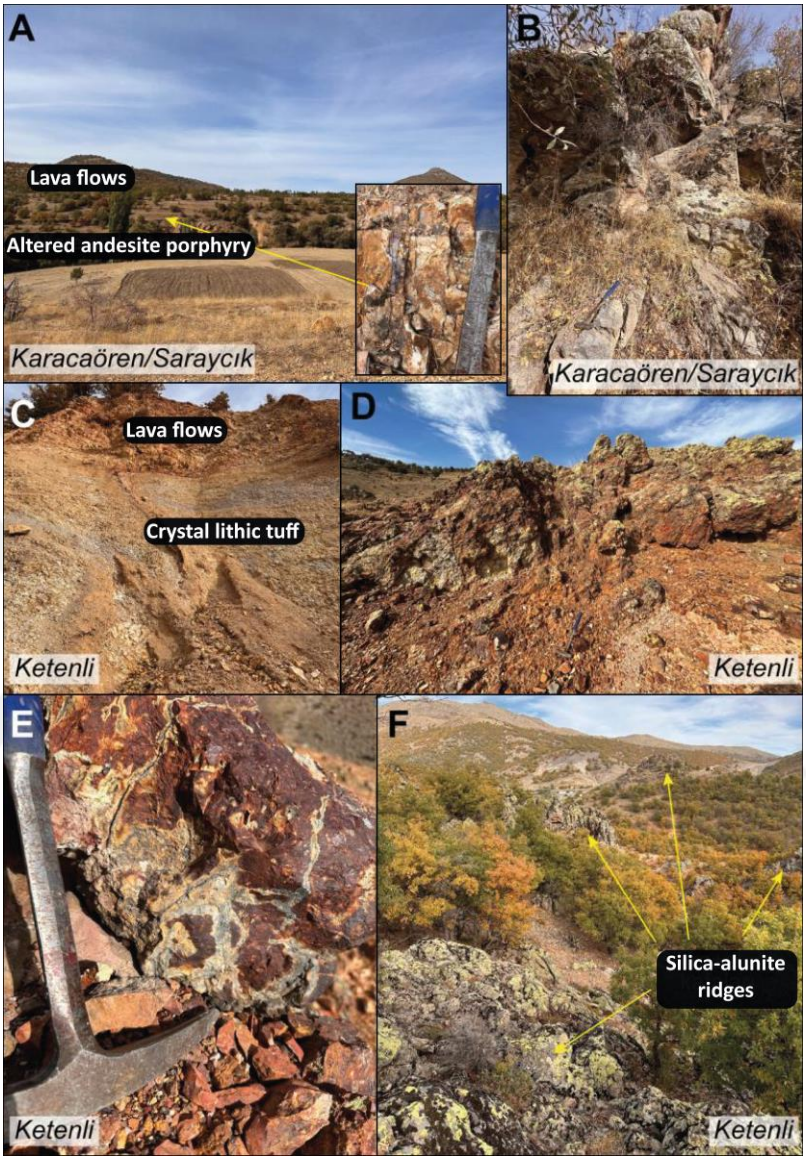


Figure 2.5. Field and outcrop photographs from the Karacaören and Ketenli prospects within the KVC. (A) Altered andesite porphyries overlain by Pliocene lavas within the Karacaören license area; inset shows representative outcrop of quartz veins hosted in the alteration zone. (B) Andesite porphyry outcrop exposed near Saraycık Village within the Karacaören license. (C) Tuffs overlain by weathered lavas near Ketenli Village. (D) Moderately weathered andesitic agglomerates

containing fresh andesite clasts, southern part of the Ketenli license. (E) Outcrop of silicified breccia with fine-grained disseminated pyrite in the matrix, southern Ketenli sector. (F) Silica ridges with approximate NNE orientation in southern Ketenli; fresh andesitic lavas and agglomerates are visible in the background hills.

Further south in Ketenli, similar alteration styles occur around dome structures. In the Ortakaraören area, thick agglomerate sequences crop out along a roughly N–S trending valley. Here, intense clay alteration and Fe‑(hydr)oxide staining are observed in weathered outcrops, while less altered blocks preserve andesitic–dacitic clasts containing fresh biotite, hornblende, and plagioclase (Figure 2.5D). Locally, pyrite‑cemented brecciated silica veins and erosion‑resistant alunite–silica caps are present, although no direct evidence of mineralization has yet been identified at surface (Figure 2.5E–F).

2.1.2 Karacadağ-Melendiz Volcanics (7–1 Ma)

Numerous volcanic centers of Late Miocene–Pliocene and Quaternary age are exposed across a broad region between Niğde and Aksaray provinces (Figure 1.7). Among these, the Melendiz Mountain and the Karapınar volcanic field to its west host multiple volcanic cones, caldera structures, and andesitic–dacitic domes. Thick accumulations of volcaniclastic deposits, interlayered basaltic–andesitic–dacitic lava flows, agglomerates, and tuffs are widespread within and around these volcanic edifices.

For the Melendiz volcanic complex, which rises immediately west of the Niğde city center and extends westward toward Mount Hasan, Türkecan et al. (2003) reported K/Ar ages ranging between 8 and 4 Ma. More recent $^{40}Ar/^{39}Ar$ hornblende–biotite and U–Pb zircon geochronology has refined this range, indicating a younger magmatic episode between ~4.5 and 3.5 Ma (Kuşcu et al., 2019; Rabayrol et al., 2019a). These data confirm that the Melendiz volcanic field, characterized by

pervasive low‐ temperature alteration, hosts some of the youngest known epithermal systems not only in Central Anatolia but across Türkiye.

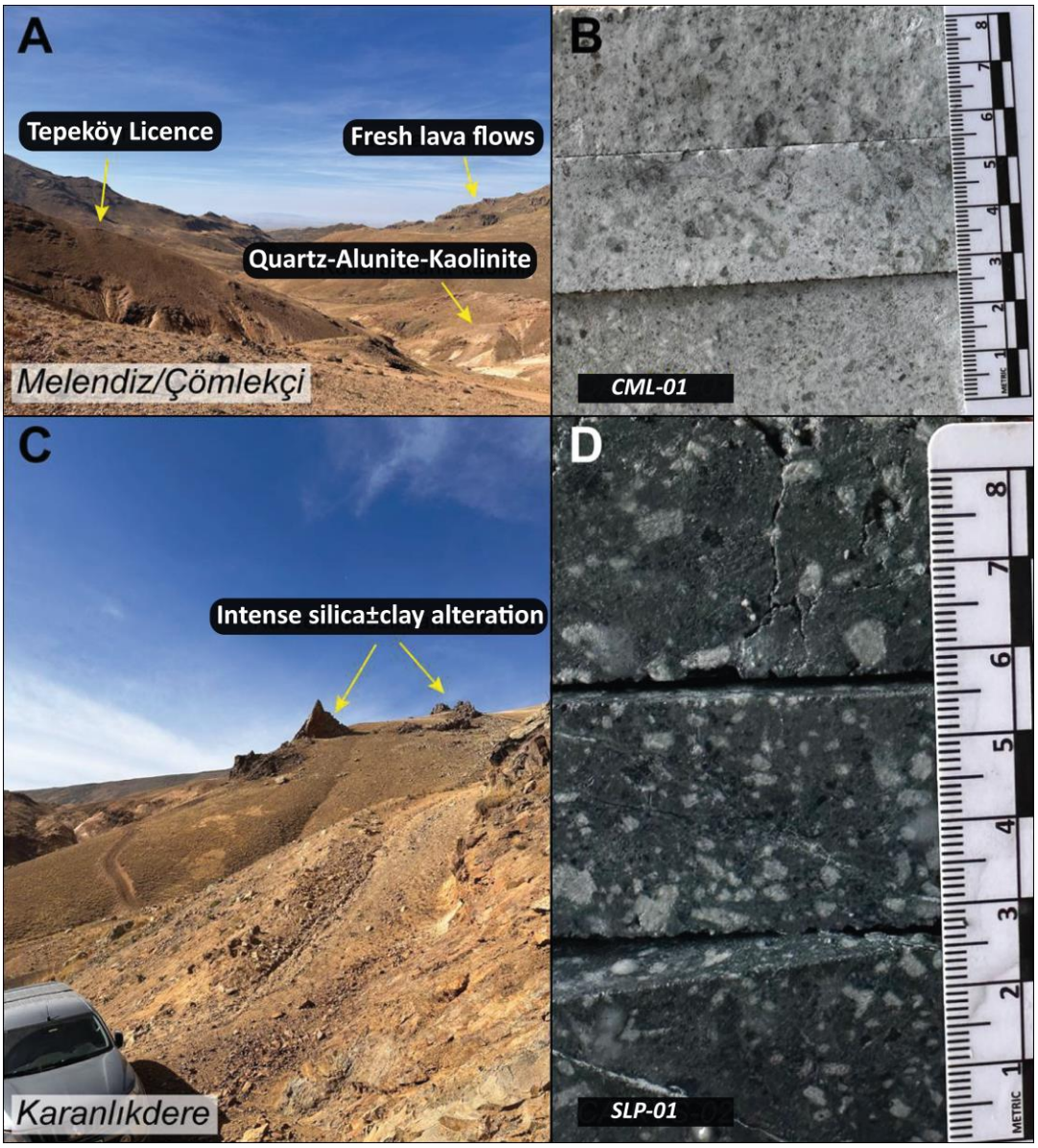


Figure 2.6. Field views and core photographs from sampling locations in Melendiz area. (A) Hydrothermally-altered units within the Melendiz Dağ volcanic complex, located east of Niğde (view looking west). (B) Agglomerate displaying quartz–illite–chlorite(?) alteration in drill core from the Çömlekçi prospect. (C) Erosion-resistant

altered lava flows at the Karanlıkdere locality. (D) Altered (chlorite–illite?) massive basaltic andesite/andesite sample from Karanlıkdere.

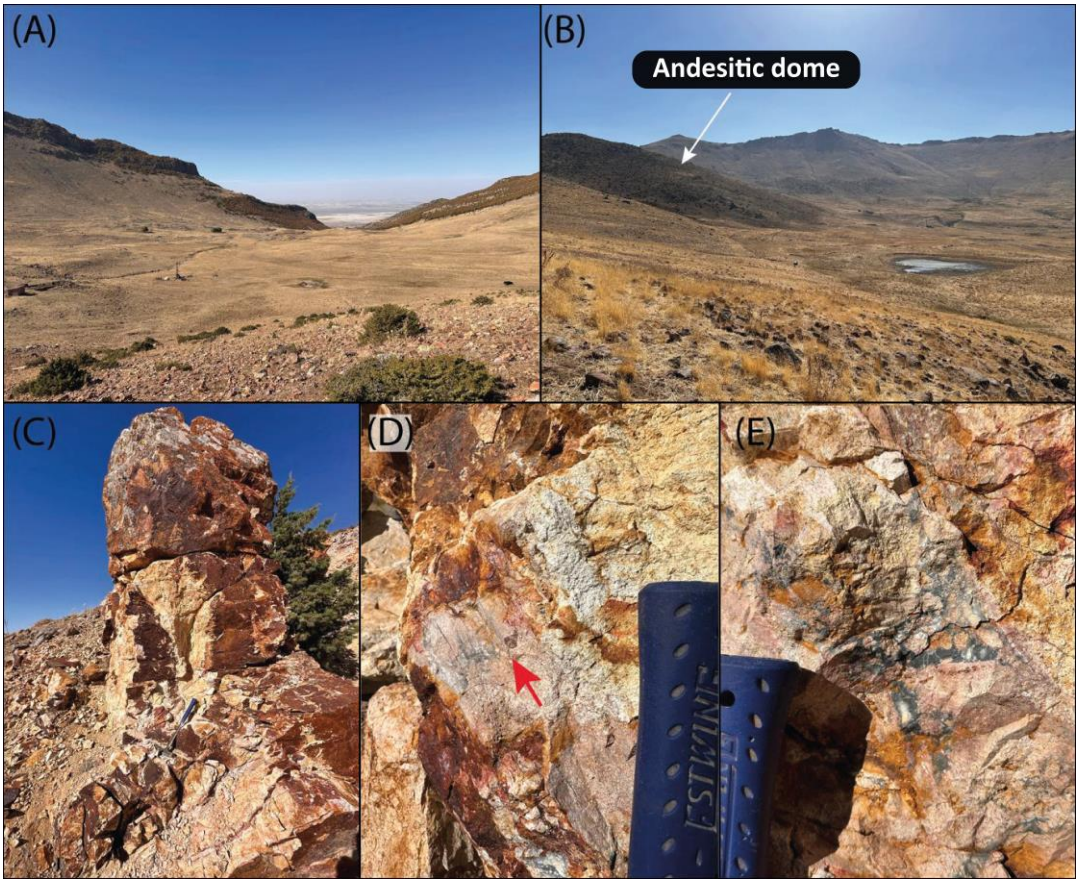


Figure 2.7. Field photographs of the Karacadağ caldera. (A) Layered lava flows and volcaniclastic deposits (block faulted to the left of image) rimming the caldera (view toward the west with town of Yeşilyurt in the background). (B) An andesitic(?) dome developed in the eastern part of the caldera center. (C, D) Strongly clay-silica-altered, Fe-(hydr)oxide-stained andesite porphyry. Red arrow in (D) show fault striations (E) Brecciated andesite porphyry with dark gray silica matrix.

Hydrothermal alteration in the Melendiz region is spatially extensive, with the most intense zones localized along structural lineaments and near volcanic vents. Volcanic rocks affected by quartz–clay–alunite alteration were first investigated in the early 2000s by Stratex plc. for their potential to host high‐sulfidation (HS) epithermal Au ± Ag ± Cu mineralization. More recently, Centerra Gold and ESAN Eczacıbaşı

have conducted exploration drilling in adjacent Tepeköy, Süleymanpınarı, and Çömlekçi prospects, as well as in the nearby Karanlıkdere license (Figure 2.6A–D).

At the Süleymanpınarı prospect, advanced argillic and argillic alteration zones developed within andesitic–dacitic lavas and volcaniclastic units are well‐exposed at surface (Figure 2.6A). These alteration assemblages, readily distinguished by their bleached and orangish/reddish color due to pervasive clay alteration and pyrite oxidation, extend over a ~1 km‐wide ridge trending NW–SE. Toward the south, the alteration halo merges with the Tepeköy prospect, where Centerra's earlier drilling intersected thick zones of silica-clay-pyrite alteration and narrow intervals of barren quartz–alunite–kaolinite assemblages (Figure 2.6A). On the eastern flank of the ridge, advanced argillic alteration grades into argillic assemblages dominated by quartz–kaolinite, chlorite, and minor illite/smectite, particularly well‐expressed within volcaniclastic lithologies. Hematite–goethite oxidation halos are common in pyrite‐rich intervals, and residual cryptocrystalline silica is locally observed, especially within matrices of volcaniclastic units.

Drill cores from the Süleymanpınarı license revealed porphyritic andesitic to basaltic andesitic units retaining primary textures despite alteration (Figure 2.6B). Plagioclase phenocrysts up to 1 cm in length are hosted within a dark gray groundmass, accompanied by altered biotite and hornblende phenocrysts.

In the nearby Çömlekçi license, two drill holes (ÇMLD‐001 and 002) were examined and sampled. Shallow intervals intersect a fine-grained and groundmass dominant porphyritic unit, locally overprinted by intense quartz–alunite alteration. These zones are cut by narrow andesitic dykes and chaotic breccias interpreted to be a part of a diatreme complex, with phenocrysts in the dykes showing strong kaolinization. At depth, drilling intercepted thinly bedded volcaniclastics intercalated with volcanic units affected by quartz–chlorite–kaolinite–smectite–

pyrite (argillic) alteration, cut locally by partially altered and variably magnetic dykes.

The Karanlıkdere license occupies the northern extension of the NW–SE‐oriented altered structural corridor mapped at Süleymanpınarı (Figure 2.6C). The two prospects are separated by a NE–SW ridge, yet lithologies and alteration styles are continuous between them. Along a fault‐controlled stream valley at Karanlıkdere, intense alteration is accompanied by erosion‐resistant silica caps forming sharp ridges (Figure 2.6C), some coated with hematite–iron oxide staining. Drill cores document quartz–kaolinite and quartz–illite–chlorite alteration as the dominant assemblages, with narrow zones of vuggy silica and quartz–alunite ± kaolinite developed near surface.

Fieldwork within the Melendiz volcanic field focused on the Çömlekçi and Karanlıkdere prospects, where core samples were collected from basaltic andesite–andesite–dacite lava flows and andesitic agglomerates showing varying intensities of quartz–kaolinite and quartz–illite–chlorite alteration (Figure 2.6B-D).

Additional sampling was conducted in the Karacadağ volcanic field near Karapınar in Konya province. The Karapınar–Karacadağ volcanic succession forms a collapse caldera structure (Figure 2.7A–B) approximately 4 km SSE of the town of Yeşilyurt. Volcanic activity at Karacadağ occurred from ~6 Ma to ~2.5 Ma (Platzman et al., 1998; Reid et al., 2017; Doğan‐Kulahcı et al., 2018; Gençoğlu Korkmaz et al., 2022). Around the caldera margins, fresh andesitic–dacitic lava flows display well‐developed layering (Figure 2.7A), while outer flanks are dominated by agglomerate–tuff sequences. At the caldera center, an andesitic dome exhibits pervasive silica ± alunite ± clay alteration (Figure 2.7B). Relatively fresh exposures within the dome complex contains a gray-colored andesite porphyry that is highly magnetic and comprising phenocrystic biotite, hornblende, and plagioclase set in a

dark groundmass. Hydrothermal alteration in Karacadağ is localized along radial ring faults extending outward from the caldera core, where andesite porphyry has been brecciated and pervasively replaced by silica-pyrite-clay assemblages (Figure 2.7C–D) partly weathered into Fe-(hydr)oxides (Figure 2.7E).

2.1.3 Develidağ Volcanic Complex (6–5 Ma)

Located approximately 45 km south of Kayseri city center and ~29 km south of the Erciyes stratovolcano, the Develidağ Volcanic Complex (DVC) is situated along the eastern margin of the Sultansazlığı pull-apart basin, forming part of the Ecemiş Fault Zone (Figure 2.8A). The complex, which developed during the Late Miocene to Early Pliocene, has been partially dissected by the NW–SE–trending Develi Fault that defines the eastern structural boundary of the basin. At the core of the complex lies a prominent dome structure composed of massive basaltic andesite to andesite lava flows (Figure 2.8A). This dome is encircled by a succession of ignimbritic units, which are in turn overlain by younger basaltic lava flows, indicating a prolonged and multi-phase eruptive history.

The Öksüt high-sulfidation (HS) epithermal Au–Cu mineralization is genetically linked to the basaltic andesite–andesite dome located at the center of the DVC. Radiometric age data suggests that mineralization occurred between 6.0 and 5.5 Ma (Rabayrol et al., 2019; Aluç et al., 2020; Yurdakul et al., 2021; Figure 2.8A–B). The mineralized zone is characterized by steeply dipping silica ledges localized along steep oblique faults with strong normal components. These structures are hosted within a diatreme-like breccia that does not appear to widen significantly toward the surface, suggesting presence of a relatively confined vertical hydrothermal system.

Within the silica ledges – similar to those observed at the İnlice deposit – well-developed alteration zonation is evident, with a central core of residual vuggy silica

surrounded by concentric zones of quartz–alunite and quartz–kaolinite alteration. Au–Cu mineralization is predominantly associated with breccias hosted within the vuggy silica and quartz–alunite zones, often displaying intense oxidation (Aluç et al., 2020; Yurdakul et al., 2021).

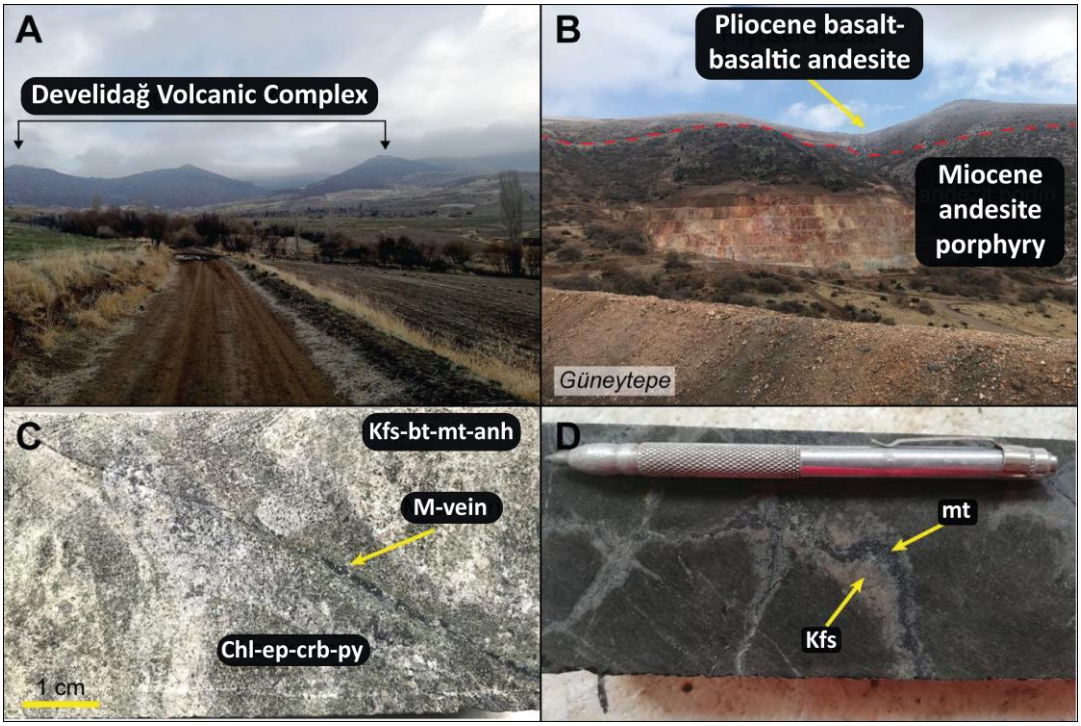


Figure 2.8. Field and drill core photographs from the DVC and the associated Öksüt HS epithermal Au-Cu deposit. (A) Andesitic dome occupying in the northern part of the DVC, which is also the host to Öksüt gold mineralization (view to the north from the Öksüt village). (B) View of the Güneytepe open pit, looking east. The upper part of the pit exposes Early Pliocene basalt to basaltic andesite lava flows overlying altered and mineralized andesite porphyry. (C) Drill core of potassically-altered (biotite-K-feldspar-magnetite) andesite porphyry from the deeper part of the Keltepe pit. Green color is due to late propylitic alteration (D) Deformed magnetite vein with K-feldspar halos in potassically-altered andesite porphyry.

These ledges transition laterally and vertically into a broader argillic alteration zone, which is composed primarily of quartz–kaolinite–illite–smectite assemblages. At deeper structural levels—particularly within the Keltepe open pit—this argillic

assemblage gradually gives way to potassic alteration (Yurdakul et al., 2021). The potassic zone at the base of the HS epithermal system is characterized by secondary biotite, K-feldspar, magnetite, and anhydrite (Figure 2.8C–D). Although classic A- and B-type veins typically associated with porphyry systems are absent, hairline M-type magnetite veinlets are locally present (Figure 2.8C), occasionally surrounded by K-feldspar selvages (Figure 2.8D).

Drill core samples of andesite porphyry were obtained from intervals of weak to moderate intensity potassic alteration underlying the Keltepe sector of the Öksüt HS epithermal Au mineralization. In its weakly altered form, this intrusive unit contains abundant plagioclase phenocrysts alongside subordinate clinopyroxene and orthopyroxene phenocrysts, and magnetite microphenocrysts.

2.2 Mineralogy and Petrography

2.2.1 Konya Volcanic Complex (16–8 Ma)

Within the Erenlerdağ-Alacadağ sector of the KVC, samples collected from the İnlice, Doğanbey, Çukurağıl, and Damlapınar tenements display varying degrees of hydrothermal alteration. Some of the samples, especially those collected from areas distal to mineralized domains, show weak to no alteration, and thus retain their primary mineralogy and magmatic textures. However, the majority of samples collected originate from ore-proximal areas exhibit where alteration intensity is high. All fresh or least-altered samples are of andesitic composition and display groundmass‐dominant porphyritic texture (Figure 2.9).

In the least-altered samples from the İnlice open pit and core samples from INES‐201, the principal phenocryst phases are plagioclase, hornblende, and biotite (Figure 2.9A–C). Selective alteration is evident, with hornblende crystals commonly

replaced by fine clay minerals (Figure 2.9A, C), whereas biotite tends to remain relatively well-preserved in most cases (Figure 2.9A–C). In the andesitic dyke sample collected from the İnlice open pit, opacitization due to replacement by Fe–Ti oxides is common particularly in the rims of biotite and hornblende. Formation of such Fe-Ti-oxides likely reflects rapid magma ascent and associated decompression effects during emplacement (Rutherford and Hill, 1993; Chambefort et al., 2013; Figure 2.9).

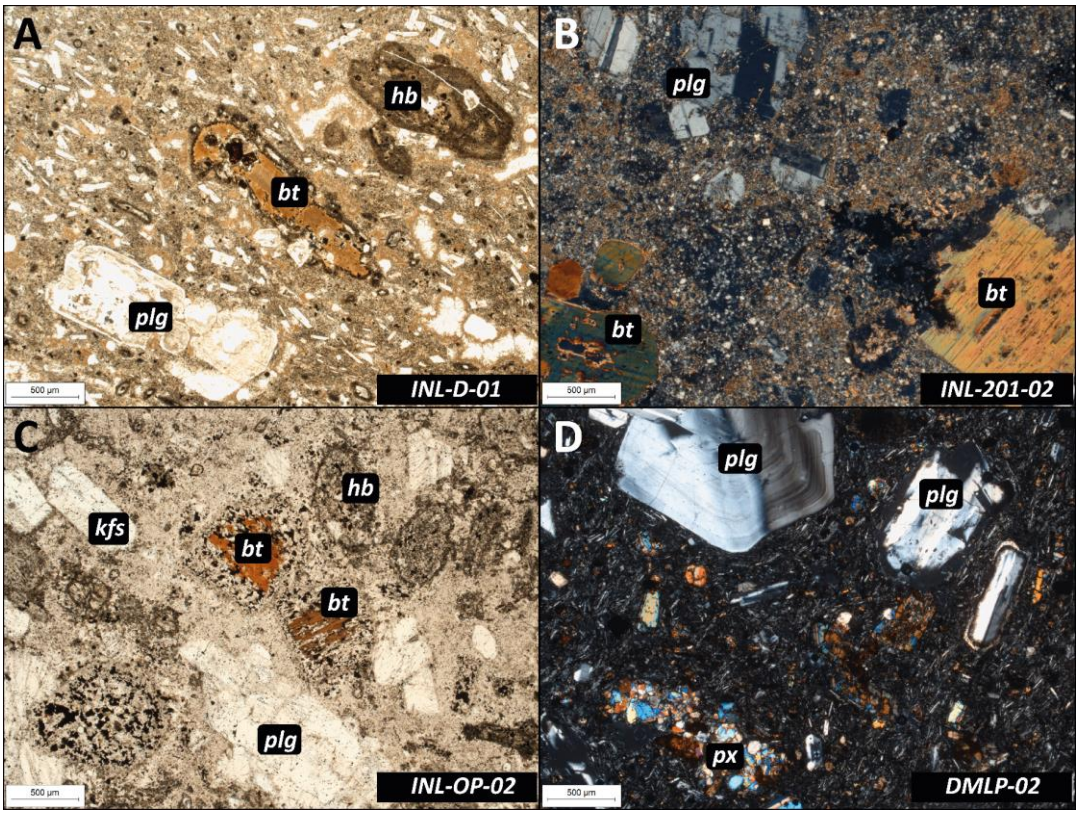


Figure 2.9. Transmitted light microphotographs of igneous rock samples from İnlice and Damlapınar areas in KVC. (A) Strongly altered andesite dyke within the İnlice open pit. Hornblende is completely replaced, whereas plagioclase in both groundmass and phenocrysts is partially kaolinized; biotite shows partial opacitization and clay alteration (PPL). (B) Weakly-altered andesite porphyry from drill hole INES-201 with relatively well-preserved plagioclase and biotite phenocrysts (XPL) (C) Strongly kaolinized andesite porphyry host to the İnlice HS

epithermal Au mineralization (PPL). (D) Weakly-altered pyroxene-bearing andesite porphyry from the Damlapınar prospect (XPL).

A second sample from the İnlice open-pit displays partial chlorite–sericite alteration of biotite (Figure 2.9). Rare sanidine phenocrysts were also observed in this sample, although they are subordinate compared to plagioclase and ferromagnesian phases (Figure 2.9C). In all samples showing only low to moderate degrees of alteration, plagioclase phenocrysts are generally fresh, exhibiting minor sericitization (Figure 2.9A–B). Oscillatory and complex zoning patterns are common in phenocrystic plagioclase, reflecting dynamic magmatic conditions during crystallization.

Drill core samples from the Doğanbey prospect and surface samples collected near drill sites in the Çukurağıl license are strongly affected by quartz–alunite–clay alteration and such as their primary rock types and original mineralogy could not be determined accurately. Despite this extensive overprint, a porphyritic texture remains evident in both areas. In contrast, a basaltic andesite specimen from the Damlapınar prospect exhibits a groundmass‐dominated porphyritic texture similar to that was observed at İnlice (Figure 2.9D). However, unlike the andesite porphyry samples, the Damlapınar basaltic andesite porphyry contains plagioclase and biotite phenocrysts accompanied by clinopyroxene and sparse orthopyroxene, but no hornblende (Figure 2.9D) where pyroxene phenocrysts are locally present in clusters resulting in glomeroporphyritic textures. In addition, some biotite phenocrysts in this sample enclose plagioclase microphenocrysts, indicating co-crystallization of both phases (Figure 2.9D).

Although magnetite microphenocrysts are present in both the İnlice and Damlapınar samples, most have been variably replaced by hematite and other Fe–Ti oxide phases due to hydrothermal alteration and/or surface weathering. Zircon and fine prismatic magmatic apatite crystals occur as accessory phases in all samples. The groundmass enveloping phenocrysts is typically very fine‐grained and dominated by plagioclase

microlites, whereas in the İnlice andesitic dyke the groundmass is more glassy and partially devitrified (Figure 2.9A).

A moderately to weakly altered andesite porphyry sample from the Karacaören prospect is characterized by large plagioclase and hornblende phenocrysts, both of which exhibit partial carbonate alteration (Figure 2.10A). This sample also contains subordinate biotite and rare quartz phenocrysts; the biotite is better preserved relative to feldspar and hornblende, although Fe–Ti oxide rims related to opacification are also present. The groundmass hosts fine carbonate and minor chlorite–illite alteration phases (Figure 2.10A).

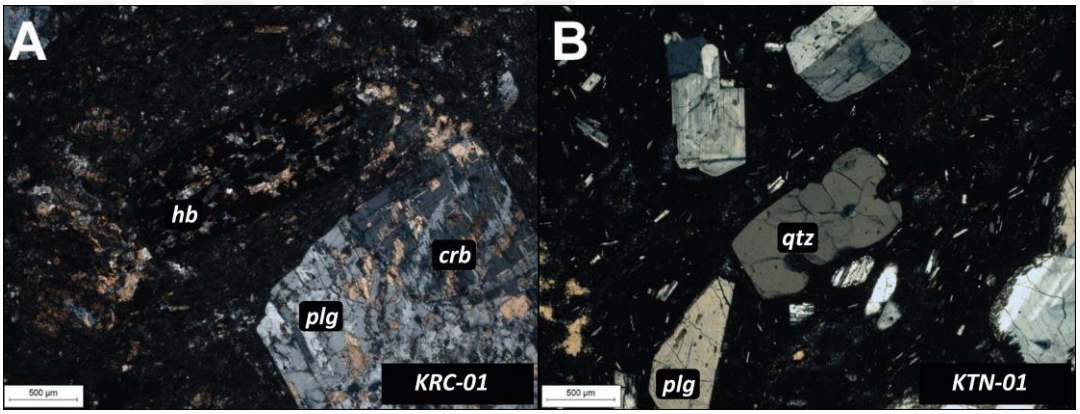


Figure 2.10. Transmitted-light microphotographs of igneous rocks from the Karacaören and Ketenli sectors of the KVC. (A) Andesite porphyry from Karacaören showing weak carbonate–chlorite–illite alteration. Plagioclase and hornblende phenocrysts have been partially replaced by carbonate, and hornblende has been partially opacitized (XPL). (B) Dacitic agglomerate from Ketenli with embayed quartz and zoned plagioclase phenocrysts set in a fine-grained matrix (XPL).

A dacitic agglomerate sample from the Ketenli prospect shows partial hydrothermal alteration combined with incipient weathering. Well‑crystallized clasts are enclosed within a clay‑rich matrix of similar mineral composition. Quartz, often showing embayed textures, and plagioclase is relatively well preserved (Figure 2.10B), while the hornblende and biotite have been selectively replaced by chlorite and illite. Strong opacitization is common in the ferromagnesian minerals. Sieve textures have

been frequently developed along the rims of plagioclase phenocrysts. This combined with widespread opacitization are interpreted to reflect decompression during rapid magma ascent.

2.2.2 Karacadağ-Melendiz Volcanics (7–1 Ma)

Within the Melendiz volcanic field, samples collected from the epithermal prospects at Çömlekçi and Süleymanpınarı/Karanlıkdere display pervasive hydrothermal alteration within andesitic–dacitic lava flows and volcaniclastic units. In a relatively well‑preserved andesite porphyry host rock from the Çömlekçi prospect, plagioclase phenocrysts retain fresh appearances, whereas all ferromagnesian phases have been extensively replaced by clay minerals (Figure 2.11A). Crystal morphologies indicate that hornblende constituted the dominant mafic phenocryst phase (Figure 2.11A), although some finer-grained crystals likely represent altered biotite. The phenocrysts are set in a fine-grained groundmass composed primarily of plagioclase laths with minor quartz and exhibit partial devitrification textures (Figure 2.11A).

At Süleymanpınarı/Karanlıkdere, the intensity of hydrothermal alteration is even higher, dominated by quartz–alunite alteration with local zones of kaolinization. In least-altered andesite porphyry samples from this area, fresh plagioclase phenocrysts are abundant and are accompanied by subordinate, generally finer-grained biotite and quartz (Figure 2.11B–C). The groundmass ranges from microcrystalline to partially glassy. Hornblende phenocrysts, identified from relict crystal habits have been almost completely replaced by illite. In other andesite porphyry samples from this prospect, intense late‑stage carbonate alteration has overprinted all phases except for plagioclase and quartz phenocrysts, as well as the groundmass itself (Figure 2.11D). Carbonate-replaced hornblende phenocrysts are readily recognized by their euhedral, rhombohedral crystal forms. Petrographic relationships suggest

that samples underwent illite–silica alteration prior to the development of the pervasive carbonate alteration.

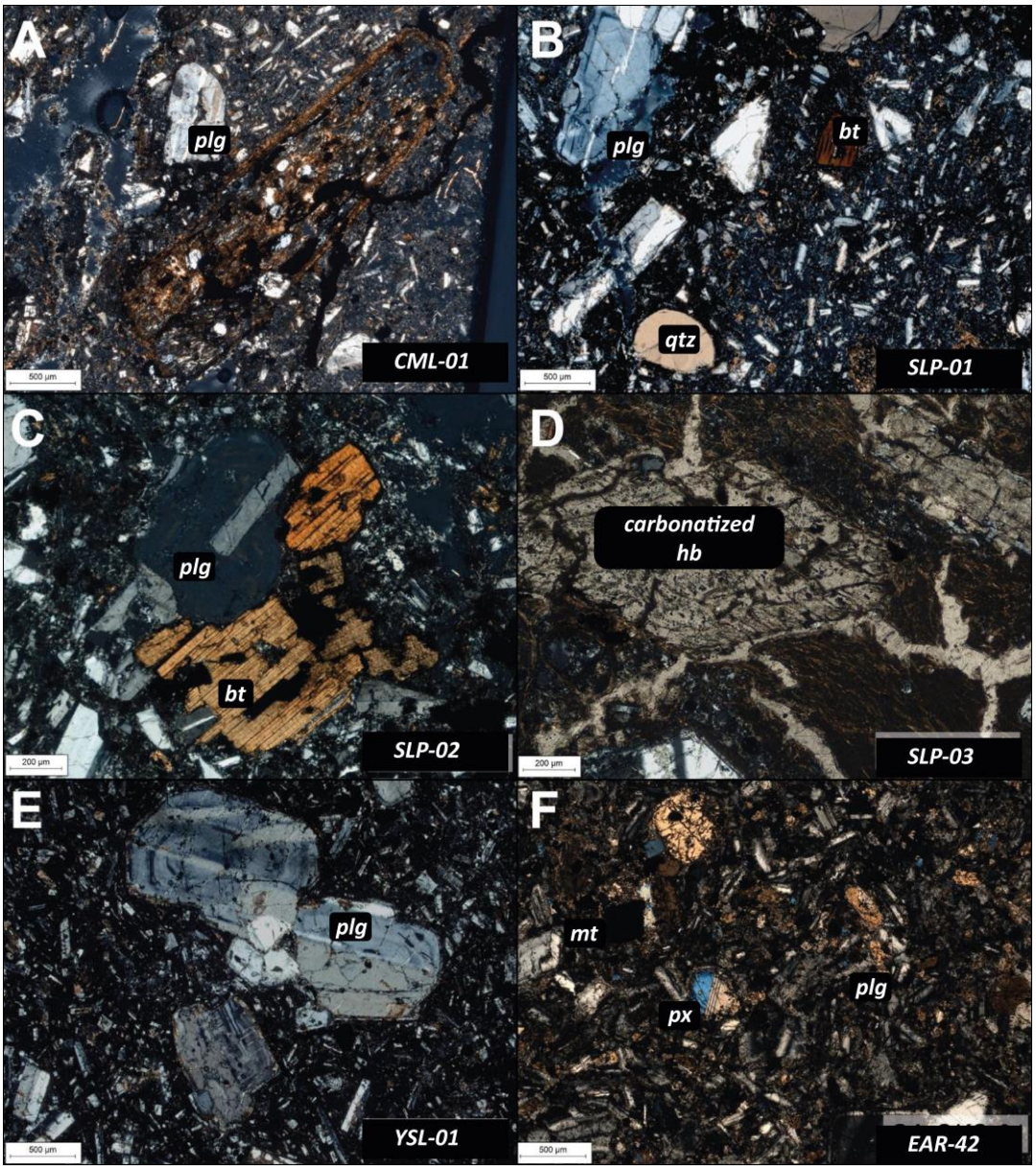


Figure 2.11. Transmitted-light microphotographs of Late Miocene–Pliocene igneous rock samples from the Niğde–Kayseri region. (A) Andesite porphyry from the Çömlekçi (Melendiz) prospect, showing low-temperature alteration; plagioclase phenocrysts are largely fresh, whereas a large hornblende crystal has been replaced

by clay minerals (XPL). (B) Least-altered andesite poprhyry from Çömlekçi displaying quartz–plagioclase–biotite as the main phenocrysts (XPL). (C) Dacitic lava flow from Süleymanpınarı containing quartz, plagioclase, and biotite phenocrysts set in partially devitrified glassy matrix (XPL). (D) Completely carbonatized hornblende phenocryst in altered andesitic lava from Karanlıkdere area (XPL)Weakly-altered dacite porphyry from Süleymanpınarı with large, medium-grained plagioclase and biotite crystals; opaque inclusions within biotite are magnetite (XPL). (E) Plagioclase-phyric andesite porphyry containing hornblende and magnetite phenocrysts from the Karacadağ caldera (XPL). (F) Clinopyroxene-bearing andesite porphyry host rock of the Öksüt HS epithermal Au-Cu deposit in the DVC (XPL).

In contrast, andesite porphyry samples collected from the Karacadağ caldera east of Karapınar/Yeşilyurt are remarkably fresh. Hand specimens are dark-colored and display coarse porphyritic textures characterized by large, euhedral plagioclase and hornblende phenocrysts with minor biotite. Plagioclase frequently exhibits oscillatory and complex zoning and commonly forms glomeroporphyritic clusters (Figure 2.11E). The opaque mineral content is high, with abundant magnetite microphenocrysts accompanied by widespread ilmenite as a secondary accessory phase.

2.2.3 Develidağ Volcanic Complex (6–5 Ma)

Within the Develidağ Volcanic Complex, the andesite porphyry unit—recognized as the principal host rock of the Öksüt high-sulfidation (HS) epithermal Au–Cu deposit and its deeper porphyry-type alteration zone—is pervasively affected by hydrothermal processes. In the shallow levels of the andesitic dome, the rock typically exhibits a groundmass‑rich porphyritic texture, whereas towards the deeper portions of the system, in proximity to the porphyry alteration zone, the same unit becomes coarser-grained and notably richer in phenocrysts.

In the least altered specimens, the dominant phenocryst phase is plagioclase, occurring as elongated rectangular prismatic crystals that constitute approximately

60 % of the rock (Figure 2.11F). These are accompanied by subordinate clinopyroxene and rare orthopyroxene, together with disseminated magnetite microphenocrysts (Figure 2.11F). The groundmass is comparatively scarce and is dominated by very fine plagioclase laths (Figure 2.11F). Zircon and prismatic apatite were consistently identified as accessory phases. This mineral assemblage and textural variation reflect the transition from shallow volcanic dome facies to deeper, intrusion-proximal porphyry domains within the magmatic–hydrothermal system.

CHAPTER 3

MAGMATISM AND METALLOGENY IN WESTERN ANATOLIA

The Late Cenozoic magmatic belt in Western Anatolia extends from the southern Balıkesir–Çanakkale region in the north to the Afyon–Isparta–Burdur line transect in the south. The widespread Cenozoic magmatism in this region is closely linked to the slab roll‐back of the northward‐subducting African oceanic lithosphere beneath the Aegean (Hellenic) arc system and extensional tectonic regime due to back-arc rifting (Dilek and Altunkaynak, 2009). One of the most prominent features of this region's tectonomagmatic history is the progressive southward younging of magmatic activity since the Late Eocene–Oligocene, reflecting the retreat of the African slab towards the south (Jolivet et al., 2013; Ersoy et al., 2017).

The sampling strategy in Western Anatolia was designed to record this temporal and spatial migration of magmatism along the Late Cenozoic belt. Accordingly, sampling locations were selected to represent a north–south transect, beginning in the Balıkesir–Kütahya region ("Northern Sector") and extending southward through the Isparta–Burdur–Afyon–Bodrum corridor ("Southern Sector").

3.1 Regional Geology and Field Observations

3.1.1 Balıkesir District (25 Ma)

Within the Biga Peninsula, including parts of the Balıkesir region, and the adjacent areas to the east, two principal Cenozoic magmatic phases have been recognized (Dilek and Altunkaynak, 2009). The first phase, active mainly between 45 and 35 Ma, is represented by calc‐alkaline, intermediate to felsic magmatic suites emplaced in a collisional setting synchronous with the convergence between the

Tauride–Anatolide Block and the Pontides. Several low‐ and high‐sulfidation epithermal systems including the Kartaldağ–Madendağ, Lâpseki, and Şahinli Au deposits dated to ~42 Ma as well as the Halilağa, Valley, and Camelback Cu–Au porphyry systems within the TV Tower license, are associated with this magmatic episode and represent some of the most significant base and precious metal deposits in the region (Ünal‐İmer et al., 2013; Brunetti, 2016; Smith et al., 2016; Kuşcu et al., 2019).

Magmatic activity waned after ~35 Ma but experienced renewed intensity around 30 Ma in response to the transition from collisional to post‐collisional extensional tectonics. This second phase is marked by the formation of the Kirazlı and Küçükdağ (~30–29 Ma) and Ağı Dağı (~26 Ma) high‐sulfidation epithermal Au–Ag systems, followed at ~25 Ma by porphyry Mo and polymetallic skarn systems at Balya and Tepeoba (Murakami et al., 2005; Smith et al., 2014, 2016; Kuşcu et al., 2019; Özel, 2024; A. İmer, unpublished Re-Os molybdenite age data).

As part of this study, sampling was conducted in the northern sector of the Balya (Balıkesir) deposit. Here, deep porphyry mineralization was encountered in deep drill holes adjacent to the well-known Balya Pb-Zn-Cu skarn system. (Özel, 2024; Figure 3.1). Shallow levels of the sampled drill holes consist of intensely argillized and locally propylitized andesitic to dacitic lavas and volcanic breccias of the Hallaçlar volcanics (Figure 3.2). The greater depths, these lithologies grade into granodiorite porphyry intrusions exhibiting quartz–sericite–illite–pyrite alteration with abundant D-type quartz–sericite–pyrite veins (Figure 3.2B). Towards the deeper parts of the drill holes, two distinct porphyry intrusions with phyllic and potassic alteration assemblages were sampled. Mineralization in these zones is typically associated with B‐type quartz–molybdenite–pyrite±chalcopyrite veinlets, locally accompanied by K‐feldspar selvages (Figure 3.2C–D).

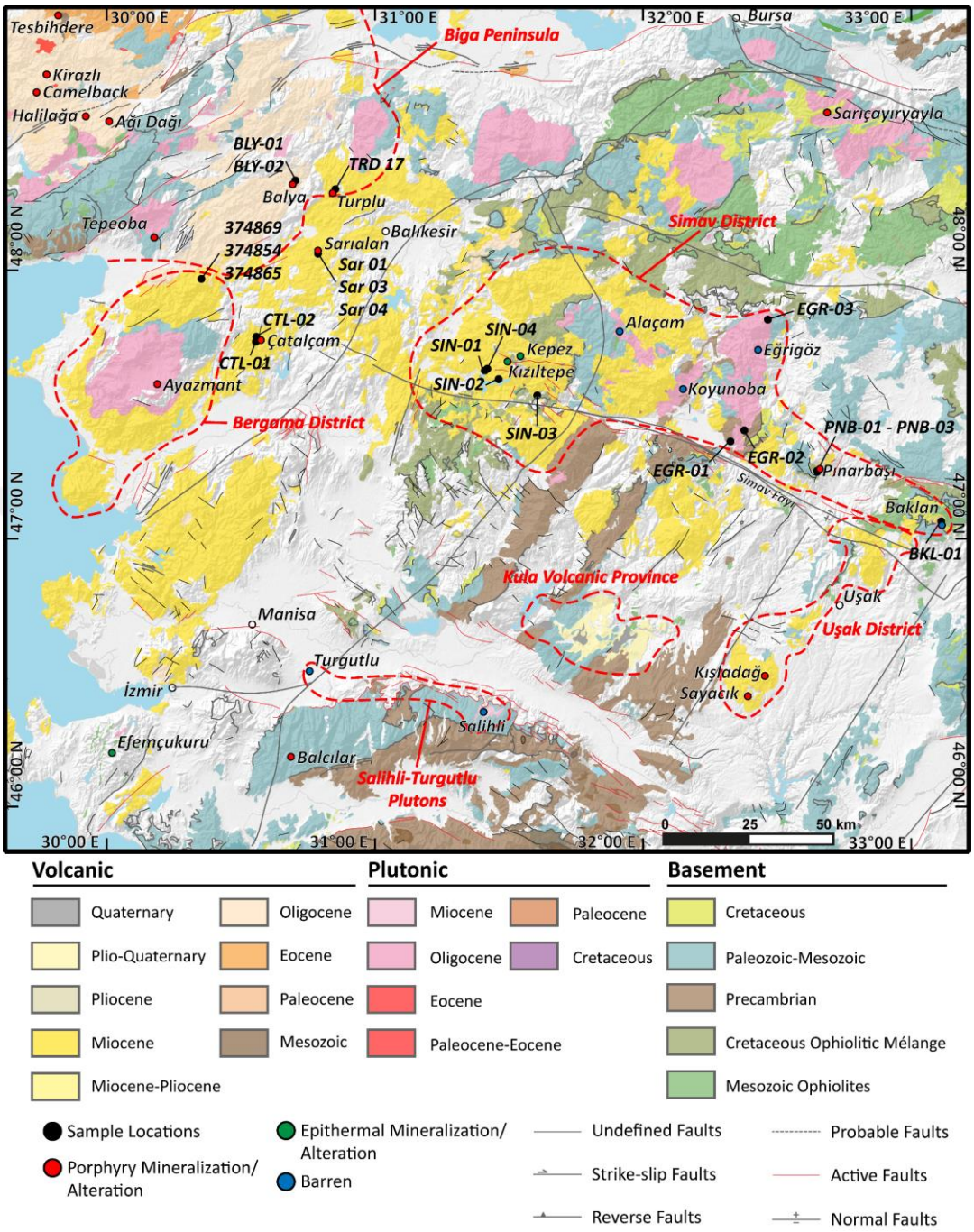


Figure 3.1. Simplified geologic map of the Biga Peninsula and the Kütahya–Simav area highlighting principal magmatic centers (Miocene–Pliocene) and the spatial distribution of porphyry and epithermal deposits/occurrences (MTA, 2002; Yılmaz et al., 2013; Bickford et al., 2016; Baker et al., 2016; Delibaş et al., 2017; Kuşcu et al., 2019; Özel, 2024).

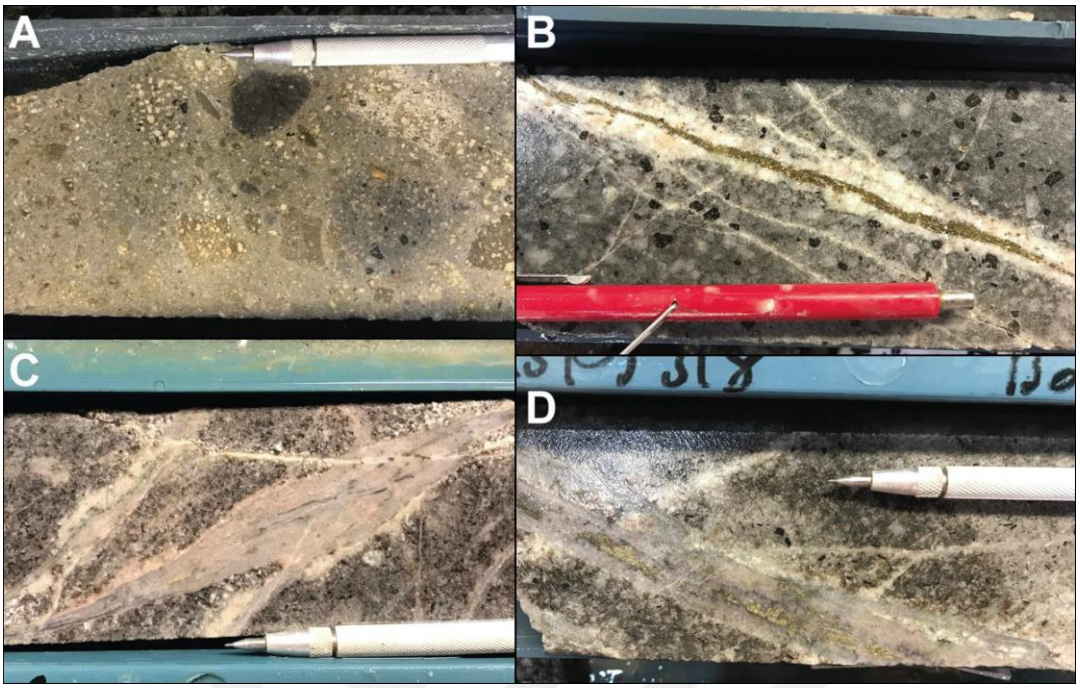


Figure 3.2. Drill core photographs from hole BKS-317, which intersects porphyry-style mineralization within the northern sector of the Balya skarn system. (A) Clay-altered agglomerate from the volcanic–volcaniclastic sequence overlying the porphyry system. Clasts include andesitic and basaltic lithologies. (B) Weakly-altered granodiorite porphyry cross-cut by a D-type quartz–pyrite vein, surrounded by a narrow sericitic halo. (C) Granodiorite porphyry exhibiting potassic alteration, cut by A- and B-type quartz–sulfide veins. Pinkish potassium feldspar halos are prominent around the veins. (D) B-type quartz–pyrite–molybdenite vein crosscutting potassically-altered granodiorite porphyry.

3.1.2 Kütahya-Simav District (22-17 Ma)

Following the Late Oligocene magmatism along the Çanakkale–Balıkesir area, magmatic activity migrated southward into the Kütahya and Manisa regions (Figure 3.1). The earliest products of this calc‑alkaline phase, emplaced between ~22 and 18 Ma, include granitic stocks and shallow felsic volcanic units dominated by dacitic to rhyolitic lava flows and associated volcaniclastic deposits (Yılmaz et al., 2001; Erkül et al., 2005; Ring and Collins, 2005; Akay, 2009; Hasözbek et al., 2011; Yılmaz et al., 2013). Granitic intrusions are well exposed along detachment faults north of Simav at Eğrigöz, Alaçam, and Koyunoba, whereas their volcanic

counterparts are best represented by extensive outcrops in the Sındırgı area (Figure 3.1).

Sındırgı and Eğrigöz: In the Sındırgı district (Figure 3.3), the units hosting the Kızıltepe LS epithermal Au–Ag mineralization comprise equigranular microgranites, massive porphyritic dacitic lavas, and agglomerates (Figure 3.4A–C). These units are only weakly affected by regional chlorite–illite–pyrite alteration and surficial weathering, with fresh ferromagnesian phases and plagioclase readily identifiable in outrcop samples. Northeast of Sındırgı, the Eğrigöz, Koyunoba, and Alaçam intrusions consistently display granitic compositions (Figure 3.4D–E). The granites are generally fresh, locally hosting mafic enclaves and crosscut by aplite dykes. Minor Fe skarn occurrences as well as IS epithermal-style mineralization are present along the NE and NW margins of the N–S‑trending Eğrigöz pluton (~21 Ma; Ring et al., 2003; Ring and Collins, 2005; Oyman et al., 2013). Sampling locations within this area (Figure 3.4E) coincide with active exploration programs targeting polymetallic skarn mineralization (Koza Gold licenses) and intermediate‑sulfidation epithermal Au–Ag systems (ESAN Eczacıbaşı licenses).

Salihli: The Salihli and Turgutlu granites, emplaced along the Alaşehir detachment within the Menderes Massif, are temporal and compositional equivalents (~20 Ma; Figure 3.1; Ring et al., 2003) of the Eğrigöz, Koyunoba, and Alaçam intrusions (Bozkurt et al., 1995; Bozkurt, 2003; Ring et al., 2003; Catlos et al., 2010). Among the Salihli and Turgutlu plutons, only the intrusive rocks at Salihli were sampled in this study (Figure 3.5). Along its southern margin, the granite is in tectonic contact with the metamorphic Bayındır Nappe and exhibits strong deformation and localized mylonitization (Figure 3.5B–C). The rock is typically coarse‑grained and fresh in appearance, with numerous flattened mafic enclaves developed in response to shearing (Figure 3.5B–C).

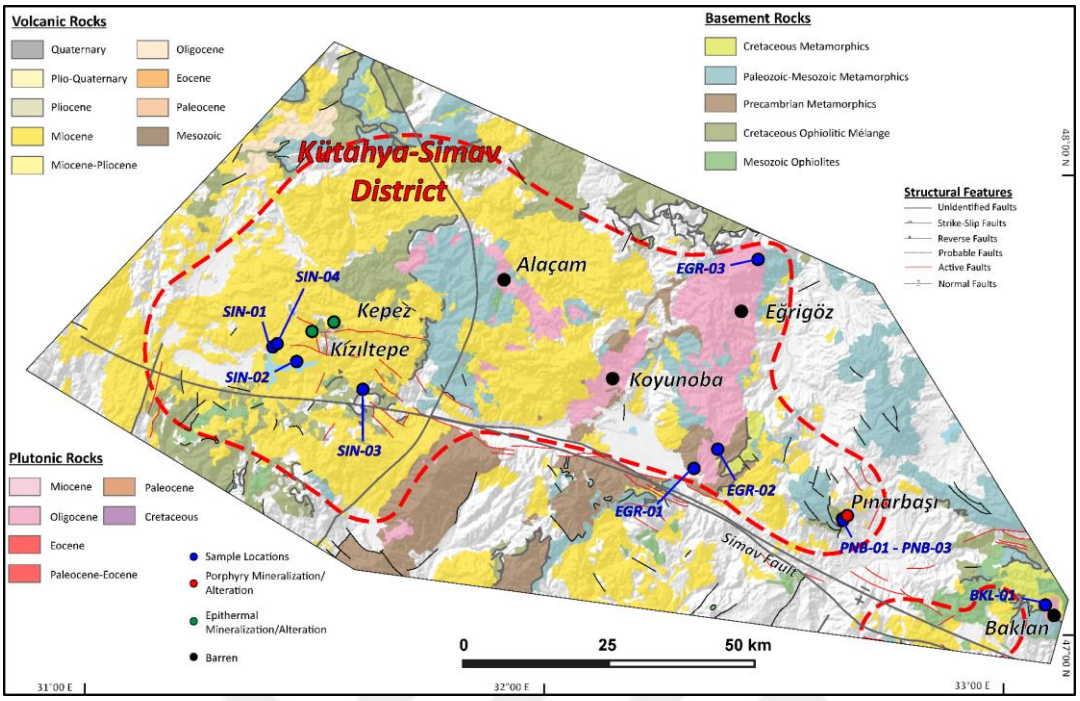


Figure 3.3. Simplified geologic map of the Kütahya–Simav region, showing major magmatic centers and the distribution of porphyry and epithermal mineralizations (MTA, 2002).

Pınarbaşı: Approximately 28 km southeast of the Eğrigöz pluton and ~1 km NW of Pınarbaşı village (Figure 3.3), the Pınarbaşı Cu–Mo prospect is spatially and temporally associated (~17 Ma; Delibaş et al., 2017; Figure 3.1) with the Pınarbaşı granodiorite (Figure 3.6A–B). Fieldwork followed historic drill roads opened by MTA, and two distinct lithological units were sampled in the outcrop. The first consists of a micro‑phaneritic granitic unit exhibiting intense quartz–sericite–pyrite alteration and dense quartz–pyrite±molybdenite stockwork veins (Figure 3.6A–B). Cross-cutting these units are dark-colored, NW–SE‑trending andesite porphyry dykes that display intense propylitic alteration (Figure 3.6C–D).

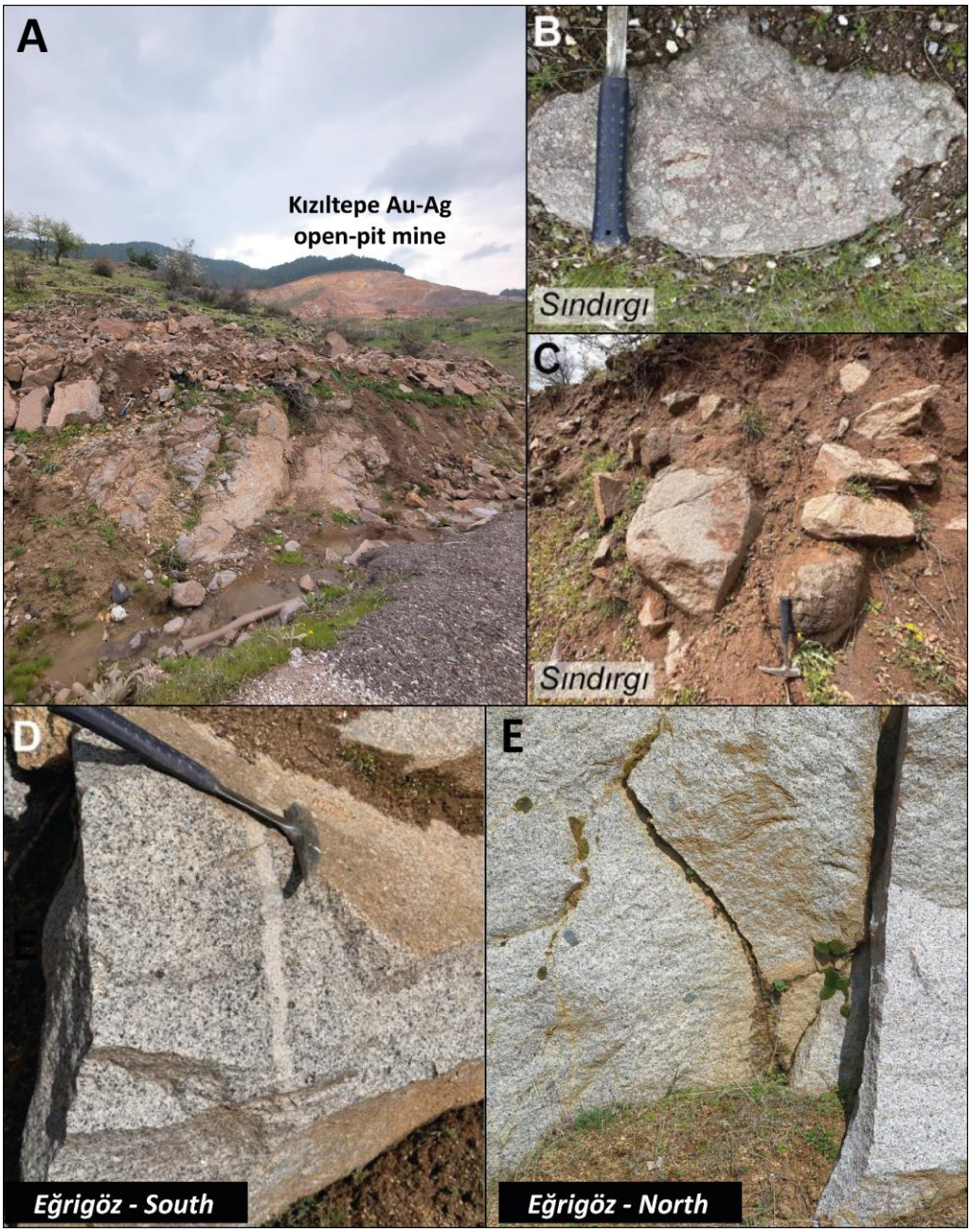


Figure 3.4. Field photographs from the Sındırgı and Eğrigöz areas in the Kütahya region. (A) Open pit at the Kızıltepe low-sulfidation epithermal Au–Ag deposit, located north of Sındırgı. Clay-altered microgranite/microgranodiorite units are exposed to the south of the pit (looking towards northeast). (B, C) Partially clay-altered and propylitized volcaniclastic units exposed ~2.5 km east of the Kızıltepe Au–Ag deposit. (D) Outcropping granite and crosscutting aplitic dike near Gökçeler village, west of Simav, situated at the southern margin of the Eğrigöz Pluton. (E) Weakly-altered granitic rocks with mafic enclaves at the northern edge of the Eğrigöz Pluton, spatially associated with skarn-type mineralization.



Figure 3.5. Field photographs from the Salihli Granite. (A) General view of the southern margin of the granitic intrusion juxtaposed against the Bayındır Nappe. This contact forms part of the E–W-trending Alaşehir Detachment. (B, C) Partially mylonitized granite at detachment contact containing flattened mafic enclaves.

Çatalçam: Located ~60 km west of Sındırgı and ~25 km NNW of Soma (Manisa), the Çatalçam project (Figure 3.1) was initially developed by MTA and later explored under the ownership of the Turkish Wealth Fund (TVF). Early investigations by MTA (Sarı et al., 2022) and subsequent studies (Kumral et al., 2022) reported occurrence of epithermal vein‐type Pb–Zn–Au–Ag mineralization within volcanic–subvolcanic units correlated with the ~17 Ma Yuntdağ Volcanics. A recent U–Pb zircon date from the same units confirmed this age (Sarı et al., 2023).

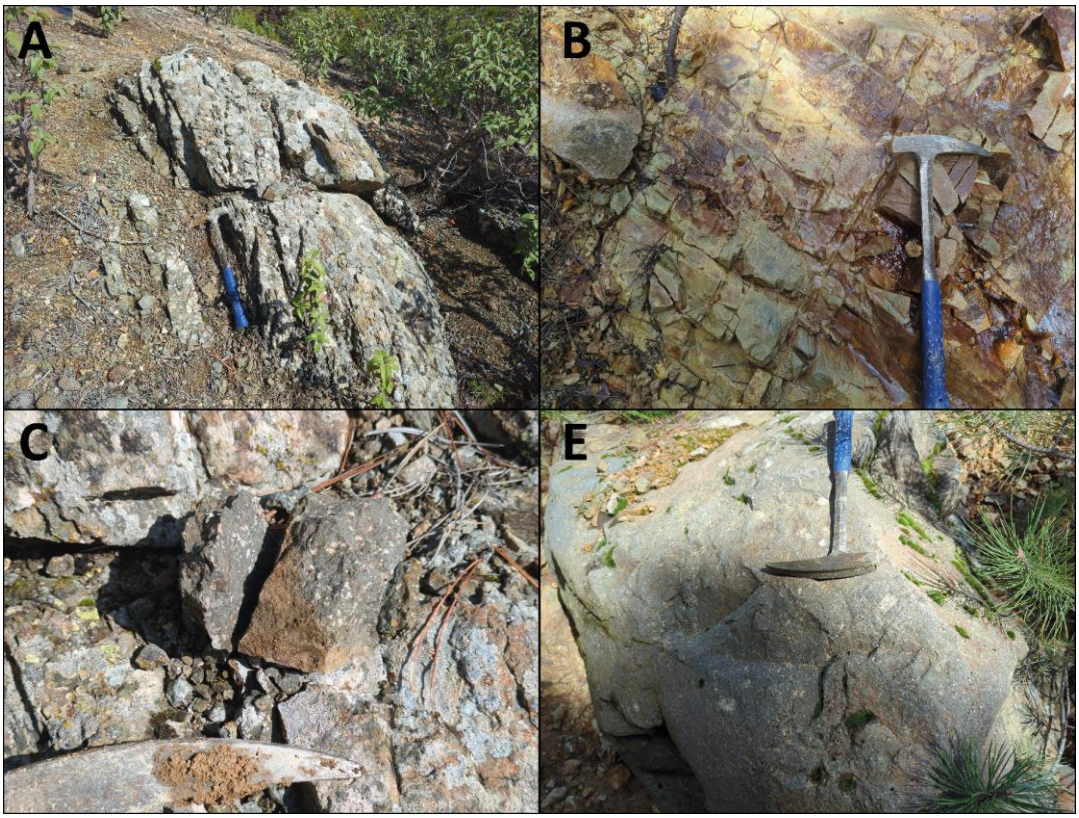


Figure 3.6. Field photographs of altered magmatic units from the Pınarbaşı Cu-Mo prospect, located approximately 1 km north of Pınarbaşı Village (NW of Gediz). (A) Surface exposure of quartz–sericite-altered microgranite, representing the main mineralized host unit. (B) Well-exposed altered microgranite along a stream bed. (C) NW-trending andesite porphyry dyke crosscutting the microgranite. (D) A transported block of andesitic porphyry containing mafic enclaves.

Surface and drill core observations at Çatalçam document a prominent massive andesite porphyry unit and narrow intervals of andesitic breccias showing moderate- to strong-intensity quartz–illite/smectite–chlorite–carbonate alteration (Figure

3.7A–C). Epithermal Pb–Zn–Au–Ag mineralization is hosted within steeply-dipping, intermediate-sulfidation quartz–carbonate–sulfide ± barite veins. Andesite porphyry has been cross-cut by basaltic andesite dykes, which have thicknesses ranging from a few centimeters to over 1 m, and following the same trends with mineralized veins. These dykes also show moderate intensity propylitic alteration characterized by abundant chlorite and lesser epidote, carbonate, and pyrite (Figure 3.7B). Ore zones are associated with both banded veins and hydrothermal‐magmatic (phreatomagmatic) breccia veins containing vein clasts derived from an underlying porphyry system (Figure 3.7C). The mineralized and altered andesite porphyries are crosscut by weakly altered andesitic volcaniclastic units (Figure 3.7D).

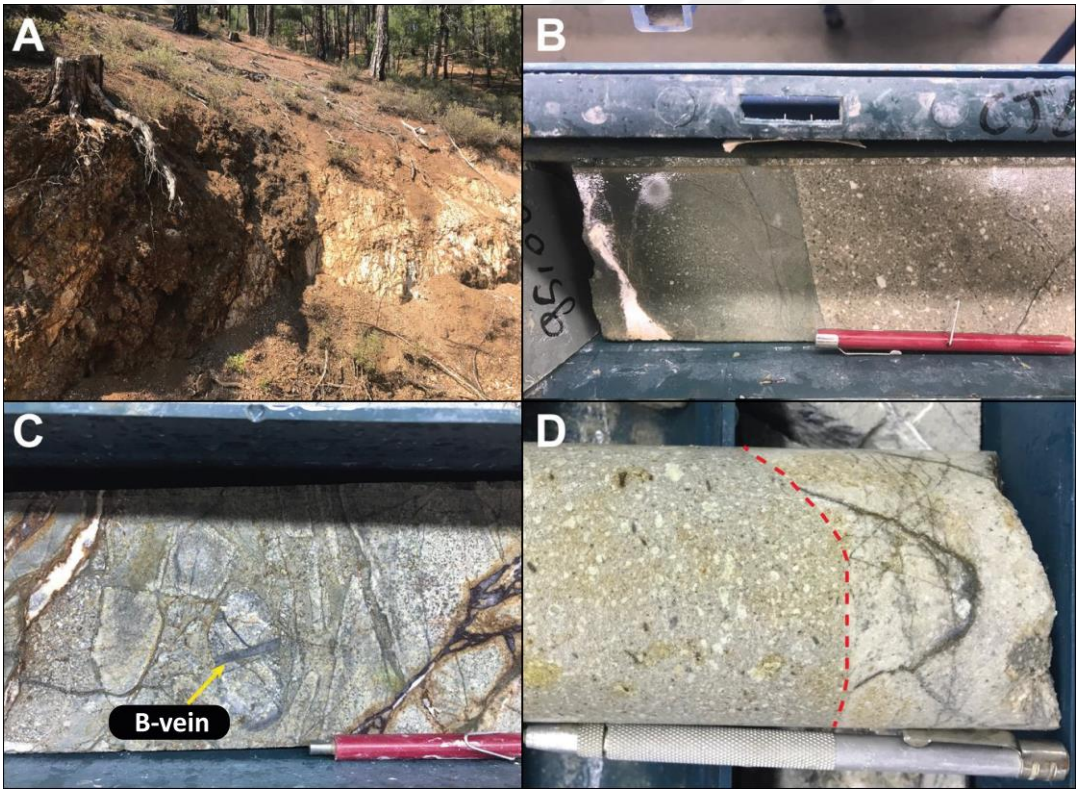


Figure 3.7. Surface and drill core photographs from the Çatalçam Au-Ag-Pb-Zn-Mo prospect. (A) Quartz–clay–carbonate–altered andesite porphyry hosting the main ore zone, exposed east of Duğla Village, crosscut by oxidized stockwork quartz–pyrite veins. (B) Andesite porphyry exhibiting quartz–illite–carbonate alteration, intruded by a propylitized basaltic andesite dyke. (C) Phreatomagmatic breccias developed

within the andesite porphyry; some breccia clasts display porphyry-style alteration and include B-type porphyry veins. (D) Quartz–illite–carbonate–altered andesite porphyry showing intense quartz–pyrite stockworking veinlets, cross-cut by basaltic andesite dyke.

Drillcore observations at Çatalçam indicated a transition from illite‐rich alteration at shallow depths to quartz–sericite–pyrite alteration in the lower intervals. Porphyry-style, sulfide-bearing quartz-rich veinlets were identified in several of the examined drill holes but no well‐developed potassic alteration zone was encountered during sampling. Nevertheless, Sarı et al. (2022) documented the presence of A‐ and B‐type porphyry veinlets in earlier MTA drilling, leading to the interpretation of Çatalçam as a shallow porphyry system overprinted by intermediate‐sulfidation epithermal Pb–Zn–Au–Ag mineralization.

3.1.3 İzmir-Afyon-Uşak District (15–9 Ma)

During the Middle to Late Miocene, progressive extension in Western Anatolia let to a southward shift in the loci of magmatism. Meanwhile, a compositional change was also observed from the typical I-type, medium‐K calc‐alkaline suites in the Late Oligocene to more alkaline magma compositions (i.e., high‐K to shoshonitic) from Middle Miocene onwards (Agostini et al., 2007; Dilek and Altunkaynak, 2009; Karaoğlu et al., 2010; Ersoy and Palmer, 2013). Volcanic, volcaniclastic, and sub‐volcanic lithologies of this magmatic phase are widely exposed in the south of Afyon and in the Eşme (Uşak) region from ~15 Ma onward. Contemporaneous volcanic rocks in western Menderes (İzmir) represent some of the earliest products of this episode.

Kışladağ: The Middle Miocene (~15–14 Ma) magmatism is particularly significant, not only in Western Anatolia but also in the broader Tethyan–Eurasian Metallogenic Belt, as it coincides with the formation of some of the region's largest ore systems. The most prominent mineralization associated with Middle Miocene magmatism in this part of the TEMB is the Kışladağ Au deposit, developed within the Beydağı Stratovolcano west of Eşme and within the Uşak–Güre basin (Figure 3.8). Currently

operated by Eldorado Gold/TÜPRAG, porphyry mineralization at Kışladağ is hosted in a shallow intrusive complex (<2 km depth) emplaced within the shallow levels of the stratovolcano. This complex, trending roughly E–W and extending over ~750 m, comprises five subvolcanic phases (INT1, INT2C, INT2A, INT2NW, INT3) as identified by Eldorado/TÜPRAG mapping (Baker et al., 2016; Figure 3.9). These intrusions cut the metamorphic basement of the Menderes Massif and the overlying ~17–16 Ma Beydağı–Payamdağı–İtecektepe volcanic pile (Karaoğlu et al., 2010).

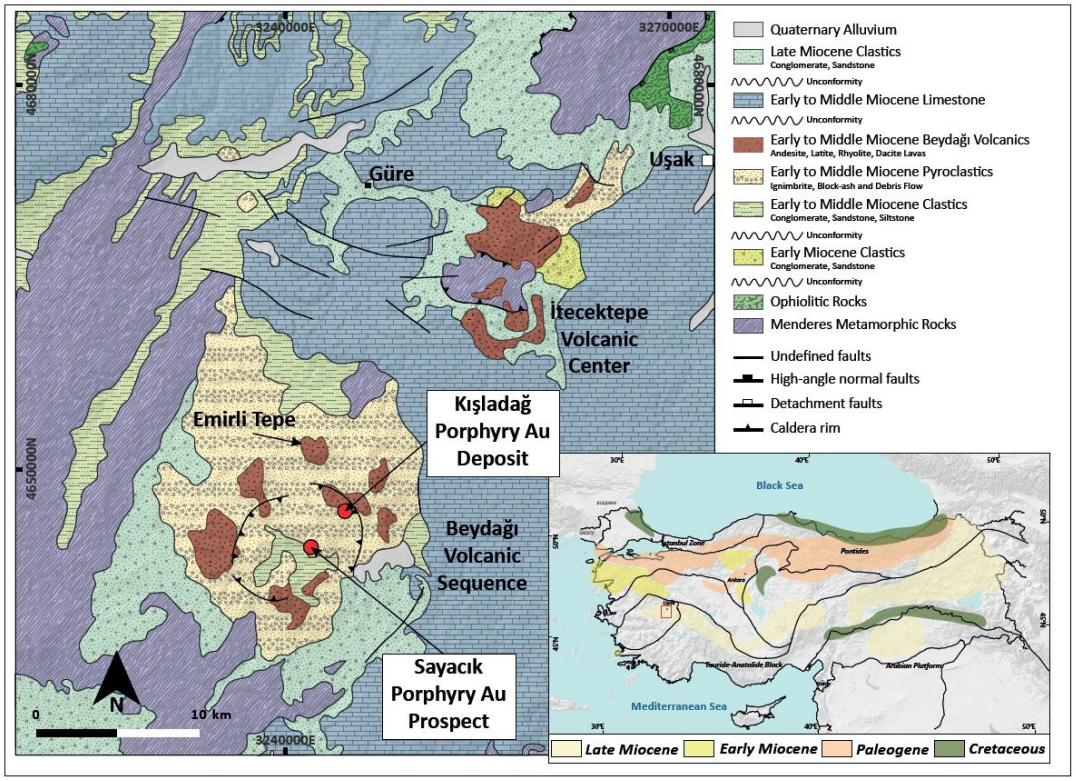


Figure 3.8. Geologic map of the Uşak-Güre basin, showing the location of the Elmadağ, Itecektepe, and Beydağı volcanic centers (modified after Karaoğlu et al., 2010). The inset map illustrates the distribution of magmatic belts across Anatolia.

High‐resolution U–Pb zircon geochronology (Paolillo et al., 2021) combined with detailed alteration mapping (Baker et al., 2016, 2020) shows progressive weakening of both mineralization intensity and potassic alteration from INT1 through INT3. INT1, the most extensive phase exposed in the open pit, is characterized by a K‐feldspar–rich groundmass hosting prismatic plagioclase, biotite, and coarse

K‑ feldspar phenocrysts (Figure 3.9A). INT2, distinguished by higher hornblende content, occurs as several bodies classified as INT2C (“central”), INT2A (“altered,” intensely clay‑ altered equivalents of INT2C), and INT2NW (“northwest”) (Figure 3.9B–E). INT3, the youngest unit, forms a steeply dipping dyke cutting INT1 and is recognized by abundant, coarse plagioclase phenocrysts and increased hornblende content (Figure 3.9F).

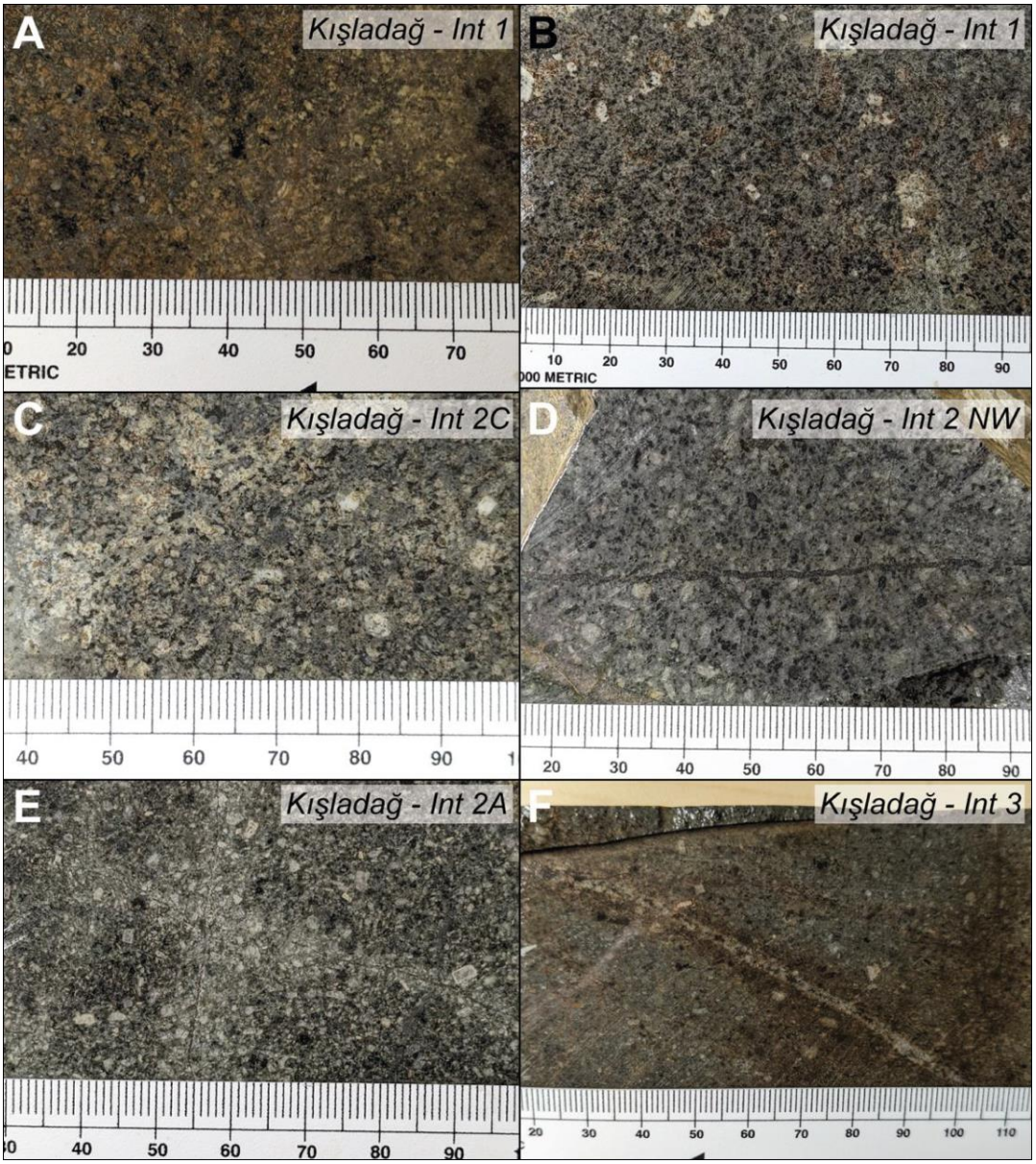


Figure 3.9. Drill core photographs representing different intrusive phases of the Kışladağ porphyry Au deposit. (A) Early-stage monzonite porphyry (INT1)

exhibiting intense potassic alteration. (B–E) Various monzonite porphyry and latite phases belonging to the syn-mineralization INT2 stage, crosscutting INT1 within the open pit. (F) Porphyritic latite dyke (INT3) with partial alteration, intruding both INT1 and INT2 phases in the open pit.

Sayacık: Located ~6 km SW of Kışladağ, the Sayacık prospect represents another mineralized center within the Beydağı Stratovolcano (Figure 3.8). Despite being discovered contemporaneously with Kışladağ, it has been less extensively explored due to the focus on the larger Kışladağ mineralization. Drilling intersected latite to quartz monzonite intrusions with hydrothermal assemblages dominated by quartz–clay–sericite–tourmaline–pyrite alteration. The low‐grade porphyry Au mineralization occurs at depths exceeding 700 m and is coeval with Kışladağ (~14.5 Ma; Re–Os molybdenite ages; Bickford et al., 2016). Core logging identified moderately preserved, medium‐grained altered quartz monzonites (Figure 3.10A) and finer‐grained latites (Figure 3.10B), although intense alteration obscures much of the original textures.

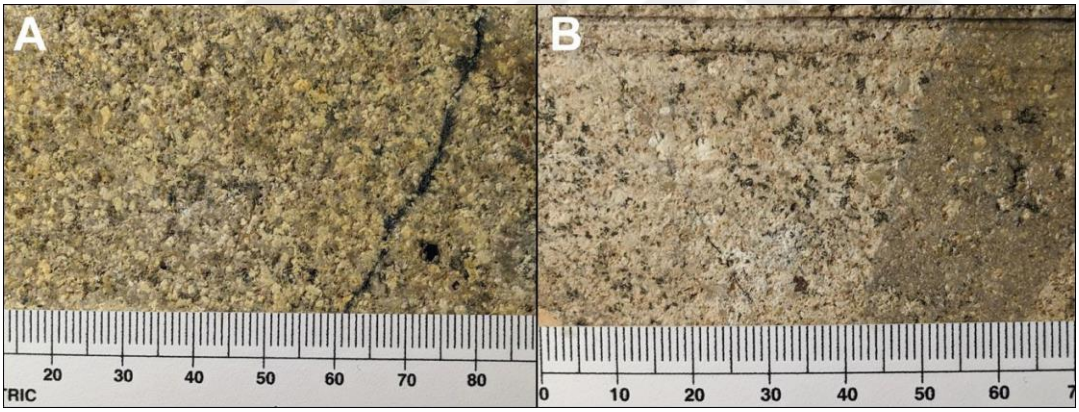


Figure 3.10. Drill core photographs from the Sayacık porphyry Au prospect. (A) Monzonite displaying intense quartz–white mica–tourmaline–pyrite alteration. The dark-colored veinlet crosscutting the sample is filled with tourmaline. (B) Altered monzonite crosscut by an altered latite porphyry intrusion.

Efemçukuru: The Efemçukuru intermediate‐sulfidation epithermal Au system near Menderes (İzmir) is also related to Middle Miocene magmatism and is one of the largest epithermal gold deposits discovered in Türkiye. Currently operated by Eldorado Gold/TÜPRAG, the ore-bearing quartz–rhodochrosite–rhodonite–sulfide

veins cut phyllites of the Bornova Flysch Zone within the Seferihisar Horst. Steep rhyolitic dykes, structurally aligned with the mineralized veins, are interpreted to exert primary control over fluid flow and ore deposition (Oyman et al., 2003). A U–Pb zircon age of 13.3 Ma from one of these rhyolite dykes was reported by Boucher (2016).

Afyon Volcanic Complex: Along the Kırka–Afyon–Isparta corridor (Figure 3.11), Miocene volcanism displays significantly more alkaline compositions compared to coeval magmatism to the west and east (Besang et al., 1977; Akal et al., 2013; Ersoy and Palmer, 2013; Prelevic et al., 2015; Seghedi and Helvacı, 2016). The Afyon Volcanic Complex, one of the most prominent expressions of this magmatic activity, covers an area of ~200 km² in the south of the Afyon city. Ages of magmatism range from ~14 Ma in the north to ~8 Ma in the south (Akal et al., 2013; Prelevic et al., 2015). The complex comprises diverse lithologies, including silica‐saturated plagioclase–amphibole lavas and ultrapotassic melilite–leucite rocks, indicating multiple mantle sources (Prelevic et al., 2015).

Northern exposures consist of ~14 Ma latitic lavas forming well‐layered volcanic sequences north of Sandıklı, whereas in the south of Sandıklı, shoshonitic 12–10 Ma volcanic and sub-volcanic units dominate. Within this zone lies the Afyon–Sandıklı ("A–S") porphyry Au–Cu prospect (Figure 3.12A), developed jointly by Eldorado Gold and Demir Export. Mineralization is associated with monzonite porphyry and latite intrusions displaying quartz–white mica–tourmaline–pyrite alteration (Sönmez and Kuşcu, 2020; Figure 3.12B–D) similar to that was observed both at Kışladağ and Sayacık. Weakly-altered feldspar‐rich latites and monzonite porphyries occur to the east of the prospect, crosscut locally by thin trachytic dykes (Figure 3.12C–F).

The southernmost part of the complex hosts an ~11 Ma ultrapotassic sequence exposed near Balçıkhisar village (Prelevic et al., 2015). This assemblage includes latitic lavas, leucitites, and lamproites, locally preserving volcaniclastics (Figure 3.13B–F).

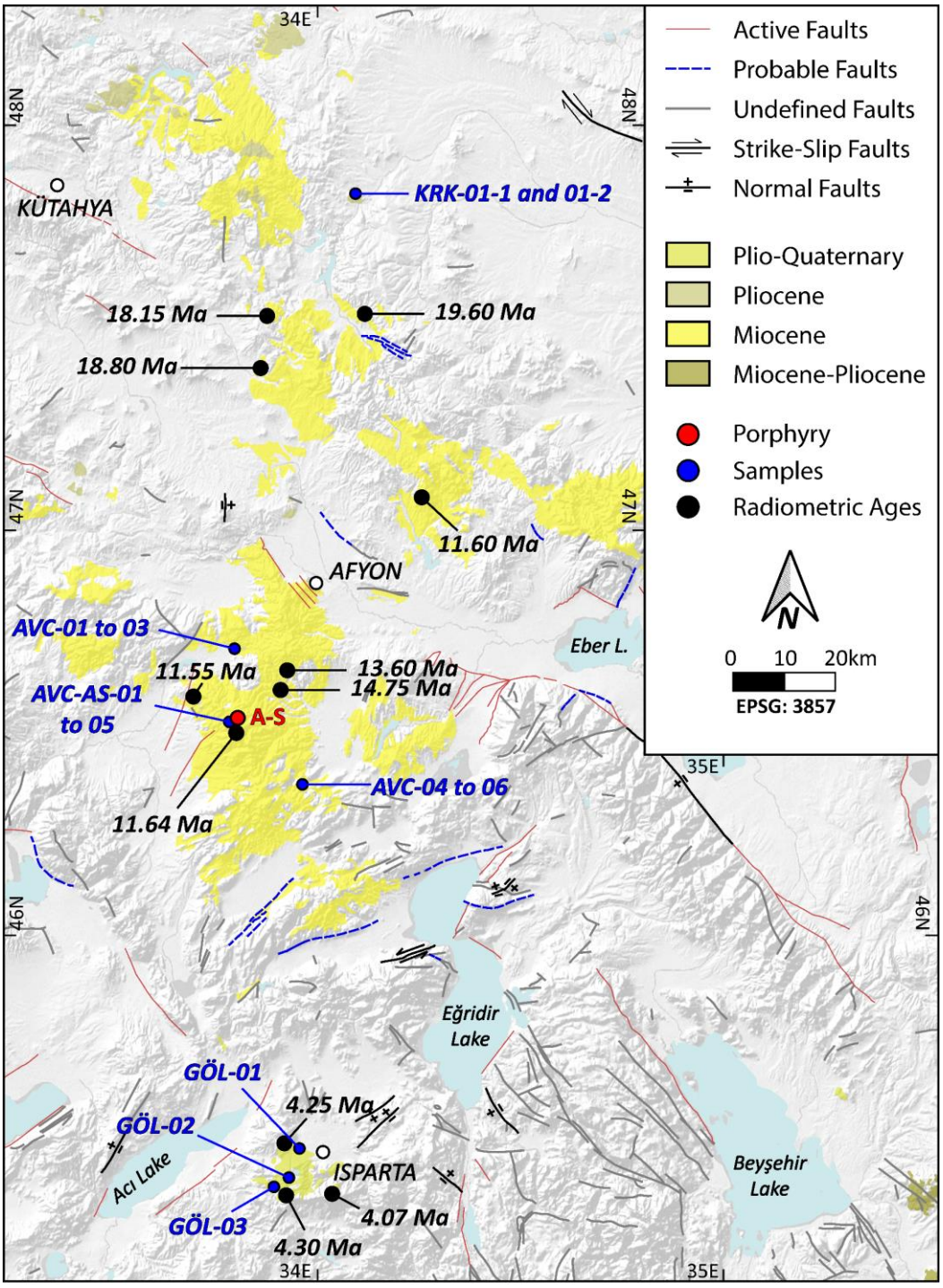


Figure 3.11. Map showing distribution of alkaline igneous rocks of Kırka-Afyon-Isparta with related fault systems, and radiometric age data determined on the volcanic rocks (Savaşcın and Oyman, 1998, modified after Savaşçın et al., 1994). Radiometric data from Sunder (1982), Besang et al. (1977), Lefevre et al. (1983), and Rabayrol et al. (2019b).



Figure 3.12. Field photographs of igneous exposures within the AVC to the north and east of Sandıklı. (A) Latitic lava flows exposed north of Sandıklı. (B) General view of the central zone of the A-S porphyry prospect, characterized by hydrothermally altered and mineralized rocks, where drilling activities have also been conducted. (C) Trachyte dykes crosscutting altered volcanic units in the central zone of the A-S porphyry prospect. (D) Altered syenite porphyry from the central zone of the A-S porphyry prospect. (E) Moderatelyaltered latite from the central zone of the A-S porphyry prospect. (F) Weakly-altered latite porphyry from the southern sector of the A-S porphyry prospect.

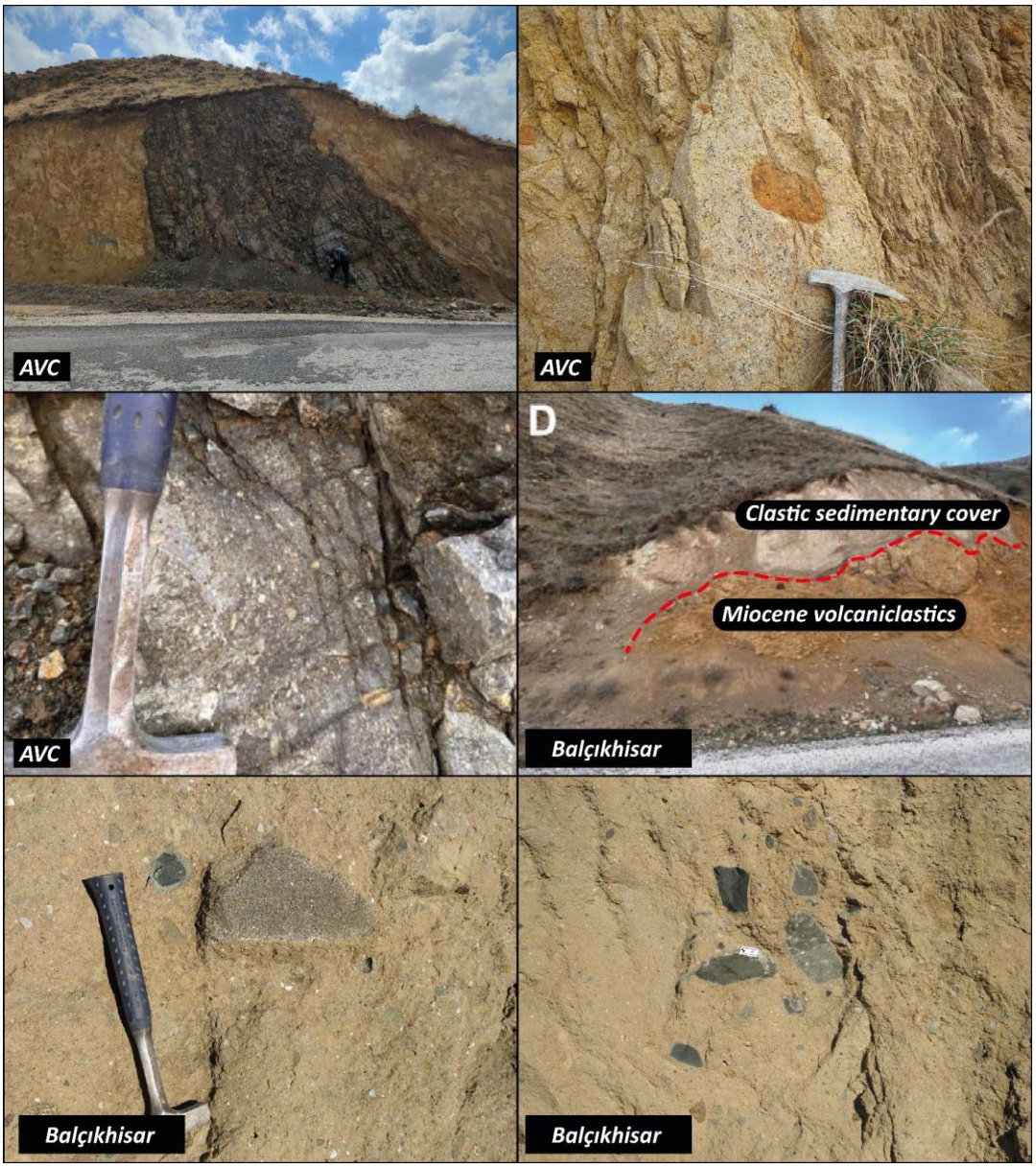


Figure 3.13. Field photographs of volcanic and volcaniclastic units from the southern Sandıklı and southern Balçıkhisar areas within the AVC. (A) Latite dyke cross-cutting a syenite porphyry unit located ~1 km east of Bektaş Village, south of Sandıklı. Close-up view of the (B) syenite porphyry and (C) latite at the same location. (D) Roadcut exposure of a volcaniclastic succession overlain by terrestrial clastic sediments ~3 km south of Balçıkhisar Village. (E–F) Syenite and lamproite clasts observed within the volcaniclastic succession south of Balçıkhisar.

3.1.4 Bodrum Peninsula (11–9 Ma)

The Bodrum Peninsula is located at the southwestern tip of the Anatolian Plate (Figure 3.2). The volcanic rocks of the region represent the products of a Miocene explosive volcanic center associated with a large caldera system.

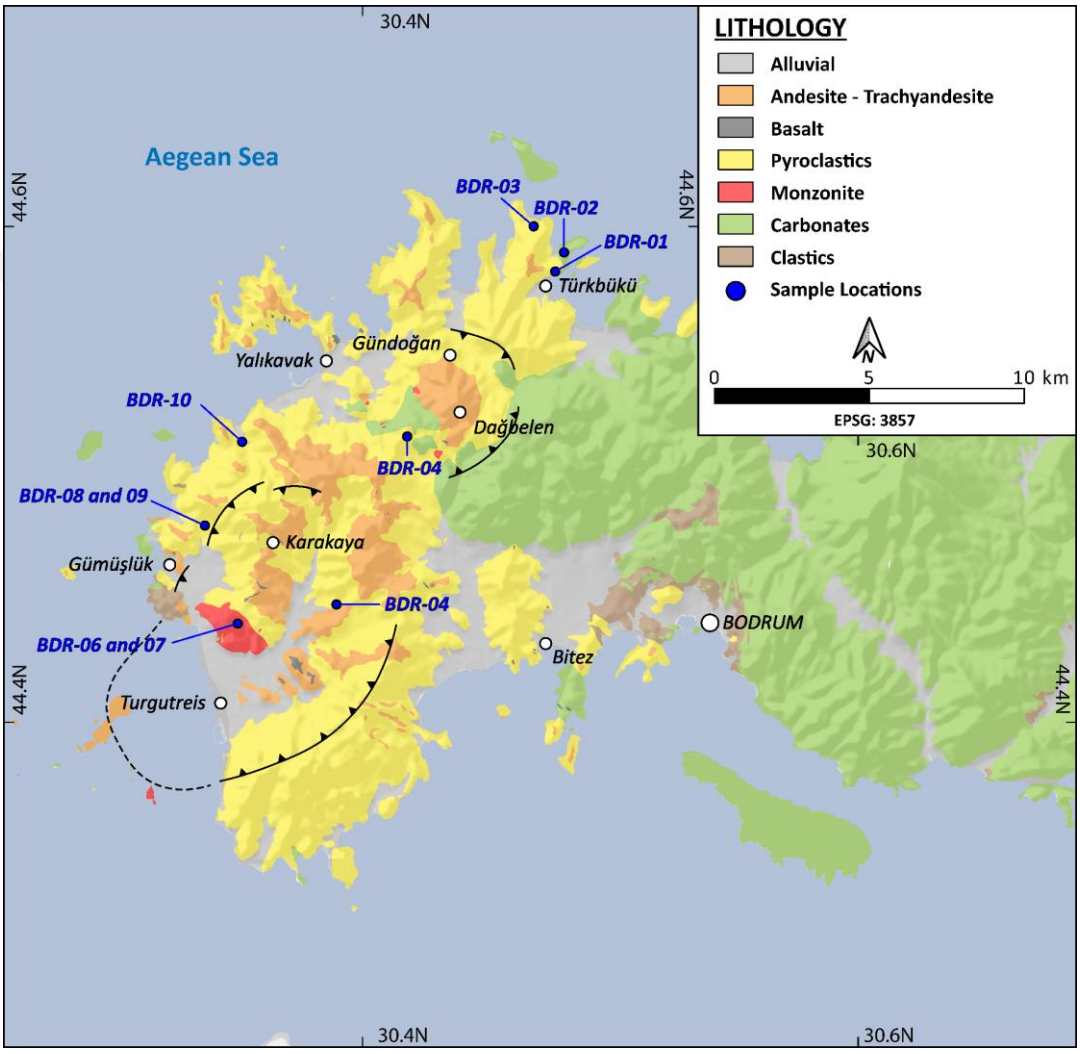


Figure 3.14. Simplified geological map of Bodrum Peninsula showing the distribution of lithological units (MTA, 2002; Çubukçu et al., 2021; modified from Ulusoy et al., 2004).

The magmatic assemblages of the Bodrum Peninsula cover a broad area and comprise lava flows, volcaniclastic deposits (block‐ and‐ ash flows, ignimbrites), and shallow intrusions bodies exposed within the caldera interior, locally exhibiting

medium‐grained or porphyritic textures (Çubukçu et al., 2021). These volcanic and volcaniclastic rocks are characterized by high‐K shoshonitic chemistry (Figure 3.15A–C) and span a wide compositional range from basaltic trachyandesite–trachyandesite to rhyolite, whereas shallow intrusions are monzonitic (Çubukçu et al., 2021; Figure 3.15D–E).

Regional volcanic activity has been subdivided "pre‐caldera," "syn‐caldera," and "post‐caldera" stages by Ulusoy et al. (2004). The pre‐caldera phase is represented by a Middle–Late Miocene monzonite porphyry intrusion emplaced into the local sedimentary and metamorphic basement (~11.2 Ma; Pişkin, 1980). Caldera‐forming ignimbrites mark the transition between pre‐ and post‐caldera stages (Ulusoy et al., 2004), while the post‐caldera phase is characterized by subvolcanic intrusions (Çubukçu et al., 2021).

Hydrothermal alteration typical of high‐sulfidation epithermal systems has been documented within the volcanic and volcaniclastic units of the Bodrum Peninsula Magmatic Complex (e.g., Dağbelen and Kadıkalesi; Figure 3.15B), while weak skarn mineralization has been observed around some of the sub-volcanic intrusions (e.g., Girelbelen; Rabayrol et al., 2019). Alteration is contemporaneous with the Afyon–Sandıklı (A–S) porphyry Au–Cu prospect (Rabayrol et al., 2019).

During this study, a total of 15 samples were collected from outcrops representing different magmatic units as previously defined in the literature, (Çubukçu et al., 2021). One sample was collected from a quarry in the southern part of the peninsula. Samples from the northern sector of the peninsula (Türkbükü) correspond to basaltic trachyandesite–trachyandesite units within a volcaniclastic succession (Figure 3.15A–C), whereas those collected from the caldera margin and interior are massive basaltic trachyandesite–trachyandesite lava flows. Samples obtained from the quarry near Turgutreis represented by monzonitic sub-volcanic intrusions (Figure 3.15D–E).

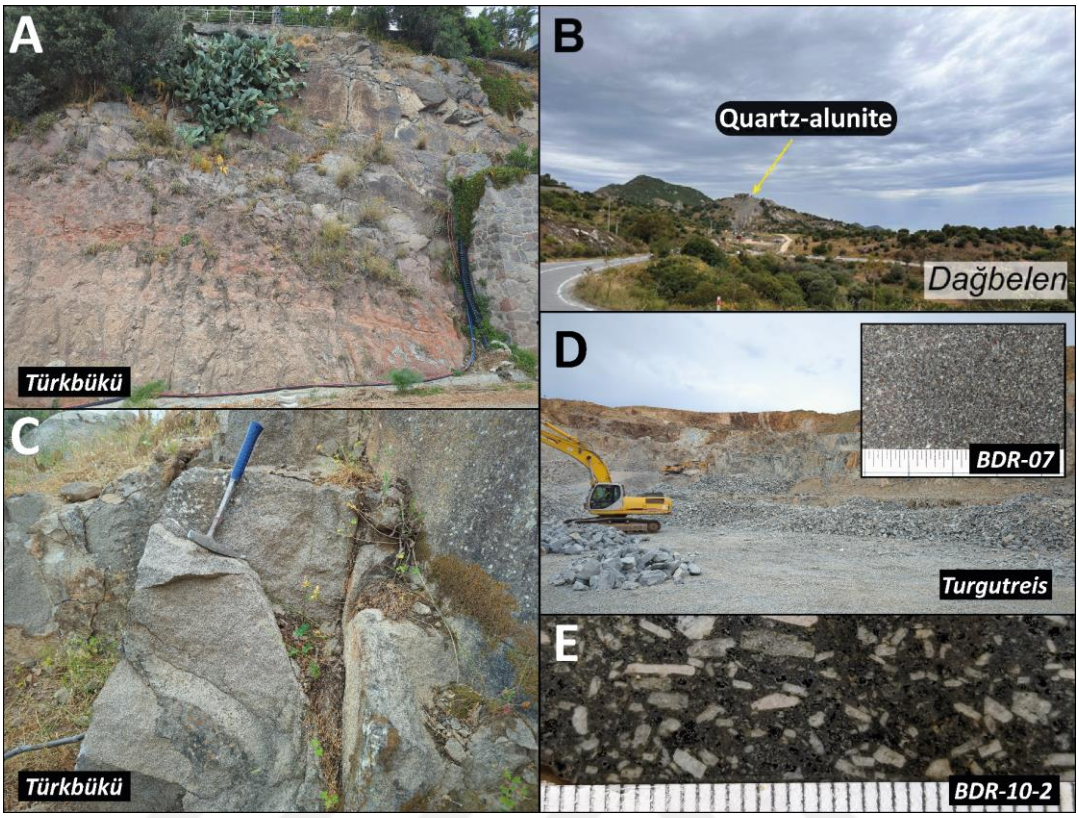


Figure 3.15. Field and hand specimen photographs of igneous rocks from the Bodrum Peninsula. (A) Pyroclastic succession exposed south of Türkbükü and hand specimen of trachyandesite clasts within this unit. (B) Resistant ridges composed of trachyandesite with pervasive quartz–alunite alteration in the Dağbelen area (view towards southwest). (C) Massive, fresh to weakly-altered trachyandesite outcrop at the same location in B. (D) Quarry near Turgutreis exposing a shallow monzonitic intrusion. (E) Weakly-altered basaltic trachyandesite outcrop near Gümüşlük.

3.2 Mineralogy and Petrography

3.2.1 Balıkesir District (25 Ma)

Drill core samples BLY‑01 and BLY‑02, obtained from the northern sector of the Balya polymetallic skarn deposit, were collected from the deep levels of drill hole BKS318 characterized by porphyry mineralization. Despite exhibiting pervasive hydrothermal alteration, both samples are representative of intermediate to felsic porphyritic intrusions. Sample BLY‑01 is a medium- to coarse-grained diorite

porphyry intrusion consisting of euhedral biotite and plagioclase phenocrysts embedded in a fine‐grained groundmass (Figure 3.16A–B). Large, euhedral biotite crystals in this sample represent primary magmatic biotite, whereas aggregates of fine-grained, anhedral biotite developed during potassic alteration. The matrix is composed of fine-grained quartz and plagioclase, the latter variably replaced by K-feldspar. Rectangular prismatic phenocrysts now entirely replaced by secondary biotite or late chlorite (Figure 3.16A) were originally hornblende (Figure 3.16A–B).

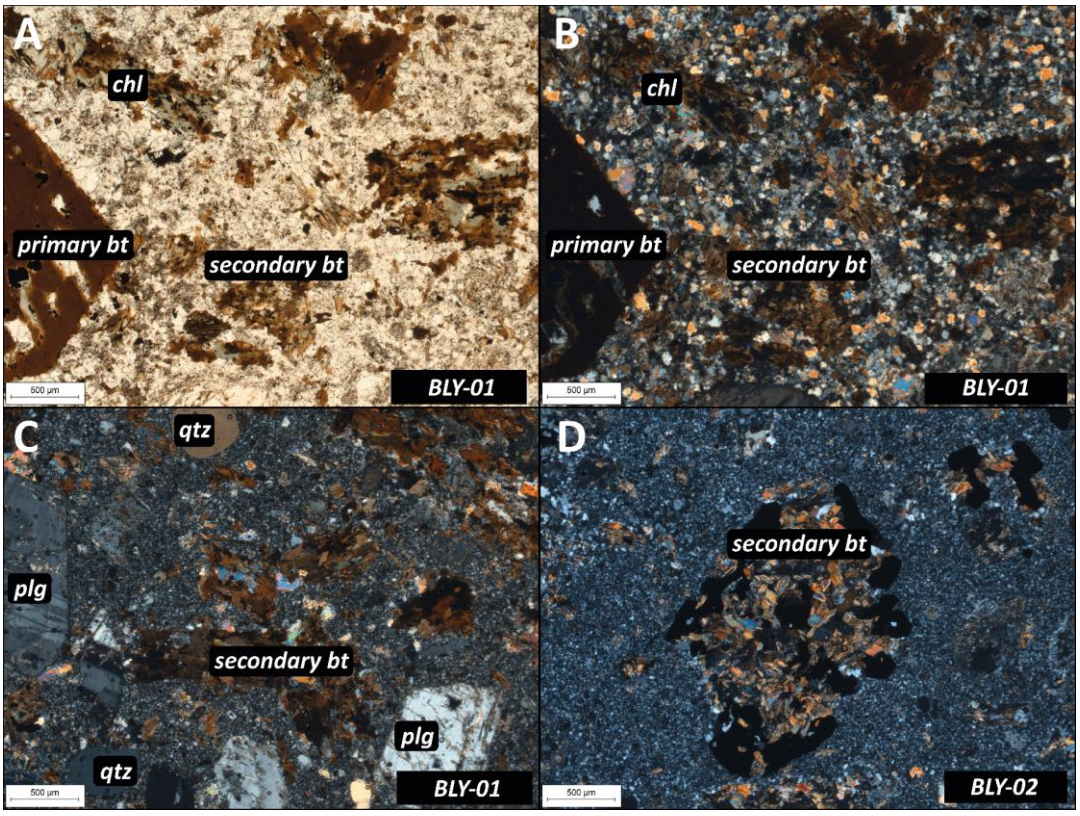


Figure 3.16. Transmitted-light microphotographs of igneous rock samples associated with porphyry-style mineralization from Balya. (A–B) Diorite porphyry affected by potassic alteration (biotite–K-feldspar); biotite phenocrysts have been partially replaced by chlorite (PPL and XPL, respectively). (C) Granodiorite porphyry overprinted by potassic alteration (XPL). (D) Hornblende phenocryst in granodiorite porphyry replaced by secondary biotite and magnetite (opaque; XPL).

In BLY‐01‐2, plagioclase, biotite, hornblende (extensively replaced by secondary biotite), and quartz phenocrysts are enclosed in a fine‐grained matrix (Figure 3.16C). The presence of relatively more abundant igneous quartz suggests a

granodiorite composition. Plagioclase crystals are partially preserved but these have been locally replaced by K-feldspar caused by potassic alteration. The BLY-02 sample, also classified as a dacite porphyry, shows mineralogical and textural characteristics comparable to BLY-01-2, with hornblende entirely replaced by secondary biotite and plagioclase altered to secondary K-feldspar (Figure 3.16D).

All samples from the Balya North Sector contain zircon and apatite as accessory phases. Magnetite is abundant in both mineralized diorite and granodiorite porphyries. Isolated, medium-grained magnetite crystals are interpreted to be magmatic in origin, whereas magnetite clusters occurring around ferromagnesian mineral domains as hornblende (Figure 3.16D) are most likely hydrothermal magnetite formed during potassic alteration.

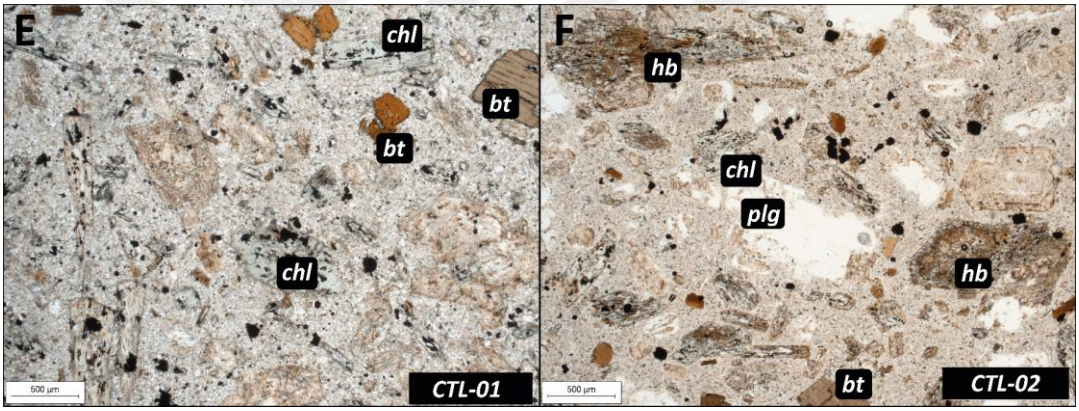


Figure 3.17. Transmitted-light microphotographs of igneous rock samples from the Çatalçam porphyry–epithermal prospect. (A) Andesite porphyry from deeper levels of the epithermal system with chloritized hornblende and illite-altered groundmass. Fine-grained opaque phases are pyrite intergrown with chlorite (PPL). (B) Altered basaltic andesite dyke with partially chloritized hornblende and better-preserved biotite. Groundmass exhibits pervasive illite alteration, and the opaque phases are disseminated pyrite grains (PPL).

Drill cores from the Çatalçam epithermal–porphyry prospect were specifically sampled from intervals representing the transition from epithermal to deeper porphyry-style mineralization, where magmatic rocks were relatively less affected from argillic alteration. Sample CTL-01 is a light-colored andesite porphyry with relatively low ferromagnesian mineral content, whereas CTL-02 is darker, fine-

grained porphyritic unit of basaltic andesite composition and occurring as dykes cross‐cutting the main andesite porphyry (Figure 3.17). Both units share a similar mineral assemblage dominated by hornblende, biotite, and plagioclase. Some quartz was also observed but is likely hydrothermal in origin. In the andesite porphyry, hornblende has been completely replaced by chlorite–sericite and plagioclase partially sericite, whereas biotite appears to be less affected from alteration (Figure 3.17A). In both units, magnetite microphenocrysts have been transformed into hematite and pyrite.

3.2.2 Kütahya-Simav District (22–17 Ma)

Samples from the Kütahya-Simav district were mainly collected from volcanic-volcaniclastic lithologies near the Kızıltepe LS epithermal Au deposit near Sındırgı and from intrusive lithologies from Eğrigöz and Pınarbaşı areas.

Sample SIN‐01, collected from immediately south of the Kızıltepe open-pit, is petrographically classified as a microgranodiorite and shows only limited alteration, preserving much of its primary texture. Outcrops of the same unit can be traced northward into the open pit with progressively increase in alteration intensity. SIN-01 exhibits an equigranular microphaneritic to weakly porphyritic texture, composed roughly of equal proportions of plagioclase and quartz with subordinate biotite (Figure 3.18A). Approximately 80 % of the rock consists of coarse- to medium‐grained crystals set in a sparse fine‐grained matrix. Biotite is notably finer‐grained than plagioclase and quartz and shows partial replacement along cleavage planes and rims to Fe‐Ti oxides (Figure 3.18A). Zircon and apatite are present as accessory minerals.

An andesitic volcaniclastic sample collected from ~2.5 km southeast of Kızıltepe, shows moderate intensity hydrothermal alteration. Sample SIN‐02 represents a volcanic breccia distinguished by abundant euhedral hornblende accompanied by biotite as the dominant ferromagnesian phases, both exhibiting opacitization (Figure

3.18B). Quartz is the most abundant mineral phase, whereas plagioclase is less common. The surrounding groundmass displays weak chlorite–sericite alteration (Figure 3.18B). At the same locality, the main volcanic unit is a dacitic tuff that lacks hornblende and is characterized instead by fine, elongate prismatic crystals of biotite intergrown with angular quartz crystals (Figure 3.18C). Biotite is notably fresh, whereas hornblende has been entirely replaced by clays or Fe‐Ti oxides. Tuff samples display well‐developed fiamme textures (Figure 3.18C).

In Eğrigöz, samples were collected along a N-S transect as the intrusive body also extends in the same trend (Figure 3.3). All samples are texturally and mineralogically similar. These are granitic in composition and differ only in overall crystal size. Predominant K-feldspar and quartz are, accompanied by subordinate plagioclase, biotite, and hornblende (Figure 3.18D–F). Hydrothermal alteration is minimal, with the exception of a single sample from the northern contact zone, which exhibits weak to moderate chlorite–sericite overprint. Magnetite and ilmenite microphenocrysts are well preserved in all samples, and zircon and apatite occur ubiquitously as accessory phases.

Samples from the Pınarbaşı Cu–Mo prospect show moderate to strong hydrothermal alteration. Sample PNB‐01 is a dark‐colored dyke rock, classified as a dacite porphyry due to its relatively high modal quartz despite the mafic matrix (Figure 3.19A). Primary biotite has been overprinted first by secondary hydrothermal biotite during potassic alteration and then by sericite during phyllic overprint. This sample also contains abundant carbonate veins and disseminated pyrite. PNB‐02 is a monzonite porphyry composed of quartz, K‐feldspar, plagioclase, and minor biotite (Figure 3.19B). Feldspars and biotite have been partially to completely sericitized. Plagioclase and possible hornblende phenocrysts have also been strongly sericitized (Figure 3.19B). Magnetite is absent in both samples, likely due to alteration, while zircon and apatite occur as accessory minerals.

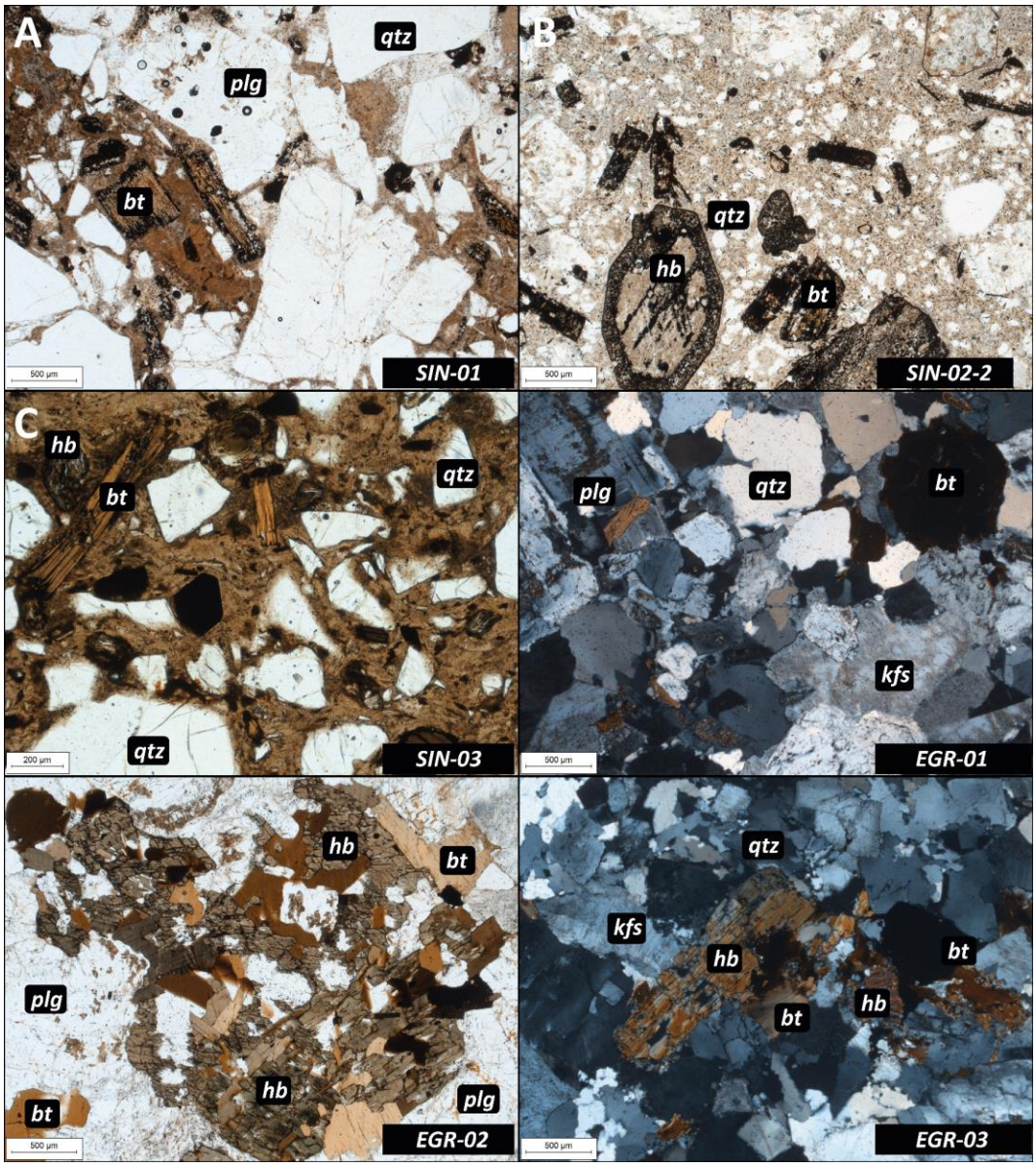


Figure 3.18. Transmitted-light microphotographs of igneous rock samples from the Sındırgı and Eğrigöz areas. (A) Weakly-altered microgranodiorite exposed north of Sındırgı, near Kızıltepe Au deposit (PPL). (B) Agglomerate from east of Kızıltepe. Hornblende and biotite are partially opacitized, whereas plagioclase-rich fine-grained groundmass shows partial alteration into clays (PPL). (C) Dacitic tuff from the same locality as (B), where hornblende crystals are completely opacitized, whereas biotite is well preserved. Quartz typically occurs as angular crystal fragments (PPL). (D) Fresh granite from the southern margin of the Eğrigöz Pluton near Gökçeler Village. (E) Granite from the northern part of the Eğrigöz Pluton, immediately north of Söğüt Village. Sample contains a higher proportion of hornblende compared to granite sample in (D) (PPL). (F) Weakly-altered granite from the northern margin of the Eğrigöz Pluton (XPL).

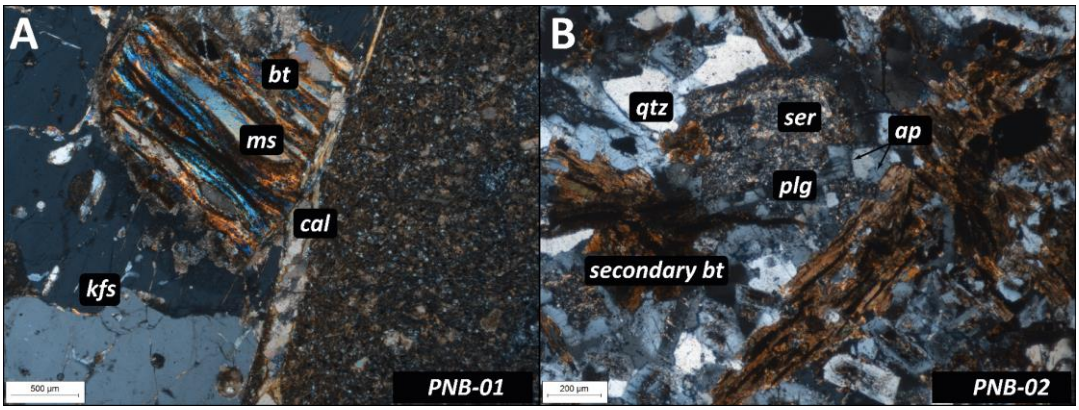


Figure 3.19. Transmitted-light microphotographs of igneous rock samples from the Pınarbaşı porphyry Cu–Mo prospect. (A) Altered dacite porphyry dyke crosscutting the monzonite. Quartz and K-feldspar are accompanied by biotite that has been variably replaced by sericite. Secondary calcite occurs as fracture-fill (XPL). (B) Altered monzonite porphyry host to the porphyry mineralization. Biotite is secondary in origin and plagioclase crystals have been partially replaced by sericite (XPL).

3.2.3 Uşak District (16–14 Ma)

Magmatic units from two porphyry Au systems formed within the Beydağı Stratovolcano (Uşak) between 15 and 14 Ma were investigated, including five intrusive phases from Kışladağ. The KSLD‐05 monzonite porphyry, representing the early INT1 phase, has undergone strongly intensity potassic alteration (Figure 3.20A). Primary biotite has been completely replaced by fine‐grained, anhedral secondary biotite forming aggregates, while the fine-grained groundmass has been almost entirely replaced by K‐feldspar. Magnetite is interpreted as hydrothermal in origin due to its association with potassic alteration. No primary hornblende or biotite were identified in this sample.

The second intrusive unit at Kışladağ (INT2), a monzonite porphyry with three sub‐phases, exhibits variable alteration intensity. KSLD‐04 shows pervasive hydrothermal alteration with abundant fine‐grained sericite, tourmaline, and disseminated pyrite (Figure 3.20B). KSLD‐06, representing the INT2‐NW phase, is less altered, preserving some primary biotite and rare hornblende phenocrysts,

while plagioclase has been only weakly sericitized (Figure 3.20C). KSLD‑09, from the INT2‑A phase, is also strongly altered, with all feldspars and ferromagnesian phases having been replaced by tourmaline–sericite–pyrite assemblages (Figure 3.20D). The youngest intrusive phase (INT3) retains its primary texture and mineralogy (Figure 3.20E-F). KSLD‑02 has a plagioclase–K‑feldspar–quartz‑rich groundmass enclosing plagioclase and biotite phenocrysts with only minor sericitization (Figure 3.20E). KSLD‑07 comprises plagioclase, hornblende, and biotite phenocrysts in a quartzofeldspathic groundmass with rarely preserved magmatic magnetite (Figure 3.20F). Zircon and apatite occur as accessory minerals in all Kışladağ samples.

Drill core samples from the Sayacık porphyry Au prospect display complete replacement of feldspars and ferromagnesian phases by sericitization (Figure 3.20G-H). Radiating clusters of prismatic tourmalines are common, and pyrite occurs as fine‑ to medium‑grained disseminations. Some quartz is likely of magmatic origin. Zircon grains are relatively coarse (150–200 μm), while fine-grained prismatic apatite crystals are abundant.

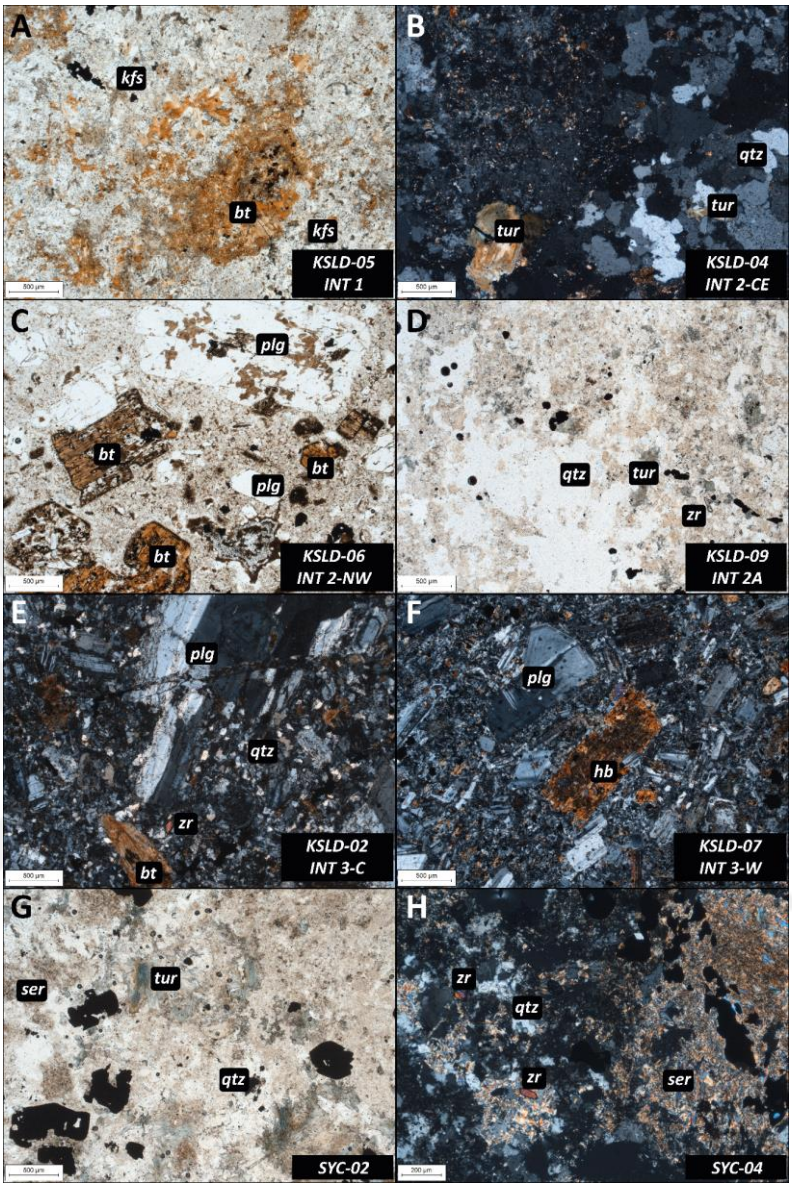


Figure 3.20. Transmitted-light microphotographs of core samples from igneous units in the Kışladağ and Sayacık porphyry Au systems. (A) Early monzonite porphyry from Kışladağ (INT1), showing abundant fine-grained biotite aggregates formed during potassic alteration. Fine-grained groundmass consists predominantly of secondary K-feldspar intergrown with quartz (PPL). (B–D) Various monzonite porphyry phases from Kışladağ (INT2) intruding early-phase monzonite porphyries. These display moderate to high intensity quartz–white mica–tourmaline alteration. Sample KSLD-06 in (C) shows lower intensity alteration, whereby ferromagnesian phases have been partially preserved (PPL and XPL). (E–F) Altered late-stage latite porphyry dyke from Kışladağ (INT3; XPL). (G–H) Monzonitic–latite porphyries from Sayacık, exhibiting intense quartz–white mica–tourmaline alteration (PPL and XPL).

3.2.4 Salihli Pluton (15 Ma)

Samples from the intrusion emplaced along the Alaşehir detachment fault south of Salihli represent fresh granitic lithologies (Figure 3.21). Sample S‐01 is intensely deformed along the detachment. It shows a coarse-grained, equigranular phaneritic texture with quartz, plagioclase, biotite, and hornblende as the principal phases, whereas titanite and magnetite are subordinate (Figure 3.21A). A second thin section prepared from a similar but highly mylonitized sample shows well-developed micro-deformation fabrics in which kinked biotite crystals define thin foliation planes, while quartz shows subgrain development and undulose extinction due to dynamic recrystallization (Figure 3.21B).

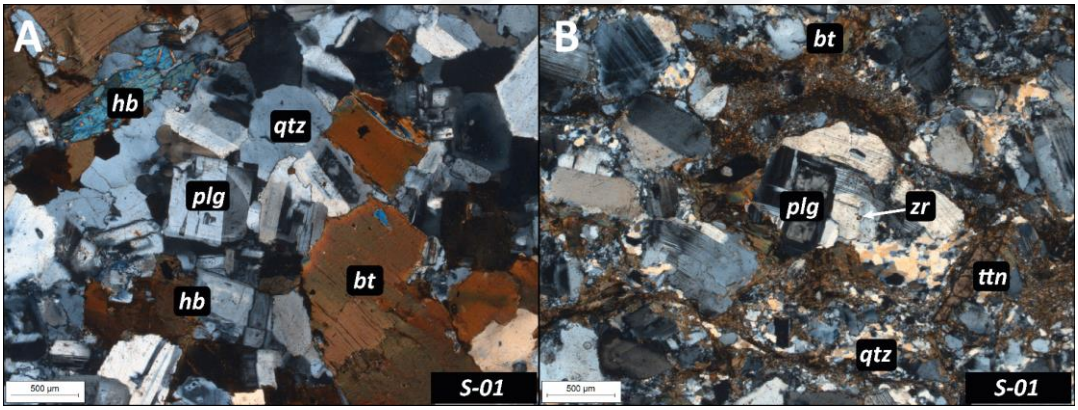


Figure 3.21. Transmitted-light microphotographs of igneous rock samples from the Salihli Granitoid. (A) Medium-grained, equigranular granite showing no evidence of deformation (XPL). (B) Foliated granite from the southern contact zone of the granitoid, which has been subjected to tectonic stress and partial mylonitization. Biotite crystals display a pronounced preferred orientation (XPL).

3.2.5 Kırka-Afyon-Isparta (21-4 Ma)

In the Afyon Volcanic Complex, sampling targeted silica‐undersaturated, feldspathoid‐rich ultrapotassic lavas and lamprophyres, alongside shoshonitic sub-volcanic units exposed in the Afyon–Sandıklı (A‐S) porphyry prospect. Sample AVC‐03 is a lamproite from the volcanic–volcaniclastic succession south of Balçıkhisar and displays a porphyritic texture with leucite, clinopyroxene, and

phlogopite phenocrysts set in a groundmass of fine-grained K‑feldspar and clinopyroxene (Figure 3.22A). Leucitites contain at least 80 modal % of variably-sized leucite crystals surrounded by a groundmass of K‑feldspar, carbonate, and minor apatite (Figure 3.22B).

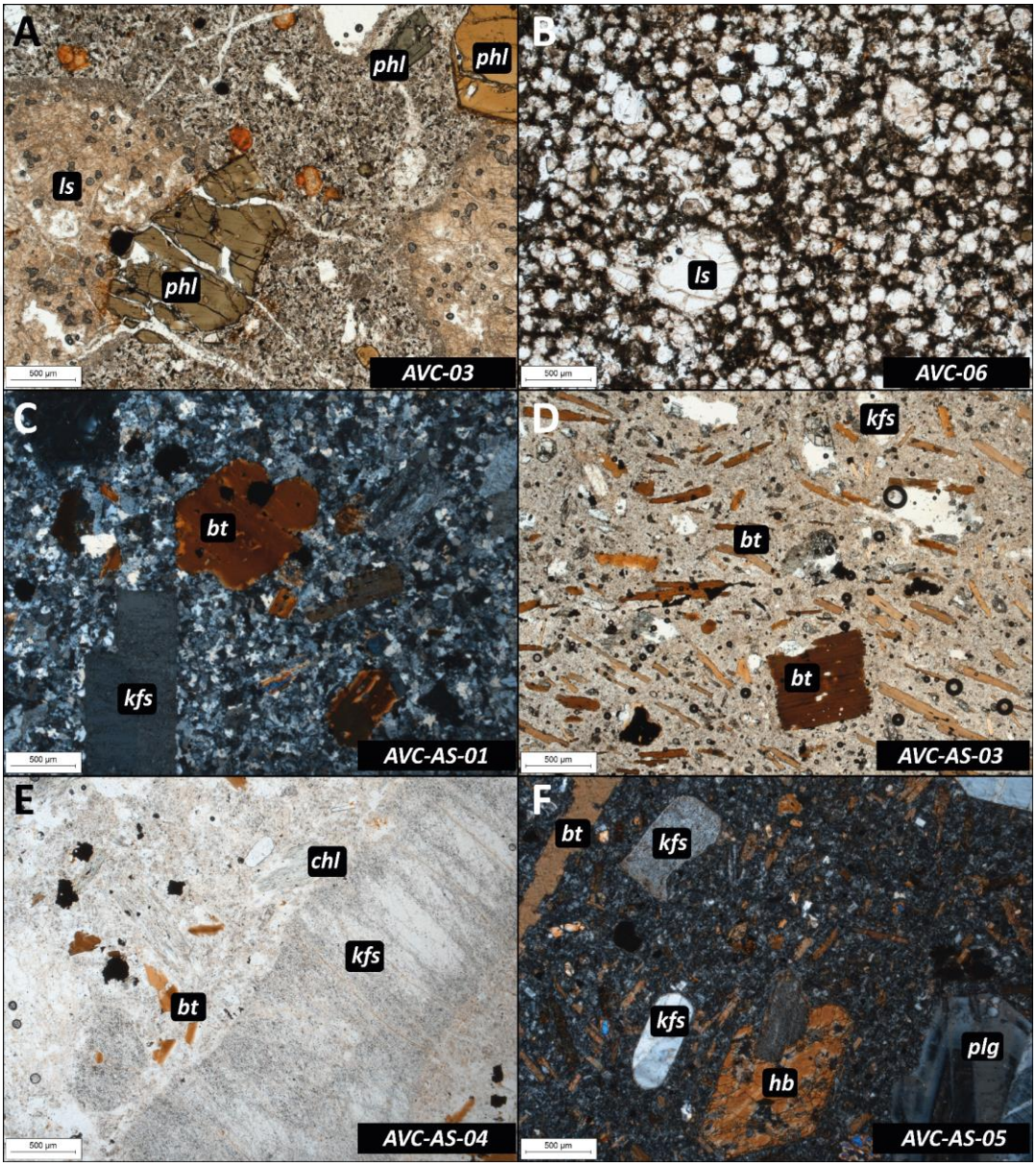


Figure 3.22. Transmitted-light microphotographs of igneous rock samples from the AVC. (A) Porphyritic lamproite from south of Balçıkhisar, containing phenocrysts of leucite, pyroxene, and phlogopite in a K-feldspar–rich groundmass (PPL). (B) Leucitite from south of Balçıkhisar, characterized by abundant leucite enclosed in a dark groundmass rich in K-feldspar and carbonate (PPL). (C) Fresh micromonzonite

from the A–S porphyry prospect, showing porphyritic texture with euhedral K-feldspar and biotite phenocrysts in a quartzofeldspathic groundmass (XPL). (D) Trachytic dyke from the A–S porphyry prospect, composed mainly of slender prismatic biotite and tabular K-feldspar phenocrysts in a fine-grained K-feldspar–rich groundmass with minor quartz; greenish minerals are tourmaline (PPL). (E) Syenite porphyry host unit of the A–S porphyry mineralization, characterized by K-feldspar, biotite, and quartz with minor chlorite (PPL). (F) Porphyritic latite from the A–S porphyry prospect, with phenocrysts of hornblende, biotite, K-feldspar, and plagioclase (XPL).

Sample AVC‑AS‑01 from A-S porphyry prospect is a porphyritic micromonzonite with blocky K‑feldspar and biotite phenocrysts accompanied by minor plagioclase and quartz, all enclosed in a groundmass consisting of quartz, feldspar, and biotite (Figure 3.22C). AVC‑AS‑03 is a weakly-altered trachyte characterized by prismatic K‑feldspar and biotite phenocrysts with fine, acicular biotite in a K‑feldspar‑rich matrix. Tourmaline locally occurs as clusters and is a product of hydrothermal alteration (Figure 3.22D). AVC‑AS‑04, a syenite porphyry from the southern part of the prospect, is distinguished by abundant coarse K‑feldspar phenocrysts with subordinate fine-grained biotite and quartz, weak chlorite–sericite–tourmaline-pyrite alteration (Figure 3.22E). AVC‑AS‑05 is a latite porphyry containing biotite, plagioclase, K‑feldspar, and subordinate hornblende phenocrysts. (Figure 3.22F) Its fine‑grained crystalline groundmass consists mainly of plagioclase and biotite with minor magnetite microphenocrysts. Zircon and apatite are present as accessory phases in all A‑S porphyry samples.

3.2.6 Bodrum Peninsula (11–9 Ma)

Petrographic analyses of the Bodrum Peninsula samples indicated compositions ranging from basaltic trachyandesite and trachyandesite to monzonite (Figure 3.23). The dominant mineral assemblage consists of feldspar, biotite, and clinopyroxene, with minor amounts of amphibole. Zircon and apatite are consistently present as accessory phases across all samples. Trachytic texture is characteristic of most samples except for the monzonite porphyry. In trachytic samples, phenocrysts are enclosed within a glassy, partially devitrified groundmass. The primary mineral

phases are typically biotite and plagioclase, while clinopyroxene occurs in lesser amounts and commonly displays clustered glomeroporphyritic textures. Orthoclase and hornblende are rare but are locally present. Most of the samples appear fresh to only weakly-altered. The monzonite porphyry sample from the quarry north of Turgutreis, however, exhibits intense carbonate-clay alteration that obscures the primary mineralogy, while retaining its primary igneous texture.

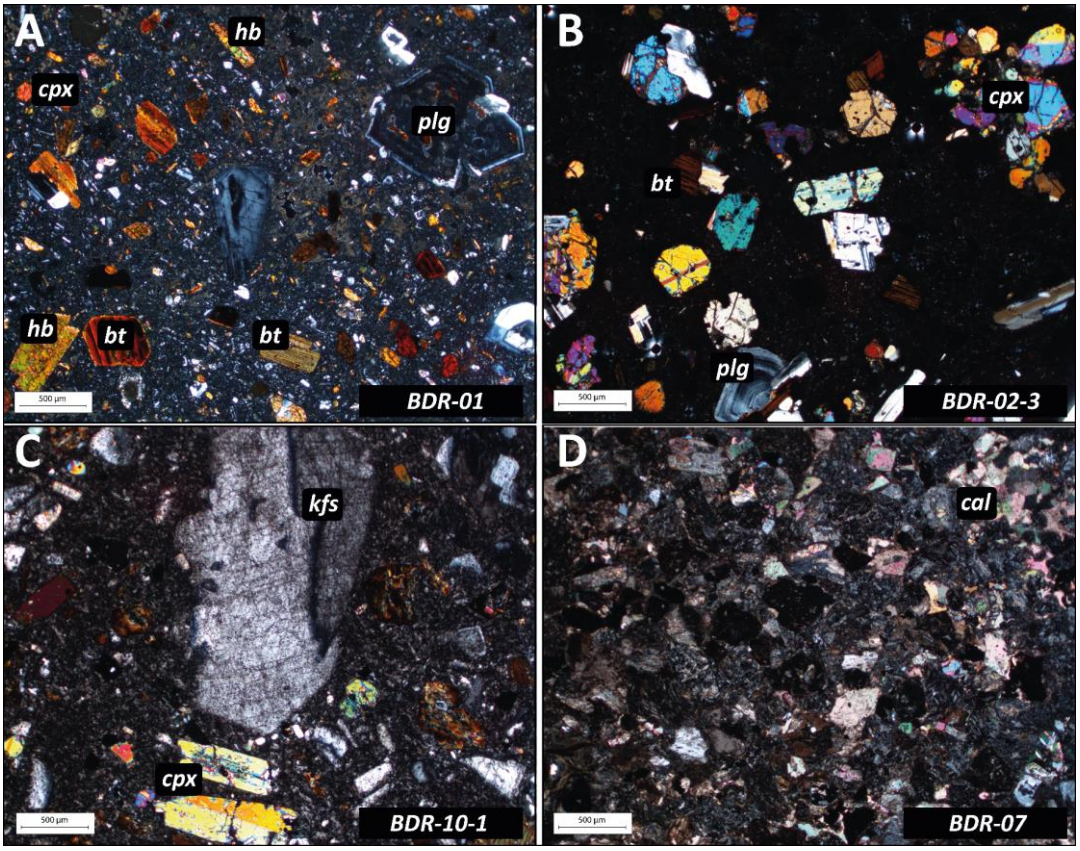


Figure 3.23. Transmitted-light microphotographs of igneous rock samples from the Bodrum Peninsula. (A) Trachyandesite containing well-preserved biotite, plagioclase, hornblende, and pyroxene (XPL). (B) Basaltic trachyandesite with trachytic texture, dominated by clinopyroxene and plagioclase with subordinate biotite (XPL). (C) Trachyandesite composed of pyroxene and plagioclase with lesser large orthoclase crystals (XPL). (D) Medium-grained monzonite showing carbonate–clay alteration (XPL).

CHAPTER 4

LITHOGEOCHEMISTRY

A comprehensive dataset of published lithogeochemical data representing the studied magmatic domains was compiled with an aim to evaluate the whole-rock major and trace element geochemical features and source compositions of igneous systems investigated in this study. Full lithogeochemical data obtained from this study is provided in Table 4.1. The initial compilation consisted of over 1,300 samples. This dataset was subsequently filtered based on loss‐on‐ignition (LOI) values to minimize the influence of secondary alteration and volatile enrichment, ultimately reducing the sample set to 500 analyses. For non‐mineralized rocks, a maximum LOI threshold of 3 wt. % was applied, while for ore‐bearing samples the cutoff was set at 7 wt.%, reflecting the higher expected volatile contents in due to hydrothermal alteration.

It is noteworthy that several mineralization‐related samples analyzed in this study yielded LOI values exceeding the 7 wt.% threshold. These data were nevertheless used and plotted on the geochemical diagrams due to their direct genetic association with the ore systems and their importance for constraining magmatic–hydrothermal processes, as well as the lack of available published data.

For geochemical classification of the studied rocks, the total alkali versus silica (TAS) scheme of Le Maitre et al. (1989) was employed as the primary framework. However, given the well‐known mobility of the major elements used in this scheme (Na, K, Si) under hydrothermal alteration (e.g., Pearce, 1975), the Zr/TiO_2 versus Nb/Y classification diagram of Winchester and Floyd (1977) was used for samples originating from mineralized localities as this diagram is based on immobile trace elements abundances that are relatively less sensitive to alteration (Figure 4.1). The

subdivision between alkaline and sub‐alkaline compositions was also evaluated on the TAS diagram following the criteria of Irvine and Baragar (1971).

To further constrain the geochemical affinities of the magmatic suites, Aluminum Saturation Index (ASI) values were plotted against SiO_2 following Shand (1927), while K_2O versus SiO_2 variation diagrams were constructed according to the classification of Peccerillo and Taylor (1976). These diagrams were prepared separately for each sector to highlight potential spatial and temporal variations in magma chemistry.

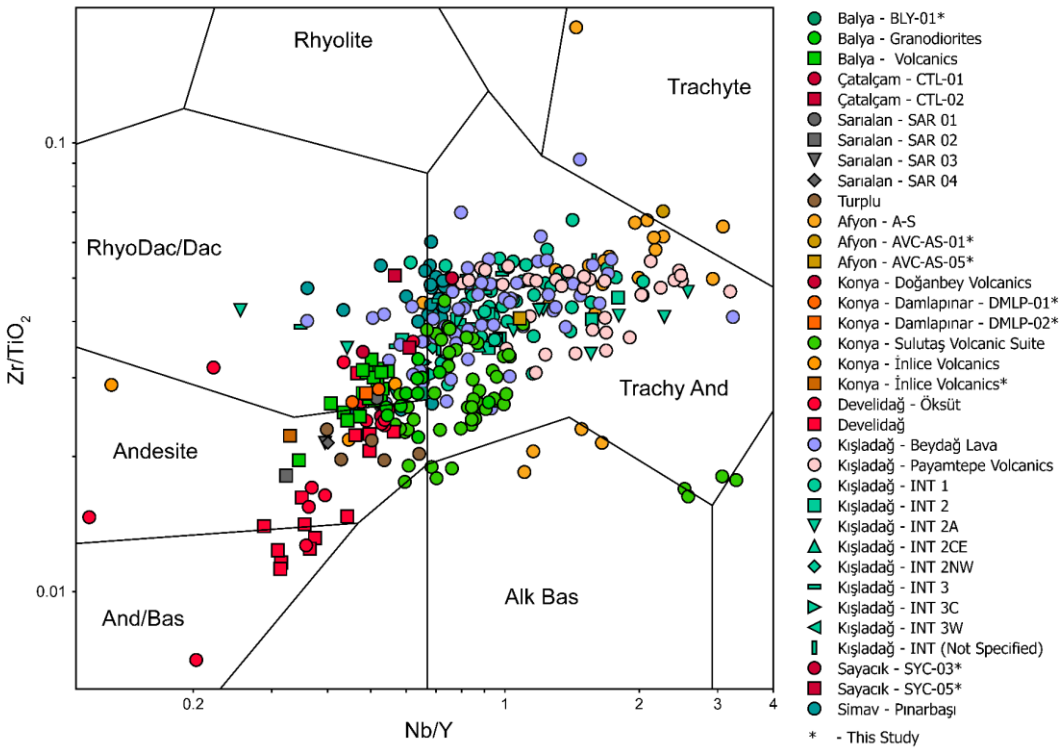


Figure 4.1. Classification diagram for mineralized samples in the Central Taurides and the Western Anatolia based on immobile trace elements (after Winchester and Floyd, 1977).

To better elucidate the trace element systematics of the studied samples, multi-element and rare earth element (REE) diagrams were constructed.

Table 4.1. Whole-rock lithogeochemistry data for the Late Cenozoic units across the Western Anatolia and the Central Taurides

Region	Biga						Uşak		Konya		
District	Sarıalan	Sarıalan	Sarıalan	Sarıalan	Çatalçam	Çatalçam	Sayacık	Sayacık	İnlice	Damlapınar	Damlapınar
Unit	SAR-01	SAR-02	SAR-03	SAR-04	CTL-01	CTL-02	SYC-03	SYC-05	INL-D-01	DMLP-01	DMLP-02
Rock	Andesite porphyry	Andesite porphyry	Basaltic andesite	Andesite	Andesite porphyry	Andesite porphyry	Monzonite porphyry	Monzonite porphyry	Andesite dyke	Basaltic andesite	Basaltic andesite
Easting	552594	552594	552594	552594	538677	538813	684048	684048	419453.06	407105	407105
Northing	4384847	4384847	4384847	4384847	4357055	4358468	4257023	4257023	4179450.9	4186658	4186658
SiO2	58.98	51.38	55.73	50.61	59.94	62.01	61.65	62.53	60.47	59.21	58.59
Al2O3	14.56	15.04	16.12	14.46	15.9	16.06	14.23	17.77	21.18	15.21	15.35
Fe2O3	5.18	6.35	7.5	7.3	5.22	4.75	11.31	5.71	3.67	6.69	6.62
MgO	1.9	3.34	3.52	3.51	2.97	2.58	1.18	1.05	0.28	3.72	3.8
CaO	4.65	7.59	7.19	7.93	2.48	3.29	0.47	0.49	2.2	6.09	6.25
Na2O	2.11	1.14	2.76	1.75	2.54	3.18	0.09	0.07	2.42	2.78	2.77
K2O	4.22	1.83	2.49	2.79	4.67	2.8	4.34	3.5	2.68	3.26	3.32
TiO2	0.5	0.67	0.69	0.66	0.53	0.5	0.48	0.57	0.89	0.77	0.78
P2O5	0.18	0.19	0.21	0.25	0.18	0.18	0.23	0.39	0.45	0.27	0.29
MnO	0.08	0.14	0.09	0.16	0.1	0.06	0.03	0.05	0.03	0.11	0.12
Cr2O3	0.002	0.004	0.005	0.004	0.004	0.005	0.006	0.006	b.d.l	0.015	0.015
LOI	7.3	12	3.3	10.2	5	3.7	5.7	7.3	5.17	1.4	1.6
SUM	99.85	99.81	99.76	99.79	99.77	99.3	99.75	99.72	100.5	99.67	99.64
Mo	0.7	4.1	1.1	0.6	4.5	1.7	11.4	4.4	2	0.5	0.5
Be	1	2	2	2	3	3	19	5	b.d.l	3	3
Ba	1440	1079	966	1107	1839	1190	402	2157	1185	1037	1078
Ni	7.5	12.9	13.9	9.3	18.8	21.1	47.4	27.8	30	12.9	14.6
As	2.2	56.5	4.2	4.5	20.1	6.2	10.5	4.7	5.2	1.9	1.2
Sc	12	21	20	21	12	11	9	10	5.2	18	19
Co	12.4	21.7	21.4	25.3	8.9	11.5	15	19.7	32	19.9	19.7
Ga	15.8	16.5	17.1	15.5	17.8	17.8	19.4	25.1	21.5	18	17.9
Nb	9.6	6.3	8.1	8.3	8.5	9.4	12.1	18.4	14	12.4	12.1
Rb	134	66.4	81.5	88.1	168.1	90.1	177.8	146	67.2	131.4	132.5
Sr	138.6	233.5	648.9	398.5	343.8	4677.1	68.1	135.9	445	1243.6	1341.4
Th	20.6	9.3	12.3	14.1	18.1	15.3	24.2	31.3	18.1	22.3	22.8
U	4.5	2.4	3	3.4	3.1	4	7.3	13	4.94	6.6	7.2
V	123	184	180	181	110	102	59	99	165	123	137
Zr	135	121.5	148.1	141.7	181.4	175	239.7	288.7	198	217.6	216
Y	18.6	19.5	20.5	20.7	17.7	15.4	15.9	32.5	42.5	23.8	24.8
Cu	15.2	36.1	35.1	6.4	71.8	67.3	10	21.7	63	24.7	29.2
Pb	3.6	37.5	5.6	9.6	28.9	16.7	482.3	199.3	18	3	3.4
Zn	70	38	44	59	124	43	584	549	1150	24	23

Table 4.1. continued

Region	Biga						Uşak		Konya		
District	Sarıalan	Sarıalan	Sarıalan	Sarıalan	Çatalçam	Çatalçam	Sayacık	Sayacık	İnlice	Damlapınar	Damlapınar
Unit	SAR-01	SAR-02	SAR-03	SAR-04	CTL-01	CTL-02	SYC-03	SYC-05	INL-D-01	DMLP-01	DMLP-02
Rock	Andesite porphyry	Andesite porphyry	Basaltic andesite	Andesite	Andesite porphyry	Andesite porphyry	Monzonite porphyry	Monzonite porphyry	Andesite dyke	Basaltic andesite	Basaltic andesite
Easting	552594	552594	552594	552594	538677	538813	684048	684048	419453.06	407105	407105
Northing	4384847	4384847	4384847	4384847	4357055	4358468	4257023	4257023	4179450.9	4186658	4186658
Sn	1	1	2	2	2	2	11	11	2.2	2	2
W	2.3	0.9	1.2	1.8	2.5	0.9	9.2	4.1	1.7	1.5	2.1
Cs	4.2	8.1	3.8	8.7	10.1	8.1	10.7	5.3	1.53	3.3	4
Hf	3.6	3.1	3.7	3.5	4.6	4.5	6.2	7.3	5.16	5.7	5.6
Ta	1.1	0.7	0.7	0.6	0.8	0.9	1.2	1.4	1	1.2	1.1
La	38.7	32.8	34.8	38.5	43.4	37	33.8	111.5	40.7	55.3	59.8
Ce	68.9	62.9	67.2	73.2	80.8	67.6	55.4	205.8	81.1	110.2	111.9
Pr	7.52	7.32	7.92	8.4	8.93	7.57	5.68	22.68	9.2	12.76	13.44
Nd	26.4	27.8	29.3	31.4	30.9	26.3	20	76.7	38.8	45.8	48.7
Sm	4.8	5.37	5.42	5.96	5.26	4.58	3.55	13.6	9.13	7.46	7.94
Eu	1.19	1.34	1.38	1.43	1.14	1.09	1.4	2.11	2.47	1.8	1.87
Gd	4.25	4.58	4.79	5.06	4.11	3.81	3.27	10	8.26	5.8	6.11
Tb	0.59	0.64	0.67	0.68	0.59	0.51	0.48	1.4	1.33	0.78	0.83
Dy	3.48	3.71	3.85	3.79	3.27	2.91	2.82	7.54	8.22	4.37	4.71
Ho	0.64	0.73	0.77	0.74	0.63	0.55	0.57	1.36	1.66	0.86	0.89
Er	1.96	2.15	2.18	2.13	1.94	1.7	1.69	3.65	4.36	2.55	2.71
Tm	0.28	0.29	0.32	0.29	0.26	0.23	0.24	0.49	0.6	0.36	0.37
Yb	1.89	1.97	2.1	1.96	1.95	1.58	1.62	3.19	4.12	2.43	2.51
Lu	0.29	0.3	0.31	0.29	0.28	0.24	0.24	0.41	0.64	0.35	0.38
Cd	0.2	<0.1	<0.1	<0.1	0.2	<0.1	2.2	1.8	1	<0.1	<0.1
Bi	<0.1	<0.1	<0.1	<0.1	0.1	<0.1	1.3	2	0.02	<0.1	<0.1
Hg	0.13	1	0.04	0.04	0.02	<0.01	0.02	0.03	0.011	<0.01	<0.01
Tl	<0.1	0.2	<0.1	<0.1	0.2	0.2	0.8	0.4	0.26	<0.1	<0.1
Se	<0.5	1.7	<0.5	<0.5	<0.5	<0.5	4.6	3.9	0.7	<0.5	<0.5
Ag	<0.1	0.2	<0.1	<0.1	0.2	<0.1	0.8	0.9	1	<0.1	<0.1
Sb	0.9	0.4	1.7	0.8	2	0.3	1.6	0.3	24.2	0.2	0.1

b.d.l. – Below detection limit n.a. – Not analyzed

The LILEs, which are characteristically mobile in the presence of fluids, generally yielded coherent patterns in the studied rocks when compared to the relatively immobile high field strength elements (HFSEs). This geochemical behavior suggests that the primary magmatic signatures are largely preserved. Nonetheless, certain

samples display localized anomalies or irregular variations in LILE abundances, which are interpreted to have resulted predominantly from secondary processes (e.g., hydrothermal alteration), and to a lesser extent, from analytical uncertainties.

Such patterns, when viewed in the context of arc-related magmatism, are consistent with subduction-modified mantle sources, where fluid–melt interactions enrich the magma in LILEs while maintaining systematic HFSE depletions. The majority of the analyzed samples display a relative depletion in HFSEs such as Ta, Nb, and Ti, manifesting as pronounced negative anomalies. In particular, the Nb–Ta negative anomaly is a well-established geochemical signature of magmas generated in subduction zone environments (e.g., Pearce and Peate, 1995). Consequently, presence of such anomalies in the studied samples can be interpreted as evidence for a subduction-related component in their mantle sources. Conversely, the absence of these anomalies in certain volcanic units suggests a lack of subduction-derived input in their source regions, implying a distinct petrogenetic history for these magmas.

Strong negative Ti and P anomalies, on the other hand, are more plausibly attributed not to subduction influence, but to fractional crystallization of accessory mineral phases such as magnetite, titanite, and apatite. The observation that these anomalies are more pronounced in the more evolved lithologies reinforces this interpretation, underscoring the significant role of fractional crystallization processes in the petrogenesis of these volcanic rocks.

In the chondrite-normalized (Sun and McDonough, 1989) multi-element diagrams, the samples exhibit enrichment in light rare earth elements (LREEs) relative to heavy rare earth elements (HREEs). Such LREE enrichment can be linked to contributions from an enriched mantle source and/or to partial melting at relatively low degrees. Examination of the HREE patterns reveals either flat or slightly negative slopes. In upper mantle peridotites, HREEs are compatible with garnet but behave incompatibly in the presence of spinel (e.g., McKenzie and O'Nions, 1991). Thus, fractionated HREE patterns (negative slopes) may indicate a contribution from melts derived from a garnet-bearing mantle source (e.g., garnet peridotite), whereas flat

HREE patterns point to a dominant melt contribution from a spinel-bearing mantle source (spinel peridotite).

Additionally, nearly all high-silica samples display a negative Eu anomaly, which is most plausibly explained by plagioclase fractionation during magmatic differentiation. This feature further supports the interpretation of extensive crystal–melt segregation processes shaping the geochemical evolution of the studied volcanic suites.

Trace elements provide critical insights into the origin, evolution, and post-formational modifications of rocks, thereby contributing significantly to the reconstruction of tectono-magmatic events. Because rocks formed in different tectonic settings acquire distinct trace element signatures characteristic of those environments, trace elements serve as geochemical archives that record the geological evolution and history of specific regions. Through systematic analysis of trace element distributions, it is possible to decipher the evolutionary pathways of minerals and rocks, offering a deeper understanding of the magmatic and tectonic processes that have shaped a given geological setting. Furthermore, specific trace element ratios (such as Eu/Eu*, Sr/Y, La/Yb, $(La/Sm)_n$, and Dy/Yb) serve as particularly informative geochemical indicators when evaluating rocks associated with porphyry-type systems (Richards, 2011; Richards et al., 2012; Loucks, 2014). These ratios can reflect key aspects of magmatic evolution, including the depth and pressure conditions of crystallization, the role of specific mineral fractionation processes (e.g., plagioclase, amphibole, garnet), and the degree of magma oxidation. When interpreted in conjunction with other geochemical and mineralogical data, they provide valuable constraints on the fertility of magmatic systems and their potential to generate economically significant porphyry-type mineralization.

It is well established that the geochemical behavior of europium (Eu) in magmatic systems is largely governed by its affinity for plagioclase (Rollinson, 1993; Rollinson and Pease, 2021). Consequently, the depletion of Eu and the development of a negative Eu anomaly may arise when this element is incorporated into the crystal

structure of plagioclase and subsequently removed from the melt, or when crystallization and fractional removal of plagioclase are strongly suppressed within the magmatic system. Therefore, the absence of a negative Eu anomaly can be interpreted as evidence for limited or negligible plagioclase fractionation during magma evolution.

Suppression of plagioclase fractionation preventing any significant Eu depletion from the source melt may occur due to elevated magmatic water contents (Richards et al., 2012; Keller et al., 2015). In addition, higher magmatic oxidation states favor the stabilization of Eu predominantly in its trivalent form (Eu^{3+}), which reduces its compatibility with the plagioclase lattice and hinders its incorporation into the crystal structure (Frey et al., 1978; Hanson, 1980; Richards et al., 2012).

Conversely, a positive Eu anomaly in magmatic systems may develop through plagioclase accumulation or, in some cases, hornblende fractionation (Green and Pearson, 1985). In this context, the increase in negative Eu anomalies observed in the majority of the studied samples with increasing SiO_2 content likely reflects the significant role of plagioclase fractionation in the petrogenesis of these rocks. On the other hand, the relatively rare occurrence of positive Eu anomalies can be attributed to localized plagioclase accumulation. Extremely high positive Eu values, however, may not necessarily reflect magmatic processes and could instead result from hydrothermal alteration and/or analytical uncertainties.

From a metallogenic perspective, magmatic rocks that are considered fertile for mineralization often display elevated Sr/Y and La/Yb ratios—geochemical signatures commonly observed in adakites (Kay and Mpodozis, 2001; Richards and Kerrich, 2007; Chiaradia et al., 2012; Richards, 2012; Richards et al., 2012; Lee and Tang, 2020). Owing to these characteristics, such rocks have frequently been genetically linked to adakitic magmas (Thieblemont et al., 1997; Sajona and Maury, 1998; Oyarzun et al., 2001).

High Sr/Y and La/Yb ratios in adakitic-type magmas arise from the contrasting geochemical behavior of the involved elements; heavy rare earth elements (HREEs), such as Y and Yb, tend to be strongly retained by garnet in the residue during partial melting, whereas Sr and light rare earth elements (LREEs) like La behave incompatibly and preferentially partition into the melt.

In the present study, in order to assess whether the analyzed samples exhibit adakite-like geochemical characteristics, Sr/Y–Y and La/Yb–Yb discrimination diagrams were constructed following the approach of Defant and Drummond (1990). These diagrams allow for the comparison of the studied rocks with the geochemical fields of adakites, providing insights into the potential petrogenetic processes and source characteristics that may have contributed to their formation.

The $(La/Sm)_n$–$(Dy/Yb)_n$ diagram serves as a valuable tool for understanding the contrasting behaviors of light and heavy rare earth elements, particularly the light rare earth elements (LREEs) and the heavy rare earth elements (HREEs). Among these element pairs, the LREEs generally display incompatible behavior, meaning they preferentially partition into the melt phase during partial melting events.

Considering the La/Sm ratio, lanthanum is more incompatible than samarium; thus, during low-degree partial melting, La is preferentially mobilized into the melt to a greater extent than Sm, resulting in an elevated La/Sm ratio. Conversely, at higher degrees of partial melting, this ratio tends to decrease because both elements are more efficiently extracted from the source.

The behavior of HREEs, such as Dy and Yb, is strongly influenced by the stability of garnet in the source region. Garnet preferentially incorporates these elements, especially Yb, into its crystal structure, thereby depleting the melt in HREEs when garnet is present in the residue. As a result, the fractionation expressed in the Dy/Yb ratio is primarily controlled by the presence or absence of garnet in the source.

In summary, while the La/Sm ratio is largely governed by the degree of partial melting, the Dy/Yb ratio is a sensitive indicator of the residual mineral assemblage—

particularly the role of garnet—within the mantle source. This relationship makes the $(La/Sm)_n$–$(Dy/Yb)_n$ diagram an effective discriminator of melting conditions and source mineralogy in magmatic systems.

4.1 Central Taurides

4.1.1 Konya Volcanic Complex

The Konya Volcanic Complex (KVC) is one of the most extensively studied volcanic regions in the area, and whole-rock geochemical data are widely available in the literature for igneous rocks of this region. Available lithogeochemical data is representative of most of the sampled prospects within the KVC, with the exception of Damlapınar. Therefore, two intensely-altered andesitic samples from this site (DMLP-01 and DMLP-02) were analyzed. In addition, an altered andesitic dyke sample from the İnlice open-pit (INL-D-01) and another sample from the Sulutaş Volcanic Suite (sample SİLLE-01) were also analyzed.

On the TAS diagram, samples from KVC define two distinct compositional clusters. The first cluster, including sample SİLLE-01, encompasses the more primitive and alkaline members of the Sulutaş Volcanic Suite (SVS), which plot within the trachybasaltic to basaltic trachyandesitic fields (Figure 4.2). The second cluster is entirely tholeiitic in character and comprises the more evolved SVS products together with the Doğanbey and İnlice samples (Figure 4.2). Within this group, the SVS rocks are dominated by andesitic to dacitic compositions, whereas the Doğanbey and İnlice suites are characterized predominantly by andesitic lithologies (Figure 4.2). Damlapınar samples also correlate with the second group as these andesitic samples display high-K calc-alkaline composition (Figure 4.2A, B).

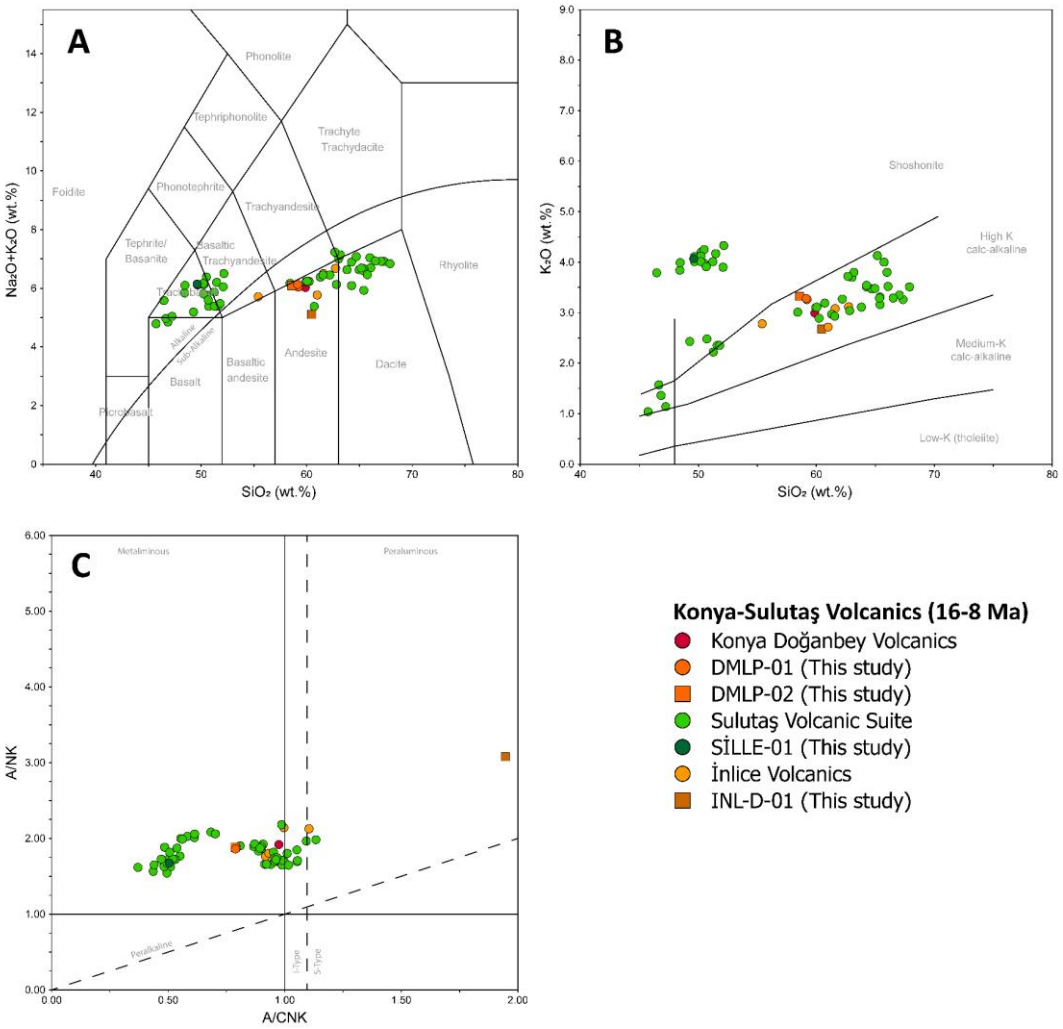


Figure 4.2. Classification diagrams based on whole-rock geochemical data for KVC. (A) TAS diagram (Le Maitre et al., 1989), with the alkaline/subalkaline division after Irvine and Baragar (1971). (B) K_2O vs. SiO_2 diagram (Peccerillo and Taylor, 1976). (C) Alumina Saturation Index (Shand, 1927). Data from Çelik, 1999, Kurt et al., 2003, Asan and Ertürk, 2013, Asan et al., 2021; Rabayrol and Hart, 2021.

The majority of the İnlice, Doğanbey, and Damlapınar samples are metaluminous, although a few are peraluminous or transitional (Figure 4.2C). In contrast, the İnlice dyke sample is an outlier compared to all other KVC samples as it is strongly peraluminous (Figure 4.2C).

Two distinct groups of samples are also noted on a primitive mantle-normalized multi-element diagram (Figure 4.3). Samples from the SVS, which exhibit trachyandesitic to basaltic andesitic compositions, are devoid of negative Nb, Ta,

and Ti anomalies typically regarded as hallmarks of subduction-related magma genesis. This absence may suggest derivation from a mantle source with limited involvement of a subduction component, or alternatively, significant crustal interaction, potentially overprinting any original subduction-related signatures. In contrast, these negative anomalies are clearly expressed in the second group of samples including those from İnlice, Doğanbey, and Damlapınar, implying a stronger subduction imprint in their mantle source regions or derivation from magmas that retained a more pristine arc-like geochemical character (Figure 4.3A).

When normalized to chondritic values, one sample from the İnlice group reveals significantly high heavy rare earth element (HREE) concentrations and an almost flat REE pattern, indicative of minimal residual garnet influence during melt generation and suggesting a relatively shallow source depth (Figure 4.3B). A broadly similar pattern is observed in the dyke sample; however, its REE pattern is comparatively more depleted, implying a more evolved melt or a greater degree of fractional crystallization.

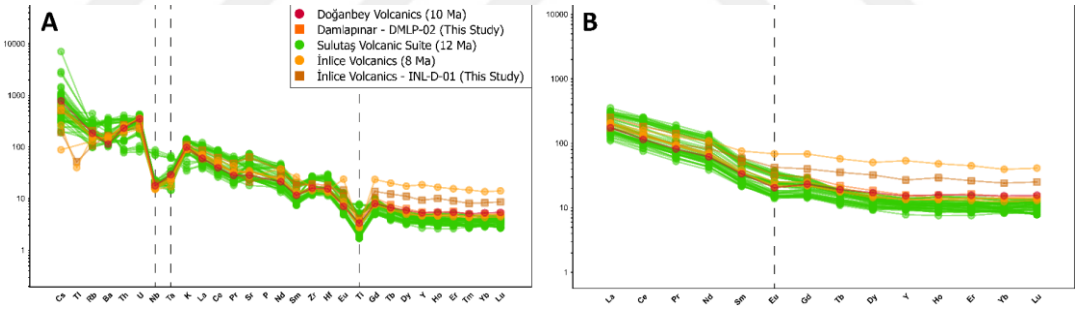


Figure 4.3. A) Primitive mantle-normalized trace element and B) chondrite-normalized REE diagrams for igneous rocks from the KVC. Normalization values are from Sun and McDonough (1989).

The combination of flat to slightly depleted HREE patterns, alongside distinct anomalies in incompatible elements, points to a magmatic evolution pathway in the İnlice system dominated by fractional crystallization processes, likely involving plagioclase and clinopyroxene as early-crystallizing phases. The variability in Nb, Ta, and Ti anomalies between the two compositional groups underscores differences

in their petrogenetic histories—ranging from magmas with attenuated subduction signatures to those retaining a robust arc-related geochemical fingerprint.

Examination of trace element ratios reveals a clear geochemical distinction within the KVC. Samples from İnlice, Damlapınar, and Doğanbey display a systematic increase in Dy/Yb ratios coupled with a decrease in La/Sm ratios (Figure 4.4A), suggesting progressive fractionation processes and potential variations in the depth and mineralogy of the melting column. In contrast, the Sulutaş Volcanic Suite is generally characterized by higher La/Sm ratios (Figure 4.4A), which may reflect a greater influence of residual garnet in the source region or derivation from melts generated at comparatively greater depths.

When Eu anomalies are plotted against SiO_2 content, the same binary grouping within the KVC becomes apparent (Figure 4.4B). Low-SiO_2 basaltic andesite/trachybasalt units exhibit moderately higher Eu/Eu* ratios, whereas increasing SiO_2 is accompanied by a marked decrease in Eu/Eu* (Figure 4.4B), a trend typically interpreted as the result of plagioclase fractionation. This indicates that in more evolved magmas, plagioclase removal played a significant role in controlling REE patterns.

The higher-SiO_2 group, which includes the İnlice, Doğanbey, and Damlapınar samples, occupies the adakite-like field in both Sr/Y versus SiO_2 and La/Yb versus SiO_2 diagrams (Figure 4.4C, D). This is consistent with magmas derived from thickened crust or from mantle sources influenced by slab melting, where residual garnet suppresses heavy rare earth element concentrations. Moreover, in Sr/Y versus Y and La/Yb versus Yb plots, KVC samples define a compositional trend from the field of normal andesites toward the adakite-like domain, with the low-SiO_2 units showing distinctly higher Sr/Y and La/Yb ratios (Figure 4.4E, F). Such enrichments are indicative of high-pressure differentiation or partial melting in the presence of garnet-bearing assemblages, further supporting a petrogenetic link to adakitic magmatism.

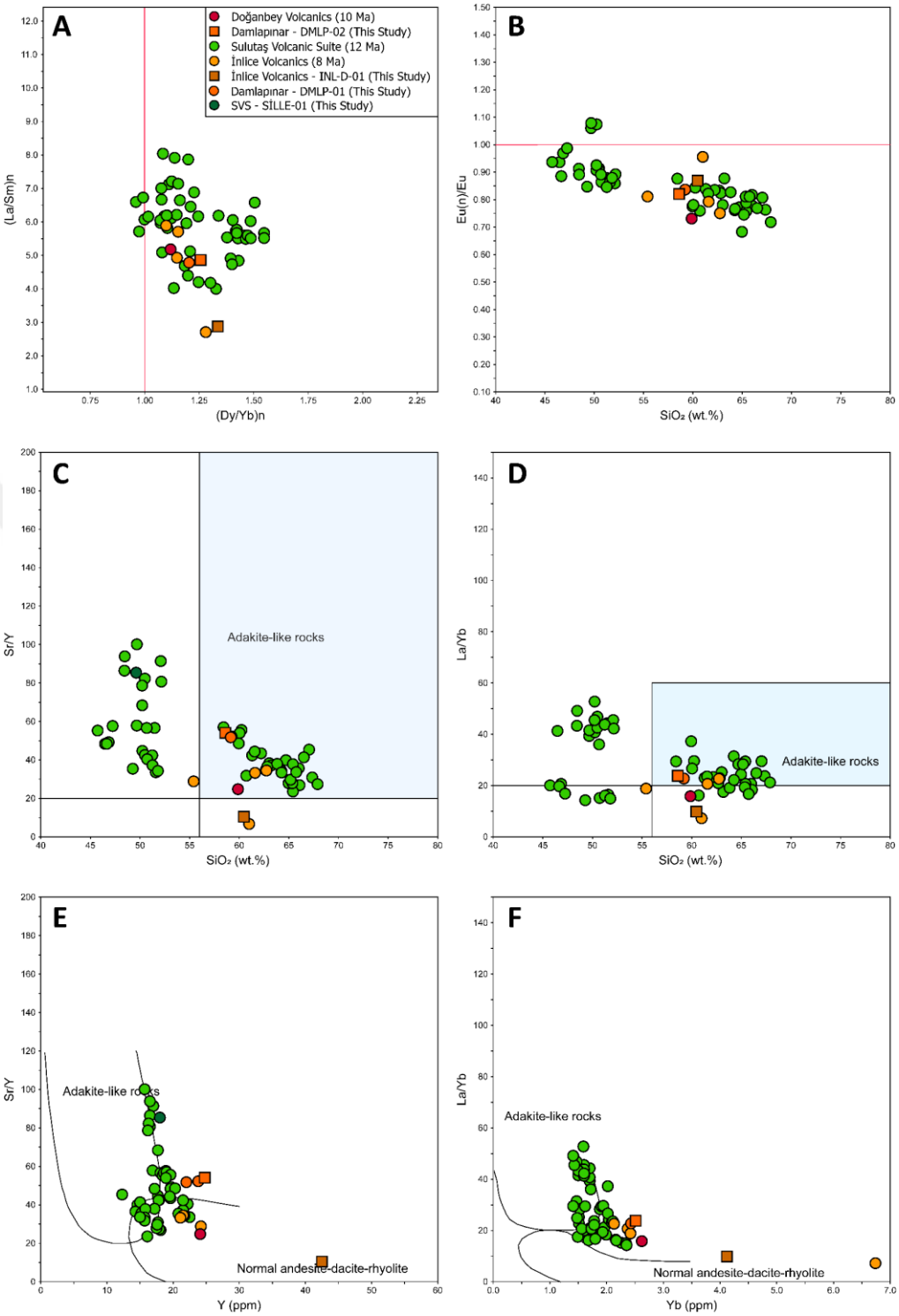


Figure 4.4. Selected trace element discrimination diagrams for igneous lithologies from the KVC and SVS: (A) $(La/Sm)_N$ vs. $(Dy/Yb)_N$, (B) Eu/Eu* vs. SiO_2, (C) Sr/Y vs. SiO_2, (D) La/Yb vs. SiO_2, (E) Sr/Y vs. Y, and (F) La/Yb vs. Yb. Normalization values are from Sun and McDonough (1989).

4.1.2 Karacadağ-Melendiz and Develidağ Volcanic Complexes

Samples from the eastern extent of the Late Cenozoic magmatic belt in the Central Taurides exhibit a remarkably broad compositional range, extending from mafic to felsic lithologies when plotted on the TAS diagram (Figure 4.5). Despite this diversity, the majority of the samples display a tholeiitic affinity, with only a small subset plotting within the alkaline field (Figure 4.5). The most primitive samples within the dataset are derived from the Karapınar and Erciyes localities, characterized predominantly by basaltic to trachybasaltic compositions.

By contrast, volcanic products from the Melendiz Volcanic Province, Tekkedağ, and Develidağ/Öksüt are dominated by andesitic compositions, with minor occurrences of basaltic andesite and dacite (Figure 4.5A). The İncesu ignimbrites, in turn, are compositionally restricted, reflecting a narrow dacitic range. In stark contrast, the Cappadocian Volcanics display an extensive compositional spectrum, spanning from basaltic andesite through to rhyolite (Figure 4.5A).

Geochemically, the Late Cenozoic Anatolian volcanic rocks from Central Anatolia are generally metaluminous and predominantly medium- to high-K calc-alkaline in character (Figure 4.5B), reflecting magmatic evolution within a subduction-related environment. An exception is observed in a subset of the Cappadocian Volcanics, which extend toward the shoshonitic field (Figure 4.5B), potentially indicating localized mantle source enrichment or variable degrees of crustal assimilation during magma evolution.

In both primitive mantle (Figure 4.6A) and chondrite-normalized multi-element diagrams (Figure 4.6B), all samples – except those from the Cappadocian Volcanics – display broadly similar geochemical patterns. In contrast, the Cappadocian suite exhibits marked internal variability, with individual samples showing distinct trace element signatures. Within this suite, whole-rock data from the Melendiz region are notably more enriched in light rare earth elements (LREEs) compared to younger volcanic products from the Erciyes and Karapınar areas.

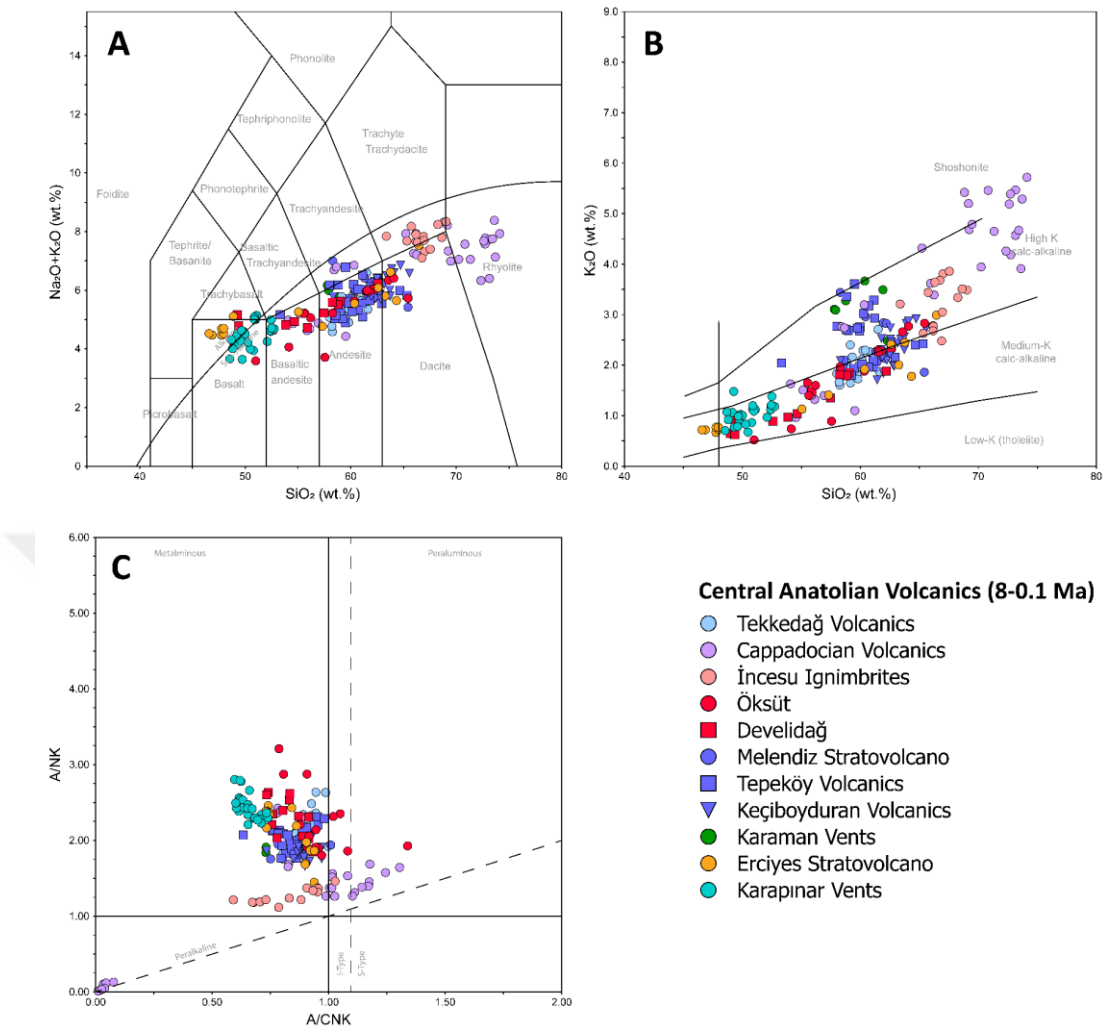


Figure 4.5. Classification diagrams based on whole-rock geochemical data for Central Taurides. (A) TAS diagram (Le Maitre et al., 1989), with the alkaline/subalkaline division after Irvine and Baragar (1971). (B) K_2O vs. SiO_2 diagram (Peccerillo and Taylor, 1976). (C) Alumina Saturation Index (Shand, 1927). Data from Innocenti et al. (1975); Temel et al. (1988); Aydın (2008); Güçtekin and Köprübaşı (2009); Gençalioğlu-Kuşcu and Geneli (2010); Koralay (2010); Kürkçüoğlu (2010); Koralay et al. (2011); Reid et. al. (2017); Di Giuseppe (2018); Aluç et al. (2020); Rabayrol and Hart (2021); Aydın et al. (2022).

A particularly striking feature is the absence of a pronounced negative Eu anomaly in the Tekkedağ Volcanic Suite, as well as in Develidağ–Öksüt samples and in the younger Melendiz, Erciyes, and Karapınar volcanic rocks (Figure 4.6B). This lack of Eu depletion implies limited plagioclase fractionation during magmatic evolution, potentially reflecting crystallization at depths where plagioclase was not stable or

was suppressed by high water content in the melt. In contrast, the presence or absence of a negative Eu anomaly within the broader Cappadocian dataset is less clear, as the expression of this feature is irregular and inconsistent across individual samples.

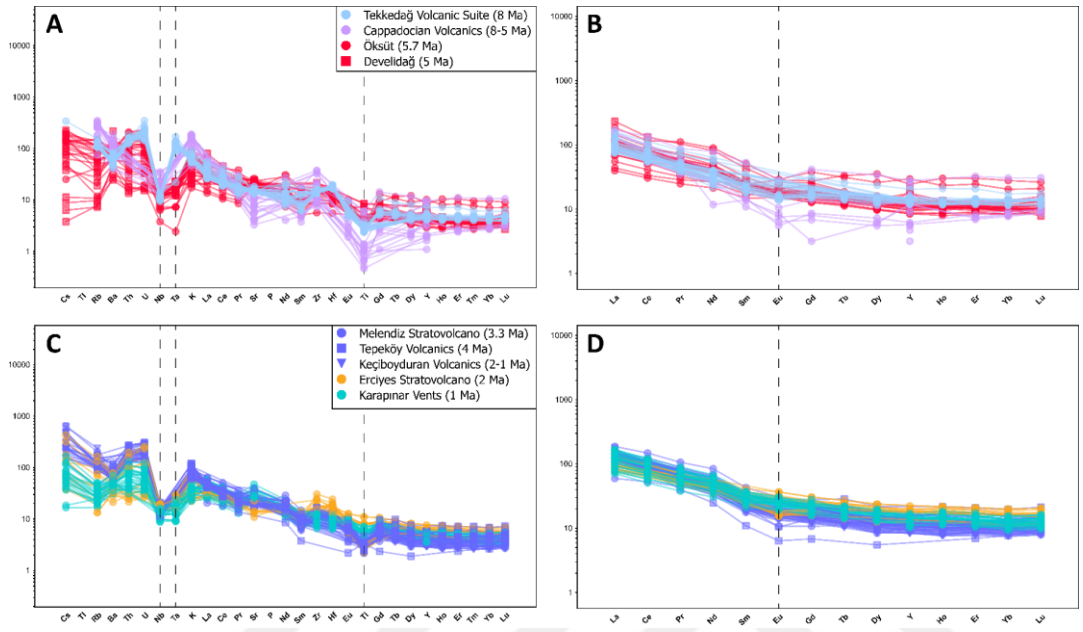


Figure 4.6. A and C) Primitive mantle-normalized trace element and B and D) chondrite-normalized REE diagrams of volcanic rocks from Central Taurides. Normalization values are from Sun and McDonough (1989).

When evaluating the trace element ratio diagrams, it becomes apparent that the Melendiz and Tekkedağ samples generally exhibit lower Dy/Yb ratios compared to those from Öksüt and Develidağ (Figure 4.7). Within the Melendiz group—particularly the Keçiboyduran volcanic suite—an increase in La/Sm ratios is notable. In fact, among the Cappadocian volcanic rocks as a whole, extremely low Dy/Yb ratios coupled with markedly high La/Sm ratios stand out as a distinctive geochemical feature (Figure 4.7A).

In the Eu(n)/Eu versus SiO_2 diagram, a clear negative correlation is observed, with Eu/Eu ratios decreasing systematically as SiO_2 content increases (Figure 4.7B). Notably, the Karapınar Vent samples record the highest average Eu/Eu* values in

the dataset (around 1.0), although certain Öksüt samples reach even higher values, up to approximately 1.1.

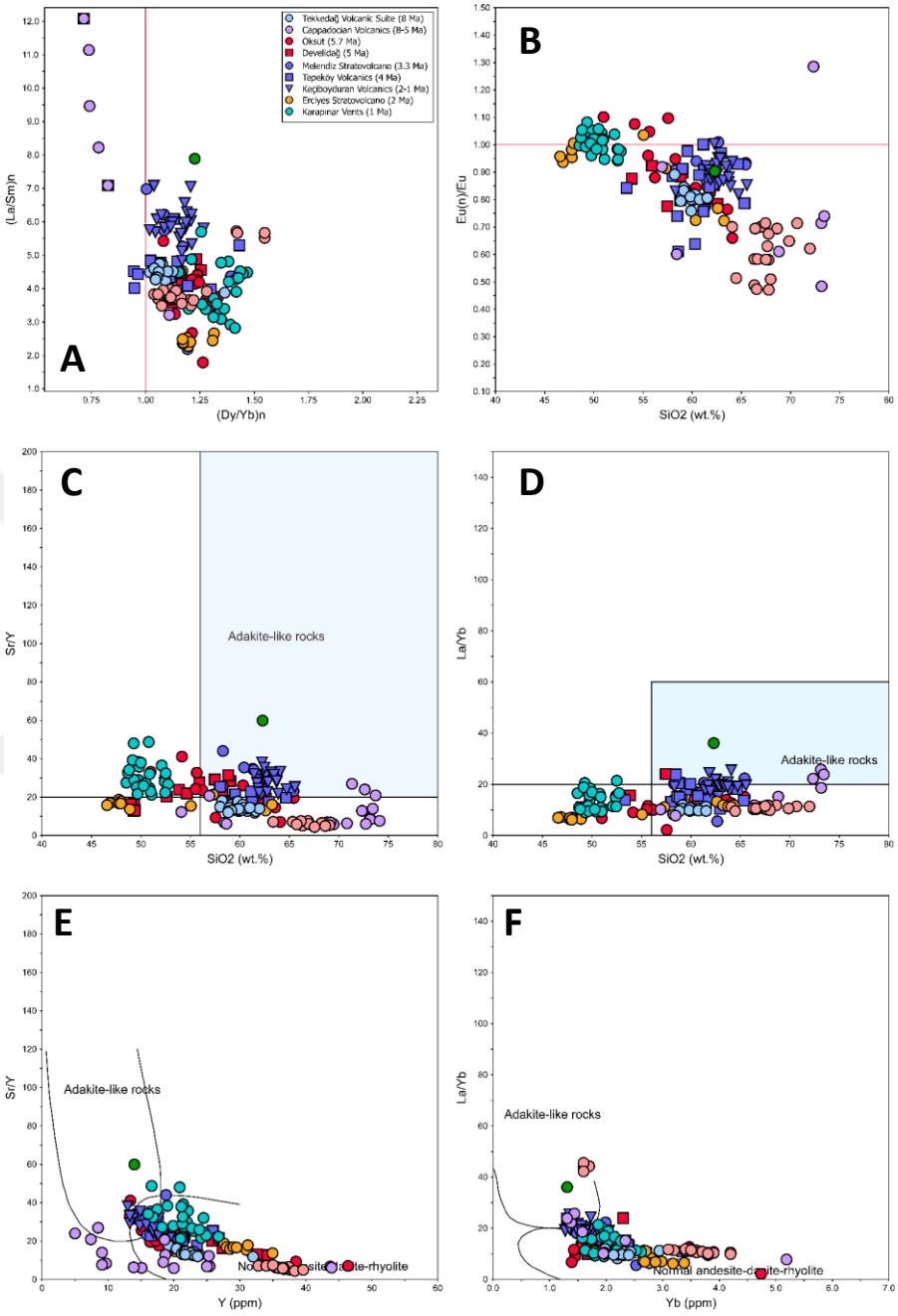


Figure 4.7. Selected trace element discrimination diagrams for igneous lithologies from the Central taurides: (A) $(La/Sm)_N$ vs. $(Dy/Yb)_N$, (B) Eu/Eu* vs. SiO_2, (C) Sr/Y vs. SiO_2, (D) La/Yb vs. SiO_2, (E) Sr/Y vs. Y, and (F) La/Yb vs. Yb. Normalization values are from Sun and McDonough (1989).

The Sr/Y versus SiO_2 diagram reveals a mildly discernible decreasing trend (Figure 4.7C). In this plot, Öksüt and Develidağ samples, along with those from Melendiz, plot within the adakite-like field. The Karapınar samples, despite exhibiting elevated Sr/Y ratios, fall outside the adakite-like field due to their relatively low SiO_2 contents. In contrast, the La/Yb versus SiO_2 diagram shows that only a limited number of samples fall into the adakite-like domain (Figure 4.7D). While a subset of the Melendiz suite trends toward this field, their La/Yb ratios generally remain low. Similarly, Sr/Y versus Y and La/Yb versus Yb diagrams yield patterns consistent with those observed in the SiO_2 -based plots, reinforcing the interpretation of subtle geochemical differences between Cappadocian volcanic centers (Figure 4.7E–F).

4.2 Western Anatolia

4.2.1 Biga Peninsula

In addition to the published lithogeochemical data for the Biga Peninsula, new whole-rock geochemical analyses were carried out on several key samples to enhance the coverage and resolution of the geochemical framework. These include one sample (BLY-01) from a granodioritic unit intersected in deep drill cores in the northern sector of the Balya district, two andesitic samples from the Çatalçam prospect (CTL-01 and CTL-02), and four core samples from the Sarıalan area. The resulting data have been incorporated into the regional geochemical compilation.

On the TAS diagram, porphyry-mineralized intrusions from Balya plot within a relatively narrow compositional range corresponding to granodiorite (dacite) and diorite (andesite) fields (Figure 4.8A). The overlying volcanic units of the Hallaçlar Volcanics, in contrast, range from basaltic andesite to andesite in composition (Figure 4.8A). Sarıalan samples exhibit a much broader compositional variability, extending from basalt to andesite, a pattern that may reflect the influence of hydrothermal alteration processes at this locality (Figure 4.8A). In the Turplu area, the majority of samples are andesitic, whereas the Eybek and Kozak plutons are

mostly granodioritic to dioritic in composition (dacite and andesite fields; Figure 4.8A). Although nearly all samples fall within the high-K calc-alkaline field, some of the samples, particularly those belonging to the volcanic units from the Balya area, trend toward the shoshonitic field (Figure 4.8B). Most samples are metaluminous, although the Çatalçam samples plot near the peraluminous boundary (Figure 4.8C).

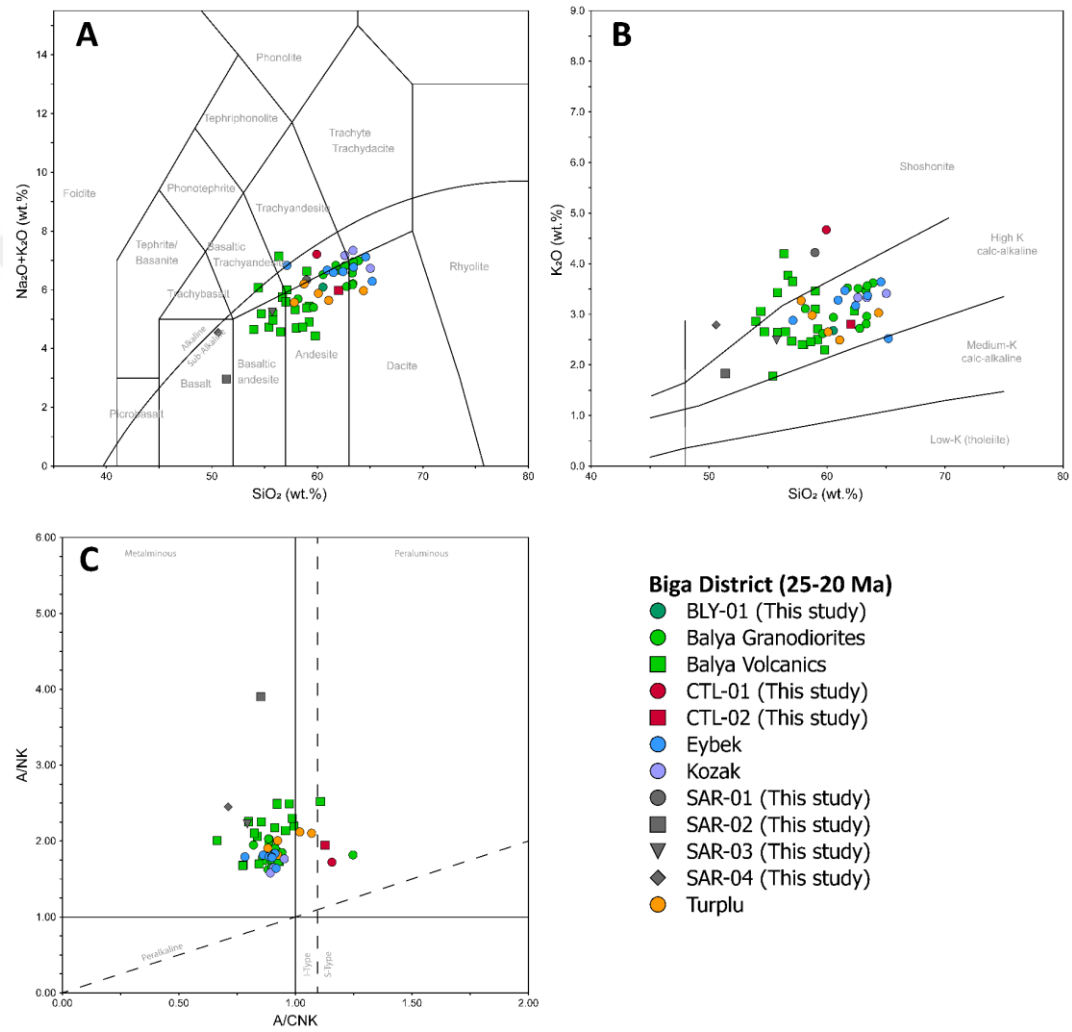


Figure 4.8. Classification diagrams based on whole-rock geochemical data for Biga Peninsula. (A) TAS diagram (Le Maitre et al., 1989), with the alkaline/subalkaline division after Irvine and Baragar (1971). (B) K_2O vs. SiO_2 diagram (Peccerillo and Taylor, 1976). (C) Alumina Saturation Index (Shand, 1927). Data from Delaloye and Bingöl (2000); Ece and Schroeder (2007); Ece and Wampler (2008); Özışık (2009); Altunkaynak et al. (2012); Aydar (2018); Özel (2024).

Primitive mantle–normalized multi-element patterns reveal a high degree of similarity among all analyzed samples. Negative Nb, Ta, and Ti anomalies are consistently observed across the dataset, indicating a subduction-related setting (Figure 4.9A). Chondrite-normalized rare earth element (REE) patterns are likewise broadly consistent among samples. Balya granodiorites display a very slight negative Eu anomaly, whereas almost all other samples show no discernible Eu anomaly (Figure 4.9B).

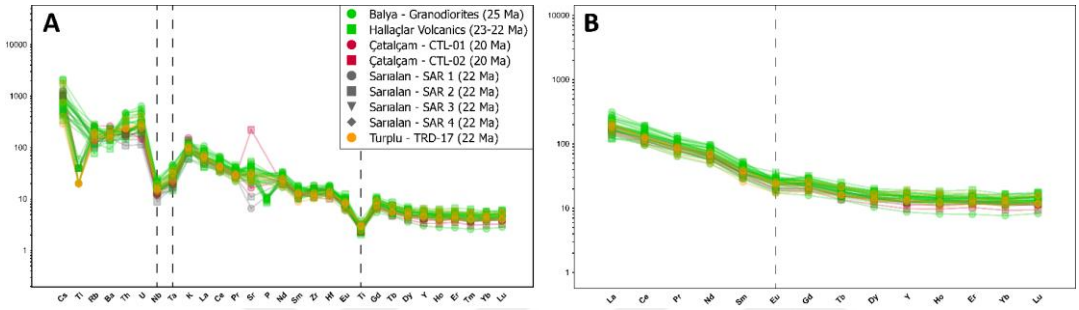


Figure 4.9. A) Primitive mantle-normalized trace element and B) chondrite-normalized REE diagrams for igneous rocks from the Biga Peninsula. Normalization values are from Sun and McDonough (1989).

Trace element ratios further underscore the geochemical coherence of the dataset. All samples have Dy/Yb ratios <1.3 and average La/Sm ratios ~5 (Figure 4.10A). In the Eu/Eu* versus SiO_2 diagram, the Sarıalan samples are particularly notable for their uniform Eu/Eu* values (~0.85), suggesting a lack of significant plagioclase fractionation during magma evolution (Figure 4.10B). Within the Balya area, volcanic and plutonic units slightly differ from each other as the volcanic units tend to have higher Eu/Eu* values compared to the intrusive rocks (Figure 4.10B).

In the Sr/Y versus SiO_2 and La/Yb versus SiO_2 diagrams, most samples plot within the adakite-like field, although the Sarıalan suite generally exhibits lower Sr/Y and La/Yb ratios (Figure 4.10C–D). Nevertheless, in the Sr/Y versus Y and La/Yb versus Yb diagrams, nearly all samples plot within or close to the field for typical calc-alkaline andesites (Figure 4.10E–F).

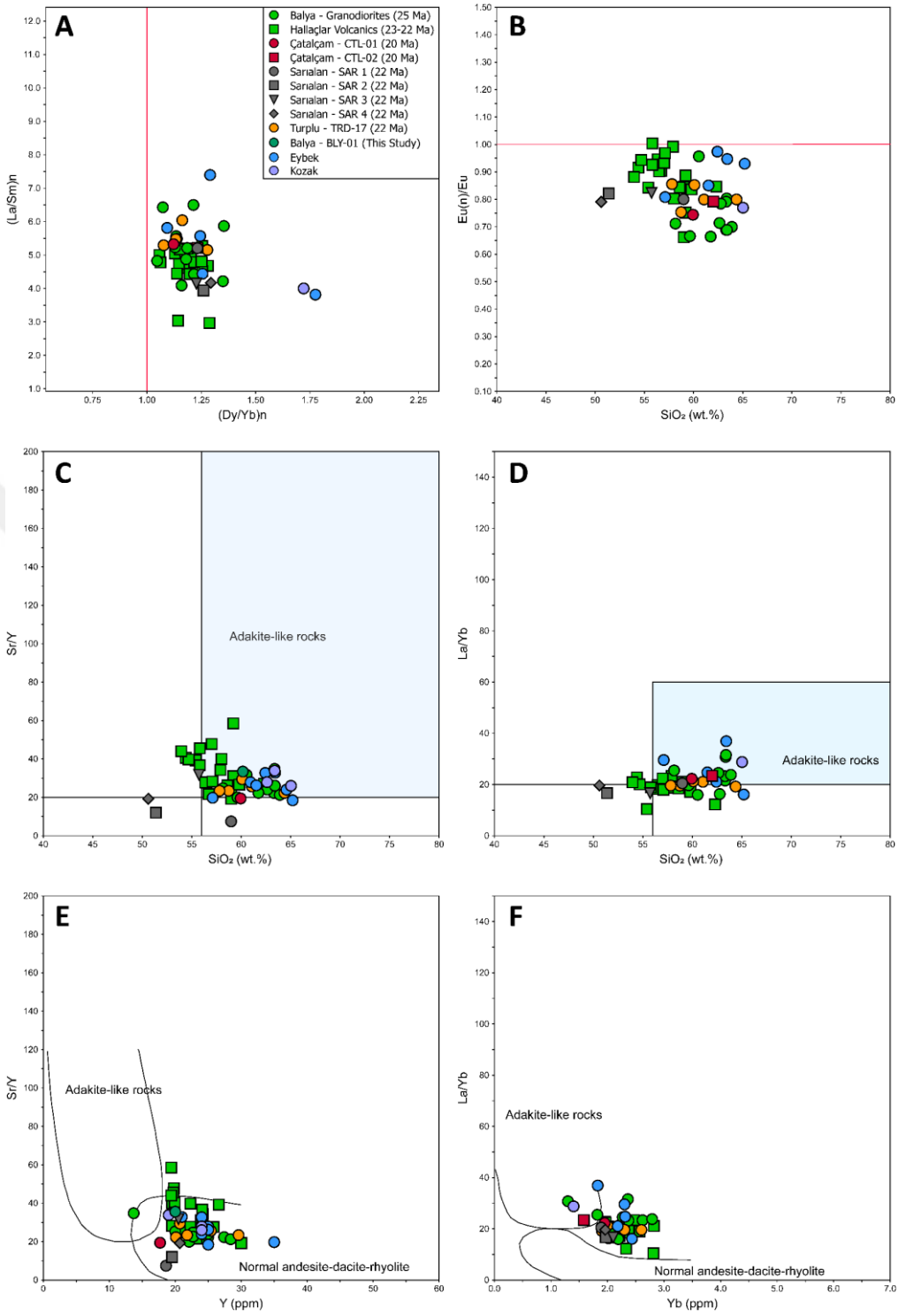


Figure 4.10. Selected trace element discrimination diagrams for igneous lithologies from the Biga Peninsula: (A) $(La/Sm)_N$ vs. $(Dy/Yb)_N$, (B) Eu/Eu* vs. SiO_2, (C) Sr/Y vs. SiO_2, (D) La/Yb vs. SiO_2, (E) Sr/Y vs. Y, and (F) La/Yb vs. Yb. Normalization values are from Sun and McDonough (1989).

4.2.2 Kütahya-Simav District

The Simav region (20.0–18 Ma) encompasses samples from Alaçam, Eğrigöz (EGR-02), Koyunoba, Pınarbaşı, Baklan, and Sındırgı (SIN-01). In the TAS diagram, the Simav samples predominantly exhibit felsic compositions. Among these, the Alaçam, Eğrigöz, and Koyunoba intrusions display the broadest silica range within the region, plotting mainly in the granodioritic (dacitic) to granitic (rhyolitic) compositional fields (Figure 4.11A). In contrast, the Pınarbaşı suite reveals a somewhat greater lithological variability, with samples distributed across the andesite, trachyandesite, trachyte/trachydacite, and dacite fields (Figure 4.11A). The Baklan suite is compositionally more restricted, with nearly all samples falling within the dacitic field. The Sındırgı suite, represented by a limited number of samples, is characterized by dacitic to rhyolitic compositions although the SIN-01 sample is plotted in the dacite field (Figure 4.11A).

Igneous rocks of the Kütahya-Simav district are predominantly high-K calc-alkaline in composition (Figure 4.11B), although a small subset of samples trends toward the shoshonitic field. This compositional framework suggests magmas that were likely generated in a continental arc setting, possibly involving significant crustal contributions during their evolution, as reflected in their slightly peraluminous signatures (on the I-type field; Figure 4.11C). All Simav samples are also distinctly peraluminous (Figure 4.11C).

The subduction signature in a continental setting is further confirmed by the primitive mantle normalized multi element diagrams as they are represented by negative Nb, Ta, and Ti anomalies (Figure 4.12A). Although all samples have similar elemental abundances, Pınarbaşı samples can be distinguished by their slight Sr and Ti enrichments (Figure 4.12A). On the chondrite-normalized diagrams however, there is a clear distinction between the seemingly barren or poorly-mineralized Eğrigöz, Koyunoba, and Alaçam plutons, and Sındırgı volcanic rocks and the porphyry-mineralized Pınarbaşı monzonite and seemingly barren Baklan pluton (Figure 4.12B). Pınarbaşı and Baklan samples lack negative Eu anomalies, whereas

other igneous suites are characterized by negative Eu anomalies suggesting the role of plagioclase fractionation in the melt source (Figure 4.12B).

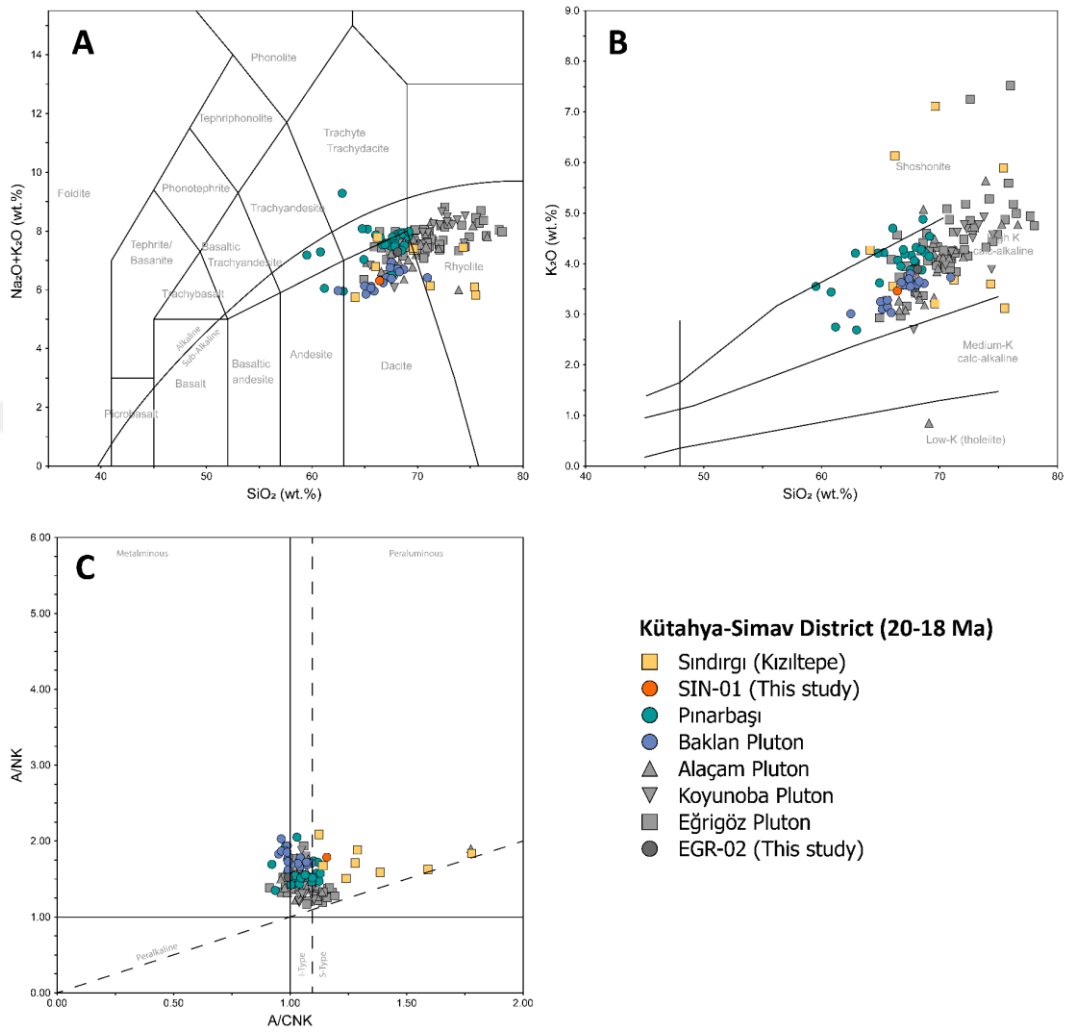


Figure 4.11. Classification diagrams based on whole-rock geochemical data for Kütahya-Simav district. (A) TAS diagram (Le Maitre et al., 1989), with the alkaline/subalkaline division after Irvine and Baragar (1971). (B) K_2O vs. SiO_2 diagram (Peccerillo and Taylor, 1976). (C) Alumina Saturation Index (Shand, 1927). Data from Tufan (2005); Aydoğan et al. (2008); Özgenç and İlbeyli (2008); Akay (2009); Hasözbek et al. (2011); Jacob (2011); Altunkaynak et al. (2012); Oyman et al. (2013); Semiz et al. (2015); Delibaş et al (2017); Özen and Arık, 2019; Rabayrol and Hart (2021).

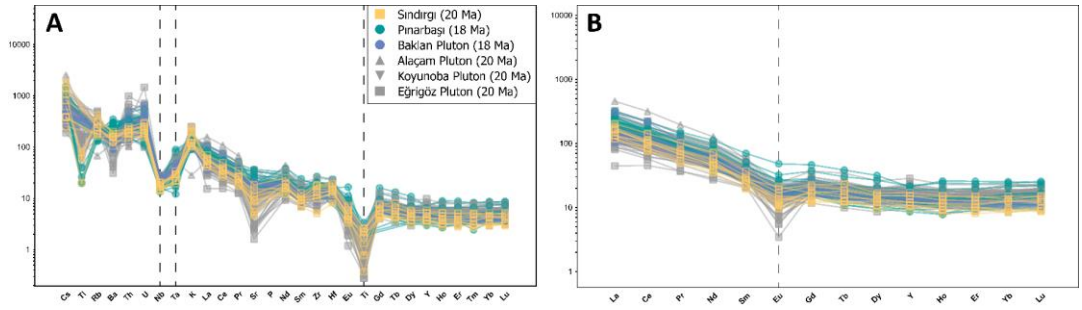


Figure 4.12. A) Primitive mantle-normalized trace element and B) chondrite-normalized REE diagrams of Late Cenozoic igneous rocks from the Kütahya-Simav region. Normalization values are from Sun and McDonough (1989).

In the La/Sm versus Dy/Yb diagram, samples from the Eğrigöz, Alaçam, and Koyunoba plutons exhibit a broad compositional variability, with Dy/Yb ratios ranging from 0.75 to 1.4 and La/Sm ratios between 2 and 7 (Figure 4.13A). Similarly, although the Baklan pluton samples display a somewhat narrower distribution compared to these three plutons, they nonetheless reveal considerable variation, but their Dy/Yb ratios do not fall below 1.0 (Figure 4.13A). The Sındırgı suite exhibits Dy/Yb ratios comparable to those of Baklan but is distinguished by consistently higher La/Sm ratios, indicating subtle differences in magma evolution or source characteristics (Figure 4.13A).

The Pınarbaşı suite presents a more restricted range in Dy/Yb ratios, yet its La/Sm ratios predominantly lie between 5.5 and 8, with some values reaching as high as 9.5 (Figure 4.13A). In the Eu/Eu* versus SiO_2 diagram, a distinctly negative correlation is observed, reflecting decreasing Eu/Eu* ratios with increasing silica content (Figure 4.13B). This trend is particularly pronounced in the poorly-mineralized/barren Eğrigöz, Alaçam, and Koyunoba plutons. In contrast, the Baklan and Pınarbaşı suites show wider scatter without any visible trends (Figure 4.13B). For the Sındırgı samples, such a correlation is difficult to establish due to limited data and compositional variability (Figure 4.13B).

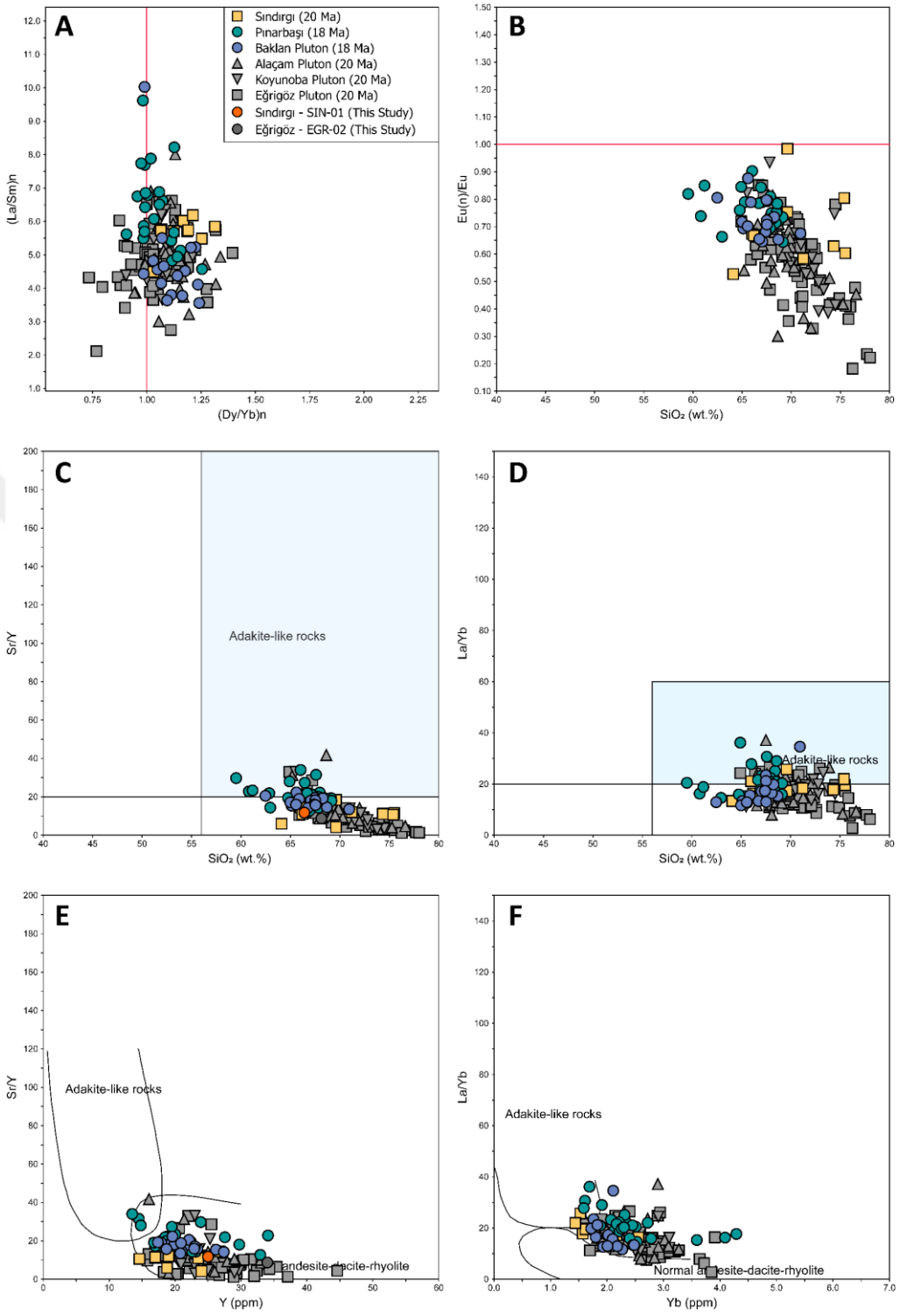


Figure 4.13. Selected trace element discrimination diagrams for igneous lithologies from the Kütahya-Simav district: (A) $(La/Sm)_N$ vs. $(Dy/Yb)_N$, (B) Eu/Eu* vs. SiO_2, (C) Sr/Y vs. SiO_2, (D) La/Yb vs. SiO_2, (E) Sr/Y vs. Y, and (F) La/Yb vs. Yb. Normalization values are from Sun and McDonough (1989).

Both Sr/Y and La/Yb ratios of the Kütahya-Simav district samples exhibit decreasing trends with increasing SiO_2 , most clearly expressed in the Eğrigöz, Alaçam, and Koyunoba plutons (Figure 4.13C–D). In the Pınarbaşı and Baklan suites, a similar declining pattern is evident in Sr/Y ratios, whereas the La/Yb trend remains ambiguous (Figure 4.13C–D). When plotted on Sr/Y versus Y and La/Yb versus Yb diagrams, nearly all samples fall within or close to the compositional field of normal andesites (Figure 4.13E–F).

These geochemical trends—particularly the variation in La/Sm and Dy/Yb ratios—suggest differences in magma fractionation histories, potential involvement of amphibole versus plagioclase as dominant fractionating phases, and possibly source composition contrasts among the studied plutonic bodies. The decreasing Sr/Y and La/Yb trends with increasing SiO_2 in several plutons are consistent with progressive differentiation and the crystallization of plagioclase and/or amphibole at mid- to upper-crustal levels.

4.2.3 Kırka-Afyon-Isparta District

When plotted on a TAS diagram, Kırka (21.0–16.1 Ma) samples display the least compositional variability within the Kırka–Afyon–Isparta region, being consistently represented by alkaline basaltic trachyandesite compositions including the sample KRK-01 (Figure 4.14A). In contrast, the Isparta and Bucak suites exhibit somewhat greater diversity, although all remain firmly within the alkaline field. Within the Isparta dataset, some samples fall into the basaltic trachyandesite, trachyandesite, and trachyte/trachydacite compositional range, whereas others plot within the phonotephrite and tephriphonolite fields. Bucak samples, in turn, form a tight cluster dominated by phonotephrite compositions. Three samples selected for the analyses in terms of their geochemistry also display the similar diversity being plotted on basaltic trachyandesite (GÖL-01), tephriphonolite (GÖL-04), and trachyte/trachydacite fields (GÖL-02).

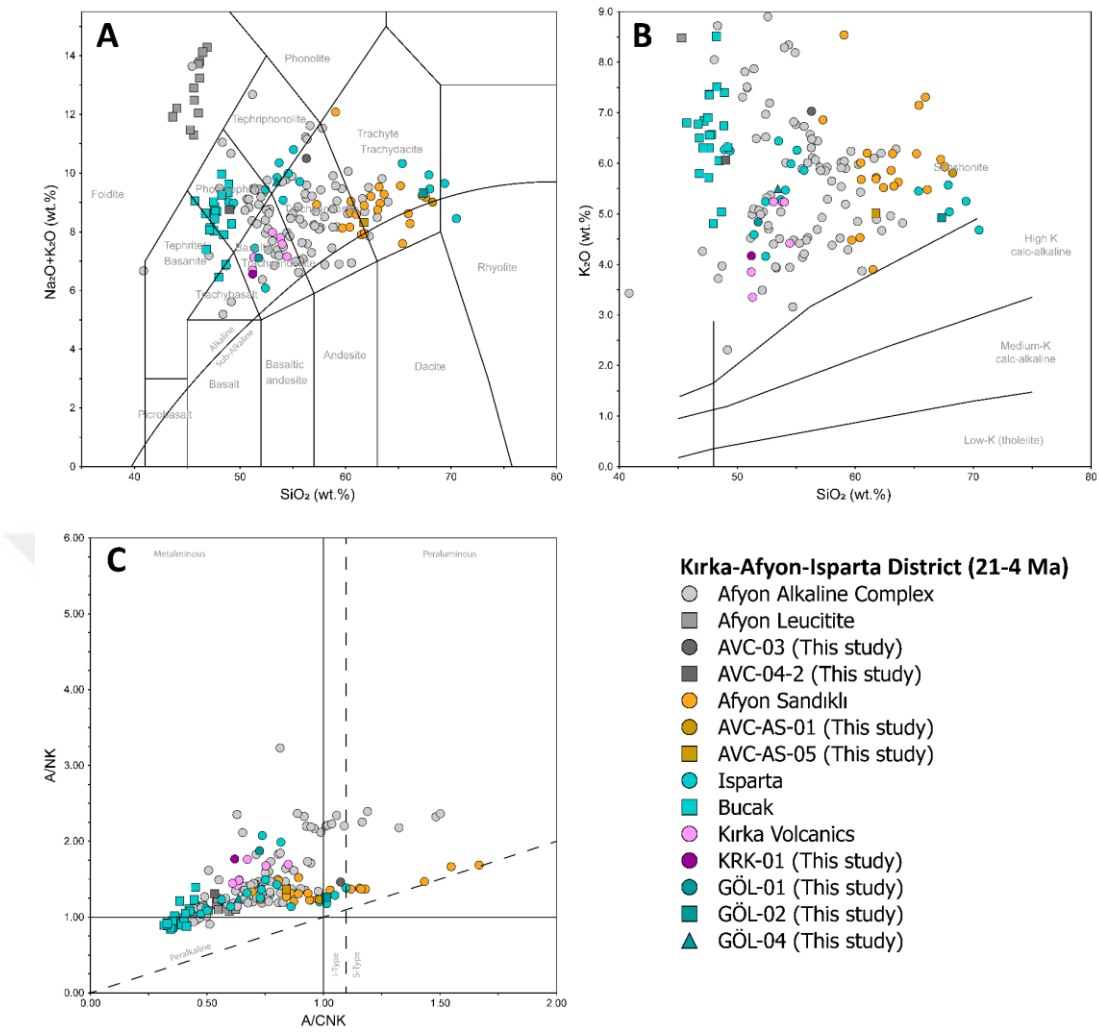


Figure 4.14. Classification diagrams based on whole-rock geochemical data for Kırka-Afyon-Isparta volcanics. (A) TAS diagram (Le Maitre et al., 1989), with the alkaline/subalkaline division after Irvine and Baragar (1971). (B) K_2O vs. SiO_2 diagram (Peccerillo and Taylor, 1976). (C) Alumina Saturation Index (Shand, 1927). Data from Francalanci et al. (2000); Akal (2003); Çoban and Flower (2006); Akal (2008); Dilek and Altunkaynak (2010); Prelevic et al. (2012); Akal et al. (2013); Prelevic et al. (2015); Kuşcu et al. (2019); Sönmez and Kuşcu (2020); Rabayrol and Hart (2021).

By comparison, the Afyon samples display the broadest compositional range in the region, with a few samples. The alkaline igneous rocks of the AVC are predominantly comprised by basaltic trachyandesite and trachyandesite (AVC-03), with subordinate trachybasalt, trachyte/trachydacite, tephrite/basanite, phonotephrite (AVC-04-2), and tephriphonolite lithologies (Figure 4.14A). The Afyon leucitites,

due to their strongly foiditic compositions, are geochemically distinct from the rest of the suite. Samples from A-S prospect are predominantly trachyte/trachydacite (AVC-AS-01 and AVC-AS-05), with minor trachyandesite, and exhibit alkaline affinities (Figure 4.14B).

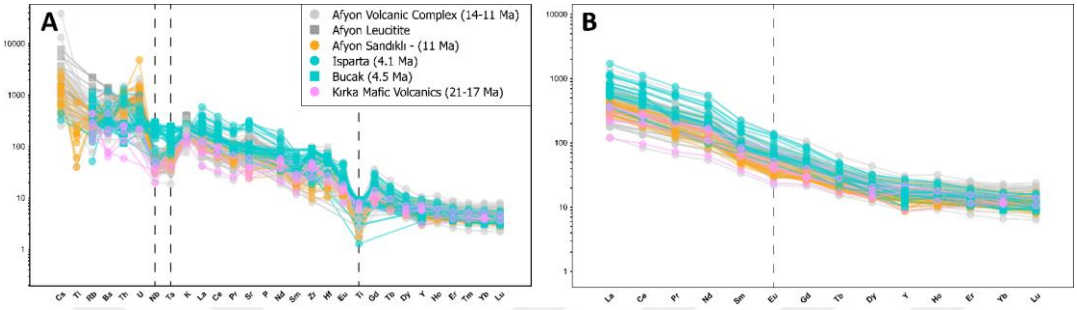


Figure 4.15. A) Primitive mantle-normalized trace element and B) chondrite-normalized REE diagrams for igneous rocks from Kırka-Afyon-Isparta region. Normalization values are from Sun and McDonough (1989).

Aluminum Saturation Index (ASI) values reveal further distinctions among the subgroups. The Kırka samples are completely metaluminous (Figure 4.14C). The Isparta and Bucak samples are predominantly metaluminous, with only a minor fraction showing peraluminous compositions (Figure 4.14C). As expected from their broader lithological diversity, the Afyon samples span a wider ASI range. Samples from the A-S porphyry prospect are peraluminous to metaluminous, whereas the leucitites are metaluminous (Figure 4.14C). The AVC as a whole displays a broad range from metaluminous to peraluminous compositions (Figure 4.14C).

In terms of their K_2 O contents, all samples from the Kırka–Afyon–Isparta region fall within the shoshonitic field (Figure 4.14B), consistent with their overall alkaline nature. This geochemical uniformity in high-K compositions, despite the observed lithological diversity, suggests that the region's magmatism was dominantly sourced from K-rich mantle-derived magmas, variably modified by fractional crystallization and, in some cases, crustal assimilation.

When examining the primitive mantle–normalized multi-element diagrams, the overall pattern of the samples appears broadly similar; however, the two distinct

geochemical groups identified in the Isparta–Bucak region are also evident here (Figure 4.15A). Notably, the volcanic rocks from the Bucak area lack the pronounced negative Nb and Ta anomalies that typically signify subduction signatures and are observed in the other samples. While a negative Ti anomaly is still present, it is less pronounced compared to the rest of the dataset.

In the chondrite-normalized REE diagrams, the Isparta samples show marked enrichment in light rare earth elements (LREEs), whereas the Bucak sample is still moderately LREE-enriched but to a lesser extent than Isparta (Figure 4.15B).

Trace element ratio plots reveal that almost all samples display high Dy/Yb ratios, with both La/Sm and Dy/Yb spanning a wide compositional range (Figure 4.16A). Among them, the Kırka samples have the lowest La/Sm ratios, while the Isparta–Bucak samples exhibit the highest Dy/Yb ratios (Figure 4.16A). The leucitite samples from the Afyon Volcanic Complex form a tight cluster, characterized by moderately high Dy/Yb ratios and intermediate La/Sm values (Figure 4.16A). By contrast, the Afyon–Sandıklı samples show a distinct trend of decreasing La/Sm with increasing Dy/Yb (Figure 4.16A).

In most Kırka–Afyon–Isparta samples, Eu/Eu* remains largely stable with increasing SiO_2 , suggesting minimal plagioclase fractionation; however, the Afyon–Sandıklı suite shows a subtle decreasing Eu/Eu* trend, which may indicate a limited plagioclase control (Figure 4.16B).

On Sr/Y versus SiO_2 , and Sr/Y versus Y, as well as La/Yb versus SiO_2 and La/Yb versus Yb diagrams, the Afyon–Sandıklı samples fall within the adakit-like field (Figure 4.16C–F). In contrast, while nearly all other samples (except Kırka) have high Sr/Y and La/Yb ratios, the Kırka suite consistently exhibits lower values. The Isparta and Bucak samples are geochemically distinct from each other in these plots.

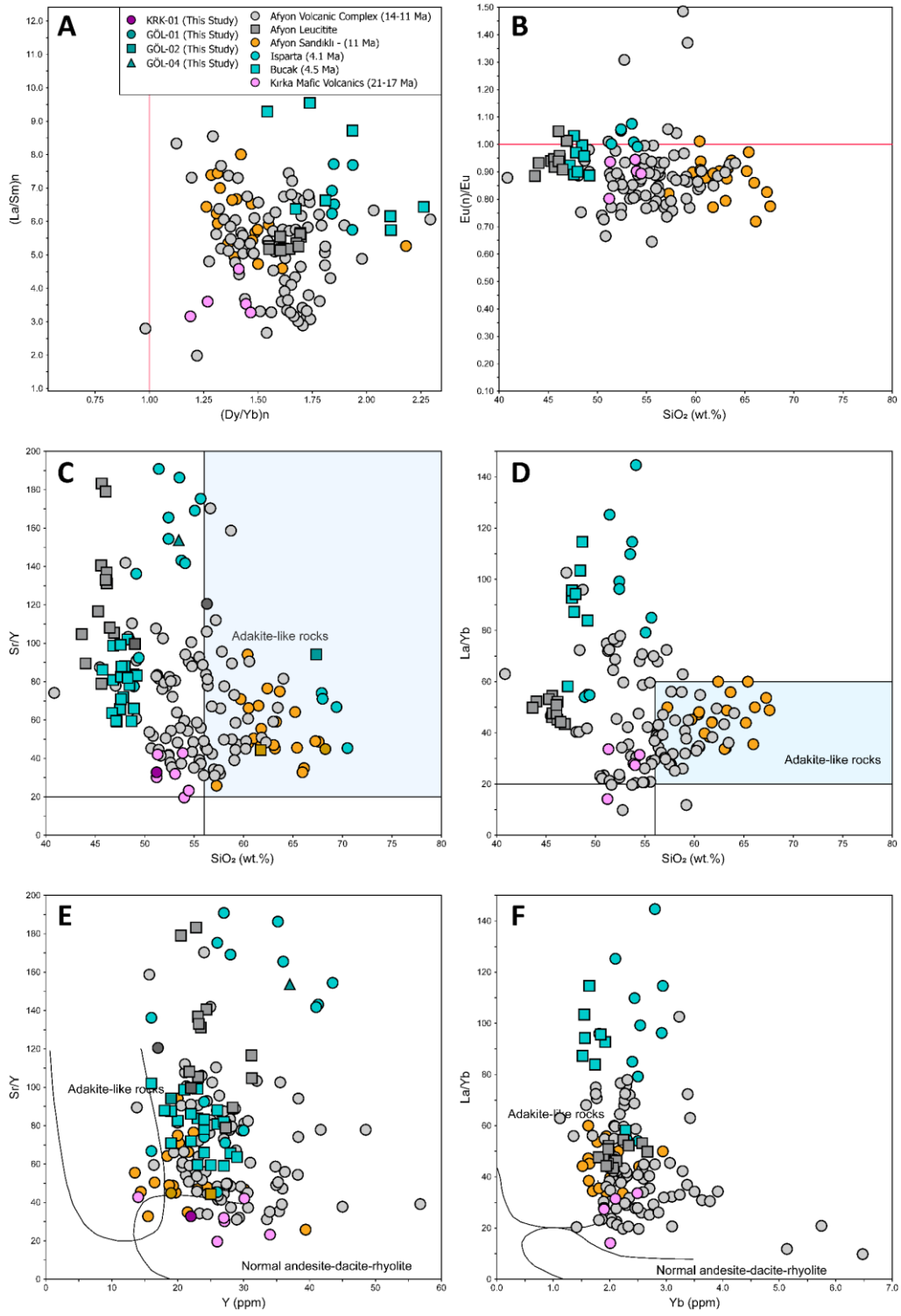


Figure 4.16. Selected trace element discrimination diagrams for igneous lithologies from the Kırka-Afyon-Isparta region: (A) $(La/Sm)_N$ vs. $(Dy/Yb)_N$, (B) Eu/Eu* vs. SiO_2, (C) Sr/Y vs. SiO_2, (D) La/Yb vs. SiO2, (E) Sr/Y vs. Y, and (F) La/Yb vs. Yb. Normalization values are from Sun and McDonough (1989).

Overall, the trace-element ratio parameters used to assess magmatic fertility partially succeed in distinguishing the Afyon–Sandıklı prospect from the other units of the Afyon Volcanic Complex, highlighting its closer geochemical affinity to fertile, adakite-like magmatic systems.

4.2.4 Uşak District

The Uşak region, mostly because of the presence of the Kışladağ porphyry Au deposit, is among the most extensively studied magmatic provinces in western Anatolia. In addition to numerous surface samples, a substantial number of drill core specimens have been analyzed for whole-rock geochemistry, enabling a detailed characterization of the local magmatic evolution. Within the scope of this study, new whole-rock geochemical data were generated only for two samples (SYC-03 and SYC-05) from the Sayacık porphyry Au prospect, a locality not previously documented in the literature.

The earliest magmatic products of the region are represented by the Payamtepe volcanic rocks, which plot mainly within the alkaline field on the TAS diagram, spanning from basaltic trachyandesite to trachyte/trachydacite (Figure 4.17A). These alkaline lavas are dominantly shoshonitic in composition (Figure 4.17B), generally metaluminous but with a minor trend toward the peraluminous field (Figure 4.17C).

In contrast, lavas from the Beydağı volcanic sequence display a much broader compositional spread in TAS space, encompassing both sub-alkaline and alkaline members and ranging from andesite to dacite (Figure 4.17A). Chemically, they straddle the high-K calc-alkaline to shoshonitic fields (Figure 4.17B) and exhibit both metaluminous and peraluminous characteristics (Figure 4.17C).

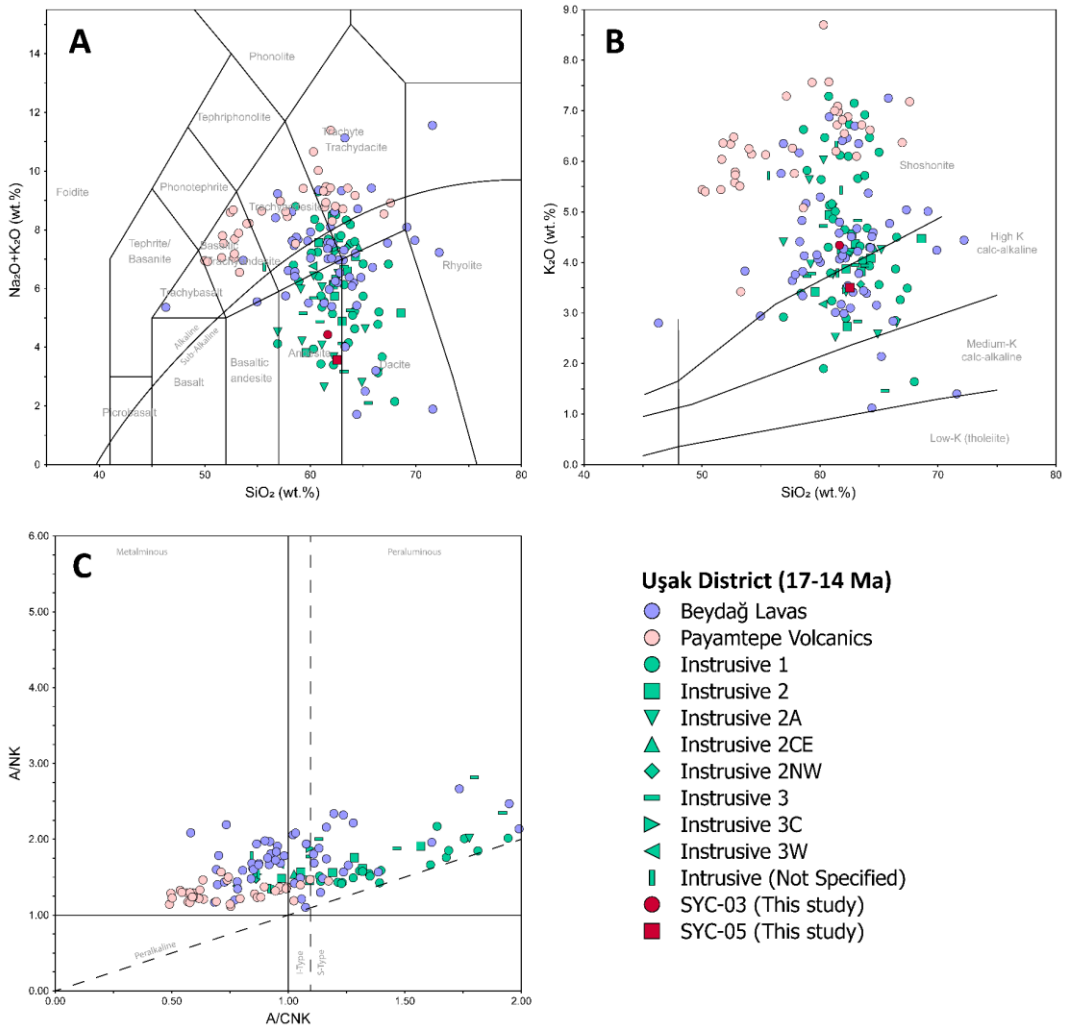


Figure 4.17. Classification diagrams based on whole-rock geochemical data for Uşak. (A) TAS diagram (Le Maitre et al., 1989), with the alkaline/subalkaline division after Irvine and Baragar (1971). (B) K_2O vs. SiO_2 diagram (Peccerillo and Taylor, 1976). (C) Alumina Saturation Index (Shand, 1927). Data from Innocenti et al. (2005); Ersoy et al. (2010); Karaoğlu et al. (2010); Prelevic et al. (2012); Baker et al. (2016); Kuşcu et al. (2019); Rabayrol and Hart (2021).

The intrusive units forming the host rocks to the Kışladağ porphyry Au mineralization consist of three main monzonitic phases, which in TAS classification plot between monzonite and diorite (Figure 4.17A). However, given that these rocks have been significantly overprinted by hydrothermal alteration (resulting in elevated LOI values) their classification of Winchester and Floyd (1977) has been prioritized (Figure 4.1). This approach places most samples in the trachyandesite field,

justifying the term “monzonite” in the context of this study (Fig. 4.1). These intrusions are dominantly high-K calc-alkaline to shoshonitic in affinity, though a few samples extend into the medium-K calc-alkaline range (Fig. 4.17B). Almost all Kışladağ samples are peraluminous (Fig. 4.17C).

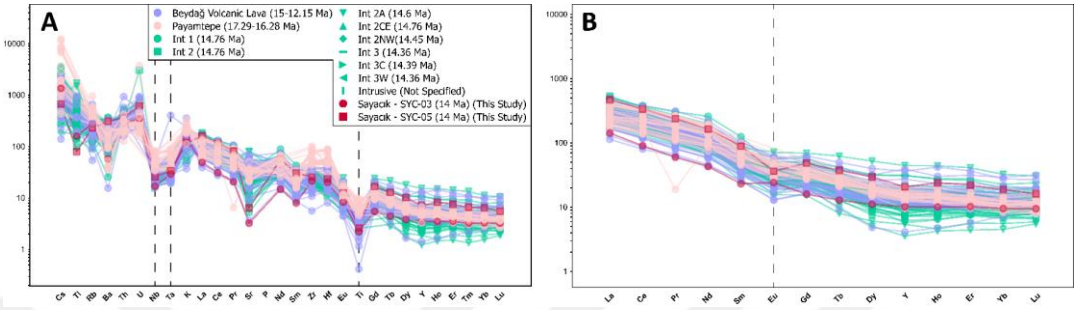


Figure 4.18. A) Primitive mantle-normalized trace element and B) chondrite-normalized REE diagrams for igneous rocks for Kışladağ and Sayacık porphyry systems and the surrounding volcanic rocks in Uşak. Normalization values are from Sun and McDonough (1989).

Two whole-rock analyses were also performed on intrusive rocks from the Sayacık porphyry Au prospect, which share petrological similarities with those of Kışladağ. These likewise fall within the high-K calc-alkaline to shoshonitic monzonite field (Figure 4.17).

Primitive mantle–normalized multi-element diagrams for the Uşak dataset Figure 4.18A) reveal a pronounced negative Nb–Ta anomaly across all samples, consistent with a subduction-related signature. In most suites (except the Payamtepe volcanics) this is accompanied by a negative Ti anomaly, which is much weaker in the alkaline lavas. The Payamtepe suite is further distinguished by prominent positive Zr and Hf anomalies. In the Kışladağ samples, a wide scatter in the heavy rare earth element (HREE) region suggests strong fractional crystallization effects (Figure 4.18B). Additionally, the SYC-03 sample from Sayacık displays a distinct positive Eu anomaly in its chondrite-normalized REE profile (Figure 4.18B), an uncommon feature among the analyzed rocks.

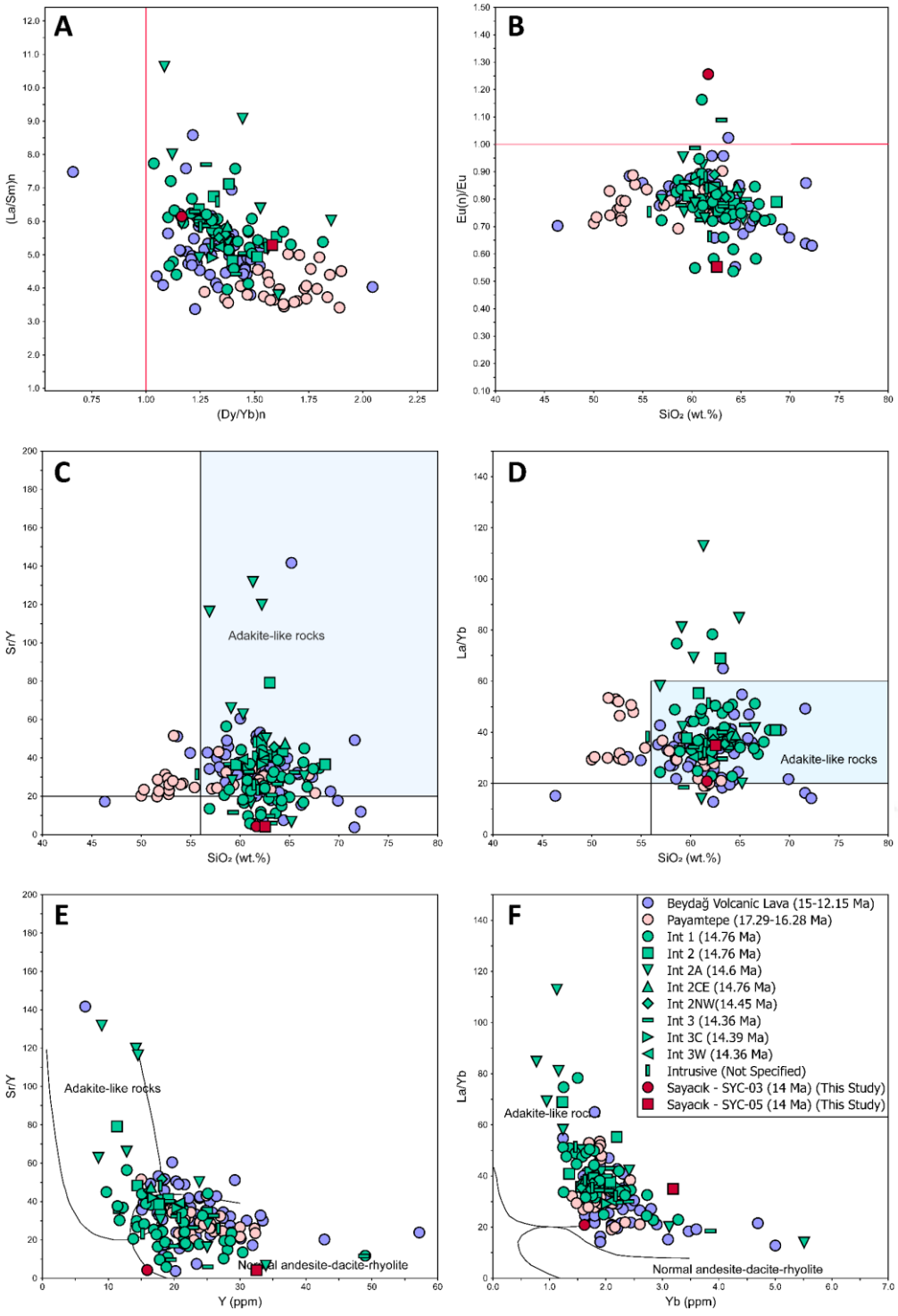


Figure 4.19. Selected trace element discrimination diagrams for igneous lithologies from the Uşak district: (A) $(La/Sm)_N$ vs. $(Dy/Yb)_N$, (B) Eu/Eu* vs. SiO_2, (C) Sr/Y vs. SiO_2, (D) La/Yb vs. SiO_2, (E) Sr/Y vs. Y, and (F) La/Yb vs. Yb. Normalization values are from Sun and McDonough (1989).

On the Dy/Yb versus La/Sm diagram, the Payamtepe alkaline volcanics plot with relatively high Dy/Yb and low La/Sm ratios, clearly separating them from the other suites (Figure 4.19A). Both Kışladağ and Sayacık intrusions exhibit a negative correlation between La/Sm and Dy/Yb (Figure 4.19A). The Eu/Eu* versus SiO_2 diagram indicates that the Kışladağ samples have a decreasing Eu/Eu* trend during magmatic evolution which can be attributed to plagioclase fractionation (Figure 4.19B).

In Sayacık samples, Sr/Y ratios are notably low (Figure 4.19C–E), most likely due to hydrothermal alteration and Sr leaching. By contrast, Kışladağ samples plot within the adakite-like field on both Sr/Y–SiO_2 and La/Yb–SiO_2 diagrams (Figure 4.19C–D), and their distribution on La/Yb versus Yb diagram (Figure 4.19F) reinforce this adakite-like affinity.

Overall, the integration of field, petrographic, and geochemical evidence underscores the petrogenetic similarities between Kışladağ and Sayacık intrusions, while also highlighting distinct geochemical signatures in the older Payamtepe alkaline suite. These differences bear directly on interpretations of magma source characteristics, fractionation processes, and the potential for porphyry-type Au mineralization in the Uşak region.

4.2.5 Manisa District

All samples from the Salihli and Turgutlu areas exhibit tholeiitic affinity and are represented by dacitic to rhyolitic compositions (Figure 4.20A). The Salihli suite is predominantly medium-K calc-alkaline, whereas the Turgutlu suite extends from high-K calc-alkaline into the shoshonitic field (Figure 4.20B). In terms of alumina saturation, Salihli plutonic rocks plot within the peraluminous field and display an I-type granitoid signature, while samples from the Turgutlu pluton extend toward the S-type granitoid field (Figure 4.20C).

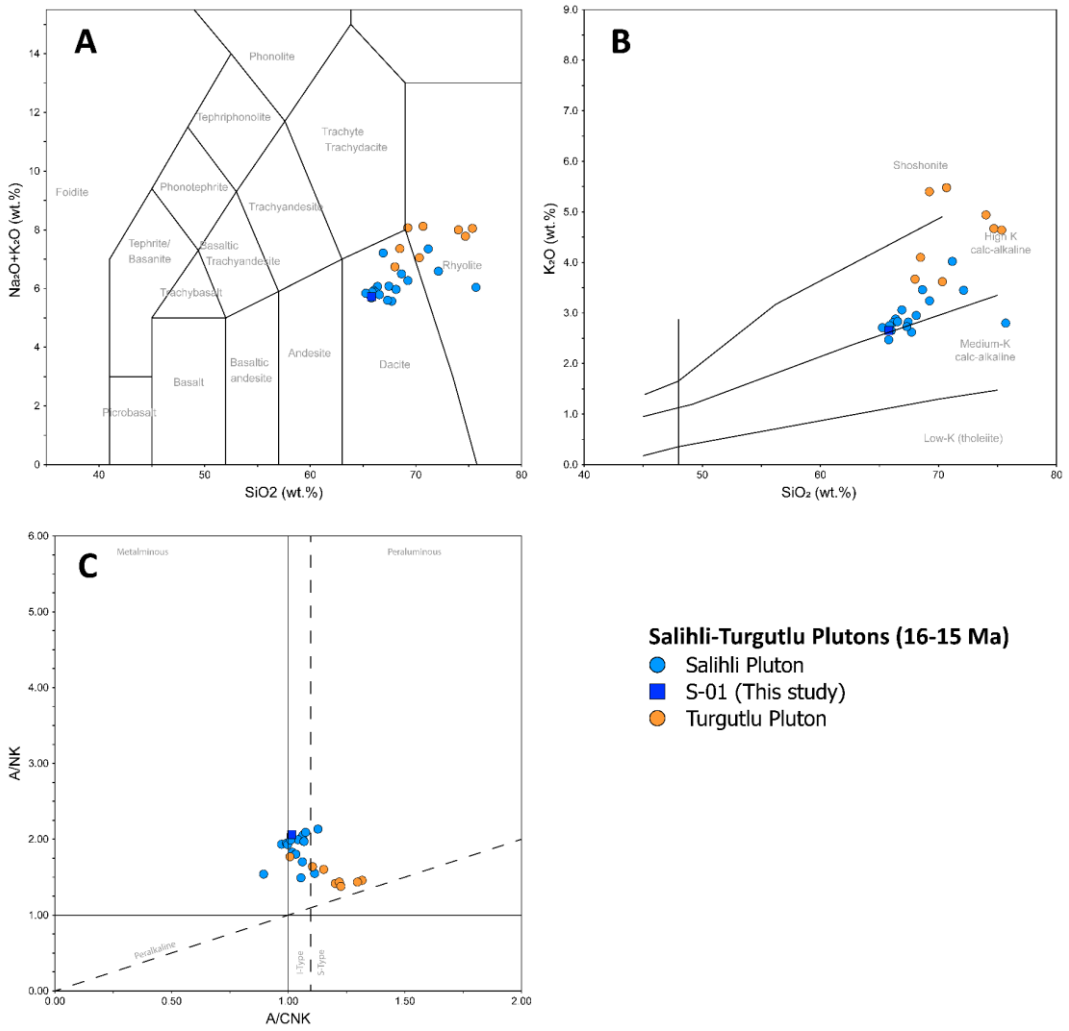


Figure 4.20. Classification diagrams based on whole-rock geochemical data for Salihli granitoid. (A) Total Alkali–SiO_2 (TAS) diagram (Le Maitre et al., 1989), with the alkaline/subalkaline division after Irvine and Baragar (1971). (B) K_2O vs. SiO_2 diagram (Peccerillo and Taylor, 1976). (C) Alumina Saturation Index (Shand, 1927).

In the primitive mantle–normalized multi-element diagrams, only samples from the Salihli pluton were included, revealing pronounced negative Nb, Ta, and Ti anomalies which are typical of subduction-related magmatism (Figure 4.21A). Chondrite-normalized REE patterns display clear light rare earth element (LREE) enrichment, notably without a strong negative Eu anomaly, a feature that may indicate limited plagioclase fractionation or partial suppression of Eu depletion during magmatic evolution (Figure 4.21B).

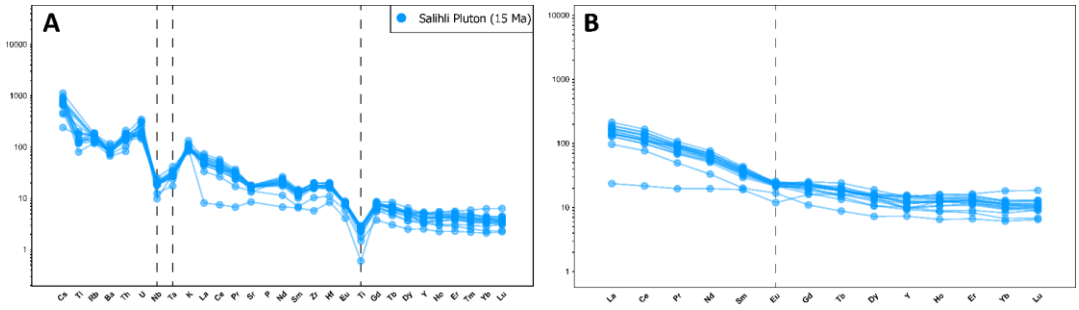


Figure 4.21. A) Primitive mantle- and B) chondrite-normalized multi-element diagrams for Salihli Pluton. Normalization values are from Sun and McDonough (1989).

On the La/Sm versus Dy/Yb diagram, Salihli samples are characterized by low La/Sm and moderate Dy/Yb ratios (Figure 4.22A). In Eu/Eu* versus SiO_2 space, these samples show both increasing and decreasing Eu/Eu* trends with rising silica content; however, aside from a few outliers, most values cluster within a relatively narrow range of 0.70–0.90 (Figure 4.22B). The Turgutlu samples, in contrast, display a broader spread in Eu/Eu*, making it more difficult to discern a consistent evolutionary trend.

Although both suites are generally represented by low Sr/Y and La/Yb ratios—features commonly associated with non-adakitic magmatism—sporadic increases in La/Yb are observed, particularly in the Salihli samples, suggesting localized variations in magma source characteristics or crystal fractionation processes (Figure 4.22).

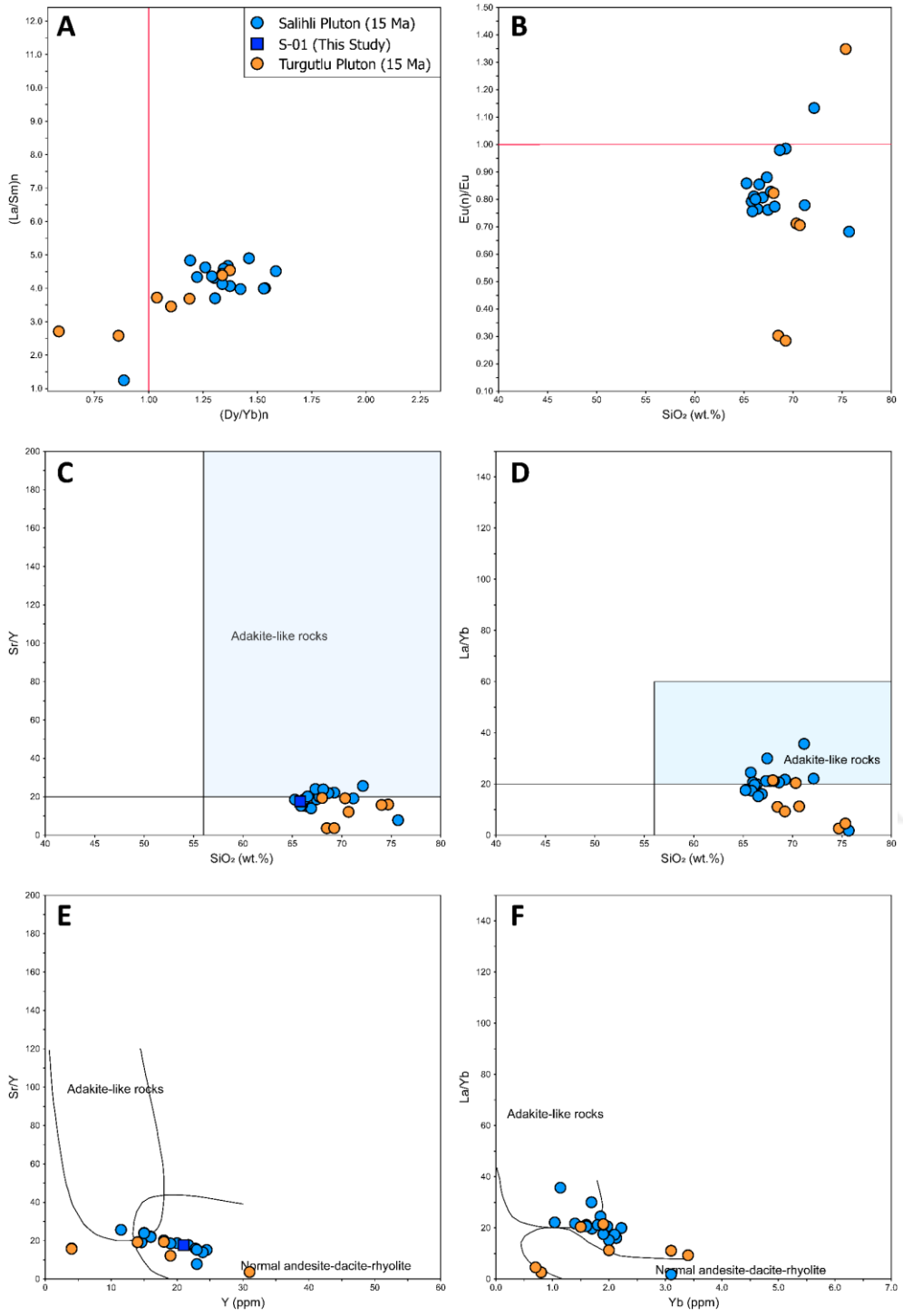


Figure 4.22. Trace element discrimination diagrams for the Salihli and Turgutlu plutons showing parameters relevant to porphyry fertility assessment: (A) $(La/Sm)_N$ vs. $(Dy/Yb)_N$, (B) Eu/Eu* vs. SiO_2, (C) Sr/Y vs. SiO_2, (D) La/Yb vs. SiO_2, (E) Sr/Y vs. Y, and (F) La/Yb vs. Yb. Subscript *N* indicates chondrite normalization (Sun and McDonough, 1989).

4.2.6 Bodrum Volcanic Complex

Within the scope of this thesis, in addition to available literature data, whole-rock geochemical analyses were carried out on two trachyandesitic samples from the Bodrum Volcanic Complex (BVC; BDR-02-2 and BDR-03). The BVC was emplaced between 10 and 7.9 Ma, and predominantly comprises alkalic volcanic rocks of basaltic trachyandesite, trachyandesite, and trachyte/trachydacite composition (Figure 4.23A). These rocks are dominantly metaluminous in character (Figure 4.23B) and display high K_2O contents, placing them within the shoshonitic compositional field (Figure 4.23C).

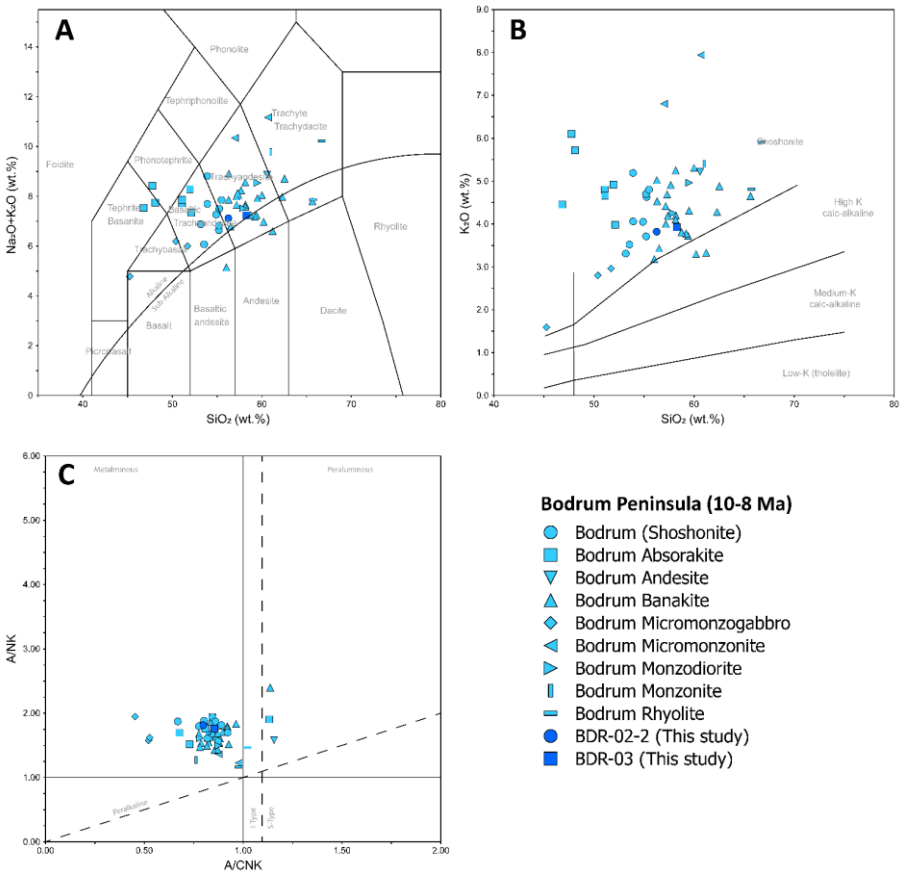


Figure 4.23. Classification diagrams based on whole-rock geochemical data for Bodrum Peninsula. (A) TAS diagram (Le Maitre et al., 1989), with the alkaline/subalkaline division after Irvine and Baragar (1971). (B) K_2O vs. SiO_2 diagram (Peccerillo and Taylor, 1976). (C) Alumina Saturation Index (Shand, 1927). Data from Çubukçu et al. (2021); Rabayrol and Hart (2021).

Multi-element variation diagrams reveal that all Bodrum samples exhibit pronounced negative anomalies in Nb, Ta, and Ti—features typically interpreted as subduction-related geochemical signatures (Figure 4.24A). Chondrite-normalized rare earth element (REE) patterns show enrichment in light REEs (LREEs) coupled with a relatively flat trend toward heavy REEs (HREEs). Notably, no significant negative Eu anomaly is observed (Figure 4.24B).

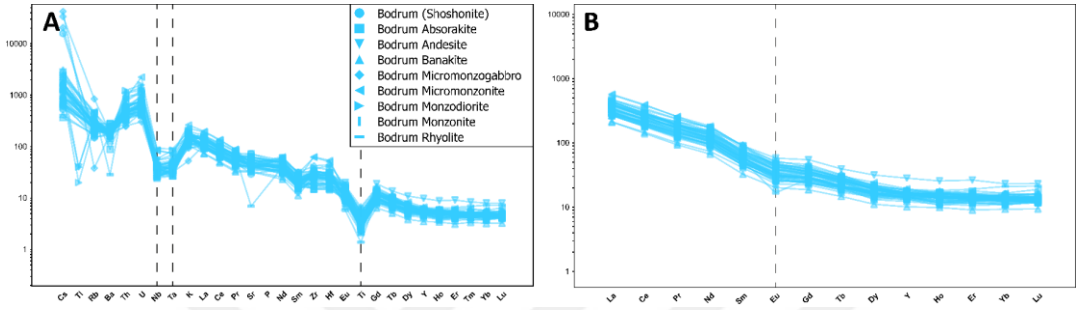


Figure 4.24. A) Primitive mantle- and B) chondrite-normalized multi-element diagrams for Bodrum Volcanic Complex. Normalization values are from Sun and McDonough (1989).

In trace-element ratio plots, an increase in Dy/Yb is accompanied by a decrease in La/Sm (Figure 4.25A). The Eu/Eu* versus SiO_2 diagram shows an essentially flat trend with increasing silica content (Figure 4.25B), consistent with the absence of a negative Eu anomaly in the chondrite-normalized REE diagram. This relationship suggests that plagioclase fractionation was suppressed during magma evolution.

Previous studies in the Bodrum region (Çubukçu et al., 2022) identified several lithological units, including shoshonite, absarokite, and micromonzogabbro, which plot outside the adakite-like field in both SiO_2 versus Sr/Y and La/Yb diagrams. In contrast, other units (such as banakite, micromonzonite, andesite, trachyandesite, rhyolite, and monzodiorite) show compositional trends toward the adakite-like field (Figure 4.25C-D). Examination of Sr/Y versus Y (Figure 4.25E) and La/Yb versus Yb (Figure 4.25F) diagrams indicates that nearly all samples plot within the typical andesite–dacite–rhyolite field in the Sr/Y–Y space, whereas in La/Yb–Yb space they

exhibit elevated La/Yb ratios that place them within the adakite-like compositional field.

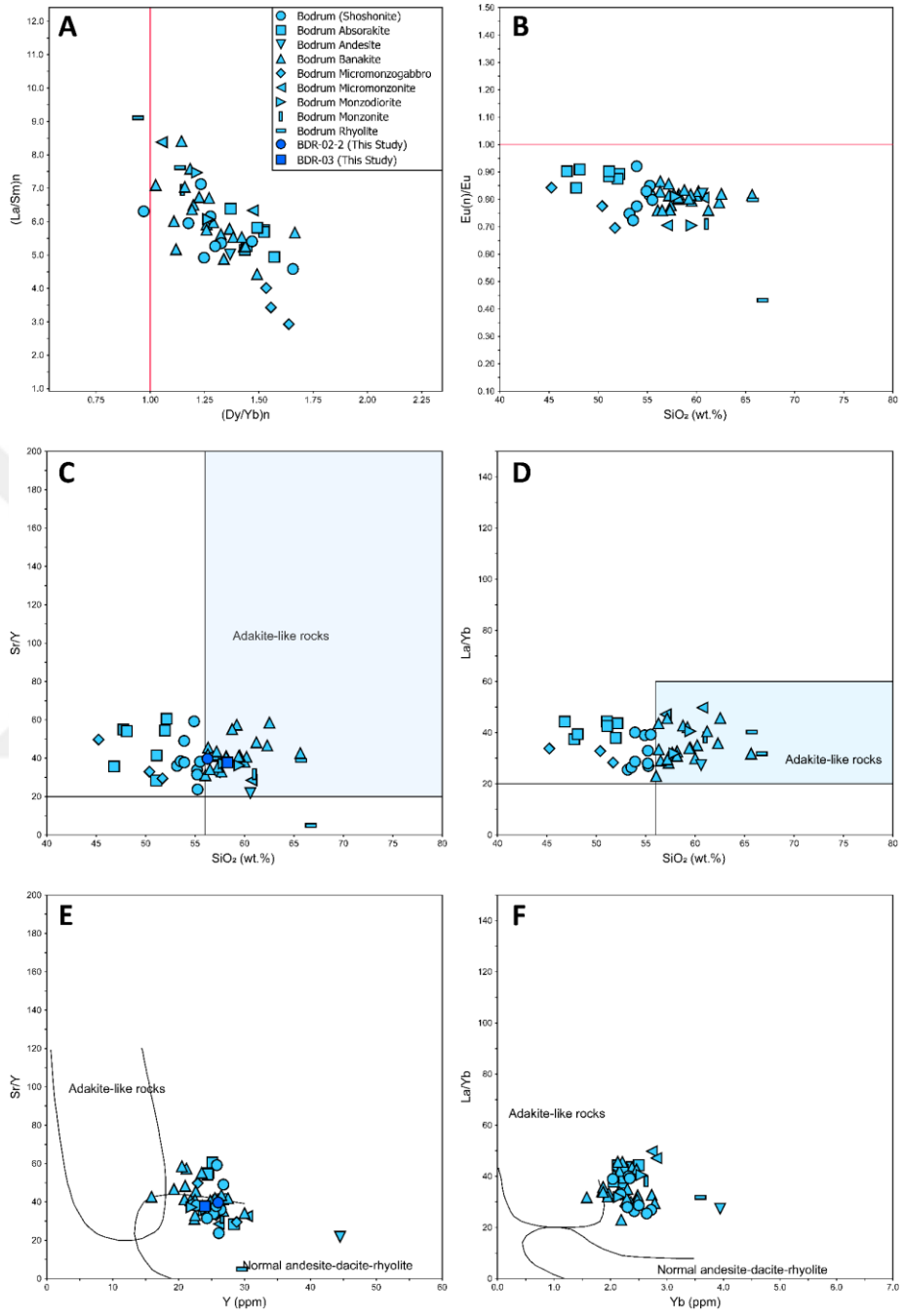


Figure 4.25. Selected trace element discrimination diagrams for igneous lithologies from the BVC: (A) $(La/Sm)_N$ vs. $(Dy/Yb)_N$, (B) Eu/Eu* vs. SiO_2, (C) Sr/Y vs. SiO_2 , (D) La/Yb vs. SiO_2, (E) Sr/Y vs. Y, and (F) La/Yb vs. Yb. Normalization values are from Sun and McDonough (1989).

CHAPTER 5

INDICATOR MINERAL ANALYSES RESULTS

5.1 Mineral Geochemistry and Isotopic Analyses

5.1.1 Zircon Analyses

Zircon grains were extracted from both surface and drill core samples using conventional mineral separation techniques. The separated grains were mounted onto epoxy and glass discs, after which cathodoluminescence (CL) imaging was conducted to facilitate precise spot selection for subsequent analyses. Both stereomicroscope observations and CL imaging were employed to examine zircon morphology and to characterize specific internal structures, allowing the selection of inclusion- and fracture-free mineral domains for analysis. Special care was taken to avoid zones containing mineral inclusions that could compromise isotopic integrity.

Zircons were successfully recovered from nearly all investigated localities, allowing U–Pb zircon dating for the majority of samples. Wherever possible, a minimum of 50 zircon grains per sample were mounted and in cases where fewer grains were available, all recoverable crystals were included to maximize analytical coverage. Samples that yielded insufficient zircon quantities were nonetheless mounted and analyzed to obtain any possible age constraints. U-Pb zircon dating was not undertaken in samples from Kışladağ since detailed zircon U–Pb chronologies of intrusions from this suite had already been established previously (Paolillo et al., 2022).

All CL images for the analyzed zircon grains are presented in the Appedix A.

Prior to constructing concordia diagrams, the internal consistency of ages derived from individual $^{206}Pb/^{238}U$ and $^{207}Pb/^{235}U$ ratios was assessed. Data points exhibiting more than 95% concordance between these two isotope systems were included in concordia plots. However, for weighted mean $^{206}Pb/^{238}U$ ages and samples without sufficient analysis points, a slightly less concordance of 90% was adopted. Measurements obtained from inherited zircon cores, identified through CL imaging and significantly older than the host magmatic population, were systematically excluded from age calculations to avoid biasing the magmatic crystallization ages.

5.1.1.1 Zircon Morphologies in Western Anatolian Samples

The CL images revealed distinct morphological and internal textural features among zircon grains extracted from samples from different localities. Zircons grains of samples (AVC-01 and AVC-02) from the AVC typically exhibit slender, elongate forms with aspect ratios approaching 1:8 and these also lack internal zoning. In contrast, zircons from the Afyon–Sandıklı sector display significant inter-sample variability. While most grains have aspect ratios around 1:4, some exhibit chunkier morphologies with aspect ratios of 1:2. These crystals frequently consist of homogeneous cores surrounded by oscillatory-zoned rims and contain abundant mineral inclusions. Zircons from sample AVC-AS-01 are also distinguished by their heavily fractured nature. From basaltic samples collected from Kırka, only a single zircon grain was recovered. This zircon grain has a dark, homogeneous core encircled by zoned rims and it also contains minor inclusions. Zircons extracted from sample Göl-02 from Isparta have generally 1:1 to 1:2 ratios with mostly homogenous appearance with occasional oscillatory zoned rims. Those without homogenous cores have complex zonation patterns.

Samples from the Biga Peninsula, including zircons from Balya, Çatalçam, and the upper volcanic sequences of the Hallaçlar area, display broadly similar morphologies

and internal textures. These grains are generally euhedral, with aspect ratios of approximately 1:4 and grain sizes ranging from 0.5 mm to ~200 μm. Mineral inclusions are relatively sparse. Turplu zircons extracted from sample TRD-17 appear to be highly fractured and include abundant inclusions. Those grains are mostly 300 to 500 microns in size with 1:4 to rare 1:8 ratios. They display complexly-zoned cores with oscillatory-zoned rims. Sarıalan zircons on the contrary, generally have sizes <250 microns. However, some grains may reach up to 400 microns length. Most of the zircon grains appear to have oscillatory zonation. In sample SAR-03, black cores surrounded by oscillatory zoned rims are also present in addition to typical oscillatory zoned grains.

In the Bodrum district, a variety of zircon morphologies was observed. Zircons from sample BDR-04-1 lack internal zoning and these generally display aspect ratios of 1:4. In contrast, zircons from samples BDR-04-2, BDR-06, BDR-08, BDR-09, and especially BDR-10 often show more elongate forms (aspect ratios of up to 1:8) with complex internal zoning and homogeneous cores. Sample BDR-07 presents an exception as zircons from this sample are chunkier grains (1:2), compositional zoning is relatively simpler, and mineral inclusions are more abundant.

Zircons extracted from the Salihli Granite are texturally consistent between the two analyzed samples, exhibiting aspect ratios of 1:2 to 1:4 with prominent oscillatory zoning and partially homogeneous cores. CL images frequently show bright central domains relative to their rims, and ages obtained from these zones are markedly older (see following section), indicating inherited cores.

In the Simav–Sındırgı sector, zircon morphologies are relatively uniform aside from variations in elongation. Zircons from the Eğrigöz samples are predominantly slender (1:8 aspect ratios), whereas those from Sındırgı and Pınarbaşı more commonly exhibit 1:4 to 1:2 proportions. Most grains show homogeneous interiors except where inherited cores are present. Zircon crystals collected from Baklan

granitoid samples have slender prismatic character (having 1:4 to 1:8 ratios, although 1:2 ratio zircons are also present) with typical oscillatory zonation. Additionally, rare homogenous or inherited cored zircons are present.

Zircons from the Sayacık Au porphyry prospect in the Uşak region are characteristically small (<500 μm). Most display aspect ratios of 1:2 or 1:4, though rare grains approach 1:8 aspect ratios. Where present, CL imaging shows dark, homogeneous cores surrounded by oscillatory zoning unless inherited cores dominate.

5.1.1.2 Zircon Morphologies in Central Tauride Samples

In the Central Taurides segment, zircons show no striking morphological differences from the Western Anatolian populations. Samples from İnlice and the nearby Damlapınar and Çukurağıl prospects span a range of aspect ratios. Damlapınar and Çukurağıl zircons predominantly exhibit 1:2 to 1:4 elongations (rarely 1:8), whereas İnlice samples more frequently contain slender 1:4 to 1:8 grains. Zoning is common in İnlice zircons, although some unzoned, highly elongate grains (1:8) are also present. Zircons separated from Sille-2 sample belong to the Sulutaş Volcanic Suite appears slightly different than the rest of the Konya samples with complex internal zonations, inherited cores, as well as black homogenous cores. Zircons mostly have the slender prismatic character with 1:4 to 1:8 ratios. Samples from Ketenli and Karacaören exhibit similar patterns, with most zircons showing aspect ratios near 1:4 and displaying intricate oscillatory zoning.

An exception within the Konya–Niğde corridor is the Yeşilyurt sample from Karacadağ Caldera, whose zircons have unusually equant forms (1:1 to 1:2) and oscillatory zoning even in their cores, unlike the homogeneous interiors seen in most other samples. Drillcore samples from Melendiz Stratovolcano (496762 and 496973)

have similar zircon morphologies and internal zonation patterns with 1:2 to 1:4 (rarely 1:8 elongated crystals) aspect ratios with oscillatory zonations although there are homogenous cores (gray and black colored) with zoned rimmed zircons are also present.

5.1.1.3 U-Pb Geochronology

LA-ICP-MS U–Pb dating was performed on zircons from a wide range of localities across Western Anatolia and the Central Taurides including localities that are known with significant mineralization porphyry (or associated epithermal/skarn mineralization), localities hosting apparently small-scale mineralization, and those that are known to be entirely barren of magmatic-hydrothermal ores.

5.1.1.3.1 Central Taurides

A total of 17 samples were dated from the Central Taurides sector of the Late Cenozoic magmatic belt. Summary results of zircon U-Pb dating are presented in Table 5.1, and detailed concordia as well as mean weighted ages are shown in Figure 5.1 and 5.2.

In the Central Taurides sector, U–Pb zircon dating was carried out on seventeen samples; twelve from İnlice and nearby prospects within the KVC and five from the Niğde area. Nearly all andesitic volcanic volcanic samples from the İnlice Au open pit, deep drill cores, and the adjacent Damlapınar and Çukurağıl prospects yielded sufficient zircon populations for analysis. The Çukurağıl sample (CKRA-01) displayed significant common Pb contamination; therefore, instead of an isochron age, the Tera–Wasserburg regression was preferred during calculation of the crystallization age. This yielded a concordia age of 10.70 ± 0.01 Ma and a weighted mean $^{206}Pb/^{238}U$ age of 10.69 ± 0.05 Ma (Figure 5.1).

Table 5.1. Summary table of U-Pb zircon ages of Central Tauride samples

District	Field	ID	Concordia Age		Weighted Mean $^{206}Pb/^{238}U$ Age	
			Age (Ma)	Error (2s)	Age (Ma)	Error (2s)
Konya	Çukurağıl	CKRA-01	10.699	0.011	10.689	0.054
Konya	Damlapınar	DMLP-01	10.241	0.071	10.182	0.075
Konya	Damlapınar	DMLP-02	10.310	0.110	10.360	0.130
Konya	İnlice	INL-201-01	8.968	0.062	8.865	0.066
Konya	İnlice	INL-201-02	8.961	0.040	8.913	0.044
Konya	İnlice	INL-201-03	8.965	0.089	8.900	0.100
Konya	İnlice	INL-D-01	9.035	0.061	9.102	0.068
Konya	İnlice	INL-OP-01	8.997	0.065	8.890	0.061
Konya	İnlice	INL-OP-02	9.078	0.060	9.104	0.630
Konya	SVS	Sille-02	12.854	0.039	12.796	0.041
Konya	Karacaören	KRC-01	4.772	0.048	4.788	0.044
Konya	Ketenli	KTN-01	3.013	0.028	3.015	0.027
Niğde	Melendiz	496918	1.767	0.085	1.768	0.085
Niğde	Melendiz	496762	1.502	0.074	1.501	0.074
Niğde	Çömlekçi	CML-01	1.938	0.028	1.925	0.290
Niğde	Süleymanpınarı	SLP-01	3.948	0.049	3.949	0.045
Niğde	Yeşilyurt	YSL-01	4.770	0.160	4.730	0.120

Among the two samples from the Damlapınar prospect the first sample (DMLP-01) produced a concordia age of 10.24 ± 0.07 Ma and a weighted mean $^{206}Pb/^{238}U$ age of 10.18 ± 0.07 Ma based on twenty-six concordant analyses (Fig. 7.15). The second sample (DMLP-02) yielded a concordia age of 10.31 ± 0.11 Ma and a weighted mean age of 10.36 ± 0.13 Ma from nine concordant zircon analyses (Figure 5.1).

For the İnlice drill core samples (INL-201-01, INL-201-02, INL-201-03), a total of 14, 46, and 13 concordant zircon analyses were obtained, respectively. The resulting concordia ages are 8.97 ± 0.06 Ma, 8.96 ± 0.04 Ma, and 8.96 ± 0.09 Ma, while the corresponding weighted mean $^{206}Pb/^{238}U$ ages are 8.86 ± 0.07 Ma, 8.91 ± 0.04 Ma, and 8.90 ± 0.10 Ma (Figure 5.1). An andesitic dyke (INL-D-01) that cross-cutting the altered and mineralized volcanic sequence within the open pit yielded seventeen

concordant analyses, producing a concordia age of 9.04 ± 0.06 Ma and a weighted mean $^{206}Pb/^{238}U$ age of 9.10 ± 0.07 Ma (Figure 5.1). Two additional samples from the open pit (INL-OP-01 and INL-OP-02) yielded twenty-two and twenty concordant zircon analyses, with concordia ages of 8.99 ± 0.06 Ma and 9.08 ± 0.06 Ma, and weighted mean $^{206}Pb/^{238}U$ ages of 8.89 ± 0.06 Ma and 9.10 ± 0.06 Ma, respectively (Figure 5.1).

A sample from the Ketenli area (KTN-01) yielded a weighted mean $^{206}Pb/^{238}U$ age of 3.02 ± 0.03 Ma (Figure 5.1). Because of its very young age, there might be possibility of significant common Pb effect. Therefore, the Tera–Wasserburg age of 3.01 ± 0.03 Ma was adopted as the preferred crystallization age instead of the isochron age (Figure 5.1).

An andesite porphyry from the Konya Karacaören area (KRC-01) yielded twenty-seven concordant analyses, producing a concordia age of 4.77 ± 0.05 Ma and a weighted mean $^{206}Pb/^{238}U$ age of 4.79 ± 0.04 Ma (Figure 5.1).

Only one of the two samples collected from the SVS forming the northern part of the KVC yielded zircons. Twenty-six concordant analyses from this andesitic volcanic unit (sample Sille-02) produced concordia age of 12.854± 0.039 Ma, and weighted mean $^{206}Pb/^{238}U$ age of 12.796± 0.041 Ma (Figure 5.1).

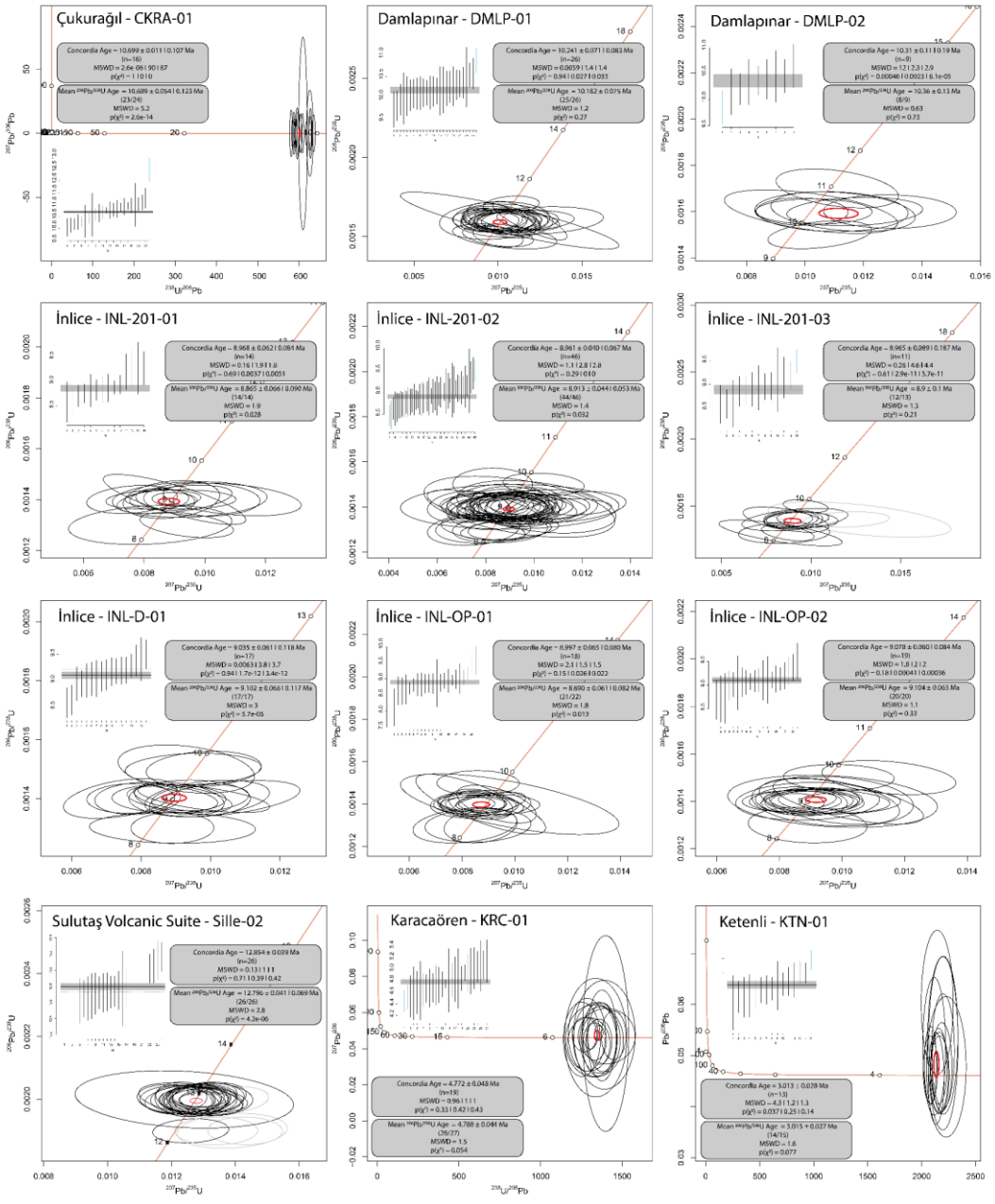


Figure 5.1. Concordia and weighted mean age diagrams of U-Pb dated zircons from KVC.

Further east within the Central Tauride sector, U–Pb dating was performed on five volcanic rock samples collected from areas with epithermal alteration with or without Au mineralization. The Melendiz Dağ volcanic field near Niğde, like Ketenli, represents a young magmatic system; thus, preferred ages were again derived from Tera–Wasserburg plots rather than standard isochrons. Dacitic porphyry from the Çömlekçi prospect (CML-01) yielded twenty-two concordant analyses and produced a concordia age of 1.94 ± 0.03 Ma with a weighted mean $^{206}Pb/^{238}U$ age of 1.93 ± 0.29 Ma (Figure 5.2). The youngest samples from the Melendiz Stratovolcano were obtained from two drill-core samples (496918 and 496762) from the Çömlekçi prospect. These samples yielded concordia ages of 1.77 ± 0.09 Ma and 1.50 ± 0.07 Ma, and weighted mean $^{206}Pb/^{238}U$ ages of 1.77 ± 0.09 Ma and 1.50 ± 0.07 Ma respectively (Figure 5.2). Another altered andesitic porphyry from the Süleymanpınarı prospect (SLP-01) in Melendiz, returned concordia and weighted mean ages of 3.95 ± 0.05 Ma and 3.95 ± 0.04 Ma from twenty-four concordant analyses, respectively (Figure 5.2).

The final sample from this sector, an andesite porphyry from the Karacadağ caldera east of Yeşilyurt (YSL-01), yielded a concordia age of 4.77 ± 0.16 Ma and a weighted mean $^{206}Pb/^{238}U$ age of 4.73 ± 0.12 Ma (Figure 5.2). Collectively, these results capture the Late Miocene to Pliocene evolution of the İnlice–Ketenli–Melendiz magmatic corridor, highlighting both the prolonged Miocene porphyry mineralization phase and the onset of much younger Pliocene volcanic activity in the Central Taurides.

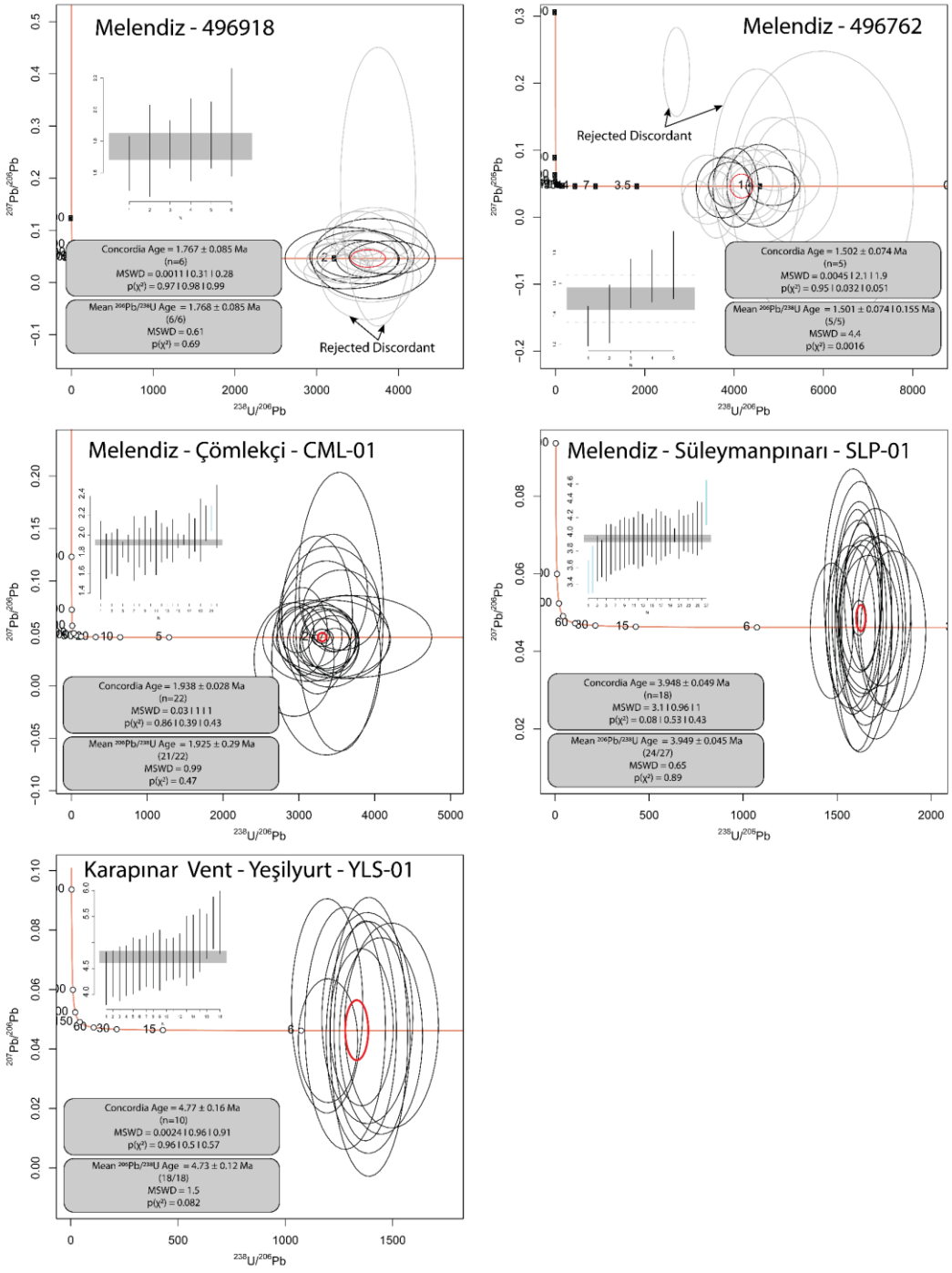


Figure 5.2. Concordia and weighted mean age diagrams of U-Pb dated zircons from prospects near Melendiz Stratovolcano and from Karacadağ caldera from the Karapınar Volcanic Vent.

5.1.1.3.2 Western Anatolia

A total of 45 samples were dated from the studied magmatic centers distributed in six different districts in the Western Anatolia sector of the Late Cenozoic magmatic belt. Summary results of zircon U-Pb dating are presented in Table 5.2, and detailed concordia as well as mean weighted ages are shown in Figure 5.3–5.8.

Table 5.2. Summary table of U-Pb zircon ages obtained from samples collected from the Western Anatolia sector.

District	Field	ID	Concordia Age		Weighted Mean $^{206}Pb/^{238}U$ Age	
			Age (Ma)	Error (2s)	Age (Ma)	Error (2s)
Biga	Balya	BLY-01	25.480	0.110	25.560	0.095
Biga	Balya	BLY-02	25.659	0.108	25.535	0.088
Biga	Hallaçlar	374869	22.740	0.110	22.720	0.120
Biga	Hallaçlar	374857	22.873	0.140	22.898	0.093
Biga	Hallaçlar	374865	23.290	0.210	23.180	0.230
Biga	Turplu	TRD-17	22.120	0.120	22.140	0.130
Biga	Sarıalan	SAR-01	22.200	0.110	22.160	0.120
Biga	Sarıalan	SAR-03	22.830	0.110	22.780	0.120
Biga	Sarıalan	SAR-04	22.240	0.160	22.320	0.170
Biga	Çatalçam	CTL-01	19.830	0.140	19.820	0.130
Biga	Çatalçam	CTL-02	20.056	0.092	20.050	0.085
Simav	Sındırgı (Kızıltepe)	SIN-01	20.100	0.140	19.570	0.096
Simav	Sındırgı (Kızıltepe)	SIN-02	19.844	0.144	19.880	0.080
Simav	Sındırgı (Kızıltepe)	SIN-04	19.890	0.140	19.890	0.140
Simav	Eğrigöz	EGR-01	19.486	0.140	19.468	0.095
Simav	Eğrigöz	EGR-02	19.072	0.071	19.069	0.071
Simav	Eğrigöz	EGR-03	19.291	0.114	19.203	0.079
Simav	Baklan	BKL-01	18.410	0.120	18.430	0.130
Simav	Pınarbaşı	PNB-01	18.162	0.068	18.146	0.064
Simav	Pınarbaşı	PNB-02	18.160	0.130	18.100	0.110
Bodrum	Bodrum	BDR-04-1	10.720	0.120	10.700	0.120
Bodrum	Bodrum	BDR-04-2	10.400	0.120	10.600	0.100
Bodrum	Bodrum	BDR-05	10.470	0.120	10.510	0.120
Bodrum	Bodrum	BDR-06	10.217	0.072	10.233	0.076

Table. 5.2. continued

District	Field	ID	Concordia Age		Weighted Mean $^{206}Pb/^{238}U$ Age	
			Age (Ma)	Error (2s)	Age (Ma)	Error (2s)
Bodrum	Bodrum	BDR-07	8.971	0.084	8.998	0.087
Bodrum	Bodrum	BDR-08	7.734	0.068	7.899	0.072
Bodrum	Bodrum	BDR-09	8.247	0.050	8.137	0.039
Bodrum	Bodrum	BDR-10	8.778	0.075	8.778	0.075
Kırka-Afyon-Isparta	Kırka	KRK-01-2	18.560	0.180	18.430	0.180
Kırka-Afyon-Isparta	Afyon-Sandıklı	AVC-AS-01	11.680	0.130	11.704	0.071
Kırka-Afyon-Isparta	Afyon-Sandıklı	AVC-AS-02	12.020	0.150	11.990	0.150
Kırka-Afyon-Isparta	Afyon-Sandıklı	AVC-AS-03	11.590	0.130	11.430	0.110
Kırka-Afyon-Isparta	Afyon-Sandıklı	AVC-AS-04	11.595	0.096	11.451	0.079
Kırka-Afyon-Isparta	Afyon-Sandıklı	AVC-AS-05	11.590	0.110	11.480	0.110
Kırka-Afyon-Isparta	Afyon Volcanic Complex	AVC-01	11.763	0.058	11.914	0.062
Kırka-Afyon-Isparta	Afyon Volcanic Complex	AVC-02	11.780	0.220	11.690	0.220
Kırka-Afyon-Isparta	Afyon Volcanic Complex	AVC-05	11.810	0.180	11.980	0.180
Kırka-Afyon-Isparta	Isparta	GÖL-02	2.635	0.033	2.633	0.034
Uşak	Sayacık	SYC-01	13.918	0.058	13.914	0.061
Uşak	Sayacık	SYC-02	13.903	0.051	13.867	0.054
Uşak	Sayacık	SYC-03	14.270	0.110	14.200	0.100
Uşak	Sayacık	SYC-04	14.050	0.110	14.140	0.110
Uşak	Sayacık	SYC-05	14.090	0.090	14.122	0.084
Salihli-Turgutlu	Salihli	S-01	14.800	0.100	14.900	0.100
Salihli-Turgutlu	Salihli	S-02	14.780	0.079	14.825	0.068

5.1.1.3.2.1 Kırka-Afyon-Isparta Region

In the Kırka-Afyon-Isparta region, U–Pb geochronological analyses were conducted on ten samples: five are derived from the Afyon–Sandıklı (A–S) porphyry prospect, and three from the volcanic units of the AVC near Sandıklı, one from Kırka, and one sample from the young volcanic formations near Isparta (Figure 5.3).

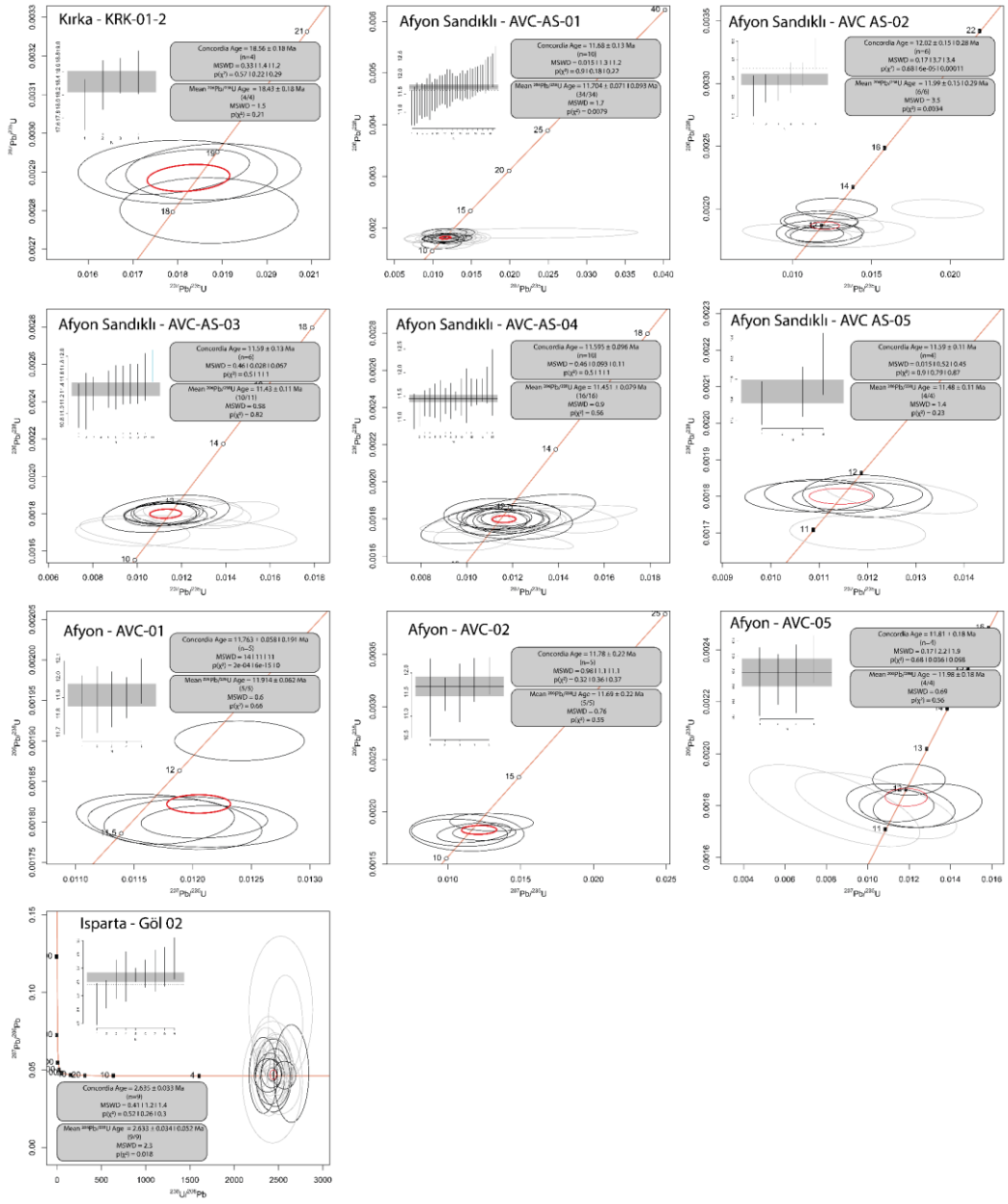


Figure 5.3. Concordia and weighted mean age diagrams of U-Pb dated zircons from Kırka-Afyon-Isparta district.

A single zircon grain was obtained from Kırka from which several analyses spots were selected to obtain a meaningful age for interpretation. Because of the absence of abundant zircon grains, the concordance limit was relieved to maximize the

amount of analysis. Four analysis spots were used to generate the concordia and weighted mean plots and the ages calculated from these plots are 18.56 ± 0.18 Ma and 18.43 ± 0.18 Ma, respectively (Figure 5.3). However, it must be noted that a single grain likely will produce similar results and may not reflect the actual age of the sample. Therefore, obtained ages are only considered to be preliminary.

Thirty-four and eleven individual zircon spots were analyzed, respectively, from the monzonitic samples from the A–S system (AVC-AS-01 and AVC-AS-02). Ten concordant analyses were included in the concordia plot, yielding an age of 11.68±0.13 Ma, while all thirty-four analyses contributed to the weighted mean $^{206}Pb/^{238}U$ age of 11.70 ± 0.07 Ma for AVC-AS-01 (Figure 5.3), and six concordant analyses were included in the concordia plot having an age of 12.02±0.15 Ma, and weighted mean $^{206}Pb/^{238}U$ age of 11.99 ± 0.15 Ma for the sample AVC-AS-02 (Figure 5.3). A trachyte sample from the same locality (AVC-AS-03) produced a concordia age of 11.59 ± 0.13 Ma based on six concordant analyses and a weighted mean $^{206}Pb/^{238}U$ age of 11.43 ± 0.11 Ma calculated from eleven concordant analyses (Figure 5.3). A syenite porphyry (AVC-AS-04) sample yielded a concordia age of 11.59 ± 0.10 Ma and a weighted mean $^{206}Pb/^{238}U$ age of 11.45 ± 0.08 Ma based on ten and sixteen concordant analyses, respectively (Figure 5.3). The final dated sample from the A–S system is a latite porphyry which yielded a concordia age of 11.59 ± 0.11 Ma and a weighted mean $^{206}Pb/^{238}U$ age of 11.48 ± 0.11 Ma age from four concordant analysis spots (Figure 5.3).

Three additional samples from the alkaline volcanic rocks of the AVC yielded only a limited number of zircon grains, and thus concordance thresholds were adjusted to maximize usable data. The first of these, a latite sample (AVC-01) provided five analyses with a concordia age of 11.76 ± 0.06 Ma and a weighted mean $^{206}Pb/^{238}U$ age of 11.91 ± 0.06 Ma (Fig. 7.8). The second sample (AVC-02), also yielding only five measurements, produced concordia and weighted mean ages of 11.78 ± 0.22 Ma

and 11.69 ± 0.22 Ma, respectively (Figure 5.3). The final sample dated from the AVC is a lampropyre, which yielded concordia and a weighted mean $^{206}Pb/^{238}U$ ages from four concordant spots of 11.81 ± 0.18 Ma and 11.98 ± 0.18 Ma, respectively.

The last sample from the Kırka-Afyon-Isparta district is collected from the Isparta segment (GÖL-02) which also is the youngest volcanic activity among the studied locations. The GÖL-02 sample yielded a concordia age of 2.64 ± 0.03 Ma and a weighted mean $^{206}Pb/^{238}U$ age of 2.63 ± 0.03 Ma (Figure 5.3). It must be noted that rather than Wetherill concordia diagram, Tera-Wasserburg plot was chosen to eliminate the potential common Pb problem with this sample.

5.1.1.3.2.2 Biga Peninsula

Zircon U–Pb dating was performed on samples from several mineralized systems within the Biga Peninsula including Balya, Çatalçam, Turplu, and Sarıalan, as well as from the thick volcanic sequences of the Hallaçlar Formation, which overlie the Balya skarn–porphyry system (Figure 5.4). The first Çatalçam andesite porphyry sample (CTL-01) yielded twenty-four concordant analyses defining a concordia age of 19.83 ± 0.14 Ma, with a weighted mean $^{206}Pb/^{238}U$ age of 19.82 ± 0.13 Ma based on thirty analyses (Figure 5.4). A second andesite porphyry (CTL-02) produced a concordia age of 20.06 ± 0.09 Ma from twenty-nine concordant analyses and a weighted mean age of 20.05 ± 0.09 Ma from thirty-six analyses (Figure 5.4).

Two andesite porphyry samples from Balya (BLY-01 and BLY-02) yielded older ages, with concordia ages of 25.48 ± 0.11 Ma and 25.66 ± 0.09 Ma from twenty-two and thirty-two concordant zircons, respectively (Figure 5.4). The corresponding weighted mean $^{206}Pb/^{238}U$ ages are 25.56 ± 0.09 Ma and 25.54 ± 0.09 Ma based on thirty and thirty-three analyses (Figure 5.4). Zircons from three different samples belonging to the Hallaçlar volcanics produced a concordia ages of 22.87 ± 0.09 Ma,

23.29 ± 0.21 Ma and 22.74 ± 0.11 Ma, and a weighted mean $^{206}Pb/^{238}U$ ages of 22.90 ± 0.09 Ma, 23.18 ± 0.23 Ma and 22.72 ± 0.12 Ma from twenty-three, five and nineteen concordant analyses, respectively (Figure 5.4).

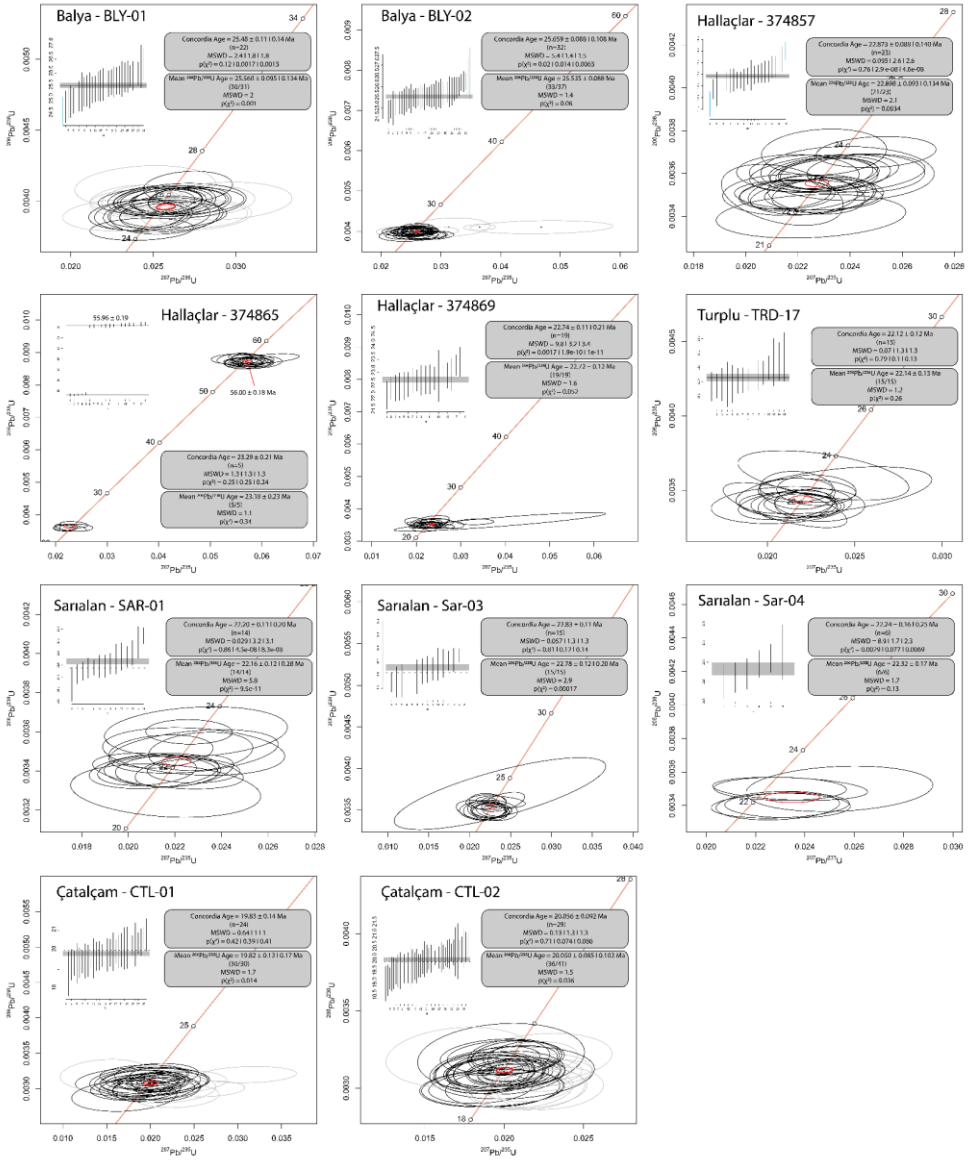


Figure 5.4. Concordia and weighted mean age diagrams of U-Pb dated zircons from the Biga Peninsula.

One granodiorite porphyry sample (TRD-17) analyzed from the Turplu porphyry Cu-Mo-Au prospect returned a concordia age of 22.12 ± 0.12 Ma and a weighted mean $^{206}Pb/^{238}U$ age 22.14 ± 0.13 Ma are obtained from fifteen concordant analysis spots (Figure 5.4).

Three volcanic rock samples from the Sarıalan HS epithermal Au deposit were dated. All samples yielded overlapping concordia ages of 22.20 ± 0.11 Ma, 22.83 ± 0.11 Ma and 22.24 ± 0.16 Ma, weighted mean $^{206}Pb/^{238}U$ ages of 22.16 ± 0.12 Ma, 22.78 ± 0.12 Ma and 22.32 ± 0.17 Ma (Figure 5.4).

5.1.1.3.2.3 Bodrum Peninsula

A total of eight samples representing different magmatic phases of volcanism within the Bodrum Peninsula were analyzed to constrain the temporal evolution of the magmatic activity (Figure 5.5). The oldest magmatic units represented by basaltic trachyandesites (samples BDR-04-1, BDR-04-2) and trachyandesite (sample BDR-05) yielded concordia ages of 10.72 ± 0.12 Ma, 10.40 ± 0.12 Ma, and 10.47 ± 0.12, and weighted mean $^{206}Pb/^{238}U$ ages of 10.70 ± 0.12 Ma, 10.60 ± 0.10 Ma and 10.51 ± 0.12 Ma, respectively (Figure 5.5).

Zircons from a monzosyenite sample from near Turgutreis (BDR-06) produced concordia and weighted mean ages of 10.22 ± 0.07 Ma and 10.23 ± 0.08 Ma, respectively (Figure 5.5). Another monzosyenite unit (BDR-07) returned slightly younger ages of 8.97 ± 0.08 Ma (concordia) and 8.99 ± 0.09 Ma (weighted mean).

Three other trachyandesite samples from (samples BDR-08, BDR-09, BDR-10) yielded progressively younger concordia ages of 7.73 ± 0.07 Ma, 8.25 ± 0.05 Ma, and 8.81 ± 0.07 Ma, with corresponding weighted mean $^{206}Pb/^{238}U$ ages of 7.90 ± 0.07 Ma, 8.14 ± 0.04 Ma, and 8.78 ± 0.08 Ma, respectively (Figure 5.5). These results collectively document a protracted Miocene magmatic history in the Bodrum

area, spanning more than 2.5 million years and capturing both early mafic-intermediate and later felsic phases.

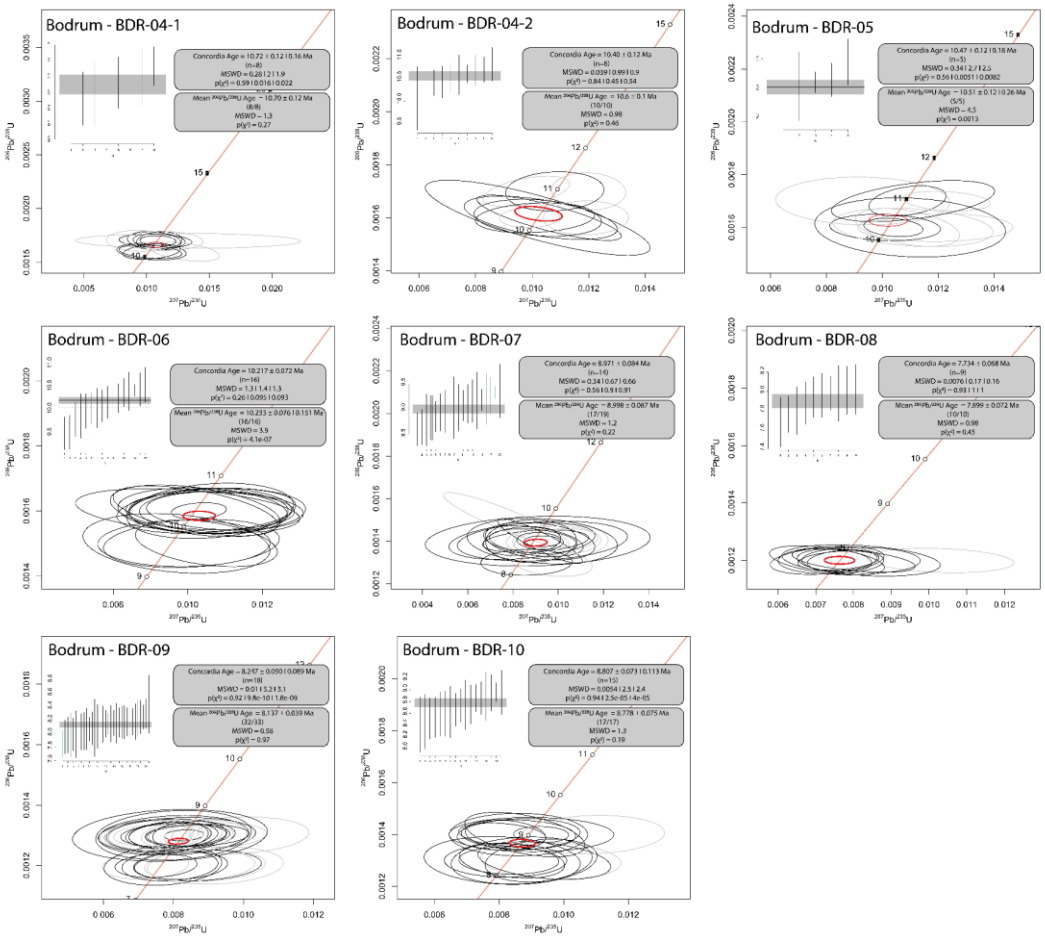


Figure 5.5. Concordia and weighted mean age diagrams of U-Pb dated zircons from the Bodrum Peninsula.

5.1.1.3.2.4 Salihli-Turgutlu Granitoids

U–Pb geochronology was performed on two samples from the Salihli Granitoid. Several zircons from the cores of these samples yielded inherited ages, which were displayed on the concordia diagrams but deliberately excluded from the final age calculations to avoid skewing of the magmatic crystallization ages. For the two

samples (S-01 and S-02), the concordia ages were determined as 14.80 ± 0.10 Ma and 14.78 ± 0.08 Ma, respectively, while the weighted mean $^{206}Pb/^{238}U$ ages were calculated as 14.90 ± 0.10 Ma and 14.83 ± 0.07 Ma (Figure 5.6).

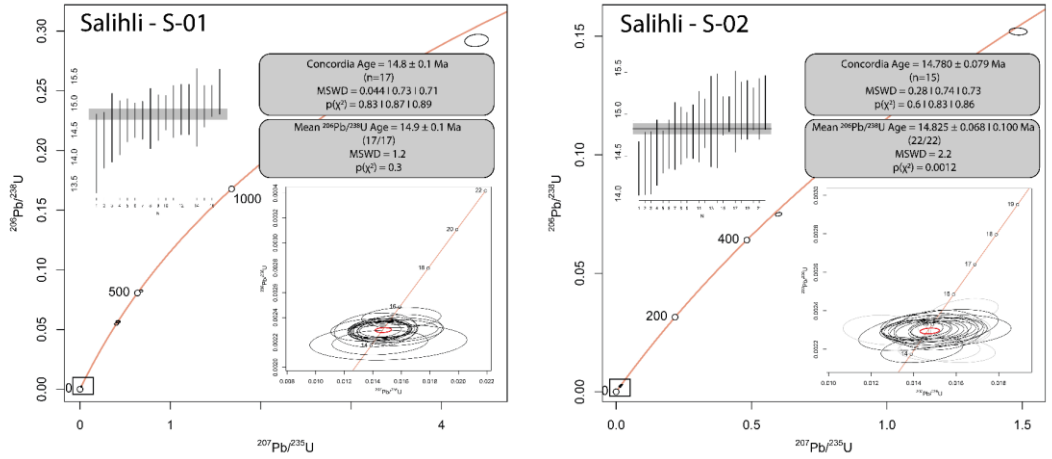


Figure 5.6. Concordia and weighted mean age diagrams of U-Pb dated zircons from the Salihli Pluton.

5.1.1.3.2.5 Kütahya-Simav District

A total of nine samples were dated from the Simav region, including three samples from Sındırgı, three samples from the Eğrigöz Granitoid, one from the Baklan pluton and two from the Pınarbaşı porphyry Cu-Mo prospect (Figure 5.7). Zircons from all localities except Pınarbaşı contained inherited cores, producing significantly older age domains that were plotted on concordia diagrams but excluded from final weighted mean calculations. The dacitic Sındırgı samples (SIN-01, SIN-02, SIN-04) yielded concordia ages of 20.10 ± 0.10 Ma, 19.84 ± 0.09 Ma, and 19.89 ± 0.14 Ma, respectively. The corresponding weighted mean $^{206}Pb/^{238}U$ ages are 19.57 ± 0.10 Ma, 19.88 ± 0.08 Ma, and 19.76 ± 0.14 Ma (Figure 5.7).

Three samples from the Eğrigöz (EGR-01, EGR-02, EGR-03) yielded concordia ages of 19.49 ± 0.09 Ma, 19.07 ± 0.07 Ma, and 19.29 ± 0.07 Ma, with corresponding

weighted mean $^{206}Pb/^{238}U$ ages of 19.47 ± 0.09 Ma, 19.07 ± 0.07 Ma, and 19.20 ± 0.08 Ma, respectively (Fig. 7.13).

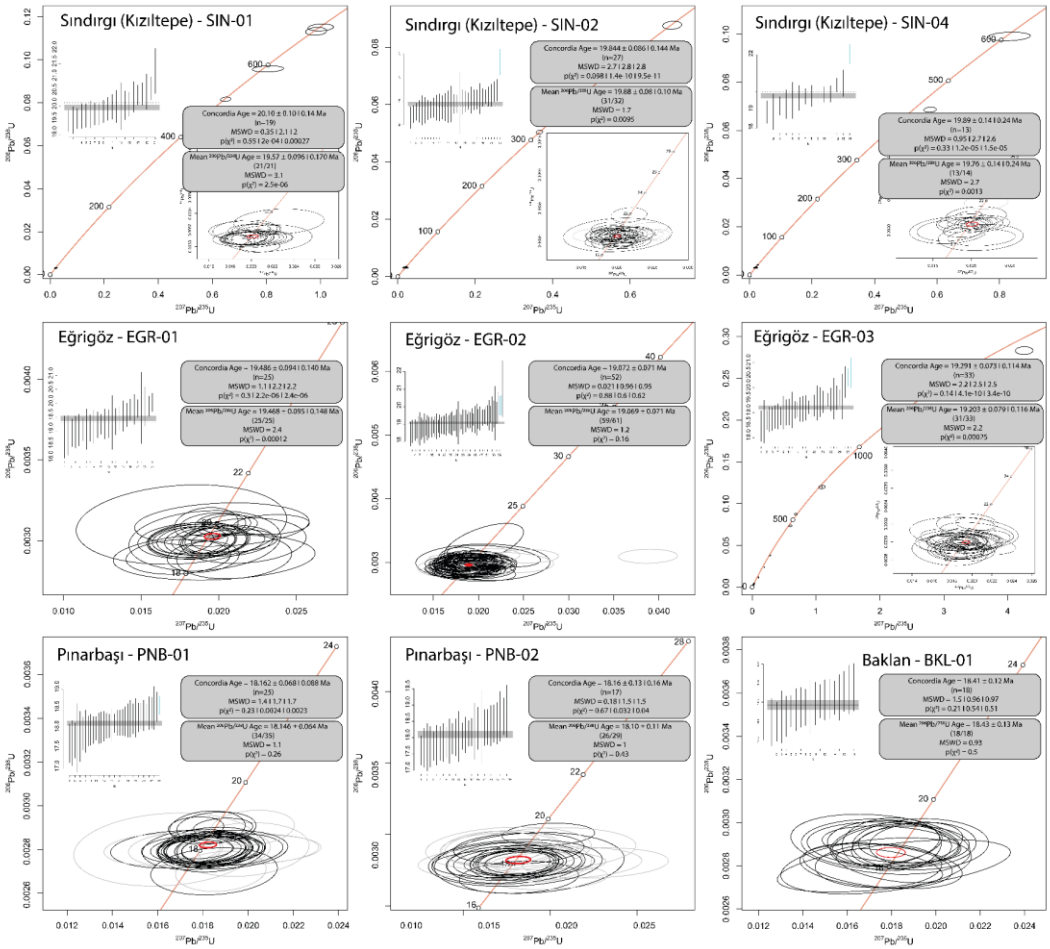


Figure 5.7. Concordia and weighted mean age diagrams of U-Pb dated zircons from the Kütahya-Simav district.

A granite sample from the Baklan Granitoid (BKL-01) yielded eighteen concordant spots from zircons, which returned a concordia age of 18.41 ± 0.12 Ma (Figure 5.7). Weighted mean $^{206}Pb/^{238}U$ age of this sample is calculated as 18.43 ± 0.13 Ma (Figure 5.7).

The Pınarbaşı samples represent the youngest units within this group. The first dated sample, a basaltic andesite (PNB-01), yielded a concordia age of 18.16 ± 0.07 Ma and a weighted mean $^{206}Pb/^{238}U$ age of 18.15 ± 0.06 Ma (Figure 5.7). A second sample from the Pınarbaşı locality, of monzonitic composition (PNB-02), produced similar results with a concordia age of 18.16 ± 0.13 Ma and a weighted mean $^{206}Pb/^{238}U$ age of 18.10 ± 0.11 Ma (Figure 5.7).

5.1.1.3.2.6 Uşak District

Another key locality dated within the Western Anatolian sector is the Sayacık Au porphyry prospect near Uşak. Drill core samples obtained from various depths represent strongly altered monzonite porphyries (SYC-01 through SYC-05). The resulting concordia ages are 13.92 ± 0.06 Ma, 13.90 ± 0.05 Ma, 14.27 ± 0.11 Ma, 14.05 ± 0.11 Ma, and 14.09 ± 0.09 Ma, respectively (Fig. 7.14), whereas corresponding weighted mean $^{206}Pb/^{238}U$ ages are 13.91 ± 0.06 Ma, 13.87 ± 0.05 Ma, 14.20 ± 0.10 Ma, 14.14 ± 0.11 Ma, and 14.12 ± 0.08 Ma (Fig. 7.14).

These ages closely overlap with the intrusive phases of the Kışladağ Au porphyry system as determined by Paolillo et al. (2022), indicating that the magmatic centers responsible for porphyry Au mineralization at both Sayacık and Kışladağ were emplaced synchronously and are likely derived from the same regional magmatic event.

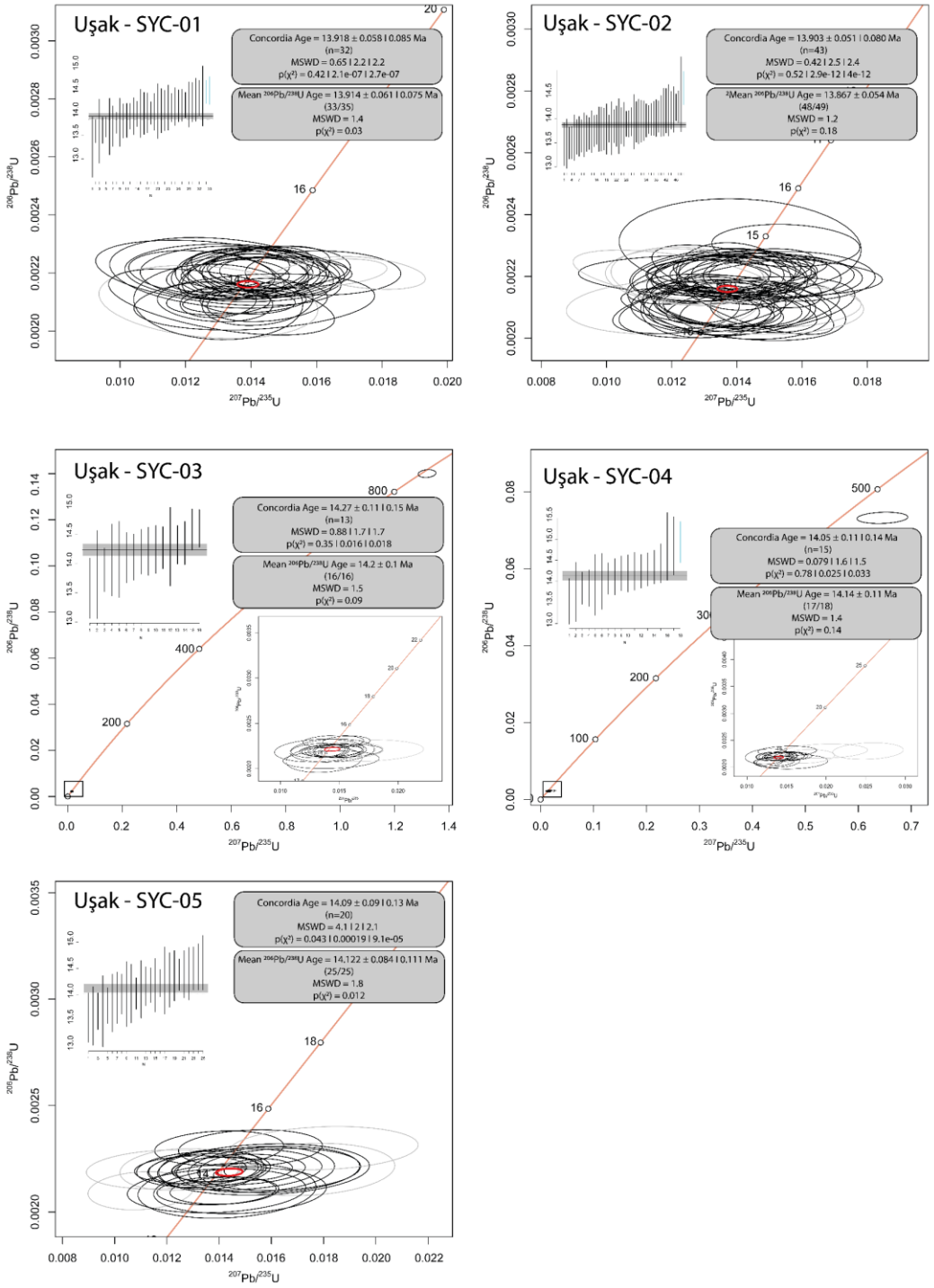


Figure 5.8. Concordia and weighted mean age diagrams of U-Pb dated zircons from the Uşak district.

5.1.1.4 Trace and Rare Earth Element Geochemistry

Dated zircon grains were subsequently analyzed through LA-ICP-MS to determine their trace and rare earth element (REE) compositions. In some samples, a high abundance of mineral inclusions—particularly apatite—was observed, leading to potential overlap with inclusions during laser ablation. To minimize the influence of such inclusions on the zircon geochemical dataset, all trace and REE data were systematically filtered prior to interpretation. Specifically, analyses with La concentrations greater than 1 ppm were excluded due to the likelihood measurement of apatite inclusions, while those with Ti concentrations exceeding 20 ppm were removed due to potential contamination from oxide phases such as rutile or titanite.

From the filtered dataset, interpretations focused on key zircon parameters that provide insights into magmatic evolution and porphyry fertility. These include absolute abundances of Ti, Hf, and Y, as well as trace element ratios such as Eu/Eu*, Ce/Ce*, Th/U, and Dy/Yb. Additionally, zircon crystallization conditions—namely temperature and magma oxidation state (fO_2)—were estimated.

Zircon crystallization temperatures were calculated using the Ti-in-zircon thermometer proposed by Ferry and Watson (2007). This model incorporates activity coefficients for SiO_2 and TiO_2, which were determined based on petrographic observations. During thin section analysis, samples were assessed for the presence of magmatic quartz in phenocrysts or groundmass; when quartz was observed, the activity of SiO_2 was set to 1. For samples containing titanite as an accessory phase, TiO_2 activity was set to 0.7 following the recommendations of Claiborne et al. (2010) and Dilles et al. (2015).

$$T(°K) = \frac{-4800 \pm 86}{logTi\ (ppm) + logaSiO2 - logaTiO2 - (5.711 \pm 0.072)} \qquad \text{(Equation 1)}$$

Pressure variations during zircon crystallization may introduce a potential source of uncertainty in Ti-in-zircon temperature estimates. Ferry and Watson (2007) acknowledged a pressure dependency of approximately 5°C/kbar for the Ti-in-zircon thermometer, which was originally calibrated at a pressure of 1 GPa (10 kbar). Since the sampled magmatic systems generally formed at shallow crustal depths—consistent with the conditions typical for porphyry mineralization—the calculated crystallization temperatures are expected to be up to ~30°C higher than the actual values. However, given that zircon crystallization likely occurred under similar conditions across all studied localities, the relative temperature comparisons among different samples are considered reliable. The temperature estimates derived from this method are summarized in Table 5.3.

Magmatic oxidation states (fO_2) were estimated using the empirical approach proposed by Loucks et al. (2020), which establishes a correlation between zircon trace element composition and magma fO_2. Unlike Ti-in-zircon thermometry, this method does not rely on temperature estimates and instead calculates fO_2 values directly from zircon Ti, U, and Ce concentrations. The equation provided by Loucks et al. (2020) is presented as Equation 2. The resulting oxidation state values are reported relative to the fayalite–magnetite–quartz (FMQ) buffer and are summarized in Table 5.3.

$$logfO_{2(sample)} - logfO_{2(FMQ)} = 3.998(\pm 0.124) x log\left[Ce/\sqrt{U_i x T_i}\right] + 2.284(\pm 0.101) \quad \text{(Equation 2)}$$

Table 5.3. Summary table of zircon trace element abundances and other key parameters.

Region		Konya											
Field		SVS	Konya	Konya	Konya	Konya	Konya	Konya	Konya	Konya	Konya	Konya	Konya
Sample		Sille-02	CKRA-01	DMLP-01	DMLP-02	INL-201-01	INL-201-02	INL-201-03	INL-D-01	INL-OP-01	INL-OP-02	KTN-01	KRC-01
U-Pb Age (Ma)		12.80	10.70	10.24	10.31	8.97	8.96	8.97	9.04	9.00	9.08	3.01	4.77
Ti (ppm)	Min	2.04	3.06	3.72	4.86	3.66	3.06	3.78	3.36	3.12	3.66	2.64	1.92
	Max	12.41	15.95	22.84	11.45	18.46	12.59	10.79	10.85	17.99	13.19	8.27	12.77
	Mean	3.88	6.14	8.38	8.31	6.77	6.34	6.57	6.77	6.21	6.99	4.93	4.18
	2std	2.64	3.31	5.30	2.28	3.88	2.28	2.15	2.43	3.94	2.91	1.16	2.72
Hf (ppm)	Min	8403.73	8338.20	8125.83	8791.24	9280.89	8167.47	7607.37	8516.55	7869.00	7935.73	8013.75	8991.45
	Max	12809.69	14322.68	12390.92	11763.76	12272.30	11902.99	11361.09	12758.83	11215.61	12614.41	12767.88	22588.42
	Mean	11845.82	10759.58	10338.39	10680.90	11119.30	10078.88	9146.13	10473.10	9908.57	10638.97	11130.76	12231.28
	2std	880.13	1577.20	1511.28	1009.48	992.90	1000.83	1210.07	1215.89	1120.96	1570.82	949.47	2956.82
Y (ppm)	Min	965.83	597.85	487.30	583.20	436.16	312.17	356.78	187.23	337.62	357.58	411.14	1000.45
	Max	3252.60	3612.89	2192.92	2050.86	5689.89	5572.36	3627.50	5516.29	4396.05	6257.95	2911.05	18845.47
	Mean	1865.51	1519.05	1089.33	919.29	1534.69	1192.02	948.82	1786.42	1348.35	2200.58	1007.90	3192.83
	2std	564.15	917.10	552.33	454.23	1618.29	941.84	937.58	1658.59	1232.88	1756.80	556.63	4655.76
Total REE (ppm)	Min	704.29	524.38	434.09	508.91	381.84	289.77	323.44	182.28	307.15	338.77	399.78	800.67
	Max	2243.58	3179.01	1633.87	1434.88	4041.73	3861.74	2638.68	3876.93	2861.15	4349.68	2288.59	12417.57
	Mean	1334.97	1198.86	842.83	733.20	1139.72	909.54	788.51	1371.35	1016.21	1597.19	848.69	2316.10
	2std	369.58	689.71	365.77	280.51	1091.22	632.69	640.88	1157.83	796.26	1205.23	431.43	3078.21
Th/U	Min	0.23	0.25	0.35	0.41	0.48	0.40	0.41	0.24	0.39	0.43	0.27	0.21
	Max	0.73	1.40	1.05	0.87	2.12	1.48	1.24	1.77	1.69	1.60	0.79	0.93
	Mean	0.33	0.61	0.52	0.53	0.85	0.67	0.65	0.74	0.69	0.78	0.53	0.41
	2std	0.13	0.30	0.20	0.13	0.49	0.24	0.27	0.41	0.38	0.40	0.12	0.20
Ce/Nd	Min	6.90	2.23	3.66	4.50	6.42	5.08	5.07	7.34	7.87	2.05	13.61	12.11
	Max	57.64	69.67	53.67	39.17	49.74	49.74	40.86	50.13	59.78	63.74	43.62	49.17
	Mean	43.01	32.46	23.12	24.35	32.79	28.33	25.56	25.02	33.12	22.82	28.53	32.17
	2std	11.72	17.37	15.64	10.95	15.13	12.99	14.26	13.88	18.19	16.45	8.93	11.19
Dy/Yb	Min	0.16	0.13	0.16	0.16	0.16	0.15	0.15	0.15	0.15	0.15	0.14	0.13
	Max	0.24	0.43	0.26	0.25	0.33	0.31	0.28	0.28	0.34	0.49	0.20	0.30
	Mean	0.19	0.21	0.20	0.19	0.21	0.20	0.19	0.21	0.20	0.23	0.16	0.19
	2std	0.02	0.08	0.04	0.03	0.06	0.04	0.05	0.05	0.06	0.09	0.01	0.05
Hf/Y	Min	3.15	2.31	4.98	4.29	1.63	1.55	2.14	1.74	1.79	1.36	2.75	0.85
	Max	9.82	17.35	25.43	19.82	28.14	34.91	25.71	68.14	32.29	34.72	28.80	15.59
	Mean	6.82	9.26	11.94	13.48	13.42	12.08	15.27	15.68	11.94	9.67	13.56	7.44
	2std	1.67	4.30	6.29	4.61	8.02	7.24	7.64	17.95	7.88	8.58	5.68	3.67
Eu/Eu*	Min	0.33	0.21	0.31	0.31	0.41	0.41	0.45	0.40	0.41	0.16	0.46	0.09
	Max	0.57	0.66	0.50	0.50	0.53	0.60	0.64	0.65	0.56	0.68	0.64	0.62
	Mean	0.44	0.45	0.40	0.41	0.46	0.49	0.53	0.49	0.48	0.44	0.54	0.52
	2std	0.05	0.10	0.07	0.06	0.04	0.05	0.05	0.07	0.04	0.12	0.04	0.15
Ce/Ce*	Min	24.15	5.45	12.96	15.43	24.73	17.97	19.06	24.54	27.11	10.74	61.91	53.00
	Max	602.59	556.53	330.35	205.92	262.02	287.75	212.69	315.96	422.45	369.53	250.58	411.88
	Mean	353.88	185.42	114.97	121.68	166.14	143.19	120.83	122.79	182.36	114.03	149.87	219.45
	2std	145.17	135.48	97.66	63.31	87.16	77.90	72.12	86.89	117.36	91.90	57.56	112.86
ΔFMQ	Min	-0.36	-0.06	-2.64	0.18	0.67	0.23	-0.01	-0.47	0.63	-1.24	0.21	0.17
	Max	1.63	3.31	2.24	0.92	2.79	2.78	1.79	2.35	2.38	2.30	2.20	2.57
	Mean	0.41	1.36	0.32	0.54	1.38	1.16	0.90	1.26	1.30	1.13	0.96	0.95
	2std	0.40	0.78	1.38	0.24	0.67	0.49	0.49	0.85	0.48	0.88	0.44	0.62
Ti-in-zircon (T °C)	Min	641.84	673.61	689.71	712.66	688.35	673.61	691.06	681.25	675.18	688.35	661.79	637.27
	Max	802.67	829.58	870.57	794.31	845.94	804.18	788.23	788.80	842.97	809.08	761.83	805.67
	Mean	684.13	725.40	752.77	759.35	735.04	732.13	736.39	738.04	725.35	739.63	711.98	690.28
	2std	40.85	42.94	49.31	28.17	41.21	32.16	29.99	34.23	44.77	38.54	20.92	42.68

Table 5.3. continued

Region		Central Anatolia				
Field		Yeşilyurt	Melendiz	Melendiz	Süleymanpınarı	Melendiz
Sample		YLS-01	496762	496918	SLP-01	CML-01
U-Pb Age (Ma)		4.77	1.50	1.77	3.95	1.94
Ti (ppm)	Min	14.51	5.22	5.34	2.88	3.66
	Max	21.10	11.63	8.75	18.94	11.33
	Mean	16.38	7.33	6.76	9.76	6.69
	2std	1.60	1.70	0.96	4.05	2.23
Hf (ppm)	Min	8739.13	8932.33	9278.43	9028.33	8289.53
	Max	10032.96	10765.32	10831.56	11365.27	10757.99
	Mean	9623.24	9914.56	9926.21	9802.53	9629.23
	2std	313.27	552.36	426.70	694.22	708.14
Y (ppm)	Min	509.10	458.84	388.40	454.49	348.00
	Max	1289.35	1621.66	2313.32	1009.54	3776.41
	Mean	787.25	751.24	709.48	705.62	913.01
	2std	261.26	286.53	453.82	173.92	820.36
Total REE (ppm)	Min	376.59	425.57	333.47	376.59	330.49
	Max	842.24	1222.41	1974.96	811.07	2790.14
	Mean	575.60	610.08	603.60	594.18	745.09
	2std	151.44	192.20	382.19	129.01	590.79
Th/U	Min	0.55	0.53	0.58	0.44	0.50
	Max	0.91	0.91	0.93	0.97	1.50
	Mean	0.74	0.69	0.72	0.71	0.74
	2std	0.10	0.12	0.12	0.15	0.23
Ce/Nd	Min	4.78	5.18	8.52	3.95	6.23
	Max	18.98	42.43	58.26	39.99	52.45
	Mean	11.51	21.25	31.46	22.29	29.67
	2std	4.90	10.11	11.30	11.58	11.06
Dy/Yb	Min	0.20	0.14	0.14	0.13	0.13
	Max	0.30	0.22	0.19	0.25	0.24
	Mean	0.24	0.17	0.16	0.19	0.17
	2std	0.02	0.03	0.02	0.04	0.03
Hf/Y	Min	7.46	6.15	4.68	9.16	2.24
	Max	18.70	22.76	25.46	24.98	29.47
	Mean	13.39	14.76	16.78	14.78	15.56
	2std	3.87	4.83	5.49	4.03	7.36
Eu/Eu*	Min	0.34	0.42	0.37	0.29	0.20
	Max	0.40	0.59	0.51	0.59	0.54
	Mean	0.37	0.52	0.47	0.38	0.42
	2std	0.02	0.05	0.04	0.10	0.09
Ce/Ce*	Min	18.76	18.14	30.98	3.82	24.34
	Max	106.10	206.53	294.22	220.90	257.85
	Mean	56.53	95.98	149.64	113.60	148.98
	2std	29.46	51.67	58.97	70.15	59.34
ΔFMQ	Min	-0.12	-0.16	0.22	0.12	0.13
	Max	0.52	1.09	2.27	1.67	2.10
	Mean	0.28	0.36	0.65	0.70	0.74
	2std	0.15	0.31	0.53	0.39	0.56
Ti-in-zircon (T °C)	Min	819.28	718.98	721.01	668.72	688.35
	Max	861.28	795.92	767.32	848.86	793.23
	Mean	832.15	748.30	741.88	770.37	737.95
	2std	10.28	21.32	12.94	45.97	29.74

Table 5.3. continued

Region		Biga										
Field		Balya	Balya	Turplu	Sarıalan	Sarıalan	Sarıalan	Hallaçlar	Hallaçlar	Hallaçlar	Çatalçam	Çatalçam
Sample		BLY-01	BLY-02	TRD-17	SAR-01	SAR-03	SAR-04	374865	374857	374869	CTL-01	CTL-02
U-Pb Age (Ma)		25.48	25.66	22.14	22.16	22.78	22.32	23.18	22.90	22.74	19.83	20.06
Ti (ppm)	Min	1.98	2.22	4.44	3.72	4.08	4.98	5.10	3.60	5.10	3.06	2.16
	Max	10.61	7.49	12.29	6.71	22.42	8.21	7.73	15.41	13.49	8.81	21.76
	Mean	4.72	4.05	6.58	5.01	7.00	6.40	6.56	5.56	7.53	5.60	5.02
	2std	1.83	1.05	2.03	0.87	4.48	1.27	0.94	2.22	2.13	1.13	2.88
Hf (ppm)	Min	8048.65	10792.62	8691.28	9836.53	10150.43	9823.52	11320.97	8558.35	9824.12	9592.28	9285.47
	Max	26898.50	12996.97	11650.94	12805.53	15170.07	12313.89	13541.69	13058.91	13565.22	12906.92	14078.66
	Mean	11995.38	11685.51	9982.13	11134.05	12686.32	11060.23	12042.85	11716.47	12176.79	11007.77	11738.72
	2std	2970.85	530.08	830.19	810.35	1751.43	761.67	817.59	1018.73	884.62	750.18	939.97
Y (ppm)	Min	378.19	661.13	251.33	541.27	651.04	330.02	515.44	361.82	719.53	230.00	392.60
	Max	3845.06	3413.02	1365.58	2166.22	2485.77	2182.26	1219.95	2031.17	2751.15	2460.45	2257.42
	Mean	1200.57	1431.97	805.51	893.40	1272.87	887.59	951.40	1092.96	1174.70	808.11	1137.25
	2std	605.37	619.07	320.38	371.33	499.80	651.02	268.20	334.49	511.93	405.42	431.82
Total REE (ppm)	Min	371.93	580.07	259.84	424.01	606.21	318.94	395.87	323.85	594.50	213.99	345.50
	Max	2665.32	2565.38	960.49	1403.39	1666.53	1527.64	772.27	1202.94	1731.67	1845.17	1716.01
	Mean	967.35	1170.34	645.66	689.30	939.53	669.08	658.78	754.07	887.53	661.73	904.06
	2std	415.20	444.41	209.08	220.17	280.19	419.09	141.79	176.57	278.17	301.33	319.57
Th/U	Min	0.16	0.17	0.47	0.45	0.47	0.40	0.56	0.44	0.58	0.35	0.20
	Max	1.62	0.43	0.95	1.03	0.86	1.15	0.63	0.84	1.15	1.06	1.16
	Mean	0.43	0.26	0.59	0.62	0.65	0.62	0.61	0.61	0.70	0.69	0.61
	2std	0.28	0.06	0.12	0.14	0.12	0.26	0.03	0.10	0.15	0.18	0.20
Ce/Nd	Min	15.58	14.32	9.35	12.48	5.29	21.63	23.48	5.18	4.77	4.91	8.17
	Max	53.38	64.84	42.95	53.01	47.68	40.71	40.25	48.09	43.13	45.46	47.19
	Mean	32.91	32.17	25.20	32.55	26.37	32.70	31.36	35.43	28.96	25.75	31.08
	2std	7.83	9.29	10.76	12.05	12.53	6.89	6.90	9.83	11.68	10.50	9.01
Dy/Yb	Min	0.13	0.14	0.14	0.13	0.15	0.14	0.20	0.14	0.20	0.15	0.13
	Max	0.29	0.21	0.20	0.23	0.24	0.21	0.22	0.24	0.30	0.24	0.22
	Mean	0.18	0.16	0.16	0.16	0.19	0.17	0.21	0.19	0.22	0.18	0.18
	2std	0.04	0.02	0.02	0.02	0.03	0.02	0.01	0.02	0.03	0.02	0.02
Hf/Y	Min	2.09	3.46	7.15	5.21	5.56	5.01	10.04	4.21	3.57	5.06	5.37
	Max	29.89	17.96	39.86	23.38	20.92	37.31	22.75	27.51	16.80	52.08	26.50
	Mean	11.85	9.36	15.55	13.89	11.22	18.62	13.69	11.77	11.75	16.66	12.05
	2std	5.48	3.24	9.50	4.32	4.04	11.95	4.69	4.08	3.70	8.76	5.14
Eu/Eu*	Min	0.40	0.37	0.48	0.42	0.29	0.41	0.30	0.30	0.25	0.43	0.43
	Max	0.63	0.59	0.59	0.59	0.55	0.62	0.38	0.63	0.41	0.59	0.62
	Mean	0.51	0.53	0.54	0.51	0.43	0.51	0.33	0.39	0.32	0.53	0.51
	2std	0.06	0.04	0.03	0.04	0.08	0.06	0.03	0.07	0.04	0.04	0.04
Ce/Ce*	Min	70.10	73.51	34.22	28.77	16.46	110.49	119.06	21.33	15.50	15.13	11.34
	Max	348.07	908.99	206.23	297.09	299.49	200.15	236.40	294.84	278.29	457.35	481.95
	Mean	190.72	238.94	110.89	154.92	129.14	156.14	172.18	188.29	156.61	136.64	188.92
	2std	68.06	138.37	55.75	72.99	77.86	36.24	51.51	64.30	77.74	89.86	97.76
ΔFMQ	Min	-0.12	0.05	-0.54	0.68	-0.19	0.18	0.66	0.24	0.58	-0.18	-0.61
	Max	2.33	0.99	1.33	1.60	1.86	1.96	1.46	1.90	1.52	1.83	2.00
	Mean	1.00	0.50	0.69	1.13	1.16	0.75	1.21	1.35	1.20	1.11	1.25
	2std	0.66	0.31	0.47	0.25	0.65	0.63	0.31	0.32	0.23	0.42	0.53
Ti-in-zircon (T °C)	Min	639.58	648.29	704.78	689.71	697.52	714.81	716.92	686.97	716.92	673.61	646.19
	Max	786.52	752.33	801.65	741.99	868.38	761.13	755.34	825.81	811.47	767.99	864.87
	Mean	705.79	694.88	737.30	714.38	736.66	736.25	739.21	721.16	750.25	723.89	708.79
	2std	30.07	20.91	25.63	15.21	44.07	18.16	13.74	26.23	24.48	18.76	36.00

Table 5.3. continued

Region		Kütahya-Simav								
Field		Eğrigöz	Eğrigöz	Eğrigöz	Sındırgı	Sındırgı	Sındırgı	Baklan	Pınarbaşı	Pınarbaşı
Sample		EGR-01	EGR-02	EGR-03	SIN-01	SIN-02	SIN-04	BKL-01	PNB-01	PNB-02
U-Pb Age (Ma)		19.49	19.07	19.29	20.10	19.84	19.89	18.43	18.16	18.16
Ti (ppm)	Min	2.16	2.28	2.40	1.86	1.80	1.62	3.66	2.94	3.84
	Max	9.95	13.01	8.45	4.92	12.05	12.17	29.02	19.06	12.11
	Mean	5.80	6.32	5.43	2.91	3.76	6.01	6.28	4.61	5.74
	2std	2.52	2.77	1.76	0.78	2.45	4.15	4.89	3.16	2.20
Hf (ppm)	Min	7902.77	7893.85	8777.55	10251.39	8835.35	8832.32	8235.38	9111.27	8473.36
	Max	12517.46	11577.43	11421.30	13561.21	13270.34	13086.97	13519.49	11705.14	11051.38
	Mean	10568.30	9745.15	9989.09	11834.39	11896.82	10862.70	11508.00	10782.27	10256.04
	2std	1127.14	913.85	791.25	841.39	1123.95	1328.01	1056.35	489.19	645.56
Y (ppm)	Min	727.27	822.08	373.24	743.19	532.19	135.46	605.41	420.74	954.57
	Max	1966.94	3726.64	2630.83	2587.45	1932.23	2794.88	3155.52	1643.93	2613.31
	Mean	1377.64	1637.13	1489.86	1582.17	1303.62	1497.12	1091.06	1147.63	1409.45
	2std	295.99	648.93	507.32	520.28	400.61	730.85	504.19	270.92	344.09
Total REE (ppm)	Min	570.05	496.76	190.23	556.43	463.85	126.53	494.42	343.84	737.43
	Max	1424.38	2339.11	1757.42	1841.66	1438.21	1884.89	2518.01	1503.21	1811.45
	Mean	1037.21	1109.98	1038.33	1153.22	985.88	1061.12	832.13	1051.70	1060.13
	2std	226.02	392.64	328.72	356.30	284.88	476.33	400.02	260.67	216.55
Th/U	Min	0.25	0.08	0.19	0.18	0.26	0.02	0.38	0.35	0.50
	Max	0.77	0.98	0.73	0.81	0.64	0.83	0.84	0.84	1.37
	Mean	0.50	0.58	0.52	0.35	0.39	0.39	0.52	0.56	0.75
	2std	0.12	0.21	0.12	0.13	0.12	0.19	0.09	0.13	0.20
Ce/Nd	Min	2.38	2.30	2.76	4.93	4.01	1.75	9.91	6.76	4.92
	Max	34.07	29.60	42.87	42.85	47.02	44.70	51.32	83.51	56.87
	Mean	15.04	12.71	12.01	19.61	22.62	14.07	32.50	50.12	39.05
	2std	7.82	9.54	9.15	10.45	13.32	14.48	14.11	18.21	15.14
Dy/Yb	Min	0.20	0.17	0.18	0.17	0.17	0.12	0.13	0.10	0.16
	Max	0.30	0.39	0.78	0.25	0.24	0.31	0.20	0.23	0.29
	Mean	0.23	0.26	0.25	0.21	0.21	0.22	0.17	0.14	0.21
	2std	0.03	0.06	0.11	0.02	0.02	0.06	0.02	0.03	0.03
Hf/Y	Min	4.86	2.39	3.78	4.53	6.33	3.80	2.61	6.45	3.67
	Max	11.97	11.97	25.94	14.58	18.91	89.77	19.45	23.68	10.74
	Mean	7.98	6.83	7.78	8.22	10.05	14.43	12.03	10.07	7.67
	2std	1.70	2.56	4.21	2.55	3.41	23.91	3.92	3.32	1.78
Eu/Eu*	Min	0.22	0.19	0.24	0.13	0.14	0.20	0.35	0.34	0.28
	Max	0.62	0.44	0.39	0.48	0.52	0.59	0.57	0.55	0.52
	Mean	0.30	0.28	0.29	0.24	0.25	0.29	0.45	0.42	0.37
	2std	0.10	0.06	0.04	0.07	0.10	0.11	0.04	0.05	0.06
Ce/Ce*	Min	1.60	2.07	13.29	17.04	11.94	5.67	39.63	27.95	19.43
	Max	233.17	226.73	394.38	396.52	394.65	259.87	289.13	442.63	417.80
	Mean	84.98	74.66	70.73	147.51	165.86	94.28	170.00	261.21	235.10
	2std	54.53	70.49	77.08	104.08	119.98	99.57	83.13	111.74	112.37
ΔFMQ	Min	-0.65	-1.81	-3.07	-0.90	-1.55	-4.40	-0.33	-0.20	0.96
	Max	2.62	2.38	1.98	0.85	1.49	1.11	1.81	1.99	2.50
	Mean	0.60	0.57	0.28	0.15	0.46	-0.78	1.21	1.48	2.05
	2std	0.74	0.72	0.89	0.49	0.72	1.47	0.47	0.59	0.37
Ti-in-zircon (T °C)	Min	646.19	650.34	654.31	634.90	632.46	624.71	688.35	670.38	692.38
	Max	780.05	807.63	763.92	713.74	799.60	800.63	899.60	849.58	800.12
	Mean	721.47	729.27	718.48	667.55	681.19	713.44	726.52	700.63	723.52
	2std	41.21	40.91	31.09	21.01	42.04	67.22	40.73	35.92	29.27

Table 5.3. continued

Region		Uşak					Salihli	
Field		Sayacık	Sayacık	Sayacık	Sayacık	Sayacık	Salihli	Salihli
Sample		SYC-01	SYC-02	SYC-03	SYC-04	SYC-05	S-01	S-02
U-Pb Age (Ma)		13.92	13.90	14.27	14.05	14.09	14.80	11.78
Ti (ppm)	Min	2.28	2.76	3.36	2.70	2.70	1.08	0.78
	Max	10.31	6.95	7.55	9.59	9.23	12.83	6.35
	Mean	5.19	4.92	6.17	5.05	4.78	4.55	2.27
	2std	1.67	1.20	1.37	1.81	1.42	3.03	1.46
Hf (ppm)	Min	7891.34	8030.42	9003.98	8129.97	8670.07	9201.76	12393.33
	Max	11470.18	11432.67	10646.44	11235.32	12296.76	16475.89	15620.29
	Mean	10101.35	10243.15	9730.69	10406.45	11087.07	12724.67	13377.06
	2std	937.48	772.25	671.48	847.39	778.35	2087.84	1007.00
Y (ppm)	Min	377.63	458.70	758.88	533.94	390.24	313.07	646.91
	Max	2085.17	2143.78	2281.25	1179.57	1764.68	3508.50	2012.89
	Mean	862.98	935.67	1294.00	813.33	933.11	1405.39	1088.48
	2std	388.62	385.26	514.07	225.65	343.32	853.08	360.99
Total REE (ppm)	Min	329.11	371.57	607.73	432.33	349.65	130.54	502.07
	Max	1407.86	1438.39	1649.51	873.87	1257.32	2530.30	1473.44
	Mean	654.47	692.27	959.63	640.16	706.60	1015.51	780.55
	2std	253.77	241.41	343.84	148.84	229.40	601.89	255.51
Th/U	Min	0.41	0.39	0.50	0.40	0.31	0.03	0.05
	Max	0.94	1.07	0.90	0.80	0.80	0.49	0.24
	Mean	0.60	0.61	0.75	0.53	0.50	0.19	0.12
	2std	0.14	0.14	0.15	0.12	0.12	0.12	0.05
Ce/Nd	Min	6.63	2.73	7.32	8.26	8.83	0.84	3.84
	Max	36.58	38.72	36.34	34.25	63.53	35.92	15.72
	Mean	26.81	25.64	18.61	24.91	30.87	6.62	7.56
	2std	9.39	10.10	11.23	9.16	12.14	6.59	3.71
Dy/Yb	Min	0.18	0.19	0.20	0.17	0.16	0.10	0.16
	Max	0.33	0.35	0.32	0.29	0.28	1.61	0.34
	Mean	0.24	0.25	0.27	0.23	0.22	0.28	0.22
	2std	0.04	0.04	0.05	0.04	0.03	0.27	0.04
Hf/Y	Min	4.22	4.42	4.15	8.79	5.97	4.63	7.76
	Max	28.58	24.13	13.40	19.58	31.51	44.18	21.11
	Mean	13.92	12.74	8.59	13.68	13.88	13.47	13.18
	2std	6.13	5.09	3.24	3.91	6.52	10.83	3.46
Eu/Eu*	Min	0.50	0.29	0.55	0.52	0.49	0.08	0.10
	Max	0.69	0.65	0.61	0.62	0.62	0.69	0.26
	Mean	0.58	0.55	0.56	0.57	0.55	0.18	0.15
	2std	0.05	0.07	0.02	0.03	0.03	0.11	0.05
Ce/Ce*	Min	21.10	12.78	27.91	27.18	33.89	3.51	28.10
	Max	183.19	198.93	173.55	183.76	449.77	378.28	189.84
	Mean	122.90	120.07	78.29	116.72	159.04	68.66	80.36
	2std	50.59	54.00	56.01	47.85	88.70	78.06	51.85
ΔFMQ	Min	0.80	-1.04	0.95	0.92	0.85	-4.35	-3.77
	Max	2.33	2.73	2.67	2.19	2.17	-1.56	-1.23
	Mean	1.63	1.69	2.00	1.59	1.55	-2.76	-2.71
	2std	0.39	0.65	0.47	0.35	0.32	0.72	0.70
Ti-in-zircon (T °C)	Min	650.34	665.32	681.25	663.57	663.57	596.09	574.40
	Max	783.62	745.28	753.09	776.37	772.57	806.16	736.89
	Mean	715.14	711.71	732.26	712.48	708.62	692.17	641.62
	2std	28.13	21.71	23.13	28.77	23.72	56.57	39.74

Table 5.3. continued

Region		Kırka-Afyon-Isparta									
Field		Kırka	Afyon	Afyon	Afyon	A-S	A-S	A-S	A-S	A-S	Isparta
Sample		KRK-01-2	AVC-01	AVC-02	AVC-05	AVC-AS-01	AVC-AS-02	AVC-AS-03	AVC-AS-04	AVC-AS-05	GÖL-02
U-Pb Age (Ma)		18.56	11.76	11.78	11.98	11.68	11.99	11.59	11.60	11.48	2.63
Ti (ppm)	Min	3.54	38.85	33.75	3.10	7.07	3.24	9.95	8.21	2.76	5.52
	Max	4.86	146.40	42.44	10.50	17.81	10.78	15.65	17.69	13.29	19.48
	Mean	4.16	95.66	37.85	7.30	11.15	6.79	11.84	11.82	6.74	10.53
	2std	0.66	53.18	4.37	2.67	2.52	2.81	2.11	3.37	3.81	2.98
Hf (ppm)	Min	11227.76	7215.84	9584.61	9476.49	9594.46	9373.72	11698.84	10216.23	11214.48	7059.17
	Max	13754.98	9045.40	10721.79	11331.04	13163.94	13572.06	13493.05	11935.51	11726.02	11038.83
	Mean	12455.75	8156.85	10183.37	10626.08	11708.86	10942.25	12476.87	10880.57	11495.04	8453.61
	2std	1265.12	792.55	570.99	859.31	693.86	1280.88	659.44	592.06	177.05	1069.33
Y (ppm)	Min	815.38	2003.86	351.46	352.21	319.85	436.45	229.46	238.84	661.52	359.95
	Max	2379.40	3898.81	788.56	1016.97	933.61	1100.38	807.69	746.60	953.98	3244.54
	Mean	1418.48	2914.65	593.44	619.39	488.71	740.68	523.71	454.73	801.66	1330.54
	2std	841.17	674.30	222.28	224.47	141.68	219.95	173.25	164.92	111.21	696.54
Total REE (ppm)	Min	712.51	1382.05	260.73	291.06	272.34	347.49	199.19	197.73	528.04	321.14
	Max	1775.21	2546.86	554.33	749.43	671.19	929.17	633.21	549.20	754.53	2477.04
	Mean	1130.58	1962.84	423.66	469.25	395.28	572.94	428.31	360.73	632.26	1013.23
	2std	566.42	414.10	149.43	154.96	98.17	170.71	130.70	117.58	84.42	524.32
Th/U	Min	0.43	1.22	0.69	0.42	0.38	0.23	0.43	0.40	0.45	0.47
	Max	0.79	1.84	0.92	0.86	0.83	0.90	0.60	0.58	0.50	1.79
	Mean	0.58	1.57	0.84	0.65	0.54	0.58	0.53	0.49	0.48	1.07
	2std	0.19	0.26	0.13	0.18	0.08	0.20	0.06	0.07	0.02	0.33
Ce/Nd	Min	6.97	1.90	2.61	2.06	8.94	3.87	13.08	9.37	26.77	7.77
	Max	46.52	5.26	7.24	42.33	36.71	41.66	46.12	33.83	34.37	38.01
	Mean	32.36	2.67	4.16	18.17	25.51	20.96	25.20	20.96	31.16	23.65
	2std	22.04	1.45	2.67	15.71	6.99	14.70	10.12	8.05	2.90	8.72
Dy/Yb	Min	0.17	0.48	0.34	0.22	0.21	0.14	0.22	0.21	0.23	0.18
	Max	0.24	0.55	0.39	0.40	0.28	0.34	0.26	0.27	0.25	0.38
	Mean	0.20	0.51	0.36	0.29	0.24	0.24	0.24	0.24	0.24	0.26
	2std	0.03	0.03	0.03	0.08	0.02	0.06	0.01	0.02	0.01	0.05
Hf/Y	Min	4.72	2.32	12.99	10.91	12.05	10.14	16.08	14.09	12.29	2.26
	Max	16.87	3.71	30.51	31.33	37.04	26.96	57.59	49.97	17.26	22.90
	Mean	11.09	2.89	19.49	19.07	25.63	16.03	26.95	27.62	14.56	8.64
	2std	6.10	0.52	9.59	7.23	6.42	5.30	12.34	12.30	1.89	5.71
Eu/Eu*	Min	0.16	0.13	0.38	0.50	0.30	0.54	0.45	0.35	0.54	0.45
	Max	0.25	0.23	0.44	0.59	0.64	0.70	0.60	0.61	0.59	0.85
	Mean	0.20	0.17	0.42	0.53	0.50	0.61	0.50	0.50	0.56	0.67
	2std	0.05	0.05	0.03	0.03	0.07	0.05	0.04	0.09	0.02	0.09
Ce/Ce*	Min	12.33	4.21	7.52	5.02	38.26	12.78	60.32	44.03	111.13	22.75
	Max	359.97	16.58	31.63	249.46	183.22	217.99	246.73	174.82	151.80	153.19
	Mean	216.68	7.27	15.71	89.46	120.17	97.31	122.02	95.62	134.35	83.66
	2std	181.68	5.23	13.79	92.46	37.85	77.79	61.40	44.94	15.52	38.81
ΔFMQ	Min	0.95	-1.36	-1.28	0.47	-0.62	0.31	-0.13	-0.98	0.83	1.17
	Max	2.30	-0.30	-1.07	1.11	0.75	1.96	0.41	0.01	2.17	3.43
	Mean	1.60	-0.89	-1.21	0.82	0.32	0.92	0.17	-0.28	1.51	2.53
	2std	0.68	0.42	0.12	0.26	0.31	0.58	0.18	0.29	0.47	0.48
Ti-in-zircon (T °C)	Min	685.57	937.06	918.72	674.86	746.88	678.36	780.05	761.13	665.51	723.98
	Max	712.66	1142.69	948.91	785.42	841.84	788.09	827.50	841.08	809.93	852.06
	Mean	698.58	1050.29	933.17	744.64	789.64	736.68	796.62	794.89	732.02	782.77
	2std	13.58	103.89	15.14	39.54	22.20	40.53	17.89	27.67	53.59	27.53

Table 5.3. continued

Region		Bodrum							
Field		Bodrum	Bodrum	Bodrum	Bodrum	Bodrum	Bodrum	Bodrum	Bodrum
Sample		BDR-04-1	BDR-04-2	BDR-05	BDR-06	BDR-07	BDR-08	BDR-09	BDR-10
U-Pb Age (Ma)		10.70	10.40	10.51	10.22	8.97	7.73	8.25	8.81
Ti (ppm)	Min	7.91	7.73	8.69	6.11	9.35	3.30	3.06	8.27
	Max	10.13	48.08	28.24	14.57	17.21	7.49	10.61	13.91
	Mean	8.85	24.56	14.95	7.93	14.67	5.12	5.76	10.44
	2std	0.65	14.45	5.81	2.02	2.25	1.40	1.36	1.58
Hf (ppm)	Min	8395.92	8398.71	7555.04	9437.30	7646.69	9526.22	8048.62	8591.06
	Max	9185.49	10385.90	9938.68	11382.77	8870.14	12628.19	12540.11	9705.60
	Mean	8694.77	9224.63	8416.83	10335.07	8312.06	11030.44	10429.87	9030.30
	2std	248.12	535.30	736.66	595.37	308.45	806.65	869.78	395.42
Y (ppm)	Min	372.96	345.23	683.74	433.89	616.99	472.07	378.19	362.52
	Max	740.84	3918.64	2087.31	3663.41	4304.47	2787.19	3845.05	1186.95
	Mean	573.98	964.27	1156.06	796.10	1344.31	1007.13	1077.03	589.49
	2std	95.12	1001.17	449.55	748.51	881.74	654.47	603.49	270.20
Total REE (ppm)	Min	298.11	260.29	486.76	341.44	400.24	436.06	371.93	287.46
	Max	530.11	2367.70	1398.93	2433.21	2806.74	1941.81	2665.31	775.05
	Mean	425.64	654.04	785.80	578.83	861.18	772.86	863.97	443.74
	2std	61.94	582.06	293.29	479.14	565.46	425.41	424.31	167.10
Th/U	Min	0.48	0.56	0.64	0.39	0.70	0.34	0.34	0.54
	Max	0.64	1.37	1.20	0.91	1.07	0.94	1.62	0.95
	Mean	0.57	0.72	0.94	0.50	0.90	0.56	0.62	0.68
	2std	0.04	0.23	0.19	0.12	0.09	0.16	0.20	0.13
Ce/Nd	Min	7.79	2.70	3.30	3.65	1.99	17.03	13.80	3.80
	Max	17.75	16.48	16.56	20.78	11.24	54.00	53.39	22.22
	Mean	13.74	8.10	8.65	14.08	7.39	34.19	32.24	14.60
	2std	2.70	5.28	5.57	5.17	3.34	12.67	8.82	5.42
Dy/Yb	Min	0.23	0.25	0.28	0.21	0.31	0.14	0.14	0.23
	Max	0.28	0.37	0.37	0.31	0.42	0.28	0.29	0.30
	Mean	0.26	0.31	0.33	0.24	0.36	0.20	0.21	0.25
	2std	0.01	0.04	0.03	0.03	0.03	0.04	0.03	0.02
Hf/Y	Min	11.97	2.14	3.75	2.87	2.06	3.42	2.09	7.38
	Max	22.85	26.62	11.38	24.51	13.11	26.75	29.89	26.48
	Mean	15.58	14.40	8.12	17.13	7.91	13.83	11.77	17.62
	2std	2.97	7.08	2.58	5.76	3.35	6.30	4.94	6.01
Eu/Eu*	Min	0.43	0.32	0.26	0.26	0.08	0.44	0.38	0.28
	Max	0.49	0.49	0.57	0.43	0.22	0.55	0.66	0.40
	Mean	0.47	0.37	0.46	0.33	0.15	0.47	0.48	0.34
	2std	0.02	0.05	0.09	0.05	0.05	0.03	0.05	0.03
Ce/Ce*	Min	31.51	7.95	11.80	14.35	3.45	63.05	57.40	11.99
	Max	80.53	75.54	73.54	96.27	38.78	259.39	266.56	85.96
	Mean	56.15	32.03	33.79	64.99	24.71	163.71	149.85	56.79
	2std	12.18	24.18	24.25	25.59	12.81	69.32	50.56	23.80
ΔFMQ	Min	-0.11	-1.77	-0.99	-0.60	0.14	0.93	1.13	-0.01
	Max	0.41	0.36	0.62	1.64	2.19	2.24	2.52	0.56
	Mean	0.17	-0.63	-0.19	-0.21	0.92	1.48	1.68	0.25
	2std	0.18	0.79	0.55	0.49	0.42	0.36	0.28	0.20
Ti-in-zircon (T °C)	Min	757.54	755.34	766.65	733.35	773.85	679.77	673.61	761.83
	Max	781.85	965.99	896.22	819.72	838.00	752.33	786.52	814.74
	Mean	768.23	861.46	817.64	755.81	819.38	714.91	726.01	784.07
	2std	7.08	78.46	37.67	21.55	18.19	24.02	20.21	14.68

5.1.1.4.1 Trace and Rare Earth Element Compositions of Zircons from the Central Taurides Belt

Within the scope of this study, trace element analyses were conducted on samples collected from various magmatic domains across the Central Taurides region. The results of these analyses are comprehensively presented in Table 5.3.

5.1.1.4.1.1 Konya Volcanic Complex

In the Erenlerdağ–Alacadağ segment of the KVC, the early-stage calc-alkaline magmatic products are well-represented by exposures in the Çukurağıl (~10.7 Ma) and Damlapınar (~10.3–10.2 Ma) prospects. In comparison, core and surface samples obtained from the İnlice region yielded crystallization ages of approximately 9 Ma—values that are consistent within analytical uncertainty—suggesting that magmatic activity at İnlice postdates those of Çukurağıl and Damlapınar.

Zircons separated from these three areas (Çukurağıl, Damlapınar, İnlice) display remarkably consistent trace and rare earth element (REE) signatures. These are derived from basaltic andesite, andesite porphyry, and diorite porphyry samples. On average, the Ti content in zircon ranges from 6.14 to 8.38 ppm, Hf from 9146 to 11119 ppm, Y from 919 to 2201 ppm, and total REE contents span from 733 to 1597 ppm. Notably, two Damlapınar samples (DMLP-01 and DMLP-02) show relatively elevated Ti and suppressed Y concentrations, distinguishing them slightly from the regional trend (Table 5.3).

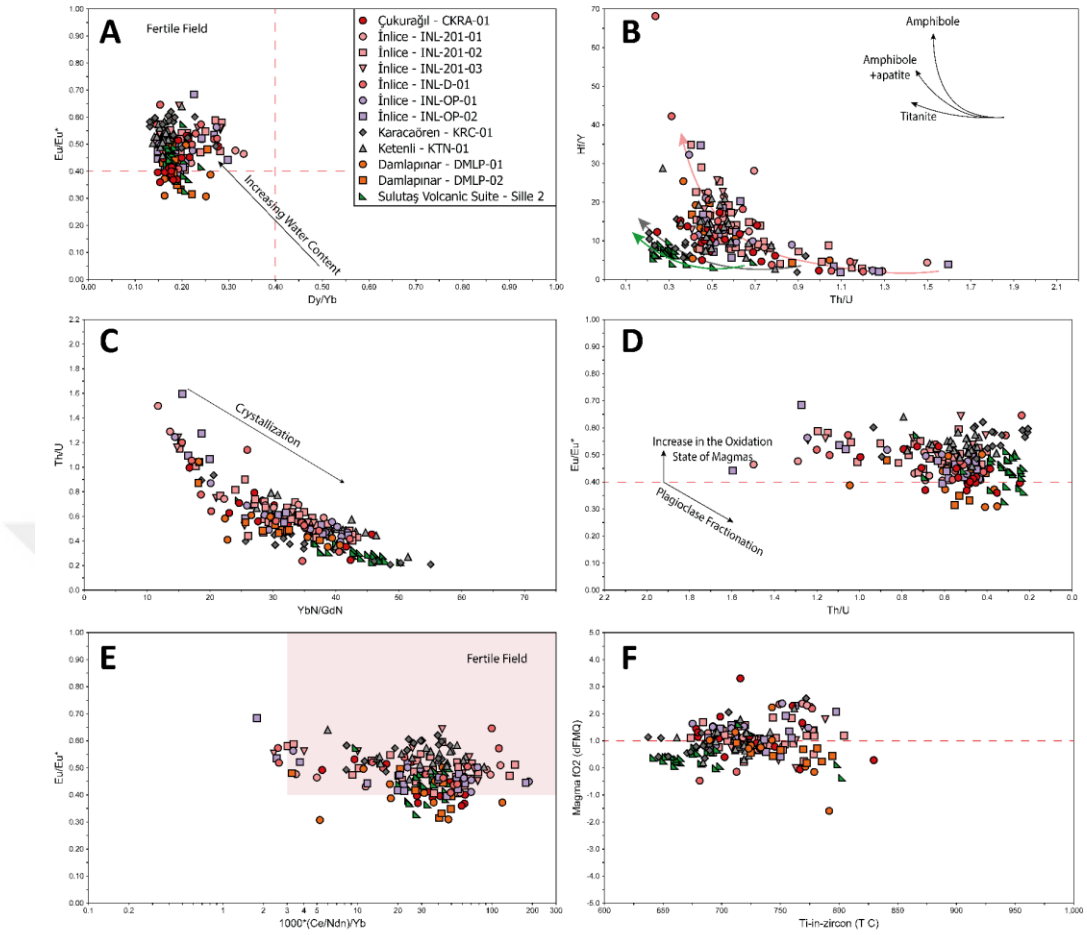


Figure 5.9. Diagrams illustrating the geochemical relationships of zircons analyzed from the Konya region of Central Anatolia. A) Eu/Eu* vs. Dy/Yb, B) Hf/Y vs. Th/U, C) Th/U vs. Yb_N/Gd_N, D) Eu/Eu* vs. Th/U, E) Eu/Eu* vs. $1000\times(Ce/Nd)_n/Yb$, and F) Magma fO_2 (ΔFMQ) vs. Ti-in-zircon temperature (°C).

Zircons from all three locations have high Eu/Eu* (>0.3) and Ce/Nd (>5) ratios—both indicative of high magma oxygen fugacities—while Dy/Yb values remain low (<0.30), likely suggesting amphibole fractionation at the source. Oxygen fugacity values calculated from zircon chemistry (ΔFMQ_{zircon}) are notably lower in the two Damlapınar samples (0.32 and 0.54) compared to the higher values (>0.90) calculated from İnlice and Çukurağıl samples. This disparity may reflect localized variations in magma source or redox evolution during crystallization.

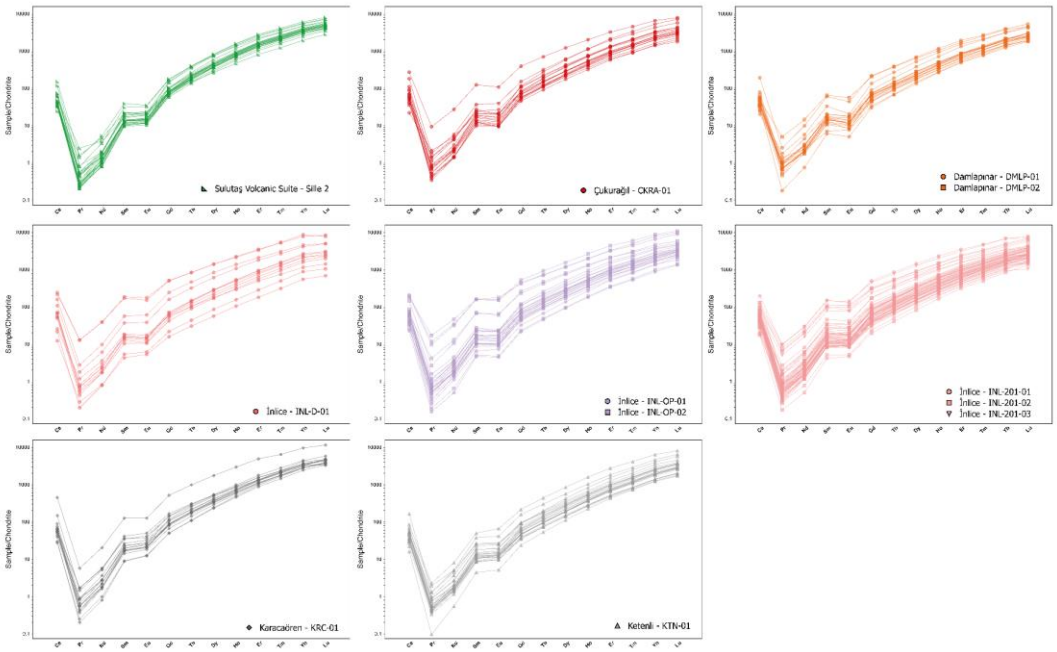


Figure 5.10. Zircon multi-element variation diagrams of the Konya district.

In the İnlice area, zircon ΔFMQ values vary between 0.90 and 1.38, suggesting relatively oxidized magmatic conditions. Trace element trends, including increasing Hf/Y and Eu/Eu* ratios with decreasing Th/U, are consistent with derivation from amphibole-dominated sources, potentially with accessory titanite or apatite (Figure 5.9). Crystallization temperatures calculated from Ti-in-zircon thermometry range between 725°C and 740°C for İnlice and Çukurağıl samples, whereas the Damlapınar samples yielded slightly higher temperatures of 753°C and 759°C.

In the southern segment of the İnlice district, zircons from the Karacaören prospect (4.8 Ma), hosted in hydrothermally altered andesite porphyry, yielded lower average Ti (4.18 ppm) but elevated Hf (12231 ppm) and Y (3193 ppm) contents, with a total REE content of 2316 ppm. The Eu/Eu* (0.52), Dy/Yb (0.19), and Ce/Nd (32.17) ratios are comparable to those of İnlice samples, and ΔFMQ values are likewise consistent (avg. ~0.95). However, Karacaören zircons exhibit markedly lower Th/U

and Hf/Y ratios, suggesting increased influence from amphibole ± titanite ± apatite fractionation. The average crystallization temperature from KRC-01 zircons is calculated as 690°C. Zircon population of KTN-01 mirrors that of Karacaören in most geochemical parameters but displays a wider range in trace element concentrations and fO_2 values. Notably, Hf/Y and Th/U ratios are elevated, and a minor subset of analyses show anomalously low Eu/Eu* values, suggesting either outlier behavior or a deviation toward a different fractionation path.

The Sille-02 sample, which belongs to the older Sulutaş Volcanic Suite (SVS) of the KVC exhibits distinctive geochemical characteristics. This unit displays only a slight increase in Hf/Y ratios (average 6.82) with decreasing Th/U values (average 0.33), which suggests that titanite, rather than amphibole, was the dominant fractionating phase during magma evolution (Figure 5.9). The Eu/Eu* ratio in Sille-02 (average 0.44) is broadly comparable to those observed in other samples from the KVC. Among all analyzed samples, Sille-02 the zircons show the highest Ce/Ce* value (353.88), indicating notable enrichment in cerium and potentially pointing to oxidizing magmatic conditions during crystallization. With an average zircon crystallization temperature of approximately 684.13 °C, Sille-02 records the lowest crystallization temperature within the region, supporting the interpretation of a more evolved magma crystallized at lower temperatures. Furthermore, the pronounced increase in Yb_N/Gd_N ratios with decreasing Th/U implies derivation from a highly evolved magmatic system (Figure 5.9). The multi-element diagram reveals that while Sille-02 shares a broadly similar pattern with other units from the region, it is characterized by notably low concentrations of light rare earth elements (LREEs) coupled with relatively elevated heavy rare earth elements (HREEs), as well as a slight negative Eu anomaly — a signature consistent with plagioclase fractionation and magmatic differentiation (Figure 5.10).

5.1.1.4.1.2 Karacadağ, Melendiz, and Develidağ Volcanics

Moving eastward into the Melendiz–Karacadağ–Develidağ region, magmatic rocks span from 5.6 to 1.9 Ma. Among these, Develidağ andesitic porphyry zircons (the oldest in this subset) have Eu/Eu* ratios between 0.25–0.45 (avg. 0.31), Dy/Yb from 0.21 to 0.38, and Ce/Nd from 3.1 to 28.6 (avg. 10.87). While a few ΔFMQ_{zircon} values exceed +1, the majority are significantly lower, with an average of just 0.12. Increasing Hf/Y ratios with declining Th/U again suggest amphibole ± titanite ± apatite fractionation.

Trace element chemistry of zircons from a 4.8 Ma andesite porphyry from the Karacadağ caldera, Yeşilyurt, resemble those from Develidağ but with narrower compositional ranges. YLS-01 zircons have average contents of 16.38 ppm Ti, 9623 ppm Hf, 787 ppm Y, and a total REE conten of 575 ppm. Eu/Eu* (0.13–0.23), Dy/Yb (0.48–0.55), and Ce/Nd (1.90–5.26) values imply low oxygen fugacity and moderate degrees of crystal fractionation, and ΔFMQ_{zircon} values range from –1.36 to –0.30 (avg. –0.89), the lowest measured values in this study. Average zircon crystallization temperatures reach up to 1050°C.

Among the younger Süleymanpınarı (3.9 Ma) and Çömlekçi (1.9 Ma) samples—both located within the Melendiz Stratovolcano—zircons from the former exhibit Ti content of 9.76 ppm and moderate Hf, Y, and REE values. Trace element ratios (Eu/Eu* = 0.29–0.59, Dy/Yb = 0.13–0.25, Ce/Nd = 4–40) imply derivation from amphibole-dominated sources. ΔFMQ_{zircon} values average 0.70, and crystallization temperatures peak at 770°C.

Zircons from the Çömlekçi dacite (CML-01) and two other samples (496762 and 496918) to the northwest, represent the youngest dated sample in this region, closely resemble Süleymanpınarı in all major geochemical parameters. With Eu/Eu*, Dy/Yb, and Ce/Nd ratios aligned, and ΔFMQ values averaging 0.74, these samples

again indicate relatively high magma fO_2 conditions and the role of amphibole fractionation for these younger group of samples from the Central Taurides sector of the belt. The calculated average crystallization temperature is in the range 738–748 °C.

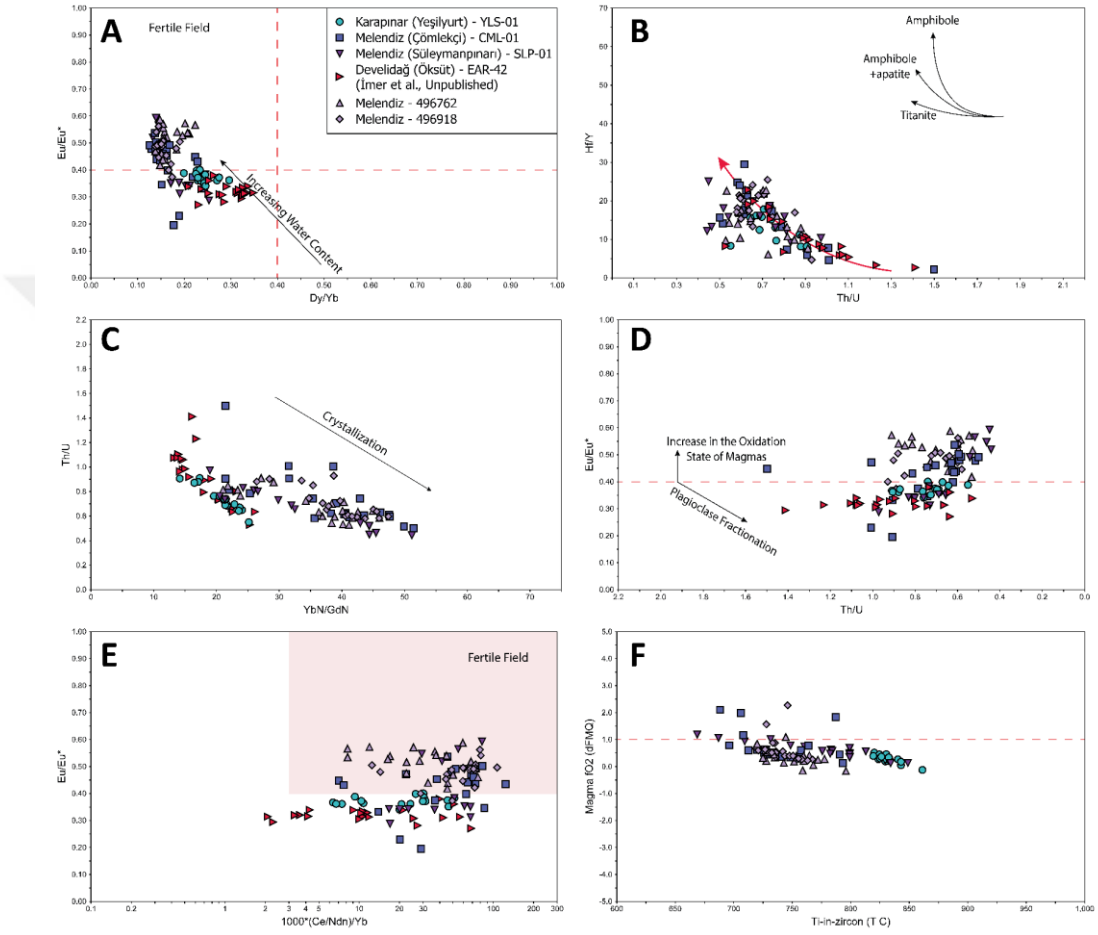


Figure 5.11. Diagrams illustrating the geochemical relationships of zircons analyzed from the Karacadağ-Melendiz-Develidağ area. A) Eu/Eu* vs. Dy/Yb, B) Hf/Y vs. Th/U, C) Th/U vs. Yb_N/Gd_N, D) Eu/Eu* vs. Th/U, E) Eu/Eu* vs. $1000\times(Ce/Nd)_n/Yb$, and F) Magma fO_2 (ΔFMQ) vs. Ti-in-zircon temperature (°C).

The Central Taurides samples represent a crystallization trend with the oldest Öksüt sample (~5.5 Ma; A. İmer, unpublished data) being the most primitive while the

youngest Melendiz samples being the most evolved (Figure 5.11). The magmatic fertility parameters such as magmatic water content and oxidation state appear to become more favorable in terms of formation of porphyry-style mineralization as the magmatism develops (Figure 5.11). All samples have more or less similar multi-element patterns with (Figure 5.12).

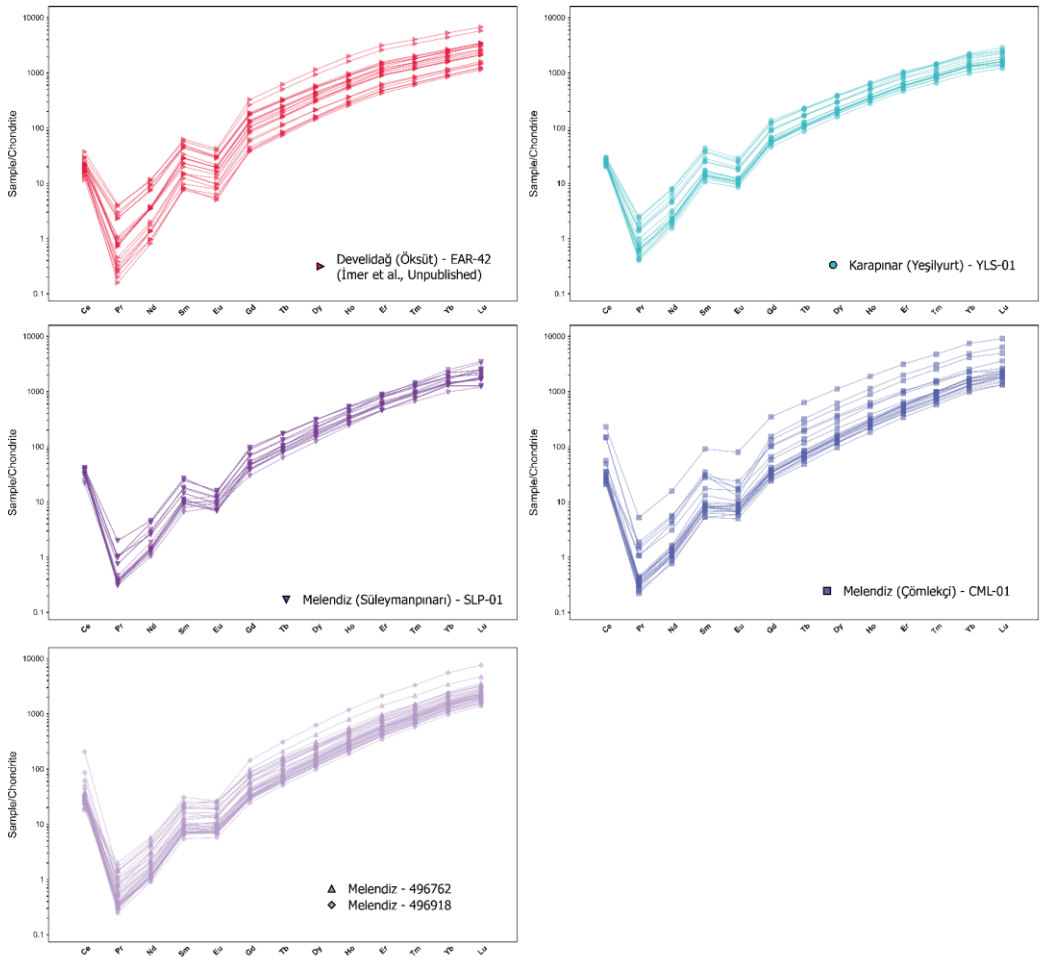


Figure 5.12. Zircon multi-element variation diagrams of volcanic and sub-volcanic rocks from the Karacadağ-Melendiz-Develidağ region.

Zircon trace element data is also plotted in various geotectonic diagrams to characterize the magmatic processes, melt evolution, and tectonomagmatic

environments, as well as to evaluate their oxidation states and water contents. When several trace element ratios (such as Nb/Hf vs Th/U, and U/Yb vs Nb/Yb) are plotted against each other, their trends can provide insight into the melt composition, fractionation, zircon source, and possibly even magmatic fertility.

5.1.1.4.2 Trace and Rare Earth Element Geochemistry of Zircons from Western Anatolia

Within the scope of this study, trace element analyses were conducted on samples collected from various magmatic domains across the Western Anatolia region. The results of these analyses are comprehensively presented in Table 5.3

5.1.1.4.2.1 Biga Peninsula

Zircon crystals extracted from two distinct granodioritic porphyry phases of the ~25 Ma Balya porphyry system were subjected to detailed trace and rare earth element analysis. The average Ti concentrations measured in zircons from samples BLY-01 and BLY-02 are 4.72 ppm and 4.05 ppm, respectively. Their corresponding Hf contents are 11,995 ppm and 11,685 ppm, while Y contents reach 1201 ppm and 1432 ppm. Total rare earth element concentrations (ΣREE) are also notably high, with values of 12,965 ppm and 12,858 ppm for BLY-01 and BLY-02, respectively (Table 5.3).

From a metallogenic perspective, these zircons exhibit trace element signatures considered favorable for porphyry fertility. Both samples yielded relatively elevated Eu/Eu* ratios (>0.5; 0.51 and 0.53), high Ce/Nd values (>30; 32.9 and 32.2), and low Dy/Yb ratios (<0.30; 0.18 and 0.16; Figure 5.13). These geochemical markers collectively indicate that the magmatic system was oxidized during zircon

crystallization which is one of the key conditions often associated with porphyry Cu-Au fertility.

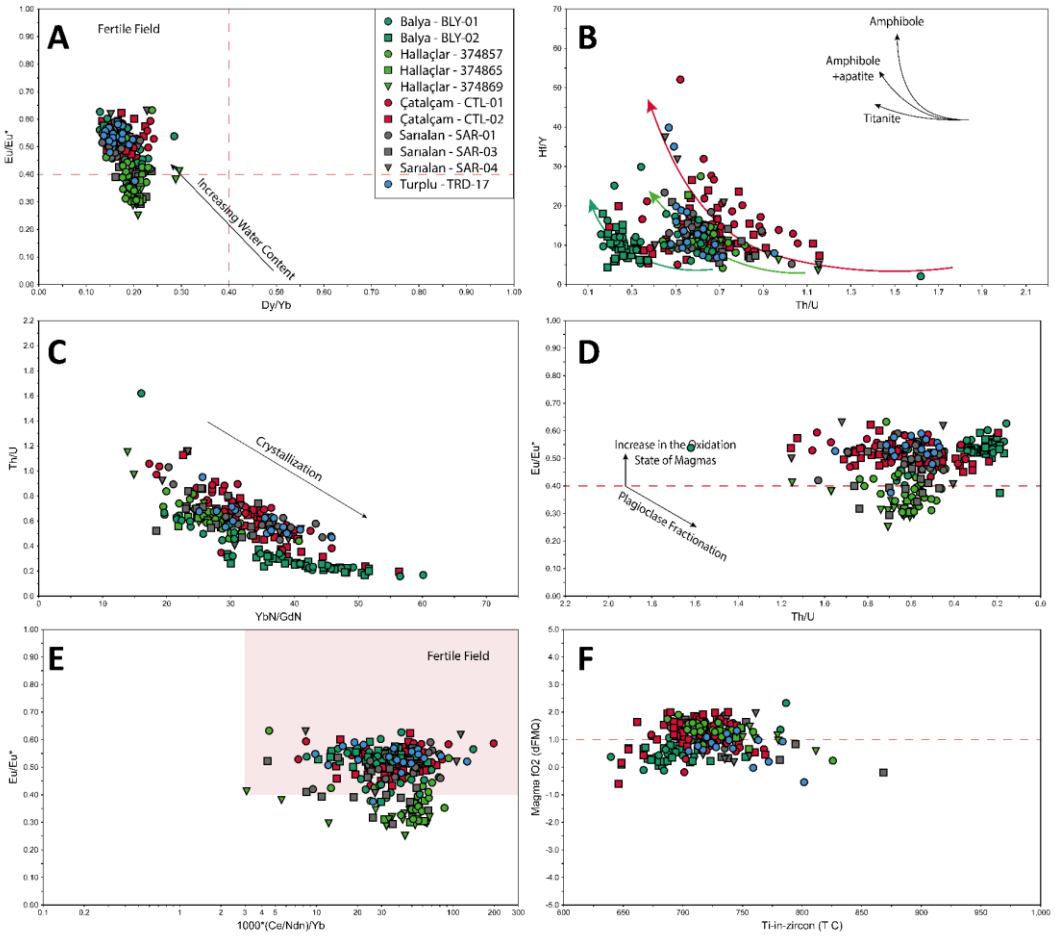


Figure 5.13. Diagrams illustrating the geochemical relationships of zircons analyzed from the Biga Peninsula. A) Eu/Eu* vs. Dy/Yb, B) Hf/Y vs. Th/U, C) Th/U vs. Yb_N/Gd_N, D) Eu/Eu* vs. Th/U, E) Eu/Eu* vs. $1000\times(Ce/Nd)_n/Yb$, and F) Magma fO_2 (ΔFMQ) vs. Ti-in-zircon temperature (°C).

The calculated ΔFMQ_{zircon} values further support this interpretation. For BLY-01, ΔFMQ ranges from -0.12 to 2.33, with an average of ~1.00. BLY-02 yielded slightly lower but still elevated values, ranging from 0.05 to 0.99 (average ~0.50; Figure 5.13). When examining trends between Th/U ratios and Hf/Y or Eu/Eu* values, it becomes apparent that the parental magmas of both porphyry phases underwent

fractionation dominated by amphibole, with possible involvement of accessory titanite ± apatite (Figure 5.13). The similarity in thermal histories is reflected in their calculated zircon crystallization temperatures, which are closely aligned at 706°C for BLY-01 and 695°C for BLY-02 (Table 5.3).

In contrast, a younger volcanic unit (22.7–23.2 Ma Hallaçlar volcanics) also sampled from the Balya region, reveals a somewhat different geochemical fingerprint. Zircons from this sample have higher average Ti contents (5.56-7.53 ppm), comparable Hf concentrations (11717-12177 ppm), and Y contents of 952-1175 ppm (Table 5.3). However, they display significantly lower Eu/Eu* ratios (averages between 0.32 and 0.39), suggesting relatively more pronounced plagioclase fractionation relative to the mineralized porphyritic intrusions. Interestingly, the Ce/Nd (averages between 29.0 and 35.4) and Dy/Yb (averages of 0.21, 0.19, and 0.22) values are similar to zircons of the Balya porphyry intrusions, implying a degree of geochemical continuity between the two systems. The ΔFMQ_{zircon} values, which range from 1.00 to 0.50 in the Balya porphyry intrusions and 1.21, 1.35, and 1.20, remain even higher and consistent with an oxidized magmatic environment (Figure 5.13). The observed decrease in Eu/Eu* with declining Th/U values is indicative of low degree effect of plagioclase-dominated fractionation in the Hallaçlar units (Figure 5.13), whereas the Eu/Eu* ratios in the Balya porphyry remain stable as Th/U decreases (Figure 5.13). The multi-element diagrams of the zircons from Hallaçlar units have more evident negative Eu anomaly further supporting the evidence of plagioclase fractionation (Figure 5.14). The average crystallization temperature calculated for the three samples are between 721°C and 750°C, slightly higher than the porphyritic intrusions (Table 5.3).

Zircons from two additional volcanic centers (Turplu and Sarıalan) located nearby Balya were analyzed to further evaluate the geochemical evolution of magmatism in this district. These centers, which show both spatial and temporal affinity with the

Hallaçlar volcanics, host both porphyry Cu-Mo-Au (Turplu) and HS epithermal Au (Sarıalan) mineralization and are slightly younger in age; dated at 22.14 Ma (for Turplu granodiorite) and between 22.16–22.78 Ma for Sarıalan andesitic porphyry and andesitic agglomerate units. Despite their proximity, the zircon trace element compositions are notable different compared to zircons from Hallaçlar volcanic units near Balya.

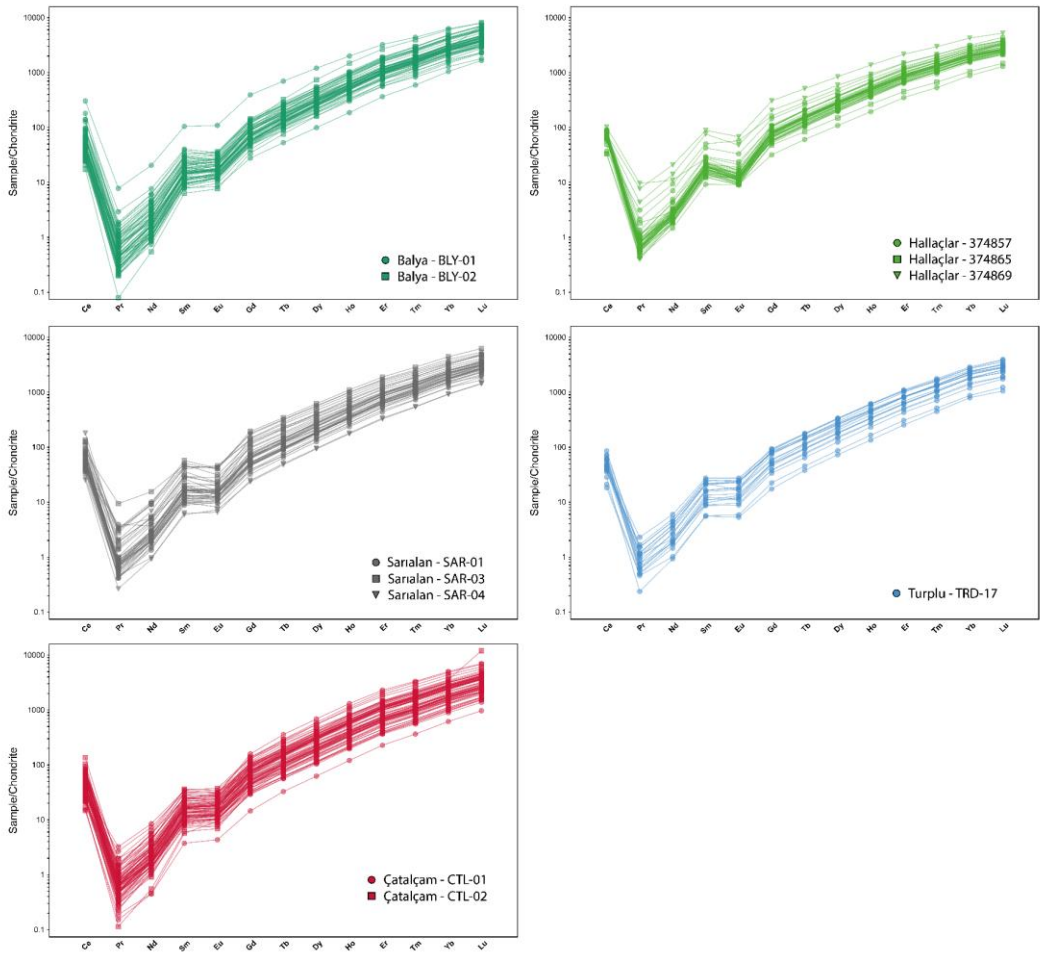


Figure 5.14. Zircon multi-element variation diagrams of the Oligo-Miocene igneous rocks from the Biga Peninsula.

The average Ti content of zircon grains from the Turplu sample (TRD-17) is 6.58 ppm, while the Sarıalan samples display a wider range of Ti concentrations, spanning

between 5.01 and 7.00 ppm (Table 5.3). Although both regions present Th/U ratios comparable to those of Hallaçlar (0.59 for Turplu, and between 0.62 and 0.65 for Sarıalan), their compositions notably diverge from the Balya North porphyry samples (Table 5.3). Additionally, Dy/Yb ratios remain below 0.20 across both Turplu and Sarıalan, supporting the interpretation of low-pressure, amphibole-dominated fractionation regimes.

When examining Eu/Eu* values—an indicator often tied to plagioclase involvement in magma differentiation—both sites exhibit slightly higher averages than Hallaçlar. Turplu zircons yielded a mean Eu/Eu* of 0.54, while Sarıalan zircons fall between 0.41 and 0.43. These values align more closely with those obtained from the fertile Balya host porphyry intrusions (Table 5.3). Multi-element diagrams further reinforce this contrast. Hallaçlar samples display a more pronounced negative Eu anomaly, pointing to stronger plagioclase control during crystallization (Figure 5.14).

Among the Sarıalan samples, the oldest sample (SAR-02; 22.78 Ma) exhibits partial geochemical overlap with Hallaçlar zircons. However, younger Sarıalan samples progressively shift toward patterns more closely resembling the zircons representing the Balya porphyry system. While increasing Hf/Y ratios with decreasing Th/U reflect a similar fractionation path to that seen in Balya North, the overall evolutionary trajectory appears more similar to Hallaçlar. This observation suggests that amphibole-dominated fractionation is a common thread across these magmatic systems, yet Balya North represents a more evolved magmatic end-member in the regional context (Figure 5.13).

The ΔFMQ_{zircon} values also reflect subtle differences across the sites. For the Turplu sample, ΔFMQ_{zircon} values range from -0.54 to 1.33, with an average of 0.69. In Sarıalan, average ΔFMQ_{zircon} values range between 0.75 and 1.16 (Table 5.3), again indicating generally high magmatic oxygen fugacities consistent with porphyry fertility models.

Zircon crystallization temperatures are slightly elevated relative to those of Balya porphyry intrusions. The average crystallization temperature for Turplu zircons is approximately 737°C, while Sarıalan samples yielded zircon crystallization temperatures in the range of ~714–737°C. These thermal conditions are comparable to those recorded in Hallaçlar, suggesting that while trace element trends may diverge, the crystallization conditions remained broadly consistent across these centers (Table 5.3).

Further south, in the Çatalçam region, one andesitic (CTL-01) and one basaltic andesite porphyries (CTL-02) dated to ~20 Ma yielded average zircon Ti concentrations of 5.60 ppm and 5.02 ppm, with corresponding Hf contents of 11,008 ppm and 11,739 ppm, and Y values of 808 ppm and 1137 ppm, respectively (Table 5.3). These samples exhibit similar fertility characteristics with Balya porphyry intrusions, including elevated Eu/Eu* values (0.53 and 0.51), high Ce/Nd ratios (~25.7), and Dy/Yb ratios <0.30 (Figure 5.13).

Their oxidized nature is also reflected in slightly higher average ΔFMQ_{zircon} values compared to Balya, at 1.11 and 1.25 (Figure 5.13, Table 5.3). Hf/Y ratios tend to increase with declining Th/U, and a parallel trend between Th/U and Eu/Eu* suggests that the magmas underwent amphibole-dominated fractionation (Figure 5.13). The average zircon crystallization temperatures for the Çatalçam porphyries are calculated as 724°C (CTL-01) and 709°C (CTL-02), again falling within the thermally moderate range typical for fertile arc-related magmatic systems (Table 5.3).

5.1.1.4.2.2 Kütahya-Simav District

Zircon samples analyzed from a series of magmatic units along the Sındırgı–Simav corridor revealed a distinct southward younging trend in magmatic activity,

beginning in the north at Sındırgı/Kızıltepe and continuing toward the Pınarbaşı porphyry Cu-Mo prospect near Simav in the south, and lastly the Baklan Granitoid at the southeastern tip of the Kütahya-Simav region. Three volcanic and volcaniclastic units from the Sındırgı region (samples SIN-01, SIN-02, and SIN-03), which are broadly coeval with the ~20.1–19.8 Ma Çatalçam magmatism, yielded average zircon Ti concentrations of 2.91, 3.76, and 6.01 ppm, respectively. Corresponding Hf contents are 11,834, 11,897, and 10,863 ppm, Y contents are 1582, 1304, and 1497 ppm, while ∑REE abundances are measured at 1153, 986, and 1061 ppm (Table 5.3).

Immediately following the Sındırgı volcanic activity, the region was intruded by the Eğrigöz Granitoid (ca. 19.5–19.1 Ma), from which three granitoid samples (EGR-01, EGR-02, and EGR-03) were analyzed. Zircons from these samples yielded average Ti concentrations of 5.80, 6.32, and 5.43 ppm, Hf contents of 10,568, 9745, and 9989 ppm, Y contents of 1378, 1637, and 1490 ppm, and ∑REE contents of 1037, 1110, and 1038 ppm, respectively (Table 5.3).

Despite some analytical outliers, zircons from both the Sındırgı and Eğrigöz samples generally display low Eu/Eu* (<0.40) and Dy/Yb (<0.30) ratios, alongside a wide variability in Ce/Nd (ranging from ~2 to 40), indicating significant heterogeneity in light REE enrichment (Figure 5.15). The calculated oxygen fugacity values (ΔFMQ_{zircon}) for these samples are mostly <1. For the Eğrigöz samples, average ΔFMQ values range from 0.28 to 0.60, while those from the Sındırgı/Kızıltepe volcanics span a broader and generally lower range from –0.78 to 0.46 (Table 5.3). The Baklan Granitoid displays different zircon geochemical characteristics compared to the Sındırgı and Eğrigöz samples despite some compositional overlap. The Ti content of the BKL-01 have an average of 6.28 ppm which is comparable with the most of the samples (Table 5.3). Similar to Pınarbaşı, high Ce/Nd (32.50), and low Dy/Yb (0.17) ratios of the Baklan Granitoid deviates from the barren

Eğrigöz and Sındırgı samples. The average Eu/Eu* ratio (0.45) appears to be the highest among the samples from Kütahya-Simav district.

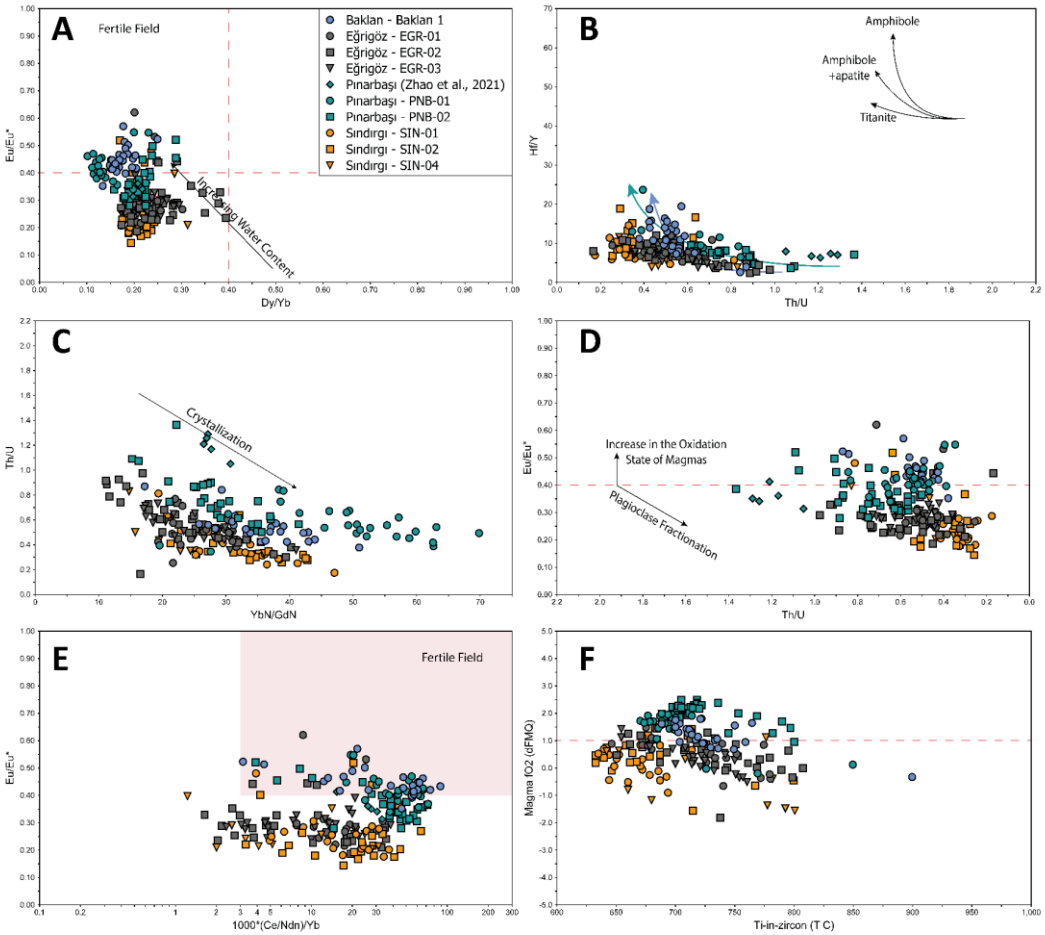


Figure 5.15. Diagrams illustrating the geochemical relationships of zircons analyzed from the Kütahya-Simav district. A) Eu/Eu* vs. Dy/Yb, B) Hf/Y vs. Th/U, C) Th/U vs. Yb_N/Gd_N, D) Eu/Eu* vs. Th/U, E) Eu/Eu* vs. $1000\times(Ce/Nd)_n/Yb$, and F) Magma fO_2 (ΔFMQ) vs. Ti-in-zircon temperature (°C).

When plotted against decreasing Th/U, both Hf/Y and Eu/Eu* ratios show weakly increasing and decreasing trends, respectively, suggesting that the Sındırgı volcanic rocks and the contemporaneous Eğrigöz Granitoid crystallized from magmas that underwent plagioclase-dominated fractionation (Figure 5.15). Multi-element

diagrams of these samples also support the plagioclase-dominated fractionation (Figure 5.16). Crystallization temperatures for zircons from the Sındırgı volcanics fall within a relatively lower temperature range of 667–713°C, whereas those from the Eğrigöz Granitoids yielded slightly higher values of 719–729°C (Table 5.3).

Further south in this magmatic corridor, two samples (PNB-01 and PNB-02) from the Pınarbaşı porphyry Cu-Mo prospect (~18 Ma) were analyzed. Zircon grains from these samples have average Ti contents of 4.61 and 5.74 ppm; Hf concentrations of 10,782 and 10,256 ppm; Y contents of 1148 and 1409 ppm; and ∑REE abundances of 1052 and 1060 ppm (Table 5.3).

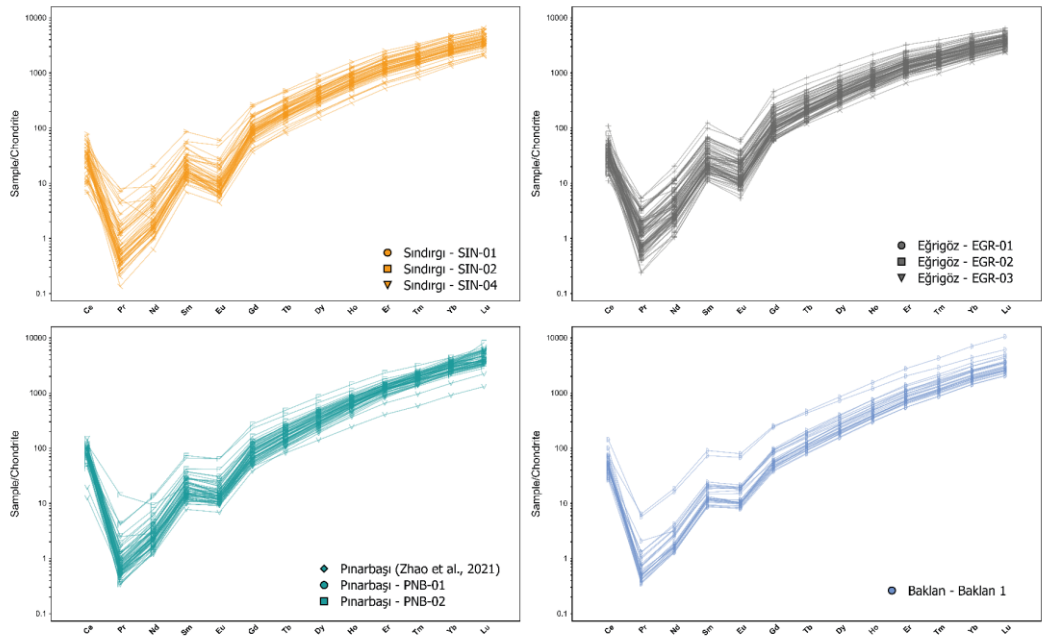


Figure 5.16. Zircon multi-element variation diagrams of Middle Miocene igneous rocks from the Kütahya-Simav region.

The Pınarbaşı zircons are geochemically distinct from both the Simav volcanic suite and the Eğrigöz Granitoid as these are characterized by relatively elevated Eu/Eu* values (>0.30; averaging 0.37 and 0.42) and low Dy/Yb values (<0.30; averaging

0.14 and 0.21). Their Ce/Nd ratios are generally >30, pointing to the oxidized nature of their source magmas (Figure 5.15). Importantly, these also exhibit notably higher ΔFMQ_{zircon} values (averaging 1.51 and 2.04), confirming the significantly more oxidizing nature of their source magmas compared to their northern counterparts (Figure 5.15).

Although Hf/Y ratios increase only marginally with decreasing Th/U, Th/U vs. Eu/Eu* plots clearly differentiate the Pınarbaşı zircons from those of Simav and Eğrigöz. These trends suggest that the Pınarbaşı magmas were likely derived from amphibole ± titanite ± apatite-dominated sources rather than plagioclase-dominated ones (Figure 5.15). Zircon crystallization temperatures calculated for PNB-01 and PNB-02 average 701°C and 723°C, respectively (Table 5.3), consistent with moderate-temperature, moderately oxidized magmatic systems commonly associated with porphyry mineralization. Similarly, the Baklan Granitoid zircons have increasing Hf/Y against decreasing Th/U indicating amphibole-dominated fractionation (Figure 5.15). The crystallization temperatures calculated through Ti-in-zircon thermometry suggest similar but slightly higher crystallization temperatures (727°C) compared to the Pınarbaşı samples (Figure 5.15).

5.1.1.4.2.3 Uşak-Manisa District

In the Uşak–Manisa region, two distinct magmatic systems—the Kışladağ and Sayacık porphyry Au systems and the Salihli Granitoid—formed almost contemporaneously at about 15 Ma. While the zircon geochemistry of the intrusions that host the Kışladağ porphyry Au system and the surrounding Emirlitepe volcanics has already been documented in detail by Paolillo et al. (2021), this study focuses on the zircon trace and rare earth element (REE) characteristics of the nearby Sayacık porphyry Au prospect, for which new analytical data have been obtained.

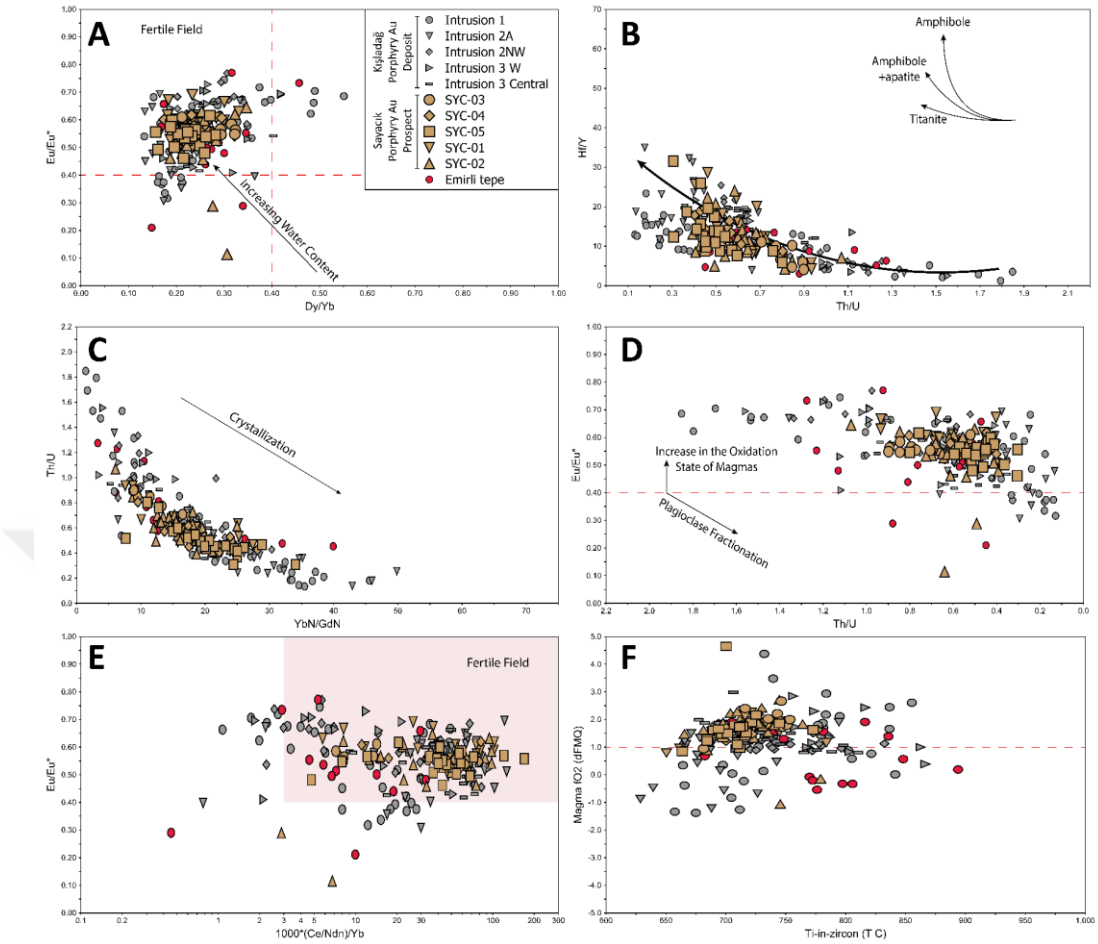


Figure 5.17. Diagrams illustrating the geochemical relationships of zircons analyzed from the Kışladağ and Sayacık porphyry Au systems in Uşak district. A) Eu/Eu* vs. Dy/Yb, B) Hf/Y vs. Th/U, C) Th/U vs. Yb_N/Gd_N, D) Eu/Eu* vs. Th/U, E) Eu/Eu* vs. $1000\times(Ce/Nd)_n/Yb$, and F) Magma fO_2 (ΔFMQ) vs. Ti-in-zircon temperature (°C).

Zircons analyzed from five different Sayacık drill core samples yielded average Ti concentrations ranging between 4.78 and 6.17 ppm, Hf contents between 9730 and 11,087 ppm, Y contents from 813 to 1294 ppm, and ∑REE concentrations from 641 to 960 ppm (Table 5.3). Among these, the oldest sample (SYC-03; 14.27 Ma) is notably distinct, with comparatively lower Hf and ∑REE contents but higher Ti and Y compositions than other samples from Sayacık. Calculated zircon crystallization

temperatures for the Sayacık samples are within the range 709–732°C, with the highest temperatures again associated with the oldest sample, SYC-03 (Table 5.3).

Despite being sampled from separate systems, the zircons from the contemporaneous Kışladağ and Sayacık porphyry Au deposits exhibit strikingly similar geochemical characteristics. Both display elevated Eu/Eu* ratios (>0.40), with Sayacık zircons consistently returning values between 0.55 and 0.58 (Figure 5.17). While Sayacık zircons occupy a narrow compositional range in terms of Dy/Yb and Ce/Nd ratios, Kışladağ zircons span much broader intervals—Dy/Yb ranging from 0.15 to 0.55 and Ce/Nd from 1 to 40—suggesting more geochemical heterogeneity. Nevertheless, the mean Dy/Yb and Ce/Nd ratios from both systems are closely correlated (Table 5.3).

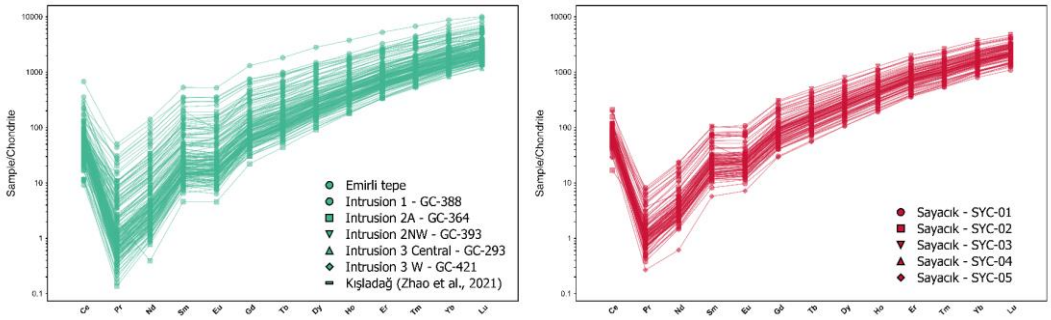


Figure 5.18. Zircon multi-element variation diagrams of igneous rock samples from the Uşak district.

Similarly, oxygen fugacity (ΔFMQ) values derived from Kışladağ zircons vary substantially, from –1.4 to as high as +4.5, although this wide range is largely influenced by two high-value outliers (Figure 5.17). In contrast, ΔFMQ values from the five Sayacık samples fall within a narrower and more consistent range of 1.55–2.00, suggesting more stable redox conditions during evolution of the Sayacık magmatic system (Figure 5.17). Th/U versus Hf/Y and Eu/Eu* plots for both systems

point to magma sources dominated by amphibole fractionation, with possible contributions from titanite ± apatite (Figure 5.17).

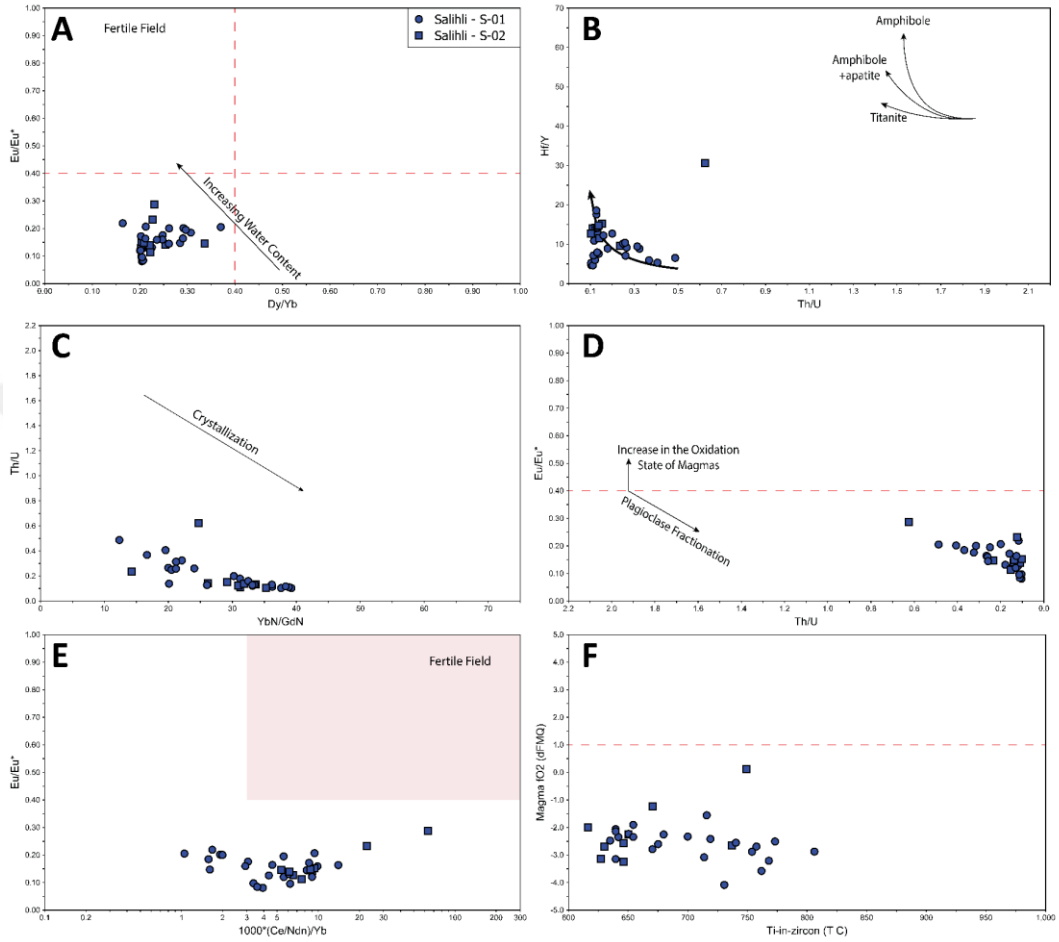


Figure 5.19. Diagrams illustrating the geochemical relationships of zircons analyzed from the Salihli Pluton. A) Eu/Eu* vs. Dy/Yb, B) Hf/Y vs. Th/U, C) Th/U vs. Yb_N/Gd_N, D) Eu/Eu* vs. Th/U, E) Eu/Eu* vs. $1000\times(Ce/Nd)_n/Yb$, and F) Magma fO_2 (ΔFMQ) vs. Ti-in-zircon temperature (°C).

The multi-element diagrams of the Kışladağ porphyry Au deposit and the Sayacık porphyry Au prospect also appear to be similar with each other with zircons from both magmatic systems showing slight negative Eu anomalies (Figure 5.18). One significant observation from this diagram is that the first intrusive phase (INT-1) in

Kışladağ display more fractionation patterns in comparison to the consecutive phases (Int-2 and Int-3; Figure 5.18). The Sayacık zircons display similar pattern with the Int-2 and Int-3 rather than Int-1 (Figure 5.18).

Two granitoid samples from the Salihli Granitoid (dated at 14.8 Ma and 11.78 Ma) show markedly different zircon compositions from those of Kışladağ and Sayacık. Samples S-01 and S-02 have average Ti concentrations of 4.55 and 2.27 ppm, Hf concentrations of 12,725 and 13,378 ppm, Y contents of 1405 and 1088 ppm, and ∑REE contents of 1016 and 780 ppm, respectively. These zircons stand out within the entire dataset due to their exceptionally low Eu/Eu* (mean values of 0.15 and 0.18) and Th/U (0.12 and 0.19) ratios, coupled with their substantially low calculated ΔFMQ values (–2.71 and –2.76), indicating highly reduced and evolved magmatic conditions (Figure 5.19, Table 5.3).

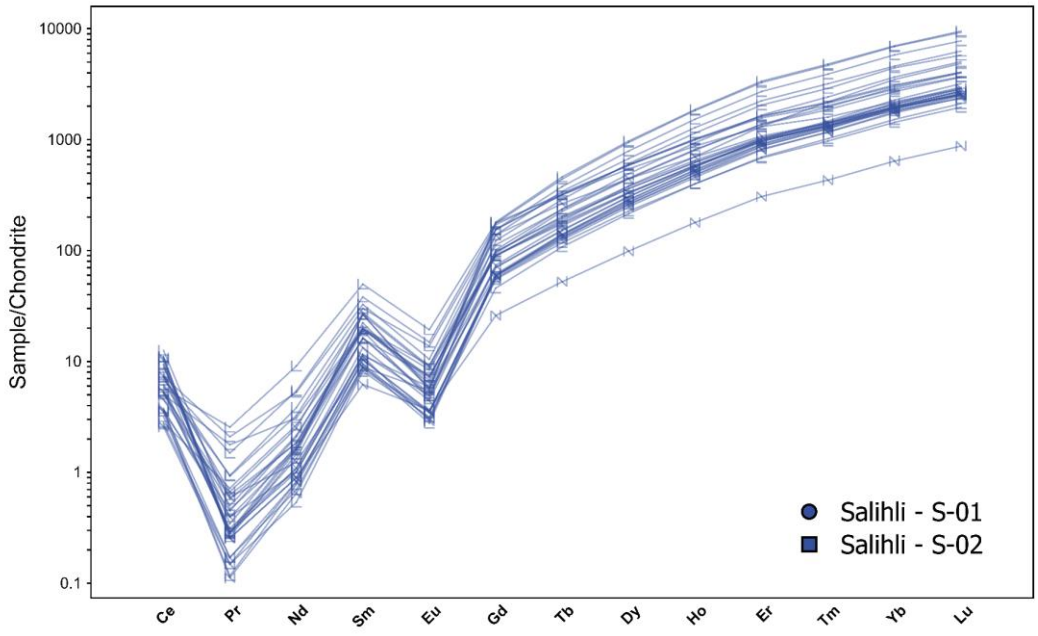


Figure 5.20. Zircon multi-element variation diagrams of granitic rocks of the Salihli Granitoid.

The Dy/Yb ratios in Salihli zircons range from 0.14 to 0.36, while Ce/Nd spans from 0.8 to 16. On the Eu/Eu* versus Th/U plot, two distinct trends are apparent; one showing an increase in Eu/Eu* above a Th/U threshold of ~0.3, and another showing a decrease (Figure 5.19D). These divergent trends likely reflect the involvement of at least two distinct magmatic sources—one dominated by amphibole fractionation and another by plagioclase. Crystallization temperatures calculated from zircon compositions for the S-01 and S-02 samples are 693°C and 642°C, respectively, placing the Salihli magmatism among the lowest temperature systems investigated in this study (Table 5.3).

The multi-element variation diagram of the zircons from the Salihli pluton have the most erratic pattern compared to the rest of the dataset having highly depleted LREE and evident negative Eu anomaly (Figure 5.20).

5.1.1.4.2.4 Kırka-Afyon-Isparta District

The earliest manifestations of magmatic activity in the Kırka–Afyon–Isparta region are recorded in the Kırka area, marking the onset of a magmatic evolution that progressively youngs toward the Afyon Volcanic Complex (~12 Ma) and subsequently to the Isparta region (~2.6 Ma). Although zircon trace element data from this region remain limited, a single zircon grain from the mafic KRK-01-2 sample, collected in the Kırka area, provides insightful, albeit statistically sparse, constraints on the geochemical characteristics of the earliest magmatic products in this sector.

The KRK-01-2 zircon displays notably low Ti concentrations (4.16 ppm), yet it stands out due to its remarkably high Hf content (12,456 ppm), which is among the highest recorded in this study (Table 5.3). Such elevated Hf levels often point to a highly evolved, silica-rich melt from which the zircon crystallized. The same zircon

is characterized by a distinctly low Eu/Eu* ratio (0.20), suggesting substantial plagioclase fractionation prior to zircon crystallization. This interpretation is further supported by a coherent trend of decreasing Eu/Eu* with decreasing Th/U ratios (Figure 5.21), which is indicative of progressive plagioclase removal from the melt.

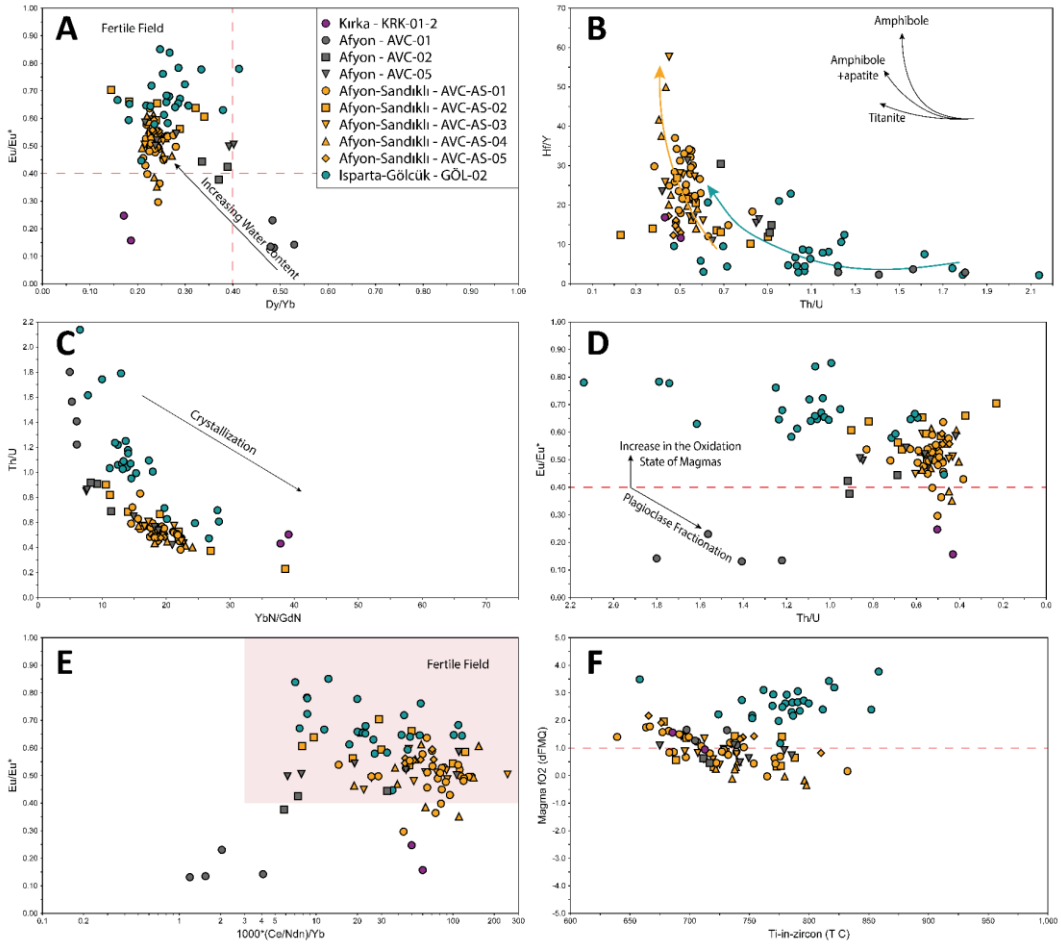


Figure 5.21. Diagrams illustrating the geochemical relationships of zircons analyzed from the Kırka-Afyon-Isparta region. A) Eu/Eu* vs. Dy/Yb, B) Hf/Y vs. Th/U, C) Th/U vs. Yb_N/Gd_N, D) Eu/Eu* vs. Th/U, E) Eu/Eu* vs. $1000\times(Ce/Nd)_n/Yb$, and F) Magma fO_2 (ΔFMQ) vs. Ti-in-zircon temperature (°C).

Multi-element patterns (Figure 5.22) reinforce this interpretation, as the trace element distribution reveals relatively low LREE concentrations compared to

HREEs, alongside a pronounced negative Eu anomaly. Additionally, the combination of low Th/U and elevated Yb_n/Gd_n ratios suggests that the source magma, while evolved, did not undergo extreme fractional crystallization. Instead, it likely reflects moderate magmatic differentiation under oxidizing to mildly reducing conditions, typical of the early to mid-Miocene magmatism that characterizes the Kırka sector.

Within the AVC, zircon trace element and REE compositions have been characterized for two distinct magmatic groups: (1) latitic volcanic rocks dated to 11.78–11.76 Ma, and (2) shallow subvolcanic intrusions comprising latitic to monzonitic compositions that post-date the volcanics. Among the analyzed samples, AVC-01 and AVC-02 represent the oldest units and exhibit significantly divergent trace element signatures. Specifically, average Ti concentrations in zircon are markedly high—95.66 ppm for AVC-01, 42.44 ppm for AVC-02, and 7.30 ppm for AVC-03. Hf contents range from 8157 ppm to 10626 ppm, while Y concentrations show variability, with AVC-01 having 2915 ppm, AVC-02 having 593 ppm, and AVC-05 having 619 ppm Hf on average. ΣREE concentrations further distinguish the two groups, with AVC-01 exhibiting an exceptionally high value of 1963 ppm, whereas AVC-02 and AVC-05 presents a much lower concentration of 424 and 469 ppm (Table 5.3).

Notably, AVC-01 sampled from the northern part of the AVC has the highest Ti, Y, and ΣREE, and the lowest Hf concentrations among all zircon samples from the AVC. Geochemically, AVC-01 zircons are characterized by low Eu/Eu* (avg. 0.17), low Ce/Nd (avg. 2.67), and Th/U ratios (avg. 1.57), accompanied by elevated Dy/Yb values (0.51) (Figure 5.21). Zircon-derived oxygen fugacity estimates (ΔFMQ_{zircon}) for this sample span from -1.36 to -0.30, indicating a relatively reduced magma state (Figure 5.21). The observed slight decrease in Eu/Eu* with decreasing Th/U is

interpreted as evidence for plagioclase-dominated fractionation exerting a stronger influence than amphibole during magma evolution.

In contrast, zircons from AVC-02 and AVC-05 are geochemically slightly different than the AVC-01 zircons, including higher Eu/Eu*, Ce/Nd, and lower Th/U, Dy/Yb (all averaging 0.42 and 0.53, 4.16 and 18.17, 0.84 and 0.65, 0.36 and 0.29 respectively). Zircon crystallization temperatures are remarkably high for both AVC-01 and AVC-02, calculated at 1050°C for AVC-01 and 933°C for AVC-02. Conversely, AVC-05 has the lowest calculated zircon crystallization temperatures among these samples (745°C). These values are the highest among all analyzed samples in the region, suggesting unusually high-temperature crystallization conditions for these early latitic units while slightly older lamprophyre are crystallized under low-temperature conditions (Table 5.3).

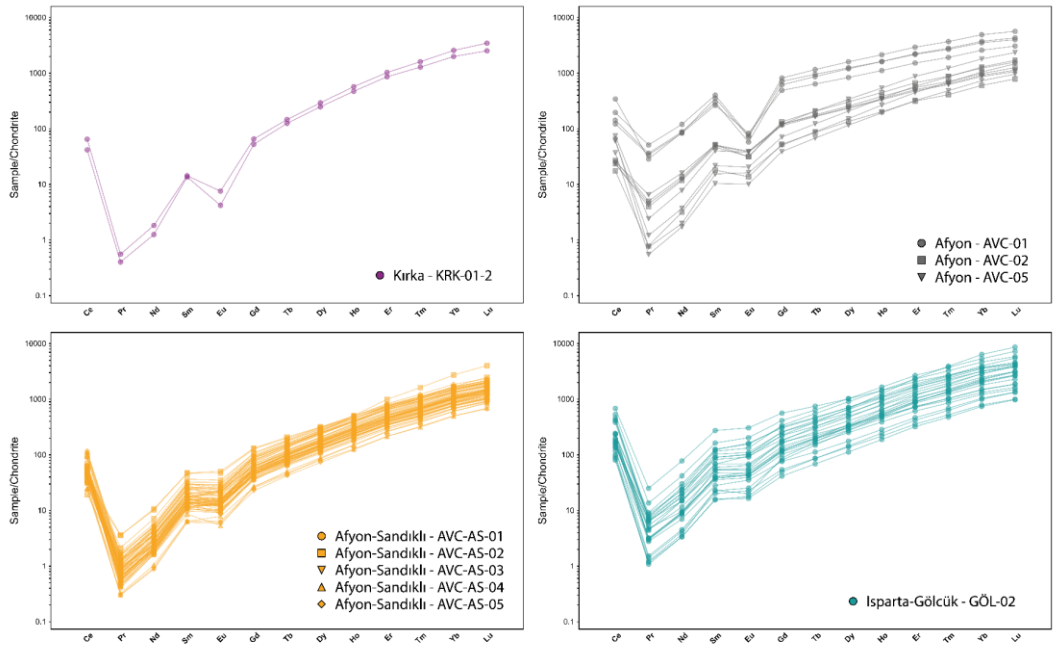


Figure 5.22. Zircon multi-element variation diagrams of the volcanic and sub-volcanic rocks from the Kırka-Afyon-Isparta region.

Subsequent magmatic activity is recorded by a suite of monzonitic to trachytic and syenitic subvolcanic intrusions (samples AVC-AS-01, AVC-AS-02, AVC-AS-03, AVC-AS-04, and AVC-AS-05) from the A-S porphyry Au prospect, emplaced between 11.99 and 11.48 Ma. Thus, intrusive rocks of the porphyry systems are slightly younger than the overlying latitic volcanic rocks. Zircons from these intrusions exhibit lower Ti (6.74–11.84 ppm) but elevated Hf contents (10881–12477 ppm) compared to AVC-01, while Y and ΣREE concentrations are moderate to low (Y: 455–802 ppm; ΣREE: 361–632 ppm) (Table 5.3).

Geochemically, zircons from the A-S porphyry phases are distinguished by significantly higher Eu/Eu* ratios (average ~0.52 across all five samples), elevated Ce/Nd (21.0–31.0), and Hf/Y (14.56–27.62), combined with lower Dy/Yb (~0.24) and Th/U ratios (0.48–0.58) (Figure 5.21; Table 5.3). The ΔFMQ_{zircon} values calculated for these intrusions (averaging -0.28–1.51, with a low of -0.98) are consistently higher than those from the latitic volcanic units, pointing to a more oxidized magmatic source (Figure 5.21).

The systematic increase in both Hf/Y and Eu/Eu* with decreasing Th/U across the Afyon-Sandıklı samples strongly suggests that these magmas experienced amphibole-dominated fractional crystallization, possibly with the involvement of titanite and apatite. Zircon crystallization temperatures for the AVC-AS-01, AVC-AS-02, AVC-AS-03, AVC-AS-04, and AVC-AS-05 samples are calculated at 790°C, 737°C, 797°C, 795°C, and 732°C respectively—considerably lower than those of the earlier latitic units (Table 5.3).

The GÖL-02 sample from Gölcük near Isparta, represents the southernmost extent of the Kırka-Afyon-Isparta transect, and plays a crucial role in elucidating the broader evolutionary trajectory of the magmatic systems in this sector. Notably, this sample exhibits a high Th/U ratio (1.07), comparable to the values observed in the

AVC suite (particularly AVC-01) which are typically associated with more primitive and less fractionated magmas (Table 5.3).

GÖL-02 zircons have notably high Eu/Eu* ratio (avg. 0.67), the highest measured among all samples examined in this region. This suggests a minimal degree of plagioclase fractionation prior to zircon crystallization. Furthermore, the calculated ΔFMQ_{zircon} value for GÖL-02 is also markedly high (+2.53), indicative of strongly oxidizing magmatic conditions (Table 5.3).

A clear trend of increasing Hf/Y with decreasing Th/U ratios is also observed in this sample (Figure 5.21), suggesting that amphibole, rather than plagioclase or pyroxene, dominated the fractionating assemblage during melt evolution. This inference is further reinforced by the inverse correlation between Th/U and Yb_n/Gd_n ratios, which may point to the involvement of garnet in the source region (potentially at deeper crustal levels) thereby implying that GÖL-02 represents a less evolved and more mantle-influenced magma (Figure 5.21).

5.1.1.4.2.5 Bodrum Peninsula

Among the zircon grains from eight distinct volcanic and sub-volcanic rock samples (each yielding U-Pb ages ranging from 10.70 to 7.73 Ma) collected from the BVC, only a single point analysis was successfully obtained from sample BDR-03. Since its trace element signature showed strong geochemical affinity with other BVC samples, it was included in plots (Figure 5.23) but excluded from the Table 5.3.

Zircons extracted from the older samples BDR-04-1, BDR-04-2 (basaltic trachyandesite), BDR-05 (trachyandesite), and BDR-06 (a micro-monzonite), dated between 10.7 and 10.2 Ma, display broadly overlapping trace element and REE profiles except for BDR-07, which clearly differs from the rest of the sample suite (Figure 5.23).

Average Ti concentrations in zircons from BDR-04-1, BDR-04-2, BDR-05, and BDR-06 are 8.85, 24.56, 14.95, and 7.93 ppm, respectively. Their Hf contents are 8695, 9225, 8416, and 10,335 ppm, Y contents are 574, 964, 1156, and 796 ppm, and ΣREE are 426, 654, 786, and 579 ppm (Table 5.3).

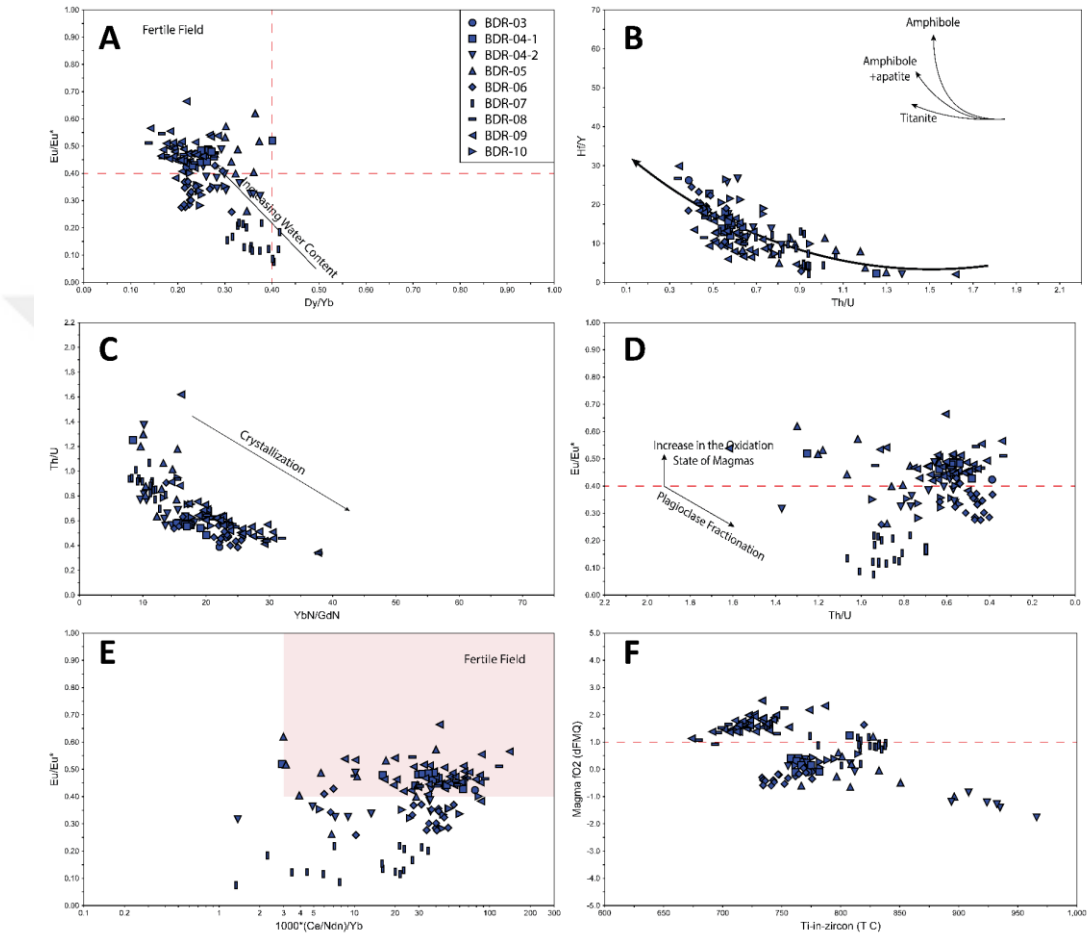


Figure 5.23. Diagrams illustrating the geochemical relationships of zircons analyzed from the Bodrum district. A) Eu/Eu* vs. Dy/Yb, B) Hf/Y vs. Th/U, C) Th/U vs. Yb_N/Gd_N, D) Eu/Eu* vs. Th/U, E) Eu/Eu* vs. $1000\times(Ce/Nd)_n/Yb$, and F) Magma fO_2 (ΔFMQ) vs. Ti-in-zircon temperature (°C).

Eu/Eu* ratios for these four samples are moderately low — 0.47 for BDR-04-1, 0.37 for BDR-04-2, 0.46 for BDR-05 and 0.33 for BDR-06 — while Dy/Yb values are 0.26, 0.31, 0.33 and 0.24, respectively. Ce/Nd ratios are 13.74 for BDR-04-1, 8.10

for BDR-04-2, 8.65 for BDR-05, and 14.08 for BDR-06 (Table 5.3; Figure 5.23). Calculated ΔFMQ_{zircon} values for BDR-04-1 range from -0.11 to 0.41 (average of 0.17), for BDR-04-2 range from -1.77 to 0.36 (average of -0.63), for BDR-05 range from -0.99 to 0.62 (average of -0.19), and those from BDR-06 span -0.60 to 1.64 (average of -0.21). These suggest that the higher magma oxygen fugacities in the oldest samples (BDR-04-1) gradually decrease through time during the development of the BVC. Importantly, zircon populations from BDR-04-2 show a pronounced increase in Eu/Eu* with decreasing Th/U, whereas an opposite trend is observed in BDR-06 zircons (Figure 5.23). These contrasting trends imply distinct fractionation histories; BDR-04-2 likely crystallized from an amphibole-dominated magma source, whereas BDR-06 reflects a plagioclase-dominated fractionation path. The average zircon crystallization temperatures for BDR-04-2 and BDR-06 are 861°C and 756°C, respectively (Table 5.3). Additionally, BDR-07 sample show an increasing trend of Eu/Eu* with decreasing Th/U similar to BDR-04-2, yet Eu/Eu* ratios are significantly lower (Figure 5.23). Low Eu/Eu* ratios can also be observed in the multi-element variation plots of the Bodrum units with pronounced negative Eu anomaly (Figure 5.24).

Younger magmatic activity in the BVC is represented by sample BDR-07 (~8.97 Ma). Zircons from this unit have average contents of 14.67 ppm Ti, 8312 ppm Hf, 1344 ppm Y, and 861 ppm ΣREE. Compared to earlier units, BDR-07 zircons are distinguished by notably lower Eu/Eu* (0.08–0.22) and Ce/Nd (1.99–11.24), alongside elevated Dy/Yb (0.31–0.42) and Th/U (0.70–1.07) values. These geochemical signatures are consistent with a plagioclase-dominated fractionation regime and a moderately oxidized magma, supported by zircon ΔFMQ values ranging from 0.14 to 2.19, with a mean of 0.92. The calculated average zircon crystallization temperature for this unit is 819°C (Table 5.3).

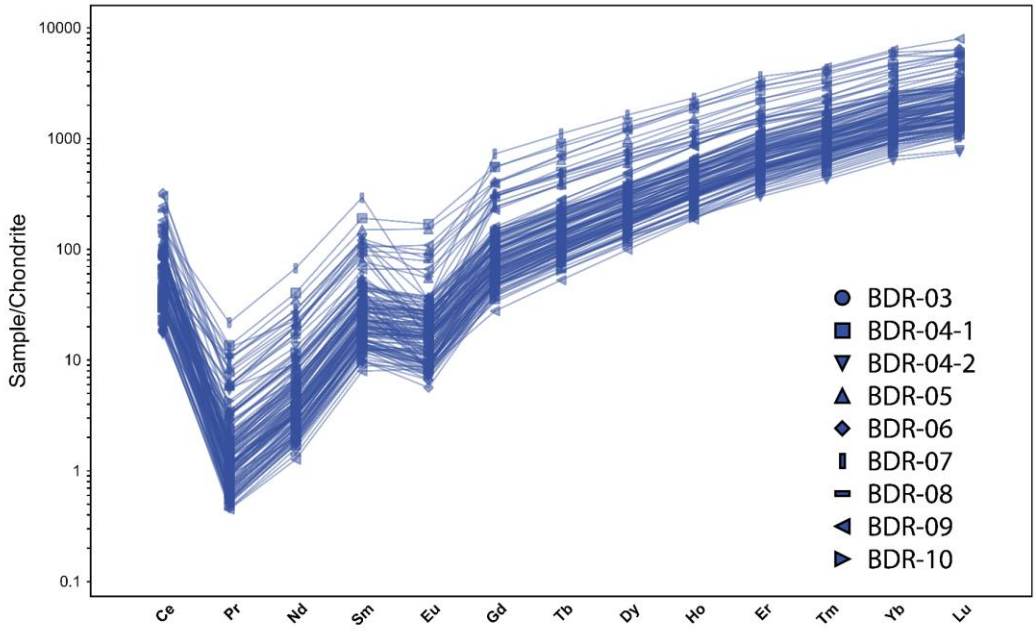


Figure 5.24. Zircon multi-element variation diagrams of volcanic, volcaniclastic, and sub-volcanic rocks of the BVC.

Following closely in time, the BDR-10 trachyandesite (8.81 Ma) records a distinct evolutionary trend. Zircons from this sample yielded average contents of 10.44 ppm Ti, 9030 ppm Hf, 589 ppm Y, and 443.7 ppm ΣREE — the lowest REE contents recorded among all BVC samples. Compared to BDR-07, BDR-10 zircons exhibit increasing Eu/Eu* (0.28–0.40) and Ce/Nd (3.80–22.22) ratios, but lower Dy/Yb (0.23–0.30) and Th/U (0.54–0.95) values. The ΔFMQ values for BDR-10 range from -0.01 to 0.56, with an average of 0.25. A clear positive correlation between decreasing Th/U and increasing Hf/Y and Eu/Eu* (Figure 5.23) suggests a shift from the plagioclase-dominated source of BDR-07 to an amphibole-dominated magmatic environment for BDR-10. The average zircon crystallization temperature for this sample is calculated at 784°C (Table 5.3).

The 8.25 Ma BDR-09 trachyandesite exhibits the most evolved geochemical signatures within the BVC. Zircon grains contain on average 5.76 ppm Ti, 10,430

ppm Hf, 1077 ppm Y, and 864 ppm ΣREE. These zircons recorded the highest Eu/Eu* (0.38–0.66; avg. 0.48) and Ce/Nd (13.80–53.39; avg. 32.24) values, and the lowest Dy/Yb (0.14–0.29; avg. 0.21) ratios among all analyzed samples. Furthermore, calculated ΔFMQ_{zircon} values from this sample — ranging from 1.13 to 2.52 with an average of 1.68 — are the highest across the entire BVC dataset, indicating the most oxidizing magma conditions. The co-variation of Hf/Y and Eu/Eu* with declining Th/U closely mirrors trends in BDR-10 and supports derivation from an amphibole-rich magma source. The average zircon crystallization temperature for BDR-09 is calculated as 726°C (Table 5.3).

The youngest dated unit in the BVC is the BDR-08 trachyandesite sample (7.73 Ma). Zircons from this sample exhibit average concentrations of 5.12 ppm Ti, 11,030 ppm Hf, 1007 ppm Y, and 723 ppm ΣREE. Similar to BDR-09, this sample displays elevated Eu/Eu* (0.44–0.55; avg. 0.47) and Ce/Nd (17.03–54.00; avg. 34.19) ratios, alongside low Dy/Yb (0.14–0.28; avg. 0.20). Its ΔFMQ values — ranging from 0.93 to 2.24 with an average of 1.48 — are also comparable to those of BDR-09, reinforcing the interpretation of a highly oxidized magma. The observed increases in Hf/Y and Eu/Eu* with declining Th/U suggest an amphibole-dominated fractionation regime, similar to BDR-09. The average zircon crystallization temperature for BDR-08 is estimated at 715°C (Table 5.3).

5.1.1.5 Hf Isotope Analyses

Hf isotope analyses were performed on zircons separated from a total of fourteen magmatic samples representing different stages of magmatic evolution in the Western Anatolian sector, several of which are associated with porphyry or associated epithermal mineralization (Table 5.4). For each analysis, initial $^{176}Hf/^{177}Hf$ ratios were calculated using a ^{176}Lu decay constant of 1.865×10^{-11} (Scherer et al., 2001), incorporating measured $^{176}Lu/^{177}Hf$ ratios and the average U–

Pb zircon crystallization ages. Initial εHf values were determined using the parameters of the chondritic uniform reservoir (CHUR) as defined by Bouvier et al. (2008). The uncertainties in the calculated initial isotopic compositions (reported as standard deviations) include both analytical errors and the reproducibility of reference materials measured across different analytical sessions. The $\varepsilon Hf_{(T)}$ values corresponding to the timing of zircon crystallization were calculated using Equation 3 of Blichert-Toft and Albarède (1997).

$$\varepsilon Hf(t) = (({}^{176}Hf/{}^{177}Hf)_S - ({}^{176}Lu/{}^{177}Hf)_S * (e^{\lambda t} - 1))/(({}^{176}Hf/{}^{177}Hf)_{CHUR,0} - ({}^{176}Lu/{}^{177}Hf)_{CHUR} * (e^{\lambda t} - 1)) - 1) * 10{,}000 \quad \text{(Equation 3)}$$

Table 5.4. Isotopic ratios obtained from zircon Hf isotope analyses.

Region	Field	Sample	$^{176}Lu/^{177}Hf$				$^{176}Hf/^{177}Hf$				εHf			
			Min	Max	Mean	2se	Min	Max	Mean	2se	Min	Max	Mean	2se
Biga	Çatalçam	CTL-01	0.0021988	0.0047294	0.0032956	0.000914	0.2826433	0.28269	0.2826684	1.509E-05	-4.5	-2.87	-3.61	0.52
	Çatalçam	CTL-02	0.0029029	0.0041662	0.0035476	0.0004608	0.2826573	0.2827049	0.2826733	1.921E-05	-3.99	-2.3	-3.42	0.68
	Balya	BLY-01	0.0033382	0.0043458	0.003842	0.0004168	0.2826481	0.2827116	0.2826683	2.418E-05	-5.52	-3.03	-4.09	0.81
	Balya	BLY-02	0.0024526	0.005267	0.0040517	0.0011539	0.282624	0.2827459	0.2826796	5.748E-05	-5.04	-4.17	-4.62	0.34
Simav	Sındırgı	SIN-01	0.0029062	0.0066114	0.0040616	0.0011432	0.2826201	0.2827755	0.2826732	5.021E-05	-5.3	-2.52	-4.14	0.76
	Sındırgı	SIN-04	0.0010561	0.0022004	0.0016282	0.0008091	0.2825353	0.2826018	0.2825685	4.705E-05	-8.24	-5.91	-7.08	1.65
	Eğrigöz	EGR-01	0.0036445	0.0065298	0.0044599	0.0011606	0.2826188	0.2826892	0.2826461	3.086E-05	-5.36	-2.9	-4.41	1.08
	Pınarbaşı	PNB-01	0.0038159	0.0057198	0.0049957	0.0006786	0.282702	0.2827702	0.2827275	2.032E-05	-2.45	-0.05	-1.56	0.72
	Pınarbaşı	PNB-02	0.0031106	0.0074128	0.0050721	0.0018536	0.2825061	0.2827434	0.2826743	7.872E-05	-9.38	-2.23	-4.46	2.39
Salihli	Salihli	S-01	0.002472	0.0044004	0.0034626	0.0007498	0.2824937	0.2825334	0.2825146	1.325E-05	-9.87	-8.46	-9.13	0.47
Uşak	Sayacık	SYC-04	0.0027104	0.0061338	0.0039871	0.0014866	0.2826996	0.2827599	0.2827184	2.817E-05	-4.04	-2.17	-2.83	0.83
	Sayacık	SYC-05	0.0022915	0.0032806	0.0027406	0.0003713	0.2826887	0.2827156	0.2827053	1.122E-05	-2.98	-2.03	-2.4	0.4
Afyon	AS	AVC-AS-01	0.001089	0.0020545	0.0014907	0.0003025	0.2826949	0.2827401	0.2827205	1.237E-05	-2.8	-1.21	-1.9	0.43
Bodrum	Bodrum	BDR-09	0.0016691	0.0027426	0.0022503	0.0003476	0.2826495	0.282763	0.282697	3.759E-05	-4.67	-2.95	-3.7	0.62

A summary of the Hf isotope analytical results for all investigated samples is presented in Table 5.4 which also lists the measured $^{176}Yb/^{177}Hf$, $^{176}Lu/^{177}Hf$, and $^{176}Hf/^{177}Hf$ ratios for each individual zircon spot. The $\varepsilon Hf_{(T)}$ values calculated from zircons representing different localities are compiled in Table 5.4, while the temporal

variation of εHf(T) is illustrated in Figure 5.25, which also displays the chondritic uniform reservoir (CHUR) evolution line for reference.

When viewed in chronological order, the two Balya samples yielded average $\varepsilon Hf_{(T)}$ values of –4.09 and –4.62. The younger Çatalçam samples exhibit slightly higher average $\varepsilon Hf_{(T)}$ of –3.61 and –3.42 (Table 5.4). In contrast, coeval samples from the Sındırgı region yielded lower $\varepsilon Hf_{(T)}$ values, with the two analyzed zircon populations averaging –4.14 and –7.08. Zircons from the more evolved Eğrigöz Granitoid returned an intermediate average $\varepsilon Hf_{(T)}$ value of –4.41 (Table 5.4)

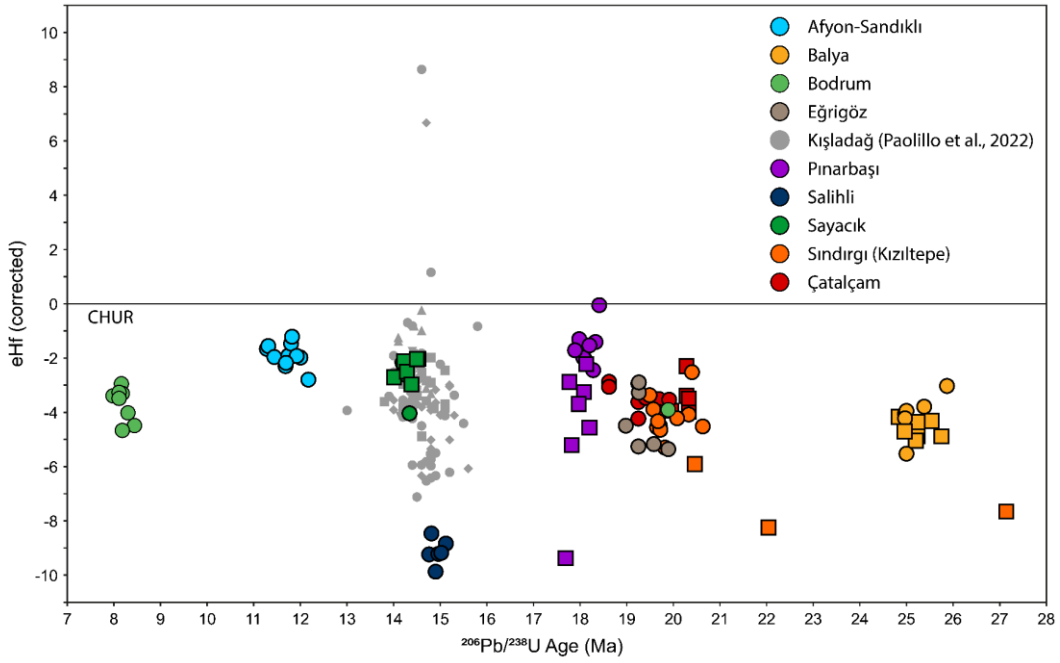


Figure 5.25. Temporal variation in εHf_{zircon} values of selected igneous systems in Western Anatolia.

Further up the temporal spectrum, two andesite porphyry samples from the Pınarbaşı porphyry prospect have average $\varepsilon Hf_{(T)}$ values of –4.46 and –1.51. Notably, the zircon populations from these samples exhibit a broader range of $\varepsilon Hf_{(T)}$ values (ranging from –9.87 to –0.05) compared to the older units, suggesting more heterogeneous

magma sources or increased crustal assimilation during this stage of magmatism (Figure 5.25).

5.1.2 Apatite Chemistry

Apatite grains separated from the collected igneous rock samples were analyzed by EPMA to determine their major oxide and volatile (Cl, F, SO_3) contents and by LA-ICP-MS to determine their trace element and REE abundances. Accessory apatite was identified and extracted from all sampled localities except for Çatalçam, Sındırgı, Karacadağ/Yeşilyurt, and Kırka.

Analyzed apatites are typically fine-grained, displaying predominantly euhedral, slender prismatic morphologies. In addition to compositionally homogenous grains observed during CL imaging, apatites that exhibit well-developed internal zoning are also common. Patchy, compositionally heterogenous domains within single crystals—likely reflecting hydrothermal overprinting—are especially widespread in samples from the Kışladağ and Sayacık porphyry Au systems.

5.1.2.1 Major Elements and Halogens

Results of the apatite EPMA analyses were evaluated to provide constraints on the oxidation state and volatile budged of the magmatic system in the study area. A summary table of the apatite EPMA data is presented in Table 5.5.

In terms of major element chemistry, apatite grains from all studied areas show relatively consistent CaO contents. In Western Anatolia, average CaO values range from 50.84 wt.% to 54.40 wt.%, while in the Central Taurides CaO abundances are between 51.27 wt.% and 54.40 wt.% (Table 5.5). In the Biga Peninsula, apatites from the porphyry mineralized Balya intrusions yielded closely similar CaO contents of

52.95 wt.% and 53.59 wt.%. Comparable CaO contents were obtained from the Eğrigöz Granite (53.91 wt.%) and the Pınarbaşı porphyry prospect (53.03 wt.%). Apatite grains from the Salihli Granitoid samples have the highest CaO contents (54.45 wt.%) among the Western Anatolian sector.

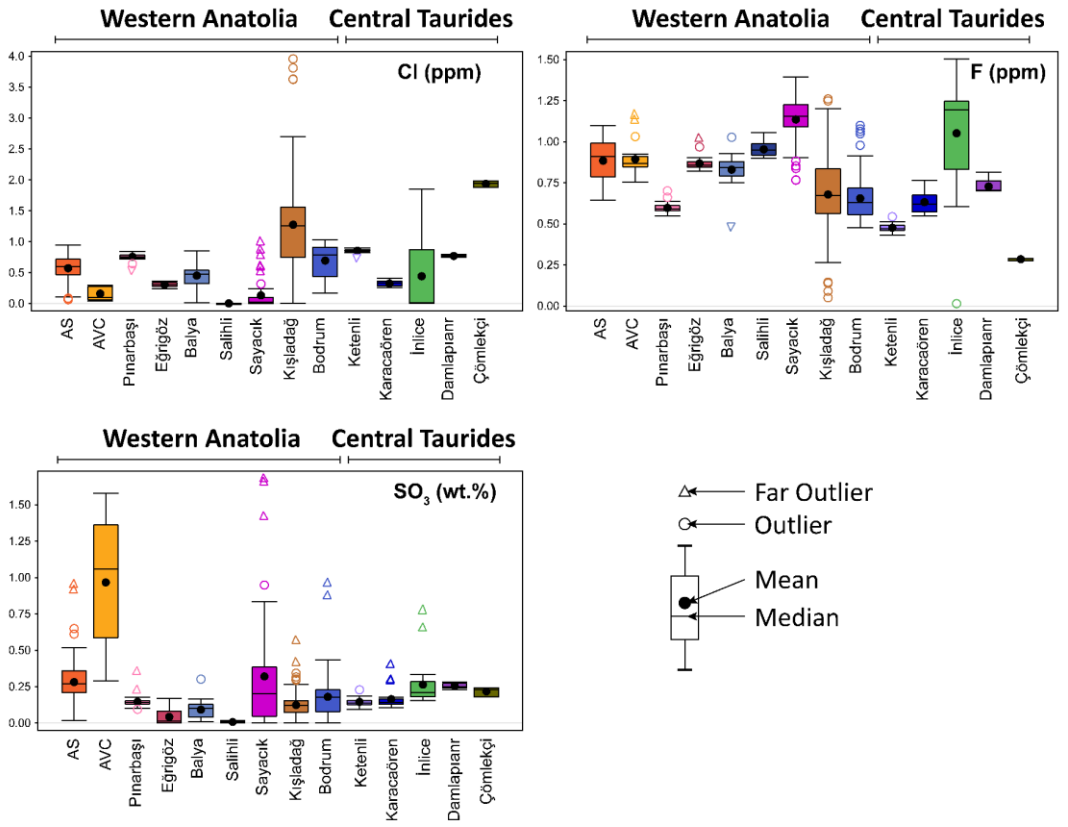


Figure 5.26. Box and whisker plots of the halogen contents of apatites from the Western Anatolia and the Central Taurides.

Apatites from different intrusive phases of the Kışladağ porphyry Au system show a clear compositional variation trend. Early-stage intrusions yielded 50.84–53.87 wt.% CaO, whereas later-stage phases record slightly higher values of 51.61–53.56 wt.%. CaO contents of apatites from the Sayacık Au porphyry system are clustered around ~53.6 wt.%, although a single sample yielded a distinctly lower value of 51.90 wt.%.

Table 5.5. Representative EPMA and LA-ICP-MS results for the apatite.

Region		Biga							Salihli-Turgutlu	Niğde
District		Balya	Balya	Hallaçlar	Hallaçlar	Turplu	Sarıalan	Sarıalan	Salihli	Çömlekçi
Sample		BLY-01	BLY-02	374857	374865	TRD-17	SAR-01	SAR-04	S-02	CML-01
U-Pb Age (Ma)		25.48	25.659	22.898	23.18	22.14	22.16	22.32	14.78	1.938
CaO (wt.%)	Min	52.50	52.49	-	-	-	-	-	54.19	51.20
	Max	53.21	54.62	-	-	-	-	-	54.65	51.32
	Mean	52.95	53.59	-	-	-	-	-	54.45	51.27
P_2O_5 (wt.%)	Min	40.42	40.87	-	-	-	-	-	41.63	38.41
	Max	41.60	42.16	-	-	-	-	-	42.53	38.69
	Mean	41.16	41.61	-	-	-	-	-	42.28	38.53
SO_3 (wt.%)	Min	0.10	0.01	-	-	-	-	-	0.00	0.18
	Max	0.14	0.30	-	-	-	-	-	0.02	0.24
	Mean	0.12	0.08	-	-	-	-	-	0.01	0.22
Cl (wt.%)	Min	1.58	0.04	-	-	-	-	-	0.00	6.14
	Max	2.85	2.18	-	-	-	-	-	0.03	6.45
	Mean	2.11	1.36	-	-	-	-	-	0.01	6.31
F (wt.%)	Min	1.35	0.87	-	-	-	-	-	1.65	0.48
	Max	1.61	1.88	-	-	-	-	-	1.93	0.51
	Mean	1.47	1.52	-	-	-	-	-	1.75	0.50
OH (wt.%)	Min	0.35	0.46	-	-	-	-	-	0.85	-0.25
	Max	0.58	1.01	-	-	-	-	-	0.99	-0.17
	Mean	0.50	0.68	-	-	-	-	-	0.94	-0.22
Eu/Eu*	Min	0.41	0.40	0.36	0.47	0.24	0.46	0.48	0.16	0.47
	Max	0.55	0.76	0.54	0.98	0.73	0.47	0.61	0.19	0.47
	Mean	0.49	0.56	0.46	0.77	0.46	0.46	0.54	0.17	0.47
Ce/Ce*	Min	0.80	0.93	0.87	0.89	0.81	0.91	0.83	0.84	1.04
	Max	0.90	1.76	1.07	1.06	1.13	1.04	0.91	1.00	1.04
	Mean	0.85	1.17	0.97	1.00	0.96	0.99	0.86	0.91	1.04
Sr/Y	Min	0.29	0.18	1.00	3.34	0.20	1.55	1.86	0.30	2.02
	Max	0.44	1.13	2.11	4.01	2.04	1.98	4.88	0.49	2.02
	Mean	0.40	0.47	1.47	3.59	0.85	1.74	3.22	0.41	2.02
La/Yb	Min	12.74	2.39	53.62	25.04	25.21	64.24	28.03	2.43	94.96
	Max	27.25	28.03	98.30	86.12	53.69	70.84	34.25	8.75	94.96
	Mean	21.56	9.53	80.59	58.97	33.11	66.68	30.50	4.63	94.96

Table 5.5. continued.

Region		Uşak									
District		Sayacık	Sayacık	Sayacık	Int 2NW		Int 3W		Int 2CE		Int 3C
Sample		SYC-02	SYC-03	SYC-04	KSLD-06	KSLD-01	KSLD-07	KSLD-08	KSLD-04	KSLD-11	KSLD-10
U-Pb Age (Ma)		13.903	14.27	14.05	14.45	14.45	14.36	14.36	14.76	14.76	14.39
CaO (wt.%)	Min	52.41	50.39	50.09	47.44	52.53	50.14	50.05	53.19	52.62	53.13
	Max	54.22	54.98	53.57	54.38	53.32	53.76	54.47	54.33	54.08	53.81
	Mean	53.62	53.73	51.90	50.84	52.93	51.61	52.00	53.85	53.47	53.56
P_2O_5 (wt.%)	Min	39.89	40.64	39.85	35.74	40.41	39.08	37.15	39.82	39.16	40.72
	Max	42.32	42.16	42.42	41.63	41.15	41.97	41.95	41.30	41.41	41.56
	Mean	41.51	41.43	41.47	38.89	40.69	39.81	39.64	40.62	40.55	41.10
SO_3 (wt.%)	Min	0.01	0.00	0.00	0.05	0.04	0.00	0.02	0.07	0.02	0.01
	Max	1.86	0.80	0.57	0.23	0.13	0.32	0.30	0.42	0.57	0.26
	Mean	0.43	0.25	0.10	0.11	0.08	0.13	0.15	0.19	0.10	0.07
Cl (wt.%)	Min	0.00	0.07	0.00	0.88	1.99	0.07	0.02	0.87	0.52	1.05
	Max	1.77	1.09	3.36	12.32	2.80	5.80	8.35	3.27	2.71	2.51
	Mean	0.18	0.41	1.28	6.21	2.33	4.45	4.15	2.05	1.24	1.77
F (wt.%)	Min	1.65	1.54	1.37	0.08	1.50	0.75	0.45	1.26	1.74	1.46
	Max	2.42	2.21	2.54	1.81	1.72	1.98	1.74	1.74	2.28	1.84
	Mean	2.13	1.91	1.94	0.87	1.59	1.15	1.17	1.49	2.00	1.57
OH (wt.%)	Min	0.49	0.53	0.17	-1.94	0.29	-0.25	-0.80	0.27	0.16	0.38
	Max	0.79	1.02	0.70	0.80	0.44	0.81	0.94	0.71	0.76	0.71
	Mean	0.70	0.75	0.48	-0.40	0.37	-0.01	0.07	0.50	0.47	0.54
Eu/Eu*	Min	0.47	0.78	0.55	0.20	0.23	0.18	0.17	0.49	0.07	0.10
	Max	1.11	2.47	4.44	0.65	0.38	0.80	0.43	0.69	0.27	0.15
	Mean	0.78	1.62	1.52	0.45	0.29	0.28	0.26	0.57	0.20	0.12
Ce/Ce*	Min	0.93	0.81	0.76	0.73	0.91	0.71	0.71	0.75	0.79	0.69
	Max	1.90	1.22	1.66	0.91	1.11	1.24	1.00	0.90	0.84	0.72
	Mean	1.17	1.08	1.20	0.85	1.04	0.78	0.80	0.81	0.82	0.70
Sr/Y	Min	0.21	0.55	0.32	1.07	0.45	0.33	0.53	2.02	0.42	0.67
	Max	3.04	13.12	12.92	6.66	2.21	1.82	1.89	3.87	0.53	0.97
	Mean	0.63	3.61	1.75	3.08	0.79	1.05	0.94	2.80	0.46	0.78
La/Yb	Min	0.37	3.94	1.04	21.79	17.01	19.61	30.65	7.12	18.17	14.86
	Max	13.97	29.20	17.54	90.17	49.12	89.61	81.50	20.51	45.53	39.28
	Mean	5.88	13.87	4.59	68.14	28.25	68.12	61.72	12.25	34.97	25.51

Table 5.5. continued.

Region		Afyon						
District		AS	AS	AS	AS	Isparta	Isparta	AVC
Sample		AVC-AS-01	AVC-AS-04	AVC-AS-05	AVC-AS-03	GÖL-01	GÖL-02	AVC-05
U-Pb Age (Ma)		11.68	11.595	11.48	11.59	-	2.633	11.98
CaO (wt.%)	Min	52.05	53.00	52.60	52.23	-	-	53.26
	Max	54.29	53.76	53.72	53.98	-	-	55.49
	Mean	53.13	53.35	53.21	52.68	-	-	54.40
P_2O_5 (wt.%)	Min	39.86	40.45	39.41	39.47	-	-	38.56
	Max	42.02	41.05	40.71	40.54	-	-	41.01
	Mean	40.81	40.77	40.20	39.80	-	-	39.91
SO_3 (wt.%)	Min	0.04	0.02	0.21	0.20	-	-	0.29
	Max	0.65	0.12	0.95	0.44	-	-	1.58
	Mean	0.29	0.06	0.31	0.35	-	-	0.97
Cl (wt.%)	Min	0.22	1.75	1.87	1.03	-	-	0.14
	Max	2.32	2.50	2.77	3.15	-	-	1.01
	Mean	1.48	2.22	2.42	2.71	-	-	0.54
F (wt.%)	Min	1.55	1.39	1.15	1.44	-	-	1.35
	Max	2.00	1.62	1.41	1.90	-	-	2.10
	Mean	1.77	1.49	1.27	1.54	-	-	1.61
OH (wt.%)	Min	0.34	0.39	0.45	0.23	-	-	0.51
	Max	0.76	0.54	0.67	0.58	-	-	1.08
	Mean	0.53	0.45	0.51	0.30	-	-	0.85
Eu/Eu*	Min	0.20	0.15	0.39	0.40	0.80	0.60	0.77
	Max	0.82	0.28	0.75	0.59	0.94	0.93	0.83
	Mean	0.41	0.21	0.58	0.52	0.91	0.79	0.81
Ce/Ce*	Min	0.73	0.75	0.93	0.79	0.63	0.68	0.77
	Max	0.94	0.91	1.18	0.89	0.72	0.87	0.85
	Mean	0.83	0.82	1.03	0.85	0.67	0.74	0.82
Sr/Y	Min	0.32	0.46	4.04	2.61	19.72	2.27	21.34
	Max	4.31	0.99	9.13	4.67	78.56	57.31	36.03
	Mean	1.03	0.64	5.89	3.04	58.52	20.95	26.14
La/Yb	Min	15.00	17.76	165.02	93.99	173.93	34.58	85.20
	Max	172.33	35.81	299.49	114.62	229.55	235.07	111.48
	Mean	81.99	23.90	233.36	101.96	207.74	128.39	99.47

Table 5.5. continued.

Region		Bodrum							Kütahya-Simav		
District		Bodrum	Bodrum	Bodrum	Bodrum	Bodrum	Bodrum	Bodrum	Eğrigöz	Baklan	Pınarbaşı
Sample		BDR-08	BDR-09	BDR-10	BDR-07	BDR-08	BDR-04-1	BDR-03	EGR-02	BKL-01	PNB-01
U-Pb Age (Ma)		7.899	8.247	8.807	8.971	7.734	10.7	-	19.072	18.43	18.162
CaO (wt.%)	Min	53.03	52.57	52.77	53.12	53.03	52.63	52.54	53.36	-	52.59
	Max	53.97	53.72	53.23	54.46	53.97	52.94	53.22	58.63	-	53.62
	Mean	53.41	52.96	53.00	53.94	53.41	52.84	53.01	53.91	-	53.03
P_2O_5 (wt.%)	Min	39.78	40.06	40.27	40.28	39.69	40.12	39.21	36.58	-	40.27
	Max	40.79	41.02	40.71	41.89	40.79	40.40	40.26	42.13	-	41.60
	Mean	40.41	40.56	40.45	41.27	40.41	40.23	39.93	41.49	-	41.05
SO_3 (wt.%)	Min	0.17	0.16	0.01	0.00	0.17	0.07	0.09	0.00	-	0.09
	Max	0.30	0.26	0.10	0.96	0.30	0.15	0.18	0.17	-	0.36
	Mean	0.23	0.19	0.04	0.25	0.23	0.09	0.14	0.05	-	0.15
Cl (wt.%)	Min	0.44	2.27	2.43	0.58	1.47	2.97	3.01	0.82	-	1.77
	Max	0.93	3.42	2.83	1.41	3.11	3.43	3.15	1.23	-	2.83
	Mean	0.67	2.95	2.66	0.96	2.25	3.14	3.10	1.04	-	2.54
F (wt.%)	Min	0.52	0.86	1.12	1.12	0.92	1.00	0.97	1.49	-	0.99
	Max	0.78	1.27	1.33	2.00	1.40	1.05	1.34	1.80	-	1.27
	Mean	0.67	1.01	1.20	1.46	1.20	1.03	1.08	1.58	-	1.08
OH (wt.%)	Min	0.53	0.37	0.44	0.57	0.47	0.34	0.33	0.59	-	0.53
	Max	0.82	0.72	0.51	0.98	0.73	0.47	0.46	0.82	-	0.70
	Mean	0.66	0.50	0.48	0.81	0.59	0.43	0.42	0.74	-	0.58
Eu/Eu*	Min	0.49	0.50	0.33	0.49	0.49	0.39	0.49	0.14	0.30	0.33
	Max	0.55	0.64	0.37	1.03	0.55	0.41	0.58	0.26	0.40	0.44
	Mean	0.52	0.57	0.35	0.69	0.52	0.40	0.54	0.20	0.33	0.38
Ce/Ce*	Min	0.89	0.86	0.89	0.72	0.89	0.85	0.80	0.50	0.92	0.77
	Max	0.93	1.02	0.92	0.85	0.93	0.87	0.95	0.94	1.30	0.93
	Mean	0.91	0.93	0.91	0.76	0.91	0.85	0.87	0.84	1.11	0.87
Sr/Y	Min	0.88	1.58	1.26	4.44	0.88	1.59	2.33	0.12	0.15	0.47
	Max	2.46	5.63	2.29	14.24	2.46	1.68	3.42	0.76	0.38	0.80
	Mean	1.62	2.91	1.60	8.19	1.62	1.63	2.88	0.33	0.22	0.59
La/Yb	Min	54.34	72.81	78.31	65.39	54.34	67.51	39.11	6.87	22.33	29.91
	Max	103.32	110.79	87.01	92.83	103.32	68.92	57.74	27.77	69.38	48.25
	Mean	83.29	93.16	81.56	77.56	83.29	68.23	48.43	16.66	48.41	35.19

Table 5.5. continued.

Region		Konya					
District		Karacaören	Damlapınar	İnlice	İnlice	SVS	Ketenli
Sample		KRC-01	DMLP-02	INL-OP-01	INL-OP-02	Sillle-02	KTN-01
U-Pb Age (Ma)		4.772	10.31	8.997	9.078	12.796	3.013
CaO (wt.%)	Min	53.53	51.39	50.42	51.48	-	52.69
	Max	54.80	53.07	53.80	54.04	-	53.49
	Mean	54.40	52.63	51.82	53.25	-	53.20
P_2O_5 (wt.%)	Min	41.11	38.62	38.79	39.12	-	40.39
	Max	41.70	40.17	41.80	41.45	-	41.04
	Mean	41.48	39.67	40.22	40.76	-	40.65
SO_3 (wt.%)	Min	0.11	0.23	0.16	0.16	-	0.10
	Max	0.40	0.28	0.33	0.78	-	0.23
	Mean	0.17	0.26	0.23	0.28	-	0.15
Cl (wt.%)	Min	0.80	2.54	0.02	0.01	-	2.43
	Max	1.39	2.67	6.04	3.89	-	3.03
	Mean	1.09	2.58	3.16	0.55	-	2.86
F (wt.%)	Min	0.99	1.26	1.06	0.03	-	0.78
	Max	1.39	1.46	2.74	2.52	-	0.98
	Mean	1.16	1.31	1.70	2.01	-	0.86
OH (wt.%)	Min	0.85	0.37	-0.46	-0.02	-	0.55
	Max	1.00	0.49	0.71	1.32	-	0.70
	Mean	0.93	0.46	0.06	0.65	-	0.59
Eu/Eu*	Min	0.57	0.77	0.38	0.34	0.42	0.51
	Max	0.92	0.77	0.46	0.49	0.52	0.56
	Mean	0.64	0.77	0.43	0.40	0.48	0.53
Ce/Ce*	Min	0.73	1.09	0.96	0.90	0.85	0.78
	Max	0.82	1.09	1.05	0.95	1.16	0.84
	Mean	0.79	1.09	1.00	0.92	0.92	0.81
Sr/Y	Min	1.80	9.64	0.56	0.59	0.61	1.63
	Max	4.08	9.64	1.81	1.09	0.92	2.75
	Mean	2.32	9.64	1.24	0.82	0.74	2.09
La/Yb	Min	17.99	259.34	55.19	43.02	8.83	43.42
	Max	80.14	259.34	96.22	75.94	13.18	51.65
	Mean	29.13	259.34	65.68	63.80	10.53	46.14

Apatites from AVC and from the A–S porphyry prospect have CaO contents of 54.40 wt.% and 52.68–53.35 wt.%, respectively. Igneous apatites from various magmatic lithologies from the BVC have CaO values ranging between 52.84 wt.% and 53.94 wt.%. Similar compositions were observed in the Central Taurides; samples from the Karacaören and Çömlekçi prospects yielded 54.40 wt.% and 51.27 wt.% CaO, respectively, while apatites from İnlice fall in the range of 51.82–53.25 wt.% (Table 5.5).

Apatites from all areas also have quite similar P_2O_5 contents. Apatite from igneous rocks of the Western Anatolian sector have P_2O_5 abundances ranging between 38.89 wt.% and 42.28 wt.%, whereas those from the Central Taurides range between 38.53 wt.% and 41.48 wt.% (Table 5.5). The Balya and Simav samples display generally consistent distributions, with P_2O_5 contents measured at 41.16–41.61 wt.% and 41.05–41.49 wt.%, respectively (Table 5.5). A granite sample from Salihli has the highest P_2O_5 concentrations with 42.28 wt.%.

Samples from the Uşak region show a broader range. In the Kışladağ porphyry system, apatite P_2O_5 values vary from 38.89 wt.% to 41.10 wt.%, while those from the Sayacık porphyry Au prospect exhibit a much narrower range of 41.43–41.51 wt.%. Apatites from the Afyon region also display highly consistent values (Table 5.5): apatites from the A–S porphyry prospect range between 39.80 wt.% and 40.81 wt.%, whereas the Afyon Volcanic Complex sample yields 39.91 wt.%.

Bodrum shows a similar pattern, with apatite P_2O_5 values ranging from 39.93 wt.% to 41.27 wt.%. In the Central Taurides, apatites from İnlice yield P_2O_5 contents between 39.67 wt.% and 40.76 wt.%. In the southern part of the same belt, apatites from the Karacaören andesite porphyry contain 41.48 wt.% P_2O_5, while those from the Çömlekçi dacite porphyry, associated with the Melendiz volcanic field, record the lowest value in the dataset at 38.53 wt.%.

Analysis of halogen and volatile contents (Cl, F, and SO_3) in apatite revealed a wide compositional range across the Western Anatolian sector: Cl varies between 0.013–6.20 wt.%, F between 0.013–2.00 wt.%, and SO_3 between 0.008–0.966 wt.% (Figure 5.26; Table 5.5). The most pronounced variations in volatile compositions are observed within the different intrusive phases of the Kışladağ porphyry Au system (Figure 5.26). In particular, Cl contents in Kışladağ apatites display significant heterogeneity, even within individual samples. When combined with major element compositions, this variability suggests that Kışladağ apatites were substantially affected by hydrothermal alteration, a conclusion also supported by patchy textures and alteration-related zoning observed in Kışladağ apatites during CL imaging.

The Salihli Granitoid contains apatites with the lowest measured Cl (0.013 wt.%) and SO_3 (0.008 wt.%) values in the current study. Some apatite crystals are also relatively poor in F (0.175 wt.%; Figure 5.26). In contrast, apatites from the porphyry-mineralized Balya intrusions in units show Cl contents of 1.37–2.11 wt.%, F contents of 1.47–1.52 wt.%, and SO_3 concentrations of 0.08–0.12 wt.%. Samples from both barren and mineralized units in the Simav region display an inverse relationship between Cl, F, and SO_3. In the Eğrigöz, apatites yielded average Cl, F, and SO_3 contents of 1.04 wt.%, 1.58 wt.%, and 0.05 wt.%, respectively, whereas those from the mineralized Pınarbaşı andesite porphyry have higher Cl (2.55 wt.%) but lower F (1.08 wt.%) and slightly elevated SO_3 concentrations (0.15 wt.%; Figure 5.26).

In Kışladağ, early-stage intrusive phases affected by hydrothermal alteration have Cl contents of 1.24–6.21 wt.%, F contents of 0.87–2.00 wt.%, and SO_3 values of 0.08–0.19 wt.% (Figure 5.26). In comparison, younger intrusive phases show slightly narrower ranges: Cl 1.77–4.45 wt.%, F 1.17–1.57 wt.%, and SO_3 0.07–0.15 wt.%. Apatites from the Sayacık porphyry Au prospect, which exhibit similar

mineralization style to Kışladağ, show much more restricted volatile compositions: Cl 0.18–1.28 wt.%, F 1.91–2.13 wt.%, and SO_3 0.09–0.43 wt.% (Figure 5.26).

In the AVC, apatites from the sub-volcanic intrusions hosting the A–S porphyry prospect have relatively consistent volatile compositions (Cl: 1.48–2.71 wt.%, F: 1.27–1.77 wt.%, SO_3 : 0.06–0.35 wt.%), whereas other volcanic units of the AVC have apatites with distinctly lower Cl (0.54 wt.%) and higher SO_3 (0.97 wt.%) contents, with an average F concentrations of1.61 wt.% (Figure 5.26).

Within the BVC, a trend of increasing Cl and decreasing F contents is observed in apatites from younger magmatic phases. Apatites from older products have ~0.96 wt.% Cl and ~0.25 wt.% F, whereas younger intrusions show elevated Cl (2.25–3.14 wt.%) and moderately higher F (1.01–1.20 wt.%). SO_3 contents in BVC apatites remain relatively uniform across samples of different stages, ranging narrowly between 0.25–0.35 wt.% (Figure 5.26).

In the Central Taurides, apatite volatile compositions are also highly variable, with Cl ranging from 0.55–6.31 wt.%, F from 0.50–2.01 wt.%, and SO_3 from 0.15–0.28 wt.%. Regionally, apatites from Karacaören and Çömlekçi show similar SO_3 values (0.17 wt.% and 0.22 wt.%, respectively), but exhibit strikingly different halogen compositions. Average Cl contents are 1.10 wt.% for Karacaören and 6.31 wt.% for Çömlekçi, while F contents show the opposite trend, with Karacaören averaging 1.16 wt.% and Çömlekçi significantly lower at 0.50 wt.% (Figure 5.26).

5.1.2.2 Trace and Rare Earth Element Geochemistry

Trace element compositions of apatite crystals provide critical insights into the oxidation states of the magmas from which they crystallized. Because certain trace element systematics in apatite are highly sensitive to magmatic redox conditions, they serve as powerful geochemical proxies for evaluating magma fertility in

porphyry-style mineral systems. To ensure that trace element data were spatially linked with previously determined major element compositions, LA-ICP-MS analyses were performed either directly on the crystal domains measured by EPMA or as close to these domains as possible. The resulting trace element concentrations, along with key elemental ratios—many of which are well-established indicators of magmatic oxygen fugacity—are presented in Table 5.5. Among these, the Eu/Eu* and Ce/Ce* ratios, both considered sensitive markers of redox state, were systematically calculated. The relationships between these two ratios, as well as apatite Sr/Y ratios, for samples from various sites within the Western Anatolia and Central Tauride sectors are illustrated in Figure 5.27.

Within the Western Anatolian sector, the highest Eu/Eu* and Ce/Ce* ratios were recorded in apatite from the Sayacık porphyry system, with values ranging from 0.78 to 1.62 and 1.08 to 1.20, respectively. In contrast, apatite from nearby Kışladağ show variable REE concentrations among distinct intrusive phases. Early intrusions, which are considered to be the most ore-productive, display Eu/Eu* ratios of 0.20–0.57 and Ce/Ce* of 0.81–1.04, whereas apatite from late-stage, weakly mineralized intrusions have significantly lower values (Eu/Eu* = 0.12–0.28; Ce/Ce* = 0.70–0.80).

In the Biga Peninsula, apatite from diorite porphyry units associated with the Balya porphyry system have Eu/Eu* and Ce/Ce* ratios of 0.49–0.56 and 0.85–1.17, respectively. In the Simav region, Ce/Ce* values show little variation between the mineralized Pınarbaşı porphyry system (0.87) and the Eğrigöz Granitoid (0.84). However, Eu/Eu* values are notably higher in the Pınarbaşı apatites (avg. = 0.38) compared to those from Eğrigöz (avg. = 0.201).

Apatite from the Salihli Pluton granite exhibits low mean Eu/Eu* (0.171) but relatively high Ce/Ce* (0.91).

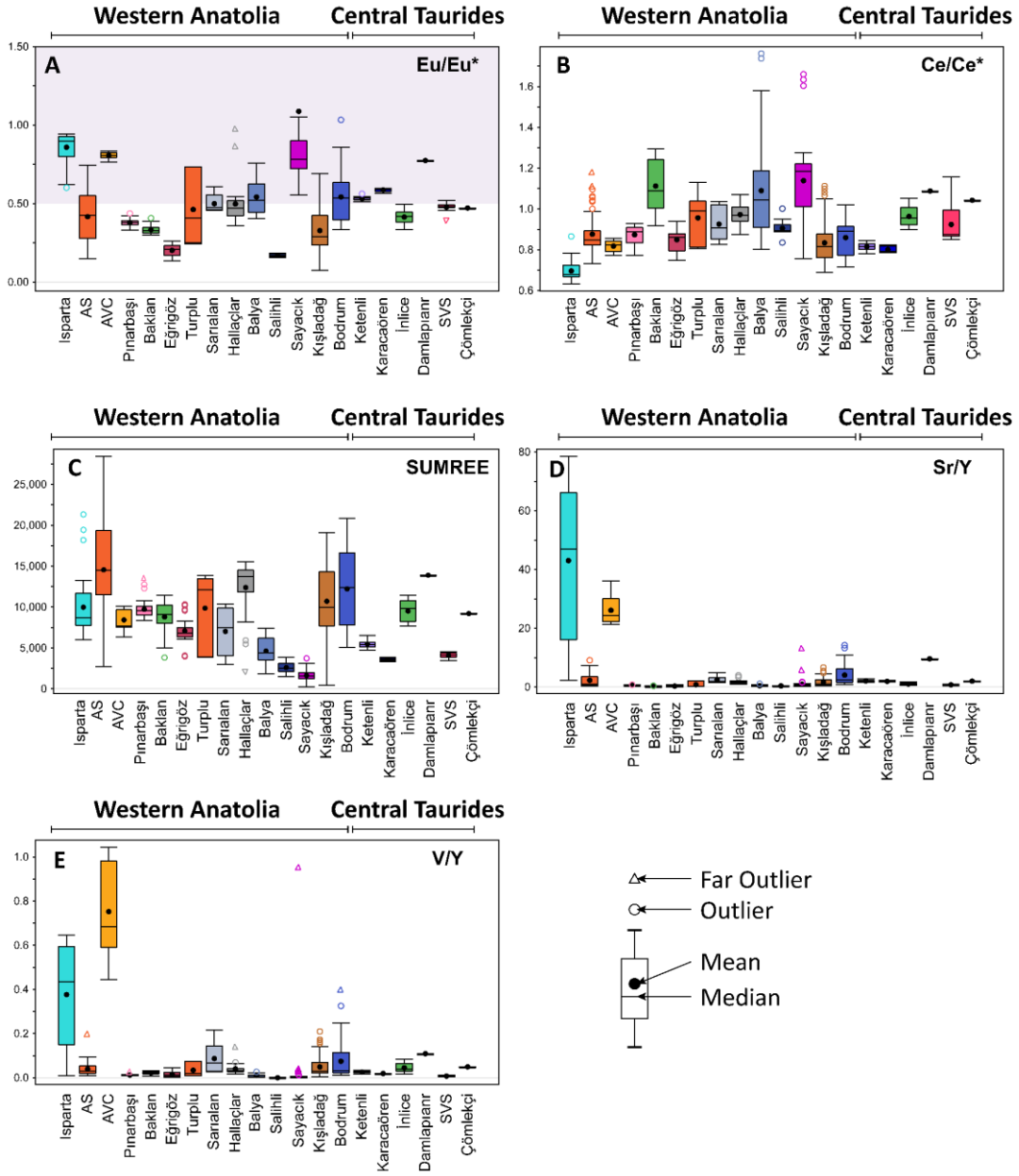


Figure 5.27. Box and whisker plots of the trace element compositions for the apatites from the Western Anatolia and the Central Taurides.

In the AVC, apatites from the host intrusions of the A-S porphyry prospect are characterized by internally consistent trace element ratios, while other volcanic units in the complex show significant variability, particularly in Eu/Eu*. Apatites from the

BVC samples have similar Eu/Eu* (0.40–0.69) and Ce/Ce* (0.76–0.93) values to those from the AVC. By contrast, apatite from the Central Tauride sector reveals a general trend of increasing Eu/Eu* accompanied by decreasing Ce/Ce*.

Apatite Sr/Y ratios also provide valuable context for magma differentiation and potential adakitic affinities. The highest average Sr/Y value recorded in the AVC is 26.14, whereas apatites from the A-S porphyry prospect have much lower Sr/Y ratios (0.65–5.89). Similarly, elevated Sr/Y values occur in samples from the BVC. The oldest unit sampled (BDR-07) has a mean Sr/Y of 8.19, whereas younger volcanic units have Sr/Y values between 1.62 and 2.91. At Kışladağ, Sr/Y ratios are highest in early, highly-mineralized intrusions (0.46–3.08) and Sr/Y ratios progressively decrease in later phases (0.78–1.04). Igneous apatite from the Salihli Granitoid has a low average Sr/Y value of 0.41.

In the Simav area, apatites from a granite sample from the barren Eğrigöz Granitoid (EGR-02) have a notably low apatite Sr/Y values (avg.= 0.33) compared to the younger and mineralized Pınarbaşı monzonite porphyry (PNB-01; avg. = 0.59).

In the Central Tauride sector, both Sr/Y and Eu/Eu* ratios decrease from older to younger igneous lithologies. Apatites from andesite porphyry samples from the Melendiz Stratovolcano have average Sr/Y ratios in the range 2.02–2.32, whereas in Konya, the Damlapınar andesite porphyry —emplaced prior to the İnlice system— has a notably high average Sr/Y ratio of 9.64. By contrast, apatite from andesite porphyry in the İnlice high-sulfidation epithermal system yielded much lower ratios (0.82–1.24). Apatites from the youngest sampled unit in the KVC, a dacitic agglomerate from Ketenli, has an intermediate mean Sr/Y value of 2.09.

5.1.3 Amphibole Geochemistry

As a substantial portion of the studied localities exhibit clear evidence of mineralization and hydrothermal alteration, many of the sampled igneous units have undergone varying degrees of chemical modification or even complete replacement of their primary magmatic assemblages. Consequently, in most of the investigated intrusions and volcanic rocks, primary phases such as feldspar, mica, and amphibole are rarely preserved in a completely unaltered state. Instead, these minerals often occur as relict phases partially replaced by secondary assemblages, or in some cases, have been entirely replaced by hydrothermal products such as sericite, chlorite, or secondary albite.

In samples only weakly affected by alteration, primary rock-forming minerals could still be identified petrographically, allowing for a more direct assessment of the magmatic crystallization conditions. These relatively better-preserved phases were selected for electron probe microanalysis (EPMA) to obtain quantitative major- and trace element compositions. EPMA analyses of such minerals are crucial in hydrothermally overprinted systems, as they provide geochemically robust constraints on original magmatic compositions despite subsequent alteration. Data obtained from feldspar and amphibole, for example, enable estimation of magmatic temperature, oxygen fugacity, and water content, while biotite compositions can be used to evaluate magmatic redox conditions.

In highly altered samples, where primary minerals were largely replaced, EPMA also served as a tool to characterize hydrothermal phases and assess the extent of element mobility during alteration. Identifying chemical zoning and replacement textures in back-scattered electron (BSE) images allowed discrimination between magmatic relicts and hydrothermal overprints, which is critical when interpreting the

petrogenetic and metallogenic evolution of the system. Representative BSE images illustrating these textures and analyzed mineral phases are provided in Figure 5.28.

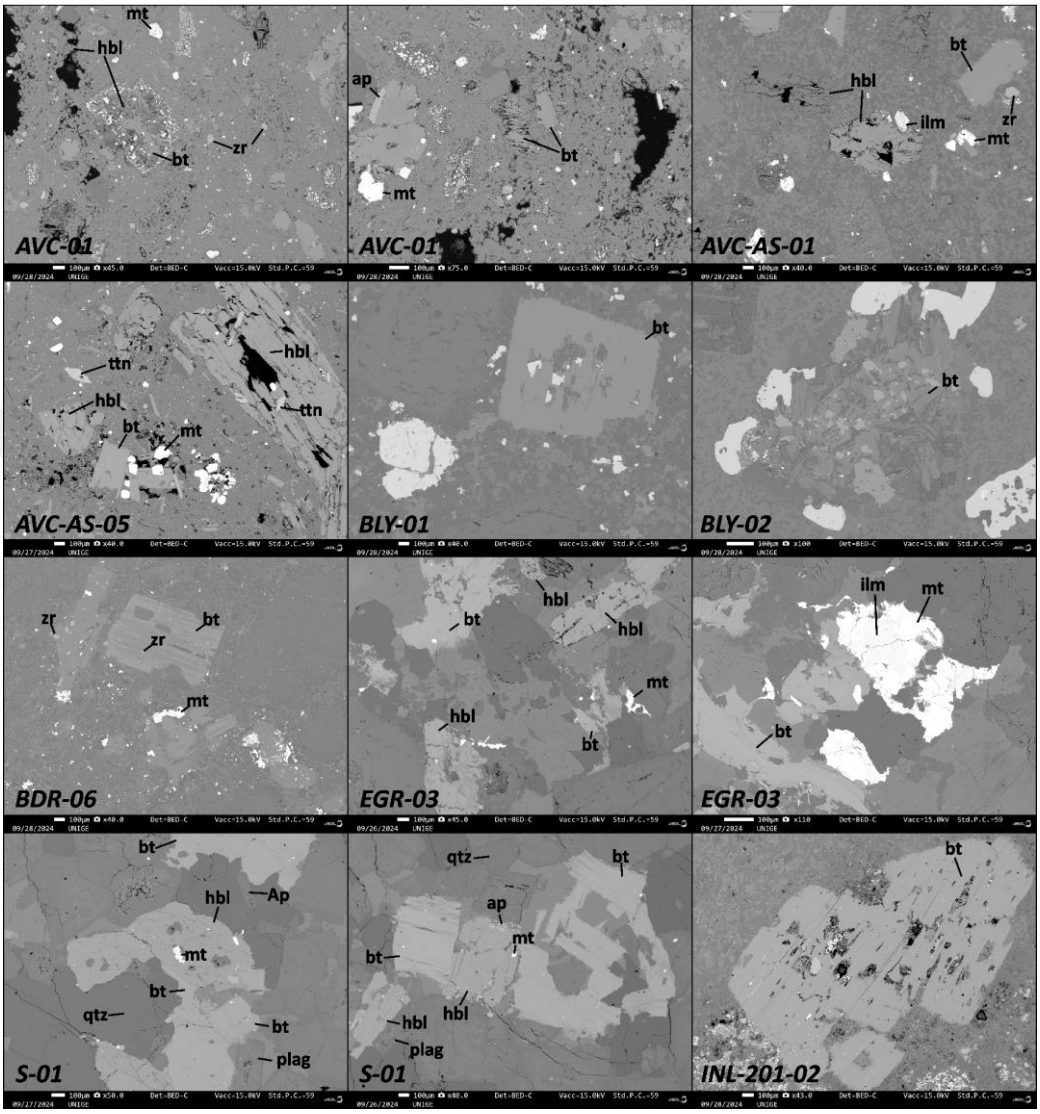


Figure 5.28. Back-scattered electron (BSE) images of amphibole, biotite, and magnetite/ilmenite grains selected for EPMA under the scanning electron microscope.

Ultimately, integrating the mineral chemistry data with whole-rock geochemistry and geochronology provides key insights into magma fertility parameters and the magmatic-hydrothermal processes responsible for ore formation, helping to

constrain the links between magma evolution, oxidation state, and mineralizing potential in the studied systems.

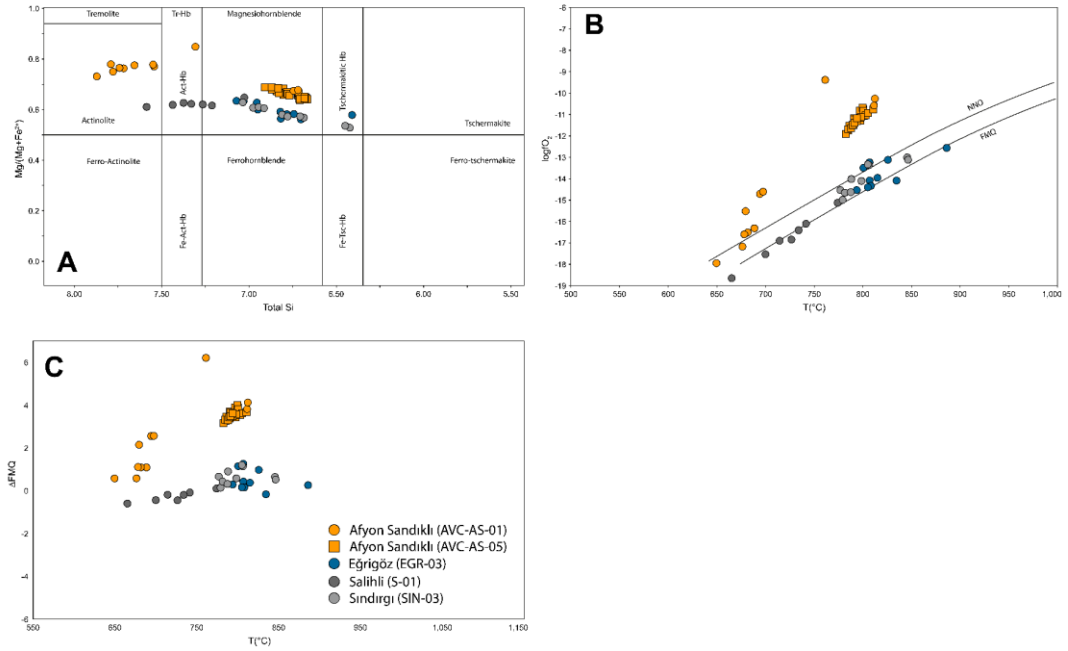


Figure 5.29. Classification diagram of amphiboles from Late Cenozoic magmatic systems (after Leake et al., 1997).

Primary amphiboles were identified in a well-preserved state in samples from the Salihli and Eğrigöz plutons, the Sındırgı volcanic rocks, and the Afyon–Sandıklı sector. In the Salihli and Eğrigöz plutons, as well as in the Sındırgı dacitic volcanics—where hydrothermal alteration is relatively weak—the amphiboles occur as euhedral, medium- to coarse-grained phenocrysts. In contrast, amphibole phenocrysts from mineralized localities commonly display pervasive chloritization and/or actinolitization. In several samples exhibiting potassic alteration, amphiboles are completely replaced by magnetite and secondary biotite, forming pseudomorphic textures indicative of intense hydrothermal overprinting. Inclusions of zircon, apatite, and magnetite are frequently observed within amphibole grains across all

studied units, suggesting co-crystallization with accessory phases during magmatic differentiation.

Mineral chemistry data obtained from EPMA of amphiboles were used to calculate magmatic crystallization temperatures and fO_2 values, which are presented in Table 5.6. The major oxide compositions obtained during EPMA were used to classify the amphiboles following the nomenclature of Leake et al. (1997; Figure 5.29). According to this scheme, amphiboles from the porphyritic trachyandesite sample AVC-AS-05 in the Afyon–Sandıklı sector, as well as most of the amphiboles from the Sındırgı dacitic volcanics and the Eğrigöz granite, are classified as magnesio-hornblende. In contrast, amphiboles from the Salihli granitoid, which has been subjected to intense deformation and partial metamorphism along fault zones, plot between the magnesio-hornblende and actinolite fields, reflecting retrograde overprinting. Amphiboles from the monzonite porphyry sample AVC-AS-01, collected from the eastern part of the Afyon–Sandıklı porphyry system, also partly classify as magnesio-hornblende; however, the majority of grains from this sample fall into the actinolitic amphibole field, indicating either lower-temperature magmatic crystallization or early hydrothermal alteration.

Based on the amphibole chemistry, magmatic crystallization temperatures, pressures, and oxidation states were calculated using the formulations proposed by Ridolfi (2021) (Table 5.6). The results reveal a broad range of crystallization temperatures, spanning from 712 °C to 818 °C. In particular, amphiboles from the Eğrigöz Pluton in the Simav region yield the highest average temperature of approximately 818 °C, whereas those from the Sındırgı volcanic rocks record significantly lower values, averaging around 722 °C (Table 5.6). Within the Afyon–Sandıklı (AS) porphyry system, the monzonite sample AVC-AS-01 produced a crystallization temperature of 712 °C, while the monzonitic latite sample AVC-AS-05 yielded a substantially higher value of 795 °C, indicating variable thermal regimes

within the same subvolcanic complex. Amphiboles analyzed from the Salihli Pluton yielded an intermediate crystallization temperature of approximately 722 °C (Table 5.6).

Table 5.6. Representative EPMA analytical results of amphiboles from the studied localities.

Region	**Salihli-Turgutlu**	**Simav**		**Afyon**	
Field	**Salihli**	**Eğrigöz**	**Sındırgı**	**Afyon-Sandıklı**	
Sample	**S-01**	**EGR-03**	**SIN-03**	**AVC-AS-01**	**AVC-AS-05**
Zircon U-Pb Age (Ma)	**14.8**	**19.291**	**-**	**11.68**	**11.48**
SiO_2	48.32	44.36	44.51	50.43	43.61
K_2O	0.41	0.75	0.83	0.39	1.04
CaO	11.07	10.94	10.88	12.03	11.29
Na_2O	0.84	1.58	1.37	0.75	1.76
MgO	11.52	10.36	10.56	15.67	12.42
Cl	0.04	0.34	0.12	0.26	0.62
TiO_2	0.57	1.24	1.76	0.39	1.28
MnO	0.64	0.85	0.54	0.47	0.36
FeO	16.47	17.83	18.82	11.03	14.93
F	0.00	0.00	0.16	0.03	0.42
Al_2O_3	5.62	7.92	8.12	3.61	7.63
Total	95.50	96.17	97.92	95.06	95.36
Si	7.32	6.83	6.77	7.49	6.76
Al^{IV}	0.68	1.17	1.23	0.50	1.24
Al^{VI}	0.32	0.27	0.21	0.14	0.15
Ti	0.07	0.14	0.20	0.04	0.15
Fe^{3+}	0.53	0.66	0.57	0.34	0.46
Fe^{2+}	1.57	1.61	1.56	1.12	1.48
Mn	0.08	0.11	0.07	0.05	0.05
Mg	2.60	2.38	2.41	3.47	2.87
Ca	1.80	1.80	1.74	1.89	1.85
Na	0.20	0.46	0.40	0.19	0.53
K	0.08	0.15	0.16	0.08	0.21
OH	1.99	1.91	1.89	1.92	1.64
Cl	0.01	0.09	0.03	0.07	0.16

Table 5.6. continued

Region	Salihli-Turgutlu	Simav		Afyon	
Field	Salihli	Eğrigöz	Sındırgı	Afyon-Sandıklı	
Sample	S-01	EGR-03	SIN-03	AVC-AS-01	AVC-AS-05
Zircon U-Pb Age (Ma)	14.8	19.291	-	11.68	11.48
P(kbar)	0.88	1.57	1.35	0.66	1.32
T(°C)	722.27	818.27	721.68	711.88	795.23
logfO_2	-16.73	-15.20	-13.37	-13.57	-13.83
ΔFMQ	-0.26	0.49	0.60	2.36	3.60

Magmatic oxygen fugacities (fO_2) were also estimated using amphibole EPMA data relative to the fayalite–magnetite–quartz (FMQ) buffer (Table 5.6). The monzonitic subvolcanic intrusions from the AS porphyry system display notably high oxidation states, with ΔFMQ values ranging from +2.36 to +3.60, consistent with oxidized, hydrous magmas favorable for porphyry-style mineralization. In contrast, the Simav region samples yield significantly lower values of +0.49 and +0.60 relative to ΔFMQ, suggesting more moderately oxidized conditions. The granite sample from the Salihli Pluton records the lowest oxidation state among all analyzed units, with a calculated value of $\Delta FMQ \approx -0.26$, indicating comparatively reduced magmatic conditions (Table 5.6).

5.1.4 Biotite Geochemistry

In samples collected from the studied localities, biotites that were petrographically identified as fresh were further examined to determine whether they were primary/magmatic, hydrothermal, or re-equilibrated. Following this petrographic classification, suitable grains were selected for quantitative electron probe microanalysis (EPMA; Figure 5.28). In samples affected by hydrothermal fluids, biotites are commonly partially to completely chloritized. In addition, secondary biotites were identified in porphyry-type systems such as Balya. To better capture

the geochemical distinction between primary/magmatic and hydrothermal or re-equilibrated biotites, a limited number of analyses were also conducted on the latter group. EPMA measurements included major element compositions as well as halogens (Cl and F). Based on these data, crystallization temperatures, magmatic fO_2, and depth estimates were calculated from the biotite chemistry (Table 5.7).

Magmatic primary biotites generally occur as euhedral to subhedral grains and often contain inclusions of magmatic accessory minerals such as zircon and apatite, supporting their primary origin (Figure 5.28). In contrast, biotites from Balya, especially in samples exhibiting intense potassic alteration (e.g., BLY-02), are fine-grained, anhedral, and occur as aggregates replacing primary ferromagnesian phases (Figure 5.28). Even the euhedral to subhedral biotites in these samples show evidence of re-equilibration. A limited number of these grains were analyzed, and the resulting crystallization parameters were compared with those of magmatic biotites from BLY-01; the similar conditions obtained justified their inclusion in the overall dataset.

No suitable biotite crystals were found in the Kışladağ, and Sayacık samples due to intense hydrothermal alteration, and biotite was likewise absent in the more mafic compositions of the Kırka and Afyon Volcanic Complex samples. All petrographic interpretations of biotite origin were cross-checked using the criteria proposed by Nachit et al. (2005), with the results showing strong consistency with the petrographic observations (Figure 5.30A).

Table 5.7. Representative EPMA analytical results of biotites from the studied localities.

Region	**Salihli-Turgutlu**	**Afyon**		**Simav**			**Bodrum**	**Biga**			**Konya**
Field	**Salihli**	**Afyon-Sandıklı**		**Sındırgı**	**Eğrigöz**	**Pınarbaşı**	**Bodrum**	**Balya**		**Çatalçam**	**İnlice**
Sample	**S-01**	**AVC-AS-01**	**AVC-AS-05**	**SIN-03**	**EGR-03**	**PNB-01**	**BDR-06**	**BLY-01**	**BLY-02**	**CTL-02**	**INL-201-02**
Age (Ma)	**14.8**	**11.68**	**11.48**	**-**	**19.291**	**18.162**	**10.217**	**25.48**	**25.659**	**20.056**	**8.961**
SiO_2	35.83	37.31	36.74	35.93	35.35	39.84	33.32	35.52	38.86	37.16	36.23
K_2O	9.66	9.56	9.05	9.18	9.29	8.9	6.12	9.34	9.5	9.06	9.57
CaO	0.01	0	0.01	0.02	0	0.05	0.06	0.01	0.01	0.01	0.03
Na_2O	0.08	0.43	0.42	0.39	0.17	0.31	0.21	0.21	0.2	0.29	0.29
MgO	9.95	16.01	13.73	10.59	10.29	11.01	13.59	14.1	17.89	15.96	16.36
Cl	0.02	0.2	0.17	0.05	0.25	0.04	0.12	0.18	0.08	0.04	0.16
TiO_2	3.12	4.23	3.7	4.98	3.83	3.56	3.47	3.48	2.5	4.02	3.56
MnO	0.34	0.18	0.18	0.27	0.46	0.23	0.23	0.1	0.07	0.18	0.23
FeO_t	19.82	11.98	16.71	21.94	20.21	13.57	17.38	15.48	10.13	14.03	12
F	0	0.14	1.03	0.2	0	0.15	0	1.41	0.9	0.17	1
Al_2O_3	14.5	13.14	13.02	13.85	13.2	18.22	15.67	13.73	14.12	14.48	13.56
Total	93.39	93.95	96.45	97.94	93.73	96.35	90.37	95.64	95.57	95.93	94.56
Si	5.63	5.63	5.5	5.44	5.58	5.75	5.38	5.35	5.65	5.51	5.43
Al^{IV}	2.37	2.33	2.3	2.47	2.42	2.21	2.56	2.44	2.35	2.48	2.4
AI^{VI}	0.32	0	0	0	0.04	0.86	0.09	0	0.07	0.05	0
Fe_2O_3	4.45	10.47	9.25	7.22	13.5	4.22	8.95	7.58	4.54	5.62	6.8
FeO	15.82	2.56	8.39	15.44	8.07	9.77	8.63	8.66	6.05	8.97	5.88
H_2O	3.8	3.63	2.78	3.71	3.56	3.95	3.72	2.4	3.11	3.83	2.84
OH*	3.98	3.65	2.8	3.75	3.75	3.81	3.88	2.41	3.02	3.78	2.84
Fe#	0.53	0.3	0.41	0.54	0.52	0.4	0.42	0.38	0.24	0.33	0.29
Mg#	0.47	0.7	0.59	0.46	0.48	0.6	0.58	0.62	0.76	0.67	0.71
T(°C)	666.7	898.2	733.7	737.3	698	750.9	805.68	735.06	758.99	817.45	820.16
P(kbar)	1.61	0.55	0.44	0.96	0.91	2.76	1.5	0.85	0.8	1.13	0.73
$\log f(O_2)$	-17.94	-11.43	-15.76	-15.63	-16.88	-15.41	-13.78	-15.71	-15	-13.64	-13.31
log(XF/XOH)	-	-1.37	-0.24	-1.28	-	-1.45	-	-0.23	-0.53	-1.43	-0.45
log(XCI/XOH)	-2.27	-1.26	-1.21	-1.85	-1.19	-2.17	-1.51	-1.12	-1.56	-2	-1.25
log(XF/XCI)	-	-0.12	0.92	0.57	-	0.72	-	0.89	1.04	0.57	0.8
$\log(fH_2O/fHF)$	-	4.49	3.69	4.56	-	4.86	-	3.69	4.06	4.74	3.77
$\log(fH_2O/fHCI)$	4.45	3.25	3.35	3.92	3.33	4.3	3.55	3.28	3.76	4.08	3.34
$\log(fHF/fHCI)$	-	-1.91	-1.02	-1.14	-	-1.2	-	-1.08	-1.11	-1.33	-1.14

The EPMA datasets were classified according to the scheme of Rieder et al. (1998), which is also adopted by the International Mineralogical Association (Figure 5.30B). Based on this classification, the analyzed grains span compositions between biotite and phlogopite. Measurements from well-preserved biotites in the Eğrigöz, Salihli, and Sındırgı regions plot firmly within the biotite field due to their high Fe contents, clearly distinguishing them from the other samples. Biotites from Pınarbaşı and Bodrum also fall within the biotite field but exhibit comparatively higher Mg contents, plotting near the biotite–phlogopite boundary.

Distinct compositional differences are observed in the AS porphyry prospect. The trachyandesite sample AVC-AS-05 plots within the biotite field but close to the biotite–phlogopite boundary, whereas the monzonite porphyry sample AVC-AS-01 is clearly plotted within the phlogopite field. A similar trend is observed in Balya; however, unlike in the AS system, the phlogopite composition of BLY-02 is attributed to the presence of secondary and re-equilibrated biotites. Samples from Çatalçam plot near the biotite–phlogopite boundary but fall on the phlogopite side, as do the biotites from the andesite porphyry in İnlice.

In terms of major element chemistry, pronounced variations are observed in FeO and MgO contents across the dataset. When plotted on the Abdel-Rahman (1994) discrimination diagram, nearly all biotite analyses (with the exception of two measurements from Pınarbaşı) are associated with calc-alkaline, orogenic I-type granitoids (Figure 5.30C). All samples show comparable Si contents (5.35–5.75 a.p.f.u.), consistent with magmatic biotite compositions from subduction-related arc environments.

Notable variations are also observed in the halogen contents of the analyzed biotites (Table 5.7). Samples from Salihli, Pınarbaşı, and Sındırgı yield the lowest chlorine concentrations, with Cl contents of approximately 0.02 wt.%, 0.04 wt.%, and 0.05 wt.%, respectively (Table 5.7). In contrast, the trachyandesite sample from the

A–S porphyry prospect and the primary biotite-bearing sample from Balya display significantly elevated fluorine concentrations, clearly distinguishing them from the rest of the dataset.

All analyzed biotites exhibit relatively narrow variations in calculated H_2O contents, ranging between 2.40 wt.% and 3.95 wt.% (Table 5.7). A systematic trend is evident in the Simav region, where H_2O contents increase from the barren porphyry systems at Sındırgı and Eğrigöz towards the mineralized Pınarbaşı porphyry prospect, suggesting a possible link between magmatic water content and ore fertility.

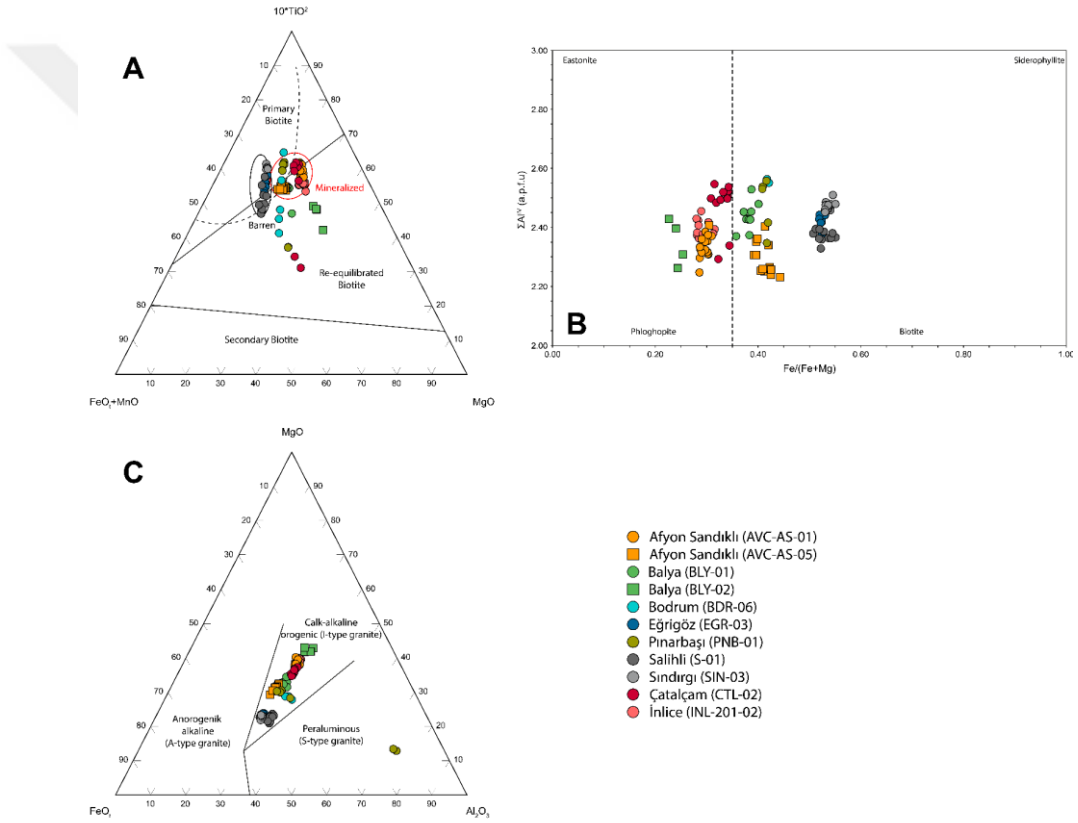


Figure 5.30. Classification diagram of biotites from Late Cenozoic magmatic systems. A) 10*TiO_2-(FeO+MnO)-MgO ternary plot to discriminate primary and secondary biotites (after Nachit et al., 2005). B) Biotite compositional plots on binary classification diagram (after Rieder et al., 1998). C) Biotite discrimination diagram (after Abdel-Rahman, 1994).

Crystallization temperature estimates derived from biotite chemistry further emphasize the thermal variability among the studied systems (Table 5.7). Within the AS porphyry prospect, a distinct difference is observed between the two analyzed samples: the monzonite porphyry AVC-AS-01 records a high crystallization temperature of 898 °C, whereas the trachyandesite sample AVC-AS-05 yields a markedly lower value of 734 °C. The granite sample from the Salihli Granitoid produced the lowest temperature of the entire dataset at 667 °C.

Samples from the Simav region yield intermediate crystallization temperatures ranging from 698 °C to 751 °C, with the Eğrigöz granite at the lower end of the range and the Pınarbaşı porphyry andesitic porphyry sample recording the highest value in this subset. In the Bodrum area, the oldest magmatic phase, represented by the basaltic trachyandesite sample, yielded a crystallization temperature of approximately 806 °C.

In the Biga Peninsula, contrasting temperature ranges are observed between the two mineralized systems. The Balya samples record crystallization temperatures between 735 °C and 759 °C, while the Çatalçam andesite porphyry yields significantly higher temperatures of ~817 °C. Finally, the andesitic porphyry wall rock of the İnlice HS epithermal system produced the highest temperature estimate of the dataset at ~820 °C, consistent with high-temperature magmatic input into the epithermal environment.

5.1.5 Magnetite-Ilmenite Geochemistry

In acidic to intermediate magmatic rocks, magnetite and ilmenite crystals—occurring either as microphenocrysts or within the groundmass of porphyritic-textured rocks—can be used in EPMA analyses to estimate magmatic crystallization temperatures and oxygen fugacity (fO_2). However, the reliability of magnetite–

ilmenite thermometry and oxybarometry depends on several critical conditions. The first requirement is that the magnetite–ilmenite pairs must not have been affected by hydrothermal alteration or re-equilibrated during post-magmatic processes. The second condition is that the two oxide phases must have crystallized in mutual equilibrium.

To ensure these criteria were met, samples exhibiting strong hydrothermal alteration, sulfide mineralization, or magnetite–ilmenite grains with exsolution textures were excluded from analysis. For this reason, samples from Çatalçam, Kışladağ, Sayacık, and Pınarbaşı were not analyzed for oxide thermobarometry, as the magnetite–ilmenite pairs in these units may have been re-equilibrated during high-temperature hydrothermal overprinting. The calculated temperatures and oxygen fugacities from the selected magnetite–ilmenite pairs are presented in Table 5.8.

In the Afyon Volcanic Complex (AVC), magnetite is present in several samples, whereas ilmenite is scarce. In sample AVC-02, magnetite accounts for less than 90 wt.% of the total Fe–Ti oxide content; therefore, the results from this sample were excluded from thermometric calculations and only major-element compositions are reported. Similarly, ilmenite was not identified in AVC-03 or in the Balya and İnlice samples, so only magnetite compositions were obtained from those localities.

Within the AVC, magnetite typically occurs as semi-euhedral grains dispersed in the groundmass of porphyritic rocks. In contrast, samples from the Afyon–Sandıklı (A–S) porphyry prospect contain euhedral to subhedral magnetite–ilmenite pairs, meeting the criteria for equilibrium crystallization. A similar textural relationship is observed in the Bodrum sample, where fine-grained magnetite occurs within a porphyritic matrix. In the Eğrigöz Granite, magnetite and ilmenite occur both as discrete euhedral to subhedral phenocrysts and as exsolution lamellae, while in the Salihli Pluton the Fe–Ti oxides are predominantly present as fine-grained inclusions within amphibole and biotite.

Table 5.8. Representative EPMA analytical results of magnetite/ilmenite from the studied localities.

Region	**Afyon**								**Simav**		**Biga**	**Konya**	**Salihli**	
Field	**A-S Porphyry**				**Afyon Volcanic Complex**				**Eğrigöz**		**Balya**	**İnlice**	**Salihli**	
Sample	**AVC-AS-01**		**AVC-AS-05**		**AVC-01**		**AVC-02**	**AVC-03**	**EGR-01**		**BLY-01**	**INL-D-01**	**S-01**	
Age (Ma)	**11.68**		**11.48**		**11.763**		**11.78**	**-**	**19.486**		**25.48**	**9.035**	**14.8**	
Mineral	**Mt**	**Ilm**	**Mt**	**Ilm**	**Mt**	**Ilm**	**Mt**	**Mt**	**Mt**	**Ilm**	**Mt**	**Ilm**	**Mt**	**Ilm**
FeO	90.01	60.71	83.43	41.7	78.78	55.46	66.16	80.43	90.21	39.7	91.7	80.18	84.23	44.46
TiO_2	0.36	30.44	5.3	53.19	5.81	35.53	11.74	7.38	1.12	49.98	0.13	5.56	5.55	49.15
MnO	0.18	1.54	0.79	5.29	0.59	0.33	0.4	0.88	0.29	8.95	0.04	0.56	0.72	5
V_2O_3	0.46	0.37	0.64	0.04	0.77	0.64	0.52	0.63	0.66	0.13	0.46	0.7	0.48	0.11
CaO	0.07	0.04	0.03	0.02	0.02	0.05	0.06	0.03	0.02	0.02	0.02	0.03	0.03	0.07
Cr_2O_3	0.21	0.15	0.27	0.01	0.34	0.29	0.07	0.07	0.09	0.05	0.04	0.47	0.23	0.02
K_2O	0.01	0	0.02	0.03	0.03	0.02	0.12	0.01	0.01	0.01	0	0.02	0.04	0.03
Na_2O	0.01	0.01	0.01	0	0.01	0	0.1	0.02	0.01	0.01	0	0.01	0.01	0.01
MgO	0.02	0.06	0.72	0.05	1.34	0.89	0.15	0.43	0.01	0.05	0.02	1.28	0.84	0.16
SiO_2	0.06	0.04	0.13	0.04	0.08	0.06	5.87	0.2	0.05	0.02	0.04	0.27	0.09	0.03
Al_2O_3	0.14	0.04	1.31	0.01	2.93	0.68	2.64	1.66	0.44	0.03	0.33	2.22	1.03	0.05
Total	91.54	93.39	92.66	100.37	90.7	93.96	87.82	91.74	92.92	98.94	92.79	91.29	93.23	99.09
Si	0	0	0.01	0	0	0	-	0.01	0	0	0	0.01	0	0
Ti	0.01	0.61	0.15	1.01	0.17	0.7	-	0.22	0.03	0.96	0	0.16	0.16	0.94
Al	0.01	0	0.06	0	0.13	0.02	-	0.08	0.02	0	0.02	0.1	0.05	0
Fe^{3+}	1.95	0.77	1.6	-0.02	1.48	0.56	-	1.46	1.89	0.08	1.96	1.52	1.61	0.12
Fe^{2+}	1	0.57	1.09	0.89	1.08	0.66	-	1.16	1.02	0.76	1	1.08	1.09	0.82
Cr	0.01	0	0.01	0	0.01	0.01	-	0	0	0	0	0.01	0.01	0
Mn	0.01	0.03	0.03	0.11	0.02	0.01	-	0.03	0.01	0.19	0	0.02	0.02	0.11
Mg	0	0	0.04	0	0.08	0.03	-	0.03	0	0	0	0.07	0.05	0.01
Ca	0	0	0	0	0	0	-	0	0	0	0	0	0	0
Na	0	0	0	0	0	0	-	0	0	0	0	0	0	0
K	0	0	0	0	0	0	-	0	0	0	0	0	0	0
V	0.01	0.01	0.02	0	0.02	0.01	-	0.02	0.02	0	0.01	0.02	0.01	0
FeO (%)	30.92	25.72	33.86	42.42	33.1	30.04	-	35.91	31.71	35.81	31.04	33.32	34.07	38.79
Fe_2O_3 (%)	66.87	38.89	55.09	-0.8	50.77	28.25	-	50.01	65.01	4.32	67.42	52.08	55.74	6.31
T(°C)	668.72		383.85		606.89		-	-	555.48		-	-	435.13	
$\log f(O_2)$	-13.27		-		-14.77		-	-	-20.9		-	-	-19.09	

The major oxide compositions of the analyzed magnetite–ilmenite pairs were classified according to two schemes: one based on their bulk oxide chemistry (Figure 5.31A) and the other on cation proportions in the crystal lattice (Figure 5.31B). The results show a clear compositional separation between magnetite and ilmenite fields, while in some samples a trend towards hematite compositions is observed in the ilmenite population (Figure 5.31).

Crystallization temperatures and magmatic oxygen fugacity values were calculated from the chemical compositions of magnetite and ilmenite using the method proposed by Andersen and Lindsley (1985). The results are presented in Table 5.8. These calculations yielded significantly lower temperature estimates compared to those obtained from amphibole- and biotite-based geothermometry. Within the Afyon–Sandıklı (A–S) porphyry prospect, a marked contrast is observed between the two analyzed samples: the monzonite porphyry AVC-AS-01 yields a crystallization temperature of 669 °C, whereas the monzonitic latite sample AVC-AS-05 produces an anomalously low value of 384 °C, well below typical magmatic crystallization ranges. The validity of these results is therefore considered questionable.

From the Afyon Volcanic Complex, the only sample containing both magnetite and ilmenite (AVC-01) produced a calculated temperature of 607 °C. Similarly, measurements from the Eğrigöz and Salihli plutons yielded temperatures of 556 °C and 435 °C, respectively—again notably lower than expected for unaltered magmatic systems. These results suggest either subsolidus re-equilibration of the Fe–Ti oxides or post-magmatic resetting during hydrothermal alteration, underscoring the necessity of cautious interpretation when applying magnetite–ilmenite thermobarometry in hydrothermally affected porphyry systems.

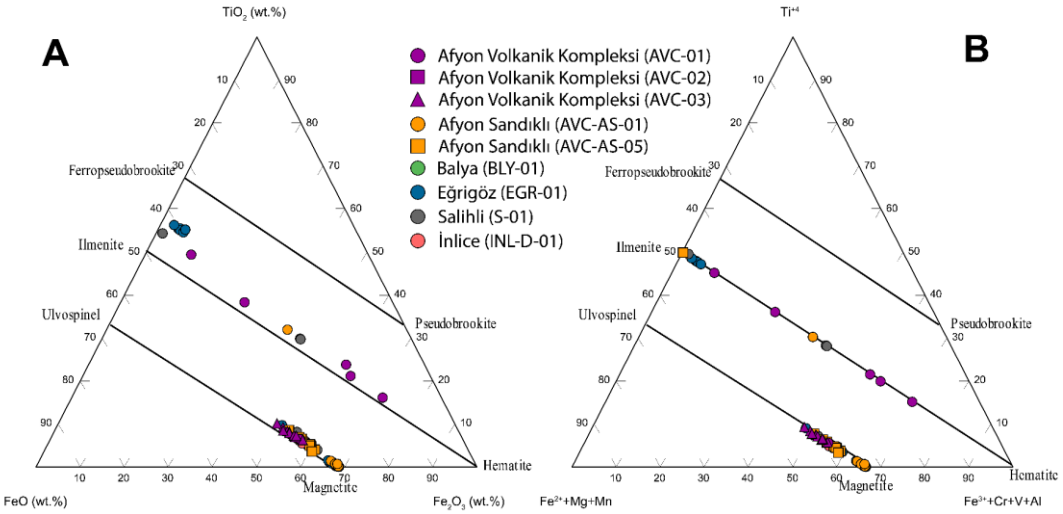


Figure 5.31. Classification of magnetite and ilmenite based on A) TiO_2-FeO-Fe_2O_3 system (after Sassi et al., 2004), and B) Ti^{+4}-Fe^{3+}+Mg+Mn-Fe^{3+}+Cr+V+Al system.

CHAPTER 6

DISCUSSION

Zircon, a ubiquitous accessory mineral in most intermediate to felsic silicate rocks, serves as a resilient geochemical archive, capable of preserving critical information about magmatic processes. It commonly incorporates substantial concentrations of uranium (U), thorium (Th), hafnium (Hf), and a range of high field strength elements (HFSE) and rare earth elements (REE) within its crystal lattice (Lu et al., 2016). In addition to these components, the abundances of titanium (Ti), cerium (Ce), and uranium in zircon have proven invaluable for quantifying key petrogenetic parameters such as magma crystallization temperatures (Watson et al., 2006; Ferry and Watson, 2007) and oxygen fugacity (Smythe and Brennan, 2016; Loucks et al., 2020)—both of which exert a fundamental influence on the metal fertility of magmatic systems.

Over the past two decades, zircon geochemistry has been increasingly employed to distinguish magmas capable of generating porphyry-type mineralization from those that are barren, leading to a substantial body of research on the geochemical fingerprints of fertile versus infertile systems (Ballard et al., 2002; Dilles et al., 2015; Lu et al., 2016; Loader et al., 2017; Lee et al., 2021; Nathwani et al., 2021; Carrasco-Godoy et al., 2024). Recently, this approach becomes an important tool to understand magmatic evolution in Türkiye (İmer et al., 2023; Moghadam et al., 2025). These studies have identified several robust discriminants, particularly in magmas emplaced at mid-crustal levels, where oxidation state plays a pivotal role in controlling ore metal transport and deposition. Among these, the europium anomaly (Eu/Eu*) and the cerium redox ratio (Ce^{4+}/Ce^{3+}, often expressed as Ce/Ce*) have emerged as primary geochemical indicators of magmatic oxidation conditions (Ballard et al., 2002).

Beyond redox-sensitive ratios, other trace element systematics—such as Hf/Y, Th/U, and Ce/Nd—offer complementary insights into the magmatic differentiation history, the identity of fractionating mineral phases, and, by extension, the volatile (particularly water) content and oxidation state of the melt. These parameters also carry implications for the thermal evolution of the magma, as they can be linked to crystallization temperature regimes and the stability fields of key mineral phases. Consequently, zircon chemistry provides not only a time-resistant record of magmatic conditions but also a framework for assessing the fertility potential of arc-related magmas in the context of porphyry deposit formation.

In the present study, zircon trace element systematics from Western Anatolia and the Central Taurides were examined within this framework to evaluate both magmatic evolution and ore-forming potential. Particular emphasis was placed on Eu/Eu* and Ce/Ce* ratios as redox-sensitive indicators, alongside Hf/Y, Th/U, and Ce/Nd ratios to constrain fractionation histories, volatile contents, and crystallization temperatures of the parental magmas. By comparing zircon chemistry from fertile porphyry-related intrusions with that from barren or weakly mineralized systems, it was possible to assess whether the Western Anatolia and Central Taurides magmas exhibit the geochemical signatures—such as elevated oxidation states, suppressed plagioclase fractionation, and distinctive REE fractionation patterns—that are characteristic of productive porphyry systems. This approach provides a robust geochemical basis for distinguishing magmatic centers with high metallogenic potential from those with limited ore-forming capacity.

6.1 Temporal and Spatial Evolution of the Late Cenozoic Magmatism

The Late Cenozoic magmatism of the Central Taurides and Western Anatolia is an intricate geological record of accretionary tectonics and collisional events, extensional tectonics, subduction-zone processes, post-subduction and post-collisional events (i.e. slab breakoff and delamination), and asthenospheric upwelling in the central and western Türkiye (Dilek and Altunkaynak, 2009, 2010,

Biryol et al., 2011; Jolivet et al., 2013; Rabayrol et al., 2019a, 2019b; Rabayrol and Hart, 2021). This magmatic history, spanning the past ~25 million years, records the transition from subduction-dominated processes along the Neotethyan suture zones to extensional and transtensional tectonic settings associated with slab break-off, lithospheric delamination, and localized mantle upwelling (Dilek and Altunkaynak, 2009; Agostini et al., 2010; Karaoğlu et al., 2018).

The distribution and timing of these magmatic events are far from uniform. Instead, they reveal a mosaic of magmatic centers that reflect variations in crustal thickness, magma source characteristics, and the degree of mantle–crust interaction. Zircon U–Pb geochronology provides one of the most reliable tools for constraining the timing of igneous activity, offering high-precision ages that allow regional magmatic events to be correlated across large distances. In this study, zircon U–Pb dates from 61 samples collected across the Central Taurides and Western Anatolia define a temporal framework that integrates the magmatic evolution of porphyry-related, epithermal, and barren intrusions.

The oldest events recorded in our dataset occur in the Biga Peninsula (Figure 6.1), more specifically in Balya. The two ages obtained from the deep drill core samples in the Balya North sector yield ages of 25.56 ± 0.10 Ma and 25.53 ± 0.09 Ma. Slightly younger mineralized systems at Turplu and Sarıalan cluster around 22.12–22.83 Ma, overlapping with barren volcanism from the nearby Hallaçlar area (22.72–23.29 Ma).

Inland from Biga, the Kütahya-Simav belt preserves a coherent ~20–18 Ma magmatic episode (Figure 6.1). Here, barren high-K calc-alkaline dacites and granites-granodiorites at Sındırgı and Eğrigöz predates the age of the host monzonites at the Pınarbaşı porphyry Cu–Mo mineralization (18.15–18.10 Ma). Zircon and apatite trace element geochemistry from these units suggest increasing role of amphibole fractionation from hydrous melts from 20 Ma towards 18 Ma. Magma oxygen fugacities (fO_2) estimated through zircon chemistry also display a progressive increase (ΔFMQ from <1.5 up to 2.6) during this time interval.

Combined whole-rock and zircon geochemical data are thus interpreted to reflect a gradual shift towards more suitable conditions for porphyry formation over a period of ~2 million years at the Kütahya-Simav District.

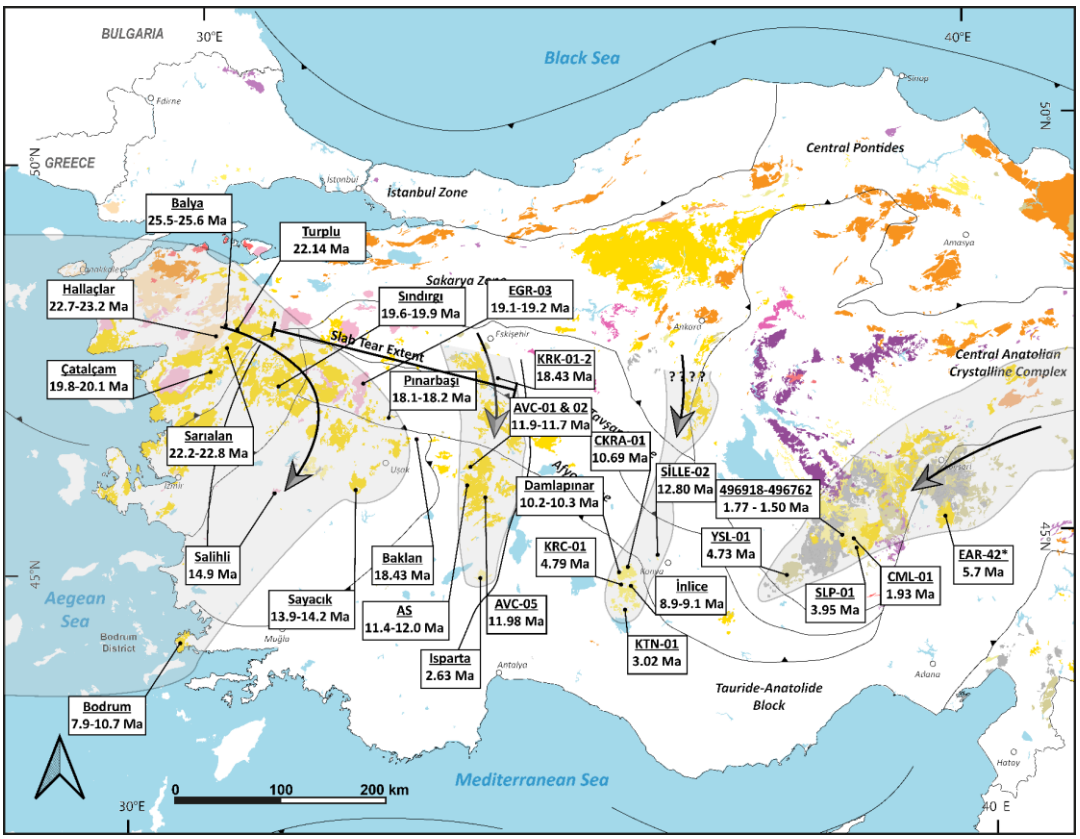


Figure 6.1. Temporal and spatial distribution of the Late Cenozoic magmatism in the Central Taurides and the Western Anatolia. The sample locations and the obtained U-Pb ages are included in the map.

Further southeast, along the Kırka–Afyon–Isparta corridor (Figure 6.1), magmatic focus progressively migrates towards the South. The northerly early Miocene calc-alkaline to alkaline magmatism in the Kırka (21–17 Ma; 18.43 from KRK-01-2) gradually shift into more alkaline in the middle Miocene (14 – 8 Ma; 12–11 Ma in analyzed samples), and eventually to the Plio-Quaternary (4 Ma to present; 2.63 Ma from GÖL-02) ultrapotassic Isparta-Gölcük magmatic rocks at the southern end.

The Uşak district hosts both the world-class Kışladağ porphyry Au deposit and the Sayacık prospect (Figure 6.1). Previous research at Kışladağ indicates that

mineralization is associated with a series of high-K calc-alkaline to shoshonitic monzonitic porphyry intrusions emplaced in a post-collisional extensional setting. Zircon U-Pb geochronology of five distinct magmatic phases revealed that Kışladağ magmatism developed within ≤0.4 M.y. (14.76–14.36 Ma). Zircons from parental intrusions at Sayacık are geochemically similar monzonitic porphyries are dated between 14.25 and 13.92 Ma, coeval with Kışladağ's late intrusions.

The formation of intrusive phases in the Kışladağ and Sayacık is also coeval with another small-volume but important granitic bodies situated at the Salihli-Turgutlu district in Manisa (Figure 6.1). Two dated samples yield crystallization ages for the Salihli pluton as between 14.90 and 14.82 Ma. The temporal coincidence between fertile and barren systems highlights the need to integrate zircon geochemistry with geochronology when discriminating between fertile and infertile magmatic pulses.

The Bodrum Peninsula located at the southwestern tip of the Anatolian plate (Figure 6.1) is represented by several million years of magmatic activity coinciding with the development of the Bodrum Caldera. The igneous activity began with the emplacement of monzonitic stock. The monzonite sample in the Bodrum Peninsula is dated between 10.7 and 10.2 Ma. This episode is identified as a barren magmatic phase as evidenced by the zircon and apatite trace element geochemistry. The second phase found through zircon U-Pb dating in this study, clusters around 8.8 to 8.9 Ma. The last phase is dated as 7.9 and 8.1 Ma, thus covering almost the entire caldera development stages. The last group appear to be the most fertile in all the samples supporting the formation of those rocks under thin-crustal settings following the caldera collapse.

The southwestward migration of the magmatic front and associated mineralization in Western Anatolia resulted from the acceleration of the Aegean slab rollback and subsequent lateral tearing (15-8 Ma).

The Central Taurides sector of this study covers relatively younger period; late Miocene in the Konya Volcanic Complex and Pliocene in the Develidağ Volcanic Complex. The Konya Volcanic Complex was emplaced at the termination of the

Akşehir normal fault. Rabayrol and Hart (2021) suggest that the KVC is a southern continuation of the early Miocene (21-17 Ma) Galatean Volcanic Province (GVP). The earliest products of the KVC within the scope of this thesis is the middle Miocene lavas and lamprophyres in the Sulutaş Volcanic Suite as confirmed by U-Pb zircon geochronology data from SVS (Sille-02 – 12.80 Ma). This alkaline magmatism shifts into calc-alkaline volcanic successions in the Erenlerdağ-Alacadağ sector in KVC. These units either contain hydrothermal alteration (Damlapınar and Çukurağıl) or host the İnlice epithermal Au mineraliation between ~10.7 and 8.9 Ma in the Çukurağıl, Damlapınar, and İnlice areas. The İnlice epithermal Au mineralization (9.10–8.89 Ma) is genetically linked to oxidized, hydrous magmas crystallizing at mid- to upper-crustal depths, as suggested by zircon trace element compositions.

Within the Konva Volcanic Complex (KVC), the widely distributed middle Miocene magmatism was succeeded further south by Pliocene magmatic activity (3–5 Ma). In the northeastern sector of the KVC, magmatic activity commenced at ca. 12 Ma, progressively younging toward the southwest. This trend corroborates the widely recognized pattern in Anatolia, whereby magmatism becomes progressively younger toward the southwest. Moreover, zircon U-Pb ages obtained in this study supports the interpretation that the KVC represents the southern continuation of the early Miocene magmatic belt of the GVP (Rabayrol and Hart, 2021; Karaoğlu et al., 2024).

Within the Central Taurides, excluding the Konva Volcanic Complex (KVC), the investigated units generally range from the Late Miocene (5.7 Ma) to the Pleistocene (1.5 Ma), representing the younger magmatic products of the region. The Öksüt sample (EAR-42; 5.7 Ma), part of the Develidağ Volcanic Complex, was not analyzed in this study but was provided by İmer et al. (unpublished). Toward the southwest, this unit is succeeded by comparatively younger volcanic products. Among these, the Melendiz volcanic rocks represent the youngest units investigated in the entire scope of this thesis, with ages ranging between 1.9 and 1.5 Ma. These units are part of the magmatic belt that originated in Eastern Anatolia during the Oligocene and subsequently propagated westward, following the trend proposed by

Rabayrol et al. (2019b). The Karapınar vent, located between the Karaman vent (<3 Ma) and the Melendiz stratovolcano, yielded an age of 4.7 Ma, thus bridging the temporal gap between Melendiz and Develidağ magmatism.

6.2 Tectonomagmatic Evolution of the Central Taurides and the Western Anatolia

In this thesis, a comprehensive geochemical database has been established through detailed trace element analyses of zircons sampled from the Late Cenozoic magmatic belt extending between the Central Taurides and Western Anatolia. These zircons were primarily characterized by U–Pb geochronology prior to trace element investigation, ensuring robust temporal constraints on the magmatic events they represent. In this section, the chemical signatures of zircons from different sectors of the belt will be examined in a comparative framework, with the dual aim of elucidating the petrogenetic characteristics of their host magmas and assessing their potential to generate porphyry-type mineralization.

In the Central Taurides segment of the belt, zircon samples were primarily examined from the Konya Volcanic Complex and the Sulutaş Volcanic Suite, with a particular focus on magmatic units associated with epithermal Au (and related porphyry Cu–Au) systems within the Erenlerdağ–Alacadağ sector. These samples represent the oldest alkaline magmatism in the north (SVS–12.8 Ma) and the magmatism from the exploration prospects of Çukurağıl (10.7 Ma), Damlapınar (10.3–10.2 Ma), İnlice (9 Ma), Karacaören (4.8 Ma), and Ketenli (3 Ma), arranged from oldest to youngest. Temporal variations in the principal porphyry fertility parameters of these sites are illustrated in Figure 6.2.

The Sille-02 sample, derived from the Sulutaş Volcanic Suite and representing the oldest magmatic activity in the region, exhibits zircon geochemical characteristics that contrast sharply with those of younger and mineralized units located farther south in the Konya region, particularly within the Erenlerdağ–Alacadağ sector.

These younger units, which occur either as altered host rocks or as directly mineralized lithologies, display distinct trace element signatures indicative of stronger subduction influence. In contrast, zircons from Sille-02 yield relatively low Th/Nb ratios coupled with elevated Nb/Hf values, pointing toward within-plate (anorogenic) magmatic conditions, more consistent with an intraplate tectonomagmatic setting.

The trace element data further suggest that the fractionation processes in Sille-02 magmas were dominated by amphibole, as evidenced by the very low Dy/Yb ratio (0.19), while garnet exerted little to no influence during crystallization. The trend observed in Th/U versus Eu/Eu* ratios—initially maintaining a relatively flat pattern before showing a progressive decrease—can be interpreted to reflect suppressed plagioclase fractionation during the early to intermediate stages of magmatic evolution, followed by enhanced plagioclase removal at later stages (Figure 5.9).

Moreover, the high Ce/Ce* values (average ~354) and moderately elevated Ce/Nd ratios (average ~43) indicate the presence of a pronounced positive Ce anomaly, suggesting crystallization from a melt characterized by high oxygen fugacity and an evolved, REE-enriched composition. While the calculated ΔFMQ_{zircon} values (> 0) indicate moderate to relatively high oxidation states—conditions that could be favorable for porphyry-style mineralization—they still fall below the threshold typically associated with the most productive porphyry systems.

In addition, the Sille-02 sample records the lowest Ti content (average 3.88 ppm) among all Konya sector samples analyzed in this study. This notably low Ti concentration directly translates into the lowest calculated zircon crystallization temperatures within the dataset, implying crystallization under relatively low-temperature conditions. Such temperatures are consistent with emplacement at shallower crustal levels, which, in turn, align with the tectonomagmatic interpretation suggested by the trace element ratios.

Of particular interest are the northern sector magmatic units, dated between 10.7 and 9 Ma, which are spatially associated with both economic mineralization (e.g., İnlice)

and with alteration styles ranging from intense silica–clay ± alunite assemblages to higher-temperature potassic–phyllic alteration zones, locally developed to considerable intensities. From the perspective of whole-rock geochemistry, these magmatic units do not exhibit pronounced differences. However, zircon trace element compositions reveal subtle but meaningful distinctions. In particular, zircons from two Damlapınar samples display slightly elevated Ti concentrations, coupled with lower Eu/Eu* and Th/U ratios, when compared to zircons from all other samples of the same age range (Figure 5.9; Table 5.3).

Although Dy/Yb_{zircon} ratios in the Damlapınar samples are broadly comparable to those from other sites, the concurrent decline in Eu/Eu* values alongside decreasing Th/U ratios suggests a somewhat greater role for plagioclase fractionation in the evolution of these magmas—albeit not overwhelmingly dominant—relative to other magmatic systems in the complex. This geochemical pattern further implies that the zircons crystallized from magmas with comparatively lower water contents. The petrographic observation that the Damlapınar samples contain pyroxene rather than hornblende reinforces this inference, as amphibole stability is typically favored in more hydrous magmatic conditions.

Moreover, Ti-in-zircon thermometry and ΔFMQ estimates for Damlapınar are systematically lower than those calculated for Çukurağıl and İnlice. Taken together, these parameters indicate that the Damlapınar magmatic system possessed more limited potential for porphyry-style mineralization. This interpretation is consistent with field evidence, as the degree of hydrothermal alteration observed at the surface is notably weaker at Damlapınar compared with both İnlice and Çukurağıl.

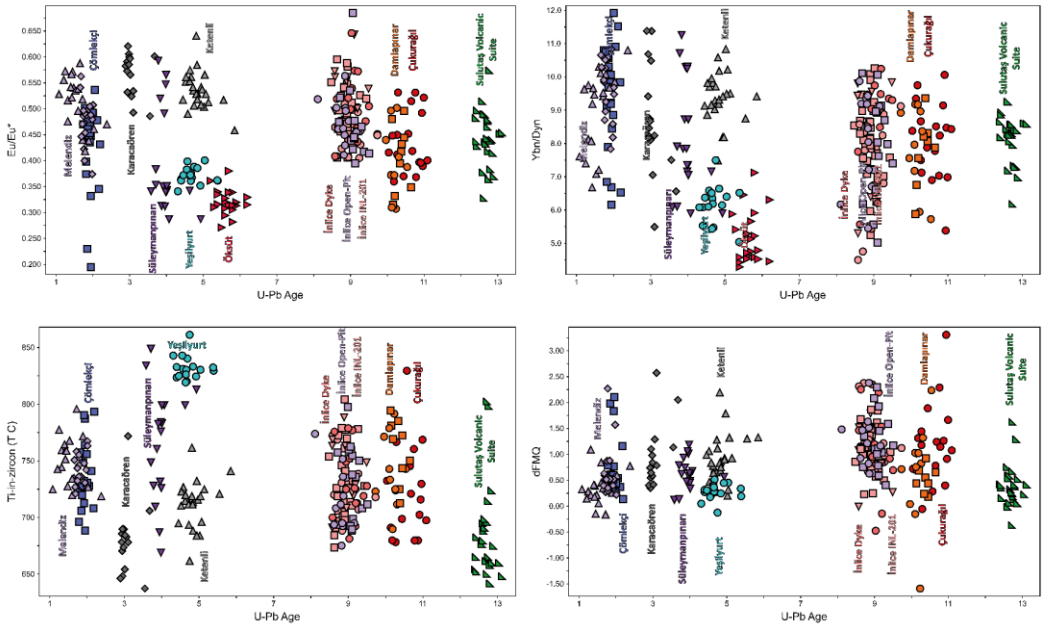


Figure 6.2. Diagrams showing temporal variations of key zircon-derived porphyry fertility parameters for Late Cenozoic magmatism in the Central Taurides.

The geochemical differences between zircons hosted in the Çukurağıl andesite porphyry volcanic units (ca. 10.7 Ma) and those from the İnlice prospect (ca. 9 Ma) are comparatively subtle. The most notable contrasts between these two sites are observed in their Eu/Eu* and Dy/Yb ratios, whereas the calculated mean zircon crystallization temperatures and ΔFMQ_{zircon} values largely overlap. These patterns suggest that the observed variations are most plausibly attributable to a modest increase in crustal thickness, coupled with a more pronounced role of amphibole fractionation in the evolution of the İnlice magmas, over the ~1.7 million years that separate the emplacement of these two systems.

Zircon trace-element data from the Konya Volcanic Complex (KVC) indicate that a significant shift in magma chemistry occurred during the transition from the Miocene to the Pliocene. Zircons from the andesite porphyry of the Karacaören prospect (4.8 Ma), located south of İnlice, and from andesitic agglomerates at the Ketenli prospect (3 Ma), situated near Seydişehir, are characterized by the lowest mean Ti contents (and hence the lowest zircon crystallization temperatures) and the lowest Th/U ratios among all samples analyzed from the KVC. The Karacaören sample, in contrast,

yields the highest mean Hf, Y, and ∑REE concentrations, as well as the highest Ce/Ce^*_{zircon} values recorded in the complex.

Despite these distinctions, the Eu/Eu* ratios and inferred fO_2 values of Karacaören and Ketenli zircons are broadly comparable to those of the older İnlice and Çukurağıl systems. This similarity suggests that their parental magmas shared certain fertility-related characteristics. Nevertheless, the relatively high abundances of incompatible elements such as Hf, Y, and REE, combined with notably low Th/U ratios, point toward a genetic model in which these younger magmas—chemically more evolved than the 11–9 Ma mineralizing systems—were generated under lower-temperature conditions (<700 °C) by low-degree partial melting. These magmas may have been derived from crustal sources that had previously hosted porphyry–epithermal mineralization but had since been depleted in metals, subsequently undergoing partial remelting. As a result, they likely retained the capacity to release hydrothermal fluids sufficient to produce widespread alteration, but lacked the metal budget necessary to form economically significant mineralization.

In the region between Karapınar (Konya), Niğde, and Kayseri, Late Miocene–Pliocene magmatic systems yield zircons whose mineral chemistry reveals important insights. Notably, the pyroxene andesite porphyry sample from the Öksüt high-sulfidation (HS) epithermal Au–Cu deposit (5.7 Ma), which forms the principal host rock to the orebody, and the andesite porphyry from the Karacadağ Caldera near Yeşilyurt (Karapınar; 4.8 Ma) exhibit several shared geochemical features. Among all zircon samples analyzed from the Central Taurides, these two sites record the highest Ti contents, accompanied by relatively high Th/U ratios, and low Eu/Eu*, Ce/Ce*, and Ce/Nd values. They also yield the lowest ΔFMQ values calculated for the sector (Figure 6.2).

The lack of any corresponding increase in Eu/Eu* with decreasing Th/U ratios—particularly in the Öksüt samples—suggests that their parental magmas underwent fractionation from a source containing significant plagioclase. The dominance of clinopyroxene and minor orthopyroxene phenocrysts, rather than hornblende, in the

Öksüt sample supports this interpretation, reflecting low magmatic water contents and aligning with the low Eu/Eu* values. Drill core studies from Öksüt have identified a potassic alteration zone at depth containing secondary biotite, K-feldspar, and magnetite (Yurdakul et al., 2021). However, the absence of porphyry-style quartz vein stockworks (e.g., A-, B-, or D-type veins) suggests a hydrothermal system characterized by limited fluid volumes, again consistent with low magmatic water content.

Zircon crystallization temperatures calculated for Öksüt and Karacadağ are exceptionally high—818 °C and 832 °C, respectively—consistent with their elevated Ti contents. Yurdakul et al. (2021) have noted that the Öksüt HS epithermal system was emplaced within the Develi segment of the Ecemiş Fault Zone during a period of strong east–west extension in the Late Miocene, with epithermal mineralization forming synchronously with explosive volcanism. In such a volcano-tectonic setting, the development of porphyry-type systems—characterized by prolonged magmatic residence, periodic magma recharge, and progressive enrichment in metals, volatiles, and sulfur—is inherently improbable.

The Öksüt zircons, with their high crystallization temperatures and elevated Th/U ratios, exhibit a positive correlation between these two parameters, consistent with derivation from relatively unfractionated, deep-seated, and thermally robust magmas (Claiborne et al., 2010). This geochemical signature is fully consistent with the field-based inferences of Yurdakul et al. (2021). Accordingly, it can be inferred that the Karacadağ Caldera and similar Early Pliocene calc-alkaline magmatic centers in the area had a low potential for generating porphyry-style mineralization.

Zircons from the Pliocene-aged volcanic systems of Süleymanpınarı (3.9 Ma) and Çömlekçi (1.9 Ma), which formed as a result of the Melendiz Dağ (Niğde) volcanic activity, display geochemical signatures distinctly different from those of Öksüt and Karacadağ, yet more closely aligned with zircons from the Konya Volcanic Complex (KVC). The Süleymanpınarı zircons, while not reaching the elevated Ti concentrations of Öksüt and Karacadağ, nevertheless exhibit comparatively high Ti

contents (9.8 ppm) relative to average zircon compositions, but lower Hf, Y, and ∑REE concentrations than those measured in KVC samples.

When considered alongside the calculated ΔFMQ_{zircon} values, their Th/U, Dy/Yb, and Hf/Y ratios closely resemble those of zircons from mineralized and/or hydrothermally altered systems examined in this study. However, the Eu/Eu* ratios of Süleymanpınarı zircons (average 0.38 and 0.42) remain notably low.

The Süleymanpınarı and Çömlekçi prospects, together with the adjacent Tepeköy and Karanlıkdere license areas, are located within the region of Central Anatolia where advanced argillic alteration—characterized by extensive silica–alunite–clay assemblages—is most prominently developed. Drill core investigations within these license areas reveal that the Melendiz Dağ volcanic units host intense hydrothermal alteration and widespread sulfide mineralization (predominantly pyrite), particularly along major structural corridors, with alteration and mineralization extending for several hundred meters below the surface.

Such extensive alteration footprints can only be sustained by magmas capable of dissolving and transporting substantial quantities of volatile components. Nevertheless, the absence of significant Au or Cu enrichment in the altered lithologies strongly suggests that the parental magmas were already depleted in metals at the time of emplacement. This metal exhaustion likely precluded the formation of economically viable mineralization, despite the favorable hydrothermal and structural conditions present in the system.

In western Anatolia, the study encompasses porphyry systems ranging in age from those that developed during the Late Oligocene in the vicinity of the Biga Peninsula in the north, to Early–Middle Miocene and subsequently Late Miocene systems further to the south. Zircons extracted from samples collected across these magmatic centers were analyzed in detail, and the temporal variations in their key porphyry fertility parameters are presented in Figure 6.3.

Within the Western Anatolia sector, the oldest system investigated is Balya, where deep drilling has intersected two distinct granodiorite porphyry phases. These phases, dated at 25.7 and 25.5 Ma, host intense porphyry-style alteration (potassic, phyllic, and argillic) accompanied locally by well-developed porphyry-type quartz vein networks. Zircons from both phases display low Ti contents (<5 ppm) and comparatively low Th/U ratios. In the older population (25.7 Ma), Th/U values remain below 0.4, whereas the younger population (25.5 Ma) exhibits values of up to 0.7. When considered alongside their slightly lower Ti and higher total REE contents (ΣREE) relative to the younger group, the older zircons appear to have crystallized from magmas that experienced stronger intracrustal fractionation. In contrast, the younger zircons likely originated from a more mafic, less evolved melt.

For both zircon populations, Eu/Eu* values increase with decreasing Th/U, suggesting that amphibole fractionation exerted a significant control on their evolution. This interpretation is further supported by the marked increase in Hf/Y ratios with declining Th/U, pointing toward a fractionation trend dominated by amphibole rather than titanite. The younger zircons yield higher calculated ΔFMQ values (average ~1) compared to the older population (average ~0.5), while their mean Eu/Eu* ratios (0.51 and 0.53, respectively) and estimated crystallization temperatures (705 °C and 695 °C) are remarkably similar. Overall, the magma oxidation states and water contents inferred from both populations are consistent with those of fertile porphyry-related magmas (Figure 6.3).

At the same locality, three more samples (ranging between 23.18-22.7 Ma) from the Hallaçlar volcanics—which are interpreted to have developed widely after the porphyry system—displays a chemical composition distinctly different from the porphyry-related zircons. These zircons exhibit significantly higher Ti contents (averages between 5.56 to 7.5 ppm) and Th/U ratios, but markedly lower Eu/Eu*, Ce/Ce*, and Ce/Nd ratios, along with higher crystallization temperatures (averages between 721 to 750 °C). They also contain lower concentrations of Hf, Y, and ΣREE. These characteristics collectively fall short of the geochemical criteria typical for porphyry fertility, suggesting that between ~25.5 Ma and ~23 Ma, the magma source

and composition at Balya underwent substantial changes, ultimately leading to the termination of the porphyry-skarn system in association with the onset of Hallaçlar volcanism.

In contrast to the zircon geochemical compositions of the Hallaçlar volcanic rocks, the mineralized Sarıalan and Turplu samples are characterized by various but still higher Ti contents than Balya samples (average values of 5 to 7 ppm in Sarıalan, and 6.58 ppm in Turplu). The Sarıalan samples have similar Hf contens wheras the Turplu sample has significantly lower average Hf contents. The Th/U ratios of the mineralized samples (average of 0.59 in Turplu, and 0.62 to 0.65 in Sarıalan samples) and are higher than the Balya samples and similar than the Hallaçlar volcanic rocks. The mineralized samples have slightly more Eu/Eu^*_{zircon} ratios (average of 0.54 in Turplu, and 0.43-0.51 in Sarıalan samples) compared to the seemingly barren Hallaçlar samples (Table 5.3).

Southward from Balya, another magmatic trend extends between Sındırgı and Simav. The oldest zircon populations from this trend are similar in age (~20 Ma) to those from Çatalçam. In the Sındırgı–Simav sector, zircon populations were analyzed from volcanic and volcaniclastic units in the Sındırgı area (20.1–19.8 Ma), granites of the Eğrigöz Pluton (19.5–19.1 Ma), and subvolcanic units from the Pınarbaşı prospect (18.2 Ma).

Following the Hallaçlar volcanism, two distinct groups of magmatic bodies developed roughly contemporaneously but within different tectonic domains. The first of these, the Çatalçam area—geographically close to and considered part of the same magmatic episode as the Kozak Pluton—hosts widespread and locally intense epithermal-type alteration (quartz–chlorite–illite–smectite), as well as intermediate-sulfidation veins. At deeper levels, there is evidence of presently weak but recognizable porphyry-style alteration (potassic–phyllic) and associated mineralization.

Although representative deep porphyry samples from Çatalçam could not be obtained in this study, the andesitic porphyries that host the shallow-level epithermal

mineralization are genetically linked to the deeper magmatic system. Zircons were also analyzed from basaltic andesite dikes crosscutting these andesitic porphyries. Zircons from the 20 Ma andesitic porphyry exhibit Hf, Y, Ti, and ΣREE concentrations similar to those from Balya, as well as overlapping Eu/Eu*, Ce/Ce*, Ce/Nd, and Dy/Yb ratios, indicating that they share the compositional hallmarks of fertile porphyry magmas. However, their relatively high Th/U ratios suggest derivation from more mafic, less fractionated magmas. Compared to Balya, the increase in Hf/Y ratios with decreasing Th/U is more pronounced, likely reflecting earlier Y depletion due to stronger amphibole fractionation.

In contrast, zircons from the 19.8 Ma basaltic andesite dike display higher Ti but lower Hf, Y, and markedly lower ΣREE contents. Relative to zircons from the andesitic porphyry, they also have slightly lower Eu/Eu*, Ce/Ce*, and calculated ΔFMQ values (Figure 6.2), though they still meet the general criteria for porphyry fertility. While both magmas appear to have experienced amphibole-dominated fractionation, the basaltic andesite dike is interpreted to have intruded after the cessation of the Çatalçam porphyry system.

Zircons from three different samples collected in the Sındırgı area—including volcanic and volcaniclastic units of andesite–dacite porphyry composition, some of which serve as the host rock for the Kızıltepe low-sulfidation epithermal Au–Ag deposit—show no significant variation in chemical composition. Furthermore, no systematic evolutionary trend is evident among these samples when considered in terms of their U–Pb zircon ages. Overall, the Sındırgı zircon populations contain Ti concentrations that are similar to or lower than those in Balya and Çatalçam (averages of 2.9, 3.8, and 6 ppm, respectively). However, they are characterized by distinctly higher Hf, Y, and ΣREE contents compared to Çatalçam zircons, a feature consistent with the more fractionated nature of the felsic Sındırgı volcanics. This interpretation is further supported by their notably lower Th/U ratios (0.3–0.4) relative to those from Çatalçam (0.6–0.7).

A pronounced decrease in Eu/Eu* values with declining Th/U suggests that the Sındırgı zircons crystallized from magmas that had undergone plagioclase fractionation. However, key porphyry fertility parameters, such as Eu/Eu* (0.24–0.29) and calculated ΔFMQ values (−0.78 to 0.46), are generally low. It is noteworthy that the sample with the highest ΔFMQ value (0.46) within this group also represents the youngest unit (19.85 Ma), hinting at subtle changes in magmatic conditions toward the end of the Sındırgı magmatism (Figure 6.3).

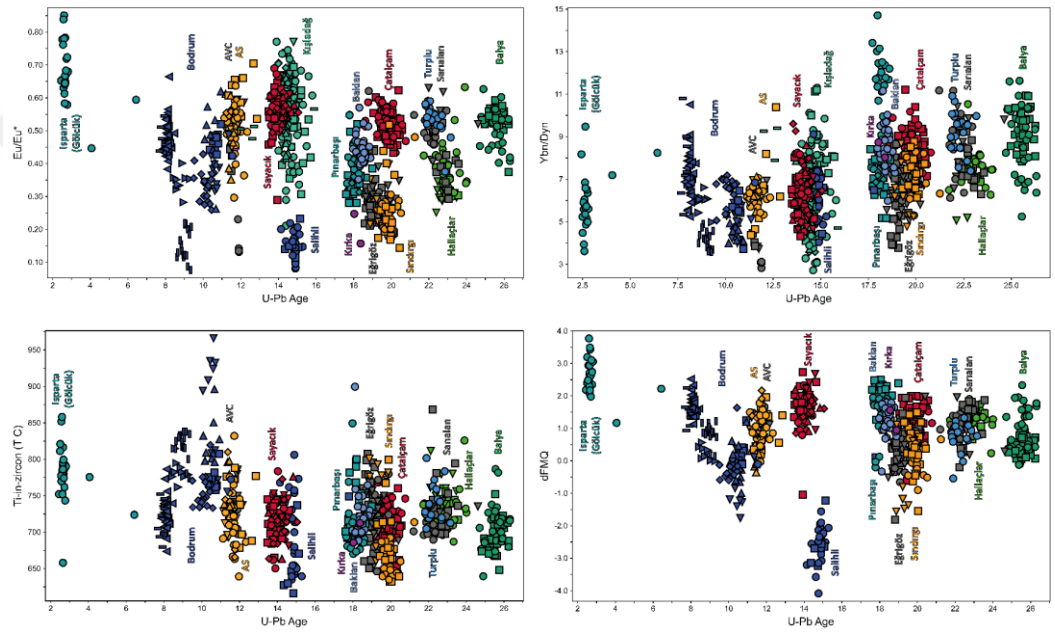


Figure 6.3. Diagrams showing temporal variations of key zircon-derived porphyry fertility parameters for Late Cenozoic magmatism in the Western Anatolia.

Immediately following the emplacement of the Sındırgı volcanic sequence, three distinct zircon populations were analyzed from the Eğrigöz Pluton, a large, homogeneously granitic intrusion. Compared to Sındırgı zircons, those from Eğrigöz display slightly higher average Ti contents but somewhat lower Y contents. The observed increase in Th/U ratios relative to Sındırgı could reflect both the high degree of fractionation in the granitic magma and the possible development of monazite within the intrusion. A weak increase in Hf/Y ratios with decreasing Th/U, coupled with declining Eu/Eu* values, indicates that plagioclase fractionation exerted a primary control on the magmas from which the Eğrigöz zircons

crystallized. Nonetheless, the Eğrigöz zircons exhibit slightly higher Eu/Eu* values (0.28–0.30) and higher calculated ΔFMQ values (0.28–0.60) than Sındırgı zircons, though these still fall short of the generally accepted thresholds for fertile porphyry magmas (Eu/Eu* > 0.4, ΔFMQ > 1.0).

Farther south, near Simav, zircon analyses were carried out on two samples from porphyritic shallow intrusions at the Pınarbaşı Cu–Mo porphyry prospect, dated at 18.2 Ma. Compositions from a third sample previously studied by Zhao et al. (2021) are also plotted in Figure 5.15 for comparison. Pınarbaşı zircons have Ti, Hf, Y, and ΣREE concentrations broadly comparable to those of Sındırgı and Eğrigöz zircons. However, they stand out by exhibiting higher Th/U, Ce/Nd, Eu/Eu*, and Ce/Ce* ratios, along with lower Dy/Yb ratios. Importantly, the calculated ΔFMQ values for Pınarbaşı zircons (averaging 1.48 and 2.05) are markedly higher than those from Balya, Çatalçam, Sındırgı, and Eğrigöz. A subtle increase in Eu/Eu* and Hf/Y ratios with decreasing Th/U suggests that the magmas feeding the Pınarbaşı porphyry system experienced amphibole–titanite fractionation.

The temporal evolution of zircon chemistry in magmatic units emplaced along the Simav–Sındırgı corridor over a period of ~2 million years reveals a gradual increase in magma oxidation state and water content from Sındırgı through Eğrigöz to Pınarbaşı (Figure 6.3). The broader range of zircon $\varepsilon Hf_{(T)}$ values at Pınarbaşı relative to the preceding Sındırgı and Eğrigöz samples further indicates that the Pınarbaşı magmas underwent more intense crustal interaction. This progressive increase in porphyry fertility is also reflected in whole-rock geochemical data from these sites, which show temporally correlated increases in Eu/Eu*, Sr/Y, and La/Yb ratios.

During the Middle Miocene, contemporaneous (~15 Ma) magmatic bodies emplaced in different sectors of western Anatolia display distinct genetic and evolutionary trends. Among these coeval systems are the Beydağı Volcanics near Eşme (Uşak), the Salihli and Turgutlu granitoids in Manisa Province, and the Cumaovası Volcanics in İzmir. Within the scope of this study, drill core samples were collected from the Kışladağ porphyry Au deposit, which is genetically linked to the Beydağı

magmatism. However, because detailed petrochronological investigations of zircons from these units have already been carried out by Paolillo et al. (2021), their dataset was directly utilized here.

Within the same magmatic system, the Sayacık porphyry Au prospect—coeval with Kışladağ and displaying similar alteration and mineralization characteristics—was examined for zircon chemical compositions and compared directly with Kışladağ. Zircons from five different Sayacık samples, with U–Pb ages ranging between 14.3 and 13.9 Ma, generally show relatively low Y and ΣREE contents (except for the oldest 14.3 Ma sample) but higher Th/U, Dy/Yb, Hf/Y, and Eu/Eu* ratios than Simav–Sındırgı zircons (Figure 5.18). Likewise, the average calculated ΔFMQ values (1.55–2.00) are among the highest oxygen fugacity values obtained from zircons in this project. The combination of a weak positive correlation between Eu/Eu* and decreasing Th/U, along with a pronounced increase in Hf/Y ratios, indicates that amphibole fractionation played a key role in the magmatic evolution of Sayacık.

Zircon compositions from five different intrusions within the Kışladağ porphyry Au system are broadly similar to those from Sayacık, but both their absolute trace element contents and trace element ratios span a much wider range. This compositional dispersion is particularly pronounced in ΔFMQ values and Dy/Y ratios for the Int1 and Int2 intrusions, which host the most intense mineralization at Kışladağ. Paolillo et al. (2021) interpreted this variability as evidence that Kışladağ magmas resided for extended periods in upper-crustal magma chambers, during which repeated recharge from deeper magma sources continually modified the melt composition.

In contrast, the narrower trace element ranges observed in Sayacık zircons—at least based on the currently available data—suggest that while the magmas were compositionally consistent with fertile porphyry systems, they likely evolved over shorter timescales in the magma chambers, experiencing more limited fractionation

and/or magma mixing. This shorter residence time would explain why the resulting mineralization is markedly weaker than at Kışladağ.

A comparison of zircon $\varepsilon Hf_{(T)}$ values further supports this interpretation: Kışladağ zircons span an exceptionally wide range but are dominated by signatures indicative of crystallization from magmas that experienced substantial crustal contamination, whereas Sayacık zircons reveal a much more restricted degree of intracrustal fractionation.

Zircons from the Salihli Granitoid—coeval with the Sayacık and Kışladağ intrusions—are chemically distinct not only from these two deposits but also from all other zircon populations investigated in this study. Two U–Pb dated samples, with crystallization ages of 14.8 Ma and 11.8 Ma, reveal that the younger zircons are characterized by exceptionally low Ti contents (average 2.3 ppm), elevated Hf concentrations, and very low Th/U (<0.2), Ce/Nd (<8), and Eu/Eu* (<0.2) ratios. The calculated ΔFMQ values for both age groups represent the lowest oxygen fugacity levels recorded in this study (average –2.76 and –2.71; Figure 5.19).

These geochemical attributes indicate that the Salihli Granitoid—and likely the nearby Turgutlu Granitoid, which was not sampled here—emplaced through processes distinct from those responsible for much of the Early–Middle Miocene magmatism in western Anatolia. Salihli zircons fail to meet any of the key geochemical thresholds for porphyry fertility. Their narrow range of Th/U ratios suggests derivation from highly evolved, strongly fractionated magmas. The marked decline in Eu/Eu* with decreasing Th/U further points to significant plagioclase fractionation in the magma source.

An additional factor contributing to the anomalously low Th/U values is the co-crystallization of monazite alongside zircon in these granites (Catlos et al., 2010). During crystallization, a substantial proportion of Th in the melt partitions into monazite rather than zircon, thereby depleting Th in the zircon lattice. Petrological interpretations by Erkül and Erkül (2012) indicate that the Salihli and Turgutlu granitoids are peraluminous leucogranitic intrusions influenced by both crustal

contamination and magma mixing. They propose that these granitoids formed from the interaction of subduction-related, depleted mantle–derived magmas with melts generated from lower-crustal anatexis. Such magmas, enriched through high degrees of fractionation and lower-crustal assimilation, are inherently ill-suited for generating porphyry-style mineralization. The intense crustal signature of the Salihli granites is further corroborated by their extremely low εHf(T) values.

Another magmatic center associated with ~15 Ma magmatism in western Anatolia is the Afyon Volcanic Complex (AVC). Within the scope of this project, zircon analyses were carried out on units from the southern sector of the complex, dated to 11.8–11.6 Ma. These include two samples from latitic lava flows located north and south of Sandıklı (11.78 and 11.77 Ma), and three samples from monzonitic subvolcanic intrusions within the Afyon–Sandıklı (A–S) porphyry Au–Cu prospect to the east of Sandıklı. The two sample groups show distinct trace-element characteristics.

The latitic lavas possess the highest Ti contents recorded among all zircon populations in this study (average 38 and 96 ppm), the highest Th/U and Dy/Yb ratios, and the lowest Ce/Nd ratios. Their average zircon crystallization temperatures are also the highest measured (933°C and 1050°C). Furthermore, significant chemical differences exist between the two lava samples. Sample AVC-01 has an exceptionally low average Hf content (8156 ppm) but high Y (average 2914 ppm), whereas AVC-02 has one of the lowest Y contents measured in this study (average 593 ppm). Their total REE contents also differ markedly (average 1962 ppm for AVC-01 vs. 424 ppm for AVC-02).

The high Th/U ratios in AVC-01 zircons indicate derivation from relatively primitive, unfractionated magmas, yet Hf/Y and Eu/Eu* vs. Th/U systematics suggest that both lava populations crystallized from magmas containing amphibole in the source. The low Eu/Eu* values in AVC-01 (average 0.7), coupled with very high Dy/Yb (>30) and negative ΔFMQ values, indicate severely limited porphyry fertility.

By contrast, zircons from the A–S porphyry prospect's monzonitic–latitic intrusions display markedly different chemical signatures from those of the volcanic lavas. With Ti contents averaging 11–12 ppm—modest but still within the range favorable for porphyry fertility—they also show generally lower Y and total REE concentrations. The sharp increase in Hf/Y and Eu/Eu* with decreasing Th/U indicates fractionation dominated by amphibole. This suggests that although the magmas retained moderate water contents, their low oxidation state likely accounts for the subdued mineralization, despite the presence of widespread and locally intense tourmaline-rich hydrothermal alteration. Additionally, the calculated zircon crystallization temperatures (>780°C) are higher than those typically associated with fertile porphyry magmas in shallow crustal settings.

The youngest zircon populations examined from the Western Anatolia sector are derived from various parts of the extensive caldera system on the Bodrum Peninsula. These samples, dated between 10.4 and 7.7 Ma, provide valuable insights into temporal changes in magma chemistry over a broad time span. Zircons from the earliest stage of magmatic activity (10.4–10.2 Ma) are characterized by elevated Ti contents, comparatively low Y concentrations, and notably low ΔFMQ values (average –0.63 and –0.21).

Following this early stage, a progressive geochemical evolution is observed: between 8.9–8.8 Ma and subsequently 8.2–7.7 Ma, Ti contents, Th/U ratios, and Dy/Yb ratios steadily decrease, while Hf/Y and Eu/Eu* ratios, along with calculated ΔFMQ values, increase. In the youngest two samples, ΔFMQ reaches values as high as 1.5–1.7. These youngest zircons also record the highest inferred magma water contents (from Eu/Eu* and Ce/Nd systematics) and the highest oxidation states within the Bodrum dataset.

Zircon crystallization temperatures likewise exhibit a temporal decline, dropping from ~812 °C in the 10.4 Ma sample to ~715 °C in the 7.7 Ma sample. This temporal pattern suggests that the earliest stages of the Bodrum caldera magmatism were dominated by magmas with limited porphyry potential, whereas from ~8 Ma onward,

the system began to generate magmatic conditions more favorable for porphyry-type mineralization.

6.3 Assessment of the Porphyry Ore Forming Potential of the Late Cenozoic Magmatism using Whole-rock, Zircon, and Apatite Fertility Indicators

Accessory minerals such as zircon and apatite have emerged as powerful petrogenetic and metallogenic indicators for evaluating the fertility of arc magmas in the context of porphyry Cu–(Au–Mo) deposit formation. Their robustness to hydrothermal alteration, resistance to weathering, and capacity to incorporate a wide array of trace elements make them particularly valuable for detrital mineral studies, where mineral chemistry can be used to assess the prospectivity of identifying igneous sources (Mao et al., 2016; Pizarro et al., 2020, 2024). In recent years, a combination of in-situ geochemical techniques—particularly LA-ICP-MS and EPMA—has enabled precise quantification of fertility-related parameters in these minerals, refining exploration models and providing constraints on magmatic processes linked to ore genesis.

Zircon, a common accessory phase in intermediate to felsic arc magmas, records a range of trace element signatures that reflect magmatic oxidation state, water content, and fractionation history. Among the most widely cited parameters are the Ce anomaly (Ce/Ce*) and the Eu anomaly (Eu/Eu*), both normalised to chondritic values (McDonough and Sun, 1995). In porphyry Cu systems, zircons tend to exhibit stronger positive Ce anomalies—reflecting elevated Ce^{4+}/Ce^{3+} ratios—and weaker negative Eu anomalies, consistent with suppression of plagioclase fractionation in hydrous, oxidised melts (Ballard et al., 2002; Loader et al., 2017; Loucks et al., 2020, 2024). Low Dy/Yb values, often ≤0.25, further indicate early hornblende ± garnet stability, which sequesters middle REE and produces steep HREE slopes, a feature characteristic of deep-seated, water-rich crystallization (Lu et al., 2016).

The ratio $(Eu/Eu^*)/Yb_N*10^4$ has been advanced as a composite index of hydrous fractionation depth and suppression of plagioclase crystallisation (Loucks and Fiorentini, 2023). High values (>3–4) are typical of fertile magmas, whereas infertile arc suites generally yield lower values. Another parameter, $Ce/\sqrt{(U \times Ti)}$, integrates oxidation state (Ce anomaly), zircon Ti-in-zircon crystallisation temperature, and U partitioning behaviour, with higher values reflecting oxidised, potentially fertile magmas (Loucks et al., 2020). Collectively, these zircon-based metrics can distinguish fertile from barren suites, though they may be less effective for certain shoshonitic, Au-rich porphyries, which require complementary proxies (Kendall-Langley et al., 2025).

Apatite's utility derives from its sensitivity to magmatic volatiles (Cl, F, OH, S, CO_2) and its capacity to host REE, Sr, and Y in its crystal lattice (Belousova et al., 2002; Li and Hermann, 2017). Elevated Sr/Y in apatite is considered a robust indicator of delayed plagioclase saturation and/or high-pressure amphibole ± garnet fractionation, combining the whole-rock Sr/Y criteria for fertile magmas (Chiaradia, 2015; Loucks, 2014). Fertile magmas commonly produce apatites with high Sr, low Y, and hence elevated Sr/Y, reflecting deep crustal crystallization under hydrous conditions (Duan and Jiang, 2018; Jia et al., 2020). Apatite LREE systematics, such as high La/Sm ratios, may further record efficient LREE enrichment in the melt during amphibole-dominated fractionation.

Melt volatile content can be reconstructed from F–Cl–OH measurements in apatite, calibrated via experimentally determined partition coefficients and constrained by Ti-in-zircon temperatures from co-crystallizing zircon inclusions (Li and Costa, 2020; Kendall-Langley et al., 2021). High Cl contents are significant because Cl-bearing fluids enhance the solubility and mobility of Cu–Au in magmatic–hydrothermal systems (Audétat et al., 2008; Seo et al., 2009). Similarly, S concentrations in apatite may serve as a qualitative oxidation proxy, since sulfur enters apatite as S^{6+} under oxidized conditions.

In Andean-type subduction settings, magmas are typically generated in a mantle wedge fluxed by slab-derived fluids, producing oxidized, hydrous, calc-alkaline magmas with high Sr/Y and low Dy/Yb signatures (Defant and Drummond, 1990; Richards, 2011). Zircon from these systems frequently displays high Eu/Eu* (>0.4–0.5), low Dy/Yb, and strong positive Ce anomalies, while apatite records elevated Sr/Y and variable but commonly high Cl contents. These signatures reflect deep-seated amphibole ± garnet fractionation, delayed plagioclase crystallization, and sustained high oxidation states, all favorable for porphyry Cu–Au formation.

By contrast, post-subduction or collisional settings often produce more reduced, dryer magmas derived from crustal anatexis and/or mixed crust–mantle sources (Collins and Richards, 2008). In such environments, zircon may show lower Ce/Ce*, stronger negative Eu anomalies (Eu/Eu* <0.4), and higher Dy/Yb, reflecting shallow-level crystallization dominated by plagioclase fractionation. Apatite in these magmas tends toward lower Sr/Y and may record reduced Cl contents and variable S, consistent with less hydrous, less oxidized melts. While exceptions occur—particularly where post-collisional magmatism taps a metasomatized lithospheric mantle—the overall fertility signal is commonly muted relative to active arc magmas.

The complementary use of zircon and apatite chemistry allows for cross-validation of fertility assessments and reduces misclassification due to late-stage alteration or degassing. Zircon offers a relatively alteration-resistant record of melt oxidation and hydrous fractionation history, whereas apatite provides direct constraints on volatile contents and trace element ratios linked to deep-seated fractionation processes. The combination of parameters such as $(Eu/Eu^*)/Yb_N*10^4$, $Ce/\sqrt{(UxTi)}$, and apatite Sr/Y enables a more nuanced discrimination of magmatic suites in different tectonic settings, facilitating targeted exploration in both exposed and covered terranes.

There are several approaches and different parameters suggested by various researchers. Loucks et al. (2024) utilized the use of $(Eu/Eu^*)/Yb_N*10^4$ and $Ce/\sqrt{(UxTi)}$ to differentiate porphyry Cu ore-forming intrusions from the infertile arc

igneous suites. Another suggested parameter among those is the approach of Tapia et al. (2025), which employs chondrite-normalized Dy and Yb/Dy ratios to distinguish fertile from barren andesite-type subduction-related systems. According to this model, systems with Yb/Dy > 10-18 and Eu/Eu* > 0.4 tend to represent fertile, arc-related porphyry Cu systems formed by a short-lived reservoir in a thin crust (<40 km). Meanwhile porphyry Cu systems that are formed by long-lived reservoir in thick crustal settings have Yb/Dy ratios spanning between ~3-10 while the Eu/Eu* ratios appear to be similar. A more recent zircon fertility model by Carrasco-Godoy et al. (2024) refines threshold values for Eu/Eu* and other parameters to identify fertile suite more efficiently. More traditional parameters suggested by Lu et al., (2016) is also utilized for the samples from the Central Taurides nad the Western Anatolia, however, those parameters failed to differentiate variations among the samples, therefore, did not included in the following discussions. One common property of these studies is that they are mostly defined for the porphyry Cu systems developed by typical Andean-type arc related settings. All three approaches are utilized in this thesis to understand fertility parameters of the Late Cenozoic magmatism the the Western Anatolia and Central Taurides.

Ultimately, while Andean-type arcs exhibit the clearest and most consistent zircon–apatite fertility signatures, recognition of more subtle variations in post-subduction magmas—especially those retaining high water contents and moderate oxidation states—remains critical. Continued integration of detrital zircon–apatite datasets with whole-rock and isotopic constraints promises to refine fertility models across diverse geodynamic environments.

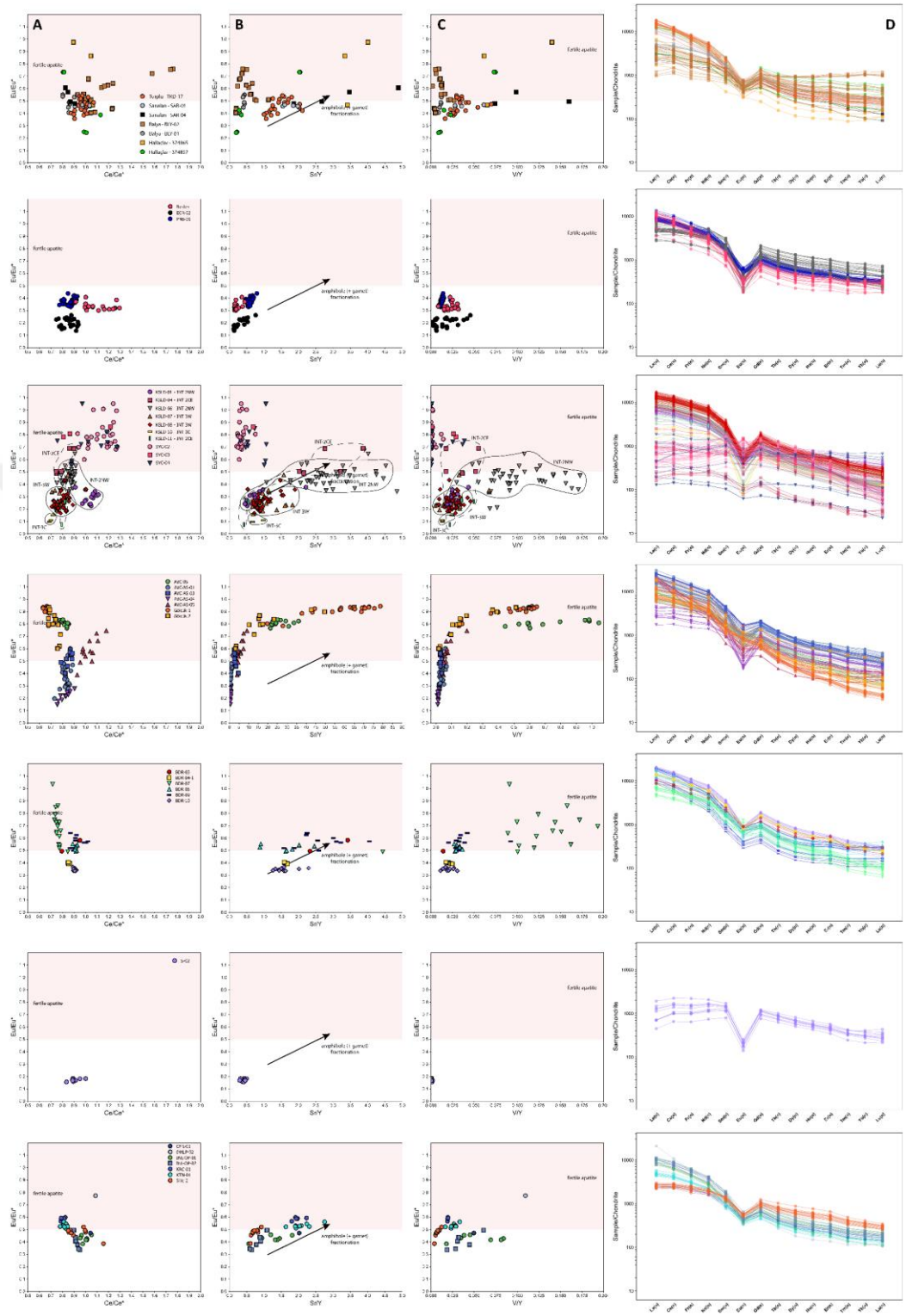


Figure 6.4. Apatite fertility diagrams (A to C) and chondrite normalized rare earth multi-element diagrams (D) for the Western Anatolian and Central Taurides samples.

Zircon and apatite crystals separated from the Late Cenozoic magmatic units of the Central Taurides and Western Anatolia were analyzed using a suite of geochemical parameters widely applied in porphyry fertility studies. These data were subsequently evaluated to assess the ore-forming potential of the studied magmatic systems.

6.3.1 Central Taurides

The Central Taurides samples are plotted on the zircon fertility discrimination diagram proposed by Loucks et al. (2024) which utilize $(Eu/Eu^*)/Yb_N*10^4$ and $Ce/\sqrt{(UxTi)}$ ratios to characterize porphyry Cu ore-forming intrusions and infertile suites. The Sulutaş Volcanic Suite sample, representing the oldest magmatism in the Konya region, stands out distinctly from the rest of the dataset as they are plotted strictly in the infertile suites field (Figure 6.5A). In contrast, the remaining samples occupy a broad range in transition between fertile and barren reference fields, yet generally fall below the thresholds defined for productive systems (Figure 6.5A).

To further explore magmatic signatures, the dataset was evaluated using the Tapia et al. (2025). When the Konya sector and Niğde–Kayseri sector samples are plotted on this diagram (Figure 6.5B), most Konya samples record Yb/Dy < 9, with the exception of the Ketenli sample—one of the youngest units in the Konya region—which predominantly yields Yb/Dy > 9 and follows the fertile porphyry trend. This suggest the weak effect of the amphibole and/or garnet fractionation for the Ketenli samples (Figure 6.5B). Conversely, the Sulutaş Volcanic Suite samples conform to the barren trend with moderate Yb/Dy ratios but increasing $Dy_{(n)}$ content. Core samples from İnlice largely display characteristics consistent with the barren field; however, their low Dy contents (100–400 ppm). Most İnlice zircons yield moderate Yb/Dy ratios between ~6 and 10, implying limited contribution of fractionation, and crystallization from magmas emplaced at relatively deeper crustal levels.

These findings for the volcanic rocks exposed in the Konya region suggest the thicker crustal settings for the oldest magmatism event where the magma differentiates at the deeper parts of the crust while the crustal thickness decreased progressively as evidenced by the shallower differentiation indications for the Ketenli samples (Figure 6.5F).

The model of Carrasco-Godoy et al. (2024) is also used to further characterize the fertility of the Konya Volcanic Complex (Figure 6.5C-E). Using this approach, a Eu/Eu* versus P (ppm) diagram reveals that nearly all Konya samples have Eu/Eu* values exceeding the proposed productivity threshold of 0.363; however, only the part of the Ketenli and subset of İnlice zircons plot towards the fertile field (Figure 6.5C). Notably, there is a subtle but systematic increase in Eu/Eu* from the oldest units of the Erenlerdağ–Alacadağ sector (Çukurağıl and Damlapınar) towards the İnlice samples, with slightly higher values in the youngest magmatic products (Figure 6.5C).

In the Ce/Nd versus Dy/Yb diagram (Figure 6.5D), however, nearly all samples plot within the fertile field—a pattern that contrasts with the more conservative separation observed in the Loucks et al. (2024) and Carrasco-Godoy et al. (2024) criteria. To evaluate the role of plagioclase fractionation, a Sr versus Eu/Eu* diagram was prepared (Figure 6.5E). The results show that Eu/Eu* remains essentially constant across a range of Sr contents, suggesting that plagioclase fractionation played a limited role in shaping the REE patterns of these zircons.

Although apatite trace-element data from the Central Taurides are limited, the available dataset is sufficient to yield meaningful insights into the region's magmatic evolution and its relationship to associated mineralization. From the Damlapınar area, only a single apatite crystal was analyzed. Given the statistical limitations of interpreting a single measurement, this sample was excluded from detailed interpretations; however, it has been retained in the plotted diagrams for completeness.

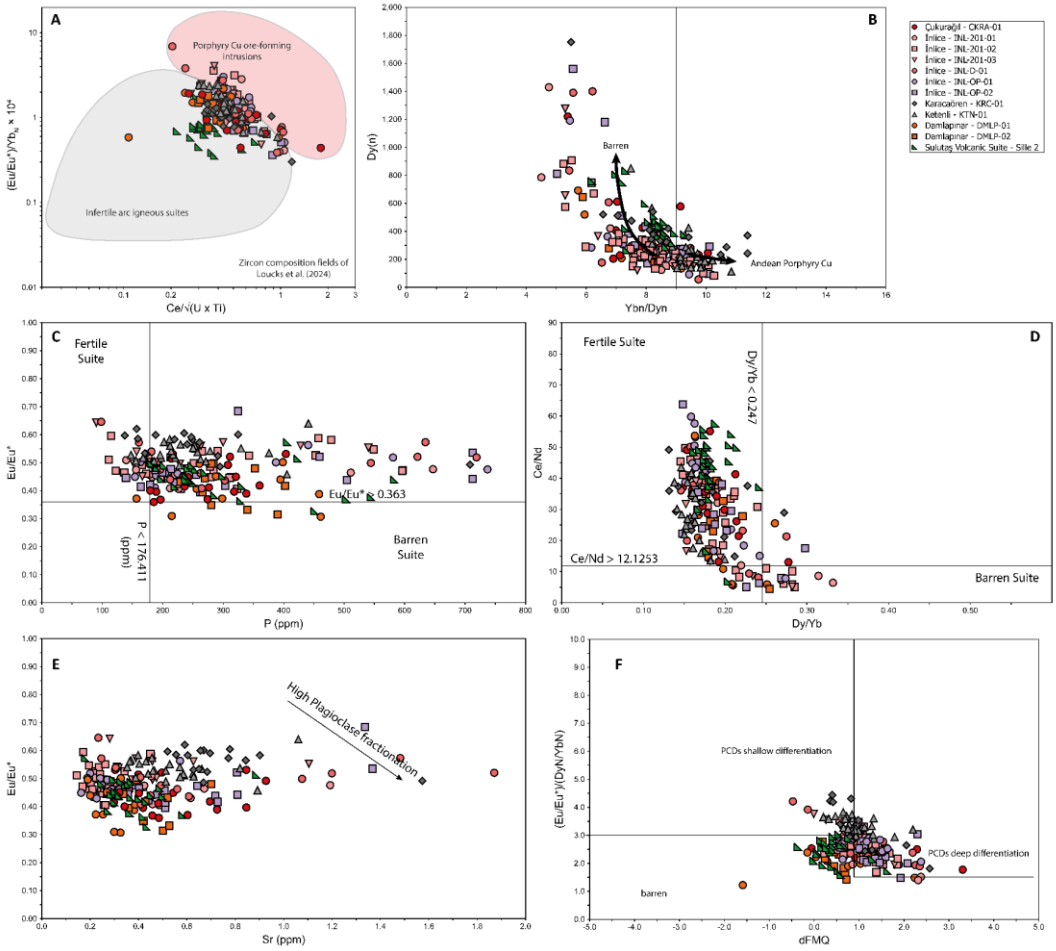


Figure 6.5. Zircon fertility parameters for the Erenlerdağ-Alacadağ Volcanics and Sulutaş Volcanic Suite. A) Zircon $(Eu/Eu^*)/Yb_N \times 10^4$ plotted against $Ce/\sqrt{(UxTi)}$ in zircon. Shaded fields are after Loucks et al. (2024) and represent ranges for zircons from porphyry Cu ore-forming intrusions and from infertile arc igneous suites. B) $Dy_{(n)}$ vs. $Yb_{(n)}/Gd_{(n)}$. C) Eu/Eu* vs. P (ppm). D) Ce/Nd vs. Dy/Yb diagram. E) Eu/Eu* vs Sr (ppm). F) ΔFMQ vs. $(Eu/Eu^*)/(Dy_N/Yb_N)$ as suggested by Tapia et al. (2025). Subscript *N* indicates chondrite-normalized values. Fertility parameters used in C, D, and E are suggested by Carrasco-Godoy et al. (2024).

For all samples, except those collected from the İnlice open pit, the Eu/Eu* ratios are close to, or slightly above, the commonly cited fertility threshold of 0.5 (Figure 6.4). Notably, in the youngest magmatic products (3–4 Ma), apatites yield Eu/Eu* values exceeding 0.5, pointing to oxidized magmatic conditions conducive to porphyry-type mineralization (Figure 6.4). This interpretation is further supported

by elevated Ce/Ce* ratios (Figure 6.4A), which also indicate high oxygen fugacity during apatite crystallization.

When Eu/Eu* is plotted against Sr/Y, the data reveal a clear increasing trend (Figure 6.4B), consistent with crystallization under conditions where amphibole was a major fractionating phase. Such a trend typically reflects moderate- to high-pressure crystallization, where amphibole stability can suppress plagioclase fractionation. Evaluation of V/Y ratios shows that the İnlice apatites fall below the fertile field (Figure 6.4C), which supports the field-based observation that these units are not associated with porphyry-type Cu mineralization.

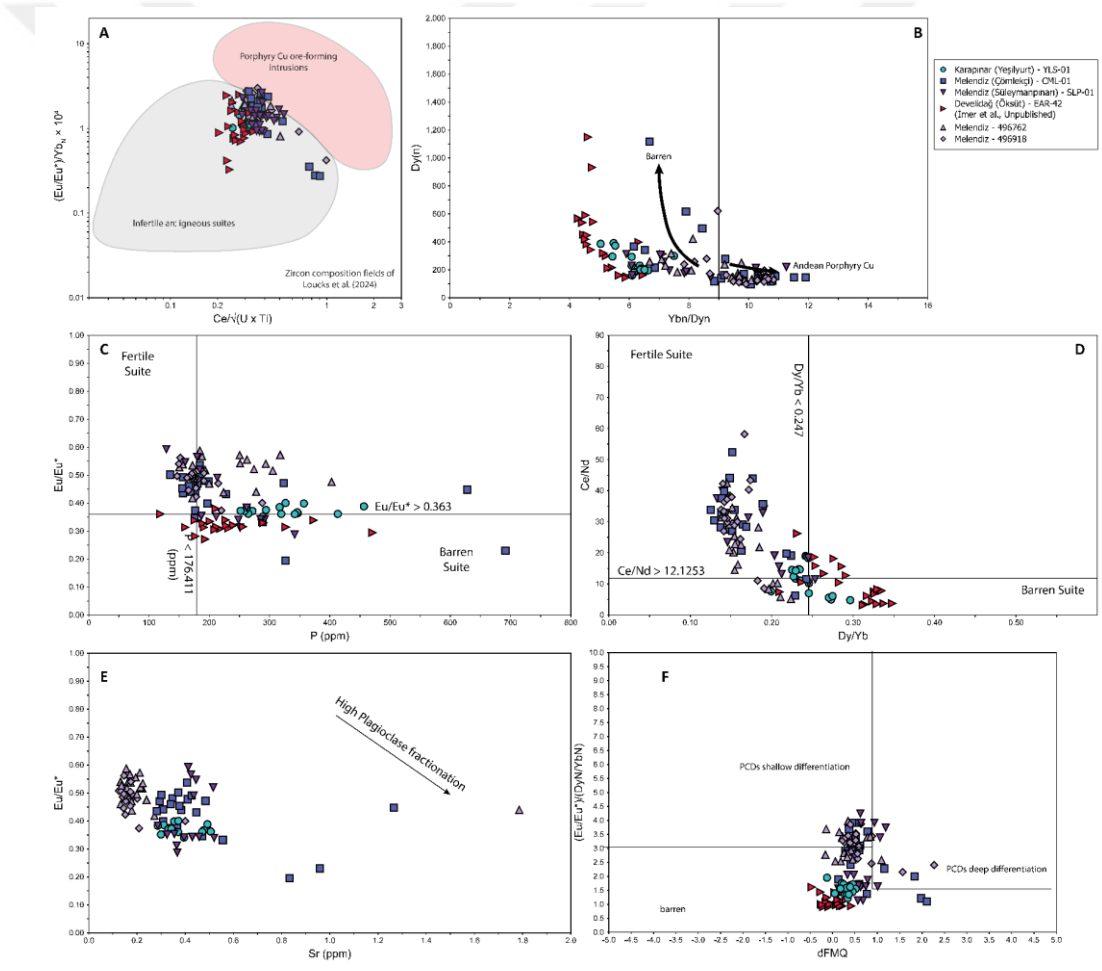


Figure 6.6. Zircon fertility parameters for the Niğde-Kayseri sector. A) Zircon (Eu/Eu*)/Yb$_N$×10^4 plotted against Ce/√(UxTi) in zircon. Shaded fields are after Loucks et al. (2024) and represent ranges for zircons from porphyry Cu ore-forming

intrusions and from infertile arc igneous suites. B) $Dy_{(n)}$ vs. $Yb_{(n)}/Gd_{(n)}$. C) Eu/Eu* vs. P (ppm). D) Ce/Nd vs. Dy/Yb diagram. E) Eu/Eu* vs Sr (ppm). F) ΔFMQ vs. $(Eu/Eu^*)/(Dy_N/Yb_N)$ as suggested by Tapia et al. (2025). Subscript *N* indicates chondrite-normalized values. Fertility parameters used in C, D, and E are suggested by Carrasco-Godoy et al. (2024).

Chondrite-normalized multi-element patterns of apatites from the region display enrichment in light rare earth elements (LREE) and depletion in heavy rare earth elements (HREE), with only a weak negative Eu anomaly (Figure 6.4D). The subdued Eu depletion suggests that plagioclase fractionation was limited during apatite crystallization, further aligning with the amphibole-dominated fractionation model inferred from Sr/Y–Eu/Eu* relationships.Integrating all zircon and apatite trace-element fertility parameters as well as the whole rock Sr/Y and La/Yb ratios, it can be suggested that the earliest alkaline magmatism in the Sulutaş Volcanic Suite (13 Ma) and the calc-alkaline Alacadağ-Erenlerdağ (including the İnlice, Çukurağıl, and Damlapınar) magmas (12–8 Ma) were derived from deeper crustal levels (progressively becoming thinner), with minor amphibole fractionation, whereas younger units (~3 Ma) crystallized at shallower depths, reflecting a progressive thinning of the crust through time. Throughout this magmatic evolution, the systems retained relatively high oxidation states, and most units, excluding the Sulutaş Volcanic Suite, exhibit characteristics consistent with a arc-related magmatic signatures capable of generating fertile porphyry systems.

Samples from the Niğde–Kayseri region, located to the east of Konya, were also plotted on the same fertility-related diagrams and interpreted accordingly. Within this region, the oldest magmatic unit investigated is the Develidağ Complex, which hosts the Öksüt epithermal Au–Cu deposit. One representative sample from this deposit, EAR-42, was not analyzed in the present study; instead, zircon trace-element data were kindly provided by İmer et al. (unpublished). The Öksüt deposit is of particular significance for understanding the magmatic evolution of the region, as porphyry-style alteration, along with well-developed A- and B-type veins, has been identified at depth beneath the epithermal mineralization zone. However, despite

these hydrothermal features, no economic mineralization has been documented (Yurdakul et al., 2021), and the zircon data is able to explain this absence.

Compared to other regional samples, the Öksüt zircons exhibit notably lower Ce/√(U × Ti) ratios, placing them well within the infertile field in the Loucks et al. (2024) classification scheme (Figure 6.6A). Low Yb/Dy ratios, combined with Ti-in-zircon thermometry results, indicate fractionation under thick-crust conditions (Figure 6.6B). Additionally, the low Eu/Eu^*_{zircon}, P_{zircon} (ppm), and ΔFMQ values demonstrate that these samples fall well below the thresholds proposed by both Carrasco-Godoy et al. (2024) and Tapia et al. (2025) for fertile porphyry systems (Figure 6.6C–F).

In contrast, the youngest volcanic field studied within the Niğde–Kayseri region—the Melendiz volcanic complex—plots closer to the fertile field defined by Loucks et al. (2024), although still within the infertile domain (Figure 6.6A). Its relatively high Yb/Dy ratios suggest that crystallization occurred at shallower crustal depths, similar to late-stage magmatic products in the Konya region, reflecting crustal thinning during the younger stages of magmatism (Figure 6.6B). Both Eu/Eu* (Figure 6.6C) and Ce/Nd (Figure 6.6D) ratios are elevated, indicating high magmatic oxidation states. Evaluation of Sr contents suggests that plagioclase fractionation was minimal in these units (Figure 6.6E). Collectively, the zircon trace-element geochemistry implies that the Melendiz system could have been prospective for porphyry-type mineralization.

In terms of apatite chemistry, the only apatite-bearing sample from the Niğde–Kayseri dataset is CML-01, derived from the Melendiz volcanic rocks. This apatite plots squarely within the fertile field on the Eu/Eu*–based fertility diagram (Figure 6.4A). A slight increase in Sr/Y ratios further supports an amphibole fractionation trend.

When zircon and apatite mineral chemistry are considered together, a scenario emerges that parallels the magmatic evolution inferred for Konya. Between approximately 8 and 5 Ma, magmatism in the Niğde–Kayseri region—particularly

in the Öksüt and Yeşilyurt areas—appears to have crystallized by less oxidized magma under thick-crust conditions at relatively high temperatures. These conditions likely limited porphyry fertility, offering a plausible explanation for the presence of porphyry-style alteration at Öksüt without associated mineralization. From ~4 Ma to ~1.5 Ma, it appears that the crust becomes progressively thinner or magma ascends rapidly into the shallower levels. This is also accompanied by rising oxidation states. The presence of documented presence of hydrothermal alteration combined with these findings suggest that the younger magmatic episodes may have inefficient metal transport or the venting of metals into subvolcanic or volcanic environments, promoting the formation of epithermal mineralization rather than forming large porphyries.

6.3.2 Western Anatolia

The oldest units among the studied Western Anatolian samples are located along the Biga Peninsula, including Balya (25.5–25.6 Ma), Çatalçam (19.8–20.1 Ma), Sarıalan (22.2–22.8 Ma), Turplu (22.14 Ma), and Hallaçlar (22.7–23.2 Ma). In the zircon discrimination diagram proposed by Loucks et al. (2024), Çatalçam samples—the youngest within this group—tend to plot toward the fertile field, whereas nearly all other samples fall within the infertile arc suite (Figure 6.7A).

A notable exception is the basaltic SAR-03 sample from the Sarıalan district, which plots in the infertile field and suggests minimal amphibole fractionation relative to other Sarıalan samples (Figure 6.7B). In Eu/Eu* vs. P (ppm) plot Hallaçlar volcanic samples are distinct from the rest of the dataset (Figure 6.7C). All samples exhibit strongly positive Eu anomalies and shift toward the fertile field with the exception of Hallaçlar volcanic rocks (Figure 6.7C).

Trace element ratios show consistently low Dy/Yb and high Ce/Nd across the dataset, plotting within the fertile field (Fig. 1D). The Sr versus Eu/Eu* diagram reveals no evidence for significant plagioclase fractionation in any of the samples

(Fig. 1E). Among the most diagnostic parameters is the relationship between zircon ΔFMQ and the (Eu/Eu*)/(Dy/Yb) ratio. This comparison indicates that Balya North, Turplu, and part of the Sarıalan suite record shallow differentiation at upper-crustal levels following rapid ascent, typical of porphyry Cu systems formed by relatively short magma residence times. In contrast, Hallaçlar samples and part of the Çatalçam suite reflect protracted fractional crystallization at mid- to lower-crustal depths, consistent with deep-seated magma differentiation (Figure 6.7F).

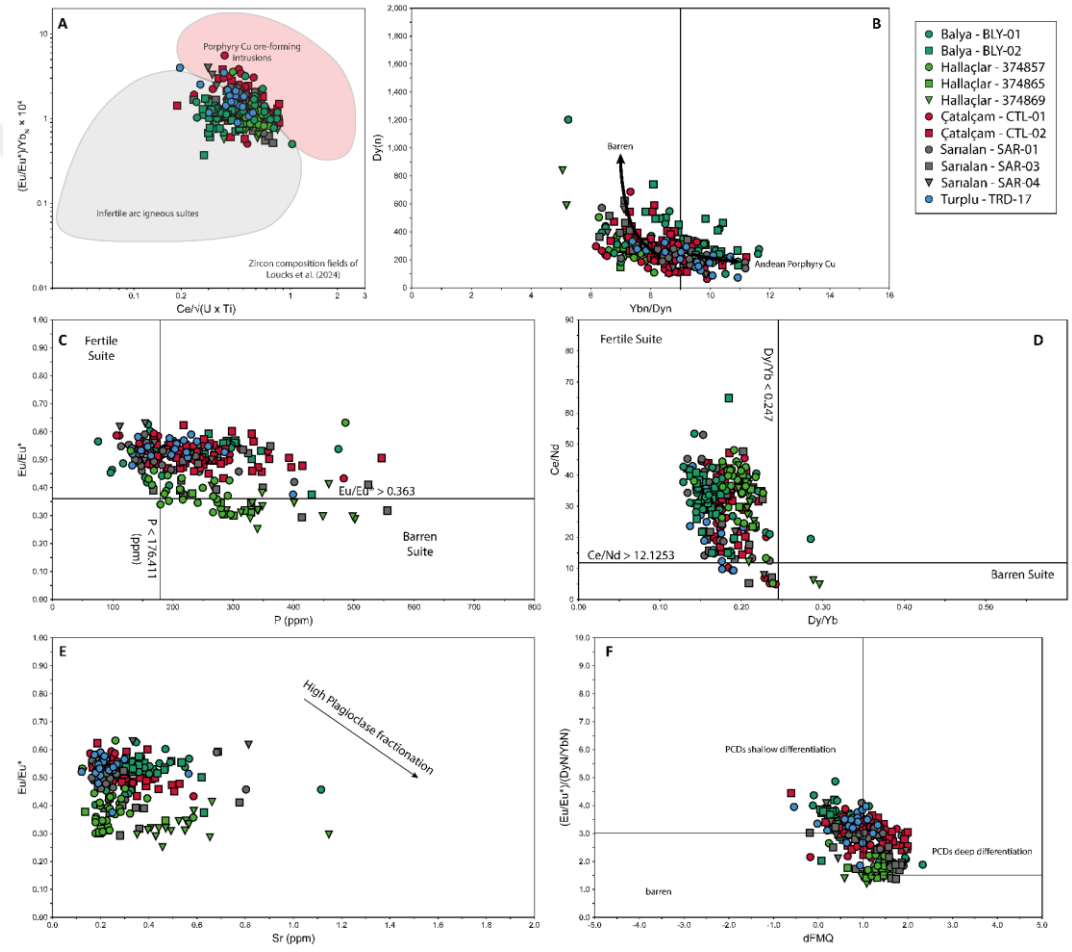


Figure 6.7. Zircon fertility parameters for the Biga. A) Zircon $(Eu/Eu^*)/Yb_N \times 10^4$ plotted against Ce/√(UxTi) in zircon. Shaded fields are after Loucks et al. (2024) and represent ranges for zircons from porphyry Cu ore-forming intrusions and from infertile arc igneous suites. B) $Dy_{(n)}$ vs. $Yb_{(n)}/Gd_{(n)}$. C) Eu/Eu* vs. P (ppm). D) Ce/Nd vs. Dy/Yb diagram. E) Eu/Eu* vs Sr (ppm). F) ΔFMQ vs. $(Eu/Eu^*)/(Dy_N/Yb_N)$ as suggested by Tapia et al. (2025). Subscript *N* indicates chondrite-normalized values.

Fertility parameters used in C, D, and E are suggested by Carrasco-Godoy et al. (2024).

While this shallow versus deep differentiation trend might suggest plagioclase dominance in the shallow systems (Balya North, Turplu, Sarıalan), the high Eu/Eu* values in these same samples indicate that amphibole remained a major fractionating phase. Consequently, the Çatalçam system is considered to have potential for porphyry-type mineralization based on zircon trace element signatures, whereas Sarıalan and Turplu—although meeting many fertility criteria (especially oxidized magma)—may lack the magmatic conditions necessary to develop large porphyry systems.

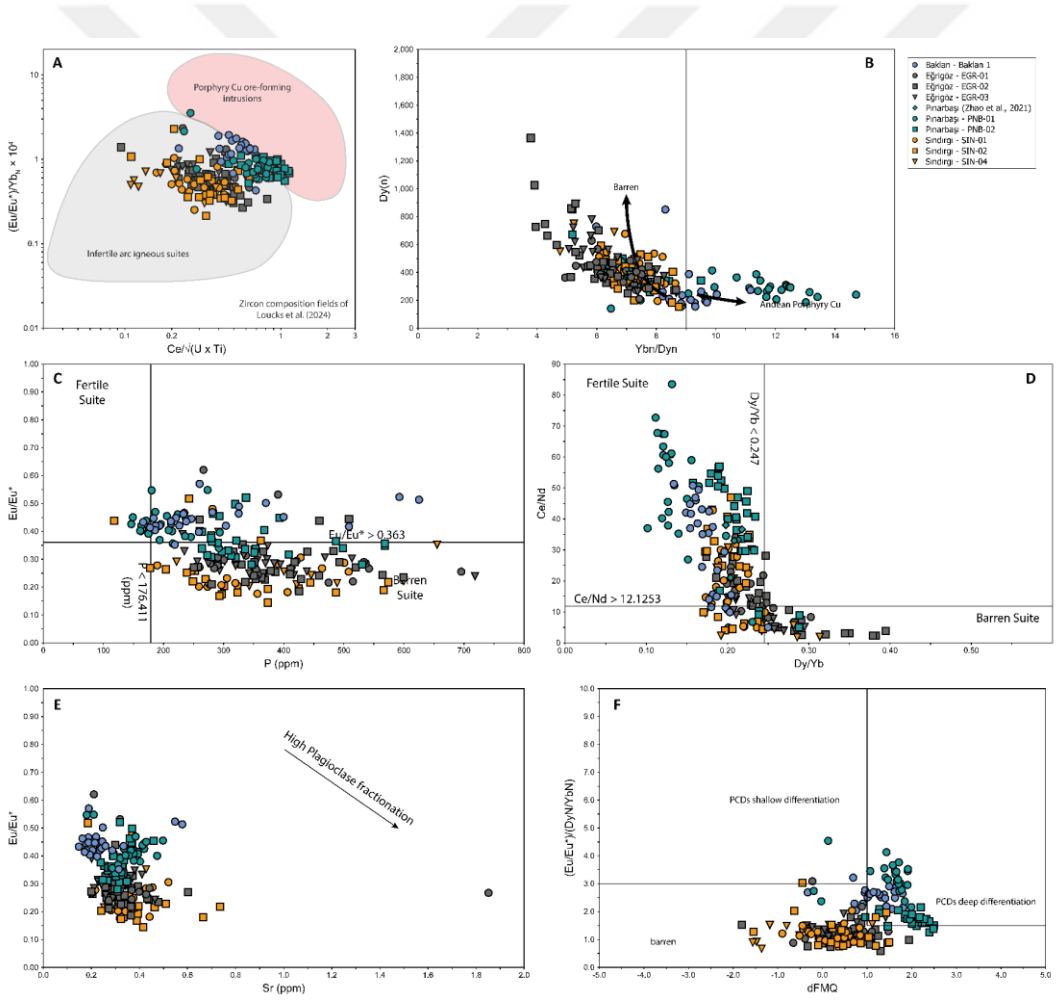


Figure 6.8. Zircon fertility parameters for the Kütahya-Simav region. A) Zircon $(Eu/Eu^*)/Yb_N \times 10^4$ plotted against Ce/√(UxTi) in zircon. Shaded fields are after Loucks et al. (2024) and represent ranges for zircons from porphyry Cu ore-forming

intrusions and from infertile arc igneous suites. B) $Dy_{(n)}$ vs. $Yb_{(n)}/Gd_{(n)}$. C) Eu/Eu* vs. P (ppm). D) Ce/Nd vs. Dy/Yb diagram. E) Eu/Eu* vs Sr (ppm). F) ΔFMQ vs. (Eu/Eu*)/(Dy_N/Yb_N) as suggested by Tapia et al. (2025). Subscript *N* indicates chondrite-normalized values. Fertility parameters used in C, D, and E are suggested by Carrasco-Godoy et al. (2024).

Apatite trace element data further support these interpretations: Balya, Turplu, and Sarıalan samples record high oxidation states, while the Hallaçlar suite shows more variable oxidation, with one sample exhibiting high Eu/Eu* and another plotting in the low field (Figure 6.4A). Moreover, both Turplu and Sarıalan show a strong positive correlation between Sr/Y and Eu/Eu*, reinforcing the role of amphibole fractionation in their evolution (Figure 6.4B).

The Biga Peninsula magmatic suites record a clear temporal and petrogenetic evolution from the early Miocene (25.6 Ma at Balya) to the late Miocene (19.8 Ma at Çatalçam). Zircon trace element systematics distinguish two principal differentiation paths: shallow, rapid ascent and upper-crustal crystallization (Balya North, Turplu, and part of Sarıalan), and deeper, prolonged fractionation at mid- to lower-crustal levels (Hallaçlar and part of Çatalçam). While amphibole fractionation is dominant across most samples, variations in Eu/Eu* and Dy/Yb indicate differing mineral control on magma evolution. Shallow systems show high Eu/Eu* and elevated oxidation states in apatite, consistent with porphyry Cu-style fertile conditions, whereas deeper systems reflect less oxidized, more protracted magmatic differentiation. Çatalçam displays the strongest geochemical potential for porphyry mineralization, whereas Sarıalan and Turplu meet many fertility criteria but may have been limited in developing large-scale systems.

In the Kütahya–Simav region, zircon geochemical parameters clearly differentiate fertile from barren systems. Over a ~2 Myr interval, from the Sındırgı volcanics to the younger Baklan and Pınarbaşı plutons, a marked shift in magmatic conditions is evident in both zircon and apatite trace element data.

The oldest units, represented by low (Eu/Eu*)/YbN$\times 10^4$ and Ce/$\sqrt{}$(U×Ti) values, consistently plot in the barren field in the fertility discrimination diagrams (Figure

6.8A). In contrast, the younger Baklan and Pınarbaşı plutons yield results that trend toward the fertile field (Figure 6.8A). Furthermore, Pınarbaşı and Baklan samples exhibit elevated Yb/Dy ratios, aligning with the porphyry Cu trend, whereas the Eğrigöz and Sındırgı samples display a negative correlation (decreasing Yb/Dy values) indicating a barren magmatic signature (Figure 6.8B). This pattern is further supported by Eu/Eu* and Ce/Nd ratios, both of which point toward higher magmatic oxidation states in the Baklan and Pınarbaşı intrusions compared to the barren counterparts (Figure 6.8C–D).

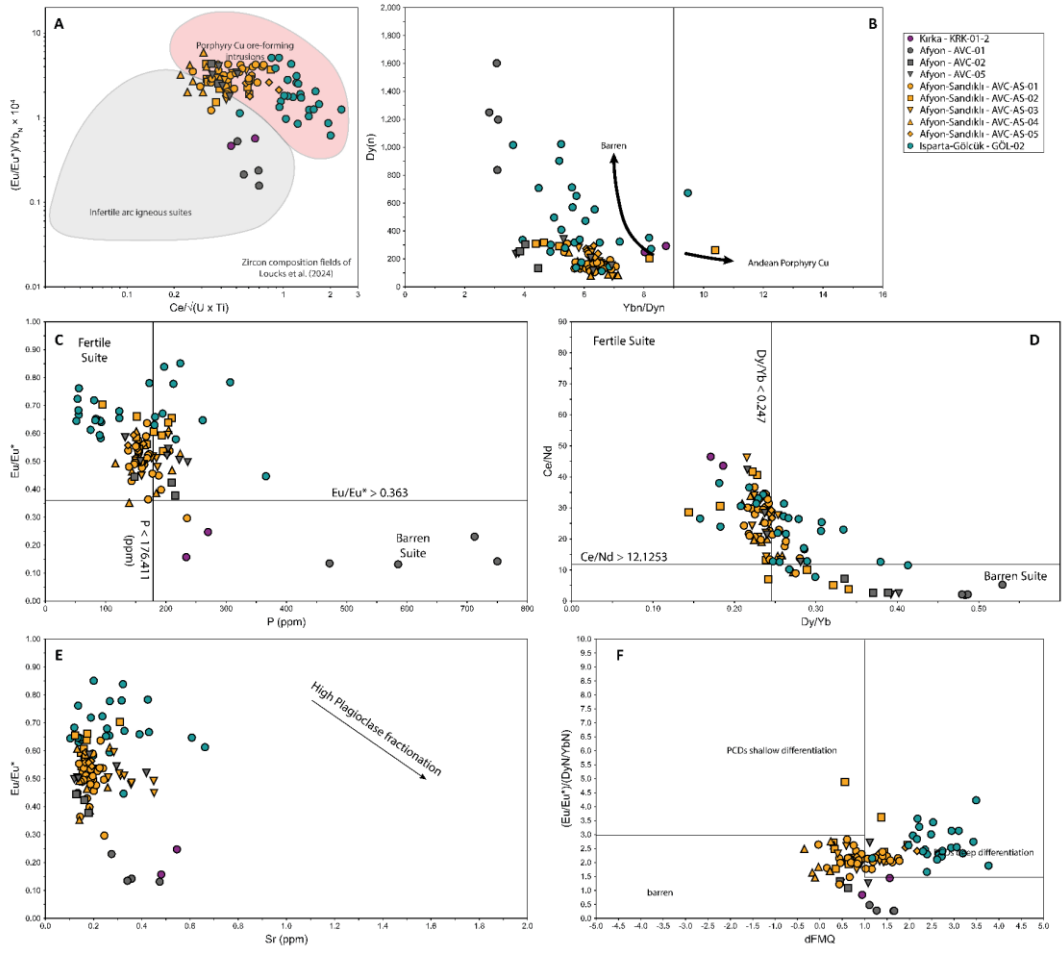


Figure 6.9. Zircon fertility parameters for the Kırka-Afyon-Isparta district. A) Zircon $(Eu/Eu^*)/Yb_N \times 10^4$ plotted against Ce/√(UxTi) in zircon. Shaded fields are after Loucks et al. (2024) and represent ranges for zircons from porphyry Cu ore-forming intrusions and from infertile arc igneous suites. B) $Dy_{(n)}$ vs. $Yb_{(n)}/Gd_{(n)}$. C) Eu/Eu* vs. P (ppm). D) Ce/Nd vs. Dy/Yb diagram. E) Eu/Eu* vs Sr (ppm). F) ΔFMQ vs. $(Eu/Eu^*)/(Dy_N/Yb_N)$ as suggested by Tapia et al. (2025). Subscript *N* indicates

chondrite-normalized values. Fertility parameters used in C, D, and E are suggested by Carrasco-Godoy et al. (2024).

In barren systems such as Eğrigöz and Sındırgı, plagioclase fractionation is clearly evident (Figure 6.8E), whereas the Baklan and Pınarbaşı systems suggest prolonged residence in deeper crustal reservoirs, likely in post-collisional settings, where magmas experienced more extensive evolution before ascent—conditions indicative of deep differentiation (Figure 6.8F). In contrast, the barren Eğrigöz and Sındırgı systems maintained signatures consistent with less oxidized, less hydrous magmas, marking a clear genetic divergence between the two groups (Figure 6.8).

Apatite trace element data reinforce these interpretations (Figure 6.4). Apatites extracted from the barren Eğrigöz granite show notably lower Eu/Eu* values, whereas those from Baklan and Pınarbaşı indicate more oxidized magmatic conditions (Figure 6.4A-C).

Combined together, these results suggest that between ~20 Ma and ~18 Ma, magmatism in the Kütahya–Simav region underwent a significant shift toward higher oxidation states and elevated magmatic water contents. This transition likely facilitated more favorable conditions for porphyry-style mineralization, marking the onset of a more fertile magmatic period in the region.

The Kırka–Afyon–Isparta magmatic corridor represents another key area for understanding the temporal and compositional evolution of late Cenozoic magmatism in western Anatolia, as it encompasses igneous suites spanning a broad age range from 18.4 to 2.6 Ma. Over this ~16-million-year period, the magmatic products in this corridor show a progressive increase in alkalinity, reflecting a gradual shift in magma chemistry through time.

Within this dataset, several samples stand out in their geochemical behavior. For instance, the Kırka sample and the oldest unit from the Afyon Volcanic Complex (AVC-01) display distinct characteristics compared to the rest, plotting clearly within the infertile igneous suites field (Figure 6.9A). By contrast, the younger AVC samples occupy a position similar to that of the Afyon–Sandıklı intrusions, falling

within the porphyry Cu–fertile field (Figure 6.9A). The youngest magmatic product of the entire corridor, sampled from the Isparta region, also lies within the fertile field (Figure 6.9A).

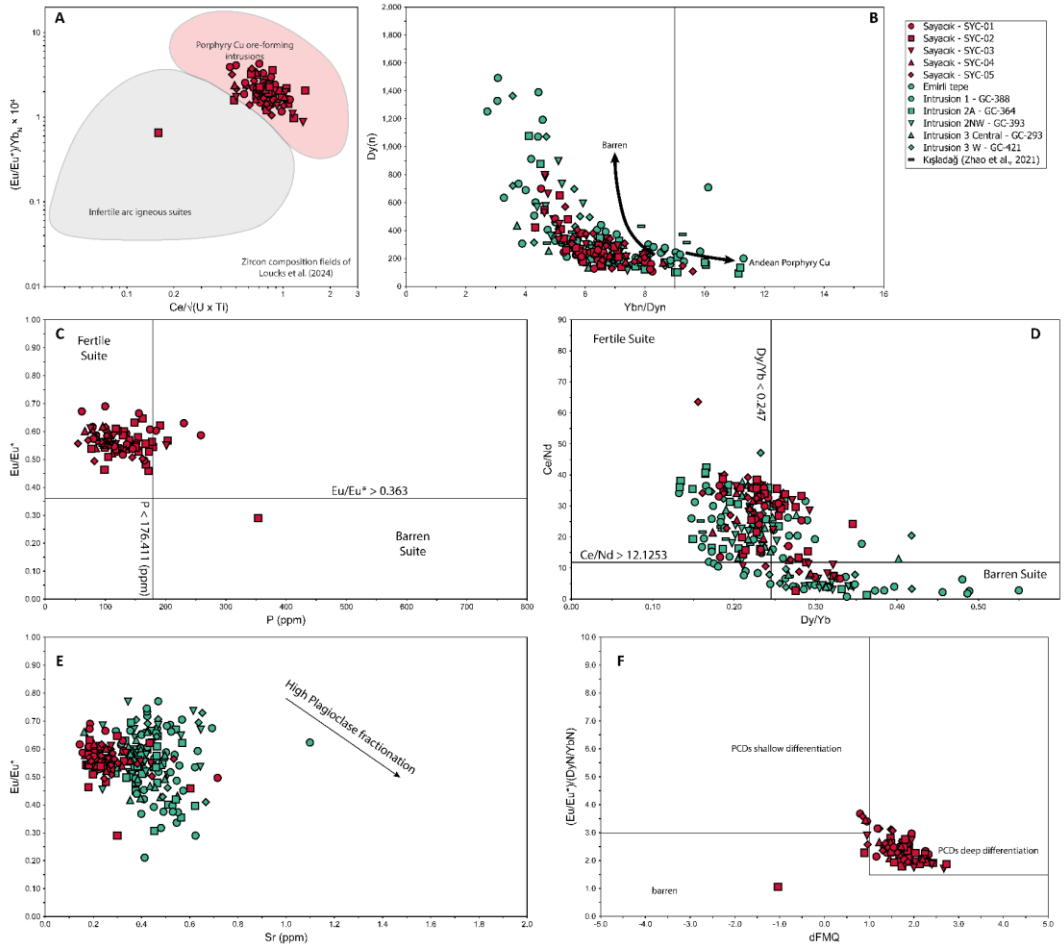


Figure 6.10. Zircon fertility parameters for the Kışladağ and Sayacık porphyry systems in Uşak. A) Zircon $(Eu/Eu^*)/Yb_N \times 10^4$ plotted against Ce/√(UxTi) in zircon. Shaded fields are after Loucks et al. (2024) and represent ranges for zircons from porphyry Cu ore-forming intrusions and from infertile arc igneous suites. B) $Dy_{(n)}$ vs. $Yb_{(n)}/Gd_{(n)}$. C) Eu/Eu* vs. P (ppm). D) Ce/Nd vs. Dy/Yb diagram. E) Eu/Eu* vs Sr (ppm). F) ΔFMQ vs. $(Eu/Eu^*)/(Dy_N/Yb_N)$ as suggested by Tapia et al. (2025). Subscript *N* indicates chondrite-normalized values. Fertility parameters used in C, D, and E are suggested by Carrasco-Godoy et al. (2024).

Although all samples exhibit low Yb/Dy ratios, the Isparta sample displays a barren geochemical trend that is particularly well-defined (Figure 6.9B). In terms of Eu anomalies, the Kırka sample and the oldest AVC sample are marked by low Eu/Eu*

values, while the younger AVC samples, Afyon–Sandıklı intrusions, and the latest alkaline magmatic products show considerably higher Eu/Eu* ratios (Figure 6.9C). This distribution suggests differing magmatic oxidation states and crystallization histories across the corridor. Furthermore, an inverse relationship between Dy/Yb and Ce/Nd ratios—characterized by increasing Ce/Nd alongside decreasing Dy/Yb—is evident in the Afyon–Sandıklı, Kırka, and Isparta samples (Figure 6.9D).

Variation in Eu/Eu* with increasing Sr contents (ppm) is clearly expressed within the AVC samples but remains indistinct in the Afyon–Sandıklı intrusions (Figure 6.9E). The Isparta sample, in contrast, shows substantial scatter, preventing the recognition of a clear trend (Figure 6.9E). Notably, the Isparta sample also preserves geochemical evidence for deep differentiation processes, setting it apart from the other units in the corridor (Figure 6.9F).

A similar pattern of separation emerges when apatite trace element compositions are examined. The Isparta and AVC samples differ significantly from the Afyon–Sandıklı intrusions (Figure 6.4). These units, which are characterized by higher Eu/Eu* ratios (Figure 6.4A), also display elevated Sr/Y ratios indicative of dominant amphibole fractionation during magma evolution (Figure 6.4B). By comparison, the Afyon–Sandıklı intrusions exhibit progressively increasing but overall low Eu/Eu* values, pointing toward relatively reduced magmatic oxidation conditions (Figure 6.4A).

Parallel to Sr/Y behavior, the AVC and Isparta samples are marked by high V/Y ratios (Figure 6.4C), further supporting the inference of oxidized magmatic conditions potentially favorable for porphyry-style mineralization. However, this highly elevated Sr/Y ratios may also be attributed to their alkaline nature. Chondrite-normalized REE patterns in apatite reveal another clear distinction: the Afyon–Sandıklı intrusions exhibit a pronounced negative Eu anomaly (Figure 6.4D), in contrast to the flatter or more positive Eu anomalies in AVC and Isparta apatites.

The Kırka–Afyon–Isparta magmatic corridor records a ~16 Ma evolution (18.4–2.6 Ma) marked by a progressive increase in magma alkalinity and notable shifts in

geochemical signatures. Early-stage magmatism, represented by the Kırka sample and the oldest Afyon Volcanic Complex unit (AVC-01), plots in the infertile igneous suites field and is characterized by low Eu/Eu* ratios. Younger AVC samples, the Afyon–Sandıklı intrusions, and the youngest Isparta rocks fall within the porphyry Cu–fertile field, with higher Eu/Eu* and elevated Sr/Y and V/Y ratios, indicative of more oxidized magmatic conditions and dominant amphibole fractionation. Despite generally low Yb/Dy ratios across all samples, the Isparta magma shows a distinctive barren trend and deep differentiation signature. Apatite trace element data reinforce these distinctions, with AVC and Isparta apatites lacking the pronounced negative Eu anomaly observed in Afyon–Sandıklı intrusions, highlighting contrasting magmatic processes and oxidation states within the corridor.

Samples from the Sayacık porphyry Au prospect in the Uşak district exhibit geochemical signatures that unambiguously point to elevated magma oxidation states, placing them within the domain typically associated with fertile porphyry systems (Figure 6.10A). Alongside this, both Kışladağ and Sayacık samples are notable for their low Yb/Dy ratios (Figure 6.10B), a feature that is complemented by their high Eu/Eu* values (Figure 6.10C). Within the framework proposed by Carrasco-Godoy et al. (2024), the Sayacık samples plot within the fertile field when Eu/Eu* ratios are considered in conjunction with P (ppm) contents (Figure 6.10C). In addition, they display elevated Ce/Nd ratios (Figure 6.10D). This combination reinforces the interpretation of high magma oxidation states. Interestingly, neither Kışladağ nor Sayacık samples show a clear correlation between increasing Sr (ppm) contents and Eu/Eu* ratios (Figure 6.10E). Based on their tectono-magmatic context, the Sayacık samples are interpreted to have formed under deep magmatic differentiation conditions (Figure 6.10F), suggesting a potential to generate large-scale porphyry systems.

To further constrain the metallogenic significance of these systems, apatite trace element data were also evaluated. At Kışladağ, apatites were separated from all intrusive phases except INT-1, which represents the earliest magmatic stage in the deposit. The analyzed apatites reveal phase-specific compositional trends, and

within-phase variability is also evident. Although the absence of apatite from INT-1 precludes a fully integrated zircon–apatite comparison for the earliest stage, meaningful relationships between the later phases were still identified. The temporal decline in mineralization intensity from INT-1 to INT-3 is mirrored in the apatite trace element chemistry (Figure 6.4). Specifically, INT-3 apatites (INT 3W and INT 3C), representing the least mineralized stage, consistently display low Eu/Eu* values with tight clustering (Figure 6.4A). By contrast, INT-2 samples (INT 2NW and INT 2CE) exhibit a broader range of Eu/Eu* values, but on average reach higher ratios, indicating higher magma oxidation states during this phase (Figure 6.4A).

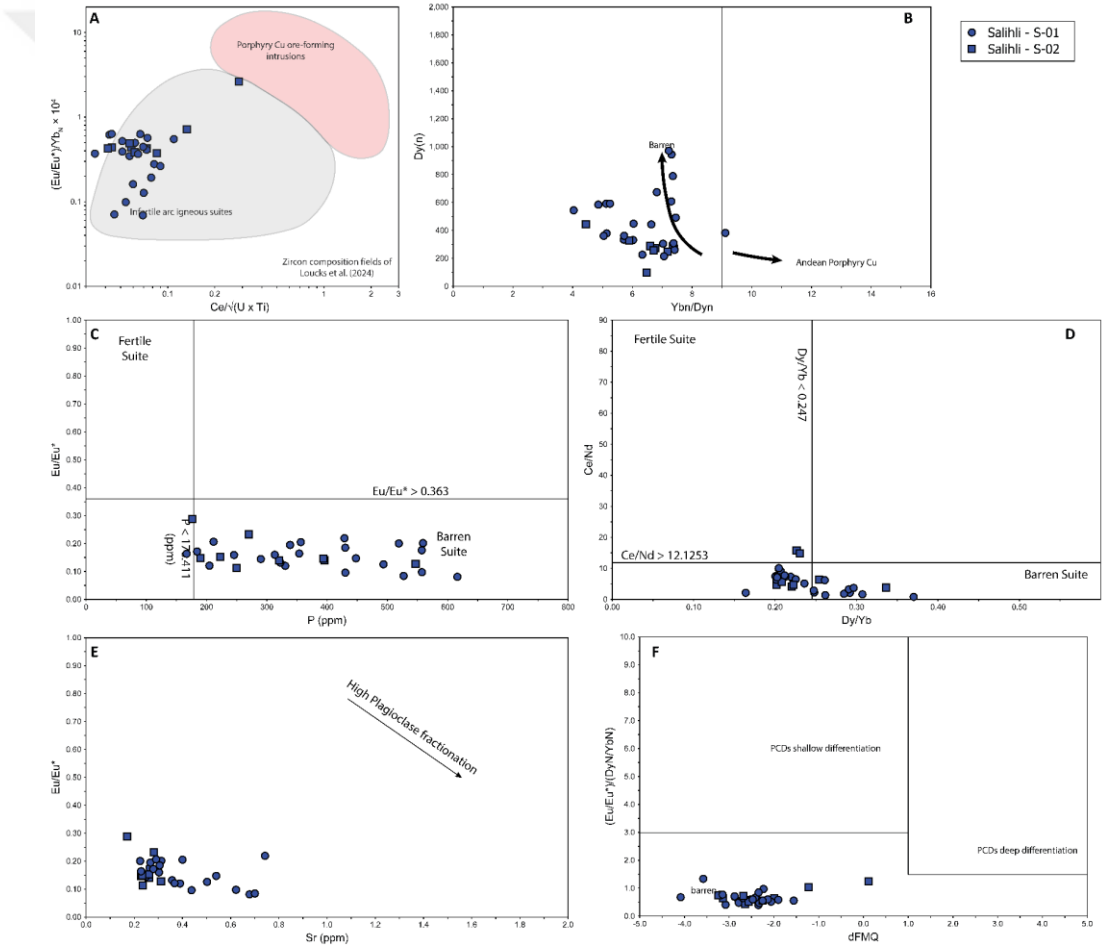


Figure 6.11. Zircon fertility parameters for the Salihli Pluton. A) Zircon $(Eu/Eu^*)/Yb_N \times 10^4$ plotted against $Ce/\sqrt{(UxTi)}$ in zircon. Shaded fields are after Loucks et al. (2024) and represent ranges for zircons from porphyry Cu ore-forming intrusions and from infertile arc igneous suites. B) $Dy_{(n)}$ vs. $Yb_{(n)}/Gd_{(n)}$. C) Eu/Eu*

vs. P (ppm). D) Ce/Nd vs. Dy/Yb diagram. E) Eu/Eu* vs Sr (ppm). F) ΔFMQ vs. (Eu/Eu*)/(Dy_N/Yb_N) as suggested by Tapia et al. (2025). Subscript *N* indicates chondrite-normalized values. Fertility parameters used in C, D, and E are suggested by Carrasco-Godoy et al. (2024).

The concurrent increase in Eu/Eu* and Sr/Y ratios—particularly pronounced in the INT-2 phase—suggests the role of amphibole fractionation (Figure 6.4), as amphibole preferentially removes middle to heavy rare earth elements while allowing Sr to remain in the melt under high-pressure conditions. The V/Y ratio provides an additional constraint: INT 2NW samples show particularly high V/Y values, which, when coupled with elevated Eu/Eu*, point toward magmatic conditions characteristic of productive porphyry systems (Figure 6.4C). Progressing from INT-2 to the younger INT-3 phase, a decrease in V/Y ratios is observed, consistent with an evolutionary shift toward more reducing magmatic conditions (Figure 6.4C). In comparison, Sayacık apatite data reveal even higher Eu/Eu* values than those from Kışladağ, reaffirming the interpretation of high oxidation states in the parental magmas (Figure 6.4A–C).

When zircon and apatite trace element data are integrated, both Kışladağ and Sayacık are shown to have been derived from oxidized magmas with high porphyry fertility potential. The declining fertility in the later stages of Kışladağ has been attributed by Paolillo et al. (2020) to an increasing mafic asthenospheric mantle contribution to the magma chamber, which reduced the system's fertility. This shift is clearly captured in both zircon and apatite trace element datasets. However, the fact that the Sayacık system, despite its geochemical signatures, did not evolve into a porphyry complex as large as Kışladağ cannot be fully explained by zircon and apatite data alone. Hafnium isotope analyses confirm the presence of asthenospheric contribution in the parental magma chamber beneath the Kışladağ and Sayacık, and the overlap of Sayacık mineralization in timing with Kışladağ's waning magmatic stages suggests a crystallization from already depleted magma chamber.

Contemporaneous with the magmatic activity in the Uşak district, the Salihli pluton stands out from all other Western Anatolian examples by exhibiting a distinctly

infertile geochemical signature when assessed across all parameters. The pluton is characterized by pronounced plagioclase fractionation (Figure 6.11E), a feature further supported by its apatite chemistry, which displays low Eu/Eu*, Ce/Ce*, Sr/Y, and V/Y ratios—collectively indicative of strongly reduced magmatic conditions (Figure 6.4). In the chondrite-normalized multi-element diagram, a distinct negative Eu anomaly is evident, reinforcing the interpretation of dominant plagioclase fractionation (Figure 6.4D).

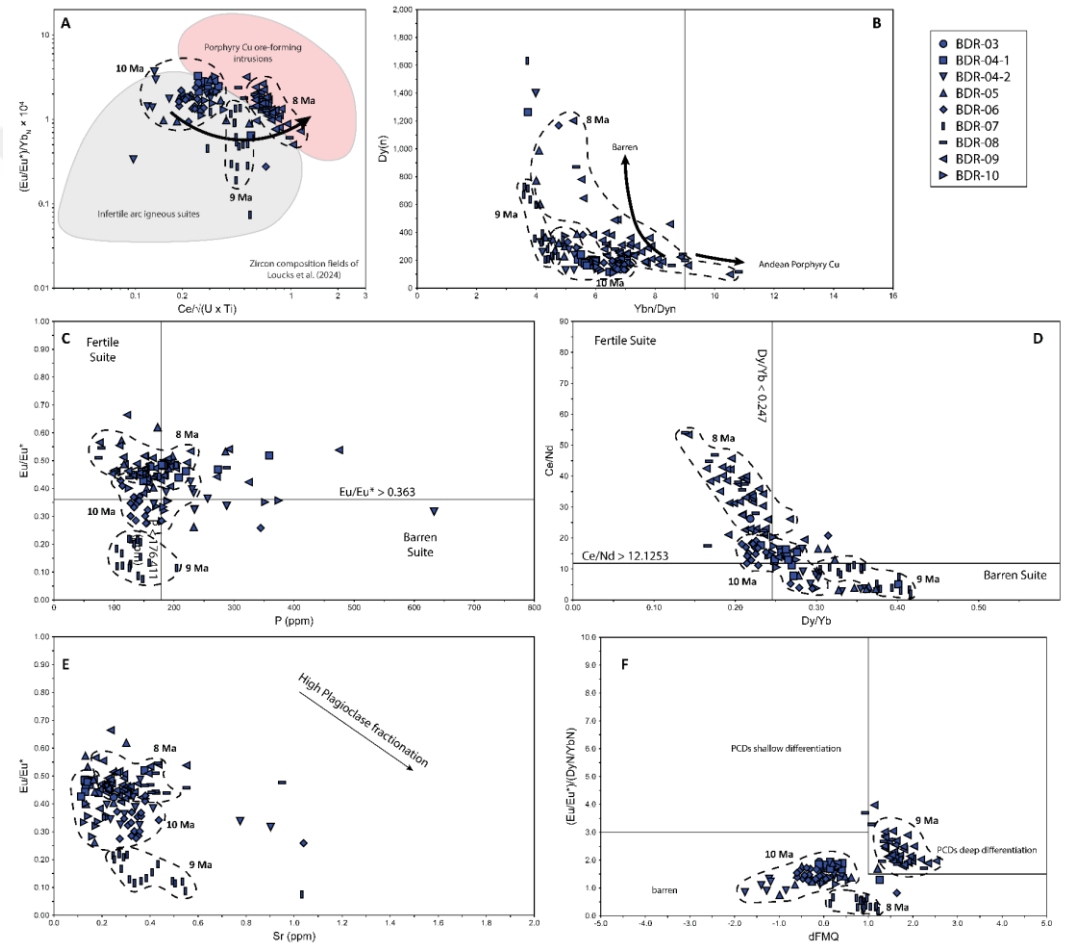


Figure 6.12. Zircon fertility parameters for the Bodrum Peninsula. A) Zircon $(Eu/Eu^*)/Yb_N \times 10^4$ plotted against $Ce/\sqrt{(UxTi)}$ in zircon. Shaded fields are after Loucks et al. (2024) and represent ranges for zircons from porphyry Cu ore-forming intrusions and from infertile arc igneous suites. B) $Dy_{(n)}$ vs. $Yb_{(n)}/Gd_{(n)}$. C) Eu/Eu* vs. P (ppm). D) Ce/Nd vs. Dy/Yb diagram. E) Eu/Eu* vs Sr (ppm). F) ΔFMQ vs. $(Eu/Eu^*)/(Dy_N/Yb_N)$ as suggested by Tapia et al. (2025). Subscript *N* indicates

chondrite-normalized values. Fertility parameters used in C, D, and E are suggested by Carrasco-Godoy et al. (2024).

The final region examined within Western Anatolia is the Bodrum Peninsula, which stands out among the study areas as the most geochemically diverse in terms of zircon trace element compositions and magmatic evolutionary history. The Bodrum samples record approximately 3 million years of magmatic evolution, spanning from 10.7 to 7.9 Ma. Based on their temporal distribution, the analyzed zircons can be grouped into three main stages. The first stage corresponds to early magmatic products dated to around 10 Ma. This is followed by a second stage concentrated near 9 Ma, and a final stage representing the youngest magmatic phase at ~8 Ma.

Zircon trace element ratios reveal a clear trend of increasing magma oxidation state from the early-stage products to the youngest units, with a progressive shift toward the porphyry fertility field (Figure 6.12A). Early-stage magmas are characterized by low Dy and moderate Yb/Dy ratios, whereas the second stage exhibits elevated Dy contents, resulting in lower Yb/Dy ratios (Figure 6.12B). The youngest magmatic products display the widest geochemical spread and the highest Yb/Dy ratios of all groups (Figure 6.12B). In terms of Eu/Eu*, early-stage units are defined by moderate values, which decrease to their lowest levels at 9 Ma before rising to peak values in the 8 Ma group (Figure 6.12C). The youngest units also exhibit the highest Ce/Nd ratios, forming a trend toward more oxidized and potentially fertile magmatic conditions (Figure 6.12D).

A negative correlation between Eu/Eu* and increasing Sr content is observed in the 9 Ma units, consistent with dominant plagioclase fractionation (Figure 6.12E). Although these 9 Ma units fall within the deep differentiation field, their geochemical signatures suggest that plagioclase—rather than amphibole—was the primary fractionating phase, implying crystallization from relatively dry magmas. This interpretation is further supported by chondrite-normalized zircon multi-element diagrams, which display a pronounced negative Eu anomaly in these units (Figure 5.24).

Apatite trace element data corroborate these zircon-based interpretations, indicating that early-stage Bodrum magmatism formed under relatively low oxidation states and subsequently evolved toward more oxidized and potentially fertile conditions through time (Figure 6.4). This temporal change is likely linked to caldera development, which may also explain the widespread hydrothermal alteration observed in the region.

The Bodrum Peninsula records a ~3 Myr magmatic evolution between 10.7 and 7.9 Ma, expressed in three main zircon age populations (~10 Ma, ~9 Ma, and ~8 Ma). Geochemical trends indicate a progressive increase in magma oxidation state from the earliest to the youngest stages, with the youngest magmas plotting toward the porphyry-fertile field. Early-stage units are marked by low Dy and moderate Yb/Dy ratios, shifting to higher Dy and lower Yb/Dy at ~9 Ma, and to the highest Yb/Dy values in the youngest stage. Eu/Eu* values decrease to a minimum at 9 Ma, then rise to their highest in the youngest units, accompanied by elevated Ce/Nd ratios. The 9 Ma units show a negative correlation between Eu/Eu* and Sr, consistent with dominant plagioclase fractionation, supported by pronounced negative Eu anomalies in chondrite-normalized zircon spectra. Apatite trace element data confirm the transition from relatively reduced early-stage magmas to more oxidized, fertile late-stage magmas, a change likely linked to caldera development and associated hydrothermal alteration.

In recent years, a number of zircon-based fertility parameters have been proposed or refined, and while these approaches have proven useful in distinguishing subduction-related systems, their application to post-collisional fertile magmatism has shown clear limitations. For example, the parameters introduced by Loucks et al. (2024) are highly effective in identifying porphyry Cu-related arc magmatism, yet they fall short in adequately characterizing Anatolian systems that display unusually high Au/Cu ratios. Similarly, although Carrasco-Godoy et al. (2024) have attempted to refine these proxies, their broader applicability remains debatable. By contrast, the parameters advanced by Tapia et al. (2025), particularly those based on ratios of heavy rare earth elements such as Yb and Dy, appear to offer more robust

discrimination compared to the other approaches. This underscores the pressing need for the development of new fertility parameters tailored to post-subduction settings, especially to enable a more precise evaluation of the Anatolian magmatic systems.

Previous studies have proposed and extensively examined several magma fertility parameters based on whole-rock, zircon, and apatite trace element compositions. Figure 6.13 presents the temporal variation of these parameters across the sampled localities in the Central Taurides and Western Anatolia, covering the interval from 25 Ma to 1.5 Ma. This compilation allows for a direct comparison of how effectively each parameter can discriminate porphyry-type mineralizing systems. The results indicate that increases in Eu/Eu^*_{zircon} and ΔFMQ_{zircon} values are particularly pronounced during transitions into fertile magmatic periods. In contrast, conventional whole-rock proxies, such as Sr/Y and La/Yb, appear to be far less effective in distinguishing fertile systems in this regional context. Apatite Eu/Eu* values, while generally less diagnostic than their zircon counterparts, still emerge as a valuable complementary tool for identifying magmas with porphyry potential. Additionally, the mineralized systems in Anatolia are represented by elevated Cl and reduced F contents compared to the barren magmas. The high Cl contents is particularly essential, as it plays a fundamental role in enhancing the capacity of magmatic–hydrothermal fluids to transport metals into the upper crustal levels where mineralization occurs. Ratios such as F/Cl, therefore, emerge as valuable geochemical proxies, offering a potential means to discriminate large-scale porphyry-style mineralization from less fertile systems.

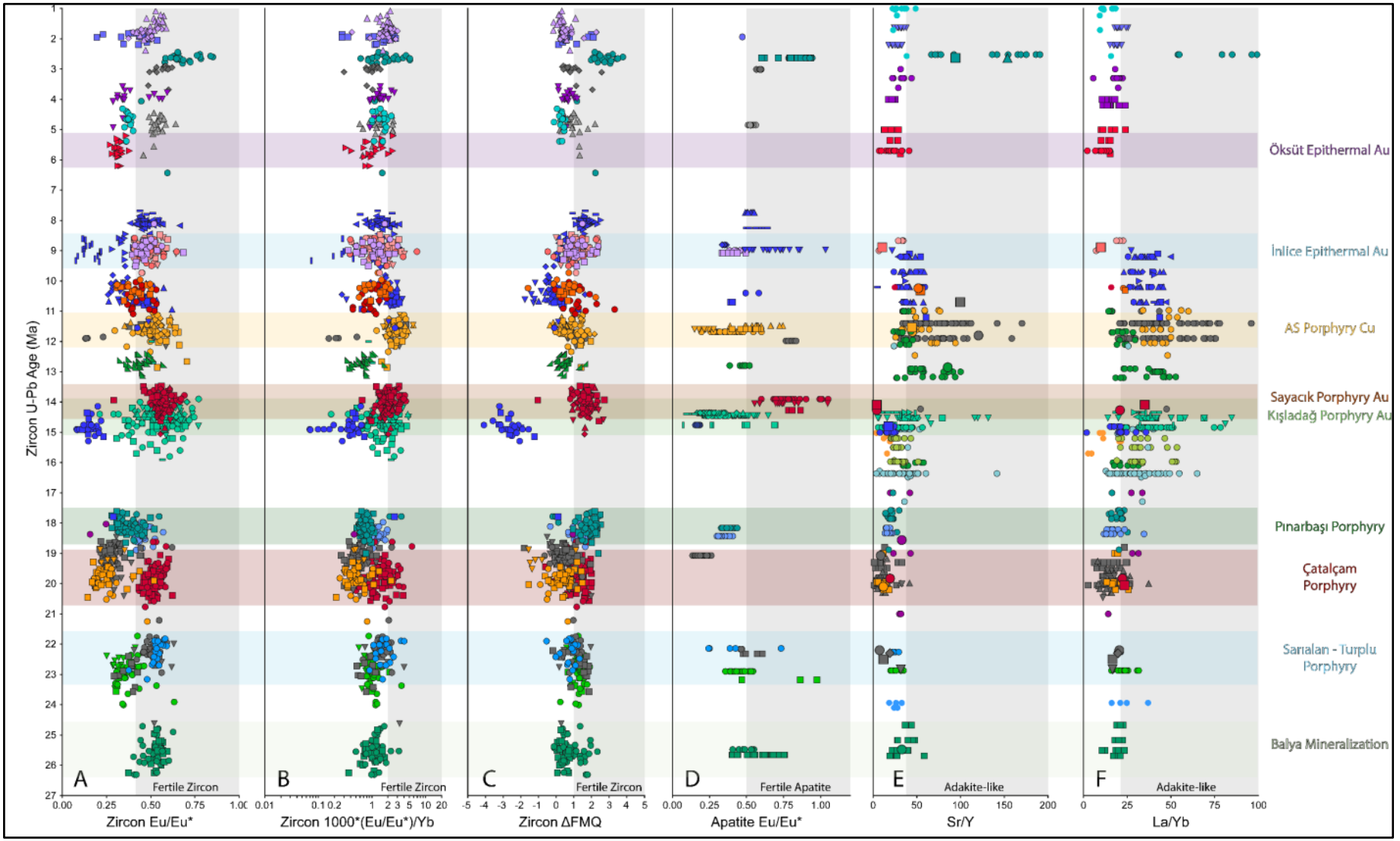


Figure 6.13. Various fertility parameters used to identify porphyry mineralization. A) Zircon Eu/Eu* (>0.4). B) Zircon 1000x(Eu/Eu*)/Yb. (>2). C) Zircon ΔFMQ (>1). D) Apatite Eu/Eu* (>0.5). E) Whole-rock Sr/Y (>40). F) Whole-rock La/Yb (>20). The gray fields for the whole rock lithogeochemistry data indicates the adakite-like field (Defant and Drummond, 1990; Richards, 2011).

CHAPTER 7

CONCLUSIONS

This thesis aims to document the magmatic fertility parameters of the Late Cenozoic (25 Ma to 1.5 Ma) in the Central Taurides and the Western Anatolia using robust and common accessory mineral phases including zircon and apatite. The findings are aimed to be supported by the field observations, petrographic investigations, whole-rock lithogeochemistry, and amphibole, biotite, and magnetite/ilmenite geochemistry and thermobarometry. To achieve this, twenty-two samples from the Central taurides and sixty-eigth samples from the Western Anatolia was collected through a couple of field excursions. Subsequently, all samples were analyzed for their mineralogy and petrography to identify the rock types, textures, and mineral assemblages, as well as the presence and the degree of alteration. The least-altered samples which contain primary hornblende, biotite, and magnetite/ilmenite were selected and prepared for the further mineral analyses. Additionally, all rock samples were processed in the sample preparation laboratory to obtain zircon and apatite separates for subsequent analytical work. Although the presence of zircon and apatite phases was confirmed through petrographic examinations, every sample was nonetheless subjected to the preparation stage to ensure that any potential recoverable grains of these minerals could be isolated. This approach was adopted to maximize the likelihood of obtaining sufficient mineral separates for detailed geochemical and isotopic analyses, even from samples where these phases appeared scarce or fine-grained under the microscope.

Following sample preparation, zircon U–Pb geochronology analyses were conducted on a total of 61 samples, comprising 17 from the Central Taurides and 44 from Western Anatolia. In Western Anatolia, the dated units range from ~25 Ma, represented by granodioritic bodies obtained from deep drill cores at the Balya deposit in the Biga Peninsula, to as young as 2.6 Ma in the Isparta region. In the

Central Taurides, magmatism spans from 13 Ma in the Sulutaş Volcanic Suite, located north of Konya, to 1.5 Ma in the Melendiz volcanic complex. Collecting additional samples from various volcanic sequences across the Central Taurides would increase the spatial coverage and enhance the resolution of magmatic evolution studies, as well as improve the assessment of the metallogenic potential in this region. Additionally, more apatite grains must be analyzed to fill the gaps and further support the magmatic fertility assessments and interpretations in the Central Taurides.

Trace element analyses of zircon grains were performed on all dated samples using the LA-ICP-MS method, producing a comprehensive dataset—particularly for Western Anatolia, where sampling covered a wide geographic area. This detailed dataset will provide a significant foundation for future studies aimed at determining the fertility parameters of magmatic units in Türkiye.

In the Central Taurides, zircon trace element data reveal a pronounced influence of crustal thickness on magmatic fertility, demonstrated through multiple geochemical parameters. Similarly, in Western Anatolia, zircon trace element analyses have successfully distinguished between fertile and barren magmatic units. In the Kütahya–Simav region, the transition from the barren 20 Ma magmatism to the fertile 18 Ma Pınarbaşı porphyry Cu magmatism was clearly documented through both zircon and apatite fertility parameters. Along the Kırka–Afyon–Isparta transect, magmatism spans from ~18 Ma in the north to 2.6 Ma in the south, with zircon and apatite fertility data providing key insights. Within these samples, the Afyon–Sandıklı porphyry Cu system demonstrates that zircon and apatite trace element signatures can be used to assess fertility. Furthermore, apatites from the alkaline magmatic products of the Afyon Volcanic Complex and Isparta units show notably high Sr/Y ratios, suggesting that apatite chemistry may serve as an effective indicator for identifying alkaline Au-bearing magmatic systems.

Zircon trace element fertility parameters from the Sayacık prospect appear broadly similar to Kışladağ. Additionally, apatites from Sayacık exhibit higher potential in

terms of porphyry mineralization. Increasing εHf values in Kışladağ over time (from -4.23 in the earliest to -1.63 in the latest intrusive phase) is interpreted as the magma chamber below Kışladağ was rejuvenated by a hotter, more mafic magma (Paolillo et al., 2022). εHf values in Sayacık, from -2.83 to -2.45, further confirm the mineralization from mafic contributed magma chamber. These findings suggest that early stages of magmatic development of the Beydağı Volcanic Complex (BVC) had a high potential to generate a world-class porphyry-style mineralization (like Kışladağ). Despite similar alteration and mineralization styles as well as comparable magmatic fertility based on zircon geochemistry, the uneconomic mineralization at Sayacık reflects an apparent temporal decline in magmatic fertility within the BVC. Progressive depletion of the fertile magma reservoir —caused by influx of mafic, dry asthenospheric magmas— possibly reduced metal and sulfur inputs during formation of the Sayacık prospect, thus limiting its economic viability.

Fertility parameters obtained from zircons and apatites separated from the Salihli pluton clearly indicate that the pluton is barren. In fact, the results from Salihli are unique in that they consistently classify the intrusion as barren across all evaluated magmatic parameters. Hf isotopes from those zircons indicate significant crustal contribution during the emplacement of the pluton.

Fertility parameters based on whole-rock geochemical ratios are generally defined for Andean-type subduction zones; therefore, they are often inadequate (even entirely ineffective in some cases) for assessing the fertility of Late Cenozoic magmatism in Anatolia. For this reason, zircon trace element geochemistry formed the core of this study, and zircon fertility parameters were applied to investigate differences between fertile and barren units in the region. However, the results also demonstrate that these parameters do not consistently provide a clear distinction in every area. While the transition to the fertile magmatic phase in the Kütahya–Simav region is well documented through changes in magmatic conditions, or the potential of the Afyon-Sandıklı prospect appears to be detected, the fertility parameters still require refinement for post-subduction or post-collisional settings. Consequently, the

dataset generated in this study, covering a broad temporal and spatial range, represents a particularly valuable resource for the future research.

REFERENCES

Abdel-Rahman, A. F. M. (1996). Nature of Biotites from Alkaline, Calc-alkaline and Peraluminous Magmas: A Comment. Journal of Petrology, 37(5).

Agostini, S., Doglioni, C., Innocenti, F., Manetti, P., and Tonarini, S. (2010). On the geodynamics of the Aegean rift. Tectonophysics, 488(1-4), 7-21.

Agostini, S., Doglioni, C., Innocenti, F., Manetti, P., Tonarini, S., and Savasçin, M. Y. (2007). The transition from subduction-related to intraplate Neogene magmatism in the Western Anatolia and Aegean area.

Akal, C. (2003). Mineralogy and geochemistry of melilite leucitites, Balçıkhisar, Afyon (Turkey). Turkish Journal of Earth Sciences, 12(3), 215-239.

Akal, C. (2008). K-richterite–olivine–phlogopite–diopside–sanidine lamproites from the Afyon volcanic province, Turkey. Geological Magazine, 145(4), 570–585. doi:10.1017/S0016756808004536

Akal, C., Helvacı, C., Prelevic, D., and Bogaard, P. van den, 2013. High-K volcanism in the Afyon region, western Turkey: from Si-oversaturated to Si-undersaturated volcanism, International Journal of Earth Sciences 102, 435-453.

Akay, E. (2009). Geology and petrology of the Simav Magmatic Complex (NW Anatolia) and its comparison with the Oligo-Miocene granitoids in NW Anatolia: implications on Tertiary tectonic evolution of the region. International Journal of Earth Sciences, 98(7), 1655-1675.

Aldanmaz, E., Pearce, J.A., Thirlwall, M. and Mitchell, J. (2000). Petrogenetic evolution of late Cenozoic, post-collision volcanism in western Anatolia, Turkey: Journal of Volcanology and Geothermal Research, v. 102, p. 67-95.

Alıcı, P., Temel, A., and Gourgaud, A. (2002). Pb–Nd–Sr isotope and trace element geochemistry of Quaternary extension-related alkaline volcanism: a case study of Kula region (western Anatolia, Turkey). Journal of volcanology and geothermal research, 115(3-4), 487-510.

Altunkaynak, Ş., and Dilek, Y. (2006). Timing and nature of postcollisional volcanism in western Anatolia and geodynamic implications, Postcollisional Tectonics and Magmatism in the Mediterranean Region and Asia, Geological Society of America, Special Paper 409, 321-351.

Altunkaynak, Ş., and Genç, Ş. C. (2008). Petrogenesis and time-progressive evolution of the Cenozoic continental volcanism in the Biga Peninsula, NW Anatolia (Turkey). Lithos, 102(1-2), 316-340.

Altunkaynak, Ş., Sunal, G., Aldanmaz, E., Genç, C. Ş., Dilek, Y., Furnes, H., Foland, K. A. and Yıldız, M. (2012). Eocene granitic magmatism in NW Anatolia (Turkey) revisited: new implications from comparative zircon SHRIMP U–Pb and 40Ar–39Ar geochronology and isotope geochemistry on magma genesis and emplacement. Lithos, 155, 289-309.

Aluç, A., Kuşcu, İ., Peytcheva, I., Cihan, M., and von Quadt, A. (2020). The late miocene öksüt high sulfidation epithermal au-cu deposit, central anatolia, Turkey: geology, geochronology, and geochemistry. Ore Geology Reviews, 126, 103795.

Annen, C., Blundy, J. D., and Sparks, R. S. J. (2006). The genesis of intermediate and silicic magmas in deep crustal hot zones. Journal of petrology, 47(3), 505-539.

Arculus, R. J. (1994). Aspects of magma genesis in arcs. Lithos, 33(1-3), 189-208.

Asan, K., and Ertürk, M. A. (2013). First Evidence of Lamprophyric Magmatism from the Konya Region, Turkey: a Genetic Link to High- K Volcanism. Acta Geologica Sinica- English Edition, 87(6), 1617-1629.

Asan, K., Gündüz, M., Korkmaz, G. G., and Kurt, H. (2024). The role of magma recharge and mixing in producing compositional modality in post-collisional volcanic rocks, Konya Volcanic Field, Central Anatolia (Türkiye). Journal of Asian Earth Sciences, 276, 106364.

Asan, K., Kurt, H., Gündüz, M., Gençoğlu Korkmaz, G., and Morgan, G. (2021). Geology, geochronology and geochemistry of the Miocene Sulutas volcanic complex, Konya-Central Anatolia: genesis of orogenic and anorogenic rock associations in an extensional geodynamic setting. International Geology Review, 63(2), 161-192.

Audétat, A., and Pettke, T. (2006). Evolution of a porphyry-Cu mineralized magma system at Santa Rita, New Mexico (USA). Journal of Petrology, 47(10), 2021-2046.

Audétat, A., Pettke, T., Heinrich, C. A., and Bodnar, R. J. (2008). Special paper: the composition of magmatic-hydrothermal fluids in barren and mineralized intrusions. Economic Geology, 103(5), 877-908.

Aydar, A. (2018). The ore forming conditions and genesis of gold-copper mineralisation in balya Pb-Zn-Ag deposit (Balikesir, Turkey). M.Sc. thesis, Muğla Sıtkı Koçman University, Muğla, 159p.

Aydar, E., Gourgaud, A., Deniel, C., Lyberis, N., & Gundogdu, N. (1995). Quaternary volcanism of central anatolia (turkey)-association of calc-alkaline and alkaline magmatisms in a zone of convergence. Canadian Journal of Earth Sciences, 32(7), 1058-1069.

Aydar, E., Schmitt, A. K., Çubukçu, H. E., Akin, L., Ersoy, O., Sen, E., Duncan, R. A., and Atici, G. (2012). Correlation of ignimbrites in the central Anatolian volcanic province using zircon and plagioclase ages and zircon compositions. Journal of Volcanology and Geothermal Research, 213, 83-97.

Aydin, F. (2008). Contrasting complexities in the evolution of calc-alkaline and alkaline melts of the Nigde volcanic rocks, Turkey: textural, mineral chemical and geochemical evidence. European Journal of Mineralogy, 20(1), 101-118.

Aydin, F., Sönmez, M., Siebel, W., Karsli, O., and Lermi, A. (2022). Slab break-off-related magnesian andesites and dacites with adakitic affinity from the early Quaternary Keçiboyduran stratovolcano, Cappadocia province, central Turkey: evidence for slab/sediment melt–mantle interaction and magma mixing. Contributions to Mineralogy and Petrology, 177(7), 65.

Aydoğan, M. S., Coban, H., Bozcu, M., and Akıncı, Ö. (2008). Geochemical and mantle-like isotopic (Nd, Sr) composition of the Baklan Granite from the Muratdagi Region (Banaz, Usak), western Turkey: Implications for input of juvenile magmas in the source domains of western Anatolia Eocene-Miocene granites.

Bai, Y., Zhang, D., Dong, D., Wu, S., and Wang, Z. (2020). Aleutian island arc magma production rates and primary controlling factors. Marine Geology, 430, 106346.

Baker, T. (2019). Gold±copper endowment and deposit diversity in the Western Tethyan magmatic belt, southeast Europe: Implications for exploration. Economic Geology, 114(7), 1237-1250.

Baker, T., Bickford, D., Juras, S., Lewis, P., Oztas, Y., Ross, K., Tukac, A., Rabayrol, F., Miskovic, A., Friedman, R., Creaser, R.A., and Spikings, R. (2016). The geology of the Kişladağ porphyry gold deposit, Turkey.

Ballard, J. R., Palin, J. M., and Campbell, I. H. (2002). Relative oxidation states of magmas inferred from Ce (IV)/Ce (III) in zircon: application to porphyry copper deposits of northern Chile. Contributions to Mineralogy and Petrology, 144(3), 347-364.

Ballhaus, C. (1993). Redox states of lithospheric and asthenospheric upper mantle. Contributions to Mineralogy and Petrology, 114(3), 331-348.

Bartol, J., and Govers, R. (2014). A single cause for uplift of the Central and Eastern Anatolian plateau?. Tectonophysics, 637, 116-136.

Belousova, E. A., Griffin, W. L., O'Reilly, S. Y., and Fisher, N. I. (2002). Apatite as an indicator mineral for mineral exploration: trace-element compositions and their relationship to host rock type. Journal of Geochemical Exploration, 76(1), 45-69.

Besang, C., Echardt, F.-J., Harre, W., Kreuzer, H., and Müller, P. (1977). Radiometrische Altersbestimmungen an neogenen Eruptivgesteinen der Turkei: Geologisches Jahrbuch, v. B25,p. 3–36

Bickford, D., Tukac, A., Öztaş, Y., and Baker, T. (2016). Exploration overview of the Sayacık and Kişladağ gold porphyries, western Anatolia volcanic province, Turkey: Society of Economic Geologists, SEG-MJD 2016: Tethyan Tectonics and Metallogeny, Çeşme, Turkey, September 25–28, 2016, Oral Presentation.

Biryol, C.B., Beck, S.L., Zandt, G., and Özacar, A.A. (2011). Segmented African lithosphere beneath the Anatolian region inferred from teleseismic P-wave tomography: Geophysical Journal International, v. 184, p. 1037–1057.

Black L.P. and Gulson, B.L. (1978). The age of the Mud Tank Carbonatite, Strangways Range, Northern Territory. Journal of Australian Geology and Geophysics, 3, 227–232.

Blichert-Toft, J., and Albarède, F. (1997). The Lu-Hf isotope geochemistry of chondrites and the evolution of the mantle-crust system. Earth and Planetary Science Letters, 148(1-2), 243-258.

Boucher, K. S. (2016). The structural and fluid evolution of the Efemçukuru epithermal gold deposit, western Turkey (Doctoral dissertation, University of British Columbia).

Bouvier, A., Vervoort, J. D., and Patchett, P. J. (2008). The Lu–Hf and Sm–Nd isotopic composition of CHUR: constraints from unequilibrated chondrites and implications for the bulk composition of terrestrial planets. Earth and Planetary Science Letters, 273(1-2), 48-57.

Boyce, J. W., Liu, Y., Rossman, G. R., Guan, Y., Eiler, J. M., Stolper, E. M., and Taylor, L. A. (2010). Lunar apatite with terrestrial volatile abundances. Nature, 466(7305), 466-469.

Bozkurt, E. (2003). Origin of NE-trending basins in western Turkey. Geodinamica acta, 16(2-6), 61-81.

Bozkurt, E., Winchester, J. A., and Park, R. G. (1995). Geochemistry and tectonic significance of augen gneisses from the southern Menderes Massif (West Turkey). Geological Magazine, 132(3), 287-301.

Brandon, A. D., and Draper, D. S. (1996). Constraints on the origin of the oxidation state of mantle overlying subduction zones: an example from Simcoe, Washington, USA. Geochimica et Cosmochimica Acta, 60(10), 1739-1749.

Brenan, J. M., Shaw, H. F., Phinney, D. L., and Ryerson, F. J. (1994). Rutile-aqueous fluid partitioning of Nb, Ta, Hf, Zr, U and Th: implications for high field strength element depletions in island-arc basalts. Earth and Planetary Science Letters, 128(3-4), 327-339.

Bromiley, G. D. (2021). Do concentrations of Mn, Eu and Ce in apatite reliably record oxygen fugacity in magmas?. Lithos, 384, 105900.

Brunetti, P. (2016). Magmatic-hydrothermal evolution and post-ore modifications of the Halilağa porphyry Cu-Au deposit. NW Turkey, University of British Columbia, Vancouver, Canada.

Buddington, A. F., and Lindsley, D. H. (1964). Iron-titanium oxide minerals and synthetic equivalents. Journal of petrology, 5(2), 310-357.

Burnham, A. D., and Berry, A. J. (2012). An experimental study of trace element partitioning between zircon and melt as a function of oxygen fugacity. Geochimica et Cosmochimica Acta, 95, 196-212.

Burnham, C. W. (1979) "Magma and hydrothermal fluids" in Barnes, H. L. (ed.), Geochemistry of Hydrothermal Ore Deposits, 2nd edition, pp. 71-136, Wiley-Interscience

Candela, P. A., and Holland, H. D. (1984). The partitioning of copper and molybdenum between silicate melts and aqueous fluids. Geochimica et Cosmochimica Acta, 48(2), 373-380.

Carrasco-Godoy, C., Campbell, I. H., and Cajal, Y. (2024). Quantifying the criteria used to identify zircons from ore-bearing and barren systems in porphyry copper exploration. Economic Geology, 119(5), 1035-1058.

Catlos, E. J., Baker, C., Sorensen, S. S., Çemen, I., and Hançer, M. (2010). Geochemistry, geochronology, and cathodoluminescence imagery of the Salihli and Turgutlu granites (central Menderes Massif, western Turkey): Implications for Aegean tectonics. Tectonophysics, 488(1-4), 110-130.

Çelik Karakaya, M. (1999). Minamiite and alunite occurences formed from volcanic emanations, West-Southwest of Konya, Turkey. Türkiye Jeoloji Bülteni, 42(2), 89-97.

Chambefort, I., Dilles, J. H., and Longo, A. A. (2013). Amphibole geochemistry of the Yanacocha Volcanics, Peru: Evidence for diverse sources of magmatic volatiles related to gold ores. Journal of Petrology, 54(5), 1017-1046.

Chelle-Michou, C., and Chiaradia, M. (2017). Amphibole and apatite insights into the evolution and mass balance of Cl and S in magmas associated with porphyry copper deposits. Contributions to Mineralogy and Petrology, 172(11), 105.

Chelle-Michou, C., Rottier, B., Caricchi, L., and Simpson, G. (2017). Tempo of magma degassing and the genesis of porphyry copper deposits. Scientific reports, 7(1), 40566.

Chiaradia, M. (2014). Copper enrichment in arc magmas controlled by overriding plate thickness. Nature Geoscience, 7(1), 43-46.

Chiaradia, M. (2015). Crustal thickness control on Sr/Y signatures of recent arc magmas: an Earth scale perspective. Scientific reports, 5(1), 8115.

Chiaradia, M. (2020). Gold endowments of porphyry deposits controlled by precipitation efficiency. Nature Communications, 11(1), 248.

Chiaradia, M., and Caricchi, L. (2017). Stochastic modelling of deep magmatic controls on porphyry copper deposit endowment. Scientific reports, 7(1), 44523.

Chiaradia, M., Ulianov, A., Kouzmanov, K., and Beate, B. (2012). Why large porphyry Cu deposits like high Sr/Y magmas?: Scientific Reports, v. 2, p. 685.

Chin, E. J., Shimizu, K., Bybee, G. M., and Erdman, M. E. (2018). On the development of the calc-alkaline and tholeiitic magma series: A deep crustal cumulate perspective. Earth and Planetary Science Letters, 482, 277-287.

Claiborne, L. L., Miller, C. F., and Wooden, J. L. (2010). Trace element composition of igneous zircon: a thermal and compositional record of the accumulation and evolution of a large silicic batholith, Spirit Mountain, Nevada. Contributions to Mineralogy and Petrology, 160(4), 511-531.

Cline, J. S., and Bodnar, R. J. (1991). Can economic porphyry copper mineralization be generated by a typical calc- alkaline melt?. Journal of Geophysical Research: Solid Earth, 96(B5), 8113-8126.

Çoban, H., and Flower, M. F. (2006). Mineral phase compositions in silica-undersaturated 'leucite'lamproites from the Bucak area, Isparta, SW Turkey. Lithos, 89(3-4), 275-299.

Cocker, H., Park, J. W., and Campbell, I. (2016). Sulfide saturation during the magmatic evolution of porphyry Cu±Au systems. 4th International Workshop on Highly Siderophile Element Geochemistry.

Collins, W. J., and Richards, S. W. (2008). Geodynamic significance of S-type granites in circum-Pacific orogens. Geology, 36(7), 559-562.

Cooke, D. R., Hollings, P., and Walshe, J. L. (2005). Giant porphyry deposits: characteristics, distribution, and tectonic controls. Economic geology, 100(5), 801-818.

Cosentino, D., Schildgen, T. F., Cipollari, P., Faranda, C., Gliozzi, E., Hudáčková, N., Lucifora, S., and Strecker, M. R. (2012). Late Miocene surface uplift of the southern margin of the Central Anatolian Plateau, Central Taurides, Turkey. Bulletin, 124(1-2), 133-145.

Cottrell, E., and Kelley, K. A. (2011). The oxidation state of Fe in MORB glasses and the oxygen fugacity of the upper mantle. Earth and Planetary Science Letters, 305(3-4), 270-282.

Crocket, J. H. (2000). PGE in fresh basalt, hydrothermal alteration products, and volcanic incrustations of Kilauea volcano, Hawaii. Geochimica et Cosmochimica Acta, 64(10), 1791-1807.

Çubukcu, H. E., Aydar, E., Ulusoy, İ., and Gourgaud, A. (2021). Shoshonitic volcanism of the Bodrum caldera (SW Turkey): Hybridization of enriched mantle-derived and crustal melts. Journal of Asian Earth Sciences, 219, 104901.

Davidson, J. P. (1996). Deciphering mantle and crustal signatures in subduction zone magmatism. Geophysical Monograph Series, 96, 251-262.

Davies, J. H., and von Blanckenburg, F. (1995). Slab breakoff: a model of lithosphere detachment and its test in the magmatism and deformation of collisional orogens. Earth and planetary science letters, 129(1-4), 85-102.

de Hoog, J. C., Taylor, B. E., and van Bergen, M. J. (2001, May). Recycling of Volatiles in Subduction Zones: Evidence from HOS Isotopic Signatures of Indonesian Arc Basalts. In AGU Spring Meeting Abstracts (Vol. 2001, pp. V41C-09).

Defant, M. J., and Drummond, M. S. (1990). Derivation of some modern arc magmas by melting of young subducted lithosphere. nature, 347(6294), 662-665.

Delaloye, M., and Bingöl, E. (2000). Granitoids from western and northwestern Anatolia: geochemistry and modeling of geodynamic evolution. International Geology Review, 42(3), 241-268.

Delibaş, O., Moritz, R., Chiaradia, M., Selby, D., Ulianov, A., and Revan, M. K. (2017). Post-collisional magmatism and ore-forming systems in the Menderes massif: new constraints from the Miocene porphyry Mo–Cu Pınarbaşı system, Gediz–Kütahya, western Turkey. Mineralium Deposita, 52, 1157-1178.

Delibaş, O., Moritz, R., Selby, D., Göç, D., and Revan, M. K. (2019). Multiple porphyry Cu-Mo events in the eastern Pontides metallogenic belt, Turkey: From Early Cretaceous subduction to Eocene postcollision evolution. Economic Geology, 114(7), 1285-1300.

Delibaş, O., Moritz, R., Ulianov, A., Chiaradia, M., Saraç, C., Revan, K. M., and Göç, D. (2016). Cretaceous subduction-related magmatism and associated porphyry-type Cu–Mo prospects in the Eastern Pontides, Turkey: new constraints from geochronology and geochemistry. Lithos, 248, 119-137.

Delph, J. R., Abgarmi, B., Ward, K. M., Beck, S. L., Özacar, A. A., Zandt, G., Sandvol, E., Türkelli, N., and Kalafat, D. (2017). The effects of subduction termination on the continental lithosphere: Linking volcanism, deformation, surface uplift, and slab tearing in central Anatolia. Geosphere, 13(6), 1788-1805.

Deng, H., Kusky, T., Bozurt, E., Chen, C., Wang, L., Dong, Z., and Meng, J. (2023). Sr-Nd-Ca isotopic variations of Cenozoic calc-alkaline and alkaline volcanic rocks above a slab tear in Western Anatolia, Turkey. Geological Society of America Bulletin.

Derman, S., Rojay, B., Güney, H., and Yıldız, M. (2003). New sedimentological data on the evolution of Şereflikoçhisar-Aksaray fault zone. Turk Assoc Petrol Geol Spec Publ, 5, 47-70.

Dewey, J. F. (1988). Extensional collapse of orogens. Tectonics, 7(6), 1123-1139.

Di Giuseppe, P., Agostini, S., Manetti, P., Savaşçın, M. Y., and Conticelli, S. (2018). Genesis of Na-alkaline and calc-alkaline magmas in a post-collisional transtensive tectonic regimes: the case study of the recent monogenetic volcanism of Cappadocia, Central Turkey. Lithos, 316, 304-322.

Dilek, Y. and Altunkaynak, Ş. (2007). Cenozoic crustal evolution and mantle dynamics of post-collisional magmatism in western Anatolia. International Geology Review, 49(5), 431-453.

Dilek, Y. and Altunkaynak, Ş. (2009). Geochemical and temporal evolution of Cenozoic magmatism in western Turkey: mantle response to collision, slab break-off, and lithospheric tearing in an orogenic belt.

Dilek, Y. and Altunkaynak, Ş. (2010). Geochemistry of Neogene–Quaternary alkaline volcanism in western Anatolia, Turkey, and implications for the Aegean mantle. International Geology Review, 52(4-6), 631-655.

Dilles, J. H., Lee, R. G., Wooden, J. L., and Koleszar, A. M. (2015, December). Temporal Evolution of Volcanic and Plutonic Magmas Related to Porphyry Copper Ores Based on Zircon Geochemistry. In AGU Fall Meeting Abstracts (Vol. 2015, pp. V41D-08).

Doğan-Kulahcı, G. D., Temel, A., Gourgaud, A., Varol, E., Guillou, H., and Deniel, C. (2018). Contemporaneous alkaline and calc-alkaline series in Central Anatolia (Turkey): Spatio-temporal evolution of a post-collisional Quaternary basaltic volcanism. Journal of Volcanology and Geothermal Research, 356, 56-74.

Du, J. and Audétat, A. (2020). Early sulfide saturation is not detrimental to porphyry Cu-Au formation. Geology, 48(5), 519-524.

Duan, D. F. and Jiang, S. Y. (2018). Using apatite to discriminate synchronous ore-associated and barren granitoid rocks: a case study from the Edong metallogenic district, South China. Lithos, 310, 369-380.

Ece, O. I. and Schroeder, P. A. (2007). Clay mineralogy and chemistry of halloysite and alunite deposits in the Turplu area, Balikesir, Turkey. Clays and Clay Minerals, 55(1), 18-35.

Ece, O. I., Schroeder, P. A., Smilley, M. J., and Wampler, J. M. (2008). Acid-sulphate hydrothermal alteration of andesitic tuffs and genesis of halloysite and alunite deposits in the Biga Peninsula, Turkey. Clay Minerals, 43(2), 281-315.

Erkül, F., Helvaci, C., and Sözbilir, H. (2005). Evidence for two episodes of volcanism in the Bigadiç borate basin and tectonic implications for western Turkey. Geological Journal, 40(5), 545-570.

Erkül, S. T., and Erkül, F. (2012). Magma interaction processes in syn-extensional granitoids: the Tertiary Menderes Metamorphic Core Complex, western Turkey. Lithos, 142, 16-33.

Ersoy, E. Y., Akal, C., Genç, Ş. C., Candan, O., Palmer, M. R., Prelević, D., Uysal, İ., and Mertz-Kraus, R. (2017). U-Pb zircon geochronology of the Paleogene–Neogene volcanism in the NW Anatolia: Its implications for the Late Mesozoic-Cenozoic geodynamic evolution of the Aegean. Tectonophysics, 717, 284-301.

Ersoy, E. Y., and Palmer, M. R. (2013). Eocene-Quaternary magmatic activity in the Aegean: Implications for mantle metasomatism and magma genesis in an evolving orogeny. Lithos, 180, 5-24.

Ersoy, E. Y., Helvacı, C., and Palmer, M. R. (2010). Mantle source characteristics and melting models for the early-middle Miocene mafic volcanism in Western Anatolia: Implications for enrichment processes of mantle lithosphere and origin of K-rich volcanism in post-collisional settings. Journal of Volcanology and Geothermal Research, 198(1-2), 112-128.

Faccenna, C., Bellier, O., Martinod, J., Piromallo, C., and Regard, V. (2006). Slab detachment beneath eastern Anatolia: A possible cause for the formation of the North Anatolian fault. Earth and Planetary Science Letters, 242(1-2), 85-97.

Ferry, J. M., and Watson, E. B. (2007). New thermodynamic models and revised calibrations for the Ti-in-zircon and Zr-in-rutile thermometers. Contributions to Mineralogy and Petrology, 154(4), 429-437.

Fisher, C. M., Hanchar, J. M., Samson, S. D., Dhuime, B., Blichert-Toft, J., Vervoort, J. D., and Lam, R. (2011). Synthetic zircon doped with hafnium and rare earth elements: A reference material for in situ hafnium isotope analysis. Chemical Geology, 286(1-2), 32-47.

Francalanci, L., Innocenti, F., Manetti, P., and Savaşçın, M.Y. (2000). Neogene alkaline volcanism of the Afyon-Isparta area, Turkey: petrogenesis and geodynamic implications. Miner. Petrol. 70, 285–312.

Frey, F. A., Chappell, B. W., and Roy, S. D. (1978). Fractionation of rare-earth elements in the Tuolumne Intrusive Series, Sierra Nevada batholith, California. Geology, 6(4), 239-242.

Frost, B. R., and Frost, C. D. (2008). A geochemical classification for feldspathic igneous rocks. Journal of Petrology, 49(11), 1955-1969.

Gencalioglu Kuscu, G., and Geneli, F. (2010). Review of post-collisional volcanism in the Central Anatolian Volcanic Province (Turkey), with special reference to the Tepekoy Volcanic Complex. International Journal of Earth Sciences, 99(3), 593-621.

Gençoğlu Korkmaz, G., Kurt, H., Asan, K., and Leybourne, M. (2022). Ar-Ar Geochronology and Sr-Nd-Pb-O Isotopic Systematics of the Post-collisional Volcanic Rocks from the Karapınar-Karacadağ Area (Central Anatolia, Turkey): An Alternative Model for Orogenic Geochemical Signature in Sodic Alkali Basalts. Journal of Geosciences, 67(1).

Georgatou, A., Chiaradia, M., and Kouzmanov, K. (2021). TP-fO2 conditions of sulfide saturation in magmatic enclaves and their host lavas. Lithos, 398, 106313.

Gessner, K., Gallardo, L. A., Markwitz, V., Ring, U., and Thomson, S. N. (2013). What caused the denudation of the Menderes Massif: Review of crustal evolution, lithosphere structure, and dynamic topography in southwest Turkey. Gondwana research, 24(1), 243-274.

Ghiorso, M. S., and Evans, B. W. (2008). Thermodynamics of rhombohedral oxide solid solutions and a revision of the Fe-Ti two-oxide geothermometer and oxygen-barometer. American Journal of science, 308(9), 957-1039.

Ghiorso, M. S., and Sack, O. (1991). Fe-Ti oxide geothermometry: thermodynamic formulation and the estimation of intensive variables in silicic magmas. Contributions to Mineralogy and Petrology, 108(4), 485-510.

Gill, J. B., and Gill, J. B. (1981). The Role of Subducted Ocean Crust in the Genesis of Orogenic Andesite. Orogenic Andesites and Plate Tectonics, 230-247.

Glodny, J., and Hetzel, R. (2007). Precise U–Pb ages of syn-extensional Miocene intrusions in the central Menderes Massif, western Turkey. Geological Magazine, 144(2), 235-246.

Göğüş, O. H., Pysklywec, R. N., Şengör, A. M. C., and Gün, E. (2017). Drip tectonics and the enigmatic uplift of the Central Anatolian Plateau. Nature communications, 8(1), 1538.

Green, T. H., and Pearson, N. J. (1985). Experimental determination of REE partition coefficients between amphibole and basaltic to andesitic liquids at high pressure. Geochimica et Cosmochimica Acta, 49(6), 1465-1468.

Grondahl, C., and Zajacz, Z. (2022). Sulfur and chlorine budgets control the ore fertility of arc magmas. Nature communications, 13(1), 4218.

Güçtekin, A., and Köprübaşı, N. (2009). Geochemical characteristics of mafic and intermediate volcanic rocks from the Hasandağ and Erciyes volcanoes (Central Anatolia, Turkey). Turkish Journal of Earth Sciences, 18(1), 1-27.

Günay, A. (2020). Origin of gold mineralization, source of ore fluid and structural controls of Keşkek hill gold mineralization (Gördes, Manisa), M.Sc. Thesis, Muğla Sıtkı Koçman University, Muğla, 131p.

Gündüz, M., Özkan, A. M., and Asan, K. (2025). The origin and emplacement dynamics of the volcaniclastic and sedimentary clastic dykes in volcanic fields: A case study from the Erenlerdağ-Alacadağ Volcanic Complex (Konya-TURKEY). Pamukkale University Journal of Engineering Sciences, 31(6), 0-0.

Hall, D. J., Foster, R. P., Yildiz, B., Redwood, S. D., and Andrew, C. J. (2007). The Inlice high-sulphidation epithermal gold discovery: Defining a potential new gold belt in Turkey. In Proceedings of the Ninth Biennial SGA Meeting (pp. 113-116).

Hall, D. J., Foster, R. P., Yildiz, B., Redwood, S. D., and Andrew, C. J. (2007). The Inlice high-sulphidation epithermal gold discovery: Defining a potential new gold belt in Turkey. In Proceedings of the Ninth Biennial SGA Meeting (pp. 113-116).

Halter, W. E., Pettke, T., and Heinrich, C. A. (2002). The origin of Cu/Au ratios in porphyry-type ore deposits. Science, 296(5574), 1844-1846.

Hamlyn, P. R., Keays, R. R., Cameron, W. E., Crawford, A. J., and Waldron, H. M. (1985). Precious metals in magnesian low-Ti lavas: implications for metallogenesis and sulfur saturation in primary magmas. Geochimica et Cosmochimica Acta, 49(8), 1797-1811.

Hanilçi, N., Bozkaya, G., Banks, D. A., Bozkaya, Ö., Prokofiev, V., and Öztaş, Y. (2020). Fluid inclusion characteristics of the Kışladağ porphyry Au deposit, Western Turkey. Minerals, 10(1), 64.

Hanson, G. N. (1980). Rare earth elements in petrogenetic studies of igneous systems. Annual Review of Earth and Planetary Sciences, 8(1), 371-406.

Hao, H., Campbell, I. H., Park, J. W. and Cooke, D. R. (2017). Platinum-group element geochemistryused to determine Cu and Au fertility in the Northparkes igneous suites, New South Wales,Australia. Geochimica et Cosmochimica Acta 216, 372-392.

Harris, N. B., Pearce, J. A., and Tindle, A. G. (1986). Geochemical characteristics of collision-zone magmatism. Geological Society, London, Special Publications, 19(1), 67-81.

Hasözbek, A., Satır, M., Erdoğan, B., Akay, E., and Siebel, W. (2011). Early Miocene post-collisional magmatism in NW Turkey: geochemical and geochronological constraints. International Geology Review, 53(9), 1098-1119.

Hawkesworth, C. J., and Kemp, A. I. S. (2006). Evolution of the continental crust. Nature, 443(7113), 811-817.

Hawkesworth, C. J., Gallagher, K., Hergt, J. M., and McDermott, F. (1993). Mantle and slab contribution in arc magmas. Annual Review of Earth and Planetary Sciences, Volume 21, pp. 175-204., 21, 175-204.

Hedenquist, J. W., and Sillitoe, R. H. (2003). Linkages between volcanotectonic settings, ore-fluid compositions, and epithermal precious metal deposits. Volcanic, geothermal, and ore-forming fluids, 315-343.

Heinrich, C. A. (2024). The chain of processes forming porphyry copper deposits—An invited paper. Economic Geology, 119(4), 741-769.

Heinrich, C. A., and Neubauer, F. (2002). Cu–Au–Pb–Zn–Ag metallogeny of the Alpine–Balkan–Carpathian–Dinaride geodynamic province. Mineralium Deposita, 37(6-7), 533-540.

Hetzel, R., Passchier, C. W., Ring, U., and Dora, O. O. (1995). Bivergent extension in orogenic belts: the Menderes massif (southwestern Turkey). Geology, 23(5), 455-458.

Hildreth, W., and Moorbath, S. (1988). Crustal contributions to arc magmatism in the Andes of Central Chile. Contributions to mineralogy and petrology, 98(4), 455-489.

Holwell, D. A., Fiorentini, M., McDonald, I., Lu, Y., Giuliani, A., Smith, D. J., Keith, M., and Locmelis, M. (2019). A metasomatized lithospheric mantle control on the metallogenic signature of post-subduction magmatism. Nature communications, 10(1), 3511.

Hoskin, P. W., and Schaltegger, U. (2003). The composition of zircon and igneous and metamorphic petrogenesis. Reviews in mineralogy and geochemistry, 53, 27-62.

İmer, A., Richards, J. P., and Creaser, R. A. (2013). Age and tectonomagmatic setting of the Eocene Çöpler–Kabataş magmatic complex and porphyry-epithermal Au deposit, East Central Anatolia, Turkey. Mineralium Deposita, 48(5), 557-583.

İmer, A., Richards, J. P., Creaser, R. A., and Spell, T. L. (2015). The late Oligocene Cevizlidere Cu-Au-Mo deposit, Tunceli Province, eastern Turkey. Mineralium Deposita, 50(2), 245-263.

İmer, A., Wang, R., Sayıt, K., and Koralay, E. (2023). Porphyry Cu fertility of Late Mesozoic-Cenozoic Magmatism along the East Anatolian Magmatic Belt based on zircon trace element compositions. In Society of Economic Geologists Conference.

İmer, E. Ü., Güleç, N., Kuşcu, İ., and Fallick, A. E. (2013). Genetic investigation and comparison of Kartaldağ and Madendağ epithermal gold deposits in Çanakkale, NW Turkey. Ore Geology Reviews, 53, 204-222.

Innocenti, F., Agostini, S., Di Vincenzo, G., Doglioni, C., Manetti, P., Savaşçin, M. Y., and Tonarini, S. (2005). Neogene and Quaternary volcanism in Western Anatolia: magma sources and geodynamic evolution. Marine Geology, 221(1-4), 397-421.

Innocenti, F., Mazzuoli, R., Pasquare, G., Di Brozolo, F. R., and Villari, L. (1975). The Neogene calcalkaline volcanism of Central Anatolia: geochronological data on Kayseri—Nigde area. Geological Magazine, 112(4), 349-360.

Irvine, T. N., and Baragar, W. R. A. (1971). A guide to the chemical classification of the common volcanic rocks. Canadian journal of earth sciences, 8(5), 523-548.

Jackson, J., and McKenzie, D. (1988). The relationship between plate motions and seismic moment tensors, and the rates of active deformation in the Mediterranean and Middle East. Geophysical Journal International, 93(1), 45-73.

Jackson, S. (2008). LAMTRACE data reduction software for LA- ICP-MS. in "Laser ablation-ICP-mass spectrometry in the earth sciences: current practices and outstanding issues", Sylvester, P., ed. Short Course Series, Vol. 40. Mineralogical Association of Canada (MAC), 305–306.

Jackson, S. E., Pearson, N. J., Griffin, W. L., and Belousova, E. A. (2004). The application of laser ablation-inductively coupled plasma-mass spectrometry to in situ U–Pb zircon geochronology. Chemical geology, 211(1-2), 47-69.

Jacob, L. R. (2011). Remote sensing, geochemistry, geochronology, and cathodoluminescence imaging of the Egrigoz, Koyunoba, and Alacam Plutons, Northern Menderes Massif, Turkey.

Jaffey, N. and Robertson, A.H.F. (2001). New sedimentological and structuraldata from the Ecemis¸ Fault Zone,southern Turkey: implications for itstiming and offset and the Cenozoictectonic escape of Anatolia. J. Geol.Soc., London, 158, 367–378

Jaffey, N., Robertson, A., and Pringle, M. (2004). Latest Miocene and Pleistocene ages of faulting, determined by 40Ar/39Ar single- crystal dating of airfall tuff and silicic extrusives of the Erciyes Basin, central Turkey: Evidence for

intraplate deformation related to the tectonic escape of Anatolia. Terra Nova, 16(2), 45-53.

Janković, S. (1997). The Carpatho-Balkanides and adjacent area: a sector of the Tethyan Eurasian metallogenic belt. Mineralium Deposita, 32(5), 426-433.

Jensen, E. P., and Barton, M. D. (2000). Gold deposits related to alkaline magmatism.

Jia, F.D., Zhang, C.Q., Liu, H., Meng, X.Y., and Kong, Z.G (2020). In situ major and trace element compositions of apatite from the Yangla skarn Cu deposit, southwest China: Implications for petrogenesis and mineralization. Ore Geol. Rev. 127, 103360.

Jiang, Y. H., Jiang, S. Y., Ling, H. F., and Dai, B. Z. (2006). Low-degree melting of a metasomatized lithospheric mantle for the origin of Cenozoic Yulong monzogranite-porphyry, east Tibet: geochemical and Sr–Nd–Pb–Hf isotopic constraints. Earth and Planetary Science Letters, 241(3-4), 617-633.

Jolivet, L., Faccenna, C., Huet, B., Labrousse, L., Le Pourhiet, L., Lacombe, O., Lecomte, E., Burov, E., Denéle, Y., Brun, J-P., Philippon, M., Paul, A., Salaün, G., Karabulut, H., Piromallo, C., Monié, P., Gueydan, F., Okay, A.I., Oberhänsli, R., Pourteau, A., Augier, R., Gadenne, L., and Driussi, O. (2013). Aegean tectonics: Strain localisation, slab tearing and trench retreat. Tectonophysics, 597, 1-33.

Jugo, P. J., Wilke, M., and Botcharnikov, R. E. (2010). Sulfur K-edge XANES analysis of natural and synthetic basaltic glasses: Implications for S speciation and S content as function of oxygen fugacity. Geochimica et Cosmochimica Acta, 74(20), 5926-5938.

Karacık, Z., Genç, Ş. C., and Gülmez, F. (2013). Petrochemical features of Miocene volcanism around the Çubukludağ graben and Karaburun peninsula, western Turkey: implications for crustal melting related silicic volcanism. Journal of Asian Earth Sciences, 73, 199-217.

Karaoğlu, Ö. (2024). Hasan Dağı Volkanı ve Çiftlik-Bozköy (Orta Anadolu) Gömülü Kalderasını Besleyen Aktif Magma Odalarına İlişkin Isı Transferi Analizleri. Türkiye Jeoloji Bülteni, 1-27.

Karaoğlu, Ö., Browning, J., Salah, M. K., Elshaafi, A., and Gudmundsson, A. (2018). Depths of magma chambers at three volcanic provinces in the Karlıova region of Eastern Turkey. Bulletin of Volcanology, 80(9), 69.

Karaoğlu, Ö., Helvacı, C., and Ersoy, Y. (2010). Petrogenesis and 40Ar/39Ar geochronology of the volcanic rocks of the Uşak-Güre basin, western Türkiye. Lithos, 119(3-4), 193-210.

Kay, S.M., and Mpodozis, C. (2001). Central Andean ore deposits linked to evolving shallow subduction systems and thickening crust: Geological Society of America Today, v. 11, p. 4–9.

Keller, C. B., Schoene, B., Barboni, M., Samperton, K. M., and Husson, J. M. (2015). Volcanic–plutonic parity and the differentiation of the continental crust. Nature, 523(7560), 301-307.

Keller, J., Jung, D., Burgath, K., and Wolff, F. (1977). Geologie und Petrologie des neogenen Kalkalkali-Vulkanismus von Konya (Erenler Dag-Alaca Dag-Massiv, Zentral-Anatolien).

Kelley, K. A., and Cottrell, E. (2009). Water and the oxidation state of subduction zone magmas. Science, 325(5940), 605-607.

Kendall-Langley, L. A., Kemp, A. I., Hammerli, J., and Blevin, P. L. (2025). An evaluation of apatite and zircon Cu–Au porphyry fertility indicators, applied to arc-related intrusions of the Lachlan Orogen, eastern Australia. Contributions to Mineralogy and Petrology, 180(6), 35.

Kendall-Langley, L. A., Kemp, A. I., Hawkesworth, C. J., EIMF Craven John Talavera Cristina Hinton Richard, and Roberts, M. P. (2021). Quantifying F and Cl concentrations in granitic melts from apatite inclusions in zircon. Contributions to Mineralogy and Petrology, 176(7), 58.

Keskin, M. (2003). Magma generation by slab steepening and breakoff beneath a subduction- accretion complex: An alternative model for collision- related volcanism in Eastern Anatolia, Turkey. Geophysical research letters, 30(24).

Kinny, P. D., and Maas, R. (2003). Lu–Hf and Sm–Nd isotope systems in zircon. Reviews in mineralogy and geochemistry, 53(1), 327-341.

Koçyiğit, A. (2003). Orta Anadolu'nun genel neotektonik özellikleri ve depremselliği. Haymana-Tuzgölü-Ulukışla Basenleri Uygulamalı Çalışma, TPJD, Özel, (5), 1-26.

Koçyiğit, A., and Beyhan, A. (1998). A new intracontinental transcurrent structure: the Central Anatolian Fault Zone, Turkey. Tectonophysics, 284(3-4), 317-336.

Koçyiğit, A., Ünay, E., and Saraç, G. (2000). Episodic graben formation and extensional neotectonic regime in west Central Anatolia and the Isparta Angle: a case study in the Akşehir–Afyon Graben, Turkey.

Koralay, T. (2010). Petrographic and geochemical characteristics of upper Miocene Tekkedag volcanics (Central Anatolia—Turkey). Geochemistry, 70(4), 335-351.

Koralay, T., Kadioglu, Y. K., and Davis, P. (2011). Weak compositional zonation in a silicic magmatic system: Incesu ignimbrite, Central Anatolian Volcanic Province (Kayseri–Turkey). Journal of Asian Earth Sciences, 40(1), 371-393.

Kreemer, C., Holt, W. E., and Haines, A. J. (2003). An integrated global model of present-day plate motions and plate boundary deformation. Geophysical Journal International, 154(1), 8-34.

Kumral, M., Kabiru, M., Aydogan, M. S., Kocaturk, H., and Unluer, A. T. (2022). The Soma polymetallic hydrothermal Pb–Zn-Cu (±Mo±Ag±Au) mineralizations in the south of Biga Peninsula, NW Turkey: constraints from mineralogy, geochemistry, and fluid inclusion data. Arabian Journal of Geosciences, 15(12), 1172.

Kürkcüoglu, B. (2010). Geochemistry and petrogenesis of basaltic rocks from the Develidağ volcanic complex, Central Anatolia, Turkey. Journal of Asian Earth Sciences, 37(1), 42-51.

Kurt, H., Özkan, A. M., and Koçak, K. (2003). Geology, petrography and geochemistry of the subduction related volcanic rocks, West of Konya, Central Anatolia. Türkiye Jeoloji Bülteni, 46(2), 39-52.

Kuscu, I., Kuscu, G. G., Tosdal, R. M., Ulrich, T. D., and Friedman, R. (2010). Magmatism in the southeastern Anatolian orogenic belt: transition from arc to post-collisional setting in an evolving orogen.

Kuşcu, İ., Tosdal, R. M., and Gençalioğlu-Kuşcu, G. (2019). Episodic porphyry Cu (-Mo-Au) formation and associated magmatic evolution in Turkish Tethyan collage. Ore Geology Reviews, 107, 119-154.

Kuşcu, İ., Tosdal, R. M., Gencalioğlu-Kuşcu, G., Friedman, R., and Ullrich, T. D. (2013). Late Cretaceous to middle Eocene magmatism and metallogeny of a portion of the southeastern Anatolian orogenic belt, east-central Turkey. Economic Geology, 108(4), 641-666.

Le Maitre, R. W. (1984). A proposal by the IUGS Subcommission on the Systematics of Igneous Rocks for a chemical classification of volcanic rocks based on the total alkali silica (TAS) diagram: (on behalf of the IUGS Subcommission on the Systematics of Igneous Rocks). Australian Journal of Earth Sciences, 31(2), 243-255.

Le Maitre, R. W. (1989). A classification of igneous rocks and glossary of terms. Recommendations of the international union of geological sciences subcommission on the systematics of igneous rocks.

Le Pichon, X., and Kreemer, C. (2010). The Miocene-to-present kinematic evolution of the Eastern Mediterranean and Middle East and its implications for dynamics. Annual Review of Earth and Planetary Sciences, 38(1), 323-351.

Leake, B. E., Woolley, A. R., Arps, C. E., Birch, W. D., Gilbert, M. C., Grice, J. D., Hawthorne, F. C., Kato, A., Kisch, H. J., Krivovichev, V. G., Linthout, K., Laird, J., Mandarino, J. A., Maresch, W. V., Nickel, E. H., Rock, N. M. S., Schumacher, J. C., Smith, D. C., Stephenson, N. C. N., Ungaretti, L., Whittaker, E. J. W., and Youzhi, G. (1997). Nomenclature of amphiboles; report of the subcommittee on amphiboles of the International Mineralogical Association, Commission on New Minerals and Mineral Names. The Canadian Mineralogist, 35(1), 219-246.

Lee, C. T. A., and Tang, M. (2020). How to make porphyry copper deposits. Earth and Planetary Science Letters, 529, 115868.

Lee, C. T. A., Lee, T. C., and Wu, C. T. (2014). Modeling the compositional evolution of recharging, evacuating, and fractionating (REFC) magma chambers: Implications for differentiation of arc magmas. Geochimica et Cosmochimica Acta, 143, 8-22.

Lee, C. T. A., Lenardic, A., Cooper, C. M., Niu, F., and Levander, A. (2005). The role of chemical boundary layers in regulating the thickness of continental and oceanic thermal boundary layers. Earth and Planetary Science Letters, 230(3-4), 379-395.

Lee, C.T.A., and Tang, M., (2020). How to make porphyry copper deposits: Earth and Planetary Science Letters, v. 529, 115868.

Lee, R. G., Dilles, J. H., Tosdal, R. M., Wooden, J. L., and Mazdab, F. K. (2017). Magmatic evolution of granodiorite intrusions at the El Salvador porphyry copper deposit, Chile, based on trace element composition and U/Pb age of zircons. Economic Geology, 112(2), 245-273.

Lee, R. G., Plouffe, A., Ferbey, T., Hart, C. J., Hollings, P., and Gleeson, S. A. (2021). Recognizing porphyry copper potential from till zircon composition: A case study from the Highland Valley porphyry district, south-central British Columbia. Economic Geology, 116(4), 1035-1045.

Lefebvre, C., Meijers, M. J., Kaymakci, N., Peynircioğlu, A., Langereis, C. G., and Van Hinsbergen, D. J. (2013). Reconstructing the geometry of central Anatolia during the late Cretaceous: Large-scale Cenozoic rotations and deformation between the Pontides and Taurides. Earth and Planetary Science Letters, 366, 83-98.

Li, H., and Hermann, J. (2017). Chlorine and fluorine partitioning between apatite and sediment melt at 2.5 GPa, 800 C: A new experimentally derived thermodynamic model. American Mineralogist, 102(3), 580-594.

Li, W., and Costa, F. (2020). A thermodynamic model for F-Cl-OH partitioning between silicate melts and apatite including non-ideal mixing with application to constraining melt volatile budgets. Geochimica et Cosmochimica Acta, 269, 203-222.

Loader, M. A., Wilkinson, J. J., and Armstrong, R. N. (2017). The effect of titanite crystallisation on Eu and Ce anomalies in zircon and its implications for the assessment of porphyry Cu deposit fertility. Earth and Planetary Science Letters, 472, 107-119.

Loucks, R. R. (2021). Deep entrapment of buoyant magmas by orogenic tectonic stress: Its role in producing continental crust, adakites, and porphyry copper deposits. Earth-Science Reviews, 220, 103744.

Loucks, R. R., and Fiorentini, M. L. (2023). Early zircon saturation in adakitic magmatic differentiation series and low Zr content of porphyry copper magmas. Mineralium Deposita, 58(8), 1381-1393.

Loucks, R. R., Fiorentini, M. L., and Henríquez, G. J. (2020). New magmatic oxybarometer using trace elements in zircon. Journal of Petrology, 61(3), egaa034.

Loucks, R. R., Henríquez, G. J., and Fiorentini, M. L. (2024). Zircon and whole-rock trace element indicators of magmatic hydration state and oxidation state discriminate copper ore-forming from barren arc magmas. Economic Geology, 119(3), 511-523.

Loucks, R.R., 2014. Distinctive composition of copper-ore-forming arc magmas: Australian Journal of Earth Sciences, v. 61, p. 5–16.

Lu, Y., Loucks, R.R., Fiorentini, M., McCuaig, T. C., Evans, N. J., Yang, Z. M., Hou, Z. Q., Kirkland, C. L., Parra-Avila, L. A., and Kobussen, A. (2016). Zircon compositions as a pathfinder for porphyry Cu ± Mo ± Au deposits: Economic Geology Special Publication 19, p.329–347.

Lustrino, M., and Wilson, M. (2007). The circum-Mediterranean anorogenic Cenozoic igneous province. Earth-Science Reviews, 81(1-2), 1-65.

McKenzie, D. (1978). Active tectonics of the Alpine—Himalayan belt: the Aegean Sea and surrounding regions. Geophysical Journal International, 55(1), 217-254.

McKenzie, D., and O'nions, R. K. (1991). Partial melt distributions from inversion of rare earth element concentrations. Journal of petrology, 32(5), 1021-1091.

Meng, X., Kleinsasser, J. M., Richards, J. P., Tapster, S. R., Jugo, P. J., Simon, A. C., Kontak, D. J., Robb, L., Bybee, G. M., Marsh, J. H., and Stern, R. A. (2021). Oxidized sulfur-rich arc magmas formed porphyry Cu deposits by 1.88 Ga. Nature Communications, 12(1), 2189.

Middlemost, E.A.K. (1994). Naming materials in the magma/igneous rock system. Earth Sci. Rev. 37 (3-4), 215–224. https://doi.org/10.1016/0012-8252(94)90029-9.

Moritz, R., Melkonyan, R., Selby, D., Popkhadze, N., Gugushvili, V., Tayan, R., and Ramazanov, V. (2016). Metallogeny of the Lesser Caucasus: From arc construction to postcollision evolution.

MTA (2002). 1:500,000 ölçekli Türkiye jeoloji haritası: Ankara, Türkiye.

Müller, D., & Groves, D. I. (1993). Direct and indirect associations between potassic igneous rocks, shoshonites and gold-copper deposits. Ore Geology Reviews, 8(5), 383-406.

Müller, D., and Groves, D. I. (2018). Tectonic settings of potassic igneous rocks. In Potassic Igneous Rocks and Associated Gold-Copper Mineralization (pp. 31-71). Cham: Springer International Publishing.

Mungall, J. E., and Brenan, J. M. (2014). Partitioning of platinum-group elements and Au between sulfide liquid and basalt and the origins of mantle-crust fractionation of the chalcophile elements. Geochimica et Cosmochimica Acta, 125, 265-289.

Murakami, H., Watanabe, Y., and Stein, H. (2005, August). Re-Os ages for molybdenite from the Tepeoba breccia-centered Cu-Mo-Au deposit, western Turkey: brecciation-triggered mineralization. In Mineral Deposit Research: Meeting the Global Challenge: Proceedings of the Eighth Biennial SGA Meeting Beijing, China, 18–21 August 2005 (pp. 805-808). Berlin, Heidelberg: Springer Berlin Heidelberg.

Mutch, E. J. F., Blundy, J. D., Tattitch, B. C., Cooper, F. J., and Brooker, R. A. (2016). An experimental study of amphibole stability in low-pressure granitic magmas and a revised Al-in-hornblende geobarometer. Contributions to Mineralogy and Petrology, 171(10), 85.

Nachit, H., Ibhi, A., and Ohoud, M. B. (2005). Discrimination between primary magmatic biotites, reequilibrated biotites and neoformed biotites. Comptes Rendus. Géoscience, 337(16), 1415-1420.

Nathwani, C. L., Simmons, A. T., Large, S. J., Wilkinson, J. J., Buret, Y., and Ihlenfeld, C. (2021). From long-lived batholith construction to giant porphyry copper deposit formation: petrological and zircon chemical evolution of the Quellaveco District, Southern Peru. Contributions to Mineralogy and Petrology, 176(2), 12.

Noll Jr, P. D., Newsom, H. E., Leeman, W. P., and Ryan, J. G. (1996). The role of hydrothermal fluids in the production of subduction zone magmas: evidence from siderophile and chalcophile trace elements and boron. Geochimica et Cosmochimica Acta, 60(4), 587-611.

Oğuz, F. (2024) Structural framework of the Tavşan Gold Deposit in Tavşanlı district/Kütahya province/Türkiye, M.Sc. Thesis, Middle East Technical University, Ankara, 221p.

Okay, A.İ, Zattin, M., and Cavazza, W. (2010). Apatite fission-track data for the Miocene Arabia-Eurasia collision: Geology, v. 38, p. 35–38.

Oyarzun, R., Márquez, A., Lillo, J., López, I., and Rivera, S. (2001). Giant versus small porphyry copper deposits of Cenozoic age in northern Chile: Adakitic versus normal calc-alkaline magmatism: Mineralium Deposita, v. 36, p. 794–798.

Oyman, T. (2019). Epithermal deposits of Turkey. In Mineral resources of Turkey (pp. 159-223). Cham: Springer International Publishing.

Oyman, T., Minareci, F., and Pişkin, Ö. (2003). Efemcukuru B-rich epithermal gold deposit (Izmir, Turkey). Ore Geology Reviews, 23(1-2), 35-53.

Oyman, T., Özgenç, I., Tokcaer, M., and Akbulut, M. (2013). Petrology, geochemistry, and evolution of the iron skarns along the northern contact of the Eğrigöz Plutonic Complex, Western Anatolia, Turkey. Turkish Journal of Earth Sciences, 22(1), 61-97.

Özel, T. E. (2024). Investigation of mineralogical and geochemical properties of igneous rocks related with porphyry copper-molybdenum mineralization in balya (Balıkesir) region, M.Sc Thesis, Haceettepe University, Ankara, 134p.

Özen, Y., and Arık, F. (2019). Geochemical, stable isotopic (S, O, H, C), microthermometric and geochronological (U-Pb) evidence on the genesis of the Pınarbaşı porphyry Cu-Mo mineralization (Gediz-Kütahya, Western Turkey). Journal of Geochemical Exploration, 204, 142-166.

Özgenç, I., and İlbeyli, N. (2008). Petrogenesis of the Late Cenozoic Egrigöz pluton in western Anatolia, Turkey: implications for magma genesis and crustal processes. International Geology Review, 50(4), 375-391.

Özışık, G. (2009). Genetical Investigation of Balya-Balikesir Lead-Zinc Mineralizations (Master's thesis, Middle East Technical University (Turkey)).

Özsayın, E., and Dirik, K. (2011). The role of oroclinal bending in the structural evolution of the Central Anatolian Plateau: evidence of a regional changeover from shortening to extension. Geologica Carpathica, 62(4), 345-359.

Özsayın, E., Çiner, A., Rojay, B., Dirik, K., Melnick, D., Fernandez-Blanco, D., Bertotti, G., Schildgen, T. F., Garcin, Y., Strecker, M. R., and Sudo, M. (2013). Plio-Quaternary extensional tectonics of the Central Anatolian Plateau: a case study from the Tuz Gölü Basin, Turkey. Turkish Journal of Earth Sciences, 22(5), 691-714.

Palmer, M. R., Ersoy, E. Y., Akal, C., Uysal, İ., Genç, Ş. C., Banks, L. A., Cooper, M. J., and Zhao, K. D. (2019). A short, sharp pulse of potassium-rich volcanism during continental collision and subduction. Geology, 47(11), 1079-1082.

Pan, L. C., Hu, R. Z., Wang, X. S., Bi, X. W., Zhu, J. J., and Li, C. (2016). Apatite trace element and halogen compositions as petrogenetic-metallogenic indicators: Examples from four granite plutons in the Sanjiang region, SW China. Lithos, 254, 118-130.

Pan, Y., and Fleet, M. E. (2002). Compositions of the apatite-group minerals: substitution mechanisms and controlling factors. Reviews in mineralogy and geochemistry, 48(1), 13-49.

Paolillo, L., Chiaradia, M., and Ulianov, A. (2022). Zircon petrochronology of the Kışladağ porphyry Au deposit (Turkey). Economic Geology, 117(2), 401-422.

Parat, F., and Holtz, F. (2005). Sulfur partition coefficient between apatite and rhyolite: the role of bulk S content. Contributions to Mineralogy and Petrology, 150(6), 643-651.

Parat, F., Dungan, M. A., and Streck, M. J. (2002). Anhydrite, pyrrhotite, and sulfur-rich apatite: tracing the sulfur evolution of an Oligocene andesite (Eagle Mountain, CO, USA). Lithos, 64(3-4), 63-75.

Parat, F., Holtz, F., and Klügel, A. (2011). S-rich apatite-hosted glass inclusions in xenoliths from La Palma: constraints on the volatile partitioning in evolved alkaline magmas. Contributions to Mineralogy and Petrology, 162(3), 463-478.

Park, J. W., Campbell, I. H., and Kim, J. (2016). Abundances of platinum group elements in native sulfur condensates from the Niuatahi-Motutahi submarine volcano, Tonga rear arc: Implications for PGE mineralization in porphyry deposits. Geochimica et Cosmochimica Acta, 174, 236-246.

Park, J. W., Campbell, I. H., Chiaradia, M., Hao, H., and Lee, C. T. (2021). Crustal magmatic controls on the formation of porphyry copper deposits. Nature Reviews Earth & Environment, 2(8), 542-557.

Park, J. W., Campbell, I. H., Malaviarachchi, S. P., Cocker, H., Hao, H., and Kay, S. M. (2019). Chalcophile element fertility and the formation of porphyry Cu±Au deposits. Mineralium Deposita, 54(5), 657-670.

Pasquare, G., Poli, S., Vezzoli, L., and Zanchi, A. (1988). Continental arc volcanism and tectonic setting in Central Anatolia, Turkey. Tectonophysics, 146(1-4), 217-230.

Patchett, P. J., and Tatsumoto, M. (1981). A routine high-precision method for Lu-Hf isotope geochemistry and chronology. Contributions to Mineralogy and Petrology, 75(3), 263-267.

Patchett, P. J., White, W. M., Feldmann, H., Kielinczuk, S., and Hofmann, A. W. (1984). Hafnium/rare earth element fractionation in the sedimentary system

and crustal recycling into the Earth's mantle. Earth and Planetary Science Letters, 69(2), 365-378.

Pearce, J. A. (1975). Basalt geochemistry used to investigate past tectonic environments on Cyprus. Tectonophysics, 25(1-2), 41-67.

Pearce, J. A., and Stern, R. J. (2006). Origin of back- arc basin magmas: Trace element and isotope perspectives. Back- arc spreading systems: Geological, biological, chemical, and physical interactions, 166, 63-86.

Peccerillo, A., and Taylor, S. R. (1976). Rare earth elements in East Carpathian volcanic rocks. Earth and Planetary Science Letters, 32(2), 121-126.

Peng, G., Luhr, J. F., and McGee, J. J., 1997. Factors controlling sulfur concentrations in volcanic apatite. American Mineralogist, 82(11-12), 1210-1224.

Piccoli, P., and Candela, P. (1994). Apatite in felsic rocks; a model for the estimation of initial halogen concentrations in the Bishop Tuff (Long Valley) and Tuolumne Intrusive Suite (Sierra Nevada Batholith) magmas. American Journal of Science, 294(1), 92-135.

Pişkin, Ö. (1980). Kadıkalesi-Girelbelen (Bodrum yarımadası) hidrotermal ve kontakt metasomatik Pb, Zn. Ege University, Cu cevherleşmelerinin mineralojik ve jeolojik incelenmesi.

Platzman, E. S., Tapirdamaz, C., and Sanver, M. (1998). Neogene anticlockwise rotation of central Anatolia (Turkey): preliminary palaeomagnetic and geochronological results. Tectonophysics, 299(1-3), 175-189.

Prelević, D., Akal, C., Foley, S. F., Romer, R. L., Stracke, A., and Van Den Bogaard, P. (2012). Ultrapotassic mafic rocks as geochemical proxies for post-collisional dynamics of orogenic lithospheric mantle: the case of southwestern Anatolia, Turkey. Journal of Petrology, 53(5), 1019-1055.

Prelević, D., Akal, C., Romer, R. L., Mertz-Kraus, R., and Helvacı, C. (2015). Magmatic response to slab tearing: constraints from the Afyon Alkaline Volcanic Complex, Western Turkey. Journal of Petrology, 56(3), 527-562.

Prelević, D., Akal, C.., Romer, R. L., and Foley, S. F. (2010). Lamproites as indicators of accretion and/or shallow subduction in the assembly of south-western Anatolia, Turkey. Terra Nova, 22(6), 443-452.

Rabayrol, F., and Hart, C. J. (2021). Petrogenetic and tectonic controls on magma fertility and the formation of post-subduction porphyry and epithermal mineralization along the late Cenozoic Anatolian Metallogenic Trend, Turkey. Mineralium Deposita, 56, 279-306.

Rabayrol, F., Hart, C. J., and Creaser, R. A. (2019a). Tectonic triggers for postsubduction magmatic-hydrothermal gold metallogeny in the late

Cenozoic Anatolian metallogenic trend, Turkey. Economic Geology, 114(7), 1339-1363.

Rabayrol, F., Hart, C. J., and Thorkelson, D. J. (2019b). Temporal, spatial and geochemical evolution of late Cenozoic post-subduction magmatism in central and eastern Anatolia, Turkey. Lithos, 336, 67-96.

Reid, M. R., Schleiffarth, W. K., Cosca, M. A., Delph, J. R., Blichert- Toft, J., and Cooper, K. M. (2017). Shallow melting of MORB- like mantle under hot continental lithosphere, Central Anatolia. Geochemistry, Geophysics, Geosystems, 18(5), 1866-1888.

Richards, J. P. (2003). Tectono-magmatic precursors for porphyry Cu-(Mo-Au) deposit formation. Economic geology, 98(8), 1515-1533.

Richards, J. P. (2005). Cumulative factors in the generation of giant calc-alkaline porphyry Cu deposits, in Porter, T.M., ed., Super Porphyry Copper and Gold Deposits: A Global Perspective: Linden Park, South Australia, Porter Geoscience Consulting Publishing, v. 1, p. 7–25.

Richards, J. P. (2009). Postsubduction porphyry Cu-Au and epithermal Au deposits: Products of remelting of subduction-modified lithosphere. Geology, 37(3), 247-250.

Richards, J. P. (2011a). Magmatic to hydrothermal metal fluxes in convergent and collided margins. Ore Geology Reviews, 40(1), 1-26.

Richards, J. P. (2012, November). Subduction-modified lithosphere as a source for post-subduction magmatic-hydrothermal ore deposits. In Geological Society of America Abstracts with Programs (Vol. 44, No. 7, p. 505).

Richards, J. P. (2014). Porphyry and Related Deposits in Subduction and Post-Subduction Settings. Acta Geologica Sinica (English Edition), 88.

Richards, J. P. (2015). The oxidation state, and sulfur and Cu contents of arc magmas: implications for metallogeny. Lithos, 233, 27-45.

Richards, J. P. (2021). Porphyry copper deposit formation in arcs: What are the odds?. Geosphere, 18(1), 130-155.

Richards, J. P., and Kerrich, R. (2007). Special paper: adakite-like rocks: their diverse origins and questionable role in metallogenesis. Economic geology, 102(4), 537-576.

Richards, J. P., and Sholeh, A. (2016). The Tethyan tectonic history and Cu-Au metallogeny of Iran.

Richards, J. P., López, G. P., Zhu, J. J., Creaser, R. A., Locock, A. J., and Mumin, A. H. (2017). Contrasting tectonic settings and sulfur contents of magmas associated with Cretaceous porphyry Cu±Mo±Au and intrusion-related iron

oxide Cu-Au deposits in northern Chile. Economic Geology, 112(2), 295-318.

Richards, J. P., Spell, T., Rameh, E., Razique, A., and Fletcher, T. (2012). High Sr/Y magmas reflect arc maturity, high magmatic water content, and porphyry Cu±Mo±Au potential: Examples from the Tethyan arcs of central and eastern Iran and western Pakistan. Economic geology, 107(2), 295-332.

Richards, J. P., Wilkinson, D., and Ullrich, T. (2006). Geology of the Sari Gunay epithermal gold deposit, northwest Iran. Economic geology, 101(8), 1455-1496.

Richards, J.P. (2011b). High Sr/Y arc magmas and porphyry Cu±Mo±Au deposits: just add water: Economic Geology, v. 106, p.1075–1081.

Richards, J.P., and Kerrich, R. (2007). Adakite-like rocks: their diverse origins and questionable role in metallogenesis: Economic Geology, v. 102, p. 537–576.

Richards, J.P., Spell, T., Rameh, E., Razique, A., and Fletcher, T. (2012). High Sr/Y magmas reflect arc maturity, high magmatic water content, and porphyry Cu±Mo±Au potential: examples from the Tethyan arcs of central and eastern Iran and western Pakistan: Economic Geology, v. 107, p. 295–332.

Ridolfi, F. (2021). Amp-TB2: an updated model for calcic amphibole thermobarometry. Minerals, 11(3), 324.

Ridolfi, F., Renzulli, A., and Puerini, M. (2010). Stability and chemical equilibrium of amphibole in calc-alkaline magmas: an overview, new thermobarometric formulations and application to subduction-related volcanoes. Contributions to mineralogy and petrology, 160(1), 45-66.

Rieder, M., Cavazzini, G., D'yakonov, Y. S., Frank-Kamenetskii, V. A., Gottardi, G., Guggenheim, S., Koval, P. W., Müller, G., Neiva, A. M. R., Radoslavich, E. W., Robert, J-L., Sassi, F. P., Takeda, H., Weiss, Z., and Wones, D. R. (1998). Nomenclature of the micas. Clays and clay minerals, 46(5), 586-595.

Ring, U. W. E., Johnson, C., Hetzel, R., and Gessner, K. (2003). Tectonic denudation of a Late Cretaceous–Tertiary collisional belt: regionally symmetric cooling patterns and their relation to extensional faults in the Anatolide belt of western Turkey. Geological Magazine, 140(4), 421-441.

Ring, U., and Collins, A. S. (2005). U–Pb SIMS dating of synkinematic granites: timing of core-complex formation in the northern Anatolide belt of western Turkey. Journal of the Geological Society, 162(2), 289-298.

Ringwood, A. E. (1977). Petrogenesis in island arc systems. Island arcs, deep sea trenches and back- arc basins, 1, 311-324.

Robertson, A. H. F., Parlak, O., Rizaoğlu, T., Ünlügenç, Ü., İnan, N., Tasli, K., and Ustaömer, T. (2007). Tectonic evolution of the South Tethyan ocean: evidence from the Eastern Taurus Mountains (Elazığ region, SE Turkey).

Rock, N. M., and Groves, D. I. (1988). Can lamprophyres resolve the genetic controversy over mesothermal gold deposits?. Geology, 16(6), 538-541.

Rollinson, H. (1993). Using trace elements data. Using geochemical data: evaluation, presentation, interpretation, 133-134.

Rollinson, H. R., Rollinson, H., and Pease, V. (2021). Using geochemical data: to understand geological processes. Cambridge University Press.

Rutherford, M. J., and Devine, J. D. (1988). The May 18, 1980, eruption of Mount St. Helens: 3. Stability and chemistry of amphibole in the magma chamber. Journal of Geophysical Research: Solid Earth, 93(B10), 11949-11959.

Rutherford, M. J., and Hill, P. M. (1993). Magma ascent rates from amphibole breakdown: an experimental study applied to the 1980–1986 Mount St. Helens eruptions. Journal of Geophysical Research: Solid Earth, 98(B11), 19667-19685.

Sajona, F. G., and Maury, R. C. (1998). Association of adakites with gold and copper mineralization in the Philippines. Comptes Rendus de l'Académie des Sciences-Series IIA-Earth and Planetary Science, 326(1), 27-34.

Sarı, R., Küçükefe, Ş., Bozkaya, G., Bozkaya, Ö., Bademler, F., Aral, Z. D., Bayrakçıoğlu, E. D., Dönmez, C., and Özkümüş, S. (2022). Geological, mineralogical-petrographical and fluid inclusion characteristics of the Çatalçam (Soma-Manisa) Au-Pb-Zn-Cu mineralization. Bulletin of the Mineral Research and Exploration, 167(167), 25-49.

Savaşcin, M. Y., and Oyman, T. (1998). Tectono-Magmatic Evolution of Alkaline Volcanics at theKırka-Afyon-Isparta Structural Trend, Sw Turkey. Turkish Journal of Earth Sciences, 7(3), 201-214.

Savasçin, M. Y., Birsoy, R., Dag, N., and Nohutcu, E. (1994). Kirka-Afyon-Isparta structural trend and alkaline rock associations (Anatolia). In Proceedings, 7th Congress of the Geological Society of Greece, with Emphasis on the Geology of Macedonia and Thrace: Bulletin of the Geological Society of Greece (Vol. 30, pp. 89-98).

Schildgen, T. F., Cosentino, D., Bookhagen, B., Niedermann, S., Yıldırım, C., Echtler, H., Wittman, H., and Strecker, M. R. (2012). Multi-phased uplift of the southern margin of the Central Anatolian plateau, Turkey: A record of tectonic and upper mantle processes. Earth and Planetary Science Letters, 317, 85-95.

Seedorff, E., Dilles, J. H., Proffett, J. M., Einaudi, M. T., Zurcher, L., Stavast, W. J., Johnson, D. A., and Barton, M. D. (2005). Porphyry deposits: Characteristics and origin of hypogene features.

Seghedi, I., and Helvacı, C. (2016). Early Miocene Kırka-Phrigian Caldera, western Turkey (Eskişehir province), preliminary volcanology, age and geochemistry data. Journal of Volcanology and Geothermal Research, 327, 503-519.

Semiz, B., Ersoy, E. Y., Özpınar, Y., Helvacı, C., Palmer, M. R., and Billor, M. Z. (2015). 40Ar/39Ar geochronology, geochemistry and petrology of volcanic rocks from the Simav Graben, western Turkey. Contributions to Mineralogy and Petrology, 170(2), 24.

Şengör, A. C., and Yilmaz, Y. (1981). Tethyan evolution of Turkey: a plate tectonic approach. Tectonophysics, 75(3-4), 181-241.

Seo, J. H., Guillong, M., and Heinrich, C. A. (2009). The role of sulfur in the formation of magmatic–hydrothermal copper–gold deposits. Earth and Planetary Science Letters, 282(1-4), 323-328.

Shafaii Moghadam, H., Xiao, W., Karsli, O., Aydin, F., He, Y., Chiaradia, M., and Griffin, W. L. (2025). Copper endowment of the magmatic rocks from Eastern Sakarya Zone (Türkiye): insights from zircon and apatite geochemical evolution. Contributions to Mineralogy and Petrology, 180(6), 38.

Shand, S. J. (1927). On the relations between silica, alumina, and the bases in eruptive rocks, considered as a means of classification. Geological Magazine, 64(10), 446-449.

Sillitoe, R. H. (2010). Porphyry copper systems. Economic geology, 105(1), 3-41.

Simon, A. C., Candela, P. A., Piccoli, P. M., Mengason, M., and Englander, L. (2008). The effect of crystal-melt partitioning on the budgets of Cu, Au, and Ag. American Mineralogist, 93(8-9), 1437-1448.

Sinclair, W. D. (2007). Porphyry deposits. Mineral deposits of Canada: A synthesis of major deposit-types, district metallogeny, the evolution of geological provinces, and exploration methods: Geological Association of Canada, Mineral Deposits Division, Special Publication, 5, 223-243.

Sisson, T. W., and Grove, T. L. (1993). Experimental investigations of the role of H2O in calc-alkaline differentiation and subduction zone magmatism. Contributions to mineralogy and petrology, 113(2), 143-166.

Sláma, J., Košler, J., Condon, D. J., Crowley, J. L., Gerdes, A., Hanchar, J. M., Horstwood, M. S. A., Morris, G. A., Nasdala, L., Norberg, N., Schaltegger, U., Schoene, B., Tubrett, M. N., and Whitehouse, M. J. (2008). Plešovice zircon—a new natural reference material for U–Pb and Hf isotopic microanalysis. Chemical geology, 249(1-2), 1-35.

Smith, M. T., Lepore, W. A., Incekaraoğlu, T., Boran, H., Barrios, A., Leroux, G., Ross, K., Büyüksolak, A., Sevimli, A., and Raabe, K. (2016). High-sulfidation epithermal Au and porphyry Cu-Au mineralization at the Karaayi target, Biga peninsula, northwestern Turkey.

Smith, M. T., Lepore, W. A., Incekaraoğlu, T., Shabestari, P., Boran, H., and Raabe, K. (2014). Küçükdağ: a new, high sulfidation epithermal Au-Ag-Cu deposit at the TV tower property in Western Turkey. Economic Geology, 109(6), 1501-1511.

Smythe, D. J., and Brenan, J. M. (2016). Magmatic oxygen fugacity estimated using zircon-melt partitioning of cerium. Earth and Planetary Science Letters, 453, 260-266.

Söderlund, U., Patchett, P. J., Vervoort, J. D., and Isachsen, C. E. (2004). The 176Lu decay constant determined by Lu–Hf and U–Pb isotope systematics of Precambrian mafic intrusions. Earth and Planetary Science Letters, 219(3-4), 311-324.

Sönmez, Ş. U., and Kuşcu, İ. (2020). Geology, geochemistry, geochronology and genesis of the late Miocene porphyry Cu-Au-Mo mineralization at Afyon-Sandıklı (AS) prospect, western Anatolia, Turkey. Ore Geology Reviews, 121, 103506.

Stavast, W. J., Keith, J. D., Christiansen, E. H., Dorais, M. J., Tingey, D., Larocque, A., and Evans, N. (2006). The fate of magmatic sulfides during intrusion or eruption, Bingham and Tintic districts, Utah. Economic Geology, 101(2), 329-345.

Streck, M. J., and Dilles, J. H. (1998). Sulfur evolution of oxidized arc magmas as recorded in apatite from a porphyry copper batholith. Geology, 26(6), 523-526.

Sun, S. S., and McDonough, W. F. (1989). Chemical and isotopic systematics of oceanic basalts: Implications for mantle composition and processes. Geological Society, London, Special Publications, 42, 313-345.

Tang, M., Erdman, M., Eldridge, G., and Lee, C. T. A. (2018). The redox “filter” beneath magmatic orogens and the formation of continental crust. Science Advances, 4(5), eaar4444.

Tang, M., Lee, C. T. A., Costin, G., and Höfer, H. E. (2019). Recycling reduced iron at the base of magmatic orogens. Earth and Planetary Science Letters, 528, 115827.

Tang, M., Lee, C. T. A., Ji, W. Q., Wang, R., and Costin, G. (2020). Crustal thickening and endogenic oxidation of magmatic sulfur. Science Advances, 6(31), eaba6342.

Tapia, M. J., Barra, F., Reich, M., Romero, R., and Ojeda, A. (2025). Large versus small Andean porphyry Cu deposits: insights from zircon petrochronology of porphyry Cu–Mo±Au deposits from the Coastal Cordillera, northern Chile. Mineralium Deposita, 1-26.

Tatar, O., Gursoy, H., and Piper, J. D. A. (2002). Differential neotectonic rotations in Anatolia and the Tauride Arc: palaeomagnetic investigation of the Erenlerdag Volcanic Complex and Isparta volcanic district, south–central Turkey. Journal of the Geological Society, 159(3), 281-294.

Tatsumi, Y. (1986). Formation of the volcanic front in subduction zones. Geophysical Research Letters, 13(8), 717-720.

Tattitch, B., Chelle-Michou, C., Blundy, J., and Loucks, R. R. (2021). Chemical feedbacks during magma degassing control chlorine partitioning and metal extraction in volcanic arcs. Nature communications, 12(1), 1774.

Temel, A., Gündoğdu, M. N., and Gourgaud, A. (1998). Petrological and geochemical characteristics of Cenozoic high-K calc-alkaline volcanism in Konya, Central Anatolia, Turkey. Journal of volcanology and geothermal research, 85(1-4), 327-354.

Terzi, M. H. (2020). İnlice (Konya) Epitermal Altın Yatağının Jeolojisi, Jeokimyası ve Kökensel İncelenmesi [Unpublished Ph.D. Thesis]. Aksaray Üniversitesi Fen Bilimleri Enstitüsü, Aksaray.

Terzi, M. H., Yılmazer, E., Kuşcu, İ., and Bozan, S. (2023). İnlice (Konya-Türkiye) Yüksek Sülfidasyon Epitermal Altın Yatağının Jeolojisi, Alterasyonu ve Jeokimyasal Karakteristikleri/Geology, Alteration and Geochemical Characteristics of Inlice (Konya-Turkey) High Sulfidation Epithermal Gold Deposit. Türkiye Jeoloji Bülteni, 66(1), 23-58.

Terzi, M. H., Yılmazer, E., Kuşcu, İ., Oyman, T., and Bozan, S. (2024). Mineralogy, fluid inclusion and stable isotope characteristics of the Inlice (Konya, Turkey) high sulfidation epithermal gold deposit: Implications for hydrothermal evolution and ore genesis. Geochemistry, 84(1), 126040.

Thiéblemont, D., Stein, G., and Lescuyer, J. L. (1997). Gisements épithermaux et porphyriques: la connexion adakite. Comptes Rendus de l'Académie des Sciences-Series IIA-Earth and Planetary Science, 325(2), 103-109.

Thirlwall, M. F., and Anczkiewicz, R. (2004). Multidynamic isotope ratio analysis using MC–ICP–MS and the causes of secular drift in Hf, Nd and Pb isotope ratios. International Journal of Mass Spectrometry, 235(1), 59-81.

Toprak, V., and Göncöoğlu, M. C. (1993). Tectonic control on the development of the neogene- quaternary central anatolian volcanic province, Turkey. Geological Journal, 28(3- 4), 357-369.

Tosdal, R. M., and Richards, J. P. (2001). Magmatic and structural controls on the development of porphyry Cu±Mo±Au deposits.

Tufan, S. T. (2005). Mineralogical and geochemical study of Kızıltepe Au-Ag deposit and surrounding prospects in the Sindirgi-Dursunbey district, Balikesir, Western Turkey. M.Sc. Thesis. Dokuz Eylül University, İzmir, 76p.

Türkecan, A., Akçay, A. E., Satır, M., Dönmez, M., and Ercan, T. (2003). Melendiz Dağları (Niğde) volkanizması. 56. Türkiye Jeoloji Kurultayı, Bildiri Özleri Kitabı, 16.

Uğurcan, O. G., and Oyman, T. (2016). Iron mineralization and associated skarn development around southern contact of the Eğrigöz pluton (northern Menderes Massif-Turkey). Journal of African Earth Sciences, 123, 309-337.

Ulianov, A., Müntener, O., Schaltegger, U., and Bussy, F. (2012). The data treatment dependent variability of U–Pb zircon ages obtained using mono-collector, sector field, laser ablation ICPMS. Journal of Analytical Atomic Spectrometry, 27(4), 663-676.

Ulusoy, I., Cubukcu, E., Aydar, E.., Labazuy, P., Gourgaud, A., and Vincent, P. M. (2004). Volcanic and deformation history of the Bodrum resurgent caldera system (southwestern Turkey). Journal of Volcanology and Geothermal Research, 136(1-2), 71-96.

Uzel, B., Kuiper, K., Sözbilir, H., Kaymakci, N., Langereis, C. G., and Boehm, K. (2020). Miocene geochronology and stratigraphy of western Anatolia: Insights from new Ar/Ar dataset. Lithos, 352, 105305.

Uzel, B., Langereis, C. G., Kaymakci, N., Sözbilir, H., Özkaymak, Ç., and Özkaptan, M. (2015). Paleomagnetic evidence for an inverse rotation history of Western Anatolia during the exhumation of Menderes core complex. Earth and Planetary Science Letters, 414, 108-125.

van Hinsbergen, D. J., Kaymakci, N., Spakman, W., and Torsvik, T. H. (2010). Reconciling the geological history of western Turkey with plate circuits and mantle tomography. Earth and Planetary Science Letters, 297(3-4), 674-686.

Wang, R., Richards, J. P., Hou, Z. Q., Yang, Z. M., Gou, Z. B., and DuFrane, S. A. (2014). Increasing magmatic oxidation state from Paleocene to Miocene in the eastern Gangdese belt, Tibet: Implication for collision-related porphyry Cu-Mo±Au mineralization. Economic Geology, 109(7), 1943-1965.

Watson, E. B., Wark, D. A., and Thomas, J. B. (2006). Crystallization thermometers for zircon and rutile. Contributions to Mineralogy and Petrology, 151(4), 413-433.

Webster, J. D., and Piccoli, P. M. (2015). Magmatic apatite: A powerful, yet deceptive, mineral. Elements, 11(3), 177-182.

Wilkinson, J. J. (2013). Triggers for the formation of porphyry ore deposits in magmatic arcs. Nature Geoscience, 6(11), 917-925.

Winchester, J. A., and Floyd, P. A. (1977). Geochemical discrimination of different magma series and their differentiation products using immobile elements. Chemical geology, 20, 325-343.

Xing, K., Shu, Q., and Lentz, D. R. (2021). Constraints on the formation of the giant Daheishan porphyry Mo deposit (NE China) from whole-rock and accessory mineral geochemistry. Journal of Petrology, 62(4), egab018.

Yiğit, O. (2009). Mineral deposits of Turkey in relation to Tethyan metallogeny: implications for future mineral exploration. Economic Geology, 104(1), 19-51.

Yılmaz, H., Sönmez, F. N., Akay, E., Şener, A. K., and Tufan, S. (2013). Low-sulfidation epithermal Au-Ag mineralization in the Sındırgı district, Balıkesir province, Turkey. Turkish Journal of Earth Sciences, 22(4), 485-522.

Yılmaz, Y., Genç, Ş. C., Karacık, Z., and Altunkaynak, Ş. (2001). Two contrasting magmatic associations of NW Anatolia and their tectonic significance. Journal of Geodynamics, 31(3), 243-271.

Yurdakul, E., İmer, A., and Cihan, M. (2021). Timing and Nature of Mineralization and Associated Hydrothermal Alteration at the Öksüt High-Sulfidation Epithermal Au-Cu Deposit (Kayseri Province, Central Anatolia).

Zajacz, Z., Seo, J. H., Candela, P. A., Piccoli, P. M., Heinrich, C. A., and Guillong, M. (2010). Alkali metals control the release of gold from volatile-rich magmas. Earth and Planetary Science Letters, 297(1-2), 50-56.

Zhang, C., Holtz, F., Ma, C., Wolff, P. E., and Li, X. (2012). Tracing the evolution and distribution of F and Cl in plutonic systems from volatile-bearing minerals: a case study from the Liujiawa pluton (Dabie orogen, China). Contributions to Mineralogy and Petrology, 164(5), 859-879.

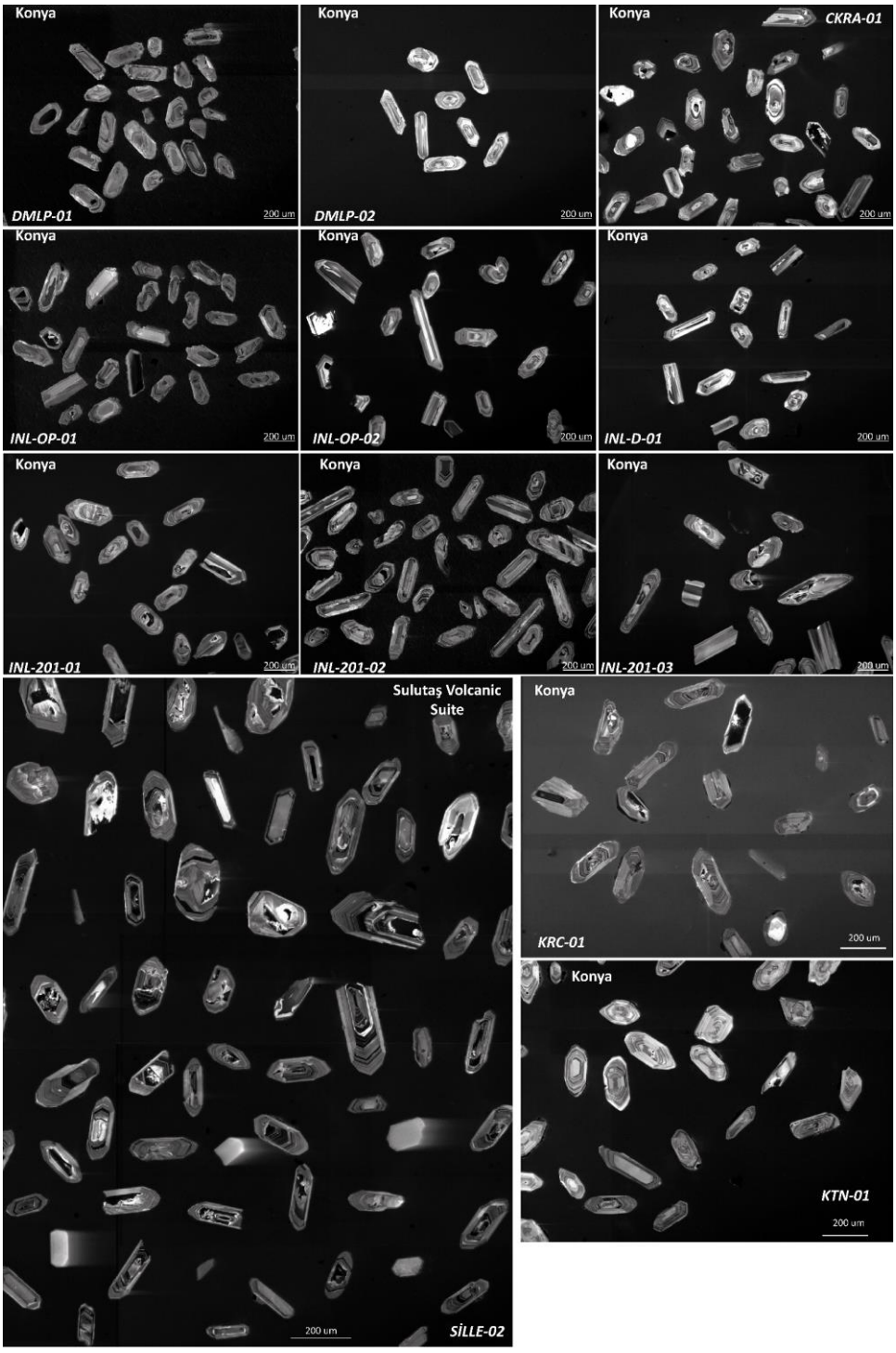
Zhu, J. J., Richards, J. P., Rees, C., Creaser, R., DuFrane, S. A., Locock, A., Petrus, J. A., and Lang, J. (2018). Elevated magmatic sulfur and chlorine contents in ore-forming magmas at the Red Chris porphyry Cu-Au deposit, northern British Columbia, Canada. Economic Geology, 113(5), 1047-1075.

Zimmer, M. M., Plank, T., Hauri, E. H., Yogodzinski, G. M., Stelling, P., Larsen, J., Singer, B., Jicha, B., Mandeville, C. and Nye, C. J. (2010). The role of water in generating the calc-alkaline trend: new volatile data for Aleutian magmas and a new tholeiitic index. Journal of Petrology, 51(12), 2411-2444.

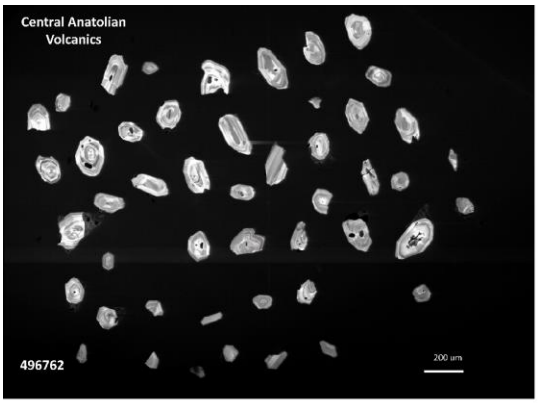
Zürcher, L., Hammarstrom, J. M., Mars, J. C., Ludington, S. D., and Zientek, M. L. (2016). Relationship between porphyry systems, crustal preservation levels, and amount of exploration in magmatic belts of the central Tethys region.

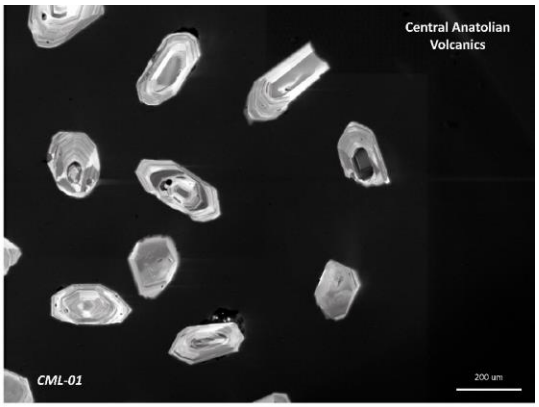
APPENDICES

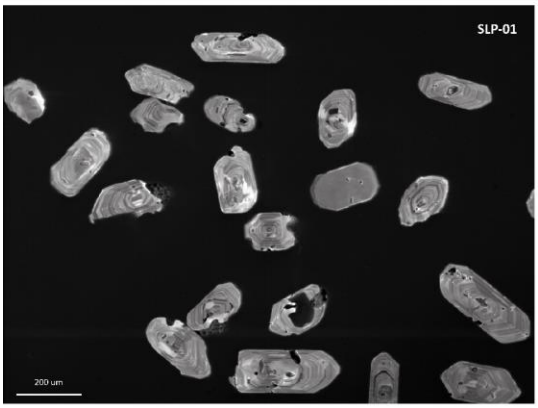
APPENDIX A. REPRESENTATIVE CL IMAGES OF THE ZIRCONS
Konya Volcanic Province

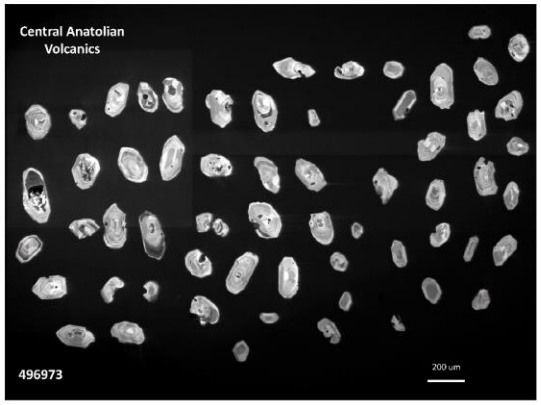


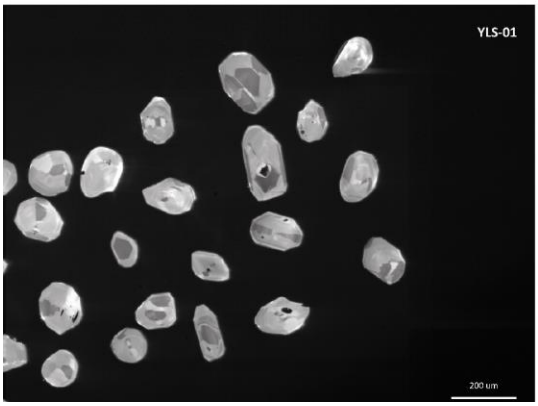
Central Anatolian Volcanics



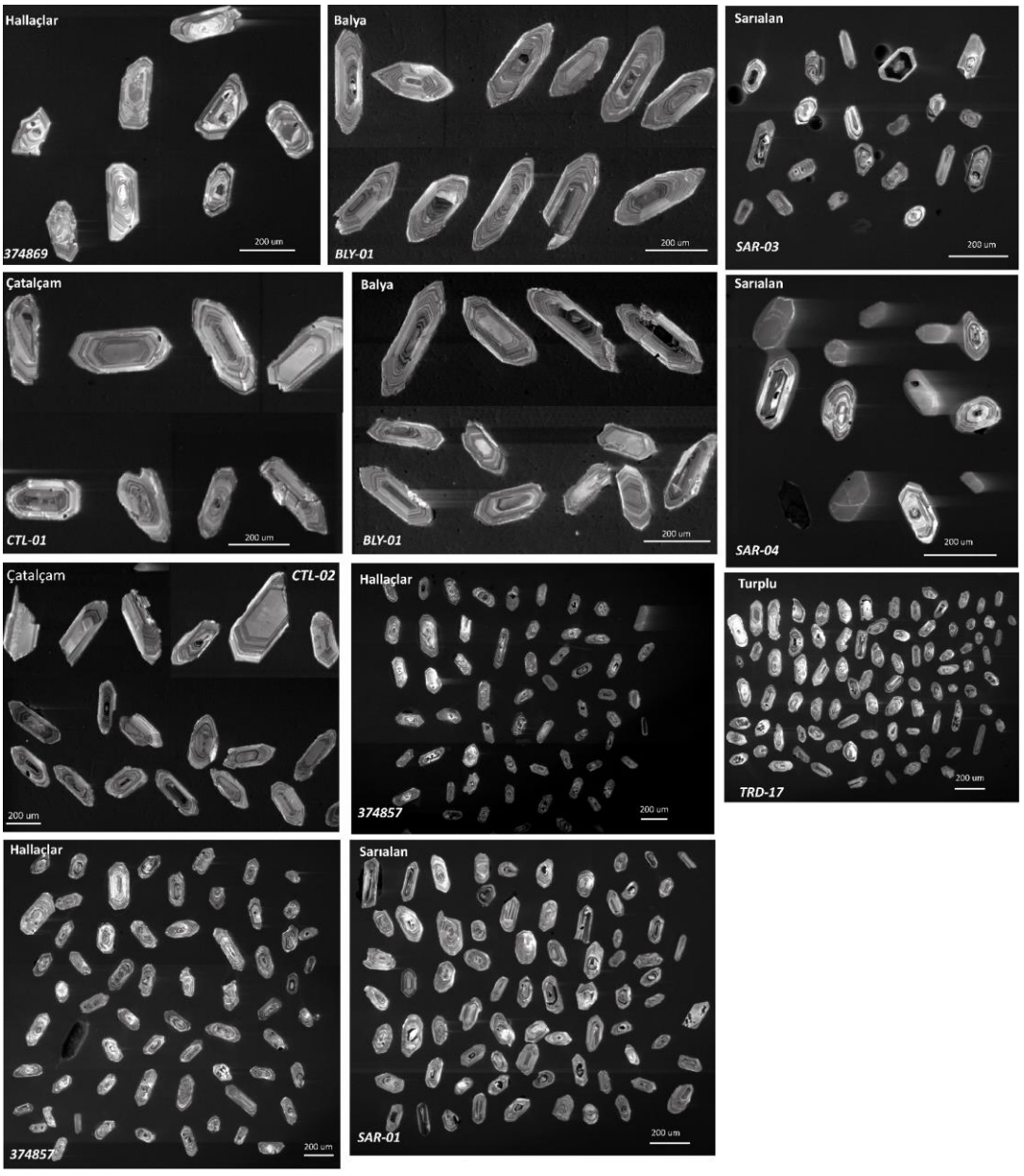




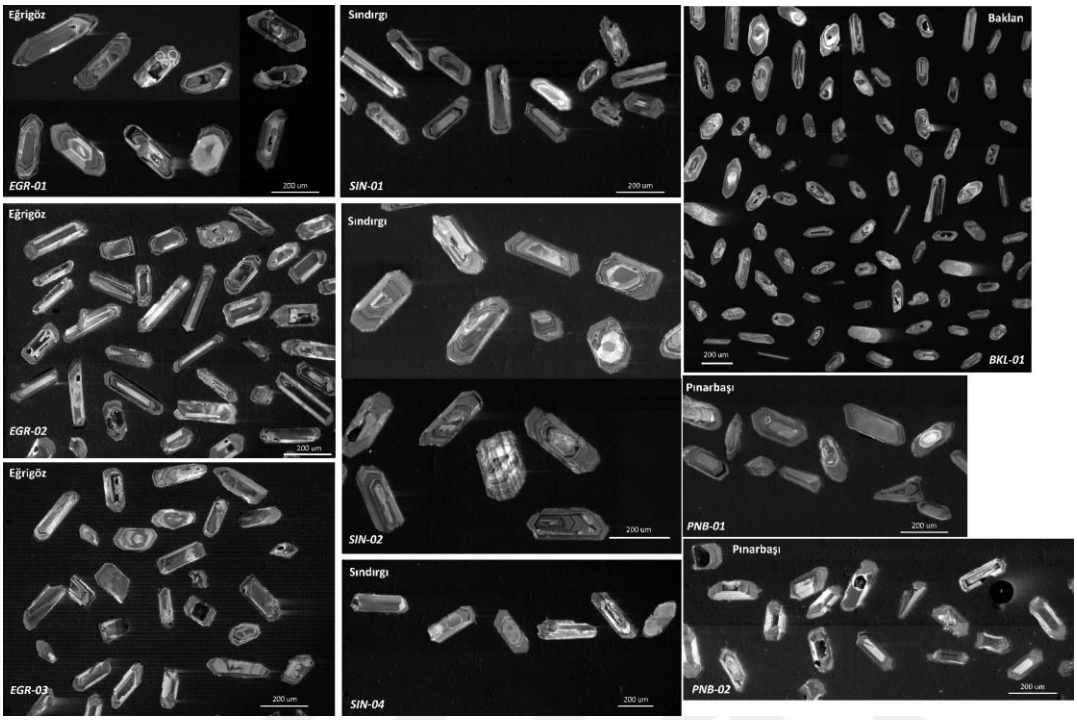




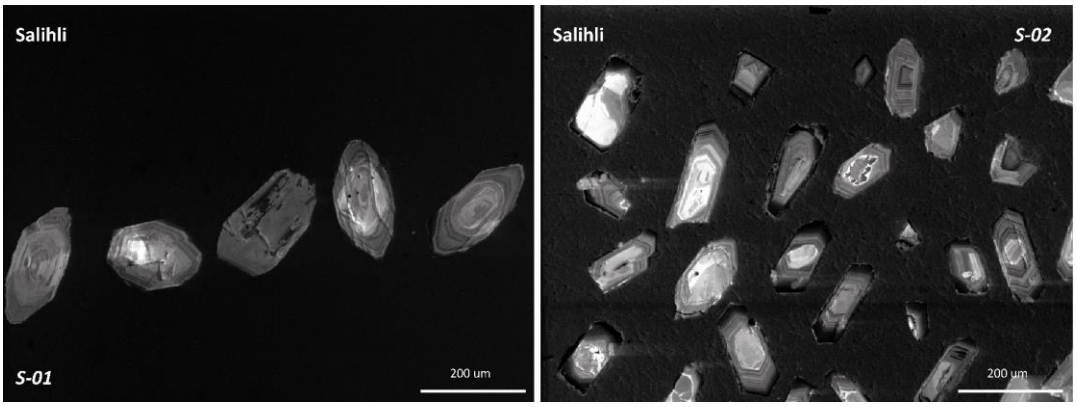
Biga Peninsula



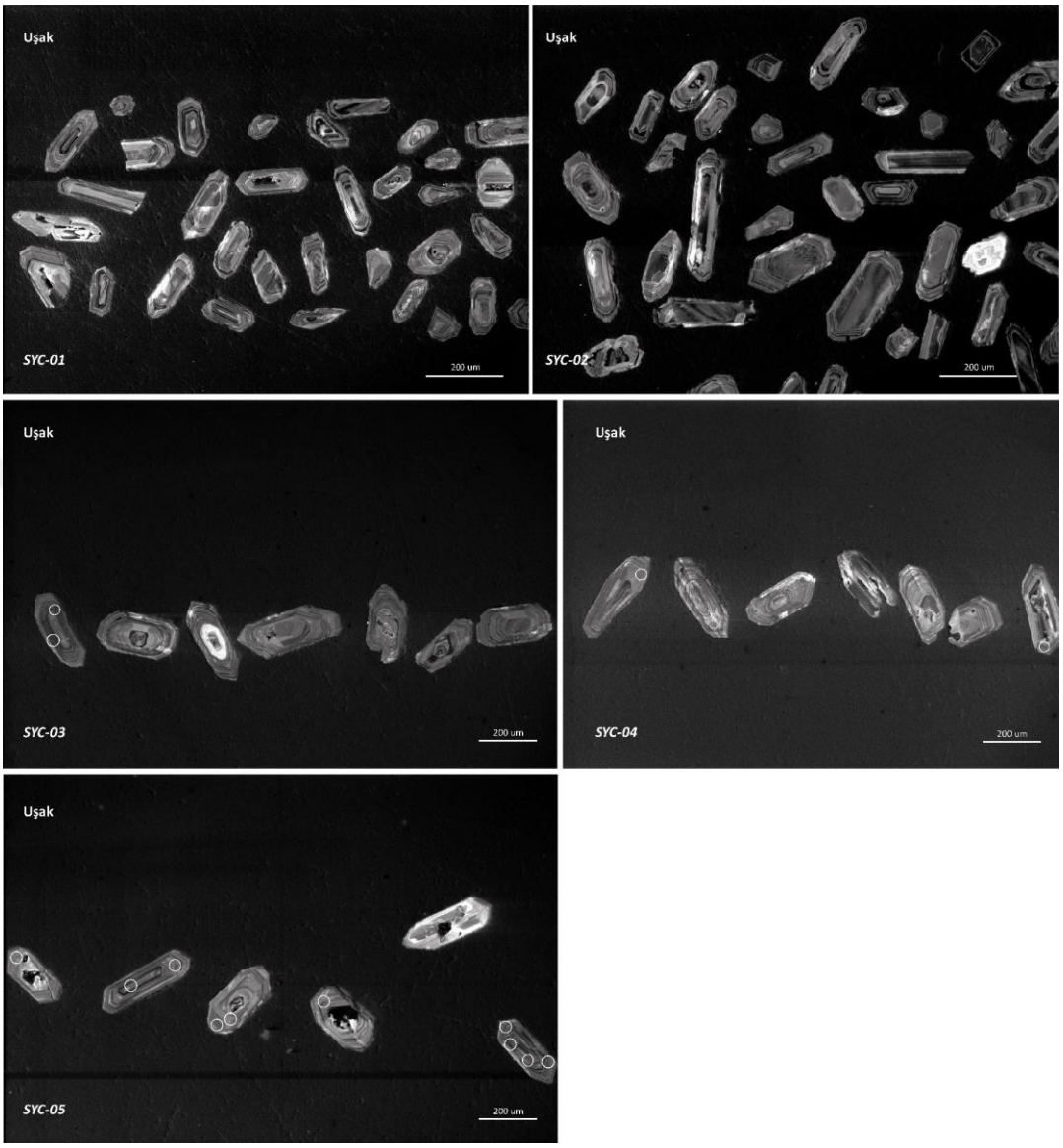
Kütahya-Simav District



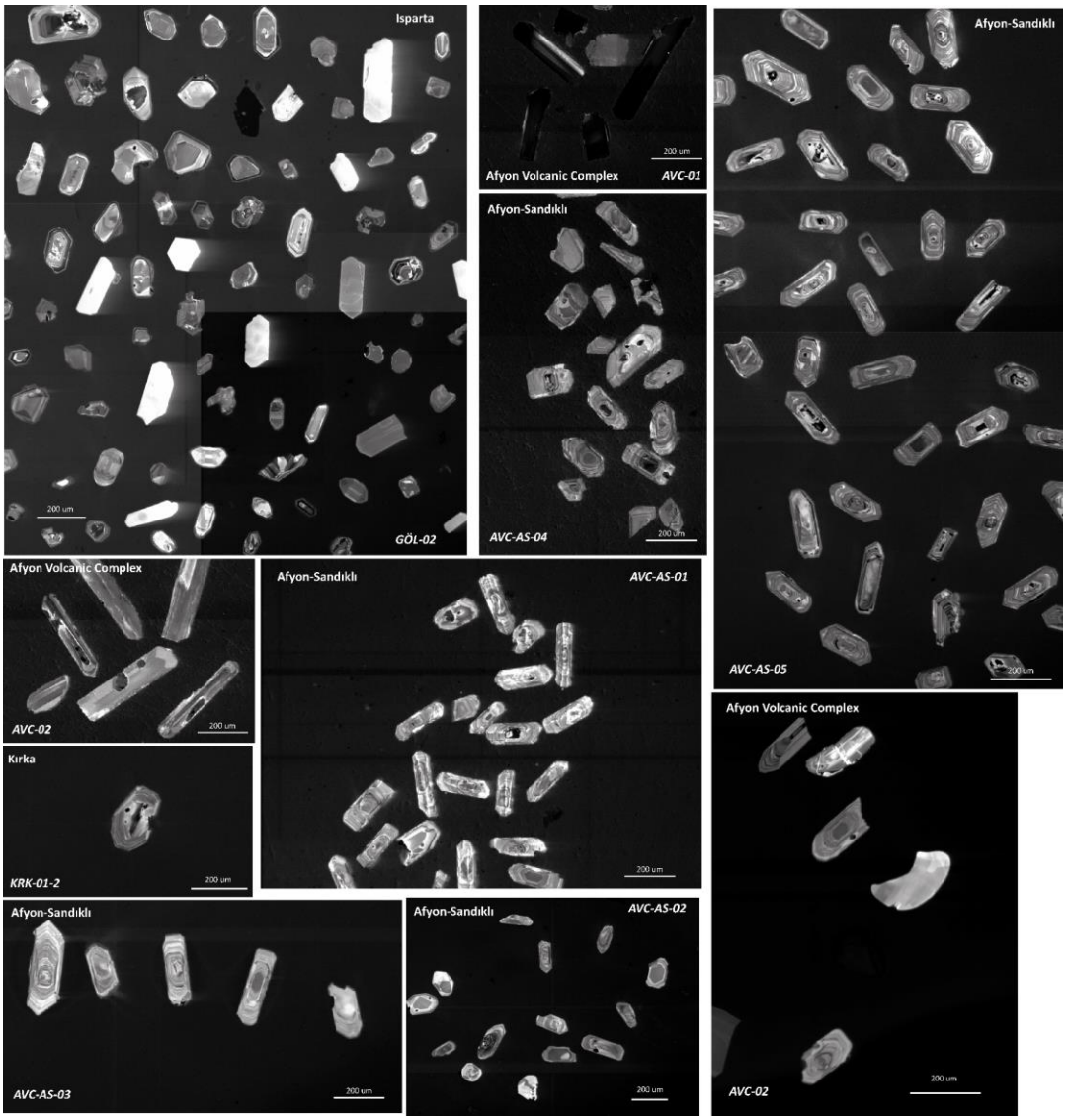
Salihli Pluton



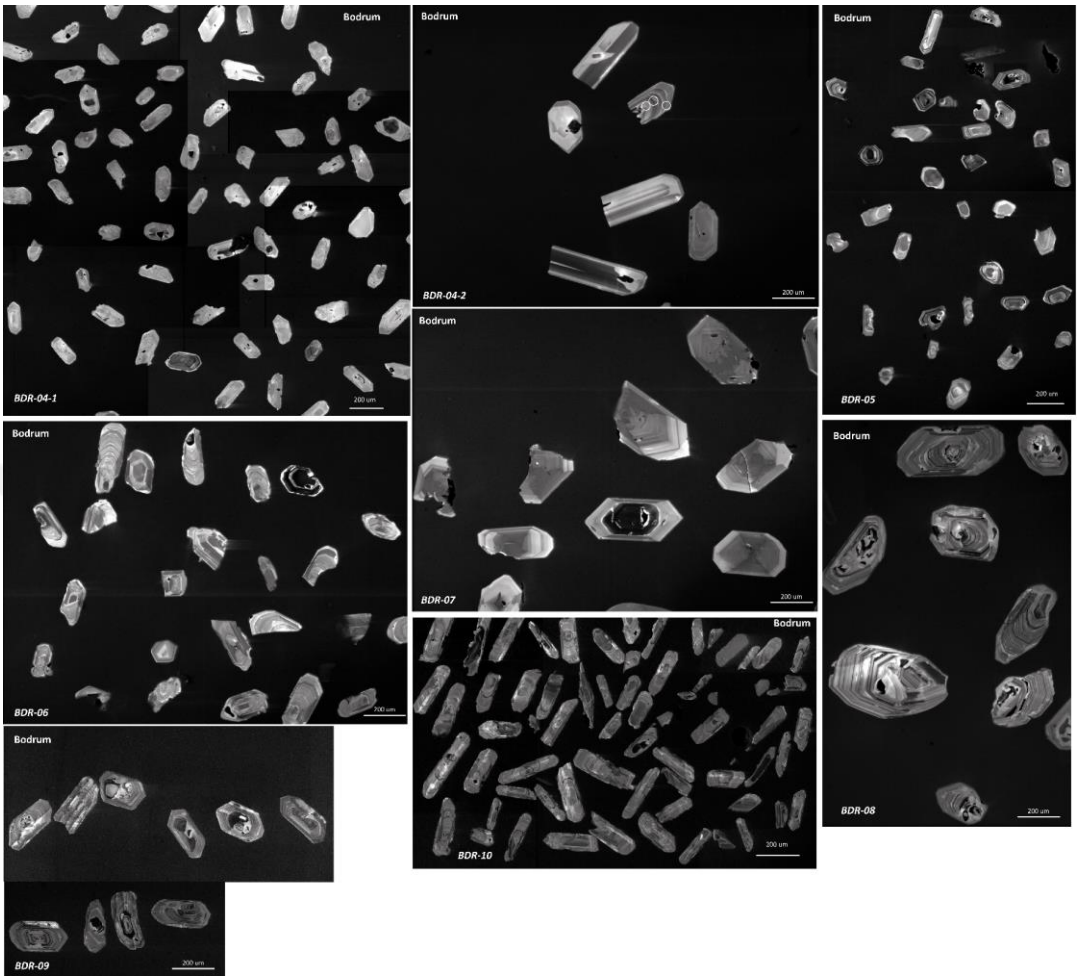
Uşak District



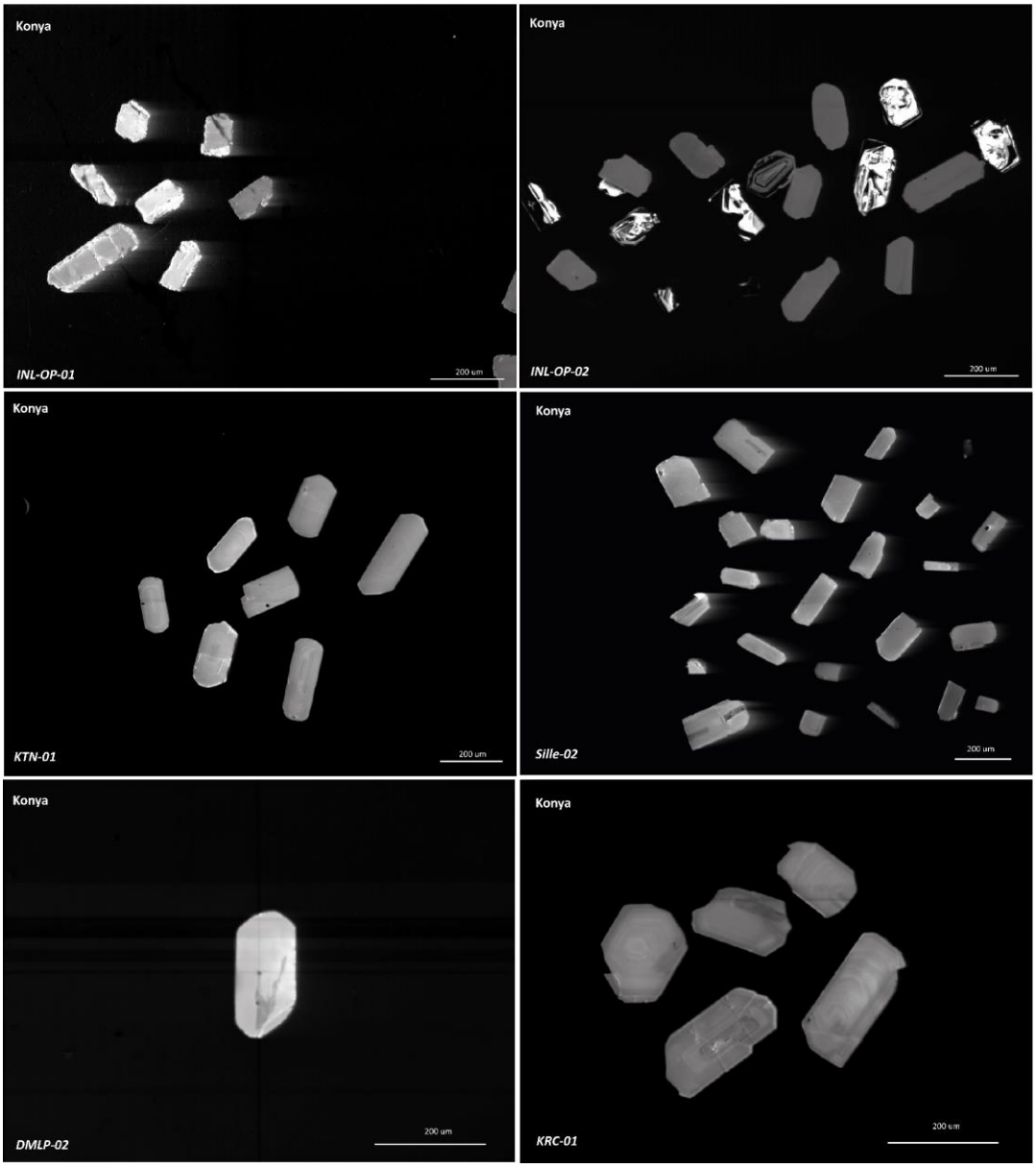
Kırka-Afyon-Isparta District



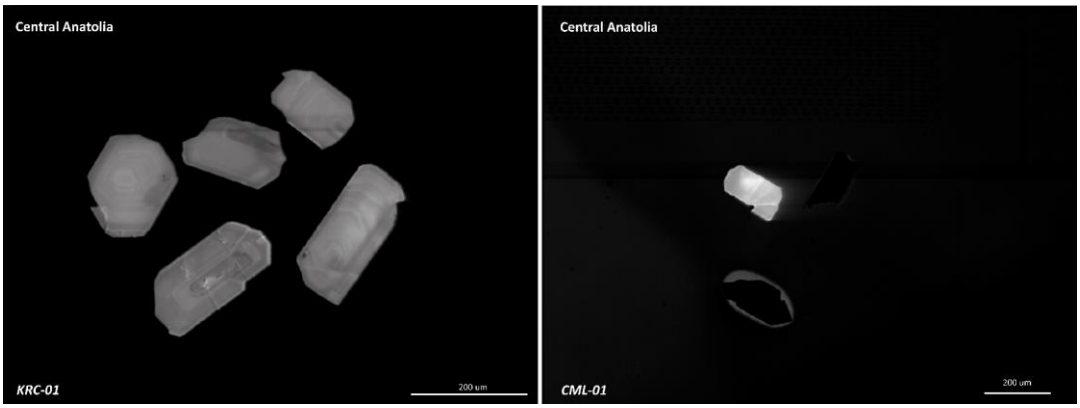
Bodrum Peninsula



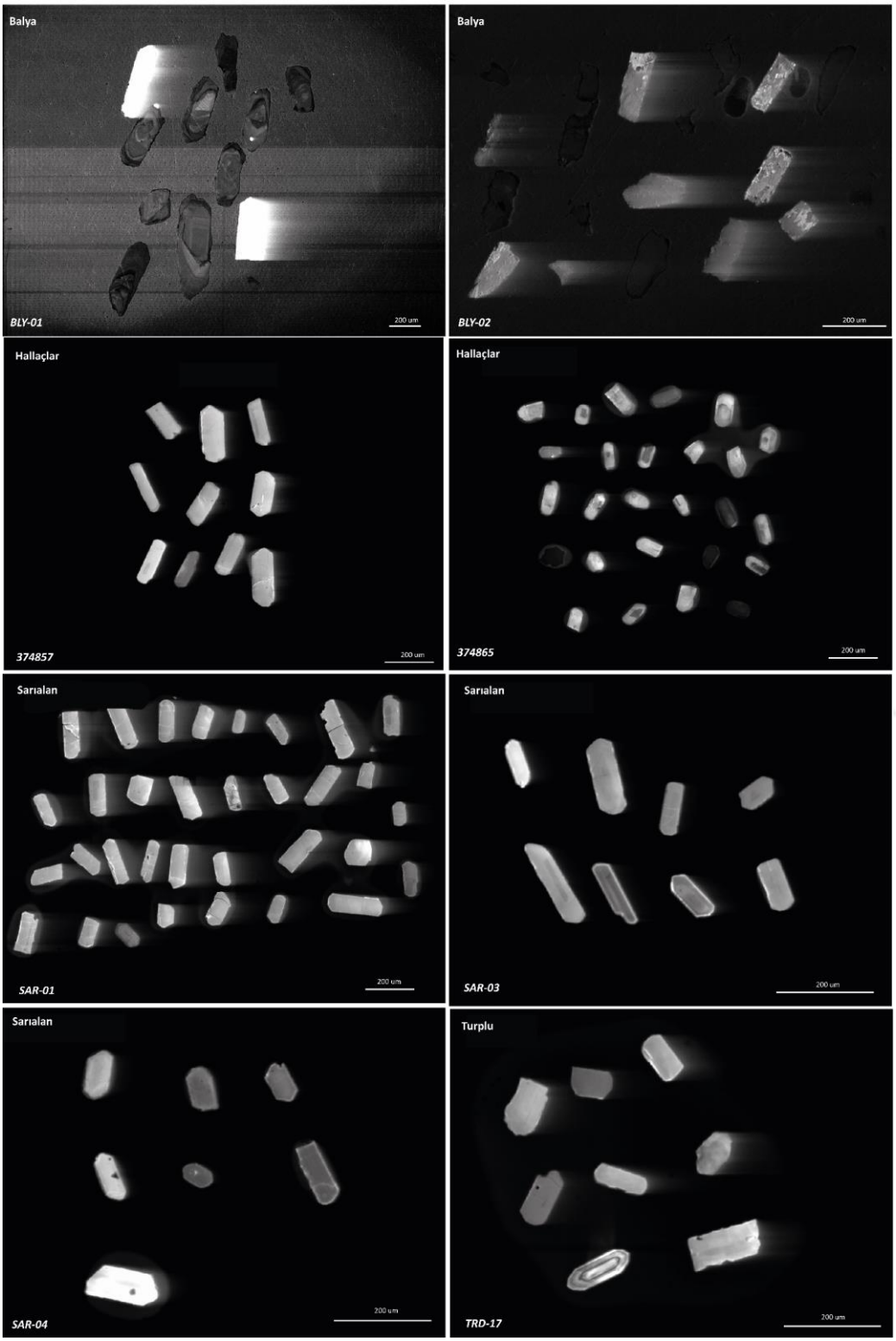
APPENDIX B. REPRESENTATIVE CL IMAGES OF THE APATITES
Konya Volcanic Province



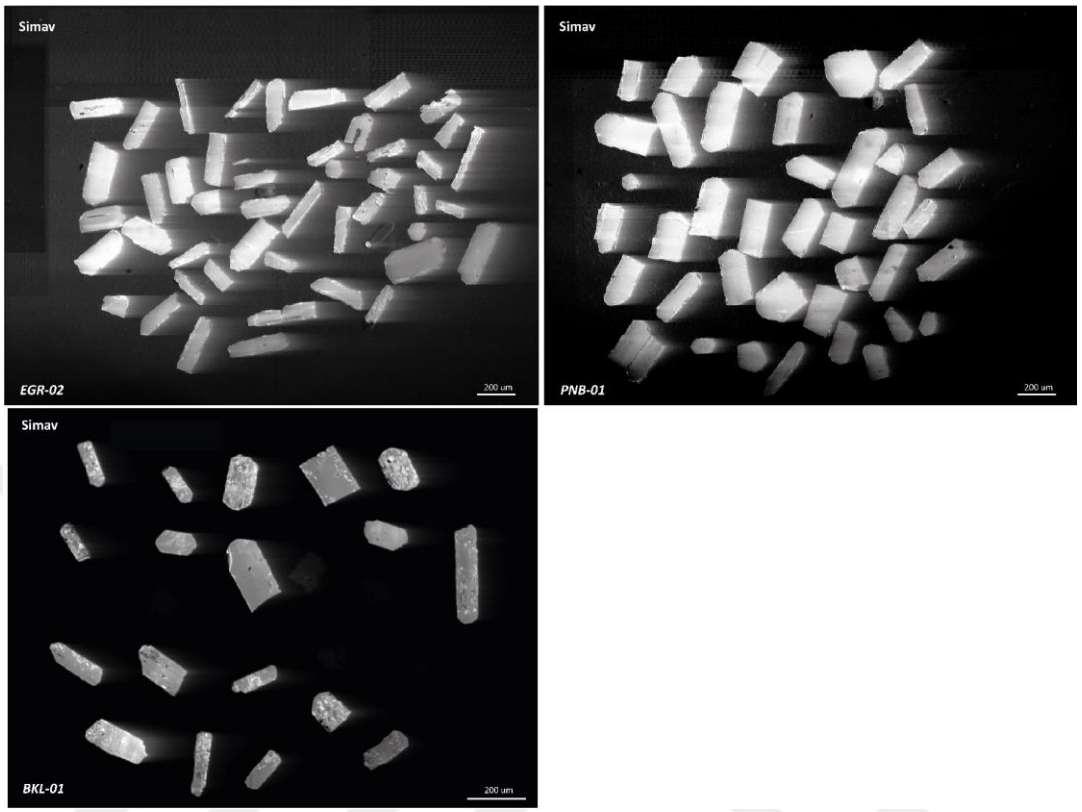
Central Anatolian Volcanics



Biga Peninsula



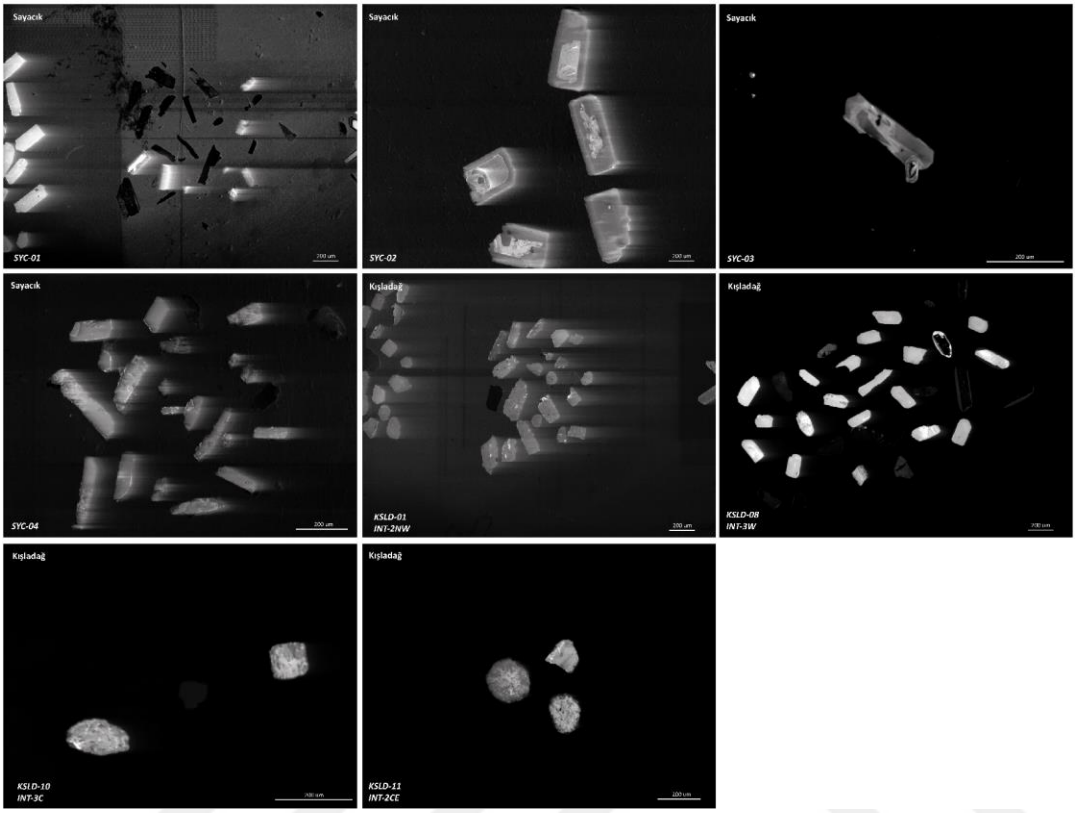
Kütahya-Simav District



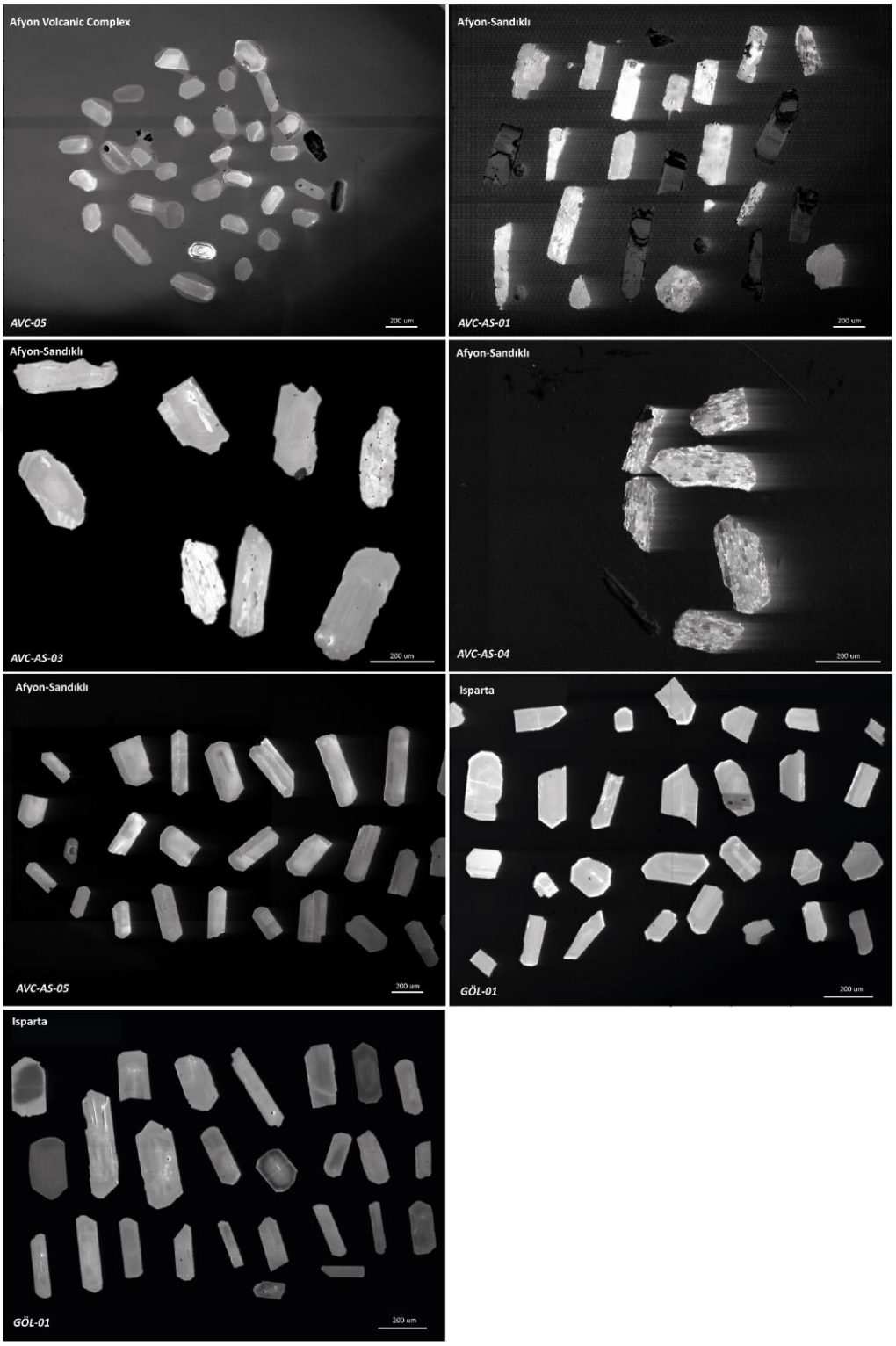
Salihli Pluton



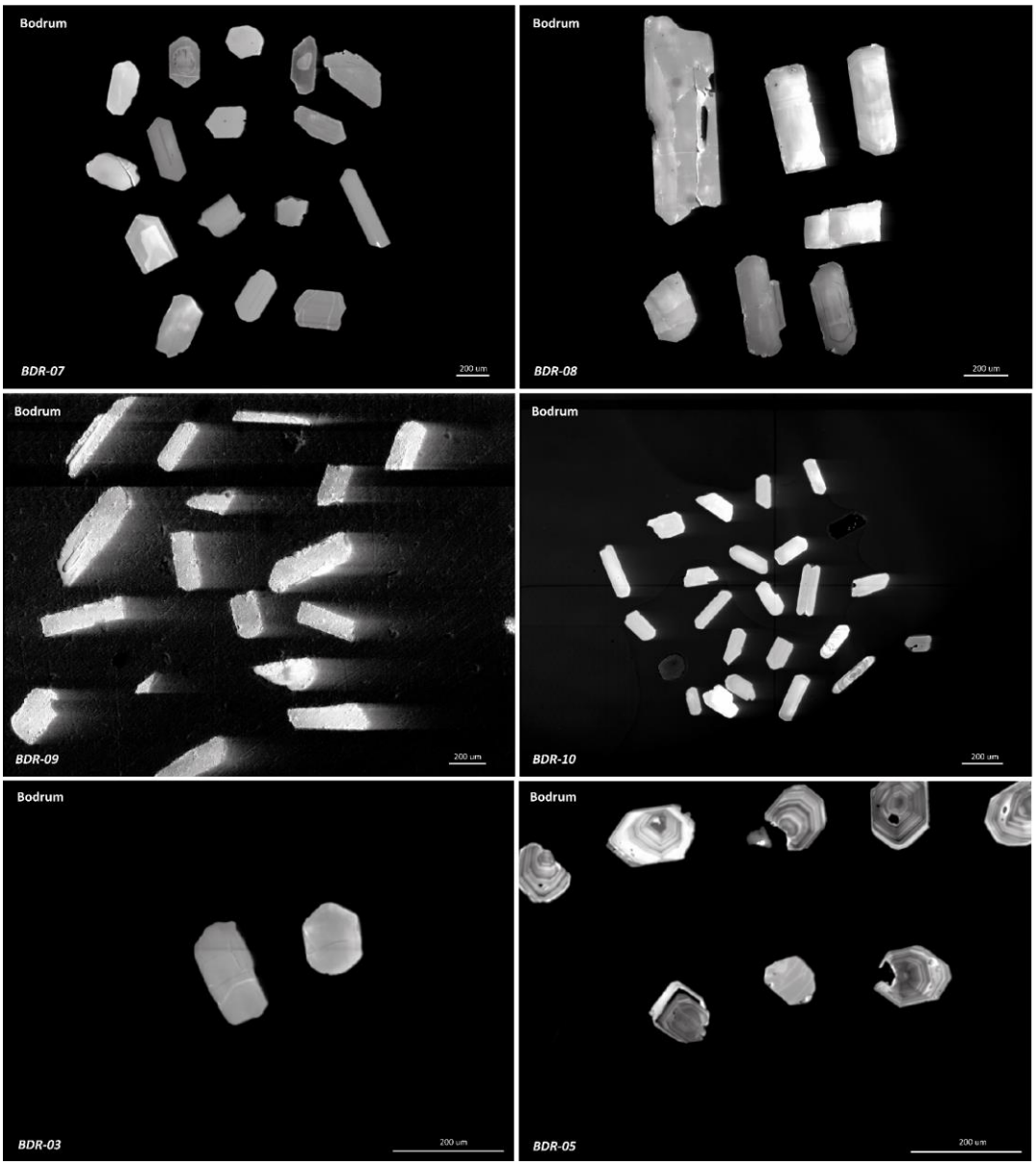
Uşak District



Kırka-Afyon-Isparta District



Bodrum Peninsula



CURRICULUM VITAE

PERSONAL INFORMATION
Surname, Name: Çil, Akın

EDUCATION

Degree	Institution	Year of Graduation
Ph.D.	METU Geological Engineering	2025 (expected)
M.Sc.	METU Geological Engineering	2019
B.Sc.	METU Geological Engineering	2016
High School	Fethiye Kemal Mumcu Anadolu High School, Ankara	20011

WORK EXPERIENCE

Year	Place	Enrollment
2018-Present	METU Geological Engineering	Teaching Assistant
2018-2017	METU Geological Engineering	Part-time Teaching Assistant
2015 Sept-Aug	Toker Drilling & Construction Engineering Consulting	Intern Engineering Student
2014 Aug-Jul	Demir Export	Intern Engineering Student

FOREIGN LANGUAGES
Advanced English

PUBLICATIONS

1. Çil A., İmer A., Sayıt K., Koralay O. E., Chiaradia M., Ulianov A., and Moritz R. "Magmatic Evolution and Fertility Constraints of the Miocene Sayacık Porphyry Au Prospect: A Comparative Study with the Kışladağ Porphyry Au Deposit, western Türkiye", Goldschmidt Conference 2025, Praha, (2025)

2. Çil A., İmer A., Sayıt K., Koralay O. E., Chiaradia M., Ulianov A., and Moritz R. " Simav Bölgesi'nde (Batı Anadolu) Erken Miyosen Döneminde Porfiri Magma Üretkenliğinde Zamana Bağlı Artış", 76th Geological Congress of Türkiye, Ankara, Türkiye, (2014)

3. Çil A. and İmer A., "Geological Setting and Mineralization of Gicik Low-sulfidation Epithermal Au-Ag±Te Deposit (Ankara, North-Central Anatolia)", Sustainable Mineral Resources Supply: Challenges for Future Generations, Geneva, Switzerland, (2022)

4. Çil A. and İmer A., "Geologic Setting and Mineralization of Gicik Low-Sulfidation Epithermal Au Deposit (North-CentralAnatolia)", SEG 100 Conference: Celebrating a Century of Discovery, Vancouver, Canada, (2021)

5. Çil A. and İmer A., "Gicik Altın Yatağı (Ankara, Orta Anadolu): Dalma-Batma Sonrası Ortamda Gelişmiş Bir Düşük-Sülfidasyonlu Epitermal Sistem", 73rd Geological Congress of Türkiye, Ankara, Türkiye, (2021)

HOBBIES

Tennis, Scuba, Gourmet, Computer Technologies, Movies, Motor Sports